

Lecture Notes in Mechanical Engineering

Mithilesh K. Dikshit
Ashish Soni
J. Paulo Davim *Editors*


Advances in Manufacturing Engineering

Select Proceedings of ICFAMMT 2022

 Springer

Lecture Notes in Mechanical Engineering

Editorial Board

Francisco Cavas-Martínez , Departamento de Estructuras, Construcción y Expresión Gráfica Universidad Politécnica de Cartagena, Cartagena, Murcia, Spain

Francesca di Mare, Institute of Energy Technology, Ruhr-Universität Bochum, Bochum, Nordrhein-Westfalen, Germany


Mohamed Haddar, National School of Engineers of Sfax (ENIS), Sfax, Tunisia

Young W. Kwon, Department of Manufacturing Engineering and Aerospace Engineering, Graduate School of Engineering and Applied Science, Monterey, CA, USA

Justyna Trojanowska, Poznan University of Technology, Poznan, Poland

Series Editors

Fakher Chaari, National School of Engineers, University of Sfax, Sfax, Tunisia

Francesco Gherardini , Dipartimento di Ingegneria “Enzo Ferrari”, Università di Modena e Reggio Emilia, Modena, Italy

Vitalii Ivanov, Department of Manufacturing Engineering, Machines and Tools, Sumy State University, Sumy, Ukraine

Lecture Notes in Mechanical Engineering (LNME) publishes the latest developments in Mechanical Engineering—quickly, informally and with high quality. Original research reported in proceedings and post-proceedings represents the core of LNME. Volumes published in LNME embrace all aspects, subfields and new challenges of mechanical engineering. Topics in the series include:

- Engineering Design
- Machinery and Machine Elements
- Mechanical Structures and Stress Analysis
- Automotive Engineering
- Engine Technology
- Aerospace Technology and Astronautics
- Nanotechnology and Microengineering
- Control, Robotics, Mechatronics
- MEMS
- Theoretical and Applied Mechanics
- Dynamical Systems, Control
- Fluid Mechanics
- Engineering Thermodynamics, Heat and Mass Transfer
- Manufacturing
- Precision Engineering, Instrumentation, Measurement
- Materials Engineering
- Tribology and Surface Technology

To submit a proposal or request further information, please contact the Springer Editor of your location:

China: Ms. Ella Zhang at ella.zhang@springer.com

India: Priya Vyas at priya.vyas@springer.com

Rest of Asia, Australia, New Zealand: Swati Meherishi at swati.meherishi@springer.com

All other countries: Dr. Leontina Di Cecco at Leontina.dicecco@springer.com

To submit a proposal for a monograph, please check our Springer Tracts in Mechanical Engineering at <https://link.springer.com/bookseries/11693> or contact Leontina.dicecco@springer.com

Indexed by SCOPUS. All books published in the series are submitted for consideration in Web of Science.

Mithilesh K. Dikshit · Ashish Soni · J. Paulo Davim
Editors

Advances in Manufacturing Engineering

Select Proceedings of ICFAMMT 2022

 Springer

Editors

Mithilesh K. Dikshit
Department of Mechanical and Aerospace
Engineering
Institute of Infrastructure Technology
Research and Management (IITRAM)
Ahmedabad, India

Ashish Soni
Mechanical Capacity Building Division
Space Applications Centre, ISRO
Ahmedabad, India

J. Paulo Davim
Department of Mechanical Engineering
University of Aveiro
Aveiro, Portugal

ISSN 2195-4356

ISSN 2195-4364 (electronic)

Lecture Notes in Mechanical Engineering

ISBN 978-981-19-4207-5

ISBN 978-981-19-4208-2 (eBook)

<https://doi.org/10.1007/978-981-19-4208-2>

© The Editor(s) (if applicable) and The Author(s), under exclusive license to Springer Nature Singapore Pte Ltd. 2023

This work is subject to copyright. All rights are solely and exclusively licensed by the Publisher, whether the whole or part of the material is concerned, specifically the rights of translation, reprinting, reuse of illustrations, recitation, broadcasting, reproduction on microfilms or in any other physical way, and transmission or information storage and retrieval, electronic adaptation, computer software, or by similar or dissimilar methodology now known or hereafter developed.

The use of general descriptive names, registered names, trademarks, service marks, etc. in this publication does not imply, even in the absence of a specific statement, that such names are exempt from the relevant protective laws and regulations and therefore free for general use.

The publisher, the authors, and the editors are safe to assume that the advice and information in this book are believed to be true and accurate at the date of publication. Neither the publisher nor the authors or the editors give a warranty, expressed or implied, with respect to the material contained herein or for any errors or omissions that may have been made. The publisher remains neutral with regard to jurisdictional claims in published maps and institutional affiliations.

This Springer imprint is published by the registered company Springer Nature Singapore Pte Ltd.

The registered company address is: 152 Beach Road, #21-01/04 Gateway East, Singapore 189721, Singapore

Preface

The first International Conference on Futuristic Advancements in Materials, Manufacturing and Thermal Sciences (ICFAMMT 2022) was jointly organized by the Department of Mechanical and Aerospace Engineering, Institute of Infrastructure, Technology, Research and Management, Ahmedabad, India, and the Space Society of Mechanical Engineers (SSME), Space Applications Centre, ISRO, Ahmedabad. This conference aims to provide splendid opportunities for academicians, researchers, industrial persons, and young scientists to address new challenges and discuss futuristic advancements in materials, manufacturing, and thermal sciences. Further, ICFAMMT 2022 also aims to facilitate technical advancement and futuristic advancement in the field of machine design, nanotechnology, composites, processing of plastics, modelling and simulations, optimization, and fluid engineering.

This book includes select peer-reviewed proceedings of the ICFAMMT 2022. The content provides an overview of the latest research in the area of manufacturing sciences such as metal cutting, metal forming, casting, joining, nonconventional machining, additive manufacturing, and concepts of design used for manufacturing. The book has four major sections such as machining, welding, additive manufacturing, and design and manufacturing. The book is useful for researchers and professionals working in the field of manufacturing sciences, and readers will be able to develop a deep understanding of manufacturing processes and possible changes for future implementations.

Ahmedabad, India
Ahmedabad, India
Aveiro, Portugal

Mithilesh K. Dikshit
Ashish Soni
J. Paulo Davim

Contents

Machining

Application of Jaya Algorithm for Minimizing Surface Finish in MQL-Based Green Machining of Titanium Alloy	3
Dhrubajit Sarma, Muthumari Chandrasekaran, and Ashok Kumar Sahoo	
Surface Roughness Analysis in High-Speed Turning of Ti-6Al-4V with Coated Carbide Inserts Using Vibration Signals	17
Grynal D’Mello and P. Srinivasa Pai	
Comparative Prediction of the Influence of Process Parameters During CAEDM and REDM of Hybrid Metal Matrix Composite	31
Paridhi Malhotra, Rajeev Agrawal, R. K. Tyagi, Nishant Singh, Jimmy Mehta, and Moti Lal Rinawa	
Effect of Different Machining and Non-machining Parameters on Machining Performance of Electrochemical Discharge Machining (ECDM): A Review	41
Dheeraj Soni, B. D. Gidwani, and R. Shringi	
Optimization of AWJM Process on Processing of Lite Bamboo Reinforced Polymer Composite by Using Grasshopper Algorithm	55
Sathish Kumar Adapa, Jagadish, Sagar Yanda, and Siva Sankara Raju	
Development of Complex Feature Extraction System from Prismatic Parts Using Hybrid Algorithms	65
Sridhar Meka, Dowluru Sreeramulu, and Lingaraju Dumpala	
Recent Trends in the Amelioration and Prediction of Surface Roughness in Turning Process: A Bibliometric Analysis	77
Vikrant Guleria, Vivek Kumar, and Pradeep K. Singh	
Experimental Design for SS 316L-Nanosecond Laser Texturing for Bioengineering Applications	91
Neelesh Sirdeshmukh and Ganesh Dongre	

Welding

Temperature Analysis of Water-Cooled Friction Stir Welding Using Spray Nozzle on Aluminium 2014 Alloy	107
Cibi Gabriel Goldwynsingh David Rajasingh, Mystica Augustine Michael Duke, and Senthil Kumar Santhanam	
A Review on the Influence of Tool Pin Profile on Microstructure and Mechanical Properties of Friction Stir Welded Joints	119
Yogendra Singh Rajpoot, Kushal Saxena, and Desh Deepak	
Effect of Weldability on Metallurgical, Mechanical, and Corrosion Behaviour of High Entropy Alloy_A Review	151
Sourabh Shukla, Anshula Gaurkar, and Tulika Bawankar	
Numerical Analysis of Conduction Mode Laser Welding of Aluminium 2024 Alloy in Lap Joint Configuration	163
Upama Dey, Aparna Duggirala, Bappa Acherjee, and Souren Mitra	
Tool Designing for Friction Stir Welding Variants	175
Namrata Thakkar and Vishvesh Badheka	
Microstructural and Mechanical Properties Characterization of Resistance Spot Welded Aluminum Alloy AA6063	195
Parth Patel, Chaitanya Sharma, Mukesh Chandra, Anil K. Rajak, and Sumit K. Sharma	
Cryogenic Behavior of TIG Welded Ni-Based Superalloy (IN617)	207
P. K. Mandal, Akash Kurian Lalu, Amal Michael Saji, and Manu M. Jacob	
Additive Manufacturing	
Thermal Modeling of Wire Arc Additive Manufacturing Process Using COMSOL Multiphysics	223
Vishal Kumar, Biplab Kumar Roy, and Amitava Mandal	
Experimental Optimization of Green FDM Process Parameters: An Integrated MCDM Approach	233
Surajit Barad, Jagadish, Sathish Kumar Adapa, and Sagar Yanda	
3-D Printing: A Review of Manufacturing Methods, Materials, Scope and Challenges, and Applications	243
Hiral H. Parikh, Rivaan Jadav, and Praas Joshi	
Influence of Infill Parameters on Flexural Properties of Bio-inspired Additively Manufactured Specimen	257
Mahesh Naik, M. C. Abhilash, and D. G. Thakur	

3D Printable Gearbox Casing 271
 T. N. Nikhil, Mayank Chutani, Gautam Mahesh,
 and Lokavarapu Bhaskara Rao

Design and Manufacturing

Design and Optimization of a 3-Stage Industrial Gearbox 297
 Shubham Sunil Patil, Swaraj Chandraparkash Parate,
 Hrushikesh Vishwas Kulkarni, and Lokavarapu Bhaskara Rao

**Electric Mobility: Key Factors, Unresolved Issues and Significance
 for Foundry Industries** 317
 Himanshu Khandelwal and Sumeet Chavan

**Response Surface Methodology to Establish Friction Model
 for Upset Forging** 329
 Karnam Thulasiram Vamsi Krishna, G. S. Amrith,
 and Lokavarapu Bhaskara Rao

Studies on Annealing Kinetics of Cold Forged AA6082 345
 Ashutosh Ranjan, Ashvani Kumar, and Rahul Kulkarni

**Evaluation of Maximum Bending Stiffness of Stranded Cables
 with Refined Kinematic Relations** 353
 Hadiya Pritesh Dulabhai, N. S. Parthasarthy,
 and Gurumoorthy S. Hebbar

**The Interest of the Longitudinal Friction Coefficient on the Slip
 Ratio of the Heavy Vehicle When Braking at 60 km/h** 367
 Luong Van Van and Nguyen Thanh Tung

**Implementation of ISO 9001 in the Manufacturing Industry,
 a Literature Review** 375
 Prashant N. Shende, Aditya Kadao, and Adithyakrishna Palery

**Improvised Model for Estimation of Cable Bending Stiffness
 Under Various Slip Regimes** 389
 Hadiya Pritesh Dulabhai, N. S. Parthasarthy,
 and Gurumoorthy S. Hebbar

Green Manufacturing: Benefits, Implementation and Challenges 403
 Ankit, Moti Lal Rinawa, and M. S. Karuna

Crack Propagation Analysis of Spur Gear 413
 Mahendra Singh Raghav, Amandeep Singh, and Shivdayal Patel

**Minimization of Structural Error of the Steering Mechanism
 of an Agricultural Harvesting Machine** 427
 Santiranjan Pramanik

Design of Differential Mounts and Rear Inboard Braking for an FSAE Vehicle	437
Shubhayu Das, Pragya Gogoi, Mihir Agrawal, Rounak Deswal, and Lokavarapu Bhaskara Rao	
A Novel Modeling Approach for Dent Identification and Sizing for Oil and Gas Pipeline	457
Aawish Kumar, Surya Prakash, Ashish Kumar Srivastava, Rajesh Kumar, and Vimal Kumar Pathak	
Solution of Lubrication Problems with Deep Neural Network	471
Saurabh Kumar Yadav and Gananath Thakre	
Structural Integrity Analysis of a Washing Machine Tripod (Front Load) and Redesign Using Taguchi Method	479
S. P. Gokul Raj, Tenzin Choney, and Lokavarapu Bhaskara Rao	

About the Editors

Dr. Mithilesh K. Dikshit is an Assistant Professor at Institute of Infrastructure Technology Research and Management (IITRAM), India. He holds a Ph.D. in Mechanical Engineering and master degree in Production Engineering. He has over nine years of experience in teaching and research. His major areas of research include high speed machining, mechanics of metal cutting, composite materials, molecular dynamics, vibration and control, optimization. He has organized number of conferences/symposium and is an editorial board member of three international journals. He has authored more than 35 research papers and journal articles.

Ashish Soni is currently working as a Senior Scientist and Division Head of Mechanical Capacity Building Division, Project and Planning Group of Space Applications Centre, ISRO, India. He is responsible for manufacturing of space components through external vendors and enhancing and exploring the scope of capacity building for SAC. He has completed his B.E. (Mechanical) in 1998 from North Gujarat University, India. He also completed his M.Tech. in CAD/CAM in 2008 from Gujarat University, India. His research interest includes design, optimization, and various mechanisms. He has published more than 40 technical research papers at national and international level.

Prof. J. Paulo Davim received his Ph.D. degree in Mechanical Engineering in 1997, M.Sc. degree in Mechanical Engineering (materials and manufacturing processes) in 1991, Mechanical Engineering degree (5 years) in 1986, from the University of Porto (FEUP), the Aggregate title (Full Habilitation) from the University of Coimbra in 2005, and D.Sc. from London Metropolitan University in 2013. He is Eur Ing by FEANI, Brussels, and Senior Chartered Engineer by the Portuguese Institution of Engineers with an MBA and Specialist title in Engineering and Industrial Management. Currently, he is a Professor at the Department of Mechanical Engineering of the University of Aveiro, Portugal. He has more than 30 years of teaching and research experience in Manufacturing, Materials and Mechanical Engineering with special emphasis in Machining and Tribology. He is the Editor-in-Chief of several international journals, guest editor of journals, books editor, book series editor, and

scientific advisory for many international journals and conferences. Presently, he is an Editorial Board member of 25 international journals and acts as reviewer for more than 80 prestigious Web of Science journals. In addition, he has also published as editor (and co-editor) more than 100 books and as author (and co-author) more than 10 books, 80 chapters, and 400 articles in journals and conferences (more than 200 articles in journals indexed in Web of Science core collection/h-index 45+/6000+ citations and SCOPUS/h-index 52+/8000+ citations).

Machining

Application of Jaya Algorithm for Minimizing Surface Finish in MQL-Based Green Machining of Titanium Alloy



Dhrubajit Sarma, Muthumari Chandrasekaran, and Ashok Kumar Sahoo

Abstract “Sustainable Manufacturing” is a recent concept to obtain efficiency in the manufacturing process in terms of economy and environmental friendliness with social aspects. Green manufacturing (GM) is a sub-set of sustainable manufacturing and aims to obtain environmentally friendly machining. Dry machining, minimum quantity lubrication (MQL) machining, and nanofluid machining are different approaches employed for minimizing the use of cutting fluid during machining, aiming toward the achievement of the green machining concept. Also, the use of cutting fluids causes several health hazards for human operators during the machining and handling processes. Machining of hard aero-space materials like titanium and nickel-based alloys with better surface finish requires a flood coolant system. This work aims to minimize the surface finish and cutting temperature and obtain optimum machining parameters during nanofluid-based MQL machining of titanium alloy Ti6Al4V. Turning experiments, conducted by Zaman et al. (*Adv Mater Process Technol* 1–21, 2020), are used for optimizing the process. A Box Behnken design of experiments with four factors at three levels is used, with 27 experimental runs. Model for Ra and T is developed with response surface methodology (RSM) as a function of four process variables (i.e., v , f , d , and C). The process is optimized using the Jaya algorithm, a popular parameter-free method. The results are compared with the conventional desirability function (DF) approach and found to be closer; the source codes developed were run in MATLAB and obtained optimum parameters with a fewer iterations.

Keywords Green manufacturing · Nanofluid-based MQL · Turning · Ti6Al4V · Jaya algorithm

D. Sarma (✉) · M. Chandrasekaran
Department of Mechanical Engineering, North Eastern Regional Institute of Science and Technology, Nirjuli, Arunachal Pradesh, India
e-mail: dhrubajitsarma123@gmail.com

A. K. Sahoo
School of Mechanical Engineering, KIIT, Bhubaneswar, India

1 Introduction

The aerospace grade materials are being immensely popular due to their high strength to weight ratio, low coefficient of thermal expansion, good fatigue life, low ductility, high wear resistance, etc. The challenge to machine these aerospace / military grade materials has always pushed the research to its boundaries. Titanium alloys are lighter in strength and have a higher resistance to high temperatures, making them suitable for use in aviation. Surface quality and friction performance during machining are becoming increasingly important in the manufacturing sector. For past times Ti6Al4V alloys have undergone hard cuts due to the possible consequences observed when cutting Ti6Al4V alloys. Ti6Al4V alloy is extensively utilized in a number of applications in the aerospace, chemical, power sectors, automotive, and sports and medical instrument manufacturing industries due to its good corrosion resistance, improved chemical resistance, higher specific strength, outstanding strength-to-weight ratio, lower density, and enhanced thermal stability. Due to all of these properties, this alloy is utilized in the production of machines, cutting tools, structural forms, and other equipment used in a number of industries [1–4].

Manufacturing industries, like any other industries, are driven by profit. Machining, being a popular material removal process, can be implemented to have a low-cost manufacturing set-up. Optimization of machining processes has always been an important key to manufacturing industries that mark critical lead to significant benefit in terms of reduced operating cost, enhanced product quality etc. and has driven various researchers to carry out research on diverse methods of optimization. The three key pillars of sustainable machining are to optimize revenue, offer a pollution-free environment, and enhance consumer–producer social relationship. A method for machining that adheres to sustainability principles while improving power usage, tool life, and surface finish was introduced by [5]. The elemental goal of sustainable manufacturing is to produce commodity cost-efficiently in line with reducing the energy consumption as well minimizing the hazardous consequences on the environment. Ti6Al4V, like other aerospace material, exhibits poor machinability and surface finish due to poor heat transfer coefficient [6]. Cutting fluid is one key factor used widely during machining the alloy to improve product quality. However, the extensive use of cutting fluid in flood cooling/lubrication leads to two major issues i.e., increased cost of coolant and health hazard to the operator [7, 8]. Researches in various times had empathized on the health issues of industry workers to be another aspect of green manufacturing [9, 10].

Minimum Quantity Lubrication (MQL) is one novel and well appreciated method to defer the disadvantages of dry machining. In MQL, coolant/lubricant in micro-scale is injected into the tool-workpiece contact using compressed air/gas. Various studies have studied and compared the use of MQL in machining hard to machine alloys with dry and wet machining. The researchers have reported the improved surface quality, tool life and reduced workpiece adherence with the tool [11–20]. To further enhance the thermal aspects or heat carrying capacity of lubricants in MQL,

a composite method instituting the nanoparticles in MQL is experimented and well appreciated by the machining industry [21].

Essentially nanofluids are new generation fluids that compromised of a base fluid with nano-sized particles (1–100 nm) suspended within the base fluid. The nanoparticles increases conduction and convection coefficients and thus allow the coolant for greater heat transfer. However, since nanoparticles have a higher thermal conductivity over base fluids, combining them with base fluids usually changes the thermo-physical characteristics of the base fluids [22]. To improve the thermal conductivity and coolant lubricity, different types of nanoparticles including alumina, silver, graphite, CuO, SiO₂, and MoS₂ are often used. The studies reported reduced cutting forces, improved surface texture, surface quality, and tool life etc. [23–26].

The employment of nanoparticles with MQL in machining has emerged to be a clean and cost efficient method in comparison to dry and MQL machining. Nevertheless, the use of optimal machining parameter leads the success of the nanofluid-based MQL machining process in terms of all the three pillars of sustainability. Taguchi, RSM, DA, and other conventional optimization algorithms have been used in multiple domains of machining by the research community. In addition to the tradition optimization techniques, popular evolutionary methods such as GA, PSO, ABC etc. are being implemented in the field of machining process optimization. However, such evolutionary algorithms function with a series of algorithm-specific parameters that have been assigned to them. The effectiveness of such algorithms is governed by the precise control of certain parameters. [27]. Rao [28] developed a parameter-free algorithm known as JAYA algorithm for solving constraint and unconstraint optimization problems. In this study, Jaya algorithm is implemented to find the optimal settings for machining Ti6Al4V in nano-MQL environment.

2 Experimental Investigations

In this investigation, the machining investigations done by Zaman et al. [29] in turning Ti6Al4V were evaluated. The Grade 5 Ti6Al4V alloy was machined using uncoated and multi-layered TiN-TiCN-Al₂O₃-TiN coated carbide insert (SNMG 120,408) mounted in a tool holder (PSBNR 2525 M12). Cutting inserts had tool geometry of -6° , -6° , 6° , 6° , 15° , 75° , 0.8 mm according to ORS tool designation system. Hybrid Al₂O₃-MWCNT-based nanofluid has been used as MQL fluid. The particle size of Al₂O₃ nanoparticle is < 50 nm. By dispersing 80% Al₂O₃ and 20% MWCNT into the base fluid, stable hybrid nanofluids with concentrations of 0.5, 1, and 1.5% were created.

Cutting speed (v), feed (f), depth of cut (d), and nanoparticle concentration (C) were considered as machining parameters. A Taylor Hobson make Surtronic 3+ surface roughness tester was used to assess average surface roughness for each experimental run. To assess cutting temperature, a tool work thermocouple approach was used. The various process variables along with the parametric levels are shown in Table 1.

Table 1 Process parameters and their levels

Variable	Unit	Level		
		1	2	3
Cutting speed (v)	m/min	40	75	110
Feed (f)	mm/rev	0.1	0.14	0.18
Depth of cut (d)	mm	0.5	1.0	1.5
Nanoparticle concentration (C)	%	0.5	1.0	1.5

In this research, the experimental work was designed employing the Box-Behnken design method. Table 2 shows the experimental design, as well as the actual machining parameters and results.

3 Development of Predictive Models

Traditional methods for developing predictive modeling include response surface methodology (RSM), multiple regression analysis (MRA), as well as the Taguchi technique. To construct a predictive model equation, RSM is a collection of both mathematical and statistical approaches. It is extensively used when numerous input parameters impact one output parameter. Equation 1 shows the RSM model in its generalized version.

$$y' = b_0 + \sum_{i=1}^3 b_i x_i + \sum_{i=1}^3 b_{ii} x_i^2 + \sum_{i=1}^2 \sum_{j=2}^3 b_{ij} x_i x_j \quad (1)$$

where b_0 is constant, and the coefficients of linear, quadratic, interaction terms are depicted by b_i , b_{ii} , b_{ij} respectively. The prediction model was created using Minitab[®] 17 statistical software. The regression confidence is represented by the R^2 value of a variable, which checks the model's adequacy. It is always preferable to have a larger R -Sq value. The R^2 value of the produced full quadratic model indicates an improved input–output relationship. Equation 2–3 represents the derived RSM model relations for the output variables, R_a and T . For all responses, R^2 and adjusted R^2 values are more than 90%, suggesting that the model equation's projected values have a superior correlation.

$$\begin{aligned} R_a = & 0.296 - (0.00083 \times v) + (11.13 \times f) - (0.546 \times d) - (0.567 \times C) \\ & - (0.000020 \times v \times v) - (25.3 \times f \times f) + (0.3483 \times d \times d) \\ & + (0.2633 \times C \times C) + (0.0179 \times v \times f) + (0.00029 \times v \times d) \\ & - (0.00143 \times v \times C) - (1.00 \times f \times d) + (0.62 \times f \times C) \end{aligned}$$

Table 2 BBD-based experimental design and the responses [29]

Trial No	Process parameters				Responses	
	<i>v</i> (m/min)	<i>f</i> (mm/rev)	<i>d</i> (mm)	<i>C</i> (%)	<i>Ra</i> (μm)	<i>T</i> (°C)
1	75	0.14	1.0	1.0	0.76	708.075
2	75	0.10	1.0	1.5	0.61	715.450
3	40	0.10	1.0	1.0	0.60	545.250
4	110	0.14	1.0	1.5	0.68	907.200
5	110	0.14	1.0	0.5	0.74	929.325
6	40	0.14	1.0	0.5	0.90	656.450
7	75	0.14	0.5	0.5	0.90	737.575
8	75	0.18	0.5	1.0	1.00	708.080
9	75	0.14	0.5	1.5	0.84	693.325
10	75	0.10	0.5	1.0	0.60	626.950
11	40	0.14	0.5	1.0	0.90	531.080
12	75	0.18	1.0	1.5	1.02	781.825
13	75	0.18	1.5	1.0	1.00	759.700
14	75	0.18	1.0	0.5	0.98	833.450
15	110	0.14	1.5	1.0	0.80	892.450
16	40	0.14	1.5	1.0	0.94	582.700
17	110	0.14	0.5	1.0	0.74	855.58
18	75	0.14	1.0	1.0	0.77	715.450
19	110	0.10	1.0	1.0	0.40	833.450
20	75	0.14	1.5	0.5	1.03	803.950
21	75	0.14	1.0	1.0	0.68	708.075
22	75	0.10	1.0	1.5	0.94	715.450
23	40	0.10	1.0	1.0	1.02	545.250
24	110	0.14	1.0	1.5	0.82	907.200
25	110	0.14	1.0	0.5	0.62	929.325
26	40	0.14	1.0	0.5	0.91	656.450
27	75	0.14	0.5	0.5	1.01	737.575

$$+ (0.0500 \times d \times C) \tag{2}$$

$$R^2 = 97.08\% \quad R^2(\text{adj.}) = 93.68\%$$

$$\begin{aligned}
 T = & 556 + (2.64 \times v) + (626 \times f) + (147.1 \times d) - (571.4 \times C) \\
 & + (0.00422 \times v \times v) + (35 \times f \times f) - (41.7 \times d \times d) \\
 & + (212.7 \times C \times C) + (1.21 \times v \times f) - (0.211 \times v \times d)
 \end{aligned}$$

$$+ (1.159 \times v \times C) + (7.4 \times d \times C) \quad (3)$$

$$R^2 = 99.15\% \quad R^2(\text{adj.}) = 98.42\%$$

3.1 Prediction Accuracy of an Empirical Model

Prediction accuracy of an empirical model can be numerically evaluated by different error measures. Among them absolute percentage error (APE), mean absolute percentage error (MAPE) are effective, simple, and widely used method for model validation. The absolute percentage error (APE), which is obtained by Eq. 4, was used to do a numerical comparison.

$$\text{APE} = \frac{|\text{Predicted value} - \text{Actual value}|}{\text{Actual value}} \times 100 \quad (4)$$

The minimum and maximum absolute percentage error for R_a is found to be 0.50% and 5.98% while the respective values for temperature T are calculated as 0.04% and 2.57%. Figures 1 and 2 enlightens visual comparison between the experimental values and the RSM predicted values of the response parameter.

MAPE is the average of the absolute percentage error where percentage errors for each experimental run are totaled irrespective of their signs. As it is an error measure, its lower value confirms better model performance. MAPE for the models was computed by utilizing the following equation,

$$\text{MAPE} = \frac{1}{N} \sum_{n=1}^N \left(\frac{|\text{Predicted value} - \text{Actual value}|}{\text{Actual value}} \right) \times 100 \quad (5)$$

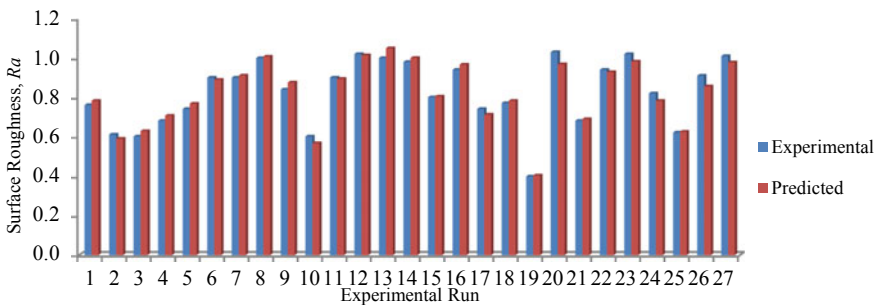


Fig. 1 Comparison of the experimental value with predicted value of surface roughness

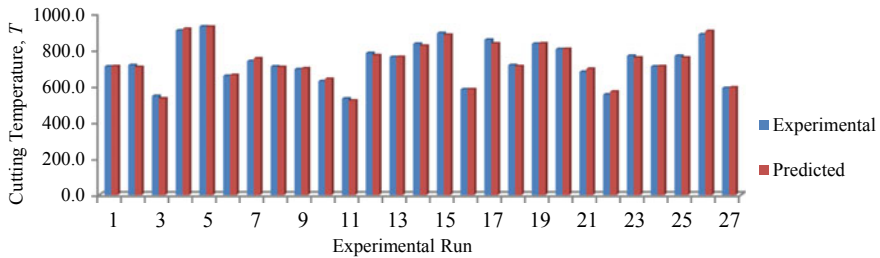


Fig. 2 Comparison of the experimental value with predicted value of cutting temperature

The MAPE for cutting temperature was determined to be 1.18%, while the MAPE for surface roughness was found to be 2.82%. For an RSM-based empirical model, these MAPE values were determined to be reasonable. Based on the results of this error analysis, all of the models are appropriate for correlating responses with process inputs with a tolerable error.

4 Parametric Optimization Using Traditional and Evolutionary Technique

It has been long understood that cutting parameters should be chosen to maximize one of the three pillars of sustainability, the economics of machining processes. Metal turning machining parameters include cutting speed, feed rate, and depth of cut. The settings of these parameters have an effect on quality attributes of turned components. Various theoretical and practical methods for optimization of machining parametrics have been explored with reference to the famous tool life equation. Geometric programming, linear programming, goal programming, and other traditional machining optimization methodologies have traditionally been successful in optimizing various turning process variables. Some of the most modern optimization techniques that have been successfully used in industrial implementations for optimal parametric selection in machining include FL, GA, scatter searches, Taguchi method, and response surface methodology.

4.1 Optimization of Process Parameter by Jaya Algorithm

Most of the evolutionary algorithms are stochastic, and they analyze common governing parameters. However, various algorithms use their own algorithm-specific control parameters. As example, particle swarm optimization employs inertia weight, social and cognitive characteristics, genetic algorithm employs mutation and crossover probability, and a selection operator; and so on. The tweaking of

algorithm-specific variables has a significant influence on the performance as well as the aforesaid algorithms' implementation possibilities. In view of the complexities of the evolutionary algorithms, Rao [28] proposed a new algorithm-specific parameter-less algorithm named Jaya in 2016.

This work was performed with four independent input variable viz. cutting speed (v), feed (f), depth of cut (d), and nanoparticles concentration (C) using coated carbide insert. Two performance characteristic, surface roughness (R_a) and cutting temperature (T) was chosen for the Investigation. The influence of process parameters on surface roughness and cutting temperature in machining Ti6Al4V alloy employing nanofluid environment in MQL was determined on the basis of experimental output and is provided by Eq. 2–3.

To estimate the minimum of the fitness function, a code for the Jaya method was built in MATLAB[®] 2013a software using Rao's inputs. The fitness function in the form of Eq. 6 can be expressed in a MATLAB file and used as an argument to the main code.

$$\text{function (z) = surface roughness (y)} \quad (6)$$

In the algorithm, maximum iteration of 100 is used for model adequacy of surface roughness and max iteration of 50 for model adequacy of cutting temperature. The fitness plot for surface roughness and cutting temperature from Jaya algorithm can be seen in Fig. 4a, b respectively (Fig. 3).

Table 3 shows the optimized values of output variables of the machining process and their corresponding values of the process parameters.

4.2 Parametric Optimization Using Desirability Function (DF)

This section employed traditional DF approach to achieve optimal cutting parameters. Using "RSM Response Optimizer" of MINITAB 17, a combination of process inputs was determined for the minimal value of temperature and roughness individually based on their empirical models. At 40 m/min speed, 0.1 mm/rev feed rate, 0.5 mm depth of cut and 1.0455 vol percent nanoparticle concentrations, a minimum cutting temperature of 537.28 °C was recorded. Likewise, cutting speed with 110 m/min, feed with 0.1 mm/rev, depth of cut with 0.8737 mm, and a nanoparticle concentration of 1.0556 vol percent were measured to generate a minimum surface roughness of 0.457 μm (Fig. 5).

The comparative statement of the optimized process response values reported by Jaya algorithm and the desirability analysis are shown in the Table 4.

In terms of performance, the evolutionary technique Jaya algorithm surpasses the classic desirability function approach by a small margin. The proximity of the optimized outputs can be attributed to a strong empirical model generated by the

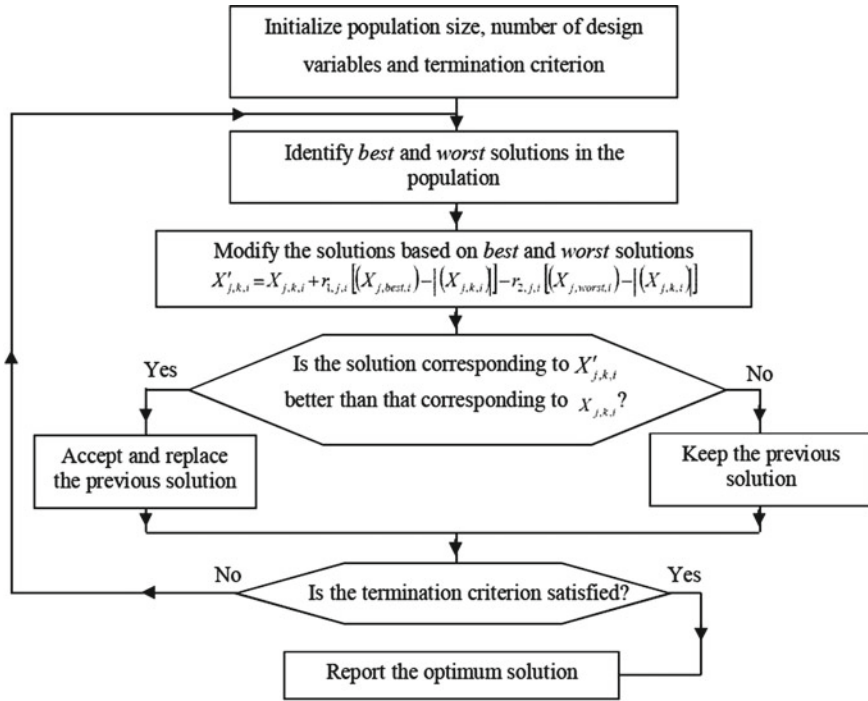


Fig. 3 Flowchart of the Jaya algorithm [28]

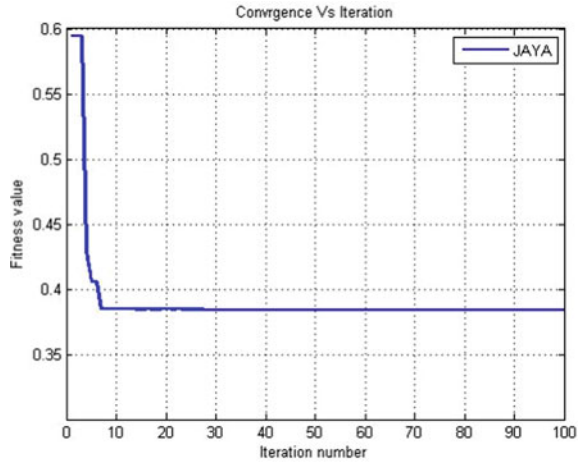
RSM. Although the improvement percentage is minor, it plays key role in reducing total machinability costs in the long term.

5 Conclusion

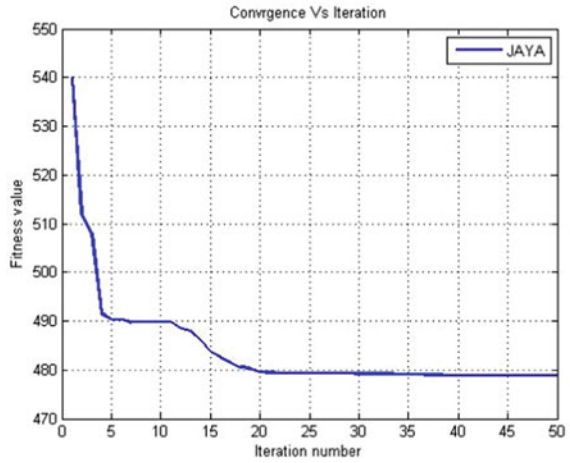
This work optimizes nanofluid-based MQL turning of Ti-6Al-4V alloy employing a popular JAYA algorithm. The effect of process parameters (i.e., v , f , d and C) is studied on surface roughness (R_a) and cutting temperature (T) using response surface models; the effectiveness of the model accuracy is assed with APE and MAPE. The following conclusions were reached as outcome of the investigation:

- Surface roughness is highly influenced by feed rate; whereas cutting temperature is influenced by cutting speed. Improved surface roughness is obtained with less feed and minimum cutting temperature is found as less cutting speed.
- For forecasting surface roughness and cutting temperature, the whole quadratic RSM models were found to be acceptable. All of the R-Sq. and adjusted R-Sq. values were higher than 90%, indicating that these models are indeed very efficient. MAPE has been determined as 2.28% for surface roughness and 1.18% for

Fig. 4 Convergence characteristics of Jaya algorithm: **a** for R_a (7 iterations) and **b** for T (19 iterations)



(a)



(b)

Table 3 Summary of the optimized surface roughness (R_a) and cutting temperature (T) value by Jaya algorithm

Sl. No.	Response	Optimum values of process parameters				Optimum value
		v (m/min)	f (mm/rev)	d (mm)	C (%)	
1	R_a (μm)	110	0.10	0.79	1.1745	0.3836
2	T ($^{\circ}\text{C}$)	40	0.10	0.50	1.225	478.778

Fig. 5 DF Optimization plot for **a** surface roughness and **b** cutting temperature

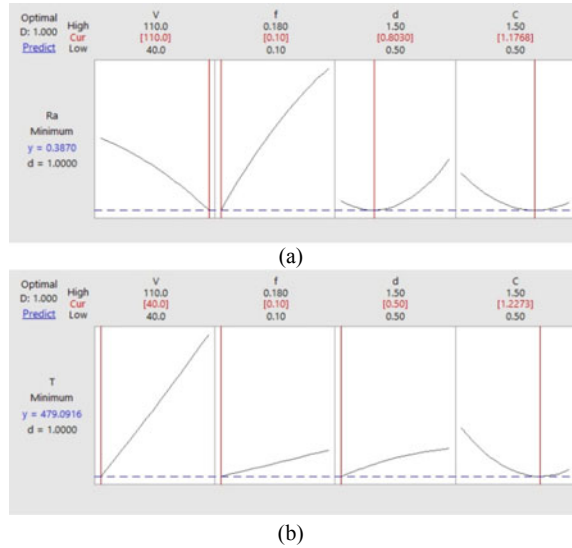


Table 4 Comparison of result (Jaya algorithm vs. DF)

Optimum R_a (μm)			Optimum T ($^{\circ}\text{C}$)		
Jaya	DF	Improvement %	Jaya	DF	Improvement %
0.383	0.387	1.05	477.778	479.09	0.27%

cutting temperature based on the experimental results. The models have excellent fit, and they may be effectively employed for response prediction and further machining optimization.

- The Jaya algorithm excels the traditional desirability function approach in terms of performance by small margin. Although the improvement margin is small, it is quite capable to reduce the overall machinability cost during long run. When NFMQL environments are taken into account, evolutionary techniques are found to be more effective in identifying the optimum process parameter of Ti6Al4V alloy.
- The least surface roughness was observed at a cutting speed of 110 m/min, feed 0.1 mm/rev, depth of cut 0.795 mm, and a nanoparticle concentration of 1.186 vol%. A speed of 40 m/min, a feed rate of 0.1 mm/rev, a depth of cut of 0.5 mm, and a nanoparticle concentration of 1.225 vol% were required to achieve a minimum cutting temperature.

References

1. Ulutan D, Ozel T (2011) Machining induced surface integrity in titanium and nickel alloys: a review. *Int J Mach Tools Manuf* 51:250–280. <https://doi.org/10.1016/j.ijmachtools.2010.11.003>
2. Machado AR, Wallbank J (2005) Machining of titanium and its alloys: a review. *Proc Inst Mech Eng Part B Manag Eng Manuf* 204:53–60
3. Dandekar CR, Shin YC, Barnes J (2010) Machinability improvement of titanium alloy (Ti–6Al–4V) via LAM and hybrid machining. *Int J Mach Tools Manuf* 50:174–182. <https://doi.org/10.1016/j.ijmachtools.2009.10.013>
4. Raza SW, Pervaiz S, Deiab I (2014) Tool wear patterns when turning of titanium alloy using sustainable lubrication strategies. *Int J Precis Eng Manuf* 15:1979–1985. <https://doi.org/10.1007/s12541-014-0554-z>
5. Pušavec F, Kopac J (2009) Achieving and implementation of sustainability principles in machining processes. *Adv Prod Eng Manag* 4:151–160
6. Singh G, Sharma VS (2017) Analyzing machining parameters for commercially pure titanium (Grade 2), cooled using minimum quantity lubrication assisted by a Ranque-Hilsch vortex tube. *Int J Adv Manuf Technol* 88:2921–2928. <https://doi.org/10.1007/s00170-016-8982-9>
7. Davoodi B, Tazehkandi AH (2014) Experimental investigation and optimization of cutting parameters in dry and wet machining of aluminum alloy 5083 in order to remove cutting fluid. *J Clean Prod* 68:234–242. <https://doi.org/10.1016/j.jclepro.2013.12.056>
8. Gupta MK, Sood PK, Sharma VS (2016) Optimization of machining parameters and cutting fluids during nano-fluid based minimum quantity lubrication turning of titanium alloy by using evolutionary techniques. *J Clean Prod* 135:1276–1288. <https://doi.org/10.1016/j.jclepro.2016.06.184>
9. Gupta MK, Mia M, Singh G, Pimenov DY, Sarikaya M, Sharma VS (2019) Hybrid cooling-lubrication strategies to improve surface topography and tool wear in sustainable turning of Al 7075–T6 alloy. *Int J Adv Manuf Technol* 101:55–69. <https://doi.org/10.1007/s00170-018-2870-4>
10. Stachurski W, Sawicki J, Wójcik R, Nadolny K (2018) Influence of application of hybrid MQL-CCA method of applying coolant during hob cutter sharpening on cutting blade surface condition. *J Clean Prod* 171:892–910. <https://doi.org/10.1016/j.jclepro.2017.10.059>
11. Priarone PC, Robiglio M, Settineri L, Tebaldo V (2014) Milling and turning of titanium aluminides by using minimum quantity lubrication. *Procedia CIRP* 24:62–67. <https://doi.org/10.1016/j.procir.2014.07.147>
12. Tamang SK, Chandrasekaran M, Sahoo AK (2017) An experimental investigation and GA optimization on tool wear during Inconel 825 turning with MQL. In: *Proceedings of 10th international conference on precision, meso, micro and nano engineering*. IIT Madras
13. Rahim EA, Ibrahim MR, Rahim AA, Aziz S, Mohid Z (2015) Experimental investigation of minimum quantity lubrication (MQL) as a sustainable cooling technique. *Procedia CIRP* 26:351–354. <https://doi.org/10.1016/j.procir.2014.07.029>
14. Mia M, Gupta MK, Singh G, Królczyk G, Pimenov DY (2018) An approach to cleaner production for machining hardened steel using different cooling-lubrication conditions. *J Clean Prod* 187:1069–1081. <https://doi.org/10.1016/j.jclepro.2018.03.279>
15. Gunda RK, Reddy NSK, Kishawy HA (2016) A novel technique to achieve sustainable machining system. *Procedia CIRP* 40:30–34. <https://doi.org/10.1016/j.procir.2016.01.045>
16. Deiab I, Raza SW, Pervaiz S (2014) analysis of lubrication strategies for sustainable machining during turning of titanium Ti–6Al–4V alloy. *Procedia CIRP* 17:766–771. <https://doi.org/10.1016/j.procir.2014.01.112>
17. Sarma D, Borah J, Chandrasekaran M (2021) Multi optimization of nano fluid based machining of titanium alloy: a green manufacturing approach. *Mater Today Proc* 46:8921–8926. <https://doi.org/10.1016/j.matpr.2021.05.362>

18. Kaynak Y, Robertson SW, Karaca HE, Jawahir IS (2015) Progressive tool-wear in machining of room-temperature austenitic NiTi alloys: the influence of cooling/lubricating, melting, and heat treatment conditions. *J Mater Process Technol* 215:95–104. <https://doi.org/10.1016/j.jmptotec.2014.07.015>
19. Sun Y, Huang B, Puleo DA, Jawahir IS (2015) Enhanced machinability of Ti-5553 Alloy from cryogenic machining: comparison with MQL and flood-cooled machining and modeling. *Procedia CIRP*. 31:477–482. <https://doi.org/10.1016/j.procir.2015.03.099>
20. Rahim EA, Sasahara H (2011) A study of the effect of palm oil as MQL lubricant on high speed drilling of titanium alloys. *Tribol Int* 44:309–317. <https://doi.org/10.1016/j.triboint.2010.10.032>
21. Amrita M, Srikant RR, Sitaramaraju AV (2014) Performance evaluation of nanographite-based cutting fluid in machining process. *Mater Manuf Processes* 29:600–605. <https://doi.org/10.1080/10426914.2014.893060>
22. Das SK (ed) (2008) *Nanofluids: science and technology*. Wiley-Interscience, Hoboken, NJ
23. Yan J, Zhang Z, Kuriyagawa T (2011) Effect of Nanoparticle lubrication in diamond turning of reaction-bonded SiC. *Int J Autom Technol* 5:307–312. <https://doi.org/10.20965/ijat.2011.p0307>
24. Chetan BBC, Ghosh S, Rao PV (2016) Application of nanofluids during minimum quantity lubrication: a case study in turning process. *Tribol Int* 101:234–246. <https://doi.org/10.1016/j.triboint.2016.04.019>
25. Sayuti M, Sarhan AAD, Salem F (2014) Novel uses of SiO₂ nano-lubrication system in hard turning process of hardened steel AISI4140 for less tool wear, surface roughness and oil consumption. *J Clean Prod* 67:265–276. <https://doi.org/10.1016/j.jclepro.2013.12.052>
26. Saravanakumar N, Prabu L, Karthik M, Rajamanickam A (2014) Experimental analysis on cutting fluid dispersed with silver nano particles. *J Mech Sci Technol* 28:645–651. <https://doi.org/10.1007/s12206-013-1192-6>
27. Abhishek K, Kumar VR, Datta S, Mahapatra SS (2017) Application of JAYA algorithm for the optimization of machining performance characteristics during the turning of CFRP (epoxy) composites: comparison with TLBO, GA, and ICA. *Eng Comput* 33:457–475. <https://doi.org/10.1007/s00366-016-0484-8>
28. Venkata Rao R (2016) Jaya: a simple and new optimization algorithm for solving constrained and unconstrained optimization problems. *Int J Ind Eng Comput* 19–34. <https://doi.org/10.5267/j.ijiec.2015.8.004>
29. Zaman PB, Tusar MIH, Dhar NR (2020) Selection of appropriate process inputs for turning Ti-6Al-4V alloy under hybrid Al₂O₃-MWCNT nano-fluid based MQL. *Adv Mater Process Technol* 1–21. <https://doi.org/10.1080/2374068X.2020.1812324>

Surface Roughness Analysis in High-Speed Turning of Ti-6Al-4V with Coated Carbide Inserts Using Vibration Signals



Grynal D'Mello and P. Srinivasa Pai

Abstract Use of vibration signals for analysis of machining processes has been done for various purposes including surface roughness evaluation and tool wear monitoring. Ti-6Al-4V is a common Titanium-based alloy that has been utilized in a variety of applications such as aerospace, automotive, biomedical etc. As Ti is a difficult-to-machine material, there have been few investigations on using vibration signals to analyze roughness of the surface in Ti-based alloys. This research investigates vibration signals generated during high-speed turning (HST) of Ti-6Al-4V employing coated carbide inserts in this context. Experiments with HST have been carried out at high speed and different feed and depth of cuts and the resulting vibration signals have been analyzed along with surface roughness. Tool wear and cutting tool vibrations, which are the major factors in machining these alloys have been considered for the study and analysis. Further, a robust artificial neural network model called Radial Basis Function Neural Networks (RBFNN) was adopted for modeling and predicting surface roughness parameters R_a and R_t . Three RBFNN models have been developed: one that considers all parameters, including tool wear and vibration, another that ignores tool wear and considers vibrations, and a third that ignores vibrations but considers tool wear. All the models developed have achieved the same prediction accuracy of 98.3607% on the test data establishing the feasibility of using this for modeling and also establishing the significance of using vibration and tool wear in surface roughness analysis of Ti-6Al-4V alloys.

Keywords Ti-6Al-4V · High-speed turning · RBFNN · Tool flank wear · Cutting tool vibration

G. D'Mello (✉) · P. S. Pai
NMAM Institute of Technology, Affiliated to Nitte (Deemed to be University), Nitte, Karkala,
Karnataka 574110, India
e-mail: grynal@nitte.edu.in

1 Introduction

Titanium alloys are widely used in various applications including petroleum industries, aerospace, automotive, and biomedical implants, and have some distinct properties like non-corrosive nature and high strength to weight ratio and are considered as a 'difficult-to-machine' material [1]. There are several issues associated with its machining and include chemical reactivity with cutting tools, lower thermal conductivity causing high temperature at the tool-workpiece interface, leading to increased tool wear, shorter tool life, lower material removal rates, and poor surface finish [2]. In spite of all the developments in cutting tool materials, cooling strategies etc., even today titanium alloys are still considered difficult to machine. Ti-6Al-4V is a popular alloy under the α - β group and has high strength to weight ratio and is used in the range, 350–400°C. They are extensively used in the aerospace sector for manufacturing fuselage, engine blades, wing, and landing gears etc. [3]. Several studies have been reported regarding machining of these group of alloys. For e.g. Arunil Sharma et al. (2013) used coated carbide tools to investigate the machining characteristics of Ti-6Al-4V at various speeds, feeds, and approaching angles in dry conditions. Increase in speeds leads to increase in cutting forces and tool tip temperature. The surface roughness was also studied with respect to these parameters and the optimal conditions were determined [4]. Younas et al. studied tool wear and specific cutting energy (SCE) during high-speed turning of Ti-6Al-4V using uncoated carbide tools under dry conditions. Tool wear was identified as a major reason for changes in SCE. They have related SCE and tool wear through a linear relationship in order to monitor wear and SCE utilization during machining, which can be used to select appropriate cutting conditions [2]. Using uncoated and coated carbide inserts, Li et al. investigated HST of Ti-6Al-4V. Coated inserts are known to have a lower wear rate than uncoated inserts with short cutting distances, but they become equivalent at a later cutting stage [5]. The machining of titanium-based alloys is different when compared to the conventional materials as the material deformation process is different, called as 'adiabatic shear or catastrophic thermoplastic shear', which results in saw-tooth chip formation. Also, titanium alloys due to their low modulus of elasticity, experience 'spring back effect' during machining that not only causes greater friction, chatter, and low clearance angle at the flank face, but affects the dimensional accuracy [1].

Vibration is a major cause of concern during a machining process, which always exists between tool and workpiece. When machining materials are difficult to machine, such as titanium alloys, the vibrations are more severe. It has been observed that during machining of these alloys, there is self-excitation between the tool and workpiece, which increases the vibrations. These self-exciting vibrations are caused due to cyclic forces [6]. The influence of spring back effect causes the tool to cause a wavy surface during material removal causing chip thickness variation, which increases the cutting forces. This results in higher amplitude of vibrations at the interface of tool and workpiece, which is called 'waviness regeneration' [1]. Chatter is also a serious issue with these alloys due to their low modulus of elasticity. The

cutting tool vibrations are caused due to the adiabatic shear happening during the chip formation process, which causes high dynamic cutting forces, leading to sudden variations in vibrations [7, 8].

Cutting tool wear and vibrations influence the surface roughness and its effect is more significant during machining of titanium-based alloys. Lower thermal conductivity of these alloys leads to increase in cutting tool temperature increasing the tool wear. They are chemically reactive with tool materials further increasing the wear. Machining with high cutting speeds can also cause catastrophic failure of inserts due to rapid chipping [9]. Adhesion and diffusion are commonly observed tool wear mechanisms [10–12].

Cutting tool vibrations affect the surface roughness. It varies from material to material and depends on its hardness and other material properties. Selection of cutting tool also helps in managing the cutting tool vibrations. Particularly the distinct characteristics associated with machining of titanium-based alloys with regard to material removal, chip formation, generation of cutting forces causing vibrations and chatter have a significant influence on surface roughness. E. Garcia Plaza and P.J. Nunez Lopez (2017) used singular spectrum analysis (SSA) on vibration signals to evaluate surface roughness in CNC finish turning operations. Individual principal component analysis (I-SSA) and grouping analysis of connected principal components were used (G-SSA). To determine the surface roughness, experiments were conducted under various cutting settings. G-SSA was shown to be the most effective method for detecting surface roughness at a low cost [13]. In a related study, Pai & Dmello studied vibration signals during HST of grade 5 titanium alloy using both uncoated and coated carbide inserts. A comparison has been made in performance between with and without coolant. Wavelet transform (WT) was used for analyzing vibration signals. It was reported that average energy of detailed coefficients at the first level can be effectively used to evaluate flank wear for both inserts, with and without coolant [14].

Machining of titanium alloys requires proper selection of cutting conditions to achieve the desired level of surface finish and reduced tool wear, at the same time increase in productivity in terms of increased metal removal rate. To achieve these objectives, there is a need for selecting proper cutting parameters, which requires lots of skill and experience. In this regard, researchers are proposing use of modeling techniques to simulate and model the relationships between the input and output variables. Surface roughness modeling and prediction in machining applications has assumed lot of significance, as it can reduce the actual number of experiments that need to be conducted. Also involving uncontrolled parameters like tool wear and cutting tool vibrations makes it easier to be modeled. In recent years, several modeling techniques like regression models & response surface methodology (RSM) [15], artificial neural networks (ANN), fuzzy logic, support vector machines etc. have been implemented for various applications.

The brief review highlights the lack of experimental investigation of tool vibrations and its correlation with roughness and use of ANN for modeling surface roughness using cutting tool vibrations. This paper presents the analysis of results of experimental investigation during HST of Ti-6Al-4V alloy using coated carbide inserts at a

high speed at three different feed and cutting depths in terms of tool wear, tool vibrations, and roughness of the surface. Further RBFNN modeling paradigm has been used to model surface roughness with and without cutting tool vibrations, establishing the feasibility of using cutting tool vibrations in surface roughness investigation and modeling studies during high-speed machining of Ti-6Al-4V alloy.

2 Experimental Setup and Details

The trials for this study were carried out on an HMT Stallion 100 SU high-speed CNC turning machine using a Ti-6Al-4V round bar with a diameter of 50 mm and a length of 200 mm in dry circumstances. Cutting speeds, feed rates, and depths of cut were all varied using a three-level full factorial experimental design. Table 1 shows the parameter levels that were employed in this study. All the parameters have been set based on its usage from literature and also by considering the limitations of the machine tool. The cutting tool insert used is CNMG120408 TS2500 coated carbide insert which is fixed on to a tool holder PCLNL 2020 K12. Both the components were supplied by SECO tools. Machining is done for a total length of 48 mm, which is one machining pass.

Cutting tool vibrations are monitored during the machining pass using an Isotron 65 triaxial (V_x (depth of cut), V_y (cutting speed), and V_z (feed) directions) accelerometer, with signals taken using a DNA cube data collecting system and analyzed using Lab View software and unit is measured in terms of g . The tool insert is removed from the tool holder after each machining pass and measured for maximum tool flank wear with a Mitutoyo tool makers’ microscope. In one round bar, three machining passes were completed. A Taylor Hobson Form Taly Surf 50 contact type profilometer is then used to measure the surface roughness of the workpiece. The roughness parameters R_a and R_t are measured at three distinct sites for a machining pass with a sampling length of 2.5 mm, and the mean value of these parameters is used for analysis. This method is repeated until the maximum tool flank wear reaches 0.4 mm, which is regarded a tool wear limiting value according to ISO 3685:1993 [16]. A total of 461 data sets have been generated from the experiments.

Table 1 Experimental design

Cutting speed V_c (m/min)	Feed rate f (mm/rev)	Depth of cut d (mm)
150	0.15	0.8
175	0.2	1
200	0.25	1.2

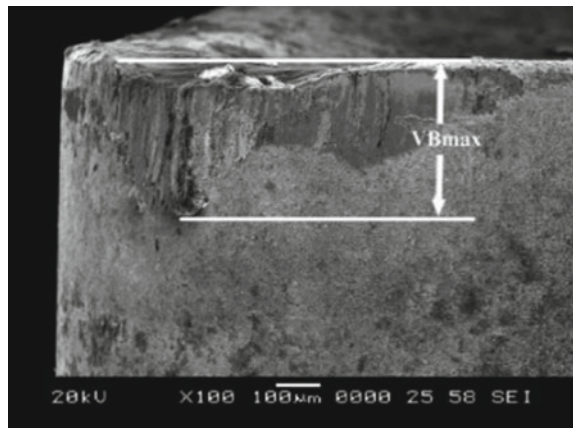
3 Results and Discussion

The major goal of this research is to figure out how tool vibration generated during turning is related to tool wear and machining parameters. The experimental conditions considered in this study are high cutting speed of 200 m/min, different feed rates, and depths of cut. Initially, the progression of tool wear is recorded with respect to number of passes. The maximum tool flank wear (VB_{max}) has been considered in this study for evaluation. The experiments were carried out till VB_{max} crossed 0.4 mm. Figure 1 shows a typical SEM photograph of the worn region of a tool showing the measurement zone of VB_{max} .

3.1 Effect of Cutting Parameters on Tool Wear

Figure 2 shows the progression of VB_{max} at 200 m/min for different feed rates and depths of cut. Tool wear progressed progressively, resulting in three distinct regions: the break-in period, the steady-state zone, and the failure region. In Fig. 2a, this kind of behavior has been observed for low and intermediate feed rates but for higher feed rate, there was a gradual increase throughout. The fastest tool wear has been observed at low feed of 0.15 mm/rev which reached the limiting value of tool wear in 9 passes. The tool wear rate decreased as the feed rate increased. In Fig. 2b, the trend of tool wear is similar to that observed in Fig. 2a. The three regions of tool wear are clearly visible for all the feed rates investigated. The fastest tool wear has been observed for low feed rate of 0.15 mm/rev which reached the limiting value of tool wear in 15 passes. In Fig. 2c, it can be seen that the trend of wear is not very clear. The fastest tool wear is observed for intermediate and high feed rate of 0.2 and 0.25 mm/rev, whereas the slowest tool wear is observed at low feed rate of 0.15 mm/rev.

Fig. 1 Maximum tool flank wear VB_{max} measurement



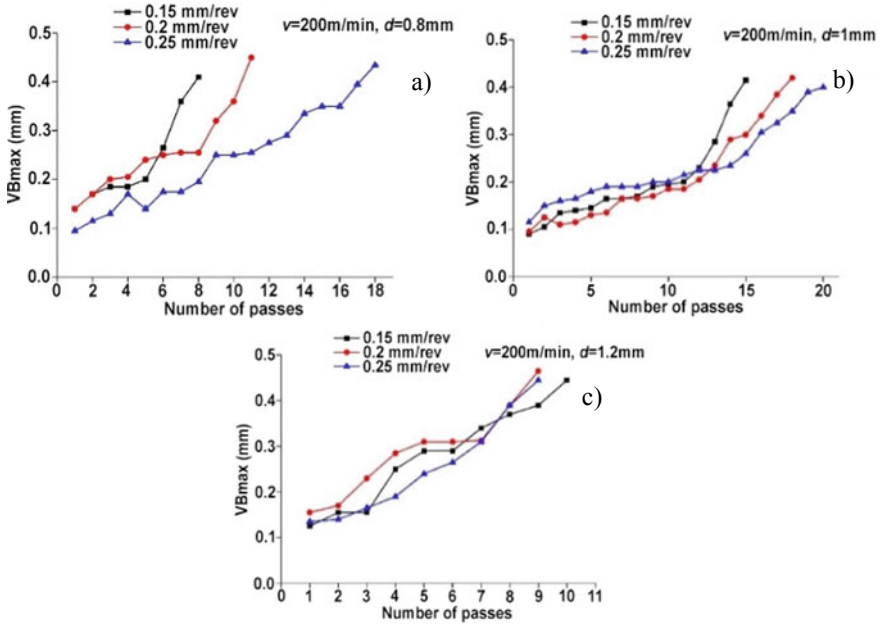


Fig. 2 Progression of VB_{max} at 200 m/min for different feed rates at **a** 0.8 mm **b** 1 mm **c** 1.2 mm cutting depth

From Figs. 2, 3 and 4, it can be seen that the trend for tool wear with variation in feed rate is not very clear. At some cases, tool wear progressed with increase in feed whereas at other cases it is vice versa. The effect of feed rate is observed in all the conditions investigated, but the trend has varied. But in majority of the cases, it is observed that the tool wear rate is slower for high feed rate of 0.25 mm/rev than at lower feed rate of 0.15 mm/rev which is opposite to what is reported in the literature [17]. As stated by Makarow [18], the tool cuts a portion of the transitory surface generated by the previous tool pass, and the amount of cold working imposed by this tool on the prior pass has an impact on the cutting conditions on the present pass. The depth of cold working in relation to the uncut chip thickness is one of the most important strain hardening properties. When cutting at low feeds, i.e. when the uncut chip thickness is less than the depth of cold working, this is very significant. When this occurs, the principal cutting edge slices the cold worked material, which has a higher strength and hardness. As a result, the rate of tool wear rises. It is assumed that a similar behavior has been observed in the current study. Moreover, Bonifacio and Diniz in a similar study, stated that because the relationship between feed rate and tool life of a coated carbide insert is not well understood and may not be influenced by feed rate [19].

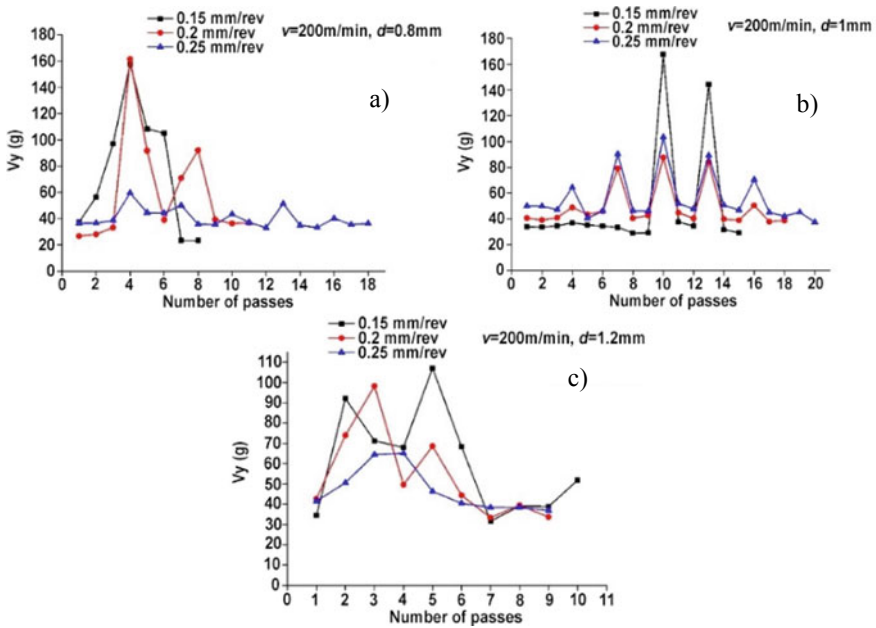


Fig. 3 Cutting tool vibrations (V_y) at 200 m/min for different feed rates at **a** 0.8 mm **b** 1 mm **c** 1.2 mm depth of cut

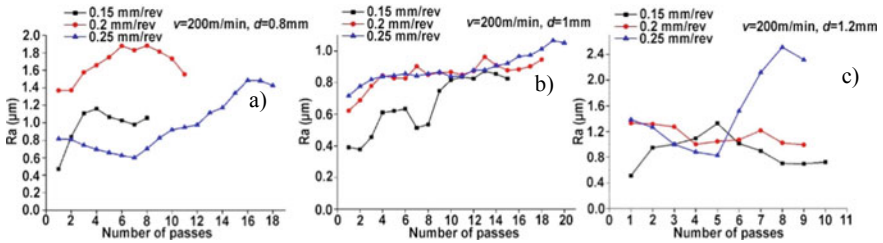


Fig. 4 R_a at 200 m/min for different feed rates at **a** 0.8 mm **b** 1 mm **c** 1.2 mm cutting depth

3.2 Effect on Cutting Parameters and Tool Wear on Cutting Tool Vibrations

Tool vibrations were measured in three speed (V_y), feed (V_z), and cutting depth (V_x). Tool vibrations are prevalent along the cutting speed direction, according to the authors’ earlier investigation (V_y) [20]. As a result, only V_y has been taken into account in this research.

Figure 3 shows the cutting tool vibrations V_y at 200 m/min for different feed and cutting depths. In Fig. 3a, the lowest vibrations have been generated at low feed rate. The tool vibrations reduced with the rise in tool wear and has minimum value at

the end of tool life in most of the cases. In Fig. 3b, the cutting tool vibrations have reached the maximum for lower feed rate and for intermediate tool wear conditions. The vibrations had a rapid increase just before 2 or 3 passes of tool reaching the limiting value of tool wear. This has been observed for some cutting conditions at different depths of cut. In Fig. 3c, the average lowest vibrations have been generated for higher rate of 0.25 mm/rev. When different depths of cut are considered, 1.2 mm depth of cut produced the lowest overall cutting tool vibrations. The tool vibrations generated at lower and intermediate feed (0.15 and 0.2 mm/rev) have found to be more than higher feed (0.25 mm/rev). A similar trend was also observed in the previous section where tool wear rate was also higher at lower and intermediate feed rate. This might have been generated due to the increased strength and hardness of the workpiece caused by the relative effect of uncut chip thickness and the depth of cold working [18]. It is also observed that the cutting tool vibrations have decreased toward the end of tool life. At the end of tool life, tool nose radius tends to increase due to wear leading to reduction in the vibration amplitude [21].

3.3 Effect of Cutting Parameters, Tool Wear, and Tool Vibration on Surface Roughness

Two profile roughness parameters R_a (Average) and R_t (Peak to valley height of the profile) have been considered in this study which is correlated with cutting parameters, VB_{max} and V_y .

Figures 4 and 5 illustrates the surface roughness parameters R_a and R_t at 200 m/min for different feed rates and depths of cut. The profile of R_a and R_t is almost similar, but there are more variations seen in R_t (Fig. 4) than R_a (Fig. 5). In all the conditions investigated, the lowest surface roughness has been obtained for lower feed rate. A similar trend is seen in vibration plots (Fig. 3). The fluctuations of vibrations and its correlation with surface roughness are more clearly visualized in R_t than R_a . Moreover, it is also observed that the values of surface roughness have gradually increased as the tool wear progressed and finally decreased approaching the end of the tool’s useful life in most of the cases. This could be due to deformation of the

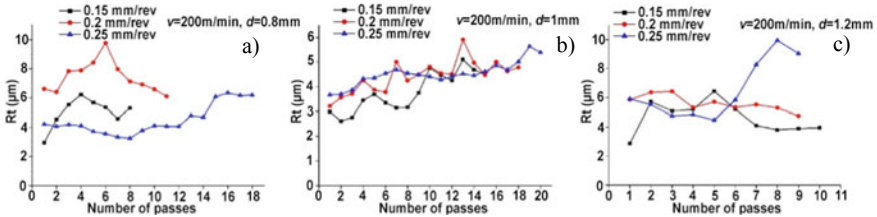


Fig. 5 R_t at 200 m/min for different feed rates at a) 0.8 mm b) 1 mm c) 1.2 mm cutting depth

flank face or workpiece material adherence to the tool nose, resulting in chamfering and a reduction in surface roughness [9].

4 Radial Basis Function Neural Network

RBFNN was created to solve multivariable interpolation problems in the real world. RBFNN refers to a feed forward network consisting of an input layer with sensory units, a hidden layer with radial basis activation functions that applies a non-linear transition from input space to hidden space, and an output layer that ties the network's output to the input layer's activation patterns [22].

The neurons in the hidden layer use Gaussian transfer functions, which are given by Eq. (1).

$$\varphi_i(\mu) = -\exp\left(\frac{\|x - \mu_i\|}{2\sigma_j^2}\right) \quad (1)$$

where x is an input vector, μ_i is the center of the RBF unit in the input vector space, and σ_j is a spread factor or width for that unit [23].

When there are K radial basis units in the intermediate layer and only one output layer in an RBF network, the output is represented by Eq. (2).

$$y = \sum_{(i=1)}^K w_i \varphi(\|x - \mu_i\|^2) + w_0 \quad (2)$$

where x and μ_i are as stated in Eq. (1), φ is the radial basis units' activation function, w_i represents the weights by which a radial unit's output is multiplied in the output layer, and w_0 is a constant [24]. The width of the activation function determines the smoothness of the function. Because the output is a non-linear function of the inputs, the gradient descent method is used to determine the weights connecting the hidden and output units. RBF models are basic and straightforward to use.

Clustering is putting data points in different number of sub groups, wherein data in a sub group (cluster) are similar to each other. In case of hard clustering, data point can be assigned to one and only one of the sub groups and the degree of membership is generally one and the sub groups have well described boundaries. But in the real world, it is not possible to classify data into one sub group and the boundaries between these groups may be fuzzy. Bezdek et al., developed several clustering algorithms that are based on fuzzy extensions of least square criterion and established their convergence to a local minimum and called them as Fuzzy C means algorithm [25]. W. Pedrycz exploited this feature and developed CFCM algorithm, which reveals a structure in the input data [26]. The RBF unit centers were created using the CFCM

algorithm as given in [27]. The centers are created using the CFCM algorithm, which was used to train the RBFNN. The same input factors were considered while creating the centers. The two output parameters are R_a and R_t , hence two RBFNN models have been created.

The CFCM has been trained with a variety of numbers of centers, with the target error set to 0.001.

The spread factor, also known as the RBF unit width, that governs the interpolating function’s fineness features. P-nearest neighbor heuristic is an effective arrangement to find the width [28]. Evaluation of width can also be done using $\sigma_j = \frac{d_{max}}{\sqrt{2m}}$, the maximum Euclidean distance between the selected centers is denoted by d_{max} , and the number of centers is denoted by m [22]. For all RBF units, it is possible to keep the width constant [29]. The widths were kept constant in this investigation and were chosen by various trials to minimize the error and maximize accuracy.

4.1 Modeling Using RBFNN

Three RBFNN models each for R_a and R_t have been developed, one considering all the parameters including tool flank wear (VB_{max}) and vibration (V_y), second neglecting VB_{max} and third neglecting V_y and considering VB_{max} . Out of 461 datasets, 400 data have been considered as training data (trg.) and 61 are considered as test data (tst.).

Throughout the investigation, the simulation parameters were maintained at a constant level. The learning rate was set to 0.85 and the momentum rate to 0.05. The RBFNN is trained by altering the width values and RBF units determined by the CFCM. Weights that have been changed during training using a gradient descent approach connect the hidden and output units. The epoch count is set to 1000. RBF units’ width was found by various trials and is maintained for all RBF units, which differ from model to model. All the models developed are evaluated by considering a Mean Squared Error (MSE) of 5% error between the predicted and experimental values and any value above the fixed error is considered to be wrong prediction. The models developed in this study have been listed in Table 2.

Model 1 and Model 2 performance is shown in Table 3 for a width of 0.1. Model 1 has the highest prediction accuracy of 99.5% on trg. and 98.36075% on tst. with an

Table 2 Models developed

Sl. No	Model	Parameters
1	Model 1 (R_a)	V_c, f, d, VB_{max}, V_y
2	Model 2 (R_t)	V_c, f, d, VB_{max}, V_y
3	Model 3 (R_a)	$V_c, f, d, VB_{max},$
4	Model 4 (R_t)	$V_c, f, d, VB_{max},$
5	Model 5 (R_a)	V_c, f, d, V_y
6	Model 6 (R_t)	V_c, f, d, V_y

Table 3 Performance of models

Model 1 (R_a)				Model 2 (R_t)			
No. of RBF units	Prediction accuracy (%)		Avg. MSE	No. of RBF Units	Prediction accuracy (%)		avg. mse
	(trg.)	(tst.)			(trg.)	(tst.)	
50	99.25	98.3607	0.007471	55	98.75	98.3607	0.00776
55	99.5	98.3607	0.00691	56	98.5	98.3607	0.00784
60	99.25	98.3607	0.00729	57	98.5	98.3607	0.00812
65	99	98.3607	0.00686	58	98.5	98.3607	0.00853
70	99	98.3607	0.0068	59	98.75	98.3607	0.00759
Model 3 (R_a)				Model 4 (R_t)			
No. of RBF units	Prediction accuracy (%)		Avg. MSE	No. of RBF Units	Prediction accuracy (%)		Avg. MSE
	(trg.)	(tst.)			(trg.)	(tst.)	
30	99.25	98.3607	0.00672	20	99	98.3607	0.00737
35	99.25	98.3607	0.01	25	99	98.3607	0.007626
40	99.75	98.3607	0.0127	30	99.25	98.3607	0.01217
45	99.5	98.3607	0.0142	35	99.5	98.3607	0.01980
50	95.75	95.08	0.0308	40	98.75	96.7213	0.02176
Model 5 (R_a)				Model 6 (R_t)			
No. of RBF0 units	Prediction accuracy (%)		Avg. MSE	No. of RBF units	Prediction accuracy (%)		Avg. MSE
	(trg.)	(tst.)			(trg.)	(tst.)	
25	99.25	98.3607	0.00765	25	99	98.3607	0.00827
30	99.5	98.3607	0.00734	30	99.25	96.7213	0.00826
35	99.25	98.3607	0.00728	35	99.25	98.3607	0.00976
40	99.5	98.3607	0.00801	40	98.5	98.3607	0.0165
45	99.75	98.3607	0.01128	45	97.75	98.3607	0.0209

error of 0.00691 for 55 RBF units, whereas Model 2 has the lowest error of 0.00759 with a highest prediction accuracy of 98.755% on trg. and 98.36075% on tst. with an average MSE of 0.00691 for 59 RBF units.

The performance of Model 3 and Model 4 has been shown for a width of 0.12. Model 3 achieved the highest prediction accuracy of 99.755% on trg. and 98.36075% on tst. with a lowest error of 0.0127 for 40 RBF units, whereas Model 4 achieved the highest prediction accuracy of 99.55% on trg. and 98.36075% on tst. with the least error of 0.01982 for 35 RBF units. The performance of the Model 5 and Model 6 has been shown for a width of 0.12. Model 5 achieved the highest prediction accuracy of 99.755% on trg. and 98.36075% on tst. with an error of 0.01128 for 45 RBF units, whereas Model 6 achieved an error of 0.00976 with a prediction accuracy of 99.255% on trg. and 98.36075% on tst. for 35 RBF units.

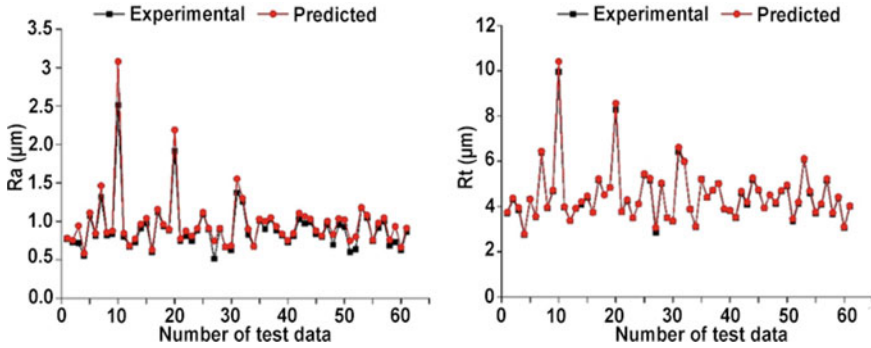


Fig. 6 Experimental and RBF forecasted values comparison **a** R_a **b** R_t

From Table 3, the same prediction accuracy of 98.36075% on the test data has been reached, demonstrating the practicality of using this for modeling and the importance of using vibration and tool wear in Ti-6Al-4 V alloy surface roughness study.

Figure 6 shows the comparison of R_a and R_t , for both investigated and forecasted values for tst. and the plots were created using the best RBFNN model available in terms of lowest error for R_a and R_t (Table 2). R_t values forecasted from the network are very similar to the investigated values, whereas R_a showed small deviations in predicted values.

RBFNN has resulted in better prediction and modeling performance due to its universal approximation capability. CFCM with RBFNN has the ability ‘to assume the patterns falling under the same fuzzy cluster and similarity in the sense of their vicinity in multidimensional space of independent variables’, which was established by Pedrycz [26] which helped in improving the RBFNN performance.

5 Conclusions

During HST of Ti-6Al-4V, vibration signals are used to analyze tool wear and surface roughness, as well as cutting parameters such as V_c , f , and d . The purpose of the experiment was to see how cutting parameters, VB_{max} , and V_y affected R_a and R_t when utilizing coated carbide inserts. In addition, an Artificial Intelligence technology known as the RBFNN was used to model and predict surface roughness characteristics in order to determine the relationship between input and output. Following are some findings that may be derived from these studies:

- The tool has worn faster at reduced feed rates in most of the experimental conditions investigated, owing to the uncut chip thickness being smaller than the depth of cold working, resulting in greater strength and hardness of the work material.

- In most cases, as tool wear advanced, surface roughness gradually increased and then decreased as tool life approached its end. Vibrations from cutting tools have likewise diminished as they near the end of tool life.
- Vibrations of the cutting tool (V_y) have a considerable impact on the surface roughness parameters R_a and R_t .
- The association between vibration fluctuations and surface roughness is more readily visualized in R_t than in R_a .
- CFCM clustering technique is highly good at determining the best location of centers in RBF units, which increases RBFNN performance.
- On the test data, all models had the same prediction accuracy of 98.36075%, illustrating the practicality of utilizing RBFNN for modeling and the usefulness of using vibration and tool wear in HST Ti-6Al-4V alloy surface roughness investigation.

References

1. Pramanik A (2014) Problems and solutions in machining of titanium alloys. *Int J Adv Manuf Technol* 70(5):919–928
2. Younas M, Jaffery SHI, Khan M, Ahmad R, Ali L, Khan Z, Khan A (2019) Tool wear progression and its effect on energy consumption in turning of titanium alloy (Ti-6Al-4V). *Mech Sci* 10(2):373–382
3. Boyer RR (2010) Titanium and its alloys: metallurgy, heat treatment and alloy characteristics. *Encyclopedia of Aerospace Engineering*, American Cancer Society, John Wiley & Sons, Ltd. ISBN: 978-0-470-68665-2
4. Sharma A, Sharma MD, Sehgal R (2013) Experimental study of machining characteristics of titanium alloy (Ti-6Al-4V). *Arab J Sci Eng* 38(11):3201–3209
5. Li YS, Deng JX, Ebbrell S, Morgan MN, Ren XJ (2012) High speed turning of Ti-6Al-4V alloy with straight cemented carbide and PVD coated carbide tools. In: *Key engineering materials*, vol 496. Trans Tech Publications Ltd. , pp 92–97
6. Fan YH, Zheng ML, Zhang DQ, Yang SC, Cheng MM (2011) Static and dynamic characteristic of cutting force when high-efficiency cutting Ti-6Al-4V. In: *Advanced materials research*, vol 305. Trans Tech Publications Ltd., pp 122–128
7. Campbell FC Jr. (2011) *Manufacturing technology for aerospace structural materials*. Elsevier, ISBN-13: 978-1-85-617495-4
8. Bhaumik SK, Divakar C, Singh AK (1995) Machining Ti-6Al-4V alloy with a wBN-cBN composite tool. *Mater Des* 16(4):221–226
9. Che-Haron CH (2001) Tool life and surface integrity in turning titanium alloy. *J Mater Process Technol* 118(1–3):231–237
10. Kennametal (2015) *High Temperature Machining Guide*
11. Jawaid A, Koksall S, Sharif S (2001) Cutting performance and wear characteristics of PVD coated and uncoated carbide tools in face milling Inconel 718 aerospace alloy. *J Mater Process Technol* 116(1):2–9
12. Molinari A, Pellizzari M, Gialanella S, Straffelini G, Stiasny KH (2001) Effect of deep cryogenic treatment on the mechanical properties of tool steels. *J Mater Process Technol* 118(1–3):350–355
13. Plaza EG, López PN (2017) Surface roughness monitoring by singular spectrum analysis of vibration signals. *Mech Syst Signal Process* 84:516–530

14. Pai PS, Mello GD (2015) Vibration signal analysis for monitoring tool wear in high speed turning of Ti-6Al-4V. *Indian J Eng Mater Sci* 226:652–662
15. Upadhyay V, Jain PK, Mehta NK (2013) In-process prediction of surface roughness in turning of Ti-6Al-4V alloy using cutting parameters and vibration signals. *Measurement* 46(1):154–160
16. Norma ISO. 3685:1993. Tool life test single point turn tools (1993)
17. Jawaid A, Che-Haron CH, Abdullah A (1999) Tool wear characteristics in turning of titanium alloy Ti-6246. *J Mater Process Technol* 92:329–334
18. Makarov AD (1976) Optimization of cutting processes. *Mashinostroenie, Moscow*, pp 9–10
19. Jang DY, Choi Y-G, Kim H-G, Hsiao A (1996) Study of the correlation between surface roughness and cutting vibrations to develop an on-line roughness measuring technique in hard turning. *Int J Mach Tools Manuf* 36(4):453–464
20. D'Mello G, Pai PS, Prashanth A (2018) Surface roughness analysis in high speed turning of Ti-6Al-4V using coated carbide inserts: experimental and modeling studies. *Tribol Ind* 40(3):457–476
21. Ince MA, Asiltürk İ (2016) Effects of cutting tool parameters on vibration. In: *MATEC web of conferences. EDP sciences*, vol 77, p 07006
22. Haykin S (2004) *A comprehensive foundation. Neural Netw* 2:41
23. Bishop CM (1995) *Neural networks for pattern recognition. Oxford University Press*
24. Pontes FJ, Ferreira JR, Silva MB, Paiva AP, Balestrassi PP (2010) Artificial neural networks for machining processes surface roughness modeling. *Int J Adv Manuf Technol* 49(9–12):879–902
25. Bezdek JC, Ehrlich R, Full W (1984) FCM: the fuzzy c-means clustering algorithm. *Comput Geosci* 10(2–3):191–203
26. Pedrycz W (1996) Conditional fuzzy c-means. *Pattern Recogn Lett* 17(6):625–631
27. Pai PS, Nagabhushana TN, Rao PR, Rao RB (2002) Radial basis function neural networks for tool wear condition monitoring
28. Moody J, Darken CJ (1989) Fast learning in networks of locally-tuned processing units. *Neural Computa* 1(2):281–294
29. Pai PS (2004) Acoustic emission based tool wear monitoring using some improved neural network methodologies. Mysore University, Ph.D. thesis [Google Scholar]

Comparative Prediction of the Influence of Process Parameters During CAEDM and REDM of Hybrid Metal Matrix Composite



Paridhi Malhotra, Rajeev Agrawal, R. K. Tyagi, Nishant Singh, Jimmy Mehta, and Moti Lal Rinawa

Abstract To attain the growing demand of industries a large number of new energies, high strength and lightweight materials are introduced and have become a major area of research for various researchers. Hybrid metal matrix composites with superior properties have found numerous applications in the aerospace and automotive industries. In present work fabrication of hybrid MMC of Al 7075/SiC/Mg and a comparative investigation of rotary electric discharge machining (REDM) and compressed air electric discharge machining (CAEDM) of hybrid MMC of Al7075 mixed with SiC and Mg has been carried out. In this investigation influence of the input variables namely duty cycle, peak current, pulse on time, and RPM of the tool electrode on output variables such as MRR and EWR were analyzed. The results showed that high MRR is achieved in CAEDM than REDM of hybrid MMC of Aluminum 7075 alloy owing to ameliorated flushing of debris from the machining gap. However, low EWR was obtained using CAEDM as compared to the REDM.

Keywords CAEDM · REDM · Hybrid composite · Peak current

1 Introduction

EDM is also known as spark eroding is often observed as the commonly used manufacturing process for the production of dies and molds by making use of the heat

P. Malhotra · R. K. Tyagi
Amity University, Noida, India

R. Agrawal
M LV Textile and Engineering College Bhilwara, Churmura, Rajasthan, India

N. Singh
Hindustan College of Science and Technology, Mathura, India

J. Mehta (✉)
Manav Rachna International Institute of Research and Studies, Faridabad, India
e-mail: jimmymehta.chd@gmail.com; jimmy.fet@mriu.edu.in

M. L. Rinawa
Government Engineering College Jhalawar, Jhalrapatan, Rajasthan, India

from sparks thus eradicating material from the surface of the hard specimen and little amount from the surface of the tool. High tool wear rate, low material evacuation rate, and flushing of the scattered fragments from the inter-electrode gap are some of them or pitfalls of the EDM process. It was observed the effect on MRR and TWR when nitrogen is supplied along the tubular rotary copper electrode in the EDM of En19 steel [1]. An increment of 62% of MRR and decrement by 35% of TWR was perceived. The process of EDM has the believability to machine intricate geometry shaped jobs. Experiments were carried out for the electrical discharge machining of a hybrid composite of Titanium carbide with varying weight % and d h-BN with constant weight % and reinforced with Al4032 [2]. The TEMP Effect of process parameters and inclusion of reinforcement were investigated on the output variables like tool wear rate, metal removal rate, micro hardness and surface roughness. Also research was done and trails of experiments were carried out of the EDM was tested under the influence of a magnetic field, and it was discovered that a magnetic field, as well as increasing values of pulse on-time and peak current, increases MRR [3]. The copper electrode provides maximum surface finish in contrast to graphite and tungsten tool electrode. It was also suggested that various mathematical models using an artificial neural network as a basis together with back propagation algorithm, ANFIS and RSM to calculate the material removal rate and surface roughness of D3 die steel during helium assisted electrical discharge machining [4]. The ANFIS model forecasted the responses more effectively compared to the other model developed. Scholars investigated the effect of EDM of a hybrid composite of AA5052 with graphite and WC as reinforcement [5]. The proportion of graphite proves to be the most superior factor that aims in enhancing the two MRR and average surface roughness. It was studied the comparison of various dielectrics and also illustrated the use of water-based dielectrics in die-sinking EDM process and also observed that adding powder in the dielectric enhances MRR and ameliorates the surface roughness [6]. Gas-assisted micro EDM revamps the performance of the process. Researchers investigated the EDM of a hybrid composite of aluminum 6061 15%SiC 6%MHA and found the peak current as of the most prevailing factor and copper electrode providing the maximum stability compared to other tools [7]. Authors analyzed the surface roughness, electrode wear ratio, power consumption and overcut using the grey rational analysis for optimizing the process variables during the EDM of functionally graded Al matrix composites. FGAMCs are the newly developed material deployed for complex engineering purpose [8]. Machinability was strenuous at particle augmented zone. At the low-level value of pulse on-time and pulse current desirable outcomes are obtained at the particle attenuated zone. Authors fabricated the setup for magnetic field-assisted EDM and witnessed an increment in MRR with the rise of peak current, pulse on-time and a reduction with pulse off-time and tool wear rate follows a reverse trend with the rise of powder concentration [9]. Scholars analyzed the effect of different tool materials and work piece material on the machining efficiency of PMND-EDM and observed variance in MRR because of the different physical properties of the electrode material [10].

1.1 Material and Method

Electronic-smart ZNC die-sinking electrical discharge machine was used for the series of studies. A multi-hole tubular rod of copper was used as tool electrode in the current procedure of experiments. The tool configuration was selected in such a manner to ensure smooth flow of compressed air. Eccentric nine holes through the tool with tooltip offering optimum heat transfer from the surface of the tool tip were selected. High precision drilling machine was used to drill holes on the bottom surface of the tool. To avoid overcut the diameter and the face corners of the copper electrode are machined and beveled properly. Experiments were carried out with the continuous flow of compressed air through the archway. Kerosene possesses excellent dielectric properties and was chosen for the present investigation.

Hybrid composite of Al7075 with 10% by weight SiC and 1% by weight Mg was selected as the work piece material. The hybrid composite was fabricated using the stir casting process. In a graphite crucible, the alloy was heated. Table 1 shows the molecular structure of Aluminum 7075 [11]. Due to high strength and low-cost material is highly recommended in the field of automobiles and airspace. The work piece has the hardness of 203 HV and tensile strength of 243.3 MPa. Figure 1 depicts the SEM image of the work piece; Figs. 2 and 3 represents the tool and schematic diagram of the experimental setup.

Peak current, Pulse on-time, duty cycle, air pressure and the rpm of the tool are selected as the input process parameters and MRR, surface roughness are considered

Table 1 Molecular structure
Aluminum 7075 alloy

Element	Weight (%)
Aluminum, Al	90
Magnesium, Mg	2.5
Zinc, Zn	5.6
Chromium, Cr	0.23
Copper, Cu	1.6

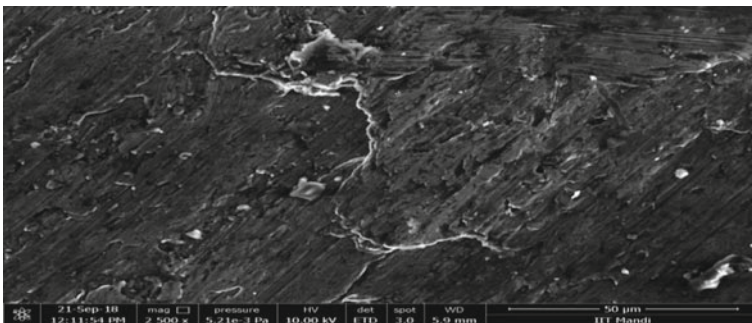


Fig. 1 SEM image of the work piece



Fig. 2 Copper tool with 9 holes

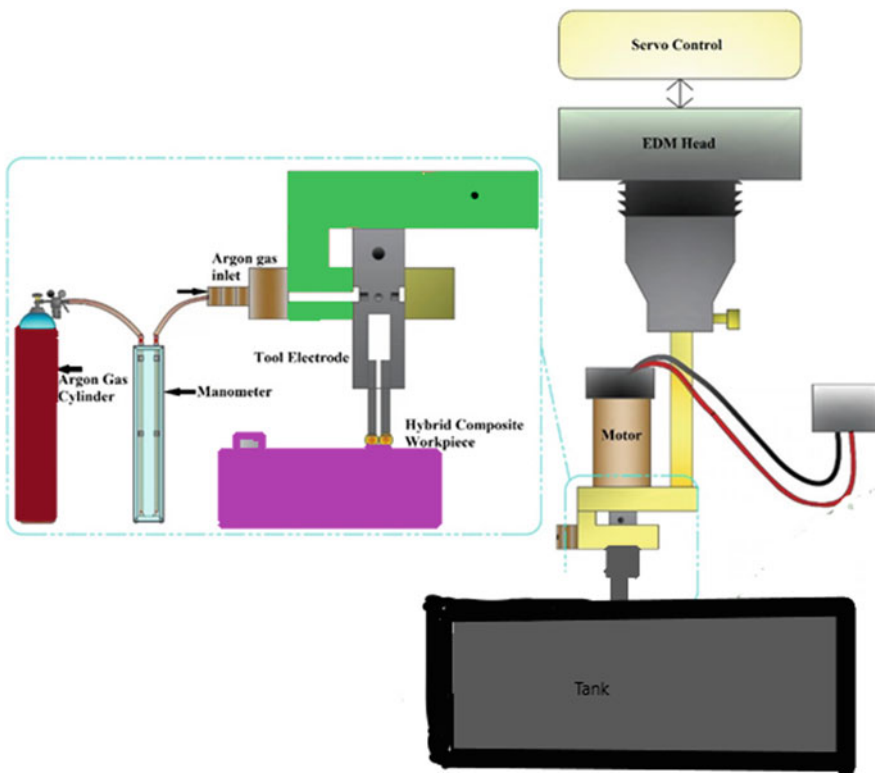


Fig. 3 Experimental setup

as the output parameters. Machining time was fixed as 15 min. To evaluate the parameters orthogonal array has been laid down. Open circuit voltage of 60 V was fixed for all the experiments. With the help of a precision electronic weighing balance with 0.1 mg least count, the relative mass of all specimens and electrode instruments is measured before and after each experiment.

MRR is measured as the material of the work piece removed per minute. EWR is calculated as the tool material removed or worn out per minute.

$$MRR = \text{Wt. of the material before machining} - \text{Wt. of the material after machining}$$

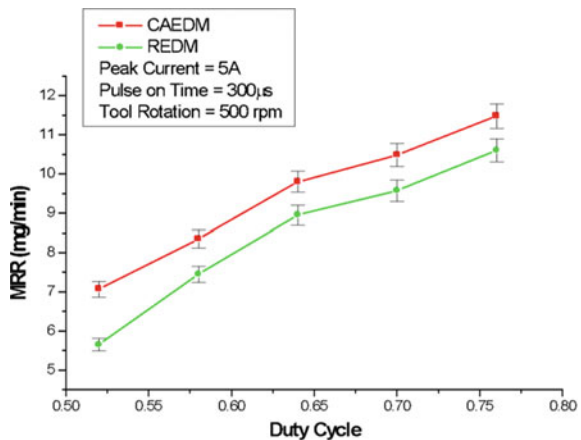
$$\text{Machining Time EWR} = (\text{Tool wear rate} / \text{Material removal rate}) * 100$$

2 Results and Discussion

2.1 Material Removal Rate (MRR)

Figure 4 represents the impact of the duty cycle on the material removal rate of CAEDM and REDM. Inference can be drawn from the fig. that the MRR rises in tandem with the duty cycle. This is mainly due to the reason that at an elevated value of duty cycle high spark energy is initiated and as the consequence the substance melts and vaporizes at a faster rate. It may be extrapolated from the figure that the MRR of CAEDM is more in contrast to the MRR of REDM because of the compressed air inoculation through the tool electrode which comes up with more melting of the work piece material and enhances the flushing of wear down particles from the machining gap.

Fig. 4 Impact of duty cycle on the MRR



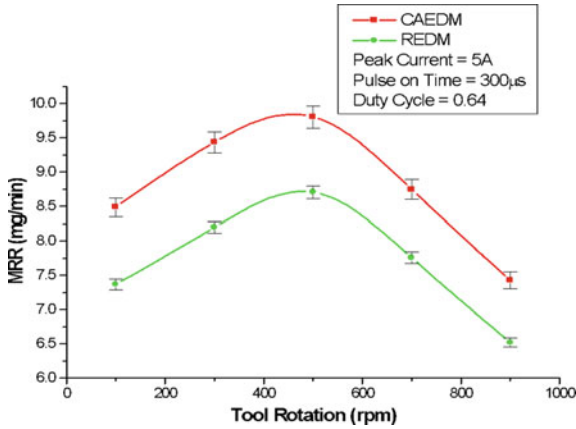


Fig. 5 Impact of tool rpm on MRR

Figure 5 manifested the impact of tool rotation on the material removal rate of CAEDM and REDM of hybrid MMC of Al7075/SiC/Mg. It can be inferred from the figure that with the increase of the tool rotation the value of MRR increases, reaches its peak value and then starts reducing gradually. It is attributable to the fact that eroded material is not sufficiently removed from the inter electrode gap at low speed of rotation of the tool. With the increase of the tool rpm, the immensity of the centrifugal force also increases which intensifies the flushing process. But after a certain value, if the tool rotation is increased further causes agitation of the plasma channel and hence the MRR gets reduced.

Figure 6 shows the impact of peak current on the MRR of CAEDM and REDM. The figure shows clearly that MRR enhances with the hike of peak current for the two processes. The reason behind this is the increase of the discharge energy in the machining gap which out-turns in more liquefying of the material. MRR of the

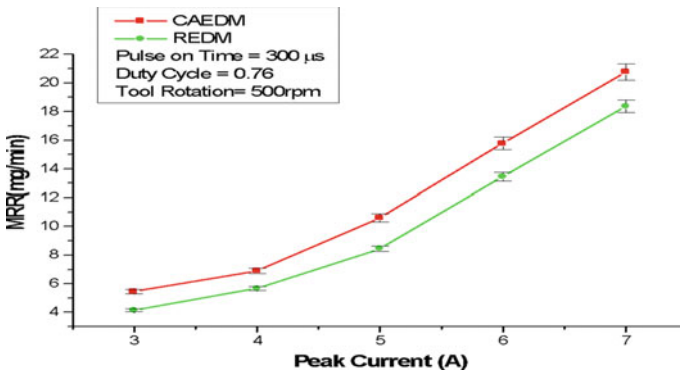
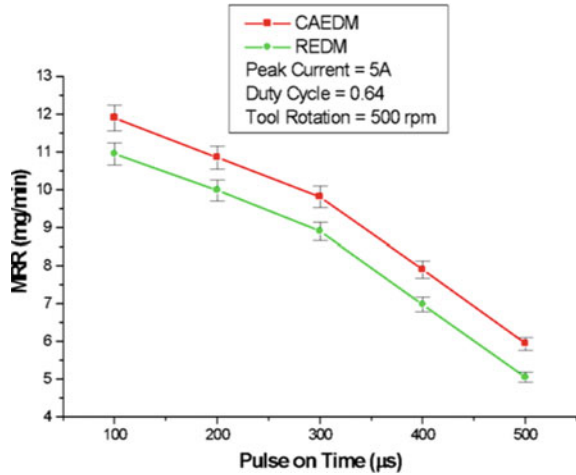


Fig. 6 Impact of peak current on MRR

Fig. 7 Impact of pulse on time on MRR



CAEDM is increased more than the MRR of the REDM because the compressed air passing through the holed electrode increases the disparity of the hydrostatical pressure, invigorating transmits of the molten metal from the cavity. The larger size of the cavity and the recast layer formed enhances the MRR as compared to the MRR of the REDM.

Figure 7 manifests the effect of pulse on-time on the MRR of both CAEDM and REDM process. The value of MRR for both the processes decline with the increase of the pulse time. Amplification of the plasma channel is noticed due to the extended time of the pulse which increases the energy density. With increased pulse duration, minimal melting of the material occurs which reduces the MRR for both the processes. Due to lengthening of the pulse duration huge craters are formed in the inter-electrode gap resulting in arcing and short circuit which further lowers down the MRR [12].

2.2 Electrode Wear Ratio (EWR)

Figure 8 represents the effect of peak current on the EWR of CAEDM and REDM of AL7075 reinforced with 10% SiC and 1% Mg. EWR of both processes enhances along with the enhancement of peak current. The discharge energy proliferates with the rise of the peak current generating additional heat in the machining area leading to amassing of the wear down particles in the gap resulting in the amplification of the EWR. The compressed air passing through the tubular electrode lowers down the temperature of the tip of the tool electrode and therefore the rise of EWR with the peak current of CAEDM is lesser as compared to REDM.

Figure 9 manifests the effect of pulse time on the EWR of both the processes. EWR is found to be negatively correlated with the pulse duration. The expansion of the

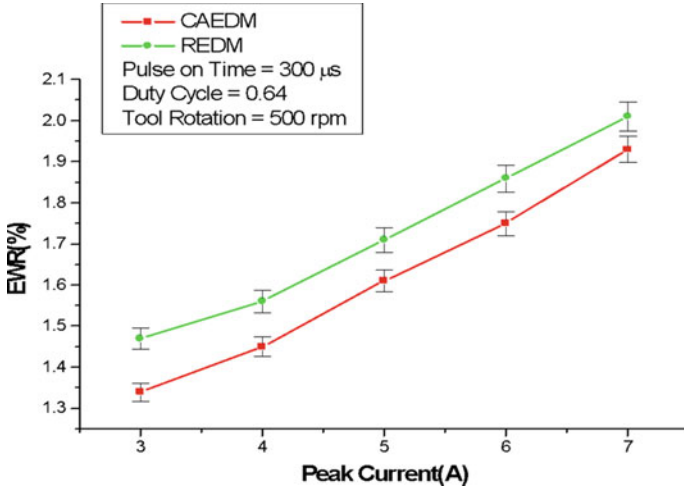


Fig. 8 Impact of peak current on EWR

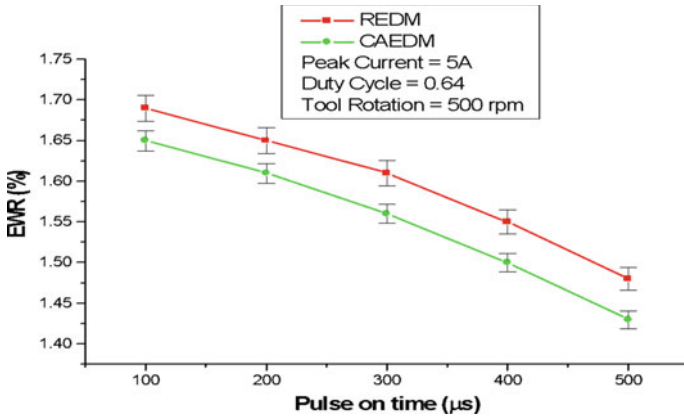


Fig. 9 Impact of pulse duration on EWR

time span of the pulse, the extension of the plasma channel takes place which results in a considerable decrease of the copper tool electrode's surface. The effused black layer of carbon provides resistance against wear because the dielectric is degrading, it sticks to the tool electrode's surface. The compressed air in case of CAEDM aims at flushing the eroded particles efficiently from the machining zone thus reducing the tool wear.

Figure 10 manifests the impact of tool rotation on the EWR of both the processes. The centrifugal force increases with the increased rpm of the tool electrode. The tool electrode resistant against the wear is improved with the deposition of the dark layer of carbon on the tool surface which is emitted out due to the decaying of the dielectric.

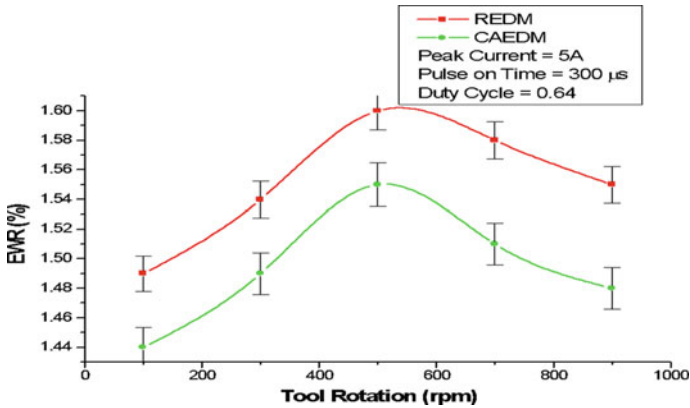


Fig. 10 Impact of tool rotation on EWR

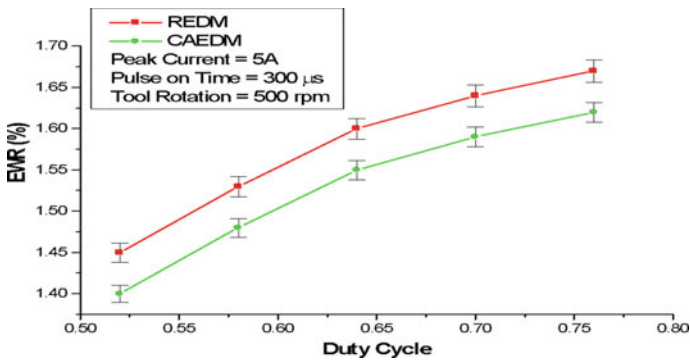


Fig. 11 Impact of duty cycle on EWR

Due to the centrifugal force, this dark layer of carbon detaches easily resulting in increased EWR.

Figure 11 manifests the effect of duty cycle on CAEDM and REDM. It clearly shows the positive relationship between the duty cycle and EWR. Increased duty cycle gives rise to high energy density originating high EWR. Due to the upgraded flushing capability of the CAEDM process of the eroded particles from the machining zone the EWR of the CAEDM is lower than EWR of REDM.

References

1. Singh NK, Agrawal S (2018) Experimental investigation of process parameters in nitrogen assisted EDM of En19 steel. *Int J Appl Eng Res* 13:165–169
2. Senthilkumar TS, Muralikannan R (2019) Role of TiC and h-BN particles on morphological

- characterization and surface effects of Al 4032 hybrid composites using EDM process. *J Mech Sci Technol* 33(9):4255–4264
3. Bains PS, Sidhu SS, Payal HS (2017) An investigation of magnetic-field- assisted EDM of composites. *Mater Manuf Processes* 33(6):670–675
 4. Singh NK, Singh Y, Kumar S, Sharma A (2019) Comparative study of statistical and soft computing-based predictive models for material removal rate and surface roughness during helium-assisted EDM of D3 die steel. *SN Appl Sci* 1(6):1–12. <https://doi.org/10.1007/s42452-019-0545-x>
 5. Dhas DS, Velmurugan C, Wins KL (2018) Investigations on the effect of tungsten carbide and graphite reinforcements during spark erosion machining of aluminium alloy (AA 5052) hybrid composite. *Silicon* 10(6):2769–2781
 6. Prakash V, Das AK, Chattopadhyay S (2019) Micro-EDM performance using different dielectrics. In Oliaei SN, Jahan MP, Perveen A (eds) *Micro EDM processes*. Springer Singapore
 7. Choudhary R (2019) Optimization of machining parameters in EDM of al6061 15% sic 6% mha composite by taguchi method. *Int J Eng Sci Math* 8(2)
 8. Uthayakumar M, Babu K, Kumaran S, Kumar S, Jappes JW, Rajan T (2017) Study on the machining of Al–SiC functionally graded metal matrix composite using die-sinking EDM. *Part Sci Technol* 37(1):103–109. <https://doi.org/10.1080/02726351.2017.1346020>
 9. Rouniyar AK, Shandilya P (2019) Fabrication and experimental investigation of magnetic field assisted powder mixed electrical discharge machining on machining of aluminium 6061 alloy, 233(12):2283–2291. <https://doi.org/10.1177/0954405419838954>
 10. Bai XP, Zhang Q, Zhang J, Kong D, Yang T (2013) Machining efficiency of powder mixed near dry electrical discharge machining based on different material combinations of tool electrode and workpiece electrode. *J Manuf Process* 15:474–482.
 11. Singh B, Kumar J, Kumar S (2013) Investigating the influence of process parameters of ZNC EDM on machinability of A6061/10% SiC composite. *Adv Mater Sci Eng* 1–8. <https://doi.org/10.1155/2013/173427>
 12. Singh NK, Pandey PM, Singh KK (2016) EDM with air-assisted multi-hole rotating tool. *Mater Manuf Process* 31(14):1872–1878.

Effect of Different Machining and Non-machining Parameters on Machining Performance of Electrochemical Discharge Machining (ECDM): A Review



Dheeraj Soni, B. D. Gidwani, and R. Shringi

Abstract In the present era of green manufacturing, non-traditional machining (NTM) processes are catering with best performance for machining of both conductive and non-conductive materials. Electro Chemical Discharge Machining (ECDM) process is materialized as a potential contender in the territory of non-traditional machining (NTM) processes. ECDM is a competent machining process which is hybridization of Electro-Chemical Machining (ECM) and Electro Discharge Machining (EDM) and also having advantages of both processes. ECDM is significantly used for machining of advanced materials, like, quartz, glass, composites, ceramics, super alloys and many more. The current article incorporates a review of various parts of the ECDM process including previous background, process variants, affecting parameters with their impact and best in class crossover approaches for upgrading the machining execution. A brief about future trends in ECDM has additionally been addressed.

Keywords ECDM · NTM · ECM · EDM · Advanced materials · Optimization techniques

1 Introduction

Manufacturing processes are in existence since Stone Age and classified as conventional and non-conventional processes. In present revolutionary market, the non-conventional or non-traditional machining (NTM) processes have completely changed the perspective of manufacturing technology [1]. These processes are widely adopted in today's manufacturing environment because of their features of micro and nano-machining with high accuracy, productivity and close degree of tolerances [2].

Numerous micro components are highly demanding in today's market. Most of these components are fabricated by advanced non-conductive materials, such as, glass, ceramics, composites, quartz etc. [3]. Due to some inherent properties of these

D. Soni (✉) · B. D. Gidwani · R. Shringi
Rajasthan Technical University, Kota, Rajasthan 324010, India
e-mail: dheeraj.soni10@gmail.com

materials like hardness and brittleness, these materials cannot be machined with traditional machining processes. Sometimes failure of cutting tool, chattering action and decreased surface quality may also cause complexity in machining [4–7].

1.1 Brief about ECDM

Nowadays, ECDM is identified as one of the best NTM process, which is capable for micro machining of both conductive and non-conductive nature of materials. ECDM is a hybrid machining process [8] based on combined principle of ECM and EDM [9, 10]. A basic ECDM experimental setup is comprised of mainly two electrodes i.e. cathode and anode with an electrolyte tank for partial immersion of work piece in electrolyte up to a few millimetres.

A number of studies have been done for identifying discharge phenomenon in ECDM process. As per observations of researchers, different titles were suggested for ECDM process. The titles are enlisted as shown in Table 1.

Table 1 ECDM titles suggested by different researchers year-wise

Title for ECDM	Researcher and year
Electrical discharge drilling [11]	Kurafuji and Suda (1968)
Discharge machining for non-conductors [12]	Cook et al. (1973)
Electro chemical arc machining [13]	Kubota (1974)
Electro chemical arc wire-machining [14]	Hofy and McGeough (1988)
Electro erosion dissolution machining [15]	Khairy and McGeough (1989)
Electro chemical discharge machining [16]	Allesu et al. (1992)
Micro electrochemical discharge machining [17]	Langen et al. (1998)
Electro chemical spark machining [18]	Jain et al. (1999)
Spark assisted etching [19]	Daridon et al. (2001)
Spark assisted chemical engraving [20]	Langen et al. (2002)

1.2 ECDM Variants

There are number of ways for performing ECDM process. These different ways are known as variants of ECDM. These variants are characterized as per their utility in machining operation adopting principle of electrochemical discharge. These variants are broadly classified as electrochemical discharge drilling (ECDD), electrochemical discharge milling, electrochemical discharge turning (ECDT), electrochemical discharge dressing, wire electrochemical discharge machining (W-ECDM), die-sinking electrochemical discharge machining (DS-ECDM) and electrochemical discharge trepanning. These variants are listed in Fig. 1 along with their utility.

Out of number of variants, ECDD is widely adopted variant of ECDM used to produce high quality precise holes. However, there are variety of hole drilling processes, such as, diamond-wheel assisted grinding [21–25], ultrasonic machining [26–29], abrasive jet machining [30, 31], laser machining [32–35], but there are certain limitations for the use of these methods, like, higher cost of machining, expensive equipments, poor quality of machined surfaces, lower material removal rates and many more.

ECDD is broadly used to fulfill the demands of micro machining of variety of non-conductive materials, such as, borosilicate glass [36, 37], pyrex glass [38, 39], soda lime glass [40, 41], glass wafers [42], other glass [10, 11, 36, 43–46], silicon

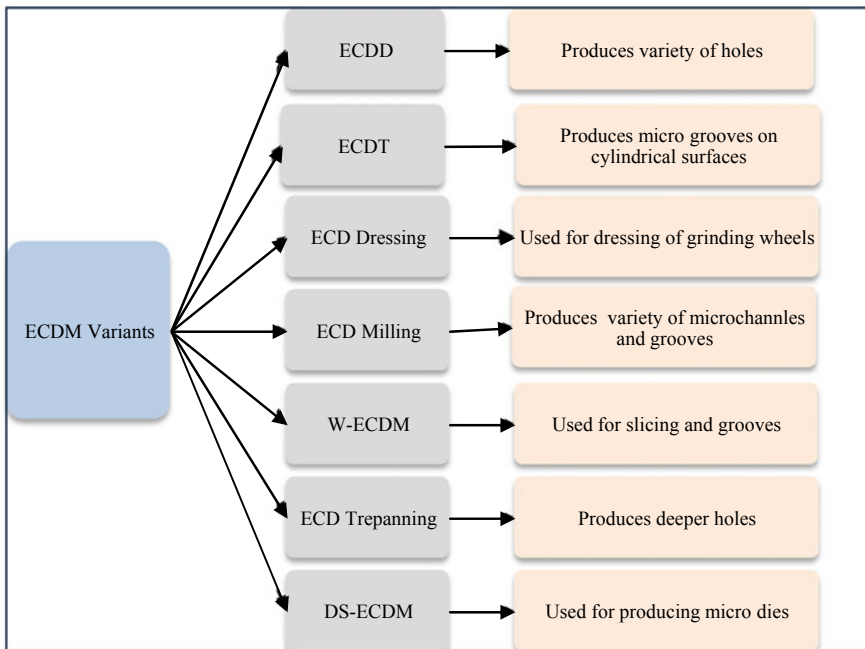


Fig. 1 Classification of ECDM variants with their utility

wafers [47], e-glass-fiber-epoxy composite [48], zirconia ceramics [26], silicon nitride ceramic [49, 50] and alumina ceramic [26, 51] and many more.

1.3 Domains of ECDM and Cause-Effect Diagram

Now days, ECDM is a trending technology and a huge number of researchers throughout the world are working for performance enhancement of this process. A huge number of researchers are working in different domains to carry out some possible outcomes, which will be helpful for commercialization of ECDM process. These domains may be in the terms of input parameters, response parameters, optimization tools and many more. The major identified domains are as shown in Fig. 2.

Process analysis always needs some initial inputs. Different studies in the field of ECDM were accomplished by taking into consideration different influencing parameters, which affect the process performance. Some parameters are highly affecting, while some have least effect on process performance. Through detailed analysis of previous studies, a number of impacting parameters are identified. These identified

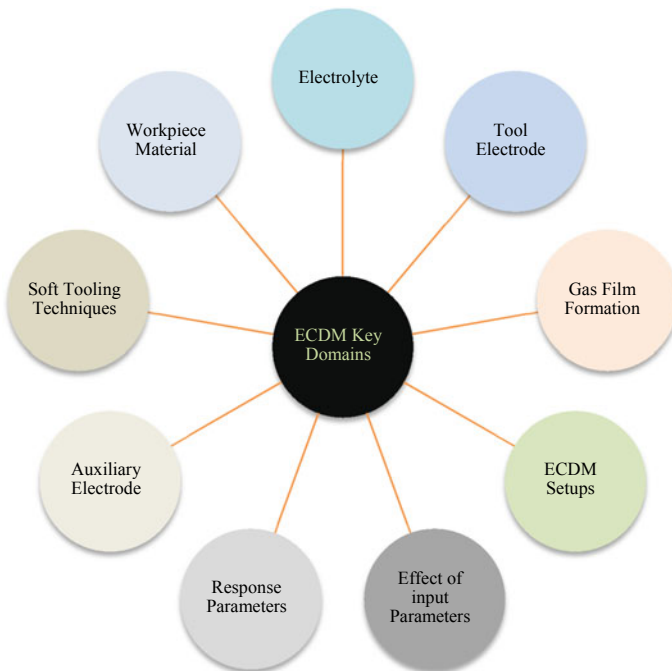


Fig. 2 Key domains of ECDM

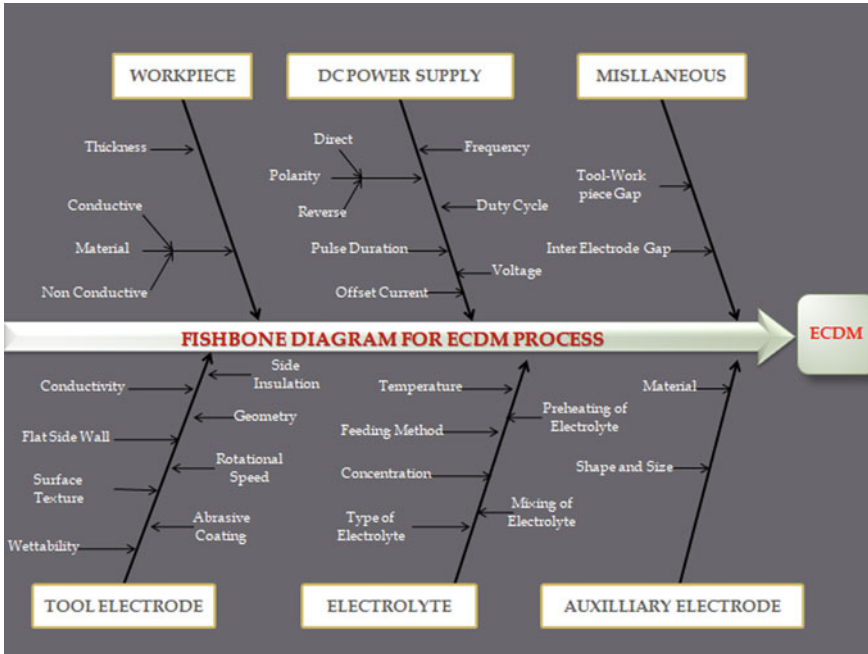


Fig. 3 Cause-effect (fishbone) diagram for ECDM

parameters have been listed in six major categories and represented by cause-effect (Fishbone) diagram as shown in Fig. 3.

2 Significance of Effective Process Parameters

Previous studies suggest that there are varieties of process parameters that regulate the process and have positive impact on performance of ECDM process. The process parameters are, such as, duty cycle, frequency, voltage, electrolyte parameters, tool electrode parameters and many more. These parameters have direct or indirect impact on response parameters of ECDM process. The major response parameters identified are, such as, material removal rate, heat affected zone, gas film formation, overcut, quality of surface, recast layer etc.

The present study deals with discussions about only electrolyte parameters, which have key role in ECDM process performance. The electrolyte parameters chosen for this study are types of electrolyte, electrolyte temperature and preheating, level of electrolyte in the tank and electrolyte flow.

2.1 Types of Electrolytes

The type of electrolyte has a major role in affecting machining performance [52]. The electrolytes are classified in three major parts i.e. acidic, neutral and alkaline. The selection is based on their stability and performance during machining process. However, out of these three varieties, alkaline electrolytes were used in most of the studies because of its observable improvement in machining performance in contrast to others. A fewer studies have also been reviewed showing the use of mixed electrolyte to improve process performance of ECDM [53–55]. Pure water was also used as an electrolyte because of its eco-friendliness and better performance [56]. Summary of literature related to use of different electrolytes and their effect on performance is as shown in Table 2.

Table 2 Summary of literature related to type of electrolytes and their effect

Type of electrolyte	Electrolyte used	Effect on performance of ECDM
Acidic electrolytes	H ₂ SO ₄ [66] HCl [67–69]	Incapable of machining glass effectively, incidence of unstable spark, reduced MRR, dimensional inaccuracy, generation of green spark
Neutral electrolytes	NaCl [54, 68, 70–73] KCl [66] NaNO ₃ [54, 70, 73]	Increased tool wear compared to the workpiece, negligible machining, poor surface roughness, cracks, non-hazardous for health, generation of red spark
Alkaline electrolytes	KOH [54, 69, 71, 72, 74, 75] NaOH [54, 68, 69, 73, 75–77] Na ₂ SiO ₃ [78, 79]	Stable spark, high spark intensity and etching rate, increased MRR compared to acidic and neutral electrolyte, negligible TWR, smooth surface finish, high thermal energy
Mixed electrolytes	NaOH + KOH [53–55]	Improved MRR, surface quality and dimensional accuracy
Water	Pure water [56]	Eco-friendly and economical
Electrolyte mixed with surfactant (soap solution)	NaOH + Soap solution [80] Surfactant added [81–83]	Improved MRR, reduced HAZ and overcut
Powder or abrasive particle mixed electrolytes	Graphite powder mixed [84, 85]	Reduction in breakdown voltage and peak current, reduced micro cracks, improvement in surface roughness

2.2 *Electrolyte Temperature*

Temperature of electrolyte is one of the impacting parameters having noticeable effect on machining performance. ECDM process is completely based on sparking action and further, sparking action is dependent on thermal conductivity of the electrolyte. The principle of ECDM suggests that the process performance can be improved with improving thermal conductivity of electrolyte and it is directly affected by its temperature.

Numbers of studies have been reviewed which show positive impact of electrolyte temperature on machining performance. Higher material removal rates and machining depth were also observed with increased electrolyte temperature [9]. Ladeesh and Manu [57] in their study for drilling process observed impact of increased temperature of electrolyte. They reported reduced micro cracks with smooth surface quality at high electrolyte temperature. The experiments were performed with range of temperature varying from 30° to 70° and reported increase MRR from 0.01 to 0.06 g/min. Lijo and Kurian [58] observed the effect of preheating of electrolyte by heating electrolyte at various temperature ranges. The study reported reduced spark intensity at high temperature but resulting in increased heat-affected zones (HAZ). Therefore, the study concluded that optimized value of temperature is always preferable.

2.3 *Electrolyte Level*

The electrolyte level in the electrolyte storage chamber is a crucial factor affecting discharge or sparking action while performing ECDM process. This is the key challenge for researcher working with ECDM to maintain the prescribed limit of electrolyte level. This is only the parameter, which affects machining results. The immersion of tool electrode in the electrolyte tank is only up to 1–2 mm. However, it's difficult task to maintain this level because of continuous evaporation of electrolyte due to sparking action [59].

This parameter decides the surface area of tool electrode in contact with electrolyte. Surface area is also an indicative parameter for formation of gas film around tool electrode. High electrolyte level indicates larger surface area in contact requiring larger quantity of gas bubbles to cover up electrode surface. This phenomenon results in decreased machining efficiency with unstable gas film formation [60]. On the other hand, a study reported that at lower electrolyte level, the tool contact within the electrolyte is minimum, resulting in quick gas film formation causing high current density with stable gas film formation and reduced machining time [61].

Arya and Divedi [37] in their study concluded about importance of injection of fresh electrolyte during machining process.

They studied about micro hole drilling process to investigate effect of vaporized electrolyte. They employed tubular electrode for supplying fresh electrolyte with

accurately controlled electrolyte flow rate (EFR) into the machining zone. The study observed improvement in machining performance with injection of fresh electrolyte. Thus, it can be concluded that if level of electrolyte is properly maintained, machining performance can be improved effectively.

2.4 Electrolyte Flow

Flow of electrolyte is a highly considerable parameter, which directly affects the machining performance. This parameter directly affects the machining performance and surface quality. This parameter is highly considerable especially for deep hole drilling operation using ECDM because of build-up of by-products produced during machining at surface of the workpiece causing obstruction in smooth machining.

Numbers of researchers are working for improvement of flow of electrolyte in machining zone. Mehrabi et al. [62] in their study for ECD machining of B270-Optical glass reported major issues in machining during deep hole drilling process. The study observed limited electrolyte circulation at deeper depths resulting in improper sparking action. For such kind of problems, hollow electrode with high-pressure electrolyte injection system has proven to be best choice to produce deep holes. Use of this system also reported improved MRR and drilling speed. Dhanvijay and Ahuja [63] in their study for micro drilling of alumina, reported improvement in MRR by 40% with proper circulation of electrolyte in comparison to stagnated electrolyte. Simultaneously, higher dimensional accuracy was also observed. Ansari et al. [64] made experimental investigations on stirring assisted ECDM to investigate machining performance of micro channels machined on borosilicate glass. The study observed improved machining performance with better surface quality. Several studies [36, 44, 65] also reported the significant effect of flushing of electrolytes for proper flow in machining zone.

3 Research Potential and Future Scopes

Although there have been broad discussions made by the research fraternity working in the domain of ECDM. However, there are huge scopes to explore process capabilities of ECDM process. From the reviewed literature, it can be concluded that still there are some domains of ECDM that are untouched and needed to be explored in future. Even after extensive research in the domain of spark analysis, gas film formation and material removal, there concluding results are still not particular. However, other responses related to ECDM, such as, HAZ, recast layer, overcut are required to be investigated further in depth for achieving better outcomes.

Through literature review, it is identified that maximum studies were done for machining of non-conductive materials, such as, quartz and glass and least studies were done using other materials such as, composites, e-glass fiber epoxy, ceramics

etc. These materials are needed to be examined in depth by varying different input parameters.

From the available literature it is identified that the alkaline electrolytes are found to perform better than other electrolytes and mostly studies were made with use of these electrolytes although these are non-eco-friendly and hazardous for health and environment. Therefore, extensive analysis is needed to explore some better alternative, which is eco-friendly and safe for health also.

The literature review shows that there are number of variants of ECDD but most of studies are focused on ECDD. On the other hand, least studies are focused on ECD milling, ECD turning, ECD grinding, die sinking ECDD. As these are high potential areas, more studies are needed to be focused in these areas.

Due to level of complexities in machining process using ECDD this process is not commercialized. This process is confined to laboratory experimentations only. More comprehensive studies are needed in this unexplored field to make it possible to commercialize this process for industrial requirements.

4 Conclusions

Based on literature survey, a detailed analysis of ECDD process has been covered in the present article. The major highlights covered are, introduction to NTM, ECDD along with its variants, key domains and affecting parameters, detailed note on electrolyte parameters are elaborated. Significance of different electrolyte parameters has been discussed, such as, types of electrolytes, electrolyte temperature and preheating, electrolyte level, electrolyte flow etc. Major conclusive remarks from this comprehensive study are as follows:

- The beauty of ECDD process is not only because of its capability to machine both conductive and non-conductive materials but it executes machining process without any intermediate process pattern making or sample preparation etc.
- ECDD is the only NTM capable of machining non-conductive materials with precision and exactness.
- Variety of ECDD variants are available that are capable of machining different micro machining operations regardless of material conductivity.
- Nature of electrolyte used significantly affects the machining quality and efficiency in ECDD process. Electrolyte of alkaline nature is identified as the best choice in comparison to neutral and acidic electrolyte. Use of mixture of electrolyte also reported significant improvement in machining performance. Addition of sodium dodecyl sulphate (SDS) surfactant and abrasive particles with electrolyte also contributes in improved machining performance.
- Role of temperature of electrolyte is a crucial factor affecting machining quality. Optimized results can be obtained with either in process heating of electrolyte or with use of preheated electrolyte.

- Level of electrolyte in electrolyte tank should be maintained in a prescribed limit to achieve better machining results and this can be achieved through supply of fresh electrolyte by a tubular electrode in the machining zone.
- Proper electrolyte circulation in the machining zone affects surface quality of ECDM process. This can be achieved with the some of the arrangements, such as, high-pressure electrolyte injection system and stirring assisted ECDM process.

References

1. EMT-2531, Manufacturing technology II (2018). <https://www.studocu.com/en/document/jomo-kenyatta-university-of-agriculture-and-technology/mechatronics-engineering/summaries/chp1-overview/4812893/view>
2. McGeough JA (1988) Advanced methods of machining. Chapman and Hall, London.
3. Temiz Y, Lovchik RD, Kaigala GV, Delamarche E (2015) Lab-on-a-chip devices: how to close and plug the lab? *Microelectron Eng* 132:156–175
4. Qin Y et al (2010) Micro-manufacturing: research, technology outcomes and development issues. *Int J Adv Manuf Technol* 47:821–837
5. Uhlmann E et al (2016) Process chains for high-precision components with micro-scale features. *CIRP Ann* 65:549–572
6. Vipindas K, Kuriachen B, Mathew J (2019) Investigations into the effect of process parameters on surface roughness and burr formation during micro end milling of Ti–6Al–4V. *Int J Adv Manuf Technol* 100:1207–1222
7. Xun LI, Chunming G, Peng Z (2018) Influences of milling and grinding on machined surface roughness and fatigue behavior of GH4169 superalloy workpieces. *Chin J Aeronaut* 31:1399–1405
8. Haerberle S, Zengerle R (2007) Microfluidic platforms for lab-on-a-chip applications. *Lab Chip* 7:1094–1110
9. Jain VK, Choudhury SK, Ramesh KM (2002) On the machining of alumina and glass. *Int J Mach Tools Manuf* 42:1269–1276
10. Gupta PK, Dvivedi A, Kumar P (2016) Effect of pulse duration on quality characteristics of blind hole drilled in glass by ECDM. *Mater Manuf Processes* 31:1740–1748
11. Kurafuji H, Suda K (1968) Electrical discharge drilling of glass. *Ann CIRP* 16:415–419
12. Cook NH, Foote GB, Jordan P, Kalyani BN (1973) Experimental studies in electro-machining
13. Kubota M (1974) Drilling of steel by using Electro-chemical Discharge Machining. In: *Proceedings of the international conference on production engineering, Tokyo*, pp 51–55
14. El-Hofy H, McGeough JA (1988) Evaluation of an apparatus for electrochemical arc wire-machining
15. Khairy ABE (1989) *Die-Sin King* 3:191–195
16. Allesu K, Ghosh A, Wuju HK (1991) Preliminary qualitative approach of a proposed mechanism of material removal in electrical machining of glass. *Eur J Mech Environ Eng* 36:201–207
17. Langen H, Breguet J-M, Bleuler H, Renaud P, Masuzawa T (1998) Micro electrochemical discharge machining of glass. *Int J Electr Mach* 3:65–69
18. Jain V, Dixit PM, Pandey P (1999) On the analysis of the electrochemical spark machining process. *Int J Mach Tools Manuf* 39:165–186
19. Daridon A et al (2001) Multi-layer microfluidic glass chips for microanalytical applications. *Fresenius' J Anal Chem* 371:261–269
20. Lange H, Fascio V, Wüthrich R, Viquerat D (2002) Three-dimensional structuring of Pyrex glass devices—Trajectory control. In: *International conference on European society for precision engineering and nanotechnology (EUSPEN)*, vol 2

21. Malkin S, Ritter JE (1989) Grinding mechanisms and strength degradation for ceramics
22. Rezaei SM, Suto T, Waida T, Noguchi H (1992) Creep feed grinding of advanced ceramics. *Proc Inst Mech Eng Part B: J Eng Manuf* 206:93–99
23. Koenig W, Popp M (1989) Precision machining of advanced ceramics. 68:550–553
24. Inasaki I, Nakayama K (1986) High-efficiency grinding of advanced ceramics. *CIRP Ann Manuf Technol* 35:211–214
25. Koenig W, Wemhoener J (1989) Optimizing grinding of SiSiC. *Am Ceram Soc Bull* 68:545–548
26. Anantharamu B, Krishnamurthy R, Gokularathnam CV (1989) Machining performance of toughened zirconia ceramic and cold compact alumina ceramic in ultrasonic drilling. *J Mech Work Technol* 20:365–375
27. Kremer D, Saleh SM, Ghabrial SR, Moisan A (1981) The state of the art of ultrasonic machining. *Cirp Ann-Manuf Technol* 30:107–110
28. Pei ZJ, Ferreira P, Kapoor SG, Haselkorn M (1995) Rotary ultrasonic machining for face milling of ceramics. *Int J Mach Tools Manuf* 35:1033–1046
29. Pei ZJ, Ferreira P, Haselkorn M (1995) Plastic flow in rotary ultrasonic machining of ceramics. *J Mater Process Technol* 48:771–777
30. Hamatani G, Ramulu M (1990) Machinability of high temperature composites by abrasive waterjet. *Journal of Engineering Materials and Technology-transactions of The Asme - J ENG MATER TECHNOL* 112, (1990).
31. Wada S, Kiyoshige M (1992) Erosion and abrasive water jet cutting of ceramics. *Ceramics Jpn* 27:970–974
32. Deng QL, Zhang YK; Tang YX, CYY (1994) Micro-crack reduction and removal in ceramic laser machining. *Electromachining* 3:2–4
33. Wallace R, Copley S, Bass M (1985) Laser machining of silicon nitride. <https://doi.org/10.1364/CLEO.1985.FP2>
34. Wallace RJ, Copley SM (1989) Shaping silicon nitride with a carbon dioxide laser by overlapping multiple grooves
35. Miyazaki T (1992) Laser machining of ceramics. *Bull Ceram Soc Jpn* 27:975–980
36. Abou Ziki JD, Wüthrich R (2013) Forces exerted on the tool-electrode during constant-feed glass micro-drilling by spark assisted chemical engraving. *Int J Mach Tools Manuf* 73:47–54
37. Arya RK, Dvivedi A (2019) Investigations on quantification and replenishment of vaporized electrolyte during deep micro-holes drilling using pressurized flow-ECDM process. *J Mater Process Technol* 266:217–229
38. Kim DJ, Ahn Y, Lee SH, Kim YK (2006) Voltage pulse frequency and duty ratio effects in an electrochemical discharge microdrilling process of Pyrex glass. *Int J Mach Tools Manuf* 46:1064–1067
39. Zheng Z-P, Su H-C, Huang F-Y, Yan B-H (2007) The tool geometrical shape and pulse-off time of pulse voltage effects in a Pyrex glass electrochemical discharge microdrilling process. *J Micromech Microeng* 17:265
40. Paul L, Hiremath SS (2013) Response surface modelling of micro holes in electrochemical discharge machining process. *Procedia Eng* 64:1395–1404
41. Goud M, Sharma AK (2016) Analysis of material removal and radial overcut during micro-drilling of soda lime glass using electrochemical discharge machining (ECDM). 213–217
42. Zheng ZP, Lin JK, Huang FY, Yan BH (2008) Improving the machining efficiency in electrochemical discharge machining (ECDM) microhole drilling by offset pulse voltage. *J Micromech Microeng* 18
43. Wüthrich R, Spaelter U, Wu Y, Bleuler H (2006) A systematic characterization method for gravity-feed micro-hole drilling in glass with spark assisted chemical engraving (SACE). *J Micromech Microeng* 16:1891–1896
44. Abou Ziki JD, Wüthrich R (2015) Nature of drilling forces during spark assisted chemical engraving. *Manuf Lett* 4:10–13
45. Wüthrich R, Despont B, Maillard P, Bleuler H (2006) Improving the material removal rate in spark-assisted chemical engraving (SACE) gravity-feed micro-hole drilling. *J Micromech Microeng* 16:N28

46. Gupta P, Dvivedi A, Kumar P (2014) A study on the phenomenon of hole overcut with working gap in ECDM. *J Prod Eng* 17:30–34
47. Paul L, Hiremath SS, Jinka R (2014) Experimental investigation and parametric analysis of electro chemical discharge machining. *Int J Manuf Technol Manage* 28:57–79
48. Manna A, Narang V (2012) A study on micro machining of e-glass-fibre-epoxy composite by ECDSM process. *Int J Adv Manuf Technol* 61:1191–1197
49. Sarkar BR, Doloi B, Bhattacharyya B (2006) Parametric analysis on electrochemical discharge machining of silicon nitride ceramics. *Int J Adv Manuf Technol* 28:873–881
50. Shanmukhi K, Vundavilli PR, Surekha B (2015) Modeling of ECDM micro-drilling process using GA- and PSO-trained radial basis function neural network. *Soft Comput* 19:2193–2202
51. Chak SK, Venkateswara Rao P (2008) The drilling of Al_2O_3 using a pulsed DC supply with a rotary abrasive electrode by the electrochemical discharge process. *Int J Adv Manuf Technol* 39:633–641
52. Zhang Z et al (2016) A study to explore the properties of electrochemical discharge effect based on pulse power supply. *Int J Adv Manuf Technol* 85:2107–2114
53. Charak A, Jawalkar CS (2017) Technological landscaping on electro chemical discharge machining of non-conducting materials. *i-Manager's J Mater Sci* 5:31
54. Sabahi N, Razfar MR (2018) Investigating the effect of mixed alkaline electrolyte (NaOH + KOH) on the improvement of machining efficiency in 2D electrochemical discharge machining (ECDM). *Int J Adv Manuf Technol* 95:643–657
55. Dhanvijay MR, Kulkarni VA, Doke A (2019) Experimental investigation and analysis of electrochemical discharge machining (ECDM) on fiberglass reinforced plastic (FRP). *J Inst Eng (India): Ser C* 100:763–769
56. Huang S, Liu Y, Li J, Hu H, Sun L (2014) Electrochemical discharge machining micro-hole in stainless steel with tool electrode high-speed rotating. *Mater Manuf Process* 29
57. Ladeesh VG, Manu R (2019) Grinding-aided electrochemical discharge drilling in the light of electrochemistry. *Proc Inst Mech Eng C J Mech Eng Sci* 233:1896–1909
58. Paul L, Kurian DG (2018) Effects of preheating electrolyte in micro ECDM process. *Mater Today: Proc* 5:11882–11887
59. Liu JW, Yue TM, Guo ZN (2010) An analysis of the discharge mechanism in electrochemical discharge machining of particulate reinforced metal matrix composites. *Int J Mach Tools Manuf* 50:86–96
60. Han MS, Min BK, Lee SJ (2008) Modeling gas film formation in electrochemical discharge machining processes using a side-insulated electrode. *J Micromech Microeng* 18
61. Cheng C-P et al (2010) Study of gas film quality in electrochemical discharge machining. *Int J Mach Tools Manuf* 50:689–697
62. Mehrabi F, Farahnakian M, Elhami S, Razfar MR (2018) Application of electrolyte injection to the electro-chemical discharge machining (ECDM) on the optical glass. *J Mater Process Technol* 255:665–672
63. Dhanvijay M, Ahuja BB (2014) Micromachining of ceramics by electrochemical discharge process considering stagnant and electrolyte flow method. *Procedia Technol* 14:165–172
64. Ansari F, Sharma AK, Karunakar DB (2013) Experimental investigations on stirring assisted electrochemical discharge machining. *i-Manager's J Mech Eng* 3:16
65. Ziki JDA, Wüthrich R (2012) Tool wear and tool thermal expansion during micro-machining by spark assisted chemical engraving. *Int J Adv Manuf Technol* 61:481–486
66. Yang CT, Ho SS, Yan BH (2001) Micro hole machining of borosilicate glass through electrochemical discharge machining (ECDM). In: *Key engineering materials*, vol 196. Trans Tech Publications, pp 149–166
67. Kulkarni A, Sharan R, Lal GK (2002) An experimental study of discharge mechanism in electrochemical discharge machining. *Int J Mach Tools Manuf* 42:1121–1127
68. Nandi D, Puri AB, Basak I (2011) Behaviour of bubbles generated in electro-chemical. *Int J Eng Sci* 3:8274–8280
69. Raghuram V, Pramila T, Srinivasa YG, Narayanasamy K (1995) Effect of the circuit parameters on the electrolytes in the electrochemical discharge phenomenon. *J Mater Process Tech* 52:301–318

70. Crichton IM, McGeough JA (1985) Studies of the discharge mechanisms in electrochemical arc machining. *J Appl Electrochem* 15:113–119
71. Basak I, Ghosh A (1997) ISM of material removal in electrochemical machining: a theoretical model and experiment. *J Mater Process Technol* 71:350–359
72. Ghosh A (1997) Electrochemical discharge machining: Principle and possibilities. *Sadhana* 22:435–447
73. Bhattacharyya B, Doloi BN, Sorkhel SK (1999) Experimental investigations into electrochemical discharge machining (ECDM) of non-conductive ceramic materials. *J Mater Process Technol* 95:145–154
74. Tang L, Zhao G (2012) Discussing the measure of improving Pyrex glass ECDM removal rate. *Adv Mater Res* 411:319–322
75. Cao XD, Kim BH, Chu CN (2009) Micro-structuring of glass with features less than 100 μm by electrochemical discharge machining. *Precis Eng* 33:459–465
76. Gautam N, Jain VK (1998) Experimental investigations into ECSD process using various tool kinematics. *Int J Mach Tools Manuf* 38:15–27
77. Wüthrich R, Fujisaki K, Couthy P, Hof LA, Bleuler H (2005) Spark assisted chemical engraving (SACE) in microfactory. *J Micromech Microeng* 15
78. Coteata M, Slatineanu L, Dodun O, Ciofu C (2008) Electrochemical discharge machining of small diameter holes. *Int J Mater Form* 1:1327–1330
79. Coteață M, Schulze HP, Slătineanu L (2011) Drilling of difficult-to-cut steel by electrochemical discharge machining. *Mater Manuf Processes* 26:1466–1472
80. Wüthrich R, Hof LA (2006) The gas film in spark assisted chemical engraving (SACE)—A key element for micro-machining applications. *Int J Mach Tools Manuf* 46:828–835
81. Jiang B, Ni J (2016) Micro-machining of glass using electrochemical discharge assisted cutting. In: ASME 2016 11th international manufacturing science and engineering conference, MSEC 2016, vol 1, pp 1–6
82. Laio YS, Wu LC, Peng WY (2013) A study to improve drilling quality of electrochemical discharge machining (ECDM) process. *Procedia CIRP* 6:609–614
83. Wüthrich R, Fascio V, Bleuler H (2004) A stochastic model for electrode effects. *Electrochim Acta* 49:4005–4010
84. Han MS, Min BK, Lee SJ (2007) Improvement of surface integrity of electro-chemical discharge machining process using powder-mixed electrolyte. *J Mater Process Technol* 191:224–227
85. Varghese A, Paul L (2018) Effect of powder mixed electrolyte in ECDM Process. *Mater Today: Proc* 5:11864–11869

Optimization of AWJM Process on Processing of Lite Bamboo Reinforced Polymer Composite by Using Grasshopper Algorithm



Sathish Kumar Adapa , Jagadish , Sagar Yanda ,
and Siva Sankara Raju 

Abstract Green composites are extensively used in wide range of applications like construction, textiles, packaging, automobile, and aerospace industries etc. due to their unique chemical and mechanical properties. This paper presents study and optimization of abrasive water jet machining (AWJM) process on processing of lite bamboo reinforced polymer (LBRP) composites by using grasshopper optimization algorithm (GOA). Further, the experimentation is performed based on Taguchi (L-9) orthogonal array to assess the AWJM processing variables like material removal rate (MRR) and surface roughness (SR) to changes in the independent variables like stand of distance (SOD), nozzle speed (NS), working pressure (WP). In addition, grasshopper optimization (GOA) is used to optimize the AWJM process variables on machining of LBRP composites. At last, parametric analysis is done to predict the statistical significance of independent variables on dependent variables of AWJM process. The optimum process variable setting is obtained exp. No. 9 with optimal condition is SOD as 1.5 mm WP as 150 Mpa and NS as 150 mm/min and the corresponding response conditions are obtained as MRR is 58.442 g/s, and SR is 0.169 μm . Parametric analysis results show that the process variables SOD and NS are most influencing variables on MRR and SR of AWJM process on LBRP composite.

Keywords LBRP composites · AWJM · Taguchi method · Optimization · Parametric analysis

S. K. Adapa (✉) · Jagadish · S. Yanda
Department of Mechanical Engineering, National Institute of Technology (NIT), Raipur-492010
Chhattisgarh, India
e-mail: adapa.satish3@gmail.com

S. K. Adapa · S. Yanda · S. S. Raju
Department of Mechanical Engineering, Aditya Institute of Technology and Management,
Tekkali, India

1 Introduction

In the current scenario manufacturing industries want to produce their products with superior quality, flexibility, durability, less in cost and high production throughput. However, the conventional machining process having certain limitations such as high rate of wear, heat affected zone (HAZ), residual stresses, production time and cost. The unconventional machining processes are one among the different manufacturing processes to overcome the issues present in conventional machining process. In addition, the work piece and tool both are non-contact to each other so that the HAZ is less and major concern in case of Non-traditional machining process. Moreover, green composites are extensively used in variety of applications due to their admirable properties like light in weight, ecofriendly, and bio-degradable, abundantly available, most economical [1]. Most of the researchers reported their research work on natural fibers processing, manufacturing, and characterization by using various manufacturing techniques, in this way NaoH solution treatment of wood saw dust natural reinforced polymer composite, enhance the mechanical properties like tensile strength, compressive strength, and specific modulus [2].

Moreover, earlier researchers have been reported some research work on bamboo fiber reinforced polymer composites. The mechanical properties like compressive, tensile, impact strength, and fracture toughness of pure bamboo fiber reinforced composite drastically effect when the fibers contain moisture [3]. In addition, mechanical properties of the bamboo fiber reinforced composite increases with alkali treatment [4, 5]. Also 10% NaoH solution and 40 wt% fiber compositions in 48 h of bamboo reinforced polymer composite produce better thermo-mechanical properties as compared to untreated bamboo fibers [6]. Furthermore, the culm wall thickness of the bamboo is significantly influencing the mechanical and physical properties. It is critical to evaluate the impact of machining settings and tool shape on remnant tensile strength and spalling damage in numerous industries and structural applications [7].

Additionally, the AWJM method has a higher material removal rate for cutting of non-conductive and ductile materials [8, 9].

Furthermore, some extent of research work has been done on machining characteristics of natural fiber reinforced polymers by using traditional and non-traditional machining processes [10–12]. However, there is a limited work on machining of LBRP composites using AWJM process. In this paper explored machinability properties of AWJM process on LBRPC based on Taguchi design. Further, the impact of process variables on response variables of AWJM process is evaluated via parametric and ANOVA statistical models. Finally, optimal process parameters setting is identified based on grasshopper optimization algorithm (GOA). The rest of the article is segregated as per the various Stages of experiment.

2 Materials and Machine-Setup Details

2.1 Specimen Preparation

In this study, the reinforcement material is lite bamboo reinforced polymer (LBRP), which has a density of 1442 kg/m^3 . At first, the lite bamboo stems are separated from the plant, with the fibers peeled out cleaned with distill water and dried in the sun for about a week [13]. The lite bamboo fiber is powdered and mixed with the matrix. cellulose, lignin, and ash are the three main components of LBF [14]. With an Epoxy density of 1230 kg/m^3 , the hardener (HY 951) has a density of 840 kg/m^3 , and these two materials are blended in a 10:8 weight ratio. 5% LBRP is added to this mixture and mechanically agitated until a homogeneous mixture is achieved [14]. After that, the slurry is poured into the mold within the vacuum glass chamber and left to cure at room temperature for two days. The $160 \text{ mm} \times 120 \text{ mm} \times 6 \text{ mm}$ specimen obtained as shown in Fig. 1, and then taken for additional machining [9].

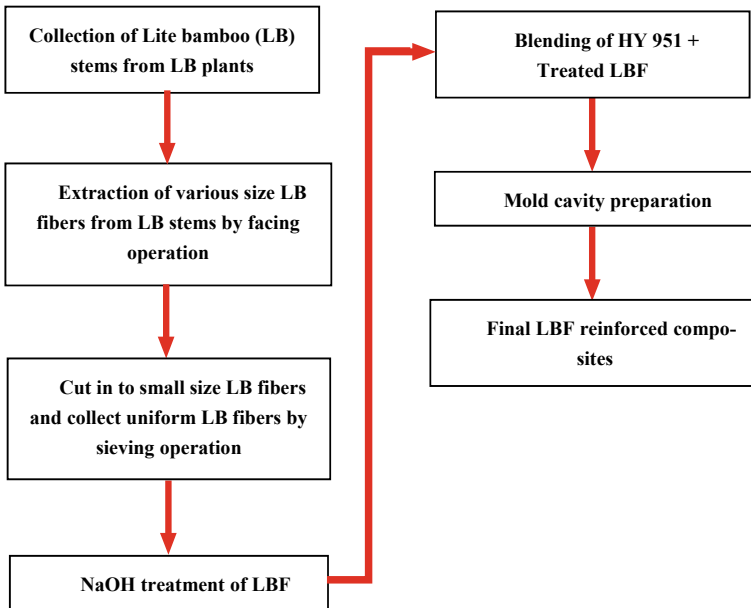


Fig. 1 Flow chart of processing and manufacturing of LBRP composite

2.2 Experimental Details

A CNC abrasive water jet cutting machine supplied by DARDI International Corporation in China was used to machine the LBRP composite with a maximum water pressure of 3800 bar, the discharge rate and orifice diameter are limited to 2.31 L per minute and 0.25 mm respectively. During the experiment, square holes of 20 mm × 20 mm were cut from an LBRP composite with dimensions of 180 mm 140 mm 6 mm [9]. The experiment was repeated three times for each set of parameter settings in accordance with the Taguchi design, with the average values used to calculate the material removal rate (MRR) and surface roughness (SR) (shown in Table 1) to get

Table 1 Investigation results of AWJM process on LBRP composite

Exp. No.	SOD (mm)	WP (Mpa)	NS (mm/min)	MRR (grm/s)	SR (μm)
1	0.5	50	100	04.132	0.142
2	0.5	100	150	13.541	0.135
3	0.5	150	200	31.816	0.167
4	1	50	150	27.743	0.129
5	1	100	200	53.237	0.133
6	1	150	100	19.432	0.176
7	1.5	50	200	69.552	0.161
8	1.5	100	100	27.367	0.101
9	1.5	150	150	58.442	0.169

precise out values with minimum percentage of errors obtained. The surface profile meter is used to examine the SR of the work piece and MRR is to be calculated by using the following Eq. (1) [15].

$$\text{MRR} = \frac{M_b - M_a}{T} \quad (1)$$

where, M_b and M_a represents mass of the work specimen before and after machining, whereas T indicates time taken for machining operation.

2.3 Grasshopper Optimization Algorithm (G.O.A)

Grasshopper Optimization Algorithm (GOA) is a modern swarm intelligence algorithm inspired by the foraging and swarming behavior of grasshoppers in nature. The GOA is extensively used to solve various optimization problems. The algorithm is basically inspired by long range and moment of adult grasshopper in a group. GOA is a population-based metaheuristic algorithm and divided in to two search spaces i.e.,

exploration and exploitation [16]. The following steps and metaheuristic equations are used in this algorithm.

Step-1: Determine the position of the grass hopper.

The grasshopper position is denoted by P_i and determined by using the following Eq. (2)

$$P_i = R_i + T_i + W_i \tag{2}$$

where R_i represents social communication, T_i is the attraction due to gravity, W_i indicates wind avocation.

Step-2: Calculate the social communication initialize parameter (R_i).

The movement of grasshopper and social communication parameter is identified based on the Eq. (3)

$$R_i = \sum_{j=1}^n k(l_{ij})\hat{l}_{ij} \tag{3}$$

where l_{ij} is the gap between i th grasshopper and j th grasshopper, n is the number of grasshoppers, k represents the function of social force and it is calculated by using the following Eq. (4)

$$k(r) = f e^{\frac{-r}{l}} - e^{-r} \tag{4}$$

where f shows the attraction intensity and l indicates length scale of the attractiveness. Regardless of the function k 's qualities, it cannot apply powerful forces between grasshoppers separated by great distances. This problem can be solved by mapping or normalizing the distance between grasshoppers [17].

Step-3: Determine the gravitational force component (T_i)

The gravitational force component of the i th grasshopper is calculated by using the Eq. (5)

$$T_i = g\hat{e}_g \tag{5}$$

where g is the gravitational constant, \hat{e}_g shows the unity vector in the wind direction.

Step-4: Adding search space parameters A stochastic method must effectively explore and exploit to construct a precise assessment of the target value for addressing optimization problems. Experimentation and exploitation should be shown in the numerical method above. The mathematical model proposed is denoted by the following Eq. (6) [18].

$$P_i^d = c \left(\sum_{j=1}^n c \frac{um_d - lm_d}{d_{ij}} \right) k \left(|p_i^d - p_j^d| \frac{p_j - p_i}{d_{ij}} \right) + \hat{N}_d \tag{6}$$

where P_i = Position of the i th grasshopper, d_{ij} = Normalize distance between i th and j th grasshoppers, um_d is upper boundary of the d th dimension, lm_d lower boundary of the d th dimension $k(r) = fe^{-\frac{r}{l}} - e^{-r}$, the value of d th dimension of the target (best solution) is represented by \hat{N}_d , and the lowering coefficient c reduces the comfort zone, repulsion zone, and attraction zone.

3 Results and Discussion

3.1 Optimization of AWJM Process Variables

Optimization of AWJM process variables is done using GOA optimization approach. Work considered process variables like SOD, WP, and NS while MRR and SR treated as response variables of AWJM process on 5% of LBRP composite. Firstly, the grasshopper position is to be calculated by using Eq. (2) which includes social communication of the grasshoppers and attraction force due to gravity and wind avocation values. Finally, the search space parameters are added to the position of the grasshopper to obtain the best solution among the nine trail runs as shown in the Table 2.

The ranking results show that, exp. No. or trail run No. 9 is obtained the highest value of P_i as 1.3564 among the other and trail run 9 is to considered as optimal process variable setting for AWJM process on 5% LBRP composite. The optimal process variables setting is obtained as SOD as 1.5 mm, WP as 150 Mpa, and NS

Table 2 GOA optimization results of AWJM process on LBRP composite

Exp. No.	Fiber composition (%)	P_i values	Rank
1	5%	0.2371	9
2		0.5934	8
3		0.9361	5
4		0.7262	7
5		1.1926	3
6		0.7517	6
7		1.2663	2
8		0.9876	4
9		1.3564	1

1.3564 value has rank 1 i.e., Exp. No. 9 produces the best results as compared to others and the parameters of Exp. No 9 is said to be the optimal parameter setting of the AWJM process

as 150 mm/min with corresponding out variables MRR as 58.442 g/s and SR as 0.169 μm . The optimal process variables setting obtained via GOA optimization provides better output results of AWJM process on LBRP composite with superior quality and higher production throughput.

3.2 Parametric Statistical Analysis

The effect of process variables like SOD, WP, and NS on response variable MRR of AWJM process on LBRP composite as shown in Fig. 2. The input parameters SOD and NS influence positively and NS impacts moderately. This is due to fact that SOD increases, then the abrasive particles contact more area of the work piece result in higher MRR, whereas NS increases then the kinetic energy of the abrasive particles also increases result in higher MRR is attained. This is notified that the process variables SOD, WP, and NS are significantly impact on output variable MRR of AWJM process on LBRP composite [19].

Moreover, the influence of process variables SOD, WP, NS on output variables SR of AWJM process on LBRP composite as shown in Fig. 3. The input variable SOD increases then the output variable SR decreases significantly. This is due to fact that the abrasive particles contact area on the workpiece increases result in better SR is obtained. In case of WP increases from 50 to 100 Mpa SR decreases from 0.144 μm to 0.123 μm and then WP increases from 100 to 150 Mpa SR increases significantly from 0.123 to 0.170 μm due to the reason that the medium values of WP particles impact on the work piece is less result in better SR values are attained. In case of NS on output variable SR is greatly impacted. This is because as the value of NS increases the kinetic energy of the abrasive particles also increases result in higher MRR with lower SR is obtained [20].

Fig. 2 Effect plots of process variables on MRR

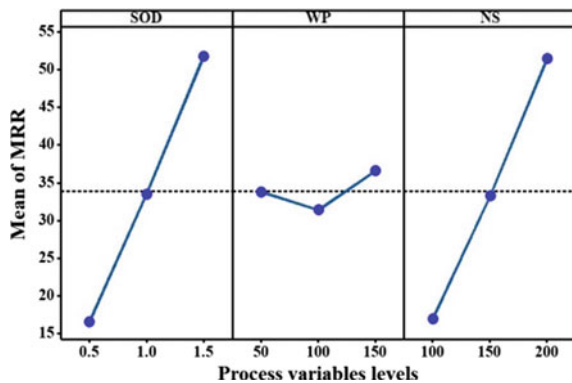


Fig. 3 Effect plots of process variables on SR

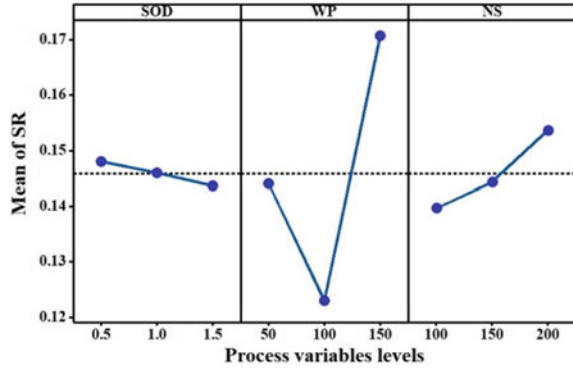


Table 3 Confirmatory test results

S. No.	Output variables	Input variables			Exp. results	Confirmatory results
		WP (Mpa)	SOD (mm)	NS (mm/min)		
1	SR	150	1.5	150	0.169	0.158
2	MRR	150	1.5	150	58.442	61.384

3.3 Confirmatory Tests

Confirmatory tests are conducted to validate the GOA results with experimental results are shown in the Table 3. The results show that, the experimental values and confirmatory values are almost all similar and acceptable. The optimal process variable setting provides optimal output results of AWJM process on LBRP composite.

4 Conclusions

This investigation explored LBRP composite applications and machinability properties of AWJM process. Optimization of process variables of AWJM process is done using GOA optimization process. Experimentation carried out considering three process variable SOD, WP, and NS while response variables taken as MRR and SR of the AWJM process on 5% LBRP composite. The optimum process variable setting is obtained exp. No. 9 with optimal condition is SOD as 1.5 mm WP as 150 Mpa and NS as 150 mm/min and the corresponding response conditions are obtained as MRR = 58.442 gm/sec SR = 0169 μm. In addition, parametric statistical analysis has been done and found the process variables SOD and NS are most significant variables on MRR whereas NS is the most influencing variable on SR of AWJM process on LBRP composite. This research work reveals that the AWJM

process well suited for machining of green composites with superior quality and higher production throughput.

References

1. Rajak DK, Pagar DD, Menezes PL, Linul E (2019) Fiber-reinforced polymer composites. *Polymers* 11:1–37
2. Yap C, Ming T, Jye WK, Ahmad H, Ahmad I (2017) Mechanical properties of bamboo and bamboo composites: a review. *J Adv Res Mater Sci* 35(1):7–26
3. Javadian A, Smith IF, Saeidi N, Hebel DE (2019) Mechanical properties of bamboo through measurement of culm physical properties for composite fabrication of structural concrete reinforcement. *Front Mater* 1–42
4. Behera S, Kumar S (2018) Study of mechanical properties of bamboo fibers before and after alkali treatment. *Int J Appl Eng Res* 13(7):5251–5255
5. Jagadish, Rajakumaran M, Ray A (2018) Investigation on mechanical properties of pineapple leaf—Based short fiber—Reinforced polymer composite from selected Indian (northeastern part) cultivars. *J Thermo Plastic Compos Mater* 33(3):324–342
6. Chin SC, Tee KF, Tong FS, Ong HR, Gimbin J (2019) Thermal and mechanical properties of bamboo fiber reinforced composites. *Materialstoday Communications* 23:1–32
7. Hossain MF, Islam MK, Islam MA (2014) Effect of chemical treatment on the mechanical and physical properties of wood saw dust particles reinforced polymer matrix composites. In: *International conference on mechanical engineering, ICME 2013, vol 90. Elsevier, Procedia Engineering*, pp 39–45
8. Zaharuddin MFA, Yunos PAA, Jiyoun Y, Mohruni AS, Yani I, Yanis M (2019) Machinability analysis of drilled bamboo fibre reinforced polymer (BFRP) composite. *J Phys: Conf Ser* 1198:1–9
9. Gupta K, Rajakumaran M (2018) Evaluation of machining performance of pineapple filler based reinforced polymer composites using abrasive water jet machining process. *Mater Sci Eng* 430:1–8
10. Karatas MA, Gokkaya H, Nalbant M (2019) Optimization of machining parameters for abrasive water jet drilling of carbon fiber-reinforced polymer composite material using Taguchi method. *Aircr Eng Aerosp Technol* 92:1–12
11. Patel JK, Shaikh AA (2014) An experimental investigation of AWJ parameters on banana fiber reinforced. *Int J Eng Res Technol* 3(12):1–6
12. Mizobuchi A, Takagi H, Sato T, Hino J (2008) Drilling machinability of resin-less green composites reinforced by bamboo fiber. *WIT Trans Built Environ* 97:185–194
13. Yusof Y, Yahya SA, Adam A (2016) Pine apple leaf fibre extractions: comparison between PALF M1 and hand scrapping. *ARP J Eng Appl Sci* 11(3):2125–2129
14. Asim M, Abdan K, Jawaid M, Nasir M, Dashtizadeh Z, Ishak MR, Hoque ME (2015) A review on pineapple leaves fibre and its composites. *Int J Polymer Sci* 2015:1–16
15. Lemma E, Chen L, Siores E, Wang J (2002) Study of cutting fiber-reinforced composites by using abrasive water-jet with cutting head oscillation. *Compos Struct* 57:297–303
16. Zahra S, Seyedali M, Shahrzad M, Hossam S, Aljarah I (2017) Grasshopper optimization algorithm for multi-objective optimization problems. *Appl Intell* 48:805–820
17. Elmi Z, Onder EFE (2018) Multi-objective grasshopper optimization algorithm for robot path planning in static environments. *IEEE international conference on industrial technology, ICIT 2018. IEEE*, pp 244–249
18. Saremi S, Mirjalili S, Lewis A (2017) Grasshopper optimisation algorithm: theory and application. *Adv Eng Softw* 105:30–47

19. Jagadish, Bhowmik S, Ray A (2016) Prediction and optimization of process parameters of green composites in AWJM process using response surface methodology. *Int J Adv Manuf Technol* 87:1359–1370
20. Kechagias J, Petropoulos G, Vaxevanidis N (2012) Application of Taguchi design for quality characterization of abrasive water jet machining of TRIP sheet steels. *Int J Adv Manuf Technol* 62:635–643

Development of Complex Feature Extraction System from Prismatic Parts Using Hybrid Algorithms



Sridhar Meka, Dowluru Sreeramulu , and Lingaraju Dumpala

Abstract In the current scenario most of the industries want to produce superior quality products with less production time and manufacturing cost to full fill the customer needs. The integration of computer-aided design (CAD) and computer-aided manufacturing (CAM) attain the industry's needs. However, the integration of CAD and CAM is most difficult task and facing lot of challenges. Feature recognition (FR) is the key link between integrate CAD and CAM and overcome the issues present in it. This paper presents a development of complex feature extraction system to extract different features like slant edges, bends, fillets, and chamfers from prismatic parts. A hybrid automatic feature recognition algorithm (HAFRA) combination of milling feature extraction algorithm (MFEA) and cylindrical feature extraction algorithm (CFEA) is proposed to identify the complex features using STEP file and then validation of the algorithm is done through case study. The developed hybrid automatic feature extraction system is well suited to extract the complex features from prismatic parts and thereby improve the downstream applications like process planning, CAPP, CAE, CAM, CAI, etc.

Keywords FR · CAD · CAM · Features · STEP file and hybrid algorithm

1 Introduction

Day by day computer revolution in manufacturing industries rapidly increasing. Most of the manufacturing industries are used computers to design the required products with superior quality, high durability, less manufacturing time with reduced cost and high production throughput. In this manner integration of computer-aided design (CAD) and computer-aided manufacturing (CAM) plays a vital role. However, the

S. Meka · L. Dumpala
Department of Mechanical Engineering, JNTUK, Kakinada, India

D. Sreeramulu (✉)
Department of Mechanical Engineering, Aditya Institute of Technology and Management, Tekkali
532201, India
e-mail: dowlurusreeram@gmail.com

integration of CAD and CAM is most difficult task and having lot of issues due to lack of proper interfacing between them. The feature recognition (FR) is a key link to integrate CAD and CAM and also acts as an interface between design and manufacturing activities. Most of the researchers carried out their research on development of automatic feature extraction algorithms to extract various features for downstream applications like computer-aided process planning (CAPP). In this way, an automatic feature extraction system is developed to recognize form features by using logical geometrical rules [1]. In addition, various issues present in feature recognition is clearly addressed and developed a hybrid approach (i.e., combination of hint-based and volume decomposition) to extract intersection features [2]. Moreover, identified different manufactured features by using reverse engineering approach [3]. The extraction process contains three phases feature reconstruction, feature extraction, and feature translation. Furthermore, a novel approach is designed to recognize primitive features in the depressions of a polyhedral machining parts by using graph-based approach [4]. A new approach to identify prismatic part features by using logical rule-based approach [5]. Classification of cylindrical and milling features based on their characteristics and developed a multi-feature extraction system to extract cylindrical and milling features by applying logical rules and concave and convex relations [6].

Furthermore, a novel approach is developed to identify 2.5D prismatic part features based on machining of pre-defined features in the database [7]. A new technique (i.e., light-ray virtual method) is established to recognize machining features [8]. A hybrid approach (combination of graph-based and hint-based) is developed to extract intersecting milling features [9]. Classified free form features like passage, protrusion, slot, and compound features based on their geometrical properties and features are recognized by using attributed adjacency graph (AAG) method [10]. Moreover, some amount of research work has been done on automatic feature recognition of constant thickness metals like sheet metal components. Classified deform features on sheet metal based on their topological properties and features are extracted by using graph-based approach [11]. A new technique (Basic deformation feature graph) is developed to identify deform features like dimple, wall, jog, louver, rib, bead, etc. [12]. Further bit amount of research work has been attempted on extraction of casted features by using automatic feature extraction systems. A new approach is addressed to identify casting and forging part features by using volume decomposition method [13].

However, very limited work has been done on identifying inclined plane features and edge fillet features in matching parts. This paper presents a new algorithm is developed to extract milling and cylindrical features on inclined planes and edge fillets by using combination of logical rules and concave and convex relations. The implementation and validation of algorithm via in house developed JAVA program is used. The rest of the paper is segregated as follows; automatic feature extraction methodology is explained in Sect. 2. Implantation and validation of the algorithm is executed via example in Sect. 3. Discussion and feature construction theory is addressed in Sect. 4. Finally, conclusions are mentioned in Sect. 4.

2 Methodology

The hybrid AFR algorithm is developed to extract various milling features like pocket, blind pocket, through hole, and fillet of a 3D model object created by CATIA software version 5.

The proposed hybrid AFR algorithm is ability to identify the features on inclined plane. Moreover, HAFRA act as a key link between CAD and CAM. In addition, HAFRA minimizes the manufacturing cost as well as stored the product information throughout its life cycle without damage of product attributes data. The milling feature extraction process from 3D modeled object is illustrated in Fig. 1.

2.1 Milling Feature Extraction Algorithm (MFEA) from B-Rep Data

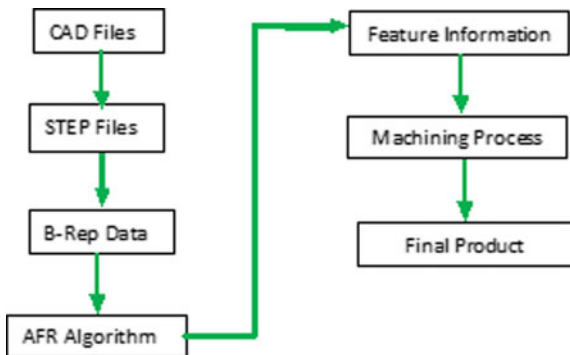
Initially, the required product is created by using CAD software. The product model is transformed into neutral file is known as STEP AP-214 file. Which plays a major role to interface between CAD and CAM. Then after boundary representation (B-rep) data extracted from STEP files by using geometric data extraction algorithm (GDEA) [5]. Further, B-rep data given as an input to MFEA as shown in Fig. 2, to extract milling feature information based on concavity relation approach. The following steps have been adopted to execute the MFEA.

Step 1: Extraction of B-rep data from STEP AP-214 file.

In this step, geometrical entities viz., plane, line, circle, edge, edge loop, inner bound, outer bound, etc. extracted by using geometrical extraction algorithm (GDE) [5] from STEP AP-214 file. Moreover, the B-rep data contains geometrical and topological attributes of the corresponding 3D modeled part.

Step 2: Identify planes, faces, and edges from B-rep data of 3D model part.

Fig. 1 Flow chart of milling feature extraction process from 3D modeled object



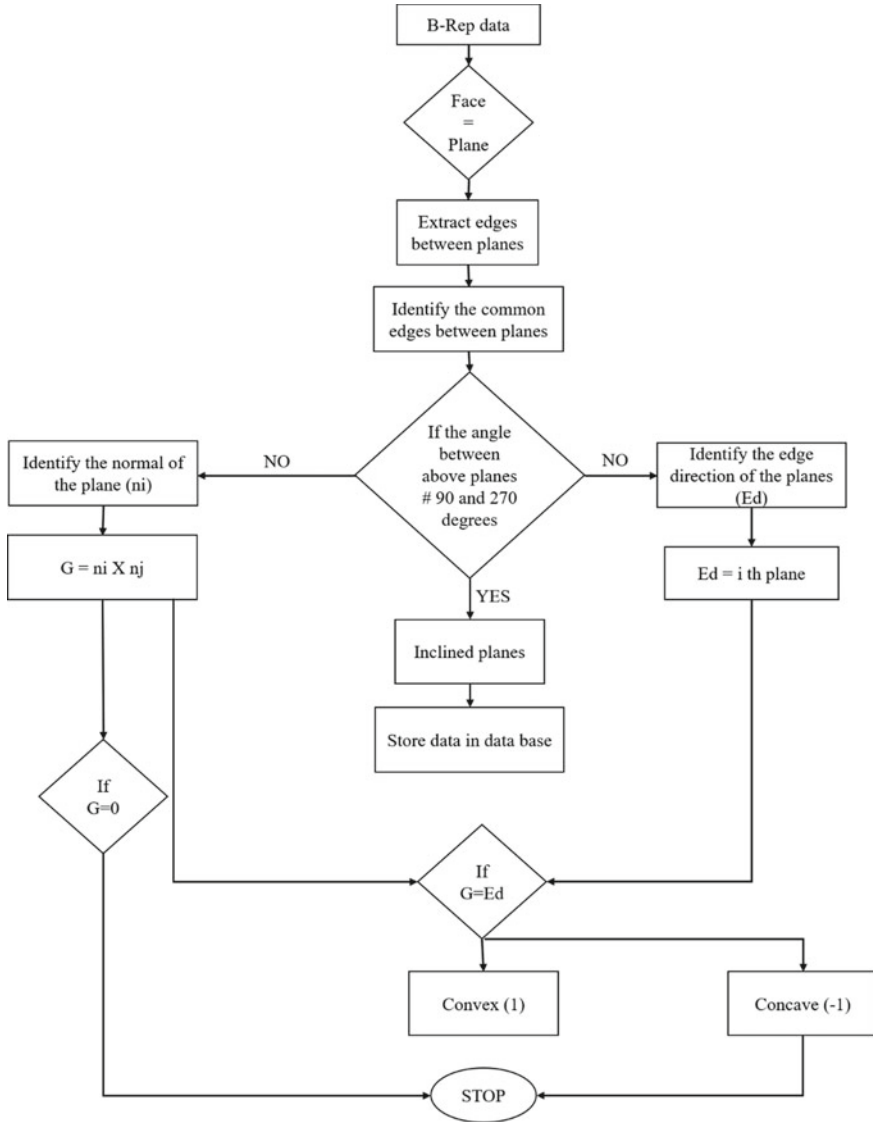


Fig. 2 Milling feature extraction algorithm (MFEA) to extract various milling features

This step collects the information like number of faces, edges, and common edges from the planes.

Step 3: Extract edges and common edges between the planes and measure angle between planes.

In this step, extract the common edges from the plane's nature and measure the angle between two common edges (i.e., angle is 90° or $\neq 90^\circ$ and $\neq 270^\circ$).

Step 4: Calculate normal with respect to planes and corresponding edge directions.

The normal of the two planes and corresponding edge direction is calculated in this step.

Step 5: Determine the cross products between the two planes.

This step involves calculate the normality index via cross-product of two normal of the corresponding planes (i.e., $n_i \times n_j$) and the normal index is denoted by C .

Step 6: Check normal index and direction of the edges.

In this step the normal index and edge direction of the correspond plane is equal then go for next step otherwise repeat the step 3–5.

Step 7: Determine concave and convex between the planes and edges.

The concave and convex relation among the faces is observed based on angle $180^\circ < \theta < 360^\circ$ and $0^\circ < \theta < 180^\circ$, respectively. The convex faces between the planes represent (1) and whereas concave faces between the planes indicate (-1) and the data is stored in the database.

2.2 *Cylindrical Feature Extraction Algorithm (CFEA) from B-Rep Data*

The cylindrical features like holes, blind holes, taper holes, boss, protrusions, etc. are extracted by using CFEA as shown in Fig. 3, based on logical rule-based approach. The following steps have been adopted to extract above listed cylindrical feature information from 3D modeled object.

Step 1: Extraction of B-rep data from STEP AP-214 file.

In this step, geometrical entities viz., cylinders, circle, radius, Cartesian points, vertex points, starting points, ending points, edge loop, inner bound and outer bound, etc. extracted by using geometrical extraction algorithm (GDE) [5] from STEP AP-214 file. Moreover, the B-rep data contains geometrical and topological attributes of the corresponding part.

Step 2: Identify cylinders and circles from the cylinders from B-rep data of 3D model part.

This step collects the information like number of cylinders and corresponding circles with their attributes of the 3D modeled part.

Step 3: Check the number of edges and vertex of the planes and type of surfaces.

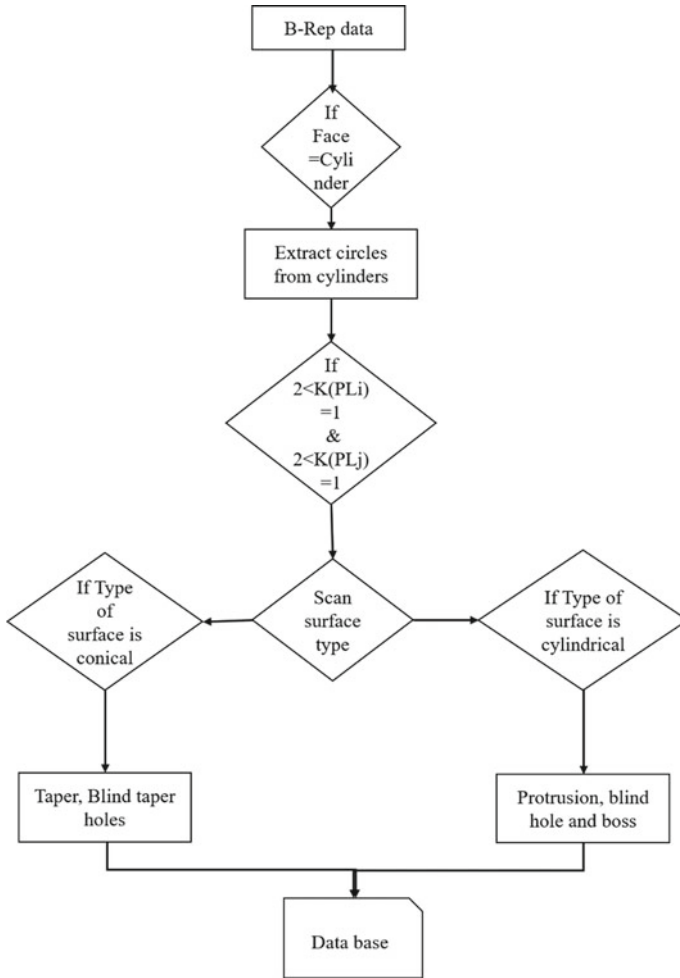


Fig. 3 CFE algorithm to extract cylindrical features

In this step, collect the surface details and check the number of edges and circle details of the corresponding plane. Further the nature information either cylindrical surface, conical surface, and toroidal surface with their geometry and correlate with circles information [6].

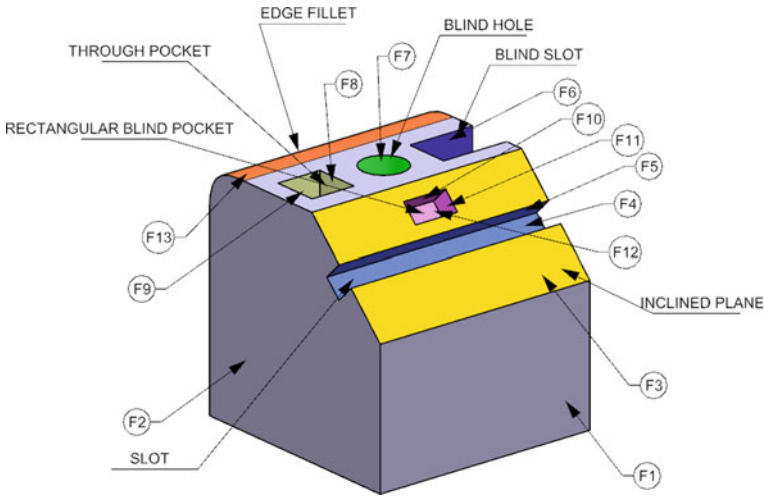


Fig. 4 Milling feature part model

3 Implementation of HAFRA Via Case Study

3.1 3D Modeling Using CATIA Software

In this study, 3D solid model is developed by using Catia software version 5. The features embedded in the model such as blind hole, blind slot, through pocket, and also features like blind pocket and through slot on inclined plane as shown in Fig. 4.

3.2 B-rep Data from GDE Algorithm

The boundary representation data (B-rep data) as shown in Fig. 5, contains geometrical information, as well as topological information of 3D model, is extracted by using GDE algorithm [5].

3.3 Results and Discussion of HAFRA

The obtained B-rep data from GDE algorithm given as an input to developed HAFRA for extraction of features from inclined plane and edge fillet by using logical rule-based theory and concavity relation. The HAFRA mechanism is the combination of both MFEA and CFEA mechanisms.

```

0|1|35.5|40.||60.||44.5|40.||60.||LINE|1.||1.||0.||0.||null||null||null||PLANE|null||50.||60.||
60.||0.||0.||1.||1.||0.||0.||
0|2|35.5|40.||60.||35.5|60.||60.||LINE|1.||0.||1.||0.||null||null||null||PLANE|null||50.||60.||
60.||0.||0.||1.||1.||0.||0.||
0|3|35.5|60.||60.||21.||60.||60.||LINE|1.||-
1.||0.||0.||null||null||null||PLANE|null||50.||60.||60.||0.||0.||1.||1.||0.||0.||
0|4|21.||60.||60.||21.||0.||60.||LINE|1.||0.||-
1.||0.||null||null||null||PLANE|null||50.||60.||60.||0.||0.||1.||1.||0.||0.||
.
.
1.||0.||null||null||null||PLANE|null||60.||41.||25.||0.||0.||1.||1.||0.||0.||
24|2|60.||41.||25.||85.||41.||25.||LINE|1.||1.||0.||0.||null||null||null||PLANE|null||60.||41.||
25.||0.||0.||1.||1.||0.||0.||

```

Fig. 5 B-rep data from GDE algorithm

3.3.1 Mechanism Involved to Extract Milling Features in MFEA

The milling features like through pocket, rectangular blind pocket, slot and blind slot, respectively. The mechanism involved in MFEA to extract above listed features based on con cavity relations among faces between the planes. The concave and convex relation among the faces is observed based on angle $180^\circ < \theta < 360^\circ$ and $0^\circ < \theta < 180^\circ$, respectively. The validation of developed MFEA is done via in house developed JAVA program and the corresponding results as depicted in Fig. 6. The following key points have been noted for extraction of milling features mechanism.

- The B-rep data as shown in Fig. 5, given as input to the MFEA and the corresponding output results of MFEA as shown in Fig. 6.

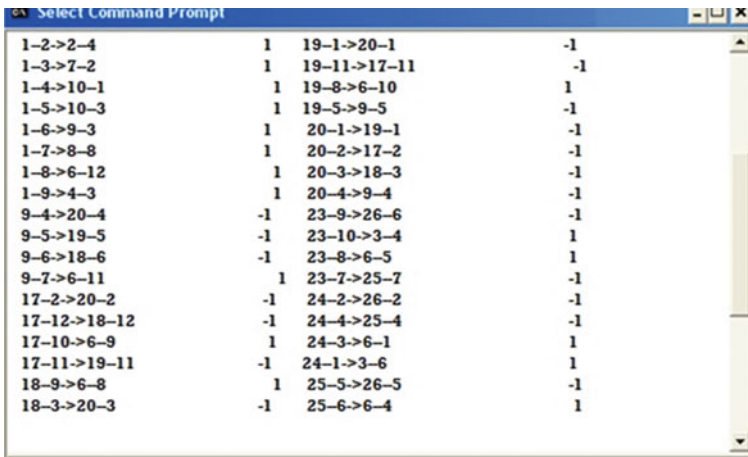


Fig. 6 Concavity relation of milling features

Table 1 Attribute relation among the faces

	0
No relation bsetween the Faces	2
Convex faces	1
Concave faces	-1

Table 2 Attributes relation between the faces based on relation matrix

FN	F4	F5	F6	F7	F8	F9	F10	F11	F12	F13	F14	F15	F16	F17	F18	F19	F20	F21	
F4	0	-1	2	2	2	2	2	2	2	2	2	2	2	2	2	2	2	2	-1
F5	-1	0	2	2	2	2	2	2	2	2	2	2	2	2	2	2	2	2	2
F6	2	2	0	2	2	2	2	2	2	1	2	2	2	2	-1	2	-1	2	2
F7	2	2	2	0	2	2	2	2	2	2	2	2	2	2	2	2	2	2	2
F8	2	2	2	2	0	-1	2	2	2	1	2	-1	2	2	2	2	2	2	2
F9	2	2	2	2	-1	0	2	2	2	2	-1	2	2	2	2	2	2	2	2
F10	2	2	2	2	2	2	0	-1	2	2	2	2	-1	-1	2	2	2	2	2
F11	2	2	2	2	2	2	-1	0	-1	2	2	2	2	-1	2	2	2	2	2
F12	2	2	2	2	2	2	2	-1	0	2	2	2	-1	-1	2	2	2	2	2
F13	2	2	1	2	1	1	2	2	2	0	1	1	2	2	1	1	1	1	2
F14	2	2	2	2	-1	-1	2	2	2	1	0	2	2	2	2	2	2	2	2
F15	2	2	2	2	-1	-1	2	2	2	1	2	0	2	2	2	2	2	2	2
F16	2	2	2	2	2	-1	2	-1	2	2	2	2	0	-1	2	2	2	2	2
F17	2	2	2	2	2	2	-1	-1	-1	2	2	2	-1	0	2	2	2	2	2
F18	2	2	-1	2	2	2	2	2	2	1	2	2	2	2	0	-1	-1	2	2
F19	2	1	2	2	2	2	2	2	2	1	2	2	2	2	-1	0	-1	2	2
F20	2	2	-1	2	2	2	2	2	2	2	2	2	2	2	-1	-1	0	2	2
F21	-1	2	2	2	2	2	2	2	2	2	2	2	2	2	2	2	2	2	0

- The face relation and corresponding attributes are depicted in Table 1.
- The attribute relationship among the faces between the planes and feature formation based on relation matrix information is mentioned in Table 2.
- From the relationship matrix concave (-1) data applied to production rules, result in corresponding milling features like through pocket, rectangular blind pocket, blind slot and slot are formed as shown in the Table 3a-d, respectively.

3.3.2 Mechanism Involved to Extract Cylindrical Features in CFEA

The cylindrical feature like blind hole, through hole, taper hole, boss and protrusion fillets, etc. The cylindrical features are extracted by using CFEA based on rule-based approach. The validation of developed CFEA is done via in house developed JAVA program and the corresponding results as shown in Fig. 7. The following mechanism points have been noted to while extracting the cylindrical features as well as edge fillet from the developed 3D model part.

Table 3 a–d Feature formation from relation matrix based on production rules

(a) Through Pocket					(b) Rectangular Blind Pocket					
FN	F8	F9	F14	F15	FN	F10	F11	F12	F16	F17
F8	0	-1	2	-1	F10	0	-1	2	-1	-1
F9	-1	0	-1	2	F11	-1	0	-1	2	-1
F14	-1	-1	0	2	F12	2	-1	0	-1	-1
F15	-1	-1	2	0	F16	2	-1	2	0	-1
					F17	-1	-1	-1	-1	0

(c) Blind Slot					(d) Slot			
FN	F6	F18	F19	F20	FN	F4	F5	F21
F6	0	-1	2	-1	F4	0	-1	-1
F18	-1	0	-1	-1	F5	-1	0	2
F19	2	-1	0	-1	F21	-1	2	0
F20	-1	-1	-1	0				

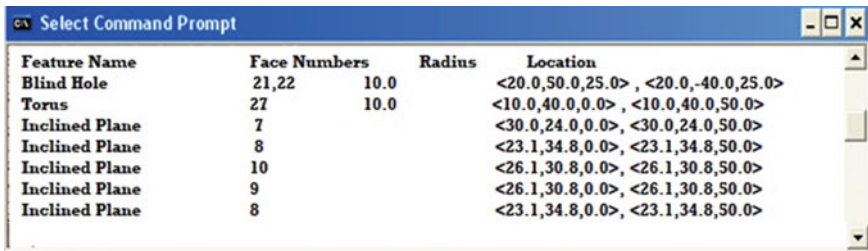


Fig. 7 Output results of CFEA of 3D modeled part

- The two cylindrical faces 21 and 22 having same geometrical information (radius) and having same center point. Moreover, if the number of edges of the cylinder one side having more than two and other side is equal to two, the obtained cylinder is blind hole and the information is stored in database.
- The cylindrical face 27 having same radius and tangent to, and join two surfaces of the corresponding planes, then the obtained plane is toroidal edge fillet and the corresponding data is stored in database for further applications.
- The inclined plane is Identified based on the cross-product of two planes not equal to 90° and not equal to 270°. The inclined plane details and the corresponding features on inclined plane information is stored in the database.

- The type of surface either cylindrical surface, conical surface, and toroidal surface and the corresponding direction (negative or positive) of the axis information with their geometry obtained the cylindrical features in the 3D modeled part.

4 Conclusions

This work developed a new HAFR algorithm to recognize milling and cylindrical features like pocket, blind slot, through slot, blind hole, edge fillet by using combination of MFEA and CFEA based on logical rules and concavity relation with relation matrix. The 3D solid model is developed by Catia version 5 software and corresponding data exchange standard STEP AP-214 is to be considered. The new HAFR algorithm is implemented through java program and the embedded features on the solid model are successfully extracted and the corresponding information is stored in the database for further downstream applications like process planning, CNC, and CAM.

References

1. Abouel Nasr ES, Kamrani AK (2006) A new methodology for extracting manufacturing features from CAD system. *Comput Ind Eng* 51:389–415
2. Woo Y, Sakurai H (2002) Recognition of maximal features by volume decomposition. *Comput Aided Des* 34(3):195–207
3. Wang M, Chamberlain MA, Joneja A, Chang T (1993) Manufacturing feature extraction and machined volume decomposition in a computer-integrated feature-based design and manufacturing planning environment. *Comput Ind* 23(1–2):75–86
4. Marefat M, Kashyap RL (2012) Geometric reasoning for recognition of three-dimensional object features. *IEEE Trans Pattern Anal Mach Intell* 12(10):949–965
5. Sreeramulu D, Rao C (2008) A new methodology for recognition of milling features from STEP file. *Int J Appl Manage Technol* 6(3):172–190
6. Adapa SK, Sreeramulu D (2021) Jagadish: Classification and automatic feature-based extraction approach for cylindrical and milling parts. *Int J Manuf Mater Mech Eng* 11(3):55–73
7. Pedagogu VM, Kumar M (2014) An intelligent feature recognition methodology study for 2.5 D prismatic parts. *Int J Comput Eng Technol* 5(4):119–125
8. Ranjan R, Kumar N, Pandey RK, Tiwari MK (2015) Automatic recognition of machining features from a solid model using the 2D feature pattern. *Int J Adv Manuf Technol* 26:861–869
9. Rahmani K, Arezoo B (2017) A hybrid hint-based and graph-based framework for recognition of interacting milling features. *Comput Ind* 58:304–312
10. Bendjebba S, Cai N, Anwer N, Lavernhe S, Mehdi-Souzani C (2018) Freeform machining features: new concepts and classification. *Procedia CIRP* 67:482–487
11. Gupta RK, Gurumoorthy B (2013) Classification, representation, and automatic extraction of deformation features in sheet metal parts. *Comput Aided Des* 45(11):1469–1484
12. Sreenu P, Gupta RK (2014) Extraction of process parameters from a sheet metal part model. *Appl Mech Mater* 592:888–893
13. Kailash SB, Zhang YF, Fuh JYH (2001) A volume decomposition approach to machining feature extraction of casting and forging components. *Comput Aided Des* 33(8):605–617

Recent Trends in the Amelioration and Prediction of Surface Roughness in Turning Process: A Bibliometric Analysis



Vikrant Guleria , Vivek Kumar , and Pradeep K. Singh 

Abstract Turning is widely used manufacturing process in industries. Quality assurance of turned products includes dimensional accuracy and surface finish. A considerable number of research papers have been published on improving and predicting surface quality during the turning process. This paper presents a study on bibliometrics of these articles since 2015. Microsoft Academic database has been collected using search terms “surface roughness” and “turning”. Co-authorship, co-organizations, keywords co-occurrence, citation analysis and source analysis networks have been developed using VOS viewer software. Main contributors viz. authors, organizations and journals in the field of amelioration and prediction of surface roughness in turning process have been identified and discussed. Research hotspots using keywords co-occurrence have been obtained and reviewed. Research hotspots are composite materials, hard to cut materials like titanium alloy, Inconel etc., MQL, Electrical Discharge Turning, nanofluid etc. This article will be helpful to researchers to understand current trends in research on improvement in surface finish during turning and provide future directions for further research.

Keywords Surface roughness · Turning · Bibliometric analysis · Microsoft academic

1 Introduction

Machining is among the major production activities in industries. Many parts in mechanical, automobiles, aerospace, electronics, and medical sectors require turning as the machining and finishing operation due to its better surface finish and dimensional tolerances [1]. Olsen [2] described the surface roughness as the function of cutting parameters. Since then, various techniques like regression, analytical studies, computer vision, artificial neural networks (ANN) and other machine learning techniques were employed to predict the surface roughness. Variables used for the

V. Guleria (✉) · V. Kumar · P. K. Singh
Department of Mechanical Engineering, Sant Longowal Institute of Engineering and Technology,
Sangrur, Punjab, India
e-mail: vikrant.guleria@hotmail.com

prediction of surface roughness are cutting parameters, tool image, material properties (e.g., hardness), vibration and acoustic features. Previous authors have categorized the prediction of surface roughness as theory-based (analytical) approach and experiment-based (empirical) approach [3]. The related publications are growing rapidly in international journals.

Bibliometrics is the science used to analyze the quantitative relation between the documents, authors, institutions, sources and many more. Bibliometrics is used by many authors to study trends of documents published in the journals [4] and also to study the change in trends in the specific fields [5]. Bibliometric study is performed using citation analysis. Different sources of citation database are Google Scholar, Scopus, Web of Science (WoS), Microsoft Academic (MA), Dimensions, CrossRef, Pubmed, OCC, Semantic Scholar. Google scholar is the most exhaustive source [6] but the records in it are retrieved in an impractical way and cannot be used for large datasets, as it requires a tedious manual process for cleaning and organizing the data [7]. The second-largest citation database is Microsoft Academic which includes 82 percent of Scopus and 86 percent of Web of Science database [6]. Next the Scopus, Dimensions and WoS have the citation database in the reduced order [6].

Hence in the present paper MA is used as the citation database to study the recent trends in amelioration and prediction of surface roughness in turning process. This paper presents an analysis on the bibliometrics of surface roughness in turning process using co-authorship, co-occurrence, citation analysis and bibliographic coupling. Co-occurrence of words in the field of study has been helpful in guiding the research scholars in this field. Co-authorship, citation analysis and source analysis have been helpful to study the link strength between different authors, organizations and sources of research.

2 Methodology

The Microsoft Academic Search (MAS) was launched in 2006, it got retired in 2012 [6]. It was relaunched in 2016 as Microsoft Academic (MA) using web crawling infra of Bing. This includes the free access to its database using Applications Programming Interface (API) [8]. The database in this research has been collected using the MA-API on VOS-viewer software. The search was conducted in August 2021. The search targets were “title” and “abstract” with inputs “surface roughness” and “turning” for the duration 2015–2021. The number of documents on 10th, 20th and 30th August, 2021 were 2257, 2277 and 2305 respectively, which means the MA is constantly updating its data. Finally, 2320 documents were retrieved for pre-processing on 13.09.2021. All documents were checked, and 9 documents were eliminated due to their non-English language. Hence 2311 documents were selected for this study. The year wise distribution of research publications from 2010 up to September 2021 is shown in Fig. 1 which shows the increasing trend in the publications up to 2020. The number of publications in 2021 is continuously increasing and is also likely to display an increasing trend by the year end.

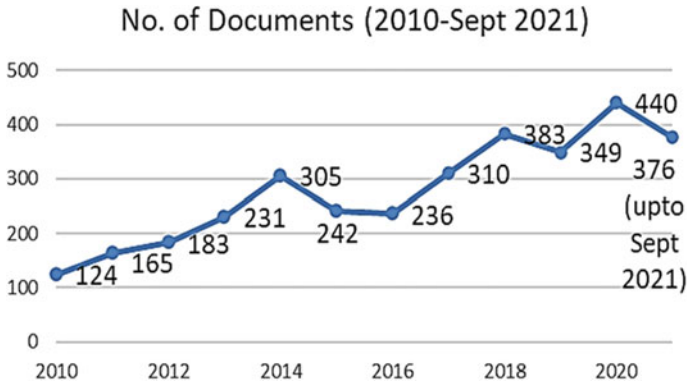
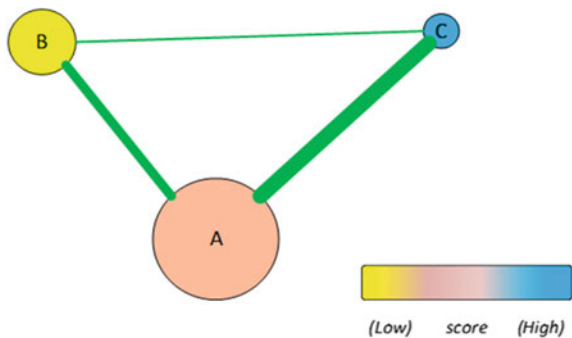


Fig. 1 Annual research publications (retrieved from MA-API on 13.09.2021)

These documents consist of 86 book chapters, 38 conference papers and the remaining journal articles. After the collection of databases, the VOS-viewer has been used to develop the network between the items which can be authors, keywords, organizations and sources. VOS-viewer is the platform independent tool that works in JAVA environment. A network is the group of items linked together with some positive value known as link strength. The group of items in the network is known as clusters. *Weight* is the positive numerical value provided by the size of the item used to show the importance, and the *score* may be used to indicate any other numerical property given by the color as shown in Fig. 2. Weight attributes include number of links and total link strength of the items e.g., in co-authorship network number of links will remain one for two authors in a cluster having 10 number of publications and the other two authors in different clusters having only five publications but the latter has less link strength as compared to the earlier one.

Fig. 2 Cluster of items showing weight, score and link strength



3 Co-authorship

Co-authorship is an important tool to study research collaboration between different authors of similar research interests [9]. International level research collaboration increasing significantly among scientists working in core area due to increasing competition and faster change in technologies. According to the collected dataset as discussed in Sect. 2 (Methodology), total 5787 authors published article to the relevant field. The threshold considered for building co-authorship map was minimum five documents which were passed by 190 authors. Top ten authors with highest number of documents in this field and with highest total link strength are given in Table 1.

Out of 190 authors, 61 authors are connected to each other with 13 clusters. The size of circle associated with the author is proportional to the number of documents published. The authors “Munish Kumar Gupta” and “Mozammel Mia” have the highest number of documents published with the mutual link strength of 22. These two authors can be considered as the pioneer in this field. Figure 3 shows the overlay visualization diagram depicting the average publication year. This figure can be used to determine the emerging authors in this field.

“Navneet Khanna”, “Mohammed Jamil”, “Qinghua Song”, “Hussien Hegab”, “Aqib Mashood Khan”, “Cagri Vakkas Yildrim”, “Chetan Agrawal” and “Rupinder Singh” are some authors with the average publication year later than 2020 and more than 50 citations. The average citations per year are calculated by dividing the number of citations with the number of years, the author is active in publishing the research. “Mozammel Mia”, “Murat Sarikaya”, “Grzegorz Krolczyk”, “N.R. Dhar”, “Vishal S. Sharma”, “D. Y. Pimenov” and “R.W. Maruda” have more than 30 citations per year and minimum 10 documents. The figure will become more complicated if all 190 authors are analyzed, because some clusters may not connect with others.

Table 1 Number of documents and link strength of authors

Name	Documents	Name	Total link strength
M.K. Gupta	42	M.K. Gupta	152
M. Mia	39	M. Mia	126
A.K. Sahoo	32	A.K. Sahoo	75
M.A. Yallese	27	M. Sarikaya	70
R. Kumar	26	R. Kumar	69
K. Abouelhossein	23	M. Jamil	65
M. Sarikaya	20	N. Khanna	63
N. Khanna	20	G. Krolczyk	62
A. Panda	20	M.A. Yallese	61
S.R. Das	20	Z. Liu	58

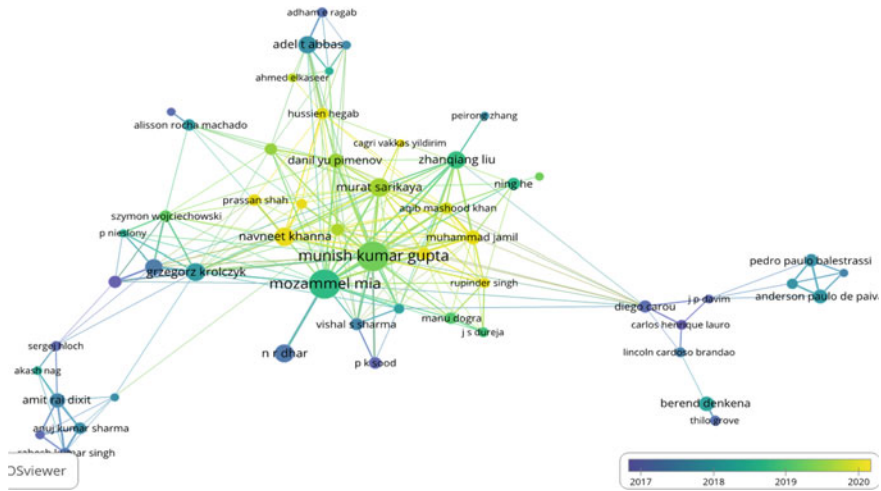


Fig. 3 Overlay visualization diagram depicting average publication year (Weight: #documents; Score: average publishing year)

4 Co-organizations

The preprocessing of the downloaded JSON data file for organizations has been performed. Thesaurus file was prepared for the same organizations with different names. A total of 936 organizations have contributed in this field. Out of these 153 meet the threshold of 5 documents. The data has been analyzed using full counting and largest set of connected items are 117 [10].

The top ranked organizations based on documents and total link strength are shown in Table 2 and the network based on average publication year is shown in Fig. 4. Top ten organizations based on number of documents published around 13% of research articles. “Munish Kumar Gupta” of “Shandong University” and later joined “Opole University of Technology” published maximum articles of approximately 2.32%. From these most of the articles published in collaboration with “Mozammel Mia” of “Imperial College, London”. Maximum mutual link strength of 14 occurs between “Shandong University, Shandong” and “Imperial College, London”. The same mutual link strength exists between “Opole University of Technology” and “University of Zielona Gora” to which the authors “Grzegorz M. Królczyk” and “Radosław Maruda” respectively are affiliated. Latest research publications are observed more from “Imperial College, London”, “IITRAM, Ahmedabad” and “PEC, Chandigarh” having mean publishing year after 2020.

Table 2 Top ranked organizations with highest number of documents and link strength

Organization	Documents	Organization	Link strength
Shandong University, Shandong	57	Shandong University, Shandong	96
IIT Dhanbad	32	Imperial College, London	86
Ahsanullah University of Science and Technology, Dhaka	30	Sinop University, Sinop	70
Opole University of Technology, Opole	30	Ahsanullah University of Science and Technology, Dhaka	67
KIIT University, Bhubaneswar	28	Opole University of Technology, Opole	62
National Institute of Technology, Rourkela	27	South Ural State University, Chelyabinsk	56
VIT University, Vellore	27	Chandigarh University, Chandigarh	46
Veer Surendra Sai University of Technology, Burla	25	Nanjing University of Aeronautics and Astronautics, Nanjing	45
Nanjiang University of Aeronautics and Astronautics, Nanjing	23	Institute of Infrastructure Technology Research and Management, Ahmedabad	44
Nelson Mandela Metropolitan University, Port Elizabeth	23	Poznan University of Technology, Poznan	40

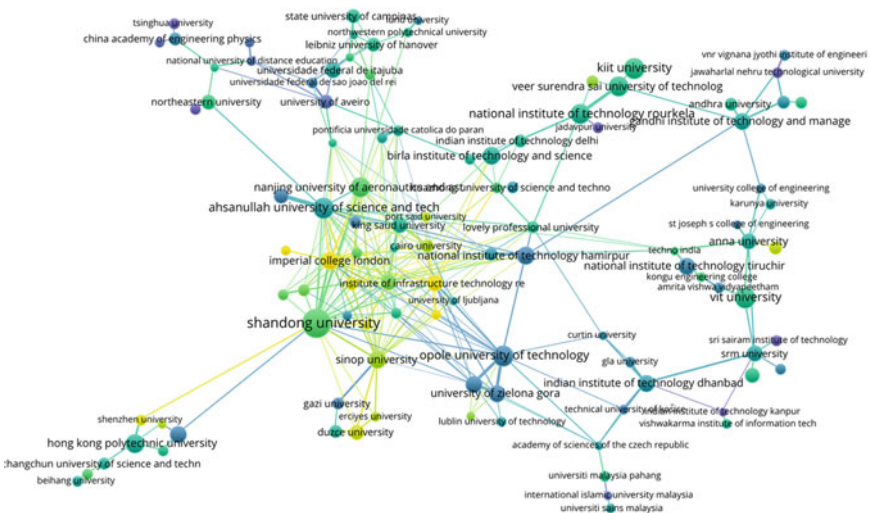


Fig. 4 Overlay visualization diagram of organizations in research collaboration based on average publishing year (Weight: #documents; Score: average publishing year)

5 Keywords Co-occurrence

The bibliometric study using co-occurrence analysis was first established in 1980s [11]. The knowledge structure is best described as “network” with two main components i.e., keywords and interrelationship among them. In this section the bibliometric analysis using keywords co-occurrence is discussed. From the total 1954 keywords, 425 meet the threshold of 5 occurrences. General keywords like “surface roughness”, “metallurgy”, “machining”, “mechanical engineering” and “process” were not considered to develop the network. Also, the links have been eliminated to avoid complexity in the network.

The network developed is based on average publishing year (Fig. 5). The font (or box) size of keywords is directly related to its occurrence. As seen from the figure, “composite material”, “design of experiments”, “tool wear” and “machinability” are the prominent keywords in the network. The research in turning is shifting from base materials toward composite materials. The researchers are developing new composite materials and test their machinability with the use of various design of experiments techniques.

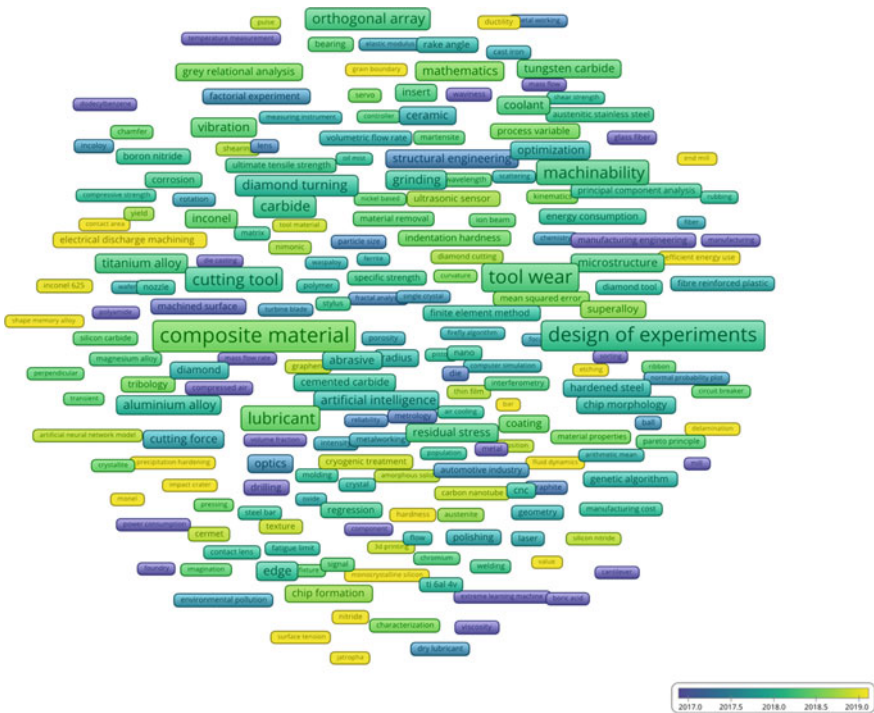


Fig. 5 Keywords’ co-occurrence network based on average publishing year (Weight: #occurrences; Score: average publishing year)

The network also shows the average publication year from where the latest keywords which contribute in the research are “shape memory alloy”, “inconel 625”, “powder metallurgy”, “electrical discharge machining”, “ionic liquid” [12], “cryogenic treatment”, “efficient energy use”, “thermal spraying”, “nano-fluid”, “coconut oil” etc. The recent research appears to focus on machining of hard and composite materials, which needs harder and tough cutting tools [13]. Hence cryogenic treatment of cutting inserts [14], minimum quantity lubrication (MQL) with nano fluids [15], internal cooling of cutting tools [16], ultrasonic vibration [17] and, electrical discharge turning [18] play an important role in recent research. Also, to reduce environmental pollution from cutting fluids for sustainable development the research in MQL seems to rise exponentially [19].

Most of the research after 2015 is based on hard to cut materials like inconel, titanium, hard steels etc. A Self Propelled Rotary Tool (SPRT) has been used to machine 41Cr4 steel leads to improve the surface finish and stabilize the cutting force values at high cutting speed and feed rate [20]. Different types of cutting fluids like nano-fluids, jojoba oil, olive oil, under MQL condition have been tested [21]. The improvement of surface finish has been noted in MQL turning for all the cutting parameters levels [22]. The feed rate has substantial effect directly on the roughness hence should be kept at low level for all conditions [23]. Under dry and MQL conditions the increase in temperature softens the material hence produce better finish at high levels of cutting speed and depth of cut [24]. The optimized surface roughness found to be at low levels under Reduced Quantity Lubrication (RQL) due to improved chip flow and reduced friction. The effectiveness of MQL has been improved by 15% using the Ranque–Hilsch vortex tube (RHVT) [25]. The MQL under cryo-environment helps in reducing the contact length of sliding sticking regions hence improves surface finish by 30–40% [26]. The magneto-rheological fluid combines with MQL to improve surface finish by 26% [27]. A new method of Electrostatic-MQL was developed by Shah et al. [28] which used charged vegetable oil droplets inside the copper tube at 25 kV. The extreme pressure/anti-wear additives had been used in combination with MQCL to improve the surface finish during machining [29]. These fluids also help in reducing the tool vibration by acting as a damper. Hence the researchers combine different techniques with MQL to improve the surface finish.

6 Citation Analysis

In this section the discussion on two networks developed considering weights as the number of times the articles cited, and normalized citations of the article. The number of citations in a document is normalized by dividing the number of citations of the document by the average number of citations in all publications published in the same year, and included in the VOS viewer data. The normalization takes into account the fact that older publications have had more time to accumulate citations than newer publications.

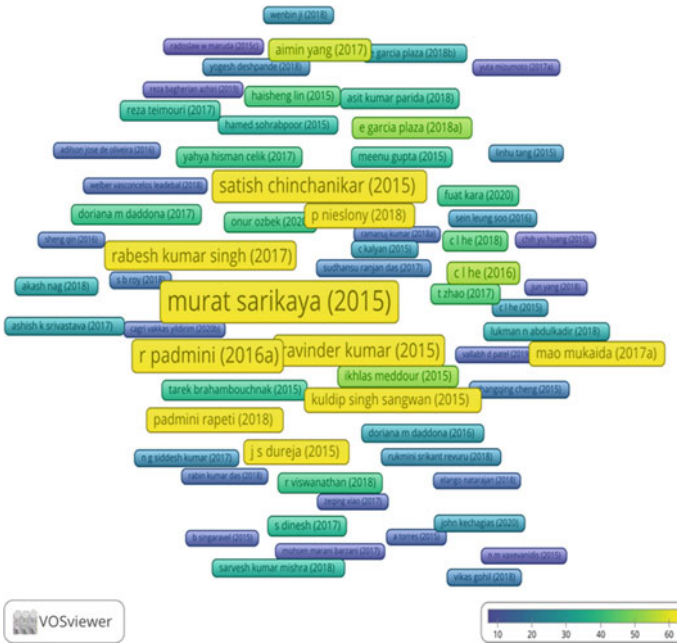


Fig. 6 Citation analysis using number of citations (Weight & Score: #citations)

Out of 2311 documents 515 meet the threshold limit of minimum 10 citations. The weights and scores both are selected as number of citations for Fig. 6, and for Fig. 7 weight is normalized citations and score is number of citations. The weight is represented by size and score is represented by color. The five most cited articles are shown in Table 3.

The latest research article with highest normalized citation count is by Gupta et al. [34]. This article deals with the turning of Ti6Al4V alloy under liquid nitrogen MQL condition which helps in reducing coolant consumption, improves surface quality with minimum tool wear and built-up edges. Most of the other top ranked normalized cited articles related with hard to cut materials, composites, cryogenic treatment and under MQL conditions. Hence these areas remain hotspots for research.

7 Sources Analysis

The data acquired from Microsoft Academic provided articles in this field from 610 sources. For developing the network minimum number of documents to be published by a source is set to five, which include 77 sources only. Also, the minimum number of citations of the source is set to 5, which reduce to 69 sources.

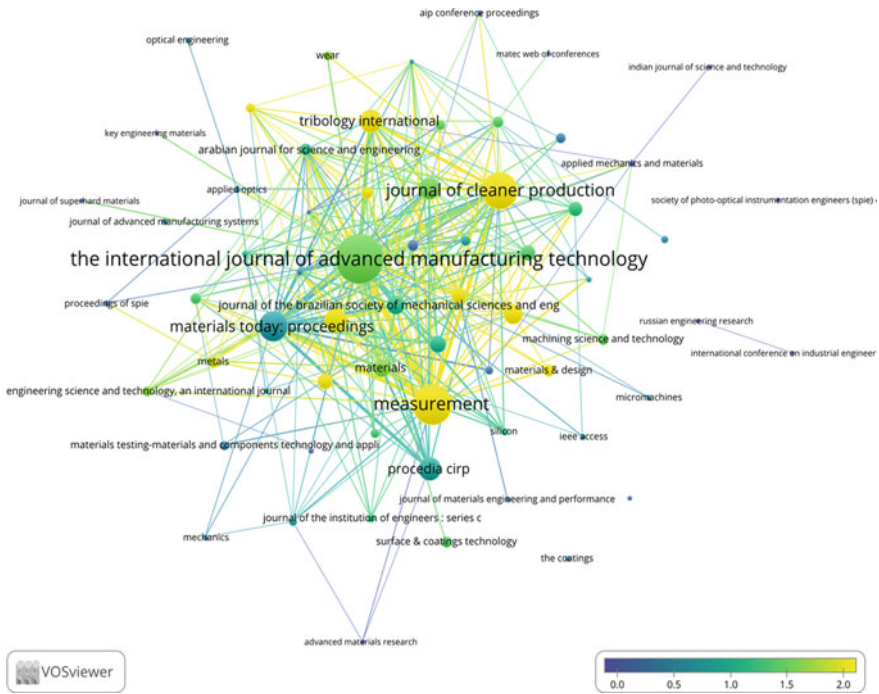


Fig. 8 Sources analysis (Weight: #citations; Score: average normalized citations)

8 Conclusion

In this paper, a bibliometric review of surface roughness in turning process during 2015–2021 has been discussed. The source of data is Microsoft Academic which provides exhaustive database after Google Scholar. The active researchers in the relevant field have been identified using and their research has been discussed. The link strength between different authors and organizations has been found using the networks developed by VOS viewer.

From the co-occurrence analysis the current research hotspot topics predicted are minimum quantity lubrication, hard to cut materials e.g., Inconel alloy, titanium alloys etc., efficient energy use, electrical discharge turning, cryogenic treatment and composite materials.

The maximum cited articles have also been discussed. An analysis with number of citations and normalized citations has been presented. Most cited articles are related to hard to cut materials and minimum quantity lubrication. At last, the sources analysis is done which will help the new researchers in this field to search for related articles and guide them for related sources.

The accuracy of bibliometric study depends on the database collected. A sincere attempt has been made to include all relevant publications in this paper. The database

has been checked manually and irrelevant articles were removed. There might be little margin of error that cannot be eliminated. This article will assist the researchers in terms of related journals, research hotspots and prominent authors in the subject area.

References

- Guleria V, Kumar V, Singh PK (2022) Classification of surface roughness during turning of forged EN8 steel using vibration signal processing and support vector machine. *Eng Res Express* 4(1):015029. <https://doi.org/10.1088/2631-8695/ac57fa>
- Olsen KV (1964) Surface roughness as a function of the cutting data when fine turning steel. *Am Soc Tool Manuf Eng* 655
- He CL, Zong WJ, Zhang JJ (2018) Influencing factors and theoretical modeling methods of surface roughness in turning process: State-of-the-art. *Int J Mach Tools Manuf* 129:15–26. <https://doi.org/10.1016/j.ijmactools.2018.02.001>
- Kamdem JP, Duarte AE, Lima KRR, Rocha JBT, Hassan W, Barros LM, Roeder T, Tsopmo A (2019) Research trends in food chemistry: a bibliometric review of its 40 years anniversary (1976–2016). *Food Chem* 294:448–457. <https://doi.org/10.1016/j.foodchem.2019.05.021>
- Saikia K, Vallès M, Fabregat A, Saez R, Boer D (2020) A bibliometric analysis of trends in solar cooling technology. *Sol Energy* 199:100–114. <https://doi.org/10.1016/j.solener.2020.02.013>
- Martín-Martín A, Thelwall M, Orduna-Malea E, Delgado López-Cózar E (2021) Google scholar, microsoft academic, scopus, dimensions, web of science, and opencitations' coci: a multidisciplinary comparison of coverage via citations. *Scientometrics* 126:871–906. <https://doi.org/10.1007/s11192-020-03690-4>
- Kiduk Y, Meho LI (2006) Citation analysis: A comparison of google scholar, scopus, and web of science. *Proc ASIST Annu Meet* 43. <https://doi.org/10.1002/meet.14504301185>
- Wang K, Shen Z, Huang C, Wu C-H, Dong Y, Kanakia A (2020) Microsoft academic graph: when experts are not enough. *Quant Sci Stud* 1:396–413. https://doi.org/10.1162/qss_a_00021
- Jalal SK (2019) Co-authorship and co-occurrences analysis using bibliometrix r-package: a case study of india and bangladesh. *Ann Libr Inf Stud* 66:57–64
- Perianes-rodriguez A, Waltman L, Jan N, Eck V (2016) Constructing bibliometric networks: a comparison between full and fractional counting. *J Informetr* 10:1178–1195. <https://doi.org/10.1016/j.joi.2016.10.006>
- Yu D, Xu Z, Wang X (2020) Bibliometric analysis of support vector machines research trend: a case study in China. *Int J Mach Learn Cybern* 11:715–728. <https://doi.org/10.1007/s13042-019-01028-y>
- Babu MN, Anandan V, Babu MD (2021) Performance of ionic liquid as a lubricant in turning inconel 825 via minimum quantity lubrication method. *J Manuf Process* 64:793–804. <https://doi.org/10.1016/j.jmapro.2021.02.011>
- Saikaew C, Paengchit P, Wisitsoraat A (2020) Machining performances of TiN plus AlCrN coated WC and Al₂O₃ + TiC inserts for turning of AISI 4140 steel under dry condition. *J Manuf Process* 50:412–420. <https://doi.org/10.1016/j.jmapro.2019.12.057>
- Kesavan J, Senthilkumar V (2020) Experimental investigations on cryo-machining of Hastelloy C-276 with tool wear characteristics. *Sadhana-Academy Proc Eng Sci* 45. <https://doi.org/10.1007/s12046-020-01477-0>
- Das A, Patel SK, Arakha M, Dey A, Biswal BB (2021) Processing of hardened steel by MQL technique using nano cutting fluids. *Mater Manuf Process* 36:316–328. <https://doi.org/10.1080/10426914.2020.1832688>
- Peng RT, Jiang HJ, Tang XZ, Huang XF, Xu Y, Hu YB (2019) Design and performance of an internal-cooling turning tool with microchannel structures. *J Manuf Process* 45:690–701. <https://doi.org/10.1016/j.jmapro.2019.08.011>

17. Teimouri R, Amini S, Mohagheghian N (2017) Experimental study and empirical analysis on effect of ultrasonic vibration during rotary turning of aluminum 7075 aerospace alloy. *J Manuf Process* 26:1–12. <https://doi.org/10.1016/j.jmapro.2016.11.011>
18. Tian WW, Zhao F, Sun Z, Shang SY, Mei XS, Chen GD (2020) A novel performance prediction model for the machining process based on the interval type-2 fuzzy neural network. *Math Probl Eng* 2020. <https://doi.org/10.1155/2020/5740362>
19. Khanna N, Shah P, Maruda RW, Krolczyk GM, Hegab H (2020) Experimental investigation and sustainability assessment to evaluate environmentally clean machining of 15–5 PH stainless steel. *J Manuf Process* 56:1027–1038. <https://doi.org/10.1016/j.jmapro.2020.05.016>
20. Nieslony P, Krolczyk GM, Chudy R, Wojciechowski S, Maruda RW, Biłous P, Lipowczyk M, Stachowiak L (2020) Study on physical and technological effects of precise turning with self-propelled rotary tool. *Precis Eng* 66:62–75. <https://doi.org/10.1016/j.precisioneng.2020.06.003>
21. Yildirim CV, Sarikaya M, Kivak T, Sirin S (2019) The effect of addition of hBN nanoparticles to nanofluid-MQL on tool wear patterns, tool life, roughness and temperature in turning of Ni-based Inconel 625. *Tribol Int* 134:443–456. <https://doi.org/10.1016/j.triboint.2019.02.027>
22. Nouioua M, Yaltese MA, Khettabi R, Belhadi S, Bouhalais ML, Girardin F (2017) Investigation of the performance of the MQL, dry, and wet turning by response surface methodology (RSM) and artificial neural network (ANN). *Int J Adv Manuf Technol* 93:2485–2504. <https://doi.org/10.1007/s00170-017-0589-2>
23. Guleria V, Kumar V, Singh PK (2022) A novel approach for prediction of surface roughness in turning of EN353 steel by RVR-PSO using selected features of VMD along with cutting parameters. *J Mech Sci Technol* 36(6):2775–2785. <https://doi.org/10.1007/s12206-022-0510-2>
24. Mikolajczyk T, Latos H, Pimenov DY, Paczkowski T, Gupta MK, Krolczyk G (2020) Influence of the main cutting edge angle value on minimum uncut chip thickness during turning of C45 steel. *J Manuf Process* 57:354–362. <https://doi.org/10.1016/j.jmapro.2020.06.040>
25. Patel T, Khanna N, Yadav S, Shah PS, Sarikaya M, Singh D, Gupta MK, Kotkunde N (2021) Machinability analysis of nickel-based superalloy Nimonic 90: a comparison between wet and LCO₂ as a cryogenic coolant. *Int J Adv Manuf Technol* 113:3613–3628. <https://doi.org/10.1007/s00170-021-06793-1>
26. Szczotkarz N, Mrugalski R, Maruda RW, Królczyk GM, Legutko S, Leksycki K, Dębowski D, Pruncu CI (2021) Cutting tool wear in turning 316L stainless steel in the conditions of minimized lubrication. *Tribol Int* 156. <https://doi.org/10.1016/j.triboint.2020.106813>
27. Arul K, Kumar VSS (2020) Magnetorheological based minimum quantity lubrication (MR-MQL) with additive n-CuO. *Mater Manuf Process* 35:405–414. <https://doi.org/10.1080/10426914.2020.1732410>
28. Shah P, Gadkari A, Sharma A, Shokrani A, Khanna N (2021) Comparison of machining performance under MQL and ultra-high voltage EMQL conditions based on tribological properties. *Tribol Int* 153. <https://doi.org/10.1016/j.triboint.2020.106595>
29. Maruda RW, Wojciechowski S, Szczotkarz N, Legutko S, Mia M, Gupta MK, Nieslony P, Krolczyk GM (2021) Metrological analysis of surface quality aspects in minimum quantity cooling lubrication. *Meas J Int Meas Confed* 171:108847. <https://doi.org/10.1016/j.measurement.2020.108847>
30. Gupta MK, Sood PK, Sharma VS (2016) Optimization of machining parameters and cutting fluids during nano-fluid based minimum quantity lubrication turning of titanium alloy by using evolutionary techniques. *J Clean Prod* 135:1276–1288. <https://doi.org/10.1016/j.jclepro.2016.06.184>
31. Padmini R, Krishna PV, Rao GKM (2016) Effectiveness of vegetable oil based nanofluids as potential cutting fluids in turning AISI 1040 steel. *Tribol Int* 94:490–501. <https://doi.org/10.1016/j.triboint.2015.10.006>
32. Chinchanikar S, Choudhury SK (2015) International journal of machine tools and manufacture machining of hardened steel—experimental investigations, performance modeling and cooling techniques: a review. *Int J Mach Tools Manuf* 89:95–109. <https://doi.org/10.1016/j.ijmactools.2014.11.002>

33. Mia M, Dhar NR (2016) Prediction of surface roughness in hard turning under high pressure coolant using artificial neural network. *Meas J Int Meas Confed* 92:464–474. <https://doi.org/10.1016/j.measurement.2016.06.048>
34. Gupta MK, Song QH, Liu ZQ, Sarikaya M, Jamil M, Mia M, Khanna N, Krolczyk GM (2021) Experimental characterisation of the performance of hybrid cryo-lubrication assisted turning of Ti-6Al-4V alloy. *Tribol Int* 153. <https://doi.org/10.1016/j.triboint.2020.106582>

Experimental Design for SS 316L-Nanosecond Laser Texturing for Bioengineering Applications



Neelesh Sirdeshmukh  and Ganesh Dongre 

Abstract Laser surface texturing of biomaterials is the most attractive technique having the potential to overcome the limitations such as inadequate osseointegration, infections, and wear of prosthetic implant material. To date, optimum dimensions and patterns are not finalized to achieve optimum performance of biomaterials. The ever-increasing demand for prosthetic implants drives the research toward developing micron-level uniform grooves with the lowest heat-affected areas, micro-cracks, and melt zones. Literature reveals the need for further efforts to investigate the optimization of response characteristics like kerf width, depth against the process parameters. This investigation analyzes the influence of input parameters like power, scan speed, and frequency of Nd: YAG nanosecond fiber laser for texturing of SS 316L. Taguchi's design of experiments and response surface methodology is applied for achieving minimum kerf width. The experimental investigation gives reproducible minimum kerf width of 23.69 μm . The incorporation of Taguchi's DOE approach and regression analysis gives 15.71 μm as the maximum Rz value. ANOVA test is employed for parametric analysis, and the mathematical models are formulated to attain consistent results. The confirmation experiment reveals a satisfactory outcome which validates the results.

Keywords Laser surface texturing · Biomaterials · SS316L

1 Introduction

As per the 2016–17 joint registry record of Canada, 6.8% knee replacements and 8.5% hip replacements are a part of revision surgery. Infections and lack of osseointegration are the prominent causes of orthopedic surgery failures [1]. Surface structuring plays

N. Sirdeshmukh (✉)
Research Scholar, V. I. T., Pune, India
e-mail: neesh.sirdeshmukh@raisoni.net

G. Dongre
Dean (R & D), Vishwakarma Institute of Technology, Pune 411037, India
e-mail: ganesh.dongre@vit.edu

a vital role in improving the life of orthopedic implants. Surface topography is crucial for achieving good osseointegration. Macro-surface roughness facilitates biomechanical interlocking which leads to good stability and longer life of implants. Micro-surface roughness promotes cell growth and tissue interlocking whereas nano-surface roughness governs protein adsorption, rapid bone healing, etc., [2, 3]. Methods like sandblasting and chemical etching are widely used for the surface structuring of implants [4]. Sandblasting method does not have control over the depth and regularity. The use of alumina abrasive particles may lead to aluminum contamination. Chemical etching is prone to fluoride contamination and micro-cracks on the surface. These cracks reduce fatigue and mechanical properties [5]. Laser surface texturing is the most attractive method which has the potential to develop reproducible micro and nanoscale textures [6]. It can modulate wettability and surface topography, roughness, and chemistry of prosthetic implant surface [7, 8, 9].

Stainless steel devices are primarily used for hip nails, plates, screws, and total hip replacement (THR) components [10]. Good corrosion resistance, toughness, and biocompatibility along with superb manufacturing ability, availability, the low price made 316L SS more applicable for bioengineering applications [8]. The laser surface texturing (LST) transforms 316L SS to good corrosion resistive material due to the newly formed thick oxide layer of Ni, Cr, and Fe [11]. Also, the process of laser ablation improves surface hardness, young's modulus, and microstructural refinement [12, 13]. Experiments reveal a decrement in the wear rate of processed AISI 304 SS material [14, 15]. Silvio et al. generated the AISI 304 SS samples having contact angles ranging from 30° to 110° . Whereas Victor et al. and Dongre et al. produce superhydrophobic samples [16, 17]. Suvranshu et al. succeeded in producing microgroove on 316L SS orthopedic material [18].

The modified surface topography controls the interaction between tissue and surface [19, 20]. Sunita et al. observe more dense, aligned osteosarcoma cells over laser textured surfaces [11]. Also, processed surfaces can modulate the migration of cells [21]. The increment in contact angle minimizes bacterial growth [22, 23, 24]. Fiorucci et al. investigated the comparative nature of 316L SS and Ti6Al4V for laser structuring [25, 26].

The literature survey reveals the need to optimize texture dimensions and patterns to obtain good osseointegration and antibacterial effects. To understand the interrelationship between process parameters and the responses like kerf width, the surface roughness R_a , R_z , an experimental design with Taguchi's design, the Response Surface Methodology, and regression analysis is used. The major influencing factors for the laser ablation phenomenon are discussed with ANOVA methodology.

2 Experimental Set-Up

The laser texturing is carried out with nanosecond fiber laser NUQA-1064-NA-0030-YZ. The laser machine specifications are given in Table 1.

Table 1 Nanosecond laser machine specification

Peak power	10.0 Kw
Output power	30.0 W
Pulse energy	1.0 mJ
Pulse width	100 ± 20 ns
Power stability	± 2.5%
Beam quality (nominal)	M2 <1.5
Mode of operation	Pulsed
Polarization	Random
Pulse repetition rate (PRR)	30–100 kHz

The experimentation is carried out on 316L SS 25 mm × 25 mm × 1.2 mm plates. For each experiment, the 6 mm × 6 mm square surface is textured with the laser beam. The composition of 316L SS is presented in Table 2.

Initially, screening tests were performed to understand the prominent parameters and their range. The surface texturing parametric influence is investigated with two different sets of experiments. The first part of the experiment is performed for interpreting the significance of variables such as power (w), scan speed (mm/s), and frequency. The investigation is carried out with Taguchi’s design of experiment L-9 orthogonal array. One replication experiment is carried out to reduce the experimental errors. Table 3 shows the process parameter range.

During the study, pitch distance 50 μm and repetition rate as one is kept constant. Three response variables, namely kerf width (μm) and surface roughness Ra, Rz (μm), are recorded. The second part of the experiment is carried out in four stages as a single factorial design. The details of the parameters are given in Table 4. Response surface methodology and regression analysis are used for parametric analysis. The kerf width is measured with a Rapid-I vision measuring system microscope. Mitutoyo SJ-210 surface roughness tester is used for measuring Ra, Rz.

Table 2 Composition of SS 316L

Grade	Cr	Mo	Si	Mn	C	P	S	Fe
Percentage	17	2.5	0.75	2.00	0.03	0.045	0.75	balance

Table 3 Process parameters for the first experiment

S. No.	Laser power (W)	Scan speed (mm/s)	Frequency (KHz)
1	6	200	70
2	9	250	80
3	12	300	90

Table 4 Parameter range for experiment part 2

S. No.	Laser power (Watt)	Scan speed (mm/s)	Frequency (KHz)	Pitch distance (μm)
1	5, 6, 7, 8, 9, 9.25, 9.5, 9.75, 10, 10.1, 10.3, 10.5, 10.75, 11, 11.25, 12, 13	200, 250	90	50, 90, 250

3 Results and Discussions

Figure 1 shows the conceptual diagram for texturing and a sample photograph of microgroove generated on the surface. The textured surface kerf width and surface roughness Ra and Rz are measured at three different cross sections and averaged. The average result values are given in Table 5.

3.1 Surface Roughness Ra, Rz and Surface Coloration

The color of the processes sample is varying with a surface roughness Ra and Rz. The variation in Ra and Rz results in the oxide layer and recast layer thickness variation. From samples number 1–6, the colors are observed as lighter as having less surface roughness and Rz values. Due to the intense power of the laser beam, surface layers get burned and re-solidified. From sample numbers 7–9, surface shows the darker wheat and brown color. The details of sample number, color, Ra, and Rz values are mentioned in Table 6 and Fig. 2 for (L-9 array)(experiments 1–9).

3.2 Signal-To-Noise (S/N) Analysis

Signal-to-noise ratio signifies the quality characteristics of the output parameters. It is used to reduce variability while finalizing the control factors. The maximum

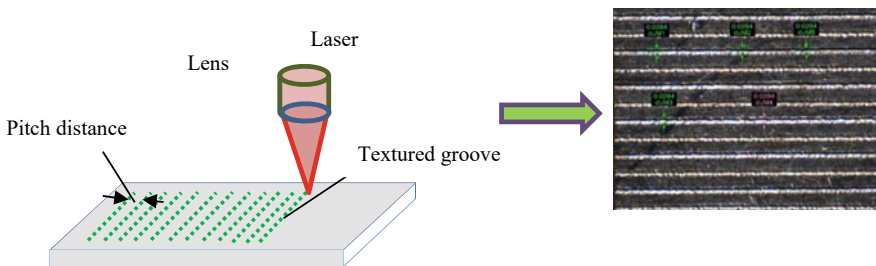


Fig. 1 Laser surface texturing and a SS 316L sample grooved surface

Table 5 Experiment dataset

Experiment No.	Power W	Frequency kHz	Scan speed mm/s	Kerf width μm	Surface roughness Ra μm	Surface roughness Rz μm
1	1	1	1	33.1	0.232	1.292
2	1	2	2	27.6	0.194	1.16
3	1	3	3	26.1	0.141	1.108
4	2	1	2	21.5	1.048	4.911
5	2	2	3	22	0.324	1.941
6	2	3	1	31.2	0.202	1.694
7	3	1	3	31.2	2.172	12.94
8	3	2	1	34.9	2.226	12.641
9	3	3	2	31.2	1.350	7.195
10	1	1	1	25.70	29.4	1.722
11	1	2	2	29.4	33.1	1.456
12	1	3	3	33.1	27.2	1.294
13	2	1	2	31.2	25.7	7.485
14	2	2	3	27.6	23.9	3.555
15	2	3	1	29.4	31.7	1.684
16	3	1	3	38.6	29.4	11.166
17	3	2	1	36.7	33.1	10.238
18	3	3	2	27.6	34.9	8.601

Table 6 Surface roughnesses Ra, Rz, and surface coloration

Surface roughness Ra μm	Surface roughness Rz μm	Surface color	Sample number
0.232	1.368	Gray	1
0.324	1.910	Silver	5
0.202	1.694	Charcoal	6
2.226	13.066	Brown	7, 8
1.350	7.349	Wheat	9

S/N ratio indicates more precise responses for expected values [27]. The kerf width is expected to be minimal for good quality. Hence, smaller the better (SB) type is selected. Surface roughness Rz value denotes the average peak to valley depth. For biomedical applications, higher Rz is planned for experimentation. Hence, higher the better (HB) is selected. Equations 1 and 2 show the signal-to-noise ratio for higher the better and smaller the better, respectively.

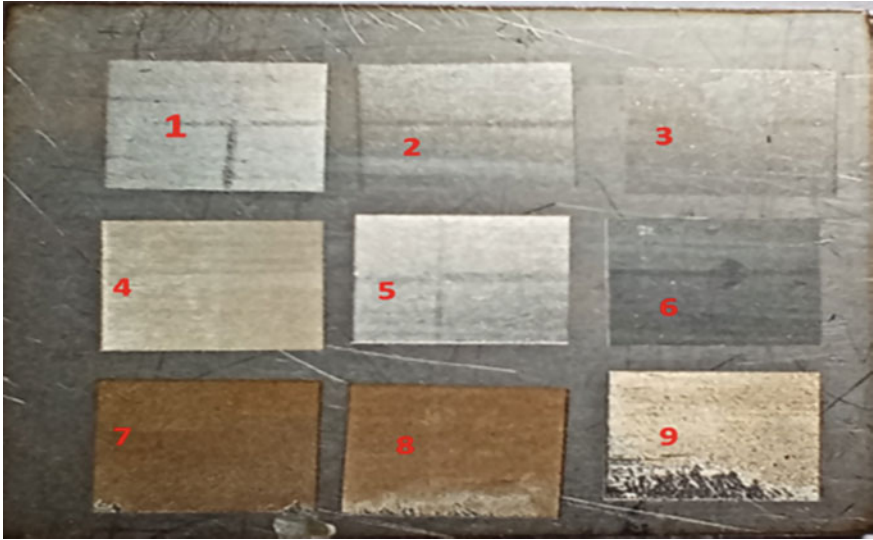


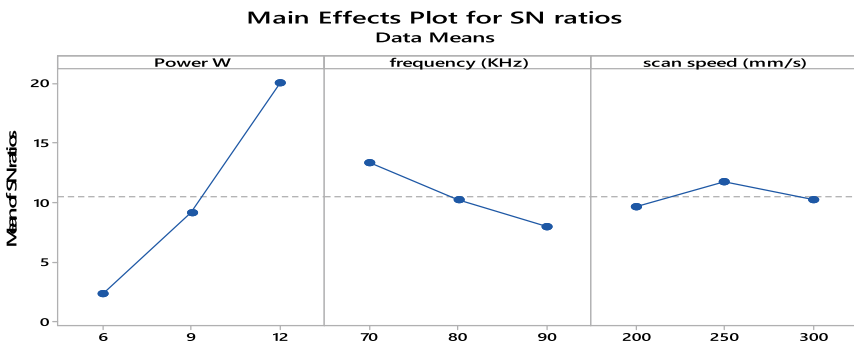
Fig. 2 Colors obtained after laser surface texturing of SS 316L

$$\eta = \text{signal to noise ratio} = -\log_{10}\left[\frac{1}{n} \sum_{i=1}^n y_i^2\right] \quad \text{For HB} \quad (1)$$

$$\eta = \text{signal to noise ratio} = -\log_{10}\left[\frac{1}{n} \sum_{i=1}^n 1/y_i^2\right] \quad \text{For SB} \quad (2)$$

Effect of process parameters on surface roughness Rz

Figure 3 shows the main effect plot for surface roughness Rz against power, frequency, and scan speed. As power increases from 6 to 12 W, the depth of the



Signal-to-noise: Larger is better

Fig. 3 S/N ratio effect plot for surface roughness Rz

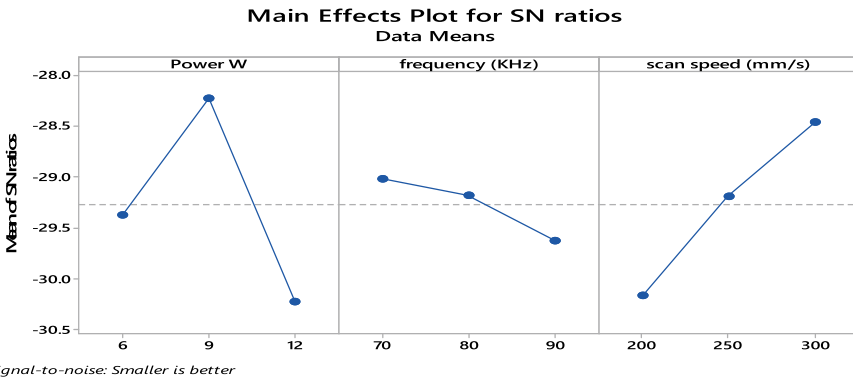


Fig. 4 S/N ratio effect plot for kerf width

groove increases. Beyond 9 W, the rise in depth is steeper due to higher power density. Lower frequency means a lower number of pulses, and each pulse will have more energy. Hence, at 70 kHz frequency gives more Rz value in comparison with 90 kHz. Scan speed is critical for the Rz value. Lower the scan speed, higher the heat interaction time and more heat input. As moving from 200 to 250 mm/s, Rz increases, and later from 250 mm/s to 300 mm/s, Rz decreases. This nature is exactly reverse as of Kerf width. Rz increases in exchange for a decrease in kerf width. Power 12 W, frequency 70 kHz, and scan speed 250 mm/s are the control factors for maximum Rz values.

Effect of process parameters on Kerf width

Figure 4 shows the signal-to-noise ratio for kerf width against power, scan speed, and frequency. Power is a critical parameter for kerf width. From 6 to 9 W, kerf width decreases and afterward increases. As power increases from 6 to 9 W, maximum heat intensity is initially utilized for the melting of the material. As it is reaching toward 9 W, elevated energy density gets utilized for evaporation and melting which results in the reduction of kerf width and heat-affected zone. Subsequently, high power intensity after 9 W melts more material along width resulting in an increment in the heat-affected zone. As scan speed moves from 200 to 300 mm/s, kerf width decreases. The lower the scan speed, the higher is the heat input rate. When frequency moves from 70 to 90, kerf width reduces. Frequency in the range of 70–80 kHz has slightly more impact as pulses have more energy as compared to the 80–90 kHz range. Power 9 W, frequency 90 kHz, and scan speed 200 mm/s are the control factors for minimum kerf width values.

Table 7 ANOVA for surface roughness Rz

Process parameter	Sum square	D.O.F	Mean sum of square	F-ratio	Percentage contribution
Power W	476.11934	2	238.0596704	109.70062	86.10312724
Frequency (KHz)	49.131545	2	24.56577256	11.320189	8.88512463
Scan speed (mm/s)	8.1824009	2	4.09120045	1.885272	1.479734691
Error	19.530765	2			3.532013434
Total	552.96405	8		Total	100

3.3 ANOVA for Kerf Width and Surface Roughness Rz

To know the significance of input parameters and find out the error in conducted experiment, an ANOVA test is carried out.

Table 7 shows the ANOVA results for surface roughness Rz. Power is the most influencing parameter over Rz control as it contributes around 86%. Frequency is the second most influencing parameter carrying an 8.88% contribution. F-ratio of three parameters is greater than 1.645 at 0.05 level which shows the significance of all parameters. The ANOVA shows a 3.53% error contribution.

Table 9 shows the ANOVA results for kerf width. Power and frequency are most significant for controlling kerf width response parameters which contribute 49% and 35% of the parameters, respectively. The value of the Z factor of all the parameters is greater than 1.645 at 0.05 level shows a significant level. Also, the error is less than 10%.

3.4 Mathematical Model for Surface Roughness Rz Response

A regression model is formulated to fit the mathematical model for Rz response. Minitab 17 software is used to formulate the model. The following regression Eq. 3 shows the parametric relationship for Rz.

$$Rz = 2.25 + 1.521 \text{ Power } W + 0.0046 \text{ scan speed(mm/s)} - 0.1495 \text{ frequency(KHz)} \tag{3}$$

where Rz is in μm .

For measuring the adequacy of the model, the ANOVA test is carried out. The P-value of the regression model is less than 0.001, and the F-ratio is 25.27 which indicates the significance of the model. Also, the R (adj) and R (pred.) show reasonably good agreement having the value 82.26% and 76.38%, respectively. Table 8 shows the ANOVA of the regression model for surface roughness Rz. F value for regression is 27.27, and P-value is less than 0.001 which shows the significance of the

Table 8 ANOVA of the regression model for surface roughness Rz

Source	DF	Adj SS	Adj MS	F-Value	P-Value
Regression	3	277.230	92.410	27.27	0.000
Power W	1	249.788	249.788	73.72	0.000
Scan speed (mm/s)	1	0.622	0.622	0.18	0.675
frequency (KHz)	1	26.820	26.820	7.92	0.014
Error	14	47.435	3.388		
Lack-of-fit	5	37.217	7.443	6.56	0.008
Pure error	9	10.218	1.135		
Total	17	324.665			

Model summary

	S	R-sq	R-sq(adj)	Rsq(pre)	
	1.84070	85.39%	82.26%	76.38%	

model. There is reasonable agreement between $R^2_{adj.}$ and $R^2_{pred.}$ values, 82.26% and 76.38%, respectively. As scan speed is less significant, the R^2 adjusted value differs from the R^2 value slightly. Figure 5 shows the normal probability plot for residuals of Rz values.

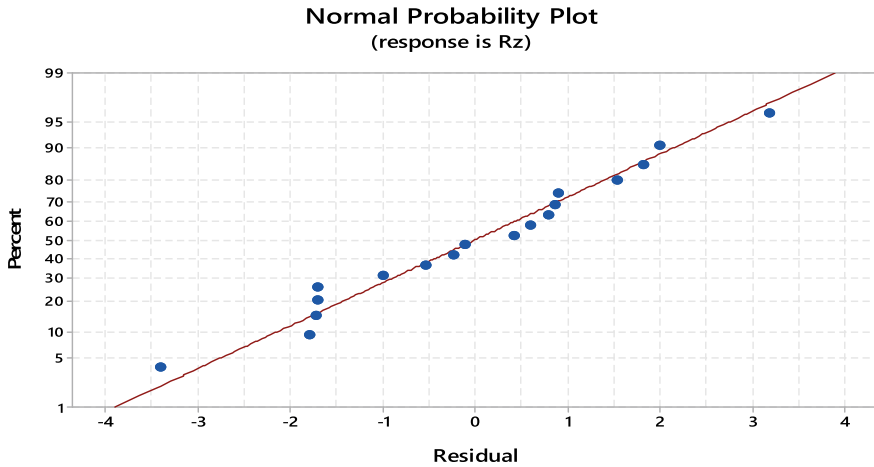


Fig. 5 Normal probability plot residuals of Rz

Table 9 ANOVA for kerf width

Process parameters	Sum square	D.O.F	Mean sum of square	F-ratio	Percentage contribution
Power W	6.190261769	2	3.095130885	23.56748336	49.50124205
Frequency KHz	0.700405744	2	0.350202872	2.666575554	5.600886609
Scan speed mm/s	4.432622961	2	2.21631148	16.87582396	35.44605225
Error	1.181975077	2			9.451819095
Total	12.50526555	8		Total	100

3.5 Response Surface Method for Process Parameter Response on Kerf Width

Central composite full quadratic RSM with a 95% confidence level is applied to draw the result. Figure 6 shows the surface plot for power, scan speed as input variables versus kerf width as a response parameter. As power is increasing from 9 to 12 W, kerf width first decreases, and from 10 to 12, it increases. From 9 to 10 W, as part of heat which is utilized for evaporation is going on increasing, ultimately resulting in a clean groove having less heat-affected zone. Later from 10 to 12 W, due to increased intensity of heat, the heat-affected zone increases. The regression equation is generated for variation in kerf width due to power and scan speed.

$$\begin{aligned}
 \text{kerf width} = & 211.7 - 22.12 \text{ Power W} - 0.574 \text{ scan speed(mm/s)} \\
 & + 1.139 \text{ Power W} * \text{Power} + 0.001162 \text{ scan speed(mm/s)} \\
 & * \text{scanspeed(mm/s)} \\
 & - 0.00346 \text{ Power W} * \text{scan speed(mm/s)}
 \end{aligned}$$

Surface Plot of kerf width vs scan speed (mm/s), Power W

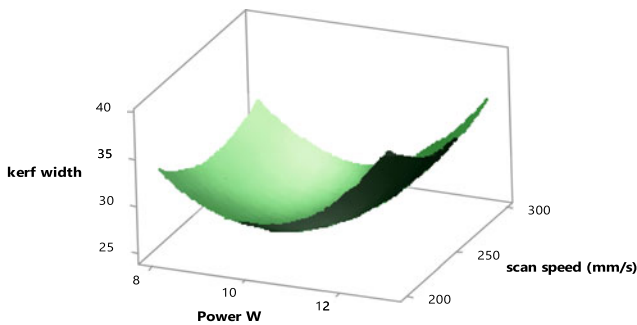


Fig. 6 Surface plot for kerf width versus scan speed, power W

Table 10 ANOVA of RSM of response parameter kerf width

Source	DF	Adj SS	Adj MS	F-Value	P-Value
Model	5	241.067	48.2135	20.12	0.000
Linear	2	54.548	27.2738	11.38	0.001
Power W	1	30.270	30.2701	12.63	0.002
Scan speed (mm/s)	2	15.776	15.7762	6.58	0.020
Square	1	193.918	96.9590	40.46	0.000
PowerW*Power W	1	96.732	96.7319	40.37	0.000
Scan speed (mm/s)*scan speed (mm/s)	1	38.042	38.0422	15.88	0.001
2-way interaction	1	0.564	0.5639	0.24	0.634
Power W*scan speed(mm/s)	17	0.564	0.5639	0.24	0.634
Error	8	40.736	2.3962		
Lack-of-fit	9	24.528	3.0660	1.70	0.222
Pure error	22	16.208	1.8009		
Total		281.803			
Model summary					
S	R-sq	R-sq(adj)	R-sq(pred)		
1.54798	85.54%	81.29%	73.37%		

The P-value of the model is less than 0.001, and the F value is 20.12 which shows the significance of the model. $R^2(\text{adj.})$ and $R^2(\text{pred.})$ are 81.19% and 73.37%, respectively. This shows reasonably good agreement between the R sq. values. Table 10 shows ANOVA for RSM of response parameter kerf width.

3.6 Experimental Validation for Optimum Process Parameters

The signal-to-noise ratio for minimum kerf width against process parameters is shown in Fig. 4. The A2B3C1 are optimum parameters to get minimum kerf width. As per Taguchi’s design, the minimum kerf width is 22.67 μm . The experimental minimum average kerf width for the process parameters power (9 W), scan speed (200 mm/s), and frequency (90 kHz) is 23.79 μm . It shows good agreement between the theoretical and experimental values resulting in a 4.94% error. Figure 7 shows the minimum kerf width groove on SS 316L plates.

The signal-to-noise ratio for maximum Rz values against process parameters is shown in Fig. 4. The A3B1C2 are optimum parameters to get maximum Rz. Taguchi’s design gives a maximum Rz value of 16.53 μm . The experimental results show 15.14 μm as average maximum Rz. It shows good agreement between theoretical and experimental results giving an 8.40% error.



Fig. 7 Minimum kerf width (in μm) received for nanosecond laser NUQA-1064-NA-0030-YZ

4 Conclusions

The laser texturing is carried out on SS 316L surface with the help of a nanosecond fiber laser. The experiment reveals the influence of input parameters such as power, scan speed, and frequency against surface roughness Ra, Rz, and kerf width as output parameters. The major conclusions drawn from the experiments are mentioned below.

- i. The power is a critical parameter for kerf width. From 6 to 9 W, kerf width decreases and later increases. Scan speed is also an influencing parameter.
- ii. The power is the major influencing parameter for surface roughness Rz. As power increases, Rz increases from 6 to 12 W.
- iii. Between 9 and 11 W, although kerf width is reducing, there is not much increment in Rz. This phenomenon occurs as most of the energy is utilized for the evaporation of material.

Acknowledgments The work has been supported under ISRO RESPOND project grant. The author is grateful to management of Vishwakarma Institute of Technology, Pune and G H Raison College of Engineering & Management, Pune, India.

References

1. Joint C, Registry R, Report A (2017) Hip and knee replacements in Canada 2016–2017
2. Barfeie AF (2015) Implant surface characteristics and their effect on osseointegration. Br Dent J 218. <https://doi.org/10.1038/sj.bdj.2015.171>

3. Zhang LF (2010) Nanomaterials for improved orthopedic and bone tissue engineering applications. *Adv Biomater Fundam Process Appl* 205–241. <https://doi.org/10.1002/9780470891315.ch7>
4. Wang K (1996) F: The use of titanium for medical applications in the USA. *Mater Sci Eng A* 213:134–137. [https://doi.org/10.1016/0921-5093\(96\)10243-4](https://doi.org/10.1016/0921-5093(96)10243-4)
5. Davis J (2003) F: Handbook of Materials for Medical Devices. *ASM Int* 205–216. <https://doi.org/10.1361/hmmd2003p001>
6. Manivasagam G (2010) F: biomedical implants: corrosion and its prevention—a review recent patents *corros. Sci* 2:40–54. <https://doi.org/10.2174/1877610801002010040>
7. Sirdeshmukh NF, Dongre GS (2021) Laser micro and nano surface texturing for enhancing osseointegration and antimicrobial effect of biomaterials: a review. *Mater Today Proc* 44:2348–2355. <https://doi.org/10.1016/j.matpr.2020.12.433>
8. Mahajan, A., F.: Surface modification of metallic biomaterials for enhanced functionality: a review. *Mater. Technol.* 33, 93–105 (2018). <https://doi.org/10.1080/10667857.2017.1377971>.
9. Shivakoti I (2021) F.: Laser surface texturing for biomedical applications: a review
10. Asri F (2017) Corrosion and surface modification on biocompatible metals: a review. *Mater Sci Eng C* 77:1261–1274. <https://doi.org/10.1016/j.msec.2017.04.102>
11. Kedia F (2021) Nanosecond laser surface texturing of type 316L stainless steel for contact guidance of bone cells and superior corrosion resistance. *Colloid Interface Sci Commun* 42:100419. <https://doi.org/10.1016/j.colcom.2021.100419>
12. Watanabe F (2009) Laser surface treatment to improve mechanical properties of cast titanium. *Dent Mater* 25:629–633. <https://doi.org/10.1016/j.dental.2008.11.006>
13. López-Cervantes A (2013) F.: Effects of surface texturing on the performance of biocompatible UHMWPE as a bearing material during in vitro lubricated sliding/rolling motion. *J Mech Behav Biomed Mater* 20:45–53. <https://doi.org/10.1016/j.jmbbm.2012.12.010>
14. Ahmed YS (2021) F: Laser surface texturing and characterization of austenitic stainless steel for the improvement of its surface properties
15. Yang L (2021) F: an experimental investigation on laser surface texturing of AISI D2 tool steel using nanosecond fiber laser. *Lasers Manuf Mater Process.* <https://doi.org/10.1007/s40516-021-00144-4>
16. Villapún F (2020) Development of antibacterial steel surfaces through laser texturing development of antibacterial steel surfaces through laser texturing. 091108. <https://doi.org/10.1063/5.0017580>
17. Dongre, G.G., F., Rajurkar, A.U., S.: Preparation of Super-hydrophobic Textures by Using Nanosecond Pulsed Laser. *Mater. Today Proc.*,2–42, 1145–1151 (2020). <https://doi.org/10.1016/j.matpr.2020.12.497>.
18. Pattanayak S (2021) F: optical fiber technology micro engraving on 316l stainless steel orthopedic implant using fiber laser. *Opt Fiber Technol* 63:102479. <https://doi.org/10.1016/j.yofte.2021.102479>
19. Fiorucci MP (2014) F.: Surface Modification Induced by UV Nanosecond Nd: YVO4 laser structuring on Biomaterials 9286:1–8. <https://doi.org/10.1117/12.2063782>
20. Patel D (2018) F.: Micro texturing on metallic surfaces: state of the art. *J Eng Manuf* 6–232. <https://doi.org/10.1177/0954405416661583>.
21. Martínez-Calderon F (2016) Surface micro- and nano-texturing of stainless steel by femtosecond laser for the control of cell migration. *Sci Rep* 6:1–10. <https://doi.org/10.1038/srep36296>
22. Lutey AHA (2018) F: towards laser-textured antibacterial surfaces, *nature scientific reports* 8–10112. <https://doi.org/10.1038/s41598-018-28454-2>.
23. Romoli L (2020) F.: CIRP annals—manufacturing technology in influence of ns laser texturing of AISI 316L surfaces for reducing bacterial adhesion. *CIRP Ann Manuf Technol* 69:529–532. <https://doi.org/10.1016/j.cirp.2020.04.003>
24. Rajab FH F.: Picosecond laser surface micro/nano texturing of stainless steel as a method to reduce the adhesion of bacteria 1–8
25. Fiorucci MP (2014) F.: Comparative study of surface structuring of biomaterials by UV nanosecond Nd:YVO4 laser. *Int J Adv Manuf Technol* 75:515–521. <https://doi.org/10.1007/s00170-014-6164-1>

26. Fiorucci MP (2018) F.: Multi-scale characterization of topographic modifications on metallic biomaterials induced by nanosecond Nd:YVO4 laser structuring. *Precis Eng* 53:163–168. <https://doi.org/10.1016/j.precisioneng.2018.03.009>
27. Wang X (2015) F.: Effect of overlap and overscan number in laser surface texturing of medical needles Effect of overlap and overscan number in laser surface texturing of medical needles. *Appl Phys A* 120:229–238. <https://doi.org/10.1007/s00339-015-9157-5>

Welding

Temperature Analysis of Water-Cooled Friction Stir Welding Using Spray Nozzle on Aluminium 2014 Alloy



Cibi Gabriel Goldwysingh David Rajasingh,
Mystica Augustine Michael Duke, and Senthil Kumar Santhanam

Abstract In-process cooling during Friction Stir Welding (FSW) has been the subject of focus in recent times because of the need to improve the various properties of conventional friction stir welded joints by reducing the excess heat dissipation. Using different cooling media during the in-process cooling of Friction Stir Welding leads to different cooling rates being induced in the tool-work piece interface. This in turn results in considerable changes across the temperature distribution along the weld line. In the present study, in-process cooling during the friction stir welding of Aluminium Alloy 2014 (AA2014) is performed using a nozzle designed to produce a spray with water and compressed air. K-type thermocouples coupled with Arduino UNO are placed on both Advancing Side (AS) and Retreating Side (RS) of the weld in order to measure the temperature distribution along the weld line. It is found that when a spray with water being maintained at a flow rate of 60 ml/min and the air at a pressure of 3 bar is used during welding, the peak temperature in the weld decreases which can attributed to the combined cooling effect caused by water and compressed air. The different phases of Friction stir welding along with cooling are simulated using a Finite Element Model (FEM) that has been developed in ABAQUS/CAE module using Coulomb's law of Friction formulation and Johnson–Cook constitutive and damage evolution model. An Explicit analysis with various mechanical and thermal boundary conditions has been performed for simulating the actual welding process. The experimental results obtained are then validated using the simulated results.

Keywords Friction stir welding · In-process cooling · Temperature distribution · AA2014 · Spray cooling · Finite element modelling

C. G. G. D. Rajasingh (✉) · M. A. M. Duke · S. K. Santhanam
College of Engineering Guindy Campus, Anna University, Chennai, Tamil Nadu 600025, India
e-mail: cibigabriel@gmail.com

1 Introduction

Friction stir welding is a solid-state joining technique used for joining metal alloys predominantly in aluminium alloys. The joining is done by utilizing the frictional heat produced by the interaction of a rotating pin tool with metal plates. The melting-related defects that usually occur in conventional welding techniques can be avoided using Friction Stir Welding as the materials are not melted and the maximum temperature during the process can be maintained within the solidus of the material [1]. The region of the plate under the tool is brought to a plastic state and then made to flow along the weld line to join the metals. Many high-strength aluminium alloys of 2xxx, 6xxx and 7xxx series that can be easily subjected to melting associated defects by conventional welding techniques, can be welded easily by FSW. AA2014 is a precipitation-hardened alloy that is most widely used in the manufacture of high-strength components used in aerospace and defense industries owing to its high strength-to-weight ratio and corrosion resistance. AA2014 offers very good machinability and also can retain its strength after heat treatment. However, welding by conventional welding techniques is not possible as it is subject to cracking. Hence Friction Stir Welding is used to join AA2014. Rajamanickam et al. [2] studied the thermal and mechanical properties in the friction stir welds of AA2014 by changing process parameter values and found that the rotational speed influences the peak temperature in the weld zone more strongly than weld traverse speed. He also reported that though the heat input during the FSW process is generally low, the strengthening precipitates dissolve when the temperature goes beyond 500 K which can considerably reduce the strength of the age-hardened aluminium alloy. Bhavesh Chaudhary et al. [3] observed that the rate of temperature rise was slow at initial stages but suddenly rises very fast and fluctuates at the center of weld length during Friction Stir Welding of AA2014 which he later attributed to an increase in friction. Kumar et al. [4] performed experiments to determine the influence of different tool pin profiles and reported that better mechanical properties and less heat generation are observed on using square pin profile due to a large amount of material being swept from the plasticized zone. Mystica et al. [5] have observed that the detrimental effects of heat produced were not only evident on the workpiece but also on other components of the machine such as the Tool Holder. Therefore, cooling is essential for Friction Stir Welding of 2014 series aluminium alloy to decrease the heat input.

Sharma et al. [6] performed Friction Stir Welding of AA7039 FSW joint under in-process cooling conditions using different cooling media and observed that the mechanical properties were enhanced greater when water is used for cooling. Sinhmar et al. [7] studied the corrosion and mechanical behavior of AA2014-T6 FSW welds cooled by spraying water and natural air and observed that flowing water caused faster heat removal leading to a reduction in high-temperature retention period and production of fine precipitate grain sizes. A novel spray cooling technique has been used in the present study.

Saad B. Aziz et al. [8] successfully simulated all the three stages of the FSW process by developing a model using an Explicit model and Arbitrary Lagrangian–Eulerian (ALE) formulation in ABAQUS. Bahman Meyghani et al. [9] have developed finite element models using temperature-dependent Young’s modulus values to provide a more accurate model because Young’s modulus values decrease when the temperature increases. Mandal et al. [10] have used a temperature and strain rate-dependent Johnson–Cook material constitutive law to show how temperature, plastic strain and strain rate are affected by the interaction of flow stress.

In the present study, a novel spray cooling technique has been used to perform the in-process cooling during the Friction Stir Welding of AA2014 alloys and the experimental results are then validated with numerical results using a Finite Element Model developed in ABAQUS.

2 Materials and Methods

2.1 Experimental Procedure

Rolled Aluminium Alloy 2014 (AA2014) plates of thickness 6 mm were initially cut into desired dimensions of 140 mm × 70 mm using a Wire-cut Electric Discharge Machine. The edge preparation was then separately done by using an end milling operation. The chemical composition of AA2014 is given in Table 1.

Initially, the plates are placed in a specially designed fixture and clamped together in butt weld configuration. H13 tool steel has been used to create the tool used for welding. The rotating tool consists of two parts: the shoulder and a square profile protruding pin. The tool has been fabricated by machining steel in a CNC Lathe Machine and subjecting to heat treatment to increase its hardness within ranges of HRC 38 and 48. The complete setup is shown in Fig. 1.

The optimized values of parameters like rotational speed and traverse velocity for spray cooled Friction Stir Welding of AA2014 plates have been obtained from past literature. Table 2 shows the welding parameters that were used for welding AA2014 plates [11].

Friction Stir Welding was performed under spray cooling conditions. The spray cooling was carried out during the welding process by using a specially designed nozzle. The nozzle was designed to atomize compressed air and water together to create a spray. The compressed air was used as a medium to transport the water particles and impinge them onto the weld line at high velocities. The flow rate of water was maintained at 60 ml/min and compressed air was maintained at a pressure

Table 1 Chemical composition of AA2014

Element	Al	Cu	Si	Mn	Mg	Fe
Percentage (%)	92.1	4.86	0.95	0.93	0.69	0.36

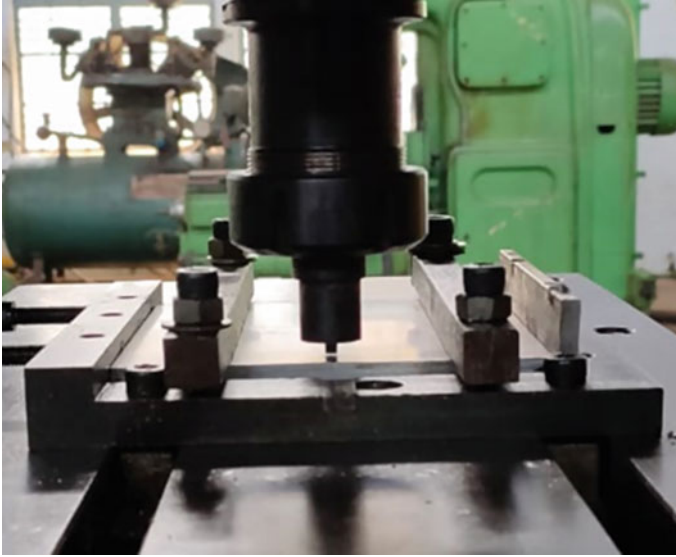


Fig. 1 Friction stir welding setup

Table 2 Welding parameters

S. No.	Process parameters	Unit	Level
1	Tool rotation speed	rpm	1000
2	Traverse speed	mm/min	44

of 2 atm. 6 mm holes are drilled onto the aluminium plates to support the probe of K-type thermocouples. During the welding process, the temperature being produced in the AS and RS of the weld is recorded in real time using these K-type thermocouples. The data acquisition is made by using an Arduino UNO that provides the interface between the thermocouples and computer. The complete FSW setup with spray cooling arrangement is shown in Fig. 2.

2.2 Numerical Model

A Non-linear, Dynamic Finite Element Model has been developed for the simulation of the FSW process of AA2014 plates with spray cooling. The actual breadth of the plate is reduced by a scale of 0.75 to improve the computational efficiency since the effects of cooling are not much evident in the region far away from the weld line. A 140 mm × 50 mm rectangle is sketched and extruded to a thickness of 6 mm to model the deformable plates. The single model is then sectioned using datum planes to form the weld line and to specify the region where the spray interacts with



Fig. 2 In-process spray cooling assisted friction stir welding setup

the plate. The rigid tool is then modeled such that only the surfaces responsible for generating heat by friction are generated. A 2D planar backing plate has also been modeled as an analytical rigid body. Tables 3 and 4 shows the various temperature-dependent material properties that have been assigned to define the AA2014 plates and the isothermal material properties to define the H13 Tool respectively.

Table 3 Temperature-dependent mechanical and thermal properties of AA2014 [12]

Temperature (°C)	Density (kg/m ³)	Thermal conductivity (W/m-K)	Young's modulus (GPa)	Specific heat (J/g-K)
25	2820	127.67	72.1	870
100	2800	137.78	69.5	910
200	2780	147.03	65.5	950
300	2760	153.38	61.1	990
400	2740	157.71	56.2	1030
500	2710	160.45	50.9	1510

Table 4 Mechanical and thermal properties of H13 [13]

Density (kg/m ³)	Young's modulus (GPa)	Poisson's ratio	Thermal conductivity (W/m-K)	Specific heat capacity (J/g-K)
7800	215	0.3	28.6	460

The Johnson–Cook model is used to define the plastic behavior of the material. Temperature and strain-dependent material model along with a Johnson–Cook material law [14] has been adopted to study deformation at a high strain rate. The model is given by the Eq. (1).

$$\sigma_o = \left(A + B\bar{\epsilon}_{pl}^n \right) \left(1 + C \ln \frac{\dot{\bar{\epsilon}}_{pl}}{\dot{\epsilon}_o} \right) \left(1 - \left(\frac{T - T_{ref}}{T_{melt} - T_{ref}} \right)^m \right) \quad (1)$$

Here, T_{ref} represents the temperature where parameters A, B and n are evaluated while T_{melt} is material solidus temperature. Table 5 lists the AA2014 material properties for the Johnson–Cook model [15].

The plates were meshed using Hex-shaped thermally coupled brick elements consisting of eight nodes with trilinear displacement and temperatures along with reduced integration and hourglass control (C3D8RT) which help increase computational efficiency while maintaining the accuracy. The meshed model has 42,000 elements as shown in Fig. 3.

Frictional contact along with temperature-dependent coefficient of friction values were used to define the contact between tool and plates. The various mechanical boundary conditions that have been used to constrain plates, tool and backing plate are shown in Fig. 4. The tool is rotated at 1000 rpm about its central axis in clockwise

Table 5 Johnson–Cook material constitutive parameters

Johnson–Cook parameters [16]					
A (MPa)	B (MPa)	N	C	M	T_{melt}
453	453	0.5948	0.013	1.08	512 °C

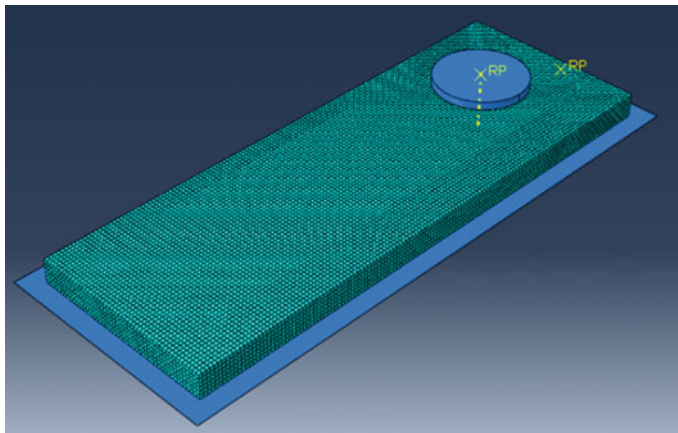


Fig. 3 Finite element model of tool and workpiece

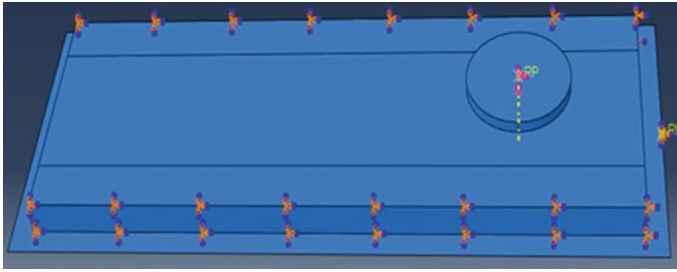


Fig. 4 Mechanical boundary conditions of the workpiece

direction. The plunging phase of FSW process is performed by defining the load in terms of displacement.

Since much of the heat loss occurs generally due to convection, the heat loss per unit area is calculated using Newton’s law of cooling as in Eq. (2) [17].

$$q_{\text{loss}} = h_{\text{conv}}(T - T_0) \tag{2}$$

where h_{conv} is the convective heat transfer coefficient, T and T_0 are the absolute and ambient temperatures respectively. As in Fig. 5, the red highlighted regions are used to show the heat loss due to convection caused by atmospheric air on the AA2014 plates.

Other computational strategies such as Arbitrary Lagrangian–Eulerian (ALE) formulation [18] and Mass scaling [19] have been used to further reduce the time required for running the simulation. During FSW, large plastic deformations occur under and around the pin tool which may result in mesh distortions. To remedy this problem, the ALE technique was used in the current finite element model. In ALE,

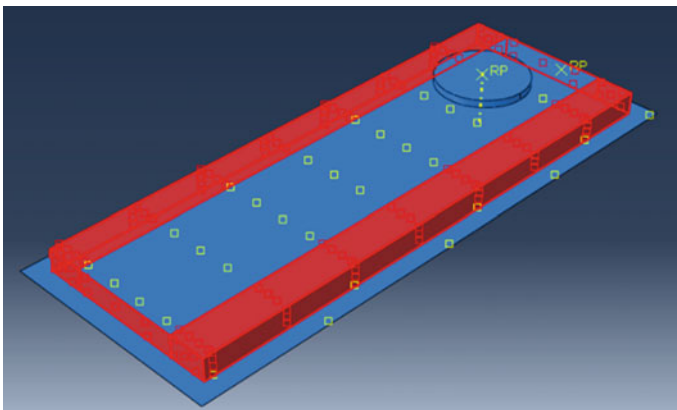


Fig. 5 Thermal boundary conditions used in the model

the movement of mesh is independent of the material which helps avoid excessive distortion, thereby maintaining a high-quality mesh during analysis. In the current simulation, the region where the spray interacts with the workpiece is defined as the adaptive mesh domain. The stable time increments of both mechanical and thermal components of the analysis are different and are given by Eqs. (3) and (4) [20] respectively.

$$\Delta t_{\max, \text{mech}} = \frac{L_e}{c_d} \quad (3)$$

$$\Delta t_{\max, \text{thermal}} = \frac{L_e^2}{2\alpha} \quad (4)$$

where L_e is the size of the smallest element, α is the thermal diffusivity and c_d is the dilatational wave speed of the material. Mass scaling algorithm has also been adopted owing to the high computational cost of solving a non-linear problem. The current analysis uses both fixed and variable mass scaling such that the material density is artificially increased to increase the stable time increment.

3 Results and Discussion

Figure 6 shows the completely welded joint obtained from the water spray assisted Friction Stir Welding process using optimized parameters and it can be seen that the weld specimen has a smoother surface without any defects.

The temperature profile recorded in real time by thermocouples on AS and RS is shown in Fig. 7. It can be seen that the temperature increases very fast for some time as the tool approaches the center of the welding length, whereas the initial temperature rise was slow and sharp. This can be caused due to sudden increase in frictional forces. The peak temperature obtained on the AS (140 °C) is higher than that of RS (130.75 °C). These values are very less when compared to peak temperature values obtained in FSW without cooling under similar processing conditions [3]. The increased heat dissipation caused by cooling effects induced by both water and compressed air has resulted in the decreased peak temperatures in AS and RS. By cooling the weld using a water spray assisted nozzle, it is found that the difference between peak temperatures as recorded by the thermocouple was only 10.25 °C which helps in the proper fixing of grain boundaries thereby producing better weld. The proposed spray cooling method has helped produce a better weld brought about by higher heat dissipation using a relatively less quantity of coolant in comparison with other cooling techniques.

The temperature values corresponding to the NodeID 11,728 which resembles the thermocouple in the AS of the weld is exported as a plot of Temperature Vs Time. The values obtained through a numerical analysis were then compared with the experimental results as in Fig. 8.

Fig. 6 Water spray cooled weld specimen



Fig. 7 Comparison of thermal cycles on AS and RS of weld

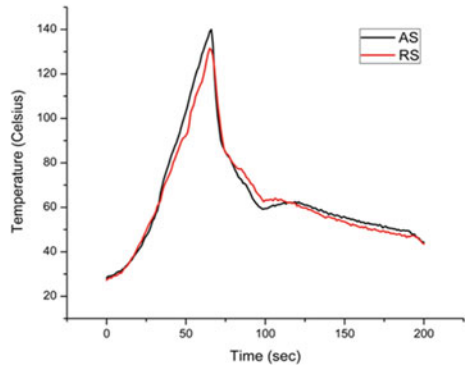
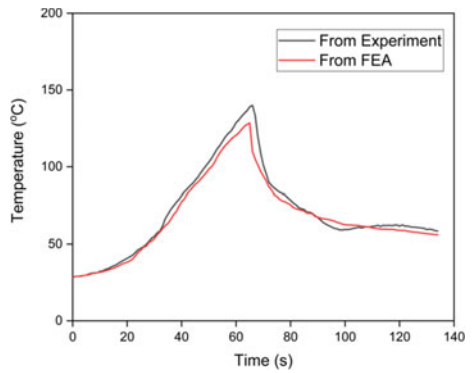


Fig. 8 Comparison between the simulated and measured temperature distribution



The peak temperature as obtained from the Finite Element Model was found to be 110.54 °C which is around 27% less than that of the experimentally observed value (140 °C). This error may be due to the uniform cooling that was introduced in the model which is not practically possible when experimenting. The calculated heat transfer coefficient value that has been used to model the spray may have caused more heat dissipation which would confirm the behavior of the temperature profile. The average error percentage was found to be in the range of 2.81%. The simulation of Spray-cooled Friction Stir Welding is done in ABAQUS CAE module as shown in Fig. 9. Since the error percentage is acceptable, the simulated model can be used to study the effect of spray cooling on the weld under different processing conditions.

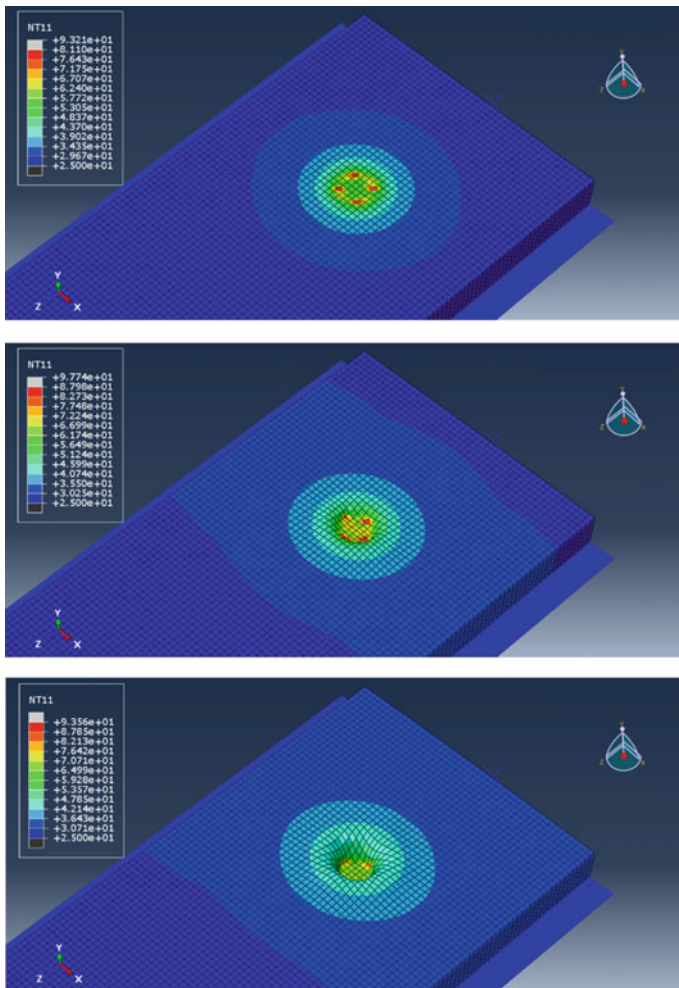


Fig. 9 Simulation of friction stir welding with spray cooling

4 Conclusion

An Explicit Finite Element Model with ALE formulation has been developed to study the thermal cycle evolution during Friction Stir Welding assisted with in-process spray cooling. The results obtained are summarized as follows:

- The FSW of AA2014 alloy along with spray nozzle cooling has been implemented using a flow rate of 60 ml/min with air pressure maintained at 3 bar at a rotational speed of 1000 rpm and weld traverse speed of 44 mm/min.
- Through experimental investigation, the maximum temperature was found to be higher on AS (140 °C) as compared to the RS (130.75 °C).
- Non-linear Explicit Analysis of Friction stir welding assisted with spray cooling is performed using techniques like ALE formulation and Mass scaling.
- The temperature profile obtained through simulation was found to be closely similar to the profile obtained from the experiment with a mean absolute error percentage of 2.81%. The percentage error is insignificant and hence the proposed model can be used to simulate the process of Spray nozzle-assisted Friction Stir Welding to study the behavior of weld under different processing conditions.

References

1. Godhani PS, Patel VV, Vora JJ, Chaudhary ND, Banka R (2019) Effect of friction stir welding of aluminum alloys AA6061/AA7075: temperature measurement, microstructure, and mechanical properties. In: Deb D, Balas V, Dey R (eds) Innovations in infrastructure: advances in intelligent systems and computing, vol 757. Springer, Singapore
2. Rajamanickam N, Balusamy V, Reddy GM, Natarajan K (2009) Effect of process parameters on thermal history and mechanical properties of friction stir welds. *Mater Des* 30(7):2726–2731
3. Chaudhary B, Patel V, Ramkumar PL, Vora J (2019) Temperature distribution during friction stir welding of AA2014 aluminum alloy: experimental and statistical analysis. *Trans Indian Inst Met* 72(4):969–981
4. Kumar A, Raju LS (2012) Influence of tool pin profiles on friction stir welding of copper. *Mater Manuf Processes* 27(12):1414–1418
5. Mystica A, Sankavi SP, Siva Sakthi V, Ganesh TS, Senthil Kumar VS (2015) Heat reduction in a tool holder during friction stir welding of aluminium alloy. In *Applied mechanics and materials*, vol 766, Trans Tech Publications Limited, pp 705–711
6. Sharma C, Dwivedi DK, Kumar P (2012) Effect of welding parameters on microstructure and mechanical properties of friction stir welded joints of AA7039 aluminum alloy. *Mater Des* 36:379–390
7. Sinhmar S, Dwivedi DK (2017) Enhancement of mechanical properties and corrosion resistance of friction stir welded joint of AA2014 using water cooling. *Mater Sci Eng, A* 684:413–422
8. Aziz SB, Dewan MW, Huggett DJ, Wahab MA, Okeil AM, Liao TW (2018) A fully coupled thermomechanical model of friction stir welding (FSW) and numerical studies on process parameters of lightweight aluminum alloy joints. *Acta Metallurgica Sinica (English letters)* 31(1):1–18
9. Meyghani B, Awang M, Emamian S, Nor MKBM (2019) Thermal modelling of friction stir welding (FSW) using calculated Young's modulus values. In *The advances in joining technology*. Springer, Singapore, pp 1–13

10. Mandal S, Rice J, Elmustafa AA (2008) Experimental and numerical investigation of the plunge stage in friction stir welding. *J Mater Process Technol* 203(1–3):411–419
11. Sinhmar S, Dwivedi DK (2019) Investigation of mechanical and corrosion behavior of friction stir weld joint of aluminium alloy. *Materials Today: Proc* 18:4542–4548
12. Kaufman JG (2016) Fire resistance of aluminum and aluminum alloys and measuring the effects of fire exposure on the properties of aluminum alloys. *ASM Int*
13. Benedyk JC (2008) Aerospace and high performance alloys database. *UNE* 36072(2)
14. Ye L (2015) Recent advances in structural integrity analysis. *Proceedings of the international congress*
15. Sharma P, Chandel P, Bhardwaj V, Singh M, Mahajan P (2018) Ballistic impact response of high strength aluminium alloy 2024-T3 subjected to rigid and deformable projectiles. *Thin-Walled Struct* 126:205–219
16. Sharma P, Chandel P, Mahajan P, Singh M (2014) Quasi-brittle fracture of aluminium alloy under ballistic impact. *Procedia engineering* 173:206–213
17. Winterton RHS (1999) Newton's law of cooling. *Contemp Phys* 40(3):205–212
18. Guerdoux S, Fourment L (2005) ALE formulation for the numerical simulation of friction stir welding. In *Proceedings of the VIII international conference on computational plasticity*. Barcelone
19. Constantin MA, Iordache MD, Nitu EL, Diakhaté M, Demmouche Y, Dhondt M, Bădulescu C (2020) An efficient strategy for 3D numerical simulation of friction stir welding process of pure copper plates. In *IOP conference series: materials science and engineering*, vol 916. IOP Publishing, p 012021
20. Smith M (2009) *ABAQUS/Standard user's manual*, Version 6.9. Dassault systèmes simulia corp

A Review on the Influence of Tool Pin Profile on Microstructure and Mechanical Properties of Friction Stir Welded Joints



Yogendra Singh Rajpoot , Kushal Saxena , and Desh Deepak 

Abstract One of the most advancements in the field of solid state joining process is friction stir welding that produces a sound quality weld. The important characteristic of a solid state welding process is the non-melting of the base material which means it is a lower temperature and a lower frictional heat input welding technology that produces joint below the melting point of materials to be joined. In present work, literature review was done to investigate the effects of various tool pin geometries on the grain structure (microstructure) and on the mechanical properties of the joints. Welded joints were fabricated by different materials in various configurations such as butt weld joint, lap weld joint and spot weld joint. The tool pins geometries were used in the most of the experiments conducted by researchers to fabricate the joint are straight cylindrical, threaded cylindrical, square, taper and triangular etc. In the entire study of the published papers, the friction stir welding is done at different traverse and rotational speeds and were considered as the most dominating parameters. Examination of microstructures of the welded joints was done with the help of optical and scanning electron microscopes. Further, the mechanical properties and most importantly hardness and ultimate tensile strength of the joints were determined by microhardness test and simple tensile test. It was observed from the literature review of various papers that the threaded and tapered cylindrical pin profile tools produce defect free sound joints and form of very fine and uniformly distributed precipitates in the stirrer zone (SZ) of the joint. Data Analysis has been made in the tabular form from which provides the details of various important data reviewed from the publications and it was concluded from table data that the tool with square pin profile exhibits better joints. However, in other literatures it can also be concluded that threaded cylinder and threaded taper pins also provide good quality joints with fine microstructure.

Keywords FSW · Recrystallization · Pin profiles · Microstructure · Ultimate tensile strength

Y. S. Rajpoot (✉) · K. Saxena · D. Deepak
Department of Mechanical Engineering, Rajkiya Engineering College Mainpuri, (Affiliated to
AKTU Lucknow), Mainpuri 205119, India
e-mail: yogendrasingh.rajpoot@recmainpuri.in

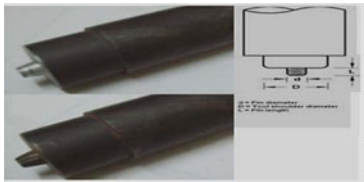
1 Introduction

Friction Stir Welding (FSW) was developed by Wayne Thomas and colleagues [1] at the welding institute (TWI) in 1991 is non-fusion joining technique best suited for welding of aluminum and other light non-ferrous metals [2]. In comparison to the conventional joining techniques, FSW can create superior mechanical as well as microstructural features in the weld zone [2]. This new technique has wide application in the aerospace, automobile and shipbuilding industries [2]. The joints created by FSW have high strength which is appreciably more in comparison to the strength of the joints obtained by fusion welding technique more specifically arc welding techniques such as TIG [3] and MIG. During friction stir welding process [4] the interaction between the surface of non-consumable tool which rotates and traverses in the longitudinal direction of weld joint line, creates a weld joint using the mechanism of plastic deformation and frictional heat dissipation which results temperature lower than the melting temperature of the materials being weld [5]. It is also the further great advantage of FSW that it is possible to make joint between alloys and combinations of various materials for which the traditional welding techniques are not suitable.

The quality of welded joint, produced by the FSW, depends up on the welding parameters [6] predominantly on tool rotational speed, traverse speed and geometry of tool pin. However, there are few parameters also which may affect the quality of weld joints are thickness of the work piece, material of the workpiece and tool pin profile. In past decade lot of research have been done to identify the influence of various FSW parameters [8] on the quality of welded [7] joints in term of mechanical as well as microstructural aspects. In order to select the best pin shape, the effect of geometry of pin will be examined incorporation with other parameters. In this review, an attempt has been made to clear the idea about the influence of tool pin geometries on microstructure and mechanical properties were evaluated in term of grain size of stir zone and ultimate tensile strength [6] (UTS) of welded joint and the data have been represented in the table.

2 Experimental Study of FSW with at Least One Threaded Tool Pin Shape

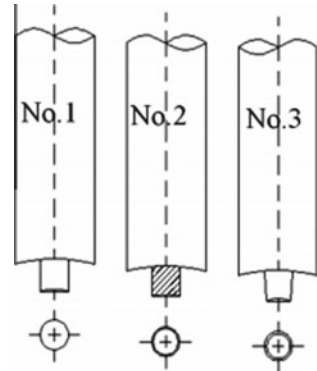
Patil et al. [5] were done Friction stir welding on AA 6082-O alloy. To perform the experiment two different tool pin shapes were used to investigate the effect of the pin on the microstructural feature and mechanical behavior. Results predict that the pin geometry has dominant effect on microstructural features and the mechanical properties of the joint. It is observed that the welding joint made by taper screw thread pin produces better tensile properties in comparison to the triflute pin profile at all the rotational speeds. This means for particular value of the welding speed, joint prepared by taper screw pin has better properties. The best tensile strength of the welded joint, which was prepared by taper screw, threaded pin (Fig. 1).



Description of the pin	Big diameter of the pin	Small diameter of the pin
Tri-flute pin	5.50mm	4.90mm
Taper screw thread pin	5.54mm	4.30mm

Fig. 1 The tool pin geometry used [5]

Fig. 2 Pin profiles: simple cylindrical (No. 1), screw threaded cylindrical (No. 2) and taper (No.3). [9]



Motaleb-nejad et al. [9] investigated the influence of pin shapes on the mechanical properties and microstructural features of AZ31B magnesium alloy friction stir welded joints. The surface of the pin profiles was utilized is shown below in the Fig. 2. The joints were made by friction stir welding at different traverse speed along the weld and rotational speeds of the tool.

The results clearly predict that the joints which were fabricated by taper surfaced pin and screw threaded cylindrical pins were free from any kind of defect. It was also observed that the taper pin produces finest grain size in the stir zone microstructure thus better mechanical properties including percentage of elongation, tensile strength and hardness.

Ilangovan et al. [10] fabricated friction stir welded Joints between two separate grades of aluminum alloys. In present work two separate grades of aluminum alloys which are AA 6061 (heat treatable) and AA 5086 (non-heat treatable) attempted to join by stirring action of friction stir welding with the utilization of different tool pin geometries shown in Fig. 3.

The microstructures of different regions of weld zone were examined and calculated by using scanning electron and optical microscopy. It was observed that the tool with threaded pin generates higher tensile strength and higher hardness in the stir zone 169 MPa and 83 HV respectively, in comparison to the other two profiles which are straight cylindrical and taper cylindrical. The improvement in the hardness value of SZ is the result of formed fine grains due to recrystallization and intermetallics in the stir/nugget zone.

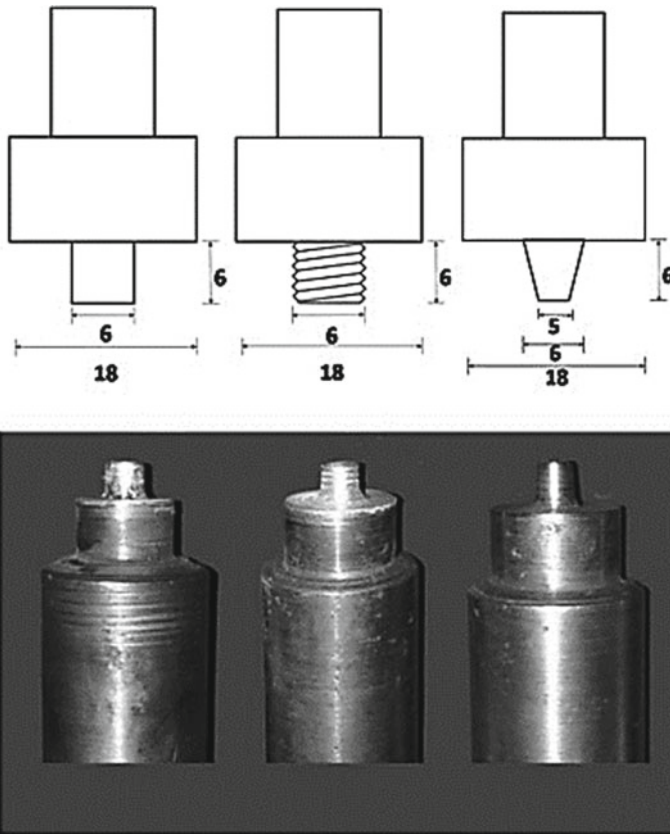


Fig. 3 Tools with different profiles of pin [10]

Khodaverdizadeh et al. [11] investigated the influence of various tool pin profile on mechanical properties and microstructure of friction stir welded joints fabricated on pure copper. Two-tool pin profiles were utilized to fabricate the joint.

The results obtained for mechanical properties like the strength at yield point, ultimate point and hardness of parent material and welded joint using two different pin profiles are shown in Fig. 4. The examination of microstructure of joints showed that stirrer zone of joint has finer recrystallized grains of size approximately $10\ \mu\text{m}$ when welding was done using tool with square pin profiles, while material welded using second tool pin profile i.e. thread cylindrical had larger grain size of around $15\ \mu\text{m}$.

Emamian et al. [12] experimentally investigated the influence of different contours tool pins on the FSW of AA6061. AA6061 is a light weighted alloy of aluminum was used in this work as the base material. H 13 tool steel was preferred to be selected as the tool material. Friction stir welding mainly relies upon the heat being generated and flow of material done by the tool. In this attempt various tool pin contours, several

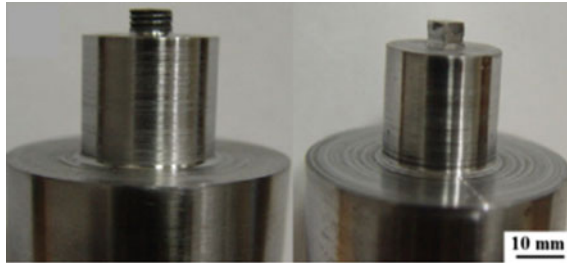


Fig. 4 Tools with two different pin shapes/geometries [11]

speeds of rotation and different welding speeds were being selected to investigate the mechanical properties of the joint. They fabricated four different contours i.e. threaded cylindrical, stepped cylindrical, conical and square on the tool pin to perform the welding. The tool developed was provided various heat treatments prior to the operation. To evaluate the effect of speeds on the welding three different values of rotational and traverse speeds were selected. Utilizing the tools total 36 joints were fabricated. Wire cut technique machine was employed to prepare the specimens for performing the tensile test. It was carried out in UTM at 100 kN as per ASTM principles. Out of the fabricated 36 joints only 11 were found suitable for tensile test to be carried out. Graphs and bar diagrams were used to depict the variations in strength of weld. With the help of diagrams it was concluded that tool pin with threaded cylindrical contour produces maximum strength at 1600 rpm and welding speed equal to 100 mm/min (Fig. 5).

Zhou et al. [13] have investigated the role of pin geometries on the friction stir spot welded plates of copper (T2) and aluminum alloy (AA1060). The sheets were used in the lap joint configuration placing the aluminum sheet at the top. Experiment was conducted by using tools viz. were created of die steel (AISI H13). Pin features play an important role on material flow during welding by stirring action. Experiments were conducted to create the spot welds using four pin features namely threaded pin, featureless pin (simple cylindrical) and threaded pin with flutes. The difference in the surface areas of each pin profile produces different amount of heat during the spot welding by friction stir process hence thermal history will differ for each

AA6061-T6	Chemical composition %							
	Mg	Cr	Ti	Zn	Mn	Fe	Si	Cu
	0.98	0.19	0.05	0.01	0.07	0.3	0.47	0.23
Mechanical Properties								
UTS (Mpa)			Yield strength (Mpa)			Elongation (%)		
305			253			12		
H13	Chemical composition %							
	C	Si	Mn	Cr	Mo	V	P	S
	0.4	0.92	0.34	5.07	1.25	0.95	0.019	0.001

Fig. 5 Material and tool properties [12]

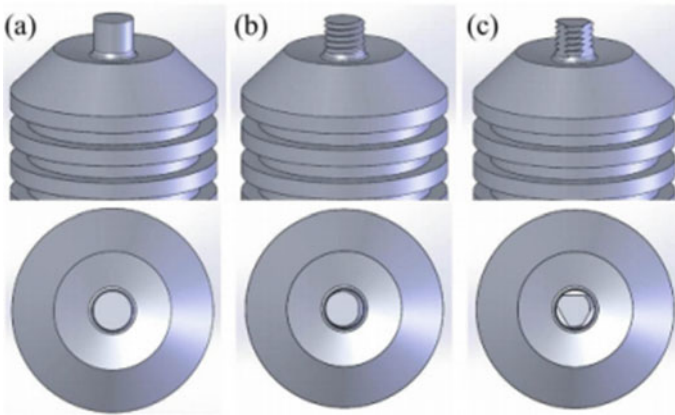


Fig. 6 FSW tool pin features **a** cylindrical **b** threaded **c** threaded with the flutes [13]

pin profile that will definitely have a significant influence on the microstructures as well as on the mechanical strength of joints. Threaded pin produces high amount of heat during welding thus the maximum temperature was recorded using threaded pin. They observed that there is no major difference in microhardness across the all welded samples and the maximum shear load was observed in the weld created by threaded pin tool (Fig. 6).

Emamikhah et al. [14] done the microstructural and mechanical examination to explore the influence of tool pin probe shape on friction stir welded joint of (CuZn40) high-zinc brass. Experiments were conducted using different pin shapes as shown in Fig. 7. The experiments were conducted at constant rotation speeds and traverse speeds to evaluate the influence of pin geometry. Mechanical and microstructural examinations indicated that tools produce sufficient heat at the bottom surface of the tool due to friction and material stirring. It was observed that high hardness at the welding zone was obtained than the parent material due to grain refinement. Better mechanical properties were observed for the friction stir welded joint fabricated by threaded cylindrical tool.

Elangovan et al. [15] investigated the different welding zone for light weight structure material AA2219 macroscopically. The evaluation of the tensile properties was done to correlate the FSP zone formation. Friction Stir welding was performed using five profiles as shown in Fig. 8 at three different speed of tool rotation. It was found that among the all tool pin with different profile the tool with square pin creates stronger joint as well as metallurgically better weld joint. It was also observed that the joints fabricated by square shape pin were free from the defects.

Izabela-Rec et al. [16] experimentally investigated the impact of different process parameters inclusive of tool rotational velocity, layout of pin and configuration of joint on the microstructural and mechanical behavior of dissimilar material joints of aluminum alloys. It is well explained in the various researches that tool rotation and the alloy placement (joint configuration) play remarkable role in the formation of

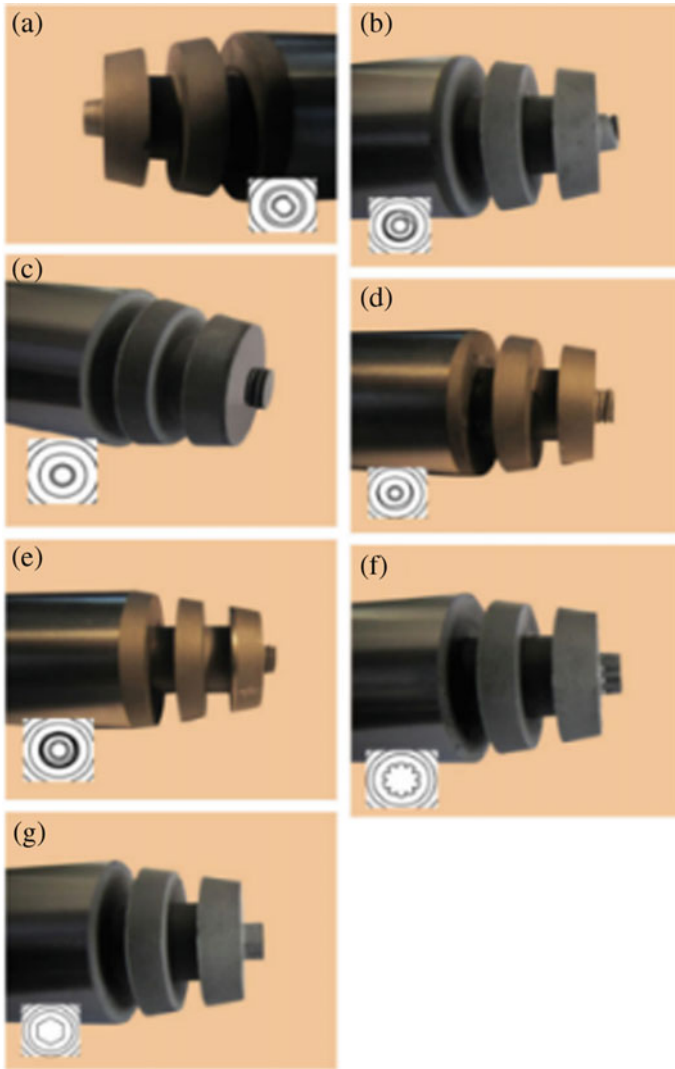


Fig. 7 Various tools: **a** taper with chamfer, **b** taper with single-thread, **c** flutes (03), **d** threaded cylinder, **e** taper with threads, **f** spline, **g** hexahedron [14]

weld. Greater mixing of materials was observed at high rotations and while keeping 5083 at the advancing facet and 7075 at the other side to make the joint configuration. From present study, it was also found that the Triflute pin ensures better tensile strength and joint efficiency. However, the weld joint configuration does not affect the mechanical properties of the joint. It was concluded that joint with maximum tensile strength and without defect was fabricated with the Triflute pin (Fig. 9).

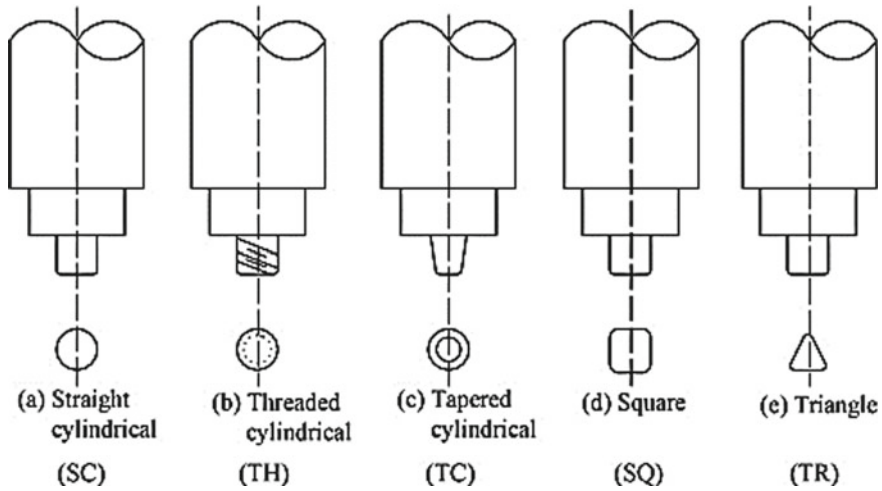
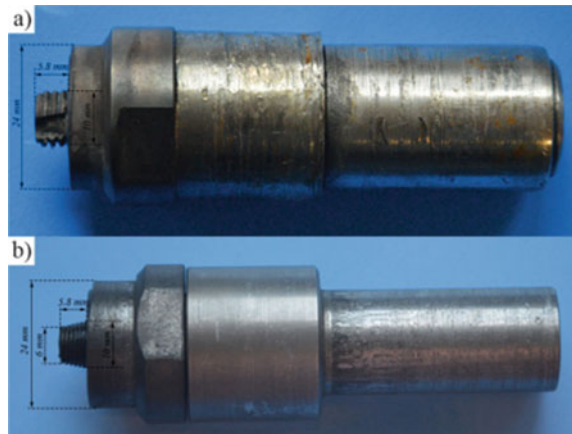


Fig. 8 Tool pin profiles used by Elangovan et al. [15] to fabricate the joint

Fig. 9 Tool pin profile a triflute pin b threaded taper pin [16]



Srujana et al. [17] predict that among the all tool pin profile the triangular tool produced better mechanical property as well as metallurgically good and defect free weld joints in comparison to other tool pin shapes (Fig. 10).

Hattingh et al. [18] analyze the effect of tool specification on forces, on torque and temperature during friction stir welding. Here in this study tool parameter related to flute design including number of flutes, depth of flute and taper angle is taken as variable parameter. This investigation provides information about the interaction between the stirred zone and tool, which can never be observed by force magnitude information only.

Das et al. [19] observed the influence of different process variables i.e. profile of tool pin, tool shoulder diameter, penetration depth, welding traverse speed and

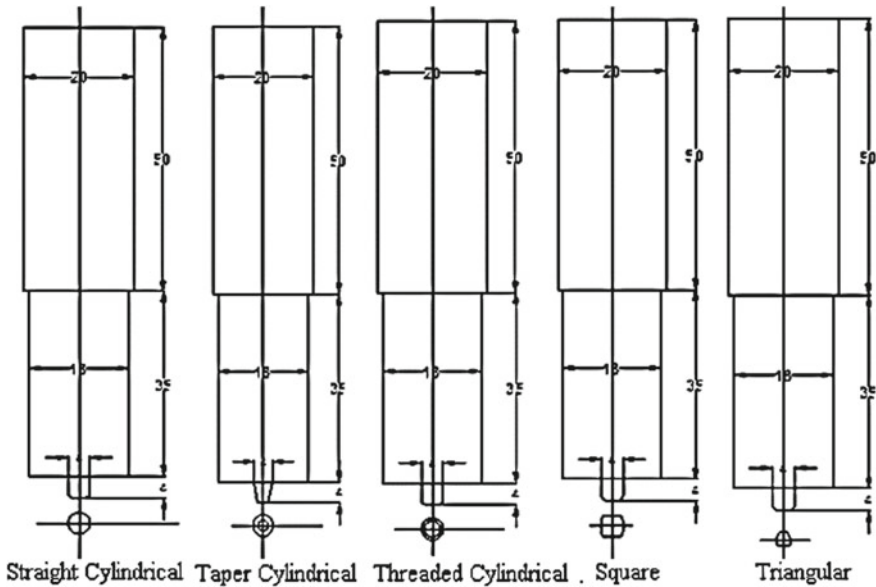


Fig. 10 Friction stir welding tool pin profiles [17]

rotation speed on the microstructural as well as mechanical behavior of welded joint. The process parameters were selected and individual influence of these variables on microstructural features and tensile strength was investigated. Out of the different selected tool pin geometries the square pin produces a sound quality weld joint which was having excellent mechanical properties due to specific stirring action by the pulsating phenomenon. It was found the tool with square profile gives best quality joint in term of mechanical and microstructural properties (Fig. 11).

Trimble et al. [20] experimentally studied the microstructure and microhardness of AA2024-T3 joints fabricated by friction stir welding. Microstructural and mechanical examination was done to observe the effect of pin geometry on the microstructural characteristics and hardness. Tapered cylinder, Triflute and Square pins were utilized in the experiments and results for each weld were reported. It was concluded from

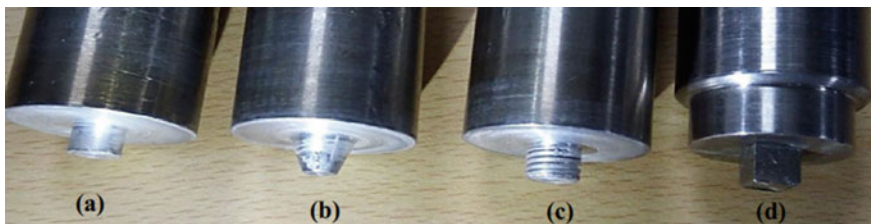


Fig. 11 Tools profiles used a straight cylindrical; b tapered cylindrical; c threaded cylindrical; d square [19]

the results that the hardness in each welding zone was less than the base material and the cylindrical pin produced the joint viz. were showing some defects however the flat surface pin profiles along with flutes or without flutes produced better joints with negligible defects (Fig. 12).

Krasnowski et al. [21] observed the influence of configuration of the weld joint and tool profile on the mechanical behavior of Al 6082 alloy joints fabricated by FSW. Three different types of tool pin shapes and different surfaces of shoulder were utilized for two configuration of the weld viz. one sided and two-sided. It was observed that all tools produce good quality butt joints which were free from all kind of defects or imperfections. It was also found that the joints fabricated by a Triflute tool give the better strength (Fig. 13).

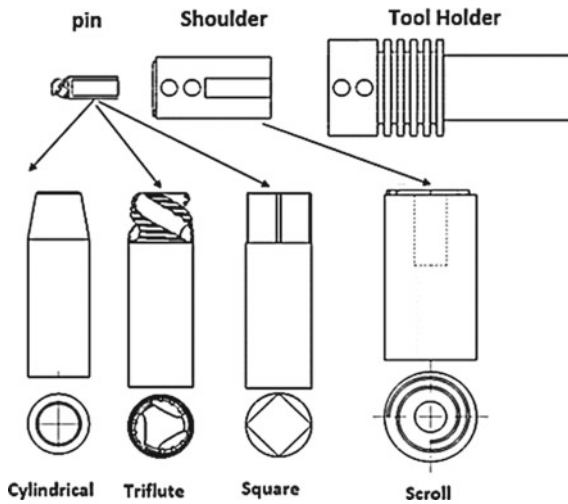


Fig. 12 The different tool pin profile used including the scroll and tool holder [20]

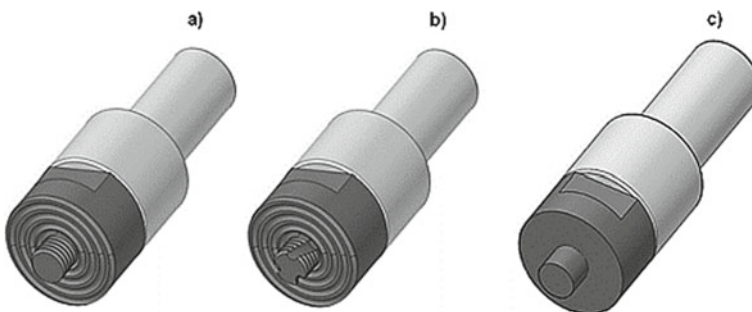


Fig. 13 Tools utilized for FSW: a) N1, b) N2 and c) N3 [21]

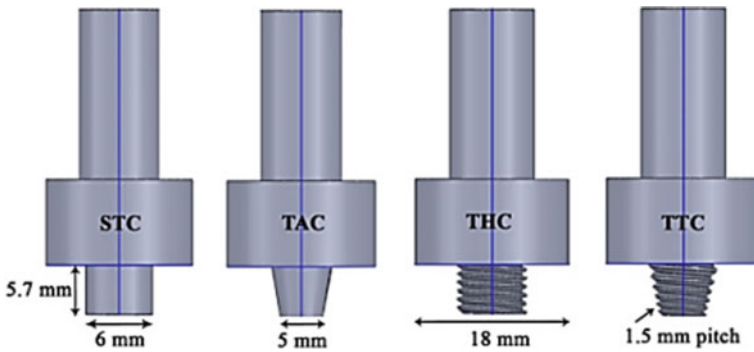


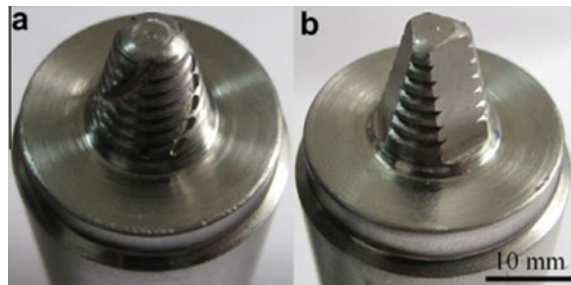
Fig. 14 Tool pin profiles [22]

Sabari et al. [22] made a comparative study to understand the act of tool pin profiles on stir zone microstructure and the tensile properties of both FSW and UWFSW joints. Three different pin geometries as shown below in Fig. 20 were used to produce welded joints. It was observed that from this investigation, that the joint created in underwater condition (water as cooling medium) by taper threaded pin tool exhibited better tensile properties with maximum ultimate tensile strength 345 MPa (Fig. 14).

Xu et al. [23] made an attempt to evaluate the microstructure distribution of second-phase particles and mechanical properties of the joint in the direction of thickness of plate. AA219 thick plate of 12 mm was welded using two different tool pin shapes. It was found that the top surface of the joints was having larger grain size with equiaxed recrystallized microstructure and finer distribution of second-phase particles in comparison to the mid-plane surface and bottom plane surfaces. Grain size obtained was much finer and dispersion of the particles too, when the joint was fabricated by tool (a) or at the lower value of the tool rotation speed i.e. 300 rpm. It was concluded that the joint prepared by using the second tool (b) exhibited lower mechanical compared to first tool (three-spiral flute) (Fig. 15).

Tamadon et al. [24] evaluated the effect of various pin shapes of tool and operating process parameters on the material properties and grain structure of an AA1100 FSW

Fig. 15 FSW tool a tool with three spiral flute b tool with threaded and tapered with triangle [23]



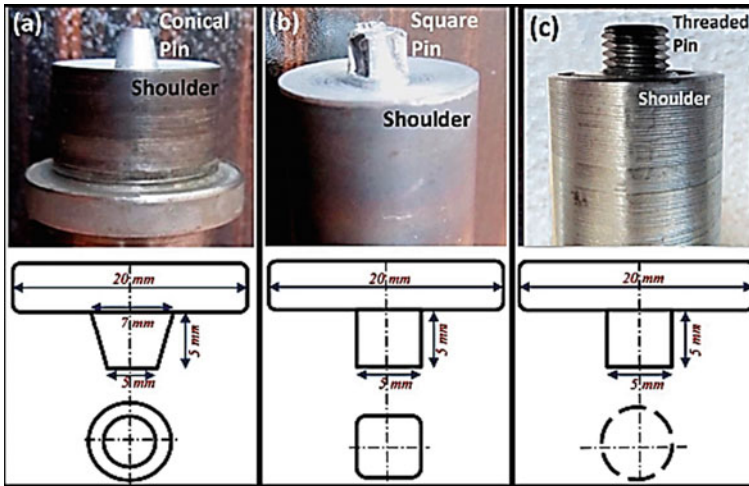


Fig. 16 Tools pin shapes utilized for the AA1100 weld preparation [24]

welded plates. Three pin profiles as shown below in Fig. 16 were utilized. For each tool pin profile, welds were fabricated for a set of welding condition viz. rotational speed 710, 1120 and 1400 rpm and tool advancing speeds or welding speed along the longitudinal direction of the weld were 150, 250 and 400 mm/min. Tensile tests as well as morphology analysis were performed on the weld samples to obtain their mechanical strength and microstructural details. Morphology examination was done using optical microscopy. Evaluation of weld composition was done with the help of SEM, EDS and XRD. It was observed that there is no weld contamination formed however there were some kind of common defects which include kissing bonds, tunnel voids and swirling lines, these defects are the inherent characteristic of the stir welding and can't be removed completely. The results obtained predict how the process parameters can be selected to produce good quality welds.

3 Experimental Study of FSW with Non-threaded Tool Pin Shapes

Muthu Krishnan Maya Krishnan et al. [25] examine the effect of profile of pin on the mechanical behavior of the friction stir welded joint prepared on AA6063 and A319. Three pin profiles namely Square tool pin shape, round tool pin shape and Hexagonal tool pin shape were used to conduct the experiment. Plates were clamped together in butt position and friction stir welding was done on automatic CNC machine of adapted milling machine at various parameters such as welding traverse speed and rotation. Joints were checked and exhibited no defects. Results obtained from the tests clearly exhibited that the joint produced by the square tool yields superior tensile

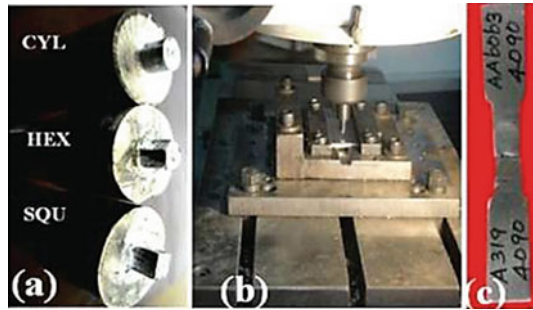


Fig. 17 Shapes of tool pin utilized for experiment [25]

strength compared to the other tool profile. The stirrer zone of the joint has very fine grain size which results in increased microhardness (Fig. 17).

Pankul Goel et al. [26] in this investigation, plates of Al 6063-T6 were friction stir welded at the two joint configuration butt and scarf. In general, the butt joint configuration was used for friction stir welding but they fabricated the Scarf joint and influence of pin shapes was observed on joint made in scarf configuration. The experimental investigation was done to determine the influence of probe shapes on the microstructural features, hardness, impact and tensile strength of joint. To make scarf joint a 26° inverted bevel was tested. For the characterization, scanning electron microscopy and optical microscopic analysis were utilized on the different regions of joints (Fig. 18).

When friction stir welded joints in butt configuration were prepared by the tool with Tapered surface showed the maximum tensile strength (162 MPa) and tool with triangular pin exhibited the minimum tensile strength (115.6 MPa). Testing was done to evaluate the impact strength of the FS welded joint in butt configuration and it was found that the joints exhibited 26 J impact strength when the welding was done with help of Tapered Cylindrical tools. New joint configuration produced low strength due to configuration.

Marzbanrad et al. [27] conducted the experiment to determine the domination of tool pin shape on mechanical properties, microstructure, flow of material, temperature history and distribution of strain of friction stir weld of AA5083 sheet. Welding was done with two different tools at 1120 rpm and 30 mm/min. Since the plunge depth

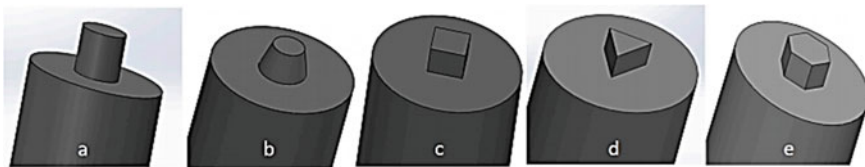


Fig. 18 Tool pin profiles [26]

of the pin was around 2.8 mm for 3 mm thick sheet. The dimensions were used to fabricate tools is shown in Fig. 19.

For particular value of the rotational speed the area of the square pin is more than the cylindrical pin and it can also be observed from the result of the literature

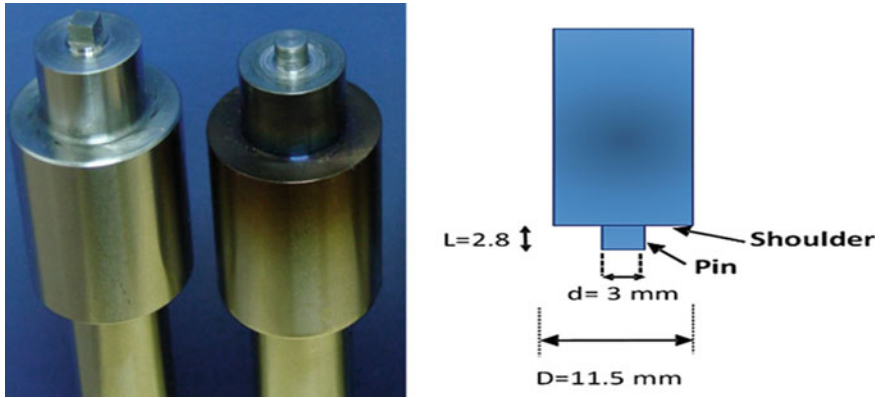


Fig. 19 Two different tool pin geometries with the dimensions of tool pin and shoulder [27]

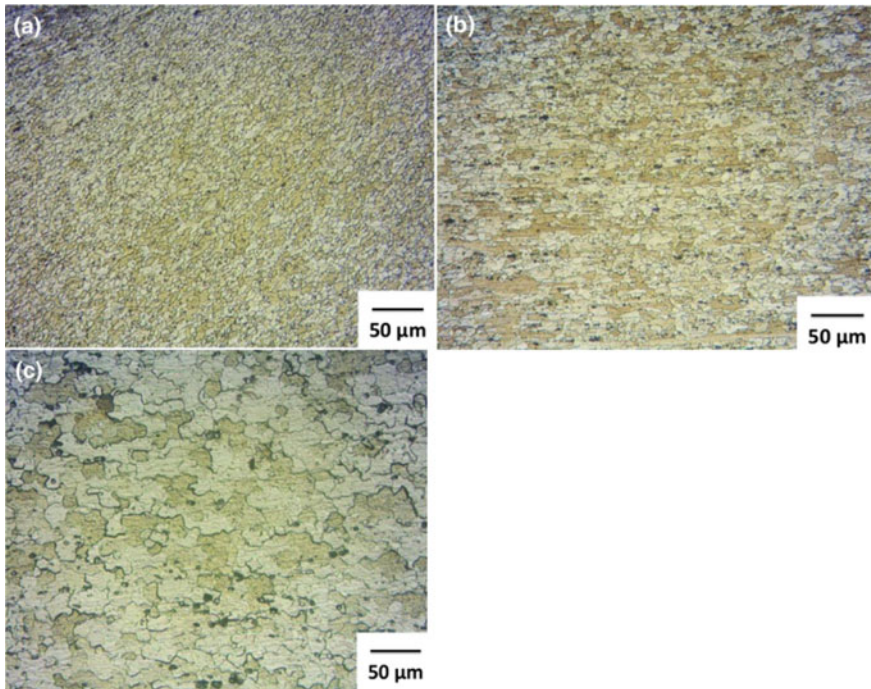


Fig. 20 Microstructural features of a nugget zone b TMAZ c HAZ [27]

that the maximum temperature is more in case of the square pin in comparison to the cylindrical pin. Higher the peak temperature during welding is the favorable condition for plasticized mixing of the material and hence it will improve the quality of the joint. It can be observed that from the results the square pin shape tool generates finer grain structure in comparison to the cylindrical pin profile tool (Fig. 20).

Two welded samples which were fabricated using two pin were tested and it was observed that both the sample is having lower UTS as compared to the base material. It was also exhibited that the joint which was created using square pin has better tensile properties compared to the cylindrical pin.

Rao et al. [28] presented the influence of the tool pin profiles on pitting corrosion and microstructure of the weld nugget formed in the dissimilar joint of AA2219 aluminum-copper alloy was observed. Fabrication of weld joint was done using different geometries of tool pin as shown in Fig. 21. It was found that the plastic deformation and high temperature is experienced by the material of the stirrer zone and thus evolved microstructure which greatly affects hardness, tensile strength and corrosion characteristics of the joint. It was observed that the three things mainly affect the corrosive behavior and hardness of the nugget zone is grain size, disorientation and precipitate dissolution. It was also observed that the resistance against pitting corrosion of joints of AA2219 was observed better for hexagon shape pin profile tool in comparison to other tool pin shapes.

Ramanjaneyulu et al. [29] attempted to investigate the act of tool pin configuration in rapid plastic deformation and frictional heat generation at the time of friction stir welding of AA2014-T6. The bottom surface of shoulder portion of tool plays

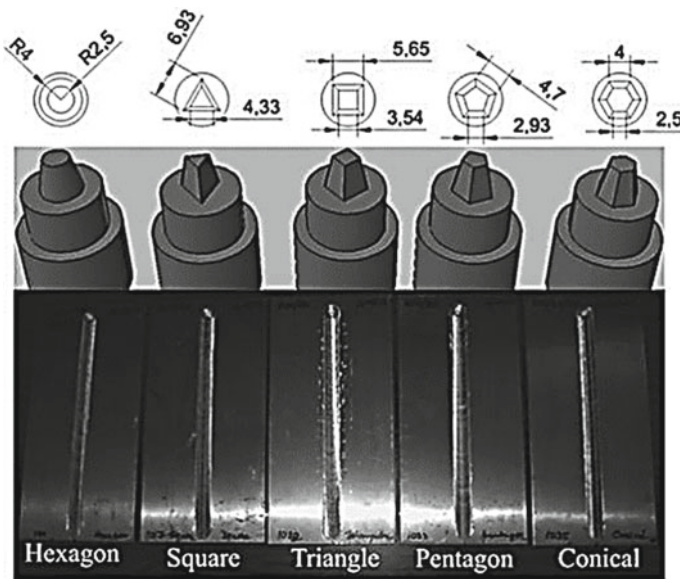


Fig. 21 Five different pin tool shapes and weld joints [28]

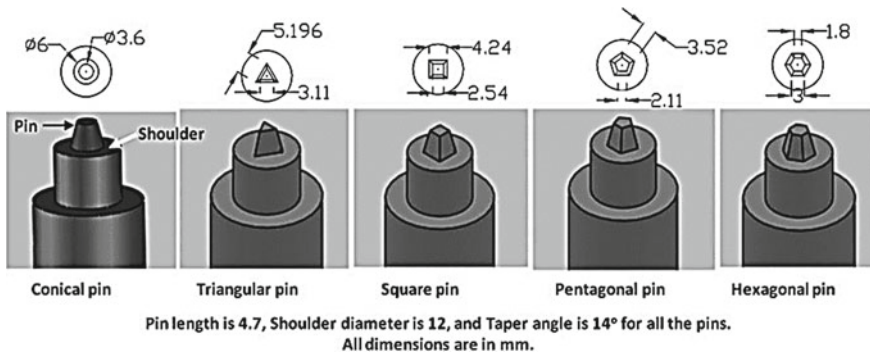


Fig. 22 Tool pin profiles [29]

very important role in the frictional heat generation and observed that the tool and base material interface friction is the dominant region for frictional heating. It was concluded that from this study the hexagonal tool pin profile produces welds which have better tensile strength, lesser width of TMAZ and higher hardness at nugget zone (Fig. 22).

Nadikudi et al. [30] studied the formability analysis of welded blanks. FSW was done at constant welding parameters. It has been observed that the blanks viz. were fabricated using tool with square profile showed greater formability against other tool pin geometries. It was also observed that the pulsating action created by the sharp edges of the square pin is the cause for this enhancement of mechanical property.

Jamshidi Aval et al. [31] attempted the investigation on the influence of tool pin shapes or profiles and post-welding heat treatment of weld on the microstructural and mechanical dissimilar joints which were fabricated on 8 mm thick plate of AA 6082-T6 and AA 7075-T6. The experimental analysis reveals that the tool pin profile viz. conical pin with three grooves generates higher temperatures compared to the square frustum probe tool. It was also found that more uniform mixing of material at nugget zone was performed by the tool pin with square in shape. It was also studied that the stir zone of each weld revealed with the highest kinetics of strength recovery and microhardness (Fig. 23).

Thube et al. [32] studied the influence of welding process parameters and tool pin shapes on formation of weld nugget zone and tensile strength of weld on 2.5 mm thick plates of AA5083 aluminum alloy. Welded joints were created using different tool pin shapes at different tool rotational speed with constant tool traverse speed. Evaluation of Tensile properties of weld was done using ultimate tensile test and these properties were correlated with the formed nugget zone the weld. It was observed from this investigation that the heat generation depends on the pin shape thus on the grain size as well as on the tensile properties, and also found that weld strength was predominantly affected by heat rather plastic deformation for thin plates. It was concluded from the above analysis that cylindrical pin profiled tool creates mechanically strong welds without defects compared to other pin shapes (Fig. 24).

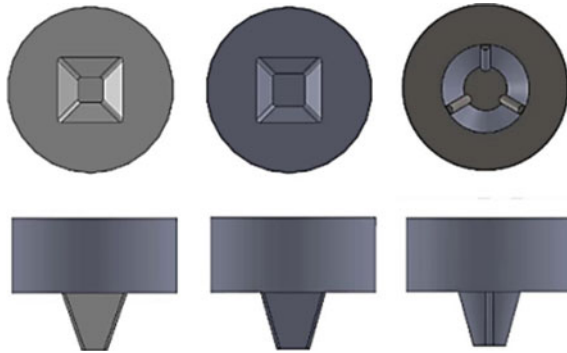


Fig.23 Tools with different profile of probe [31]

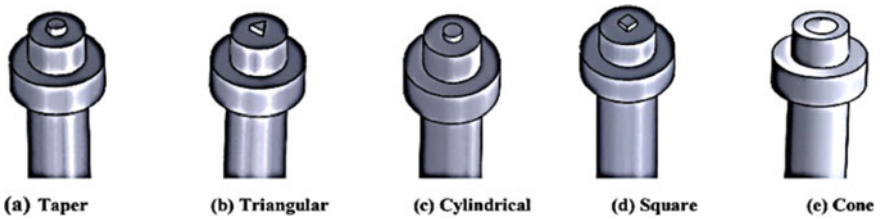


Fig. 24 Tools pin shapes utilized for the weld preparation [32]

Palanivel et al. [33] accomplished the study on 6 mm thick plate of aluminum alloys AA5083-H111 and AA6351-T6. All the regions of joint were examined and it was observed that the tool rotational speed and pin profile play considerable role in the evolvement of microstructure and tensile properties of the joints. The joint, which was created with the help of square tool pin profile at rotational speed of 950 rpm, produces maximum tensile strength of 273 MPa (Fig. 25).

Aghajani Derazkola et al. [34] investigated experimentally the influence of three-pin shapes, which are frustum, cubic and triangle on the friction stir welding (FSW) of poly (methyl methacrylate). It was observed that utilization of different pins effects the area of contact and hence mechanical evaluation revealed that tensile strength in

Fig. 25 Tools pin shapes [33]



longitudinal (LS) and transverse (TS) directions was 59 MPa and 43 MPa respectively of the joint was obtained by the frustum pin (Table 1 and Fig. 26).

4 Conclusion

It is observed from the various literatures that the shape or geometry/profile of pin of a friction stir welding tool plays a major role on the microstructural features as well as mechanical properties. The reason behind this is the amount of frictional heat generation depends upon surface area of interaction between tool material and workpiece material. There exists relationship between the heat input and evolved microstructure of weld nugget zone, after the perfect recrystallization of material higher heat input will evolve the grain size and thus it was observed in some literature that for particular pin profile of tool, the rotational speed and welding speed play significant role in the final grain structure of friction stir welded joint. It is also concluded that higher the heat input results higher hardness in the nugget zone of joints.

Among the most of the literatures, it can be concluded that the shape of tool pin will also play significant role in the final grain size and thus mechanical properties of the welded joints. It is also concluded among the various pin profiles, the square shape pin creates better quality joints with high strength and microhardness in the nugget zone due to its pulsating action on material flow. Further, it is also found that square pin shape tool produces finer grain size in the region of nugget zone of weld. However, in some literatures it was also observed that threaded cylindrical pin profile tool also creates better quality joints; this may happen be due combine effect of tool rotation and welding speeds.

Table 1 Summary of extracted critical data such as grain size, microhardness and tensile strength from reviewed literatures

Reference	Base material	Type of joint fabricated	Tool pin profile	Rotational speed (rpm)	Traverse speed (mm/min)	Mechanical properties of friction stir welded joint		
						Average grain size (SZ) μm	UTS (MPa)	Micro-hardness (HV)
Patil et al. [5]	AA6082-O	Similar Butt Joint	Taper screw thread pin	1200	60	-	103.33	-
			”	”	70	-	120	-
			”	”	75	-	106.67	-
			”	”	85	-	-	-
			Tri-flute pin	1200	60	-	76.67	-
			”	”	70	-	63.33	-
			”	”	75	-	-	-
			”	”	85	-	56.67	-
			Cylindrical	630	63	16.6	204	70
			”	800	80	18.2	192	68
Motalleb-nejad et. al [9]	Az31B Magnesium alloy	Similar Butt Joint	”	1000	100	25.8	162	60
			Taper Cylindrical	630	63	9.8	253	80
			”	800	80	13.1	243	77
			”	1000	100	17.8	223	73
			Threaded Cylindrical	630	63	8.8	242	77
			”	800	80	11.4	234	73
			”	1000	100	15.7	212	69

(continued)

Table 1 (continued)

Reference	Base material	Type of joint fabricated	Tool pin profile	Rotational speed (rpm)	Traverse speed (mm/min)	Mechanical properties of friction stir welded joint		
						Average grain size (SZ) μm	UTS (MPa)	Micro-hardness (HV)
Ilangovan et al. [10]	AA6061-T6 and AA5086-0	Dissimilar Butt Joint	Straight Cylindrical	1100	22	-	126	-
			Threaded Cylindrical	"	"	-	169	-
			Plain Taper Cylindrical	"	"	-	163	-
Khodaverdizadeh et al. [11]	Pure Copper	Similar Butt Joint	Square	600	75	Between 10 to 15 (square pin profile has finer grain structure)	221	99
			Threaded Cylindrical				202	87
Emamian et al. [12]	AA6061-T6	Similar Butt Joint	Conical	800	40	-	180.456	-
			Stepped conical	"	100	-	188.218	-
			Threaded cylindrical	"	40	-	200.709	-
			"	"	70	-	212.224	-
			"	100	-	213.173	-	

(continued)

Table 1 (continued)

Reference	Base material	Type of joint fabricated	Tool pin profile	Rotational speed (rpm)	Traverse speed (mm/min)	Mechanical properties of friction stir welded joint		
						Average grain size (SZ) μm	UTS (MPa)	Micro-hardness (HV)
Zhou et al. [13]	AA 1060 & AA 1060	Lap joint	”	1200	40	–	201.231	–
			”	”	70	–	210.047	–
			”	”	100	–	193.84	–
			”	1600	40	–	186.392	–
			”	”	70	–	208.213	–
			”	”	100	–	214.359	–
			Featureless pin	2250	–	The smallest size of SZ area and angle	Tensile shear failure load	1 mm above the interface
Threaded pin	”	”	The SZ area enlarge	2.75	113	84		
						4.3	111	83

(continued)

Table 1 (continued)

Reference	Base material	Type of joint fabricated	Tool pin profile	Rotational speed (rpm)	Traverse speed (mm/min)	Mechanical properties of friction stir welded joint					
						Average grain size (SZ) μm	UTS (MPa)	Micro-hardness (HV)			
Emamikhah et al. [14]	High-Zinc brass (CuZn40)	Butt Joint	Threaded pin with flutes	"	"	The size of SZ area and the angle are larger than that in sample 1, but a bit smaller than that in sample 2	3.2	109	85		
							-	-	64.2		
							-	-	50.96		
							-	-	50.84		
							-	-	50.49		
Elangovan et al. [15]	AA2219-T87	Square butt joint	Straight cylindrical	1600	45.6	15	100	82			
							Tapered cylindrical	"	10	84	
							Threaded cylindrical	"	-	98	
							Square	"	-	242	105

(continued)

Table 1 (continued)

Reference	Base material	Type of joint fabricated	Tool pin profile	Rotational speed (rpm)	Traverse speed (mm/min)	Mechanical properties of friction stir welded joint		
						Average grain size (SZ) μm	UTS (MPa)	Micro-hardness (HV)
Srujana et al. [17]	AA6351	Butt Joint	Triangular	"	"	-	215	101
			Straight cylindrical	900	65	-	168	40
			Taper Cylindrical	"	"	-	170	44
			Threaded Cylindrical	"	"	-	166	42
			Square	"	"	-	161	39
Jayashree Das [19]	AA2014	Butt Joint	Triangular	"	"	-	174	48
			Straight cylindrical	600	22	21	370.05	148
			Tapered cylindrical	"	"	25	372.98	151
			Threaded cylindrical	"	"	20	375.99	153
			Square	"	"	18	380.34	155
			Square	815	22	17	389.34	158
			Square	1100	22	28	377.78	153
			Square	1500	22	31	359.34	150

(continued)

Table 1 (continued)

Reference	Base material	Type of joint fabricated	Tool pin profile	Rotational speed (rpm)	Traverse speed (mm/min)	Mechanical properties of friction stir welded joint		
						Average grain size (SZ) μm	UTS (MPa)	Micro-hardness (HV)
Trimble et al. [20]	AA2024-T3	Butt Joint	Square	815	36	16	391.45	160
			Square	815	63	15	393.87	165
			Square	815	98	25	380.84	149
			Square	450	180	2.19	–	130
S. Sree Sabari [22]	AA2519-T87	FSW-Butt Joint UWFSW-Butt Joint	Taper Cylindrical	”	”	2.3	–	127
			Triflute	”	”	2.23	–	124
			Straight threaded cylindrical (THC)	1300	30	17.5	244	93
			Taper threaded cylindrical (TTC)	”	”	15	267	97
			Straight threaded cylindrical (THC)	”	”	5.2	327	105
			Taper threaded cylindrical (TTC)	”	”	3.3	345	100

(continued)

Table 1 (continued)

Reference	Base material	Type of joint fabricated	Tool pin profile	Rotational speed (rpm)	Traverse speed (mm/min)	Mechanical properties of friction stir welded joint		
						Average grain size (SZ) μm	UTS (MPa)	Micro-hardness (HV)
Weifeng Xu [23]	2219-T62 Al alloy	Butt Joint	Threaded and tapered with three spiral flutes	400	60	5.5 at top surface and 3.5 at bottom	324	97
			Threaded and tapered with triangle	400	60		313	86
Abbas Tamadon [24]	AA1100	Butt Joint	Conical pin	1120	250		250	-
			Square pin	"	"		≈ 284	-
			Threaded pin	"	"		≈ 292	-
Muthu Krishnan Maya Krishnan [25]	AA6063 & A319	Dissimilar Butt Joint	Round(CLY)	1300	25	-	92	102
			Hexagonal (HEX)	"	"	-	158	141
			Square (SQU)	"	"	-	172	159
			Tapered cylindrical	900	50	-	162	76
PankulGoel et al. [26]	Al 6063-T6	Square butt	Cylindrical	"	"	-	160	71
			Square	"	"	-	158	70
			Hexagonal	"	"	-	117	67
			Triangular	"	"	-	116	60

(continued)

Table 1 (continued)

Reference	Base material	Type of joint fabricated	Tool pin profile	Rotational speed (rpm)	Traverse speed (mm/min)	Mechanical properties of friction stir welded joint		
						Average grain size (SZ) μm	UTS (MPa)	Micro-hardness (HV)
Javad Marzbanrad et al. [27]	AA5083	Scarf joint	Tapered cylindrical	"	"	-	129	70
			Cylindrical	"	"	-	137	69
			Square	"	"	-	77	77
			Hexagonal	"	"	-	121	71
			Triangular	"	"	-	63	69
Ch. VENKATA RAO et al. [28]	AA2219 Al-Cu alloy	Square-butt joint	Square Pin	1120	30	-	269.7	-
			Cylindrical Pin	"	"	-	258.1	-
Ramanjaneyulu [29]	AA 2014-T6	Butt Joint	Conical	-	-	2.74	-	102
			Square	-	-	1.24	-	123
			Triangle	-	-	1.03	-	111
			Pentagon	-	-	0.92	-	129
			Hexagon	-	-	0.67	-	136
Ramanjaneyulu [29]	AA 2014-T6	Butt Joint	Conical	1000	600	4.6	348	146
			Triangular	"	"	Less than 4.6 and more than 2.06	432	148
			Square	"	"		434	153
			Pentagon	"	"		435	146

(continued)

Table 1 (continued)

Reference	Base material	Type of joint fabricated	Tool pin profile	Rotational speed (rpm)	Traverse speed (mm/min)	Mechanical properties of friction stir welded joint		
						Average grain size (SZ) μm	UTS (MPa)	Micro-hardness (HV)
Bhanodaya Kiran Babu Nadikudi [30]	AA6061 & AA2014	Butt Joint Similar Butt Joint	Hexagon	"	"	2.06	441	157
			Straight cylindrical (SC)	900	24	-	175	97
			Taper cylindrical (TC)	"	"	-	168	88
			Stepped cylindrical (ST)	"	"	-	170	88
			Straight square (SS)	"	"	-	183	100
			Straight hexagonal (SH)	"	"	-	173	93
Ravindra S. Thube et al. [32]	AA5083		Taper Cylindrical	900	16	-	103	-
			"	1400	"	-	122	-
			"	1800	"	-	116	-
			Triangular	900	"	-	140	-

(continued)

Table 1 (continued)

Reference	Base material	Type of joint fabricated	Tool pin profile	Rotational speed (rpm)	Traverse speed (mm/min)	Mechanical properties of friction stir welded joint		
						Average grain size (SZ) μm	UTS (MPa)	Micro-hardness (HV)
			"	1400	"	-	136	-
			"	1800	"	-	123	-
			Conical	900	"	-	126	-
			"	1400	"	-	138	-
			"	1800	"	-	114	-
			Square	900	"	-	137	-
			"	1400	"	-	143	-
			"	1800	"	-	122	-
			Cylindrical	900	"	-	132	-
			"	1400	"	-	149	-
			"	1800	"	-	140	-

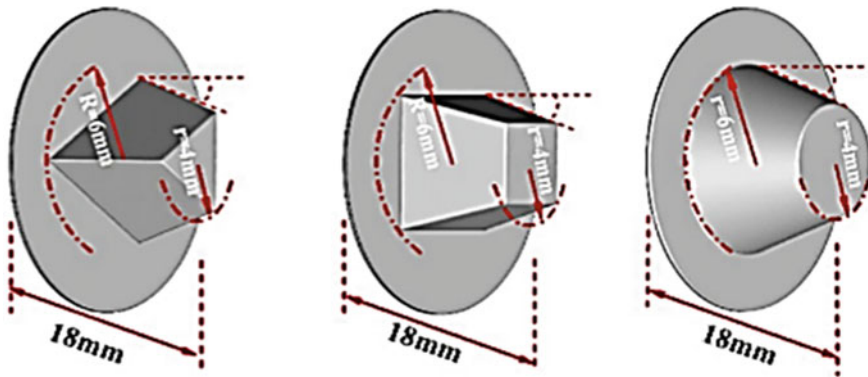


Fig. 26 Tool pin shapes utilized to fabricate the joint [34]

References

1. Thomas WM, Nicholas ED, Needham JC, Murch MG, Templesmith P, Dawes CJ (1992) Improvements relating to friction welding. International Patent Number, PCT/GB92/02203 TWI
2. Thomas WM, Nicholas ED, Watts ER, Staines DG (2002) Friction based welding technology for aluminium. *Mater Sci Forum* 396–402:1543–1548
3. Ericsson M, Sandstro R (2003) Influence of welding speed on the fatigue of friction stir welds, and comparison with MIG and TIG. *Int J Fatigue* 25:1379–1387
4. Akinlabi ET, Mahamood RM (2020) Solid-state welding: friction and friction stir welding processes. Mechanical engineering series, eBook ISBN 978–3–030–37015–2, XV, 145
5. Patil H, Soman S (2010) Experimental study on the effect of welding speed and tool pin profiles on AA6082-O aluminium friction stir welded butt joints. *Int J Eng Sci Technol* 2(5):268–275
6. Shunmugam MS, Kanthababu M (2020) Advances in additive manufacturing and joining. Springer Science and Business Media LLC
7. Asadi P, Givi MKB, Parvin N, Araei A, Taherishargh M, Tutunchilar S (2012) On the role of cooling and tool rotational direction on microstructure and mechanical properties of friction stir processed AZ91. *Int J Adv Manuf Technol* 63(9–12):987–997
8. Rajendran C, Srinivasan K, Balasubramanian V, Balaji H, Selvaraj P (2017) Identifying the combination of friction stir welding parameters to attain maximum strength of AA2014-T6 aluminum alloy joints. *Adv Mater Process Technol* 4(1):100–119
9. Motaleb-nejad P, Saeid T, Heidarzadeh A, Darzi K, Ashjari M (2014) Effect of tool pin profile on microstructure and mechanical properties of friction stir welded AZ31B magnesium alloy. *Mater Design* 59:221–226
10. Ilangovan M, Rajendra Boopathy S, Balasubramanian V (2015) Effect of tool pin profile on microstructure and tensile properties of friction stir welded dissimilar AA 6061–AA 5086 aluminium alloy joints. *Defence Technol* 11(2):174–184
11. Khodaverdizadeh H, Heidarzadeh A, Saeid T (2013) Effect of tool pin profile on microstructure and mechanical properties of friction stir welded pure copper joints. *Mater Design* 45:265–270
12. Emamian S, Awang M, Hussai P, Meyghani B, Zafar A (2016) Influences of tool pin profile on the friction stir welding of AA6061. *J Eng Appl Sci* 11
13. Zhou L, Zhang RX, Li GH, Zhou WL, Huang YX, Song XG (2018) Effect of pin profile on microstructure and mechanical properties of friction stir spot welded Al-Cu dissimilar metals. *J Manuf Process* 36:1–9

14. Emamikhah A, Abbasi A, Atefat A, Givi MKB (2013) Effect of tool pin profile on friction stir butt welding of high-zinc brass (CuZn40). *Int J Adv Manuf Technol* 71(1–4), 81–90. <https://doi.org/10.1007/s00170-013-5480-1>
15. Elangovan K, Balasubramanian V (2007) Influences of pin profile and rotational speed of the tool on the formation of friction stir processing zone in AA2219 aluminium alloy. *Mater Sci Eng* 459(1–2):7–18
16. Kalembe-Rec I, Kopyściański M, Miara D, Krasnowski K (2018) Effect of process parameters on mechanical properties of friction stir welded dissimilar 7075–T651 and 5083–H111 aluminium alloys. *Int J Adv Manuf Technol* 97(5–8):2767–2779
17. Srujana N, Umadevi O, Venkateswarlu G (2014) Influence of tool pin profile on microstructure and mechanical properties of friction stir welded 6351 aluminium alloy. *Res Rev: J Eng Technol* 3(2):13–17
18. Hattingh DG, Blignault C, van Niekerk TI, James MN (2008) Characterization of the influences of FSW tool geometry on welding forces and weld tensile strength using an instrumented tool. *J Mater Process Technol* 203(1–3):46–57
19. Das J, Robi PS, Sankar MR (2019) Assessment of parameters windows and tool pin profile on mechanical property and microstructural morphology of FSWed AA2014 joints. *SN Appl Sci* 2(1)
20. Trimble D, Mitrogiannopoulos H, O'Donnell GE, McFadden S (2015) Friction stir welding of AA2024-T3 plate—the influence of different pin types. *Mech Sci* 6(1):51–55
21. Krasnowski K, Hamilton C, Dymek S (2015) Influence of the tool shape and weld configuration on microstructure and mechanical properties of the Al 6082 alloy FSW joints. *Archives Civil Mech Eng* 15(1):133–141
22. Sabari SS, Malarvizhi S, Balasubramanian V (2016) The effect of pin profiles on the microstructure and mechanical properties of underwater friction stir welded AA2519-T87 aluminium alloy. *Int J Mech Mater Eng* 11(5)
23. Xu W, Liu J, Zhu H, Fu L (2013) Influence of welding parameters and tool pin profile on microstructure and mechanical properties along the thickness in a friction stir welded aluminum alloy. *Mater Design* 47:599–606
24. Tamadon A, Baghestani A, Bajgholi M (2020) Influence of WC-based pin tool profile on microstructure and mechanical properties of AA1100 FSW welds. *Technologies* 8(2):34
25. Krishnan MKM, Subburaj J, Ravichandran S (2020) Effect of tool pin profiles on mechanical properties of friction stir welded joints. *AIP Conf Proc* 2207:020006
26. Goel P, Siddiquee A, Khan N, Hussain M, Khan Z, Abidi M, Al-Ahmari A (2018) Investigation on the effect of tool pin profiles on mechanical and microstructural properties of friction stir butt and scarf welded aluminium alloy 6063. *Metals* 8(1):74
27. Marzbanrad J, Akbari M, Asadi P, Safaee S (2014) Characterization of the influence of tool pin profile on microstructural and mechanical properties of friction stir welding. *Metall Mater Trans B* 45(5):1887–1894
28. Venkata Rao C, Madhusudhan Reddy G, Srinivasa Rao K (2015) Influence of tool pin profile on microstructure and corrosion behaviour of AA2219 Al–Cu alloy friction stir weld nuggets. *Defence Technol* 11(3):197–208
29. Ramanjaneyulu K, Madhusudhan Reddy G, Venugopal Rao A, Markandeya R (2013) Structure-property correlation of AA2014 friction stir welds: role of tool pin profile. *J Mater Eng Perform* 22(8):2224–2240
30. Nadikudi BKB, Davidson MJ, Akasapu NR, Govindaraju M (2015) Formability analysis of dissimilar tailor welded blanks welded with different tool pin profiles. *Trans Nonferrous Metals Soc China* 25(6):1787–1793
31. Jamshidi Aval H (2015) Influences of pin profile on the mechanical and microstructural behaviors in dissimilar friction stir welded AA6082–AA7075 butt Joint. *Mater Design* 67:413–421
32. Thube RS (2014) Influences of tool pin profile and welding parameters on Friction stir weld formation and joint efficiency of AA5083 Joints produced by Friction Stir Welding. *Int J Eng Adv Technol (IJEAT)* 3(5)

33. Palanivel R, Koshy Mathews P, Murugan N, Dinaharan I (2012) Effect of tool rotational speed and pin profile on microstructure and tensile strength of dissimilar friction stir welded AA5083-H111 and AA6351-T6 aluminum alloys. *Mater Design* 40:7–16
34. Aghajani Derazkola H, Simchi A (2018) Experimental and thermomechanical analysis of the effect of tool pin profile on the friction stir welding of poly (methyl methacrylate) sheets. *J Manuf Process* 34:412–423

Effect of Weldability on Metallurgical, Mechanical, and Corrosion Behaviour of High Entropy Alloy_A Review



Sourabh Shukla, Anshula Gaurkar, and Tulika Bawankar

Abstract In recent days, cantor alloy/High entropy alloys (HEAS) have come a long way, and key challenges have developed more frequently when HEA welding is required. In this critical evaluation of the HEAs welding, we seek to report the HEAs weldability under BM and WM composition, welding parameters and their distinctive corrosion behaviour. The current advancements and issues in various HEAS welding phenomena are comprehensively studied, with the microstructures, mechanical characteristic, and functional performances of the joints all taken into account. In addition to reducing the production of intermetallic phases, personalizing welded components, and improving properties of joints, HEAS fillers have shown great potential.

Keywords Corrosion · HEAS · Weldability

1 Introduction

HEAs are an original form of metallic substance with applications in structural, transportation, food preservation, aerospace, nuclear power plants, and cryogenics. [1–6]. HEAs are alloy systems having 5–13 elements, with equi-atom or unequi-atom ratios and atomic proportions ranging from 5 to 35% for each element [5–11]. However, one of the previous works offered a new definition for these alloys, where high entropy alloys comprise a broader spectrum of materials with varying component quantities [1, 12]. Because of their fatigue resistance [13, 14], corrosion resistance [15], excellent wear resistance [16–18], high strength and hardness, significant high-temperature stability, and damping properties via eutectic-structure design or multi-phase [19–22], HEAs have attracted huge importance from researchers in recent years. As a result, metallurgical researchers are working on developing HEAs with both outstanding plasticity and great tensile strength [22–25]. As HEAs exhibit some impressive properties, they are certified as a potential structural and functional

S. Shukla (✉) · A. Gaurkar · T. Bawankar
Mechanical Engineering Department, G H Raisoni College of Engineering, Nagpur 440016, India
e-mail: sourabh.shukla@raisoni.net

materials [26, 27]. Yeh et al. [7] and Cantor et al. [28, 6] each introduced HEAs, commonly called multicomponent alloys. The entropy at a higher level of mixing in HEAs stabilizes the growth of simple solid solution phases and their multiphase [29, 30], whilst prohibiting the growth of intermetallic compounds (IMCs) [6]. It is important to note, however, that HEAs can also exhibit brittle behaviour, as demonstrated by the AlCoCrCuFeNi system [12, 31]. Co-Cr-Fe-Ni-Mn (FCC-structured) system alloys are one of the advantageous classes of HEAs that are of particular interest [5]. Several attempts have been made to enhance CoCrFeNiMn strength through heat treatment or alloying [26, 32–49]. It was discovered that after the proper heat treatment, the yield strength of a (CoCrFeNi) 94Al4Ti improves whilst sustaining enough ductility [26]. Elements with large atomic radius, such as Al, V, Nb, Mo, and others, have sparked a lot of interest in HEA research [50, 51]. The “four-core-effects” of HEAs are specified, which are the high configurational entropy of HEA solid solutions (impact on phase Gibb’s energy), the lattice distortion effect [52], the complexity of HEA compositions tends to “Cocktail effect” [53], and the sluggish diffusion effect for kinetics [54]. Because of the combination of these [55, 56] “four-core-effects”, HEAs possess excellent properties at elevated, room, and cryogenic temperatures [6].

2 Recent Update in the HEAs Welding

Material related to these alloys fundamentally varies from predictable alloys in their chemical make-up, microstructures and mechanical properties which makes weldability challenge. Calculated from science direct, Fig. 1 shows the graphic illustration

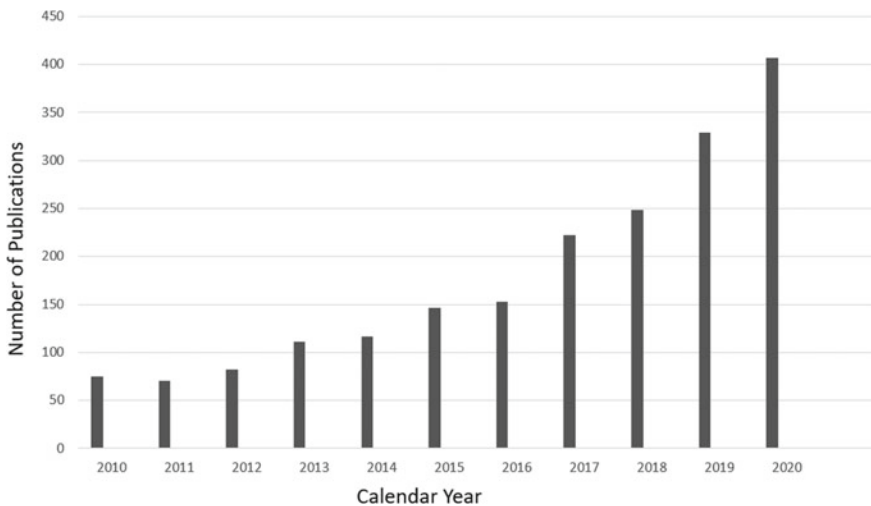


Fig. 1 Graph shows growth of publication with respect to year

of the number of peer-reviewed articles published each year in the field of “Welding of HEAs related material”.

3 Microstructural Evaluation of HEAs Joints

Hyunbin et al. [57] used a single-pass GTA welding process on the cast HEA Base Metal (BM) to feed the filler metals (HEA and STS 308L filler metals), with welding parameters of 90A, diameter of 2.1, 12.5 cm/min velocity, and Arc shielding gas. Defect free joints and full penetrating welds were observed in spite of the filler metals. The cast BM and the HAZ exhibited same coarse grain size of 1.0 ± 0.2 mm as illustrated in Fig. 2a. The undefined fusion line and continuous weld composition generated using the HEA filler metal resulted in epitaxial development of the columnar grains Fig. 2b. Inadequate epitaxial growth of the columnar grains was noticed due to a clearly visible weld-fusion line generated with 308L filler metal Fig. 2c. The columnar grains were converted into equiaxed grains along the centerline of each weld, revealing typical microstructure for GTA welding with significant heat input [58]. Furthermore, dendritic packet sizes at the WM centerline were identical. Both WM and BM revealed the similar pattern of compositional micro-segregations, however elements including Co, Fe, Cr, Mn, and Ni in WMs made with HEA and 308L filler metals showed varying degrees of segregation. In addition, the relationship between the different micro-segregations of Co and Cr in the WM utilizing STS 308L filler was not recognized in this research. The response of CoCrFeMnNi HEA welding using a high-heat input gas tungsten arc and a low energy density was

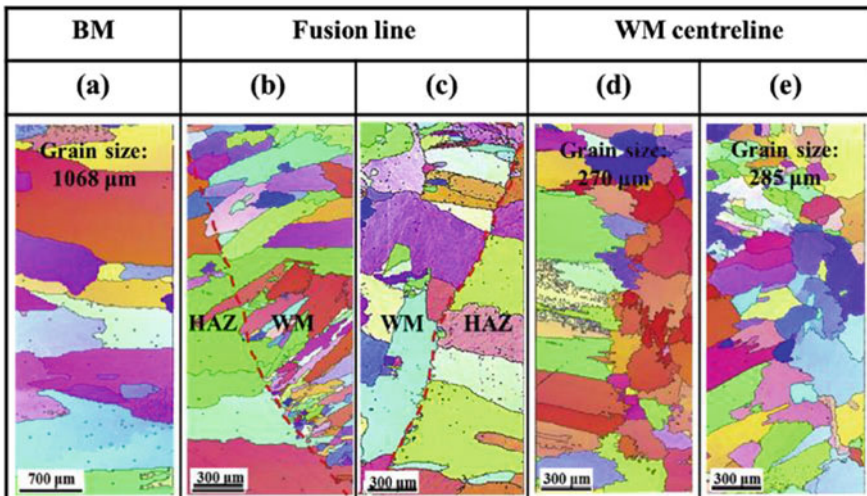


Fig. 2 EBSD image of a cast BM and various filler metals utilizing b and d and c and e STS 308 L [57]

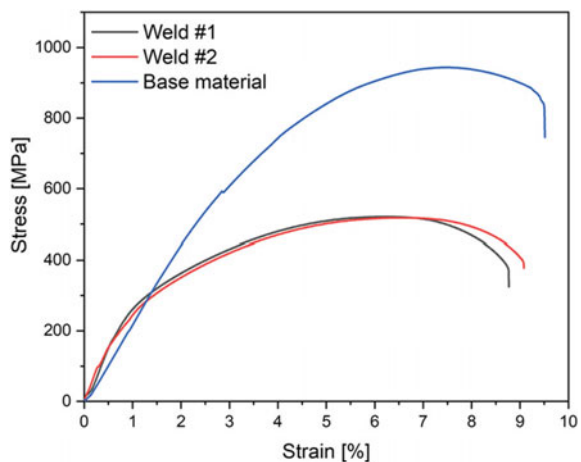
investigated by Wu et al. [59]. Furtherly, Qingkai Fan et al. [60] explored the effect of high Fe content on the various properties of AlCoCrFeNi HEA coatings prepared by gas tungsten arc cladding. Martin et al. [61] performed gas tungsten arc welding on $Al_xCoCrCu_yFeNi$ alloy systems (In molar ratio, $x = 0.5$, $y = 1.0$ and $0 \leq y \leq 1.0$). Again, the weldability of $Al_{0.5}CoCrCu_{0.1}FeNi$ alloy was explored by Martin et al. [62] using hot rolled and heat treated alloy conditions.

4 Mechanical Properties of Welded HEAs

GTA welding on CoCrFeMnNi HEAs which demonstrates the peculiarity of high cooling rate and high heat input and formation of fine dendrites in melting zone. In this case [63], the base metal was cold-rolled equiatomic CrMnFeCoNi HEAs, which was reduced $\approx 50\%$ [from 3 mm to 1.5 mm], by rolling at a normal temperature and pressure. TELWN model technology TIG182 AC/DC-LIFT equipment was used to execute GTA welding to assess the Mechanical Properties.

The study not only advances HEA decision-making research by introducing new and important view points, but it also shows potentially hidden connections between some crucial beliefs in the realm of material science [64]. In Fig. 3, the mechanical behaviour of the welds is related with those of the joints which demonstrates the amount of experiments that have been conducted to achieve consistent results in terms of weld properties. After weld there were changes in mechanical behaviour. The change in ductility behaviour was observed. As comparison to the base material there is reduction in ductility and hardness of welded joints. Most of the failure of the joints are occurred in FZ. For FZ on investigation the obtained results were large grains with soft material in significant amount. In another experiment where there was use of laser welding about the strength for joining an alloy with same

Fig. 3 Tensile testing until failure of the base material and the as-welded HEAs joints are used to derive curves illustrating their mechanical behavior [63]



composition. The amount of deformation experienced by the FZ can be recognized about the tensile direction in which material will lay. The low hardness and larger grain size in the FZ describes microstructure of the GTA welded joints about the failure. Decrease in mechanical properties which is a cause due to increase in large grain size inside the fusion zone. In recent work [65], four divisions are there, the first of which deals with general features of fusion-welding processes, second of which deals with specific elements of fusion-welding processes. In weldments, encounter of metallurgical zones takes place, and the remaining three: the fusion, partially melted, and heat-affected zones are the three types of zones.

5 Corrosion Behaviour in Welded Structures of HEAs

High entropy alloys exhibited favourable properties of superior corrosion resistance and have a vast potential compositional space, which is not widely investigated [66, 67]. Fan et al. [68] examined the effect of Fe (iron) on the electrochemical behaviour of GTA welded AlCoNiCrFe HEA and concluded that the phase changes to BCC + FCC from BCC with increase in Fe content and this new phase induces galvanic corrosion that deteriorates corrosion behaviour. According to Shi et al. [69, 70], the composition varies between FCC and BCC phase of AlCoCrFeNi HEA becomes prone to galvanic type of corrosion, provides an early passive film breakdown due to brittleness. Similarly, again Fan et al. [71] studied the effect of cladding done by GTA on the AlCoCrFeNi HEA. He concluded that AlCoCrFe₃Ni (S-180) shows more corrosion resistance than AlCoCrFeNi (S-150) as shown in Fig. 4, and mainly the corrosion mechanism is pitting and intergranular corrosion. It can be seen in the figure that the OCP of S-180 has a small peak, indicating substantial passivation. Both samples have no discernible passivation zone in their polarization curves. The anodic Tafel zone is next to the passive film breakdown region. It's possible that the passive film forms under corrosion potential, but it's so fragile that it's swiftly destroyed during anodic polarization. The Tafel extrapolation method is used to get E_{corr} (corrosion potential) and i_{corr} (corrosion current density) from the curves. S-180 is nobler than S-150 because it has a higher positive E_{corr} and a lower i_{corr} . Both S-150 and S-180 have only one time constant, proving the lack of a passive film, according to the Bode and Nyquist plot. S-180 has a higher charge transfer resistance (Rct, measured in circuit) than S-150, showing that anodic dissolution is more challenging to arise on the test surface of S-180. Overall, S-180 outperforms S-150 in terms of corrosion resistance. The HEAs corrosion behaviour has been studied at the earliest stages of the development of HEAs shown in Table 1 and Fig. 5 by Chen et al. [72]. From the study of AISI 304SS corrosion behaviour which was then compared with the corrosion behaviour of the Cu_{0.5} AlCoNiCrFeSi alloy in variety of solutions from which it was concluded that in all test solutions, Cu_{0.5} AlCoNiCrFeSi alloy had low corrosion rate than that of AISI 304SS [72].

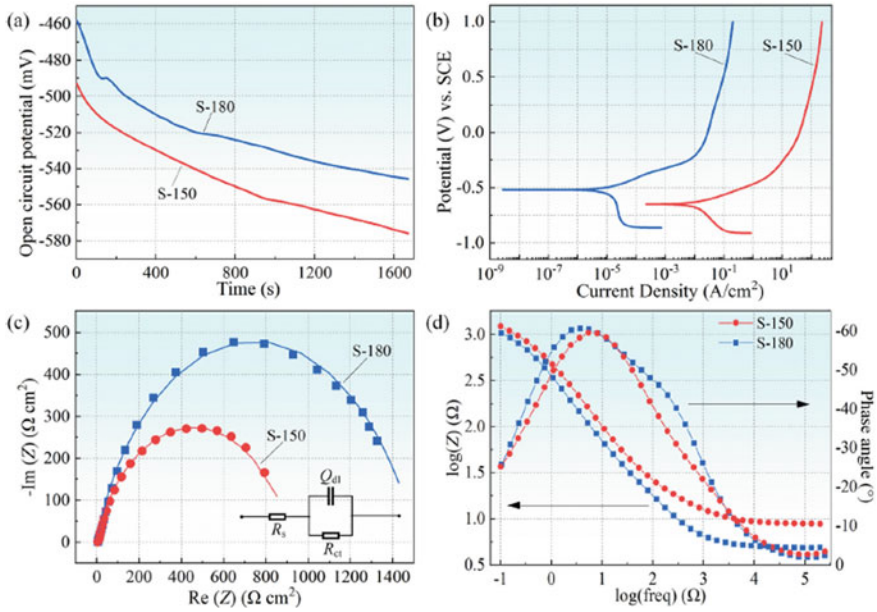
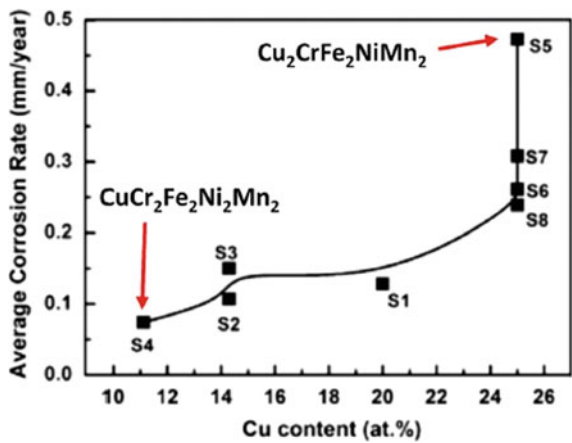


Fig. 4 Open circuit, polarization, and impedance plot showing the effect of iron on the corrosion behaviour of the GTA clad HEA [71]

Table 1 Data of potentiodynamic polarization for all the given three conditions

State	B_a (mV)	B_c (mV)	E_{corr} (mV)	i_{corr} (mA/cm ²)
Base metal	321.15	-168.45	-310.35	6.65×10^{-6}
Weld metal	152.65	-176.45	-240.35	3.85×10^{-5}
Base + weld	35.55	-80.85	-315.75	5.15×10^{-6}

Fig. 5 The impact of a copper content on the rate of corrosion [72]



6 Conclusion

This paper looked at the microstructure evolution, mechanical behaviour, and corrosion in HEA welds made with GTAW welding procedures, as well as the effect of welding settings on welded joint attributes. The welding mechanisms for HEAs were studied, and subsequently the fusion welding mechanism for HEAs was described. We talked about macro-segregation, solidification behaviour, and phase creation in the weld. Some conclusions have been pointed out:

- Numerous studies on HEAs welding have revealed that adjusting welding settings can improve the characteristics of welded connections. The use of metallic interlayers in welding of HEA could successfully prevent flaws from appearing. Numerical simulations can be utilized in the future to forecast experimental findings of HEA welding, which is important for optimizing experimental parameters.
- Furthermore, because of their superior qualities, HEAs also may available as coatings to increase the materials life by improving various properties that are welded.
- A new research direction is the use of HEAs fillers as welding fillers. It has been shown that there are still many areas of HEAs welding that need to be investigated.
- The effects of FSW, LW, and EBW on the linkage of HEAs and other metals should be further investigated.
- There are limited research on the thermal treatment of HEA weldments after they have been welded.
- Relevant studies on the property changes of HEAs weldments at low and high temperatures are required. As a result, additional research into HEAs weldments properties and their use in various fields of welding can help to improve the use value of HEAs in industries.

References

1. Miracle DB, Senkov ON (2017) A critical review of high entropy alloys and related concepts. *Acta Mater* 122:448–511. <https://doi.org/10.1016/j.actamat.2016.08.081>
2. Zhang Y, Zuo TT, Tang Z, Gao MC, Dahmen KA, Liaw PK, Lu ZP (2014) Microstructures and properties of high-entropy alloys. *Prog Mater Sci* 61. <https://doi.org/10.1016/j.pmatsci.2013.10.001>
3. Pickering EJ, Jones NG (2016) High-entropy alloys: a critical assessment of their Founding principles and future prospects. *Int Mater Rev* 183–202. <https://doi.org/10.1080/09506608.2016.1180020>
4. Tsai MH, Yeh JW (2014) High-entropy alloys: a critical review. *Mater Res Lett* 2:107–123
5. Kashaev N, Ventzke V, Stepanov N, Shaysultanov D, Sanin V, Zherebtsov S (2018) Laser beam welding of a CoCrFeNiMn-type high entropy alloy produced by self-propagating high-temperature synthesis 0966–9795/ ©. <https://doi.org/10.1016/j.intermet.2018.02.014>
6. Li J, Meng X, Wan L, Huang Y (2021) Welding of high entropy alloys: progresses, challenges and perspectiveness. 1526–6125/©

7. Yeh JW, Chen SK, Lin SJ, Gan JY, Chin TS, Shun TT, Tsau CH, Chang SY (2004) Nanostructured high-entropy alloys with multiple principal elements: novel alloy design concepts and outcomes. *Adv Eng Mater* 6:299–303. <https://doi.org/10.1002/adem.200300567>
8. Yang S, Lu J, Xing F, Zhang L, Zhong Y (2020) Revisit the VEC rule in high entropy alloys (HEAs) with high-throughput CALPHAD approach and its applications for material design—a case study with Al–Co–Cr–Fe–Ni system. *Acta Mater* 192:11–19. <https://doi.org/10.1016/j.actamat.2020.03.039>
9. Zhang W, Liaw PK, Zhang Y (2018) Science and technology in high-entropy alloys. *Sci China Mater* 61:2–22. <https://doi.org/10.1007/s40843-017-9195-8>
10. Newbury DE (2011) Mistakes encountered during automatic peak identification of minor and trace constituents in electron-excited energy dispersive X-ray microanalysis. *Scanning* 31:91–101. <https://doi.org/10.1002/sca.20151>
11. Cai YP, Wang GJ, Ma YJ, Cao ZH, Meng XK (2019) High hardness dual-phase high entropy alloy thin films produced by interface alloying. *Scr Mater* 162:281–285
12. Lopes JG, Oliveira JP A Short Review on Welding and Joining of High Entropy Alloys. *UNIDEMI, Department of Mechanical and Industrial Engineering, NOVA School of Science and Technology, Universidade NOVA de Lisboa, pp 2829–516 Caparica, Portugal; jcg.lopes@campus.fct.unl.pt
13. Hemphill MA, Yuan T, Wang GY, Yeh JW, Tsai CW, Chuang A, Liaw PK (2012) Fatigue behavior of Al_{0.5}CoCrCuFeNi high entropy alloys. *Acta Mater* 60(16):5723–5734
14. Tang Z, Yuan T, Tsai CW, Yeh JW, Lundin CD, Liaw PK (2015) Fatigue behavior of a wrought Al_{0.5}CoCrCuFeNi two-phase high-entropy alloy. *Acta Mater* 99:247–258
15. Shi YZ, Yang B, Liaw PK (2017) Corrosion-resistant high-entropy alloys: a review. *Metals-Basel* 7(2):43. <https://doi.org/10.3390/met7020043>
16. Chuang MH, Tsai MH, Wang WR, Lin SJ, Yeh JW (2011) Microstructure and wear behavior of Al_xCo_{1-5x}CrFeNi_{1-5x}Ti_y high-entropy alloys. *Acta Mater* 59(16):6308–6317. <https://doi.org/10.1016/j.actamat.2011.06.041>
17. Wu JM, Lin SJ, Yeh JW, Chen SK, Huang YS (2006) Adhesive wear behavior of Al_xCoCrCuFeNi high-entropy alloys as a function of aluminum content. *Wear* 261(5–6):513–519. <https://doi.org/10.1016/j.wear.2005.12.008>
18. Tong CJ, Chen MR, Yeh JW, Lin SJ, Chen SK, Shun TT, Chang SY (2005) Mechanical performance of the Al_xCoCrCuFeNi high-entropy alloy system with multiprincipal elements. *Metall Mater Trans A Phys Metall Mater Sci* 36(5):1263–1271. <https://doi.org/10.1007/s11661-005-0218-9>
19. Li Z, Pradeep KG, Deng Y, Raabe D, Tasan CC (2016) Metastable high-entropy dualphase alloys overcome the strength–ductility trade-off. *Nature* 534(7606):227–230. <https://doi.org/10.1038/nature17981>
20. Ma SG, Liaw PK, Gao MC, Qiao JW, Wang ZH, Zhang Y (2014) Damping behavior of Al_xCoCrFeNi high-entropy alloys by a dynamic mechanical analyzer. *J Alloys Compd* 604:331–339. <https://doi.org/10.1016/j.jallcom.2014.03.050>
21. Chen Q, Zhang HL, Zhou SL, Cai YT, Li XG, Xu Y (2019) A novel high-entropy alloy with excellent damping property toward a large strain amplitude environment. *J Alloys Compd* 802:493–501. <https://doi.org/10.1016/j.jallcom.2019.06.247>
22. Lu Y, Dong Y, Guo S, Jiang L, Kang H, Wang T, Wen B, Wang Z, Jie J, Cao Z, Ruan H, Li T (2014) A promising new class of high-temperature alloys: eutectic highentropy alloys. *Sci Rep-UK* 4:6200. <https://doi.org/10.1038/srep06200>
23. Kuznetsov AV, Shaysultanov DG, Stepanov ND, Salishcheva GA, Senkovbc ON (2012) Tensile properties of an AlCrCuNiFeCo high-entropy alloy in as-cast and wrought conditions. *Mater Sci Eng A* 533:107e118
24. Ma S, Zhang S, Gao M, Liaw P, Zhang Y (2013) A successful synthesis of the CoCrFeNiAl_{0.3} single-crystal, high-entropy alloy by Bridgman solidification. *JOM (J Occup Med)* 65:1751e1758
25. Li D, Li C, Feng T, Zhang Y, Sha G, Lewandowski J, Liaw P, Zhang Y (2017) Highentropy Al_{0.3}CoCrFeNi alloy fibers with high tensile strength and ductility at ambient and cryogenic temperatures. *Acta Mater*. 123:285e294

26. He JY, Wang H, Huang HL, Xu XD, Chen MW, Wu Y, Liu XJ, Nieh TG, An K, Lu ZP (2016) *Acta Mater* 102:187–196
27. Zhu ZG, Sun YF, Goh MH, Ng FL, Nguyen QB, Fujii H, Nai SML, Wei J, Sheka CH Friction stir welding of a CoCrFeNiAl_{0.3} high entropy alloy. <https://doi.org/10.1016/j.matlet.2017>
28. Cantor B, Chang ITH, Knight P, Vincent AJB (2004) Microstructural development in equiatomic multicomponent alloys. *Mater Sci Eng A* 375–377:213–218. <https://doi.org/10.1016/j.msea.2003.10.257>
29. Xu XD, Guo S, Nieh TG, Liu CT, Hirata A, Chen MW (2019) Effects of mixing enthalpy and cooling rate on phase formation of AlxCoCrCuFeNi high-entropy alloys. *Materialia* 100292. <https://doi.org/10.1016/j.mtla.2019.100292>
30. Choudhuri D, Gwalani B, Gorse S, Komarasamy M, Mantri SA, Srinivasan SG et al (2019) Enhancing strength and strain hardenability via deformation twinning in fcc-based high entropy alloys reinforced with intermetallic compounds. *Acta Mater* 165:420–430. <https://doi.org/10.1016/j.actamat.2018.12.010>
31. Ng C, Guo S, Luan J, Shi S, Liu CT (2012) Entropy-driven phase stability and slow diffusion kinetics in an Al_{0.5}CoCrCuFeNi high entropy alloy. *Intermetallics* 31:165–172
32. Otto F, Dlouhý A, Somsen C, Bei H, Eggeler G, George EP (2013) The influences of temperature and microstructure on the tensile properties of a CoCrFeMnNi high entropy alloy. *Acta Mater* 61. <https://doi.org/10.1016/j.actamat.2013.06.018>
33. Gludovatz B, Hohenwarter A, Thurston KVS, Bei H, Wu Z, George EP, Ritchie RO (2016) Exceptional damage-tolerance of a medium-entropy alloy CrCoNi at cryogenic temperatures. *Nat Commun*. <https://doi.org/10.1038/ncomms10602>
34. Laplanche G, Kostka A, Reinhart C, Hunfeld J, Eggeler G, George EP (2017) Reasons for the superior mechanical properties of medium-entropy CrCoNi compared to high-entropy CrMnFeCoNi. *Acta Mater*. <https://doi.org/10.1016/j.actamat.2017.02.036>
35. Stepanov ND, Shaysultanov DG, Chernichenko RS, Yurchenko NY, Zherebtsov SV, Tikhonovsky MA, Salishchev GA (2017) Effect of thermomechanical processing on microstructure and mechanical properties of the carbon-containing CoCrFeNiMn high entropy alloy. *J Alloy Comp* 693:394–405. <https://doi.org/10.1016/j.jallcom.2016.09.208>
36. Stepanov ND, Yurchenko NY, Tikhonovsky MA, Salishchev GA (2016) Effect of carbon content and annealing on structure and hardness of the CoCrFeNiMn-based high entropy alloys. *J Alloy Comp* 687:59–71. <https://doi.org/10.1016/j.jallcom.2016.06.103>
37. Stepanov N, Tikhonovsky M, Yurchenko N, Zyabkin D, Klimova M, Zherebtsov S, Efimov A, Salishchev G (2015) Effect of cryo-deformation on structure and properties of CoCrFeNiMn high-entropy alloy. *Intermetallics* 59:8–17. <https://doi.org/10.1016/j.intermet.2014.12.004>
38. Wu Z, Parish CM, Bei H (2015) Nano-twin mediated plasticity in carbon-containing FeNiCoCrMn high entropy alloys. *J Alloy Comp* 647:815–822. <https://doi.org/10.1016/j.jallcom.2015.05.224>
39. Wu Z, Gao Y, Bei H (2016) Thermal activation mechanisms and Labusch-type strengthening analysis for a family of high-entropy and equiatomic solid-solution alloys. *Acta Mater* 120:108–119. <https://doi.org/10.1016/j.actamat.2016.08.047>
40. Li Z, Tasan CC, Springer H, Gault B, Raabe D (2017) Interstitial atoms enable joint twinning and transformation induced plasticity in strong and ductile high-entropy alloys. *Sci Rep* 7:40704. <https://doi.org/10.1038/srep40704>
41. Stepanov ND, Shaysultanov DG, Tikhonovsky MA, Salishchev GA (2015) Tensile properties of the Cr-Fe-Ni-Mn non-equiatomeric multicomponent alloys with different Cr contents. *Mater Des* 87:60–65. <https://doi.org/10.1016/j.matdes.2015.08.007>
42. Wang Z, Baker I, Cai Z, Chen S, Poplawsky JD, Guo W (2016) The effect of interstitial carbon on the mechanical properties and dislocation substructure evolution in Fe_{40.4}Ni_{11.3}Mn_{34.8}Al_{7.5}Cr₆ high entropy alloys. *Acta Mater* 120. <https://doi.org/10.1016/j.actamat.2016.08.072>
43. Wang Z, Baker I, Guo W, Poplawsky JD (2017) The effect of carbon on the microstructures, mechanical properties, and deformation mechanisms of thermo-mechanically treated Fe_{40.4}Ni_{11.3}Mn_{34.8}Al_{7.5}Cr₆ high entropy alloys. *Acta Mater* 126:346–360. <https://doi.org/10.1016/j.actamat.2016.12.074>

44. Yao MJ, Pradeep KG, Tasan CC, Raabe D (2014) A novel, single phase, non-equiatomic FeMnNiCoCr high-entropy alloy with exceptional phase stability and tensile ductility, *Scripta Mater* 72–73. <https://doi.org/10.1016/j.scriptamat.2013.09.030>.
45. Deng Y, Tasan CC, Pradeep KG, Springer H, Kostka A, Raabe D (2015) Design of a twinning-induced plasticity high entropy alloy. *Acta Mater* 94. <https://doi.org/10.1016/j.actamat.2015.04.014>
46. Gwalani B, Soni V, Lee M, Mantri S, Ren Y, Banerjee R (2017) Optimizing the coupled effects of Hall-Petch and precipitation strengthening in a Al_{0.3}CoCrFeNi high entropy alloy. *Mater Des* 121:254–260. <https://doi.org/10.1016/j.matdes.2017.02.072>
47. Fu Z, Chen W, Wen H, Zhang D, Chen Z, Zheng B, Zhou Y, Lavernia EJ (2016) Microstructure and strengthening mechanisms in an FCC structured single-phase nanocrystalline Co₂₅Ni₂₅Fe₂₅Al_{7.5}Cu_{17.5} high-entropy alloy. *Acta Mater* 107:59–71. <https://doi.org/10.1016/j.actamat.2016.01.050>
48. Sun SJ, Tian YZ, Lin HR, Dong XG, Wang YH, Zhang ZJ, Zhang ZF (2017) Enhanced strength and ductility of bulk CoCrFeMnNi high entropy alloy having fully recrystallized ultrafine-grained structure. *Mater Des* 133:122–127. <https://doi.org/10.1016/j.matdes.2017.07.054>
49. Klimova M, Stepanov N, Shaysultanov D, Chernichenko R, Yurchenko N, Sanin V, Zharebtsov S (2017) Microstructure and mechanical properties evolution of the Al, C-containing CoCrFeNiMn-type high-entropy alloy during cold rolling. *Materials (Basel)* 11:53. <https://doi.org/10.3390/ma11010053>
50. Shun TT, Du YC (2009) *J Alloy Compd* 479:157–160
51. Chen S, Liu Q, Tianbing H, Lei G Inhomogeneity of microstructure and mechanics of laser welded CoCrFeNiAl_{0.3} high entropy alloy 0167–577X/© 2021
52. Wu YD, Cai YH, Chen XH, Wang T, Si JJ, Wang L, Wang YD, Hui XD (2015) Phase composition and solid solution strengthening effect in TiZrNbMoV high-entropy alloys. *Mater Des* 83:651–660
53. Dabrowa J, Zajusz M, Kucza W, Cieślak G, Berent K, Czeppe T, Kulik T, Danielewski M (2019) Demystifying the sluggish diffusion effect in high entropy alloys. *J Alloys Compd* 783:193–207
54. Pickering EJ, Muñoz-Moreno R, Stone HJ, Jones NG (2016) Precipitation in the equiatomic high-entropy alloy CrMnFeCoNi. *Scr Mater* 113:106–109
55. Shu FY, Liu S, Zhao HY, He WX, Sui SH, Zhang J et al (2018) Structure and hightemperature property of amorphous composite coating synthesized by laser cladding FeCrCoNiSiB high-entropy alloy powder. *J Alloy Compd* 731:662–666. <https://doi.org/10.1016/j.jallcom.2017.08.248>
56. Qin G, Xue W, Chen R, Zheng H, Wang L, Su Y et al (2019) Grain refinement and FCC phase formation in AlCoCrFeNi high entropy alloys by the addition of carbon. *Materialia* 6:100259. <https://doi.org/10.1016/j.mtla.2019.100259>
57. Nam H, Park S, Park N, Na Y, Kim H, Yoo SJ, Moon YH, Kang N Weldability of cast CoCrFeMnNi high-entropy alloys using various filler metals for cryogenic applications
58. Sokkalingam R, Mishra S, Cheethirala SR, Muthupandi V, Sivaprasad K (2017) Enhanced relative slip distance in gas-tungsten-arc-welded Al_{0.5}CoCrFeNi high-entropy alloy. *Metall Mater Trans A* 48:3630–3634
59. Wu Z, David SA, Leonard DN, Feng Z, Bei H (2018) Microstructures and mechanical properties of a welded CoCrFeMnNi high-entropy alloy. *Sci Technol Weld Join* 23:585–595
60. Fan Q, Chen C, Fan C, Liu Z, Cai X, Lin S, Yang C Effect of high Fe content on the microstructure, mechanical and corrosion properties of AlCoCrFeNi high-entropy alloy coatings prepared by gas tungsten arc cladding
61. Martin AC, Oliveira JP, Fink C (2020) Elemental effects on weld cracking susceptibility in Al_xCoCrCuFeNi high-entropy alloy. *Metall Mater Trans A* 51:778–787. <https://doi.org/10.1007/s11661-019-05564-8>
62. Martin AC, Fink C (2019) Initial weldability study on Al_{0.5}CrCoCu_{0.1}FeNi high-entropy alloy. *Weld World* 63:739–750. <https://doi.org/10.1007/s40194-019-00702-7>

63. Oliveira JP, Curado TM, Zeng Z, Lopes JG, Rossinyol E, Park JM, Schell N, Fernandes FMB, Kim HS (2020) Gas tungsten arc welding of as-rolled CrMnFeCoNi high entropy alloy. *Mater Des* 189:108505
64. Influence of tungsten on microstructure evolution and mechanical properties of selected novel FeCoCrMnW_x high entropy alloys. <https://doi.org/10.1016/j.intermet.2021.107161>
65. Kou S (2002) *Welding metallurgy*, 2nd edn, Wiley, Hoboken, New Jersey. www.mrs.org/publications/bulletin
66. Sokkalingam R, Sivaprasad K, Duraiselvam M, Muthupandi V, Prashanth KG (2020) Novel welding of Al_{0.5}CoCrFeNi high-entropy alloy: corrosion behaviour. *J Alloys Compd* 817:153163
67. Li QH, Yue TM, Guo ZN, Lin X (2013) Microstructure and corrosion properties of AlCoCrFeNi high entropy alloy coatings deposited on AISI 1045 steel by the electrospark process. *Metall Mater Trans A* 44:1767e1778.
68. Fan Q, Chen C, Fan C (2021) Effect of high Fe content on the microstructure, mechanical and corrosion properties of AlCoCrFeNi high-entropy alloy coatings prepared by gas tungsten arc cladding. *Surf Coat Technol* 418:127242
69. Shi YZ, Collins L, Balke N, Liaw PK, Yang B (2018) In-situ electrochemical-AFM study of localized corrosion of Al_xCoCrFeNi high-entropy alloys in chloride solution. *Appl Surf Sci* 439:533–544
70. Shi Y, Yang B, Xie X, Brechtel J, Dahmen KA, Liaw PK (2017) Corrosion of Al_xCoCrFeNi high-entropy alloys: Al-content and potential scan-rate dependent pitting behavior. *Corros Sci* 119:33–45
71. Fan Q, Chen C, Fan C, Liu Z, Cai X, Lin S, Yang C (2021) AlCoCrFeNi high-entropy alloy coatings prepared by gas tungsten arc cladding: Microstructure, mechanical and corrosion properties. *Intermetallics* 138:107337
72. Chen YY, Duval, Hung, Yeh JW, Shih HC (2005) Microstructure and electro-chemical properties of high entropy alloys (HEAs)—a comparison with type-304 stainless steel. *Corrosion Sci* 47:2257–2279

Numerical Analysis of Conduction Mode Laser Welding of Aluminium 2024 Alloy in Lap Joint Configuration



Upama Dey, Aparna Duggirala, Bappa Acherjee, and Souren Mitra

Abstract Aluminium alloys are one of the most difficult materials to weld, but those are in great demand across a wide range of industrial sectors. A three-dimensional model is designed in this study to predict heat transmission characteristics in the lap joint welding of Aluminium alloy 2024. The simulative work is carried out using COMSOL Multiphysics, a finite element software. Numerical simulations are used to investigate the impact of input process parameters (peak power, scanning speed, and frequency) on weld geometry. The Taguchi method is used for design of experiment (DOE). To build the numerical model for the conduction mode of welding, the temperature dependent material properties are used. The simulative work yields the weld width as well as the temperature history of the lap joint. The simulated results are validated with experimental results. Those are in good accord, as seen by the validated outcomes with minimum 0.9% to maximum 9.8% error.

Keywords Aluminium alloy · Laser welding · Numerical simulation · Conduction mode · Weld geometry · Lap joint

1 Introduction

Laser welding theory and practice have grown in importance in the discipline of production engineering due to considerable advantages over conventional welding processes. Due to its high aspect ratio and tiny heat-affected zone, laser welding has become a more popular advanced manufacturing process [1]. Welding simulation is another important topic that will impact the future of welding technology.

U. Dey (✉) · A. Duggirala

School of Laser Science and Engineering, Jadavpur University, Kolkata 700032, India

e-mail: upama@ieee.org

B. Acherjee

Department of Production and Industrial Engineering, Birla Institute of Technology, Mesra, Ranchi 835215, India

S. Mitra

Department of Production Engineering, Jadavpur University, Kolkata 700032, India

Numerical approaches are used to model the welding process and predict joint geometry, microstructure, and other weld characteristics, partially replacing the costly and time-consuming experimental-based trial-and-error method.

The laser welding process has been modelled by different researchers using numerical methods and experimental design of experiments (DOE). Moraitis and Labeas [2] propose a thermo-mechanical finite element model for estimating residual stress and distortion fields in aluminium lap joints. Acherjee et al. [3] developed a temporal numerical model based on conduction mode heat transfer for laser transmission welding. Akbari et al. [4] utilised computational and experimental approaches to estimate the HAZ, molten pool width, and depth. Shanmugam et al. [5] and Balasubramanian et al. Bachmann et al. [6, 7] used COMSOL Multiphysics to solve 3D heat transfer, fluid dynamics with phase change, and electromagnetic field PDEs. To model heat and fluid movement, Courtois et al. [8] utilised Comsol Multiphysics, a proprietary software. Frewin and Scott [9] show that the temperature profile and weld size are important variables in the laser beam's absorptivity and energy dispersion. Morgan and Williams [10] utilised conduction mode laser welding in AA2024 alloy to accomplish plate penetration. The Taguchi method saves time and money when designing experiments. Paul et al. [11] devised an experimental design utilising Taguchi L9 technique to explore weld width.

Despite the fact that aluminium alloys have good strength, some alloys are not in widespread usage. The cause is attributed to the poor weldability of certain alloys due to their physical and chemical properties. There is an enhanced need to conduct research on the weldability of these alloys in order to devise ways to find practical applications. Hence investigations are needed for the study of different governing parameters observed during laser welding of those aluminium alloys. This study simulates laser welding of a lap joint performed on aluminium alloy 2024 in conduction mode to better understand the thermal condition of the welds. The numerical model was created with COMSOL Multiphysics. The Taguchi approach was used to design the experiment, and the welding was done in one pass using a Gaussian beam profile pulsed laser. Finally, experimental findings verified the simulated results.

2 Model Materials and Experimental Design

This study utilized aluminium alloy 2024. The principle alloying element of this aluminium alloy is copper. This alloy can withstand high amounts of stress and strain for long periods of time; also, it has great shearing resistance and can function at high temperatures. So, it finds extensive applications in the aircraft industry. Traditional welding of this alloy gives massive micro cracking, which is often difficult to detect and can result in severe failure in operation. As a result laser welding process is choosing to weld this alloy. The material's measurements are 75 mm in length, 20 mm in width, and 2 mm in thickness.

The L9 Taguchi technique is used to create the numerical model for manufacturing lap joints, using three input variables, peak power, scanning speed, and frequency,

Table 1 DOE of lap joint numerical model

S. No.	Peak power (P) in kW	Scanning speed (V) in mm/s	Frequency (f) in Hz
1	4.43	1	6
2	4.43	1.5	7
3	4.43	2	8
4	4.79	1	7
5	4.79	1.5	8
6	4.79	2	6
7	5.14	1	8
8	5.14	1.5	6
9	5.14	2	7

as well as three levels of data chosen for the study. The Taguchi technique has the benefit of emphasising a mean performance characteristic value close to the objective value instead of a value within specified limitations, which improves product quality. Furthermore, Taguchi’s experimental design technique is simple and intuitive to use. The planned combinations of input parameters generated using the Taguchi L9 technique is shown in Table 1.

3 Numerical Modelling of Lap Joints

This numerical model is created using the COMSOL Multiphysics programme for examining the thermal and weld characteristics of AA2024 during laser welding of a lap joint. Because the physics of laser welding is tightly coupled and substantially nonlinear, the equations used to represent the laser process are reduced to ensure numerical stability within an acceptable computation time. The fundamental assumptions are utilised to simplify the computation process while yet maintaining the model’s correctness.

3.1 Assumptions

The fundamental assumptions of this simulative work are stated below.

- The laser’s intensity distribution is supposed to be Gaussian.
- The workpiece is made of a homogeneous and isotropic material.
- This study considers just solid–liquid phases.
- The model makes no consideration for the effects of shielding gas.

3.2 Simulation Modelling

The laser beam is represented as a heat flux that flows in brief pulses down the plate's y-axis. As a result, the thermal history is investigated in terms of space and time. The scanning speed and plate width are used to calculate the travel duration of the beam. The time growth is dependent on the total travel time of the beam and the amount of load stages.

Heat source with the Gaussian distribution is used to express the laser beam energy [12]:

$$Q_0 = \frac{3AP}{\pi r_b^2 h} \exp \frac{-3(x - x_c)^2}{r_b^2} \exp \frac{-3(y - y_c)^2}{r_b^2} \exp \frac{-3(z - z_c)^2}{h^2} \quad (1)$$

where, A is the absorption coefficient, P is the laser power, r_b is the radius of laser beam (m), h is the height of the volumetric heat source, which is equal to the thickness of the work-piece, and $(x - x_c)$, $(y - y_c)$, and $(z - z_c)$ shows the radial distance from the beam centre of the corresponding co-ordinates.

This simulation in COMSOL Multiphysics finite element software includes the governing equations for mass conservation, momentum conservation, and energy conservation.

- Equation of mass conservation:

$$\nabla \cdot (\rho u) = 0 \quad (2)$$

where, the density of the molten metal is denoted by ρ , and u is the fluid velocity vector.

- Equation of momentum conservation:

$$\rho \frac{\delta u}{\delta t} + \rho(u \cdot \nabla)u = \nabla \cdot \left[-pI + \mu(\nabla u + (\nabla u)^T) - \frac{2}{3}u(\nabla \cdot u)I \right] + K \quad (3)$$

where, ρ is density of the molten metal, u is the fluid velocity vector, p is the pressure, μ is the dynamic viscosity, T is the temperature, and

$$K = \frac{C_1(1 - f_l)^2}{f_l^2 + C_2}(u - u_{\text{weld}}) \quad (4)$$

C_1 is a constant operator that indicates circumstances in the mushy zone, C_2 is a positive value that is taken into account to prevent division by zero, and f_l is the liquid fraction

$$f_l = \begin{cases} 0 & 0 < T < T_s \\ \frac{T-T_s}{T_s-T_l} & T_s \leq T \leq T_l \\ 1 & T \geq T_l \end{cases} \quad (5)$$

where, T_s is the solidus temperature, and T_l is the liquidus temperature.

The energy-temperature relation is used to simulate the solidus–liquidus mushy region. From solidus to liquidus temperatures, f_l varies between 0 and 1. When the solid phase is present, $f_l = 0$, and when the liquid phase is present, $f_l = 1$.

- The equation of energy conservation:

$$\rho C_p^* u \cdot \nabla T = \nabla \cdot (\lambda \nabla T) \quad (6)$$

where, ρ is density of the molten metal, u is the fluid velocity vector, T is the temperature, λ is the effective heat conductivity, and C_p^* is the apparent specific heat capacity which defines the melting phase.

$$C_p^* = C_p + \frac{\exp\left(\frac{(T-T_{\text{melt}})^2}{\delta T}\right)}{\sqrt{\pi} \delta T} H_f \quad (7)$$

C_p is the specific heat capacity which is temperature dependent, δT is the mushy region's temperature range, and H_f is the latent heat of fusion.

The temperature in the fusion zone rises over the material's melting point during the welding process. As a result, the enthalpy method is used to include phase transition events into finite element models.

3.3 Meshing

For various processes and analysis, different mesh settings are necessary. Free triangular and sweeping meshes are used to mesh the element. A very small mesh pattern is placed along the scanning path of the laser beam to improve outcomes. To reduce calculation time and memory, the remainder of the workpiece is meshed with coarser components, as seen in Fig. 1.

The models are numerically solved in order to simulate the laser welding process. Table 3 shows the parameters that were utilised in the simulation.

3.4 Model Validation

The UW YAG 300 W pulsed laser welding system is used for all of the tests. Peak power, scanning speed, and frequency were chosen as process parameters. The lap

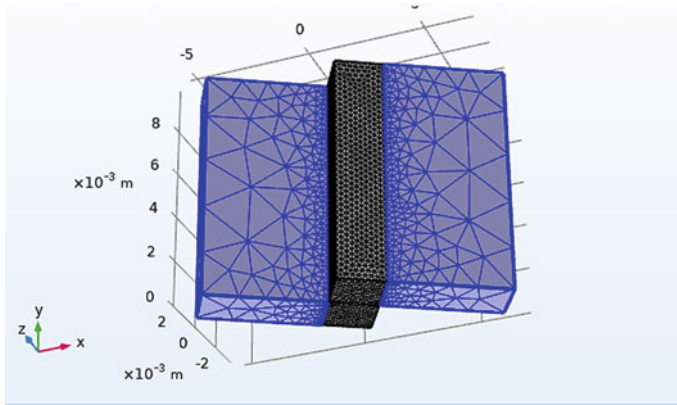


Fig. 1 Mesh patterns in the workpiece

joint studies used a sample size of 75 mm \times 25 mm \times 2 mm. The length of the overlapped portion is 30 mm. At a pressure of 3 bar, the welding was done with argon as an aid gas. During the experiment, the laser torch was positioned at a 30° angle to the perpendicular axis to concentrate the beam for the lap joint. A backing plate of the same material composition is used during welding.

The present investigation used the same material composition and size as the previous tests, as well as the same DOE. The experimental research includes information on breaking load, weld width, and throat length. Tables 2 and 3 include all of the experimental results as well as the simulated results. The research investigated the effect of process factors on results.

The model is validated by comparing the simulated and experimental results. According to Table 2, the average error is 3.84%, with experiment no. 7 having the

Table 2 Validation of the weld width dimensions

S. No.	Peak power (P) in kW	Scanning speed (V) in mm/s	Frequency (f) in Hz	Experimental result	Simulation result	Error (%)
				weld width (WW) in μm	Weld width (WW) in μm	
1	4.43	1	6	398.81	387.68	-2.79
2	4.43	1.5	7	434.79	443.82	+ 2.08
3	4.43	2	8	474.37	501.13	+ 5.64
4	4.79	1	7	713.01	680.26	-4.60
5	4.79	1.5	8	820.76	747.50	-9.80
6	4.79	2	6	496.56	506.88	+ 2.08
7	5.14	1	8	828.69	836.55	-0.94
8	5.14	1.5	6	507.23	520.45	+ 2.61
9	5.14	2	7	552.69	572.94	+ 3.66

Table 3 Validation of the throat length dimensions

S. No.	Peak power (P) in kW	Scanning speed (V) in mm/s	Frequency (f) in Hz	Experimental result	Simulation result	Error (%)
				Throat length (TL) in μm	Throat length (TL) in μm	
1	4.43	1	6	340.72	324.71	-4.93
2	4.43	1.5	7	350.95	341.82	-2.67
3	4.43	2	8	427.40	415.28	-2.91
4	4.79	1	7	731.53	720.56	-1.52
5	4.79	1.5	8	883.94	850.31	-3.95
6	4.79	2	6	369.99	342.03	-8.17
7	5.14	1	8	972.51	901.46	-7.88
8	5.14	1.5	6	385.39	380.65	-1.24
9	5.14	2	7	417.32	403.64	-3.38

lowest error rate and experiment no. 5 having the highest. In Table 3, experiment no.6 having highest error and experiment no. 8 having lowest error. The high agreement between the simulated and actual findings demonstrates the potential use of this numerical model. Tables 2 and 3 shows with the maximum peak power and frequency weld width and throat length is maximum. Figure 2 is the experiment 7’s weld width taken from the optical microscope.

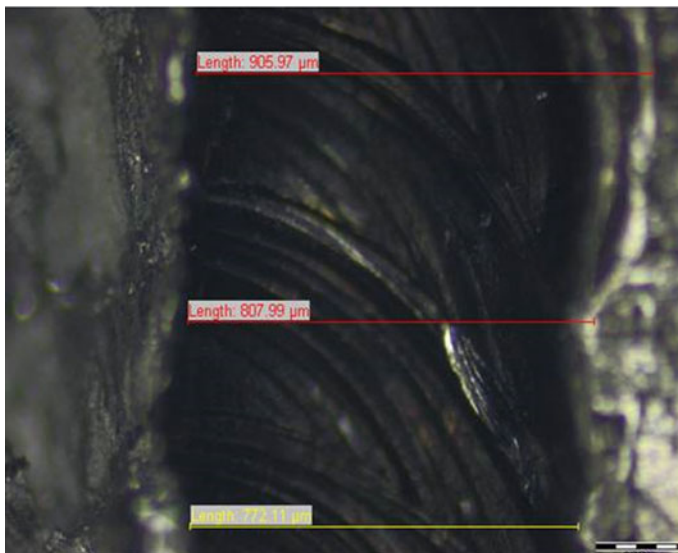


Fig. 2 Microscopic image showing weld width of experiment 7

3.5 Significance of Investigation on Weld Width and Throat Length

Weld width and depth of penetration are two objectives for determining the weld quality. Higher weld width means that the parent material gets damaged reducing the strength of the final joint. Hence, weld width needs to be as low as possible and keyhole penetration produces sound joints. Higher depth of penetration is often desirable. These two objectives effect the load bearing capacity of the joints.

4 Results and Discussion

The heat produced by absorbing the laser beam's energy is progressively transmitted from the irradiated zone to the surrounding region, causing the temperature to rise. The temperatures versus time graphs are presented in Figs. 3, 4 and 5.

Figure 3 depicts three graphs for experiments 1, 2, and 3 that illustrate the relationship between temperature and time. As can be seen in Fig. 3a–c, the first has a greater temperature than the second and third. Table 2 demonstrates that while the power in experiments 1, 2, and 3 is the same, the scanning speed and frequency are not. In experiments 2 and 3, the frequency and scanning speed are increased. However, the

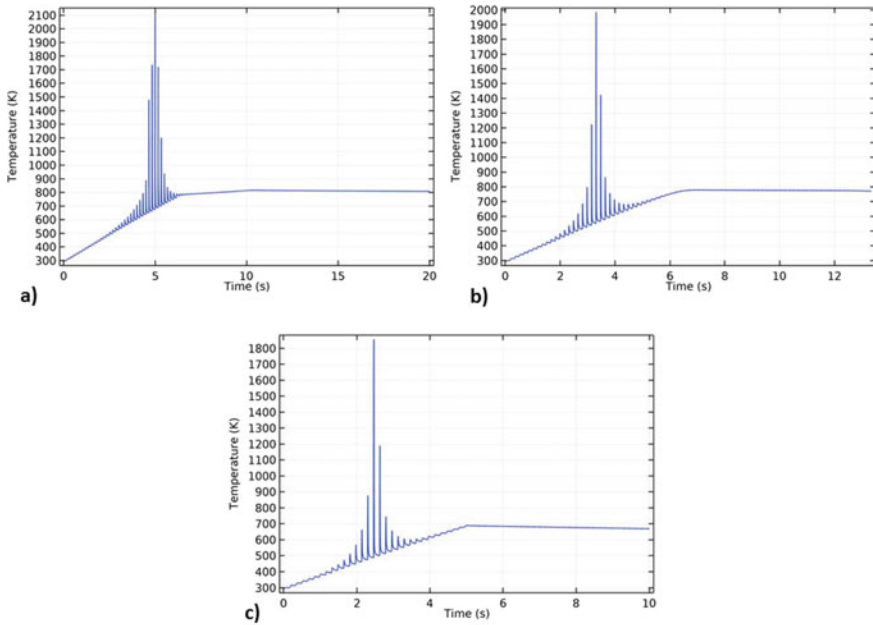


Fig. 3 The temperature versus time graphs at power 4.43 kW

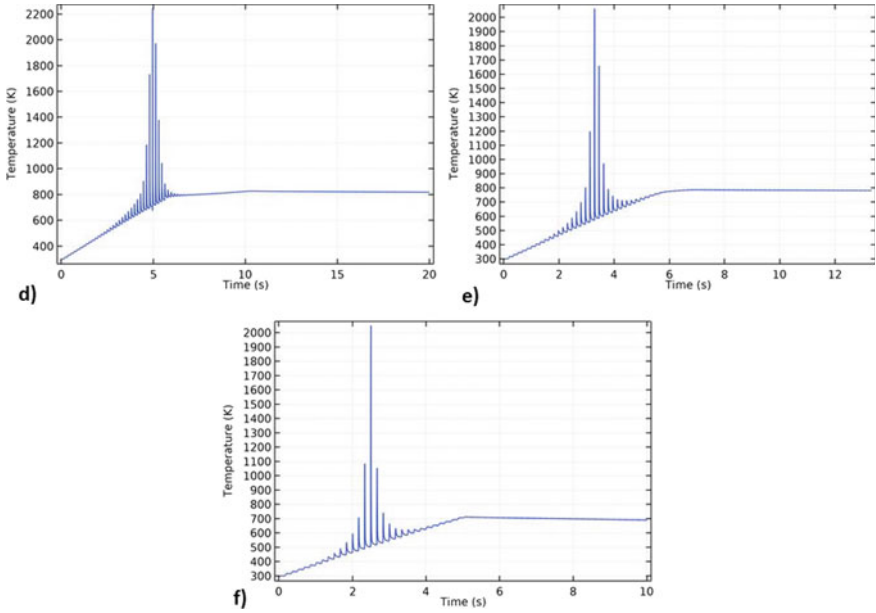


Fig. 4 The temperature versus time graphs at power 4.79 kW

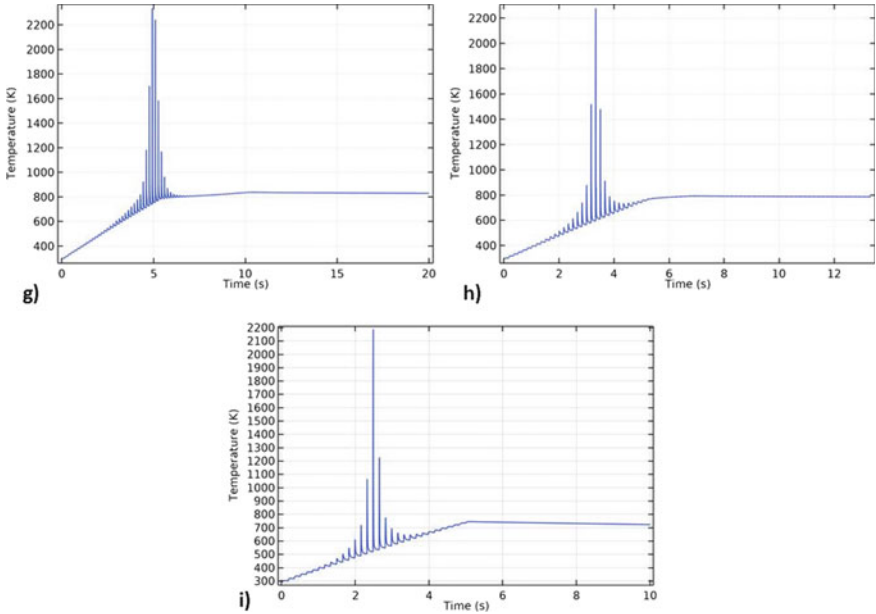


Fig. 5 The temperature versus time graphs at power 5.14 kW

greatest temperature was observed with the slowest scanning speed and frequency (in experiment no. 1 as shown in Fig. 3a). If the scanning speed is slow, the variation time will be longer, and the pulses are overlapped more. As a result, the temperature is greater there. When the laser power is increased, the temperature rises, and as the scanning speed increases, the maximum temperature lowers (Fig. 3a–c).

At 5 ms, the highest temperature was determined to be 2150 K (see Fig. 3a). Because of the increased scanning speed, the highest temperatures in the second and third experiments are 1980 and 1860 K at about 3.2 ms in Fig. 3b and 2.5 ms in Fig. 3c, respectively.

Figure 4d–f show a similar pattern to Fig. 3. The highest temperature is seen in Fig. 4d, which has same power but a lower scanning speed and frequency than Fig. 4e, f. In Fig. 4e, f, the temperature falls as the scanning speed increases. At around 5 ms, the highest temperature was discovered to be roughly 2240 K.

The highest temperatures in the fifth and sixth trials are about 2050 K at 3.15 ms in Fig. 4f and 2030 K at 2.5 ms in Fig. 4f, respectively, due to increased scanning speed.

Figure 5g–i illustrate a pattern similar to Figs. 3 and 4. As compared to Fig. 5h, i, g, which has the same power but a lower scanning speed and frequency, has the greatest temperature. Figure 5h, i demonstrate how the temperature decreases with increasing scanning speed. The maximum temperature was determined to be about 2300 K at around 5 ms (Fig. 5g). Due to the faster scanning speed, the highest temperatures in the eighth and ninth trials are about 2230 K at 3.1 ms in Fig. 5h and approximately 2200 K at 2.4 ms in Fig. 5i respectively.

The greatest temperature is seen in Fig. 5g, which has the highest laser peak power of 5.14 kW, the slowest scanning speed of 1 mm/s, and the highest frequency of 8 Hz.

5 Conclusions

- In this study, laser welding on aluminium alloy is modelled by analysing the effect of input process factors. The laser intensity and scanning speed are determined in the simulation based on machine parameters.
- The simulated result such as weld width and throat length is validated with the experimental result and that shows excellent agreement with the minimum error of 0.94% to maximum error of 9.80% for weld width, and the minimum error of 1.24% to maximum error of 8.17% for throat length.
- When the power is at its peak, the highest temperature was measured with the slowest scanning speed and frequency. The maximum temperature reached 2300 K by the complete experimental setup for laser peak power of 5.14 kW, slowest scanning speed of 1 mm/s, and highest frequency of 8 Hz and with this combination of process parameters weld width and throat length also got maximum.

References

1. Katayama S (ed) (2013) Handbook of laser welding technologies. Elsevier
2. Moraitis GA, Labeas GN (2008) Residual stress and distortion calculation of laser beam welding for aluminum lap joints. *J Mater Process Technol* 198(1–3):260–269
3. Acherjee B, Kuar AS, Mitra S, Misra D (2012) Effect of carbon black on temperature field and weld profile during laser transmission welding of polymers: a FEM study. *Opt Laser Technol* 44(3):514–521
4. Akbari M, Saedodin S, Toghraie D, Shoja-Razavi R, Kowsari F (2014) Experimental and numerical investigation of temperature distribution and melt pool geometry during pulsed laser welding of Ti6Al4V alloy. *Opt Laser Technol* 59:52–59
5. Shanmugam NS, Buvanashakaran G, Sankaranarayanan K, Kumar SR (2010) A transient finite element simulation of the temperature and bead profiles of T-joint laser welds. *Mater Des* 31(9):4528–4542
6. Balasubramanian KR, Shanmugam NS, Buvanashakaran G, Sankaranarayanan K (2008) Numerical and experimental investigation of laser beam welding of AISI 304 stainless steel sheet. *Adv Prod Eng Manag* 3(2):93–105
7. Bachmann M, Avilov V, Gumenyuk A, Rethmeier M (2013) About the influence of a steady magnetic field on weld pool dynamics in partial penetration high power laser beam welding of thick aluminium parts. *Int J Heat Mass Transf* 60:309–321
8. Courtois M, Carin M, LeMasson P, Gaied S, France L (2012) Keyhole formation during spot laser welding: heat and fluid flow modeling in a 2D axisymmetric configuration. In COMSOL Conference, Milan
9. Frewin MR, Scott DA (1999) Finite element model of pulsed laser welding. *Weld J New York* 78:15
10. Morgan SA, Williams SW (2002) Hybrid laser conduction welding. In 55th annual assembly of international institute of welding
11. Paul S, Duggirala A, Mitra S (2020) Study of laser beam welding of AA 2024 using taguchi methodology. In 2020 IEEE India council international subsections conference (INDISCON). IEEE, pp 248–253
12. Marimuthu S, Eghii RM, Pinkerton AJ, Li L (2013) Coupled computational fluid dynamic and Finite element multiphase modeling of laser weld bead formation and joint strength. *J Manuf Sci Eng* 135:011004–1. <https://doi.org/10.1115/1.4023240>

Tool Designing for Friction Stir Welding Variants



Namrata Thakkar and Vishvesh Badheka

Abstract The shoulder and probe are the major components of the rotating tool of Friction Stir Welding (FSW) technology. When it comes to producing a high-quality weld connection, tool design is crucial. The key design elements that substantially impact weldment quality and microstructure are pin length, pin diameter, shoulder diameter, shoulder profile, pin profile and surface features. A friction stir welding tool can be a fixed (conventional tool, conventional bobbin tool, conventional friction stir spot welding tool, pinless tool) or adjustable (floating bobbin tool, adjustable gap/double reacting bobbin tool, refill friction stir spot welding tool) type. Pin profiles such as square, hexagonal, cylindrical, threaded, and tapered affect the grain size and structure, hardness, heat generation and appearance of the weldment. Concave, convex, and flat shoulder profiles affect particle distribution and microstructure. The weld joint quality is determined by the combined effect of the pin and shoulder profile. This paper reviews the effect of various pins and shoulder profiles on friction stir welded joints. Empirical relationship between pin diameter, shoulder diameter and sample thickness as well as most commonly used dimensions for tools have been presented in the paper.

Keywords Friction stir welding (FSW) · Tool design · Bobbin tool · Variants of FSW

1 Introduction

Friction Stir Welding (FSW) has gained popularity as it is an environment-friendly process. FSW is a solid-state welding process performed with the help of a rotating tool. The rotating tool generates frictional heat, that plasticizes the material below its melting point, forming a weldment. It has proven to be a technique capable of welding both thick and thin sheets. The main components of a conventional FSW tool are a shoulder and a pin, whereas a bobbin tool has an additional lower shoulder that

N. Thakkar (✉) · V. Badheka
Pandit Deendayal Energy University, Gandhinagar, Gujarat, India
e-mail: namrata.tmc18@sot.pdpu.ac.in

eliminates the requirement of a backing plate. Friction Stir Spot Welding (FSSW) can be performed using a conventional tool, a pinless tool or a refill tool. The pinless variant of FSW tool consists of only a shoulder whereas the refill tool consists of a pin and a sleeve. Apart from welding parameters like rotational speed of the tool and plunge depth, tool designing plays an important role in producing a joint with higher mechanical properties. Critical design parameters include Pin Length (PL), Pin Diameter (PD), Shoulder Diameter (SD), pin and shoulder profiles and surface features. The designing of conventional tool, bobbin tool and friction stir spot welding tool has been discussed in this paper.

2 Conventional Friction Stir Welding Tool

A conventional tool is a rotating tool consisting of a pin and a shoulder. The role of the pin is to generate frictional heat and mix the softened molten material, whereas the shoulder is responsible for generating frictional heat on the surface of the workpiece and downward forging action that is required to constrain the heated softened material beneath it [1]. Conventional tool has specially designed pin and shoulder to achieve optimum characteristics for a weld. Pin profile, shoulder profile and dimensions of the tool affect the weld quality (Fig. 1).

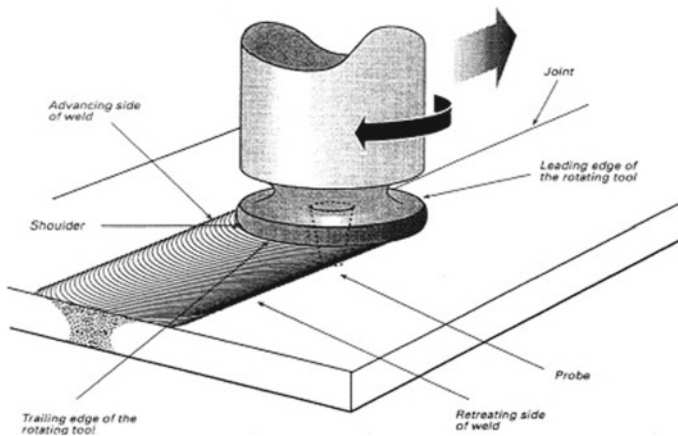


Fig. 1 Conventional friction stir welding process [2]

2.1 Conventional Tool Pin Profiles

The stirring pin profile affects the heat generation, micro-hardness, size of the deformation region, amount of plasticized material that is moved from advancing side to retreating side and the travel speed of the tool. Profiles like cylindrical, cylindrical taper, cylindrical threaded, triangular, square, pentagonal and hexagonal has been experimentally tested to obtain optimum weld quality. Threaded pins generate more heat and are efficient in moving heated material from advancing side to retreating side. Thread feature enhances the plastic material movement and accelerates the flow of plastic material by exerting a downward force [3]. Padmanaban et al. [4] concluded that the joints welded by threaded cylindrical pin are free from defects and exhibit higher tensile strength compared to other pin profiles. Pitch value of the threads determine whether the pin will act as a driller or a stirrer. The pin will act as a driller if the pitch of the threads is very high [2].

Deformation patterns and size of the deformation region depends on the pin profile. Pin profiles like square and hexagon reduce the size of the deformation region [5]. Features like flats on the pin are provided to increase the amount of material carried from advancing side to retreating side. Flat feature also helps in achieving higher temperatures in the weld zone. Pulsating action which is only achieved through providing flat features on the pin, refines the grain structure. Finer grains are obtained with square and hexagonal pin profiles [5–7]. Triangular pin profile has the least area of contact with the molten material which in turn generates least friction compared to square and hexagonal pins. Triangular profile pins sweep least amount of plasticized material due to its lowest static to dynamic volume ratio. Dynamic volume (swept volume) to static volume (pin volume), known as swept ratio quantifies the amount of material plasticized during the process [5, 7]. Less heat generation and amount of material plasticized by a triangular pin may result in lower strength and defects in a weldment. Taper feature provided to the pins help in achieving higher mechanical properties like hardness, elongation and ultimate tensile strength, defect-free joints and finer grain structure [2, 8] (Figs. 2 and 3).

TWI has recently developed the Whorl™ and MX Triflute™ tools. Frustum shaped probes in both the tools displace less material compared to cylindrical tool having the same root diameter. Whorl™ and MX Triflute™ reduce the displaced volume by about 60% and about 70% respectively. Cylindrical probes require more effort to traverse through the plasticized material than a frustum shaped probe for

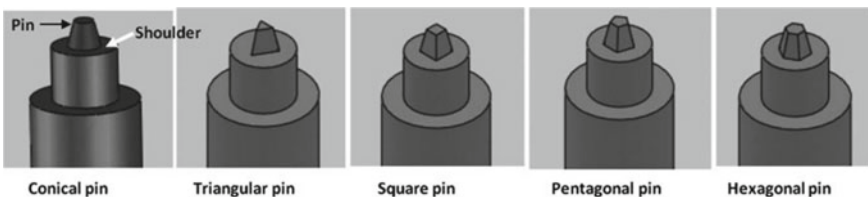
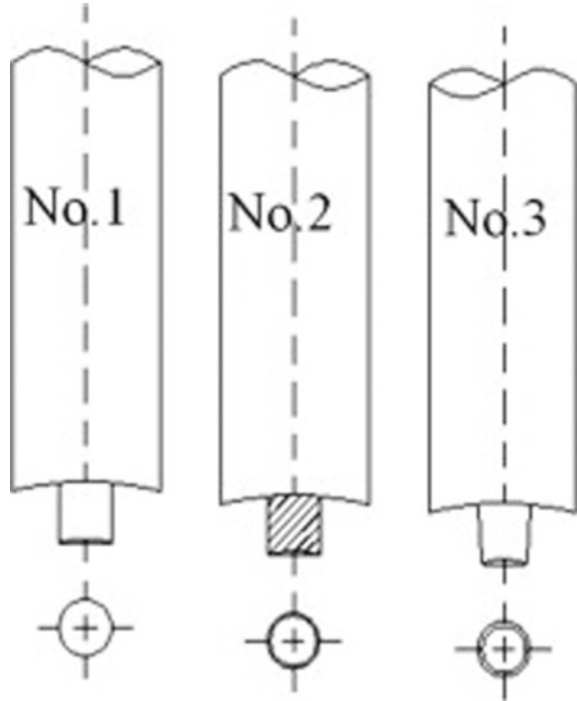


Fig. 2 Pin profiles [5]

Fig. 3 Simple cylindrical, screw threaded cylindrical, taper cylindrical [8]



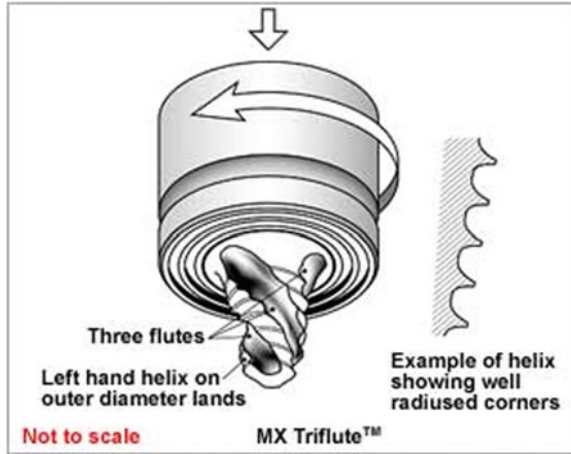
a certain minimum probe tip diameter [9]. Re-entrant feature of the Whorl™ tool, helical ridge is responsible for providing a downward augering force, ensuring that the next ridge faces less interference and to enable a more effective material flow. The ridge having a non-uniform pitch, are placed at a distance greater than the thickness of the ridge itself [9]. These specially designed probes having re-entrant features have an increased surface area compared to featureless probes.

Re-entrant features on a triflute probe can be designed according to the material and joint geometry. They can be designed with any combination of left, neutral or right-handed flutes/ridges grooves. The inclined ridges move the fragmented oxides in an upward or a lower direction by deflecting the plasticized material. In order to reduce the volume of triflute tools, an additional helical feature is provided [9, 10]. These novel designs of the tools have very high swept rates compared to conventional cylindrical probes. The dynamic to static volume ratio for MX Triflute™ probe is 2.6:1, 1.8:1 for Whorl™ probe and 1:1 for a cylindrical probe [9] (Fig. 4).

2.2 Conventional Tool Shoulder Profiles

Flat, concave and convex type shoulder profiles are the most commonly used profiles. A flat shoulder, being the simplest design, does not trap plasticized material during

Fig. 4 Trade-marked MX triflute tool [9]



the process, whereas a concave shoulder is highly used due to its material entrapment characteristic. A concave type shoulder has an inclination of about 6° – 10° compared to a flat shoulder, which entraps the material and directs its flow towards the pin. Convex shaped shoulder has gained popularity due to its ability to maintain a constant contact with the base metal. Though it is considered that the influence of outer shape of shoulder on the weld quality is minimal, the outer surface of the shoulder can have a conical or cylindrical geometry [1, 11]. Galvão et al. [12] conducted experiments using a conical shaped shoulder and concluded that conical shape of the cavity will act as a reservoir for plasticized material and will direct the material flow towards pin (Fig. 5).

Re-entrant features like grooves, concentric circles, scrolls and ridges are often provided at the end surface of the shoulder to entrap the plasticized material and direct the flow towards the pin. These features prevent the molten material flow towards the periphery of the shoulder. The scroll feature is a spiral shaped channel that move the material from the periphery to the centre of the shoulder [1, 9]. A combination of convex shoulder and scroll feature can provide sound welds due to constant contact and entrapment of material throughout the process [1]. Although, a scroll feature is not suitable for the welding of thin sheets as the feature periodically deposits the material at the rear end of the tool and, increases the thickness of the material [12]. A. Scialpi et al. [13], experimentally proved that a combination of fillet and cavity can be used to improve the weld quality. It was also observed that though shoulder geometry has reduced effect on the micro-hardness and nugget grain structure, features like fillet, cavity and scroll improved the quality of weldment.

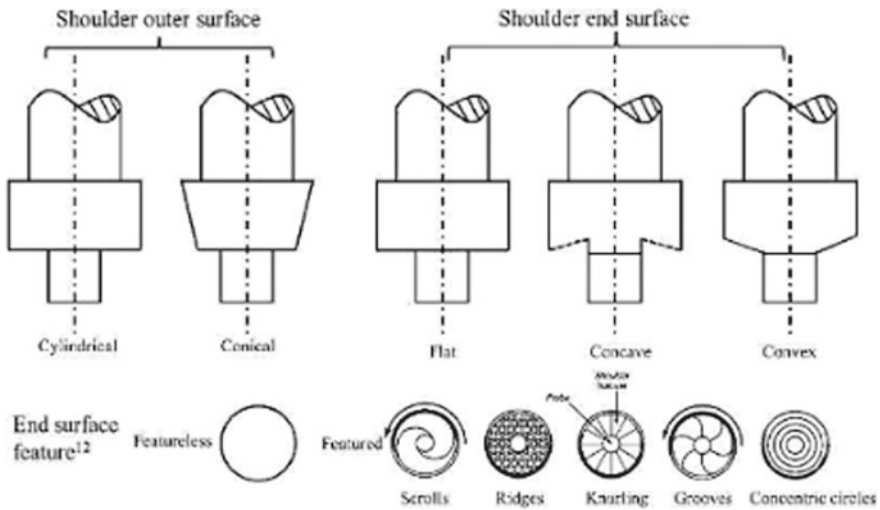


Fig. 5 Primary and secondary shoulder profiles [11]

2.3 Conventional Tool Dimensions

For designing a conventional FSW tool, shoulder and probe diameter are critical design parameters. Zhang et al. [1], deduced empirical relationships for Shoulder Diameter (SD) and Sample Thickness, Probe Diameter (PD) and Sample Thickness and Shoulder Diameter (SD) and Probe Diameter (PD) from the available literature (Fig. 6).

$$SD(\text{mm}) = 2.2 * \text{Sample thickness}(\text{mm}) + 7.3 \text{ mm} \tag{1}$$

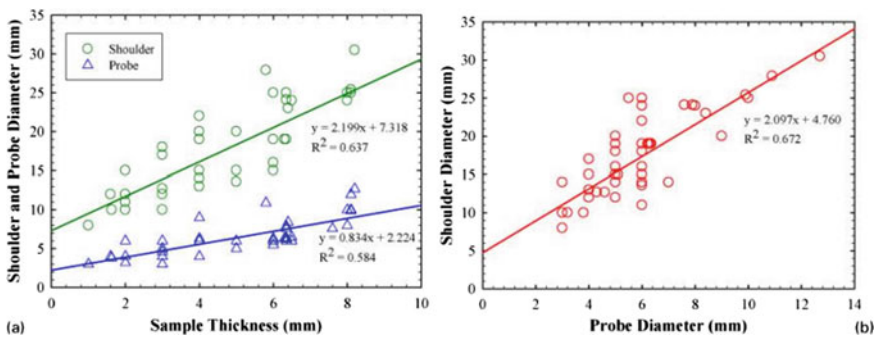


Fig. 6 a Shoulder and probe diameter versus sample thickness and b shoulder diameter versus probe diameter [1]

$$PD(mm) = 0.8 * \text{Sample thickness}(mm) + 2.2 \text{ mm} \tag{2}$$

$$SD(mm) = 2.1 * PD(mm) + 4.8 \text{ mm} \tag{3}$$

3 Bobbin Tool Friction Stir Welding

Self-reacting friction stir welding, also known as bobbin tool friction stir welding has a specially designed tool having two shoulders and a pin. During the process, both shoulders generate frictional heat. The reactive forces generated during the process, are cancelled out by the two shoulders resulting in a very low axial force [14, 15]. During a bobbin tool friction stir welding process, no backing plate is required, as the lower shoulder supports the base metal. Fixed gap bobbin tool, floating bobbin tool, adaptive or double driven bobbin tool and pinless bobbin tool are major variants of this technique. The gap between the shoulders remains constant throughout the process for a fixed gap bobbin tool. The movement of fixed gap tool about z-axis is restrained [14]. A floating bobbin tool, is designed as a fixed gap bobbin tool and is allowed to float in the axial direction. The novel design of floating bobbin tool adjusts its position according to the base metal in such a way that the axial force reduces drastically [16] (Fig. 7).

An adaptive tool or a double driven bobbin tool, is driven from both the ends, providing an enhanced flow path. Double driven tool is capable of altering the distance between both the shoulders during the process, and is allowed to oscillate in the axial (z-axis) direction. In a double driven tool, the aspect ratio of the probe can be altered [14, 17].

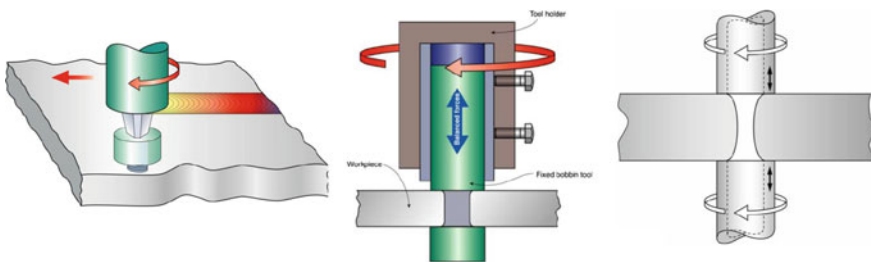


Fig. 7 Fixed gap bobbin tool, floating bobbin tool, adaptive bobbin tool [16, 17]

3.1 Bobbin Tool Pin Profiles

Bobbin Tool Friction Stir Welding (BT-FSW) process has been employed with various pin profiles like cylindrical taper, trigonal, hexagonal, outward conical and inward conical. Out of all these pin profiles, cylindrical tapered pin with flats is a commonly used profile [18]. Mohammad Hosein Mirzaei et al. [19] conducted double shoulder friction stir welding using trigonal, square, hexagonal, inward conical and outward conical pins and concluded that the heat generated by un-edged pins is more than edged pin profiles. Trigonal and outward conical pins result into joints having lower mechanical properties whereas hexagonal and square pin profiles yielded joints having superior mechanical properties like ultimate tensile strength (UTS) and elongation. As the number of edges increase from square to hexagonal profile, the material boxes moved by the pins decrease in size but increase in number. Such a material movement enhances the material coalescence, improving the joint properties [19]. Pin profiles like outward conical and trigonal should be avoided as a trigonal profile results into undesired flow of material and an outward conical profile pin reduces the mechanical properties by excessive heating [19] (Fig. 8).

Re-entrant features like flats, threads, grooves and flutes can be added to the tool pin to enhance the horizontal and vertical movement of plasticized material. Thread feature is responsible for the vertical movement of the molten material and flat feature enhances the horizontal movement [14]. While designing the tool pin, grooves shall be carefully added as they trap the material between them and resist the vertical flow. Excessive heat is generated for the materials trapped between grooves as a groove feature has a tendency to only generate heat and not axial flow [19]. A pin having three to four flat features and having threads will generate a sound weld having high mechanical properties due to combined horizontal and vertical material flow [14, 19, 20]. Wu et al. [21], designed and experimented a novel adjustable-gap bobbin tool on Al-Cu aluminium alloy. The adjustable-gap tool pin, having half-right and half-left feature enhanced material mixing in the vertical direction of the weldment. Specially designed half-right hand and half-left hand thread filled the voids by converging material flow towards the centre (Fig. 9).

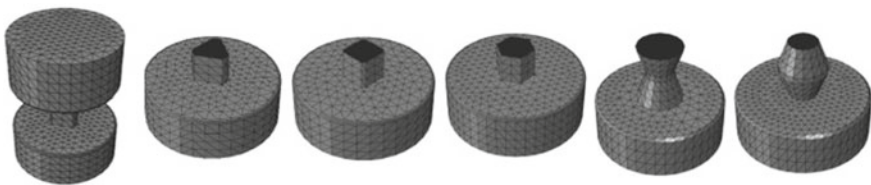
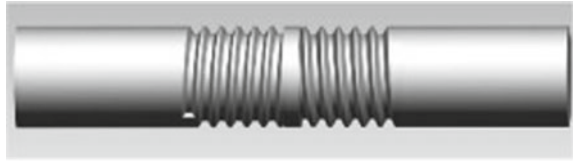


Fig. 8 Various pin profiles of a bobbin tool [19]

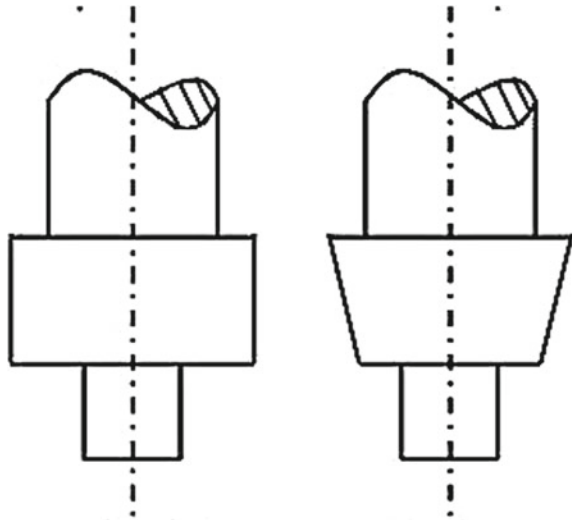
Fig. 9 Novel adjustable-gap bobbin tool pin having right and left-handed threads [21]



3.2 Bobbin Tool Shoulder Profiles

Similar to a conventional friction stir welding tool, the primary features of bobbin tool shoulder include flat, concave and convex [18]. A flat shoulder, in spite of being the simplest design, does not trap plasticized material and produces flash. Concave profile of a shoulder entraps the molten material and feeds it to the pin by acting as a reservoir. A convex shoulder acts in a unique way by remaining in a constant contact with base metal plate of varying thickness [1, 15, 18]. The outer shape of the shoulder can be cylindrical or tapered. Tapered shoulders have successfully welded flash-less joints [16]. Scroll feature is the most used secondary feature on the shoulder as it promotes the flow of plasticized material in a horizontal direction towards pin. Okamoto et al. [20] deduced that scroll feature will enhance the vertical flow and dispersion of oxide film when provided on convex shoulder instead of a flat shoulder (Fig. 10).

Fig. 10 Cylindrical and tapered shape of shoulders [11]



3.3 Bobbin Tool Dimension and Size

Pin Diameter (PD), Pin Length (PL), Upper Shoulder Diameter (USD), Lower Shoulder Diameter (LSD) and gap between upper and lower shoulder are critical parameters while tool designing. The upper and lower shoulder are generally taken to be of equal diameters [15, 20, 22–33], but it is recommended that the lower shoulder should have a smaller diameter than upper shoulder. Lesser diameter of lower shoulder results into less bending moment and torque on the pin, as well as less generation of frictional heat on the lower surface due to less contact with the plate [34–36]. The lower shoulder will provide insufficient support to the plate from the vibration if a very small value of diameter is chosen. Also, a reduced area of contact may result into premature solidification of weld zone.

Shoulder gap being an important design parameter, enhances material stirring and vertical flow. An optimum compression effect and frictional heat is produced if the shoulder gap is determined [18]. The pinching gap of the shoulders generate dragging force for the material to flow around. An optimal combination of pinching gap at the centre and periphery are required to produce sound welds [20]. In the literature available, no definite method has been suggested for the selection of shoulder and pinching gap and have been designed using a trial and error. Pin length usually kept the same as base metal thickness, can also be taken as 0.9 times the thickness of the base metal [14]. Figure provided below summarizes experiments conducted with bobbin tool and empirical relations have been obtained using least square approximation method [15, 20, 22–33, 37–40] (Fig. 11).

$$USD(mm) = 1.87 * PT(mm) + 9 \text{ mm} \tag{4}$$

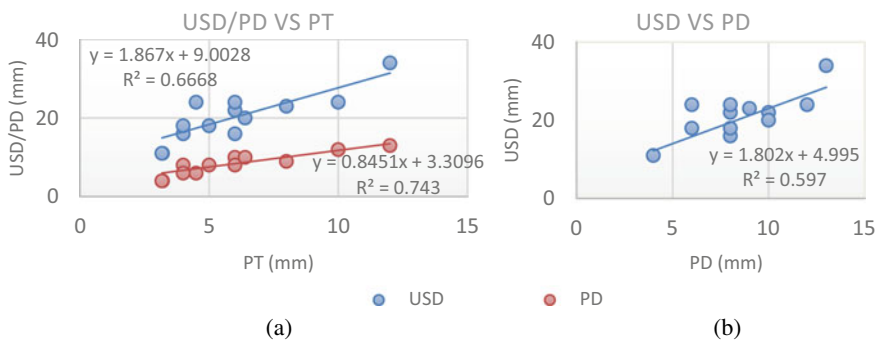


Fig. 11 **a** Upper shoulder diameter/pin diameter versus plate thickness, **b** upper shoulder diameter versus pin diameter

$$PD(mm) = 0.85 * PT(mm) + 3.31 \text{ mm} \tag{5}$$

$$USD(mm) = 1.8 * PD(mm) + 5 \text{ mm} \tag{6}$$

4 Friction Stir Spot Welding (FSSW)

A friction stir spot welding involves the rotation, plunging and retraction of the tool. The rotational speed of the tool and its plunge depth are predetermined. A conventional FSSW tool has a shoulder-pin setup, where the length of the pin is fixed. A conventional tool has a tendency to move the material in a downward direction, away from the tool shoulder. As the tool pin has a fixed length, a plate having a constant thickness can be welded. The tool is responsible for heating the base metal, inducing material flow, confine the plasticized material and prevent it from overflowing [41]. The drawback of a conventional FSSW tool is that, it can cause thinning of the top sheet due to excessive tool penetration [42]. Due to the presence of pin, a keyhole defect at the end of welding process is observed (Fig. 12).

A pinless tool, as the name suggests, is a tool only having a shoulder. The pinless tool performs welding process by rotation, plunging and retraction from the base material. This tool eliminates the occurrence of keyhole defect at the end of the welding process [43]. Features like scroll and flutes can be provided to enhance the quality of the weld (Fig. 13).

A refill FSSW tool comprises of a sleeve, pin and a clamp. The clamp is responsible for holding the sheets together whereas the sleeve and pin are responsible for spot welding the sheets. Pin plunge and sleeve plunge are the two variants of this process. For a sleeve plunge method, once the clamp has held the sheets together tightly, the sleeve plunges into the sheets till a predetermined depth and simultaneously the pin moves upwards. Once the predetermined depth has been achieved, the sleeve retracts to its original position and the pin moves towards the sheets. In this process, the hole

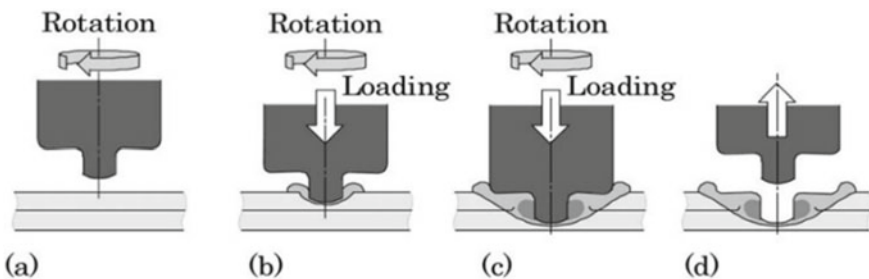


Fig. 12 a Rotation of tool, b plunging of tool, c dwell period, d drawing out of tool [41]

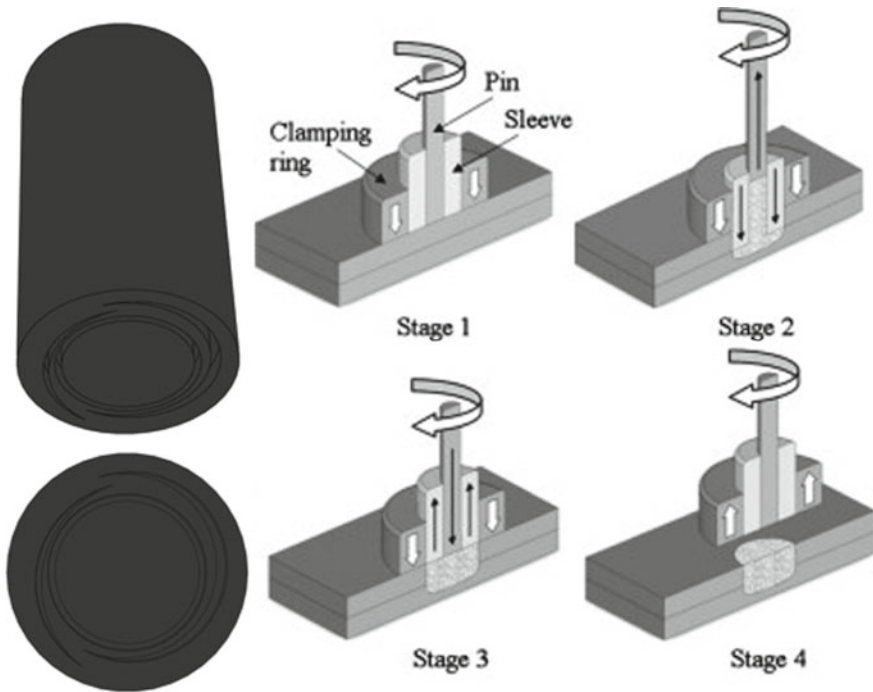


Fig. 13 Pinless FSSW tool with scroll feature, sleeve plunge variant of FSSW [41]

is completely filled with the molten material, eliminating the keyhole defect. For a pin plunge method, the pin is responsible for the penetration in the sheets, whereas the sleeve retracts. A sleeve plunged joint has a larger welded area compared to a pin plunged joint [44].

4.1 Pin Profiles

Pin profiles like triangular, square, hexagonal, spherical, inverse-tapered and other off-centre have been employed for friction stir spot welding process [45–49]. A high forging force is exerted by a cylindrical pin, but is a commonly used pin profile in a conventional FSSW process [48, 49]. It has been experimentally proven that a tapered pin forms a smaller hook compared to a conventional cylindrical pin [49]. A triangular pin generated more heat compared to a cylindrical pin due to the presence of flat features. Joints having higher mechanical strength and larger bonding area formed using triangular pins. In spite of a triangular pin having above mentioned advantages, it is recommended that, it should not be used to weld steels, as the sharp flat features will worn away after being used for some time [41, 48, 49, 50]. For an

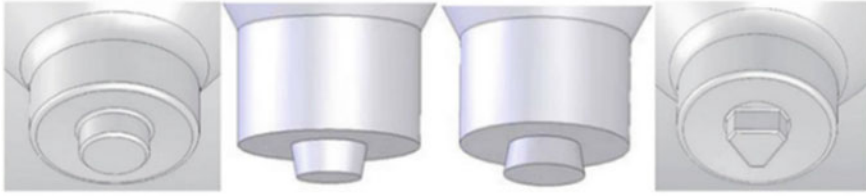


Fig. 14 FSSW tool pin profiles—cylindrical, tapered, inverse tapered, triangular [41]

inverse tapered pin, a hook feature will be extended up to the top surface, resulting a joint has low mechanical properties [45] (Fig. 14).

Secondary features such as threads, flutes and flats increase the area of contact and increase the heat generation. Such features have given improved results for lightweight materials, but for materials like steel, these features get worn out after a few spot welds. Hence, it is recommended that complex secondary features shall not be provided for materials like steel [41, 51]. Although, features like stepped-spiral and coarse thread can be provided on polycrystalline cubic boron nitride (PBCN) tools [52, 53]. A cylindrical pin is the most used pin profile for refill FSW as it is designed to move in axial direction [41].

4.2 Shoulder Profiles

The primary shoulder profiles in a conventional FSSW are the same as conventional FSW and Bobbin Tool FSW. The primary profiles include flat, concave and convex [48, 54]. A concave shoulder, the most commonly used profile produces a weld sound by the formation of a sharp hook. Concave shoulder, which acts as a reservoir for the plasticized material results into a weld joint having higher mechanical properties compared to a flat or convex shaped shoulders [45, 48, 54]. The joint properties exhibited by a convex shoulder is inferior to those exhibited by a flat shoulder, making the flat shoulder an intermediary choice. A convex shoulder welds a joint having lowest mechanical properties due to thinning of the top sheet and insufficient mixing of molten material [48, 49]. Like conventional FSW tool and bobbin tool, secondary features like scroll and concentric circles can be provided at the end surface of concave and convex shoulders (Fig. 15).

Re-entrant features like long and short wiper flutes, scroll flutes and proud wiper are the most important features for a pinless tool to produce a joint of good quality. Welds exhibit higher mechanical properties with use of re-entrant features, due to an enhanced flow of molten material and deeper penetration of the plastic zone [55]. Uematsu et al. [56] experimentally obtained joints having higher tensile-shear strength using a scroll grooved tool compared to a conventional tool having concave shoulder and a probe (Fig. 16).



Fig. 15 Concave, flat and convex shoulder profiles [41]

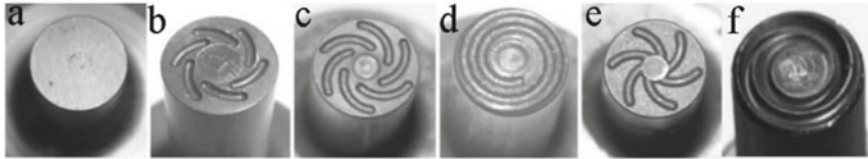


Fig. 16 Re-entrant features for pinless tool [41]

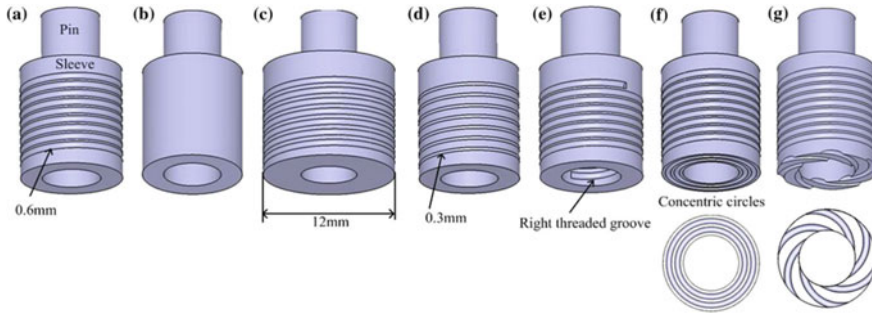


Fig. 17 Secondary features of a refill FSSW sleeve [58]

Shude Ji et al. [57] studied sleeve features like grooves on the wall and concentric circles and grooves at the bottom surface of the sleeve. It was observed that, groove width is negatively proportional to flow velocity. Provision of threaded grooves on sleeve walls alters the behavior of material flow. Experiments proved that scrolled grooves on the bottom surface of sleeve are more efficient than concentric circles (Fig. 17).

4.3 Tool Dimensions

Shoulder Diameter (SD), Pin Diameter (PD), Pin Length (PL) and angle of concave shoulder are critical design parameters that need to be determined in a correct way to obtain a sound weld. Heat generation depends on the pin and shoulder diameter.

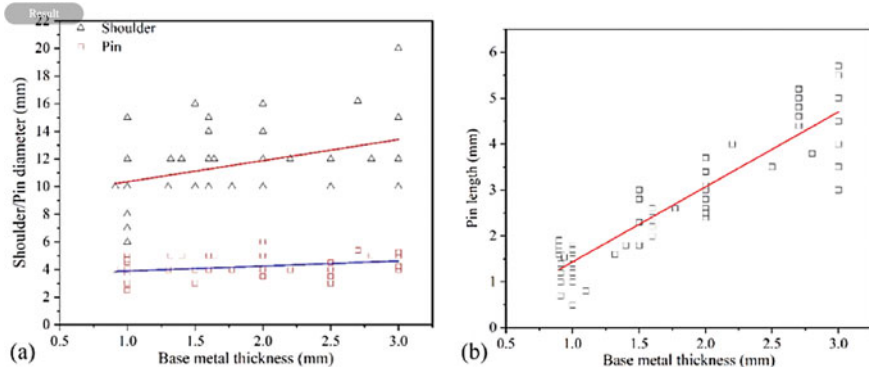


Fig. 18 a Shoulder and pin diameter versus base metal thickness b pin length versus base metal thickness [41]

Larger diameters result into more frictional heat [1, 58]. Pins having larger diameters have proven to bond larger area, but produces excessive flash [45, 59]. Design of concave shoulder for a conventional FSSW tool must not have an extreme angle. Extreme angles for a concave shoulder result into insufficient axial force, decreasing the weld quality (mechanical strength) of the joint [58]. Zhikang Shen et al. [41] graphically represented the linear increase of pin length with the plate thickness. It was also observed that the shoulder diameter linearly increased with the plate thickness. For a conventional FSSW tool, a pin diameter of 4 mm can be employed, irrespective of the plate thickness [5]. The pin length for thin workpiece has less importance and the tool can be considered to be pinless [42]. From the available literature for pinless tool, it can be observed that a shoulder diameter of 10 mm is the most used diameter [42, 43, 56, 60, 61] (Fig. 18).

External and internal sleeve diameter, pin diameter and groove width on sleeve are important dimensions for designing a refill friction stir welding tool. The outer diameter and groove width influence the material flow velocity whereas threaded grooves on the inner wall affect the bonding ligament thickness [57]. From the literature available, it can be deduced that, a diameter of 9 mm for sleeve and 5–6.4 mm for a pin diameter is commonly employed in a refill friction stir spot welding process [41].

5 Conclusion

In this paper, pin profiles, shoulder profiles and tool dimensions for conventional tool, bobbin tool and friction stir spot welding tools were reviewed.

For a conventional tool, pin profiles like cylindrical, cylindrical tapered, triangular, square, pentagonal and hexagonal have been used for friction stir welding. Similarly, pin profiles like cylindrical, trigonal, hexagonal, inward and outward conical have

been used for bobbin tool friction stir welding. In a refill friction stir spot welding tool, cylindrical and triangular pin profiles result into joints having superior mechanical properties. Secondary features like flats, flutes, threads and grooves can be provided to increase the contact area between plate and pin, increase heat generation and to acquire joints with superior qualities. Although, for friction stir spot welding of steels it is recommended that complex secondary features shall not be provided as it decreases the tool life.

Flat, concave and convex profiles are common to conventional, bobbin and friction stir spot welding tools. Re-entrant features like scroll, concentric circles and grooves can be provided on the bottom surface of shoulder to improve the weld quality.

Empirical relationship between Pin Diameter (PD), Shoulder Diameter (SD) and sample thickness have been mentioned for a conventional tool. Similarly, empirical relationship between Upper Shoulder Diameter (USD), Pin Diameter (PD) and Plate thickness (PT) have been established using least square approximation method. From the available literature, it has been concluded that a pin with 4 mm diameter can be used for conventional spot welding process irrespective of the plate thickness. For refill spot welding tool, a sleeve diameter of 9 mm and a pin diameter of 5–6.4 mm can be used. For a pinless spot welding tool, a shoulder diameter of 10 mm can be used to obtain defect-free joints.

Acknowledgements Special thanks go to Pandit Deendayal Energy University (PDEU), Mechanical Engineering Department. Also, special thanks to IIW-PDEU Students Chapter for extending registration fee support.

References

1. Zhang YN, Cao X, Larose S, Wanjara P (2012) Review of tools for friction stir welding and processing. *Can Metall Q* 51(3):250–261. <https://doi.org/10.1179/1879139512y.0000000015>
2. Boz M, Kurt A (2004) The influence of stirrer geometry on bonding and mechanical properties in friction stir welding process. *Mater Des* 25(4):343–347. <https://doi.org/10.1016/j.matdes.2003.11.005>
3. Zhao YH, Lin SB, Wu L, Qu FX (2005) The influence of pin geometry on bonding and mechanical properties in friction stir weld 2014 Al alloy. *Mater Lett* 59(23):2948–2952. <https://doi.org/10.1016/j.matlet.2005.04.048>
4. Padmanaban G, Balasubramanian V (2009) Selection of FSW tool pin profile, shoulder diameter and material for joining AZ31B magnesium alloy – An experimental approach. *Mater Des* 30(7):2647–2656. <https://doi.org/10.1016/j.matdes.2008.10.021>
5. Ramanjaneyulu K, Madhusudhan Reddy G, Venugopal Rao A, Markandeya R (2013) Structure-property correlation of AA2014 friction stir welds: role of tool pin profile. *J Mater Eng Perform* 22(8):2224–2240. <https://doi.org/10.1007/s11665-013-0512-4>
6. Sharma N, Siddiquee AN, Khan ZA, Mohammed MT (2017) Material stirring during FSW of Al–Cu: Effect of pin profile. *Mater Manuf Process* 33(7):786–794. <https://doi.org/10.1080/10426914.2017.1388526>
7. Kumar A, Raju LS (2012) Influence of tool pin profiles on friction stir welding of copper. *Mater Manuf Process* 27(12):1414–1418. <https://doi.org/10.1080/10426914.2012.689455>

8. Motalleb-nejad P, Saeid T, Heidarzadeh A, Darzi K, Ashjari M (2014) Effect of tool pin profile on microstructure and mechanical properties of friction stir welded AZ31B magnesium alloy. *Mater Des* 59:221–226. <https://doi.org/10.1016/j.matdes.2014.02.068>
9. Friction stir welding—tool developments (February 2001) (2001b) TWI. <https://www.twi-global.com/technical-knowledge/published-papers/friction-stir-welding-tool-developments-february-2001>
10. Thomas W, Johnson K, Wiesner C (2003) Friction stir welding—recent developments in tool and process technologies. *Adv Eng Mater* 5(7):485–490. <https://doi.org/10.1002/adem.200300355>
11. Mishra A, Tiwari A, Shukla M, Rose R (2018) Analysis of tools used in friction stir welding process. *Int J Curr Eng Technol* 8. <https://doi.org/10.14741/ijcet/v.8.6.2>
12. Galvão I, Leal RM, Loureiro A, Rodrigues DM (2010) Material flow in heterogeneous friction stir welding of aluminium and copper thin sheets. *Sci Technol Weld Joining* 15(8):654–660. <https://doi.org/10.1179/136217110x12785889550109>
13. Scialpi A, de Filippis L, Cavaliere P (2007) Influence of shoulder geometry on microstructure and mechanical properties of friction stir welded 6082 aluminium alloy. *Mater Des* 28(4):1124–1129. <https://doi.org/10.1016/j.matdes.2006.01.031>
14. Fuse K, Badheka V (2018) Bobbin tool friction stir welding: a review. *Sci Technol Weld Joining* 24(4):277–304. <https://doi.org/10.1080/13621718.2018.1553655>
15. Longhurst WR, Cox CD, Gibson BT, Cook GE, Strauss AM, Wilbur IC, Osborne BE (2016) Development of friction stir welding technologies for in-space manufacturing. *Int J Adv Manuf Technol* 90(1–4):81–91. <https://doi.org/10.1007/s00170-016-9362-1>
16. Martin J, Wei S (2015) Friction Stir Welding Technology for Marine Applications. *Friction Stir Welding and Processing VIII*, 217–226. <https://doi.org/10.1002/9781119093343.ch24>
17. Thomas WM, Norris IM, Staines DG, Clarke PJ, Horrex NL (2007) Friction stir welding—variants and process techniques. In *The first international conference 'joining of aluminium structures'*, Moscow, Russian
18. Sued M, Pons D, Lavroff J, Wong E (2014) Design features for bobbin friction stir welding tools: Development of a conceptual model linking the underlying physics to the production process. *Mater Des* 1980–2015(54):632–643. <https://doi.org/10.1016/j.matdes.2013.08.057>
19. Mirzaei M, Asadi P, Fazli A (2020) Effect of tool pin profile on material flow in double shoulder friction stir welding of az91 magnesium alloy. *Int J Mech Sci* 183:105775. <https://doi.org/10.1016/j.ijmecsci.2020.105775>
20. Okamoto K, Sato A, Park SHC, Hirano S (2012) Microstructure and mechanical properties of FSWed aluminum extrusion with bobbin tools. *Mater Sci Forum* 706–709:990–995. <https://doi.org/10.4028/www.scientific.net/msf.706-709.990>
21. Wu D, Li W, Gao Y, Yang J, Su Y, Wen Q, Vairis A (2020) Effect of an improved pin design on weld formability and mechanical properties of adjustable-gap bobbin-tool friction stir welded Al-Cu aluminum alloy joints. *J Manuf Process* 58:1182–1188. <https://doi.org/10.1016/j.jma pro.2020.09.015>
22. Wang F, Li W, Shen J, Hu S, dos Santos J (2015) Effect of tool rotational speed on the microstructure and mechanical properties of bobbin tool friction stir welding of Al–Li alloy. *Mater Des* 86:933–940. <https://doi.org/10.1016/j.matdes.2015.07.096>
23. Zhao Y, Wang C, Dong C (2018) Microstructural characteristics and mechanical properties of water cooling bobbin-tool friction stir welded 6063–T6 aluminum alloy. *MATEC Web Conf* 206:03002. <https://doi.org/10.1051/mateconf/201820603002>
24. Xu W, Luo Y, Fu M (2018) Microstructure evolution in the conventional single side and bobbin tool friction stir welding of thick rolled 7085–T7452 aluminum alloy. *Mater Charact* 138:48–55. <https://doi.org/10.1016/j.matchar.2018.01.051>
25. Zhang H, Wang M, Zhang X, Yang G (2015) Microstructural characteristics and mechanical properties of bobbin tool friction stir welded 2A14–T6 aluminum alloy. *Mater Des* 1980–2015(65):559–566
26. Yang C, Ni D, Xue P, Xiao B, Wang W, Wang K, Ma Z (2018) A comparative research on bobbin tool and conventional friction stir welding of Al–Mg–Si alloy plates. *Mater Charact* 145:20–28

27. Fuse K, Badheka V (2020) Hybrid self-reacting friction stir welding of AA 6061–T6 aluminium alloy with cooling assisted approach. *Metals* 11(1):16. <https://doi.org/10.3390/met11010016>
28. Li G, Zhou L, Luo S, Dong F, Guo N (2020) Quality improvement of bobbin tool friction stir welds in Mg–Zn–Zr alloy by adjusting tool geometry. *J Mater Process Technol* 282:116685. <https://doi.org/10.1016/j.jmatprotec.2020.116685>
29. Zhao S, Bi Q, Wang Y, Shi J (2016) Empirical modeling for the effects of welding factors on tensile properties of bobbin tool friction stir-welded 2219–T87 aluminum alloy. *Int J Adv Manuf Technol* 90(1–4):1105–1118. <https://doi.org/10.1007/s00170-016-9450-2>
30. Esmaily M, Mortazavi N, Osikowicz W, Hindsefelt H, Svensson J, Halvarsson M, Martin J, Johansson L (2016) Bobbin and conventional friction stir welding of thick extruded AA6005–T6 profiles. *Mater Des* 108:114–125. <https://doi.org/10.1016/j.matdes.2016.06.089>
31. Singh P, Biswas P, Kore SD (2018) Finite element method and experimental study of self-reacting friction stir welding of aluminium alloy A6061–T6. *Lecture Notes on Multidisciplinary Industrial Engineering*, 79–102. https://doi.org/10.1007/978-981-10-8518-5_3
32. Chen S, Li H, Lu S, Ni R, Dong J (2015) Temperature measurement and control of bobbin tool friction stir welding. *Int J Adv Manuf Technol* 86(1–4):337–346. <https://doi.org/10.1007/s00170-015-8116-9>
33. Sued MK, Pons D, Lavroff J (2014) Compression ratio effects in bobbin friction stir welding. In *Proceedings of the 10th international friction stir welding symposium*, Beijing, China, pp 292–310
34. Thomas WM, Wiesner CS, Marks DJ, Staines DG (2009) Conventional and bobbin friction stir welding of 12% chromium alloy steel using composite refractory tool materials. *Sci Technol Weld Joining* 14(3):247–253. <https://doi.org/10.1179/136217109x415893>
35. Wan L, Huang Y, Wang Y, Lv S, Feng J (2014) Friction stir welding of aluminium hollow extrusion: weld formation and mechanical properties. *Mater Sci Technol* 31(12):1433–1442. <https://doi.org/10.1179/1743284714y.0000000721>
36. Huang YX, Wan L, Lv SX, Feng JC (2013) Novel design of tool for joining hollow extrusion by friction stir welding. *Sci Technol Weld Joining* 18(3):239–246. <https://doi.org/10.1179/1362171812y.0000000096>
37. Węglowska A (2018) The use of a bobbin tool in the friction stir welding of plates made of aluminium alloy EN AW 6082–T6. *Biuletyn Instytutu Spawalnictwa* 5:35–43. <https://doi.org/10.17729/ebis.2018.4/4>
38. Hou JC, Liu HJ, Zhao YQ (2014) Influences of rotation speed on microstructures and mechanical properties of 6061–T6 aluminum alloy joints fabricated by self-reacting friction stir welding tool. *Int J Adv Manuf Technol* 73(5–8):1073–1079. <https://doi.org/10.1007/s00170-014-5857-9>
39. Sahu PK, Vasudevan NP, Das B, Pal S (2019) Assessment of self-reacting bobbin tool friction stir welding for joining AZ31 magnesium alloy at inert gas environment. *J Magnes Alloys* 7(4):661–671. <https://doi.org/10.1016/j.jma.2019.05.011>
40. Zhou L, Li GH, Zha GD, Shu FY, Liu HJ, Feng JC (2018) Effect of rotation speed on microstructure and mechanical properties of bobbin tool friction stir welded AZ61 magnesium alloy. *Sci Technol Weld Joining* 23(7):596–605. <https://doi.org/10.1080/13621718.2018.1432098>
41. Shen Z, Ding Y, Gerlich AP (2019) Advances in friction stir spot welding. *Crit Rev Solid State Mater Sci* 45(6):457–534. [https://doi.org/10.1080/10408436.2019.1671799\(sameasref5inshoulderdimensioning\)](https://doi.org/10.1080/10408436.2019.1671799(sameasref5inshoulderdimensioning))
42. Bakavos D, Prangnell PB (2009) Effect of reduced or zero pin length and anvil insulation on friction stir spot welding thin gauge 6111 automotive sheet. *Sci Technol Weld Joining* 14(5):443–456. [https://doi.org/10.1179/136217109x427494\(sameasref6inshoulderdim\)](https://doi.org/10.1179/136217109x427494(sameasref6inshoulderdim))
43. Tozaki Y, Uematsu Y, Tokaji K (2010) A newly developed tool without probe for friction stir spot welding and its performance. *J Mater Process Technol* 210(6–7):844–851. <https://doi.org/10.1016/j.jmatprotec.2010.01.015>
44. Tier M, Rosendo T, dos Santos J, Huber N, Mazzaferro J, Mazzaferro C, Strohaecker T (2013) The influence of refill FSSW parameters on the microstructure and shear strength of 5042 aluminium welds. *J Mater Process Technol* 213(6):997–1005. <https://doi.org/10.1016/j.jmatprotec.2012.12.009>

45. Badarinarayan H, Yang Q, Hunt F (2008) Effect of pin geometry on static strength of friction stir spot welds. SAE Technical Paper Series. Published. <https://doi.org/10.4271/2008-01-0147>
46. Bilici MK, Yüklér AR (2012) Influence of tool geometry and process parameters on macrostructure and static strength in friction stir spot welded polyethylene sheets. *Mater Des* 33:145–152. <https://doi.org/10.1016/j.matdes.2011.06.059>
47. Ohishi K, Sakamura M, Ota K, Fujii H (2015) Novel dissimilar spot welding of aluminium alloy and steel sheets by friction stirring. *Weld Int* 30(2):91–97. <https://doi.org/10.1080/09507116.2014.921088>
48. Badarinarayan H, Shi Y, Li X, Okamoto K (2009) Effect of tool geometry on hook formation and static strength of friction stir spot welded aluminum 5754-O sheets. *Int J Mach Tools Manuf* 49(11):814–823. <https://doi.org/10.1016/j.ijmactools.2009.06.001>
49. Hirasawa S, Badarinarayan H, Okamoto K, Tomimura T, Kawanami T (2010) Analysis of effect of tool geometry on plastic flow during friction stir spot welding using particle method. *J Mater Process Technol* 210(11):1455–1463. <https://doi.org/10.1016/j.jmatprotec.2010.04.003>
50. Retracted: “Effect of Pin and Shoulder Geometry on Stir Zone and Mechanical Properties of Friction Stir Spot-Welded Aluminum Alloy 2024-T3 Sheets” (2015) *J Eng Mater Technol* 137(3). <https://doi.org/10.1115/1.4030197>
51. Santella M, Hovanski Y, Frederick A, Grant G, Dahl M (2010) Friction stir spot welding of DP780 carbon steel. *Sci Technol Weld Joining* 15(4):271–278. <https://doi.org/10.1179/136217109x12518083193630>
52. Miles MP, Ridges CS, Hovanski Y, Peterson J, Santella ML, Steel R (2011) Impact of tool wear on joint strength in friction stir spot welding of DP 980 steel. *Sci Technol Weld Joining* 16(7):642–647. <https://doi.org/10.1179/1362171811y.0000000047>
53. Hartman T, Miles M, Hong ST, Steel R, Kelly S (2015) Effect of PCBN tool grade on joint strength and tool life in friction stir spot welded DP 980 steel. *Wear* 328–329:531–536. <https://doi.org/10.1016/j.wear.2015.03.001>
54. Lin P, Pan J, Pan T (2008) Failure modes and fatigue life estimations of spot friction welds in lap-shear specimens of aluminum 6111-T4 sheets. Part 2: Welds made by a flat tool. *Int J Fatigue* 30(1):90–105. <https://doi.org/10.1016/j.ijfatigue.2007.02.017>
55. Bakavos D, Chen Y, About L, Prangnell P (2010) Material interactions in a novel pinless tool approach to friction stir spot welding thin aluminum sheet. *Metall Mater Trans A* 42(5):1266–1282. <https://doi.org/10.1007/s11661-010-0514-x>
56. Uematsu Y, Kakiuchi T, Tozaki Y, Kojin H (2012) Comparative study of fatigue behaviour in dissimilar Al alloy/steel and Mg alloy/steel friction stir spot welds fabricated by scroll grooved tool without probe. *Sci Technol Weld Joining* 17(5):348–356. <https://doi.org/10.1179/1362171812y.0000000014>
57. Ji S, Wang Y, Li Z, Yue Y, Chai P (2016) Effect of tool geometry on material flow behavior of refill friction stir spot welding. *Trans Indian Inst Met* 70(6):1417–1430. <https://doi.org/10.1007/s12666-016-0937-1>
58. Lacki P, Kucharczyk Z, ŚLiwa R, Gałaczyński T (2013) Effect of tool shape on temperature field in friction stir spot welding. *Arch Metall Mater* 58(2):595–599. <https://doi.org/10.2478/amm-2013-0043>
59. Shen J, Wang D, Liu K (2012) Effects of pin diameter on microstructures and mechanical properties of friction stir spot welded AZ31B magnesium alloy joints. *Sci Technol Weld Joining* 17(5):357–363. <https://doi.org/10.1179/136217112x13333824902125>
60. Xu L, Wang L, Chen YC, Robson JD, Prangnell PB (2015) Effect of interfacial reaction on the mechanical performance of steel to aluminum dissimilar ultrasonic spot welds. *Metall Mater Trans A* 47(1):334–346. <https://doi.org/10.1007/s11661-015-3179-7>
61. Reilly A, Shercliff H, Chen Y, Prangnell P (2015) Modelling and visualisation of material flow in friction stir spot welding. *J Mater Process Technol* 225:473–484. <https://doi.org/10.1016/j.jmatprotec.2015.06.021>

Microstructural and Mechanical Properties Characterization of Resistance Spot Welded Aluminum Alloy AA6063



Parth Patel, Chaitanya Sharma, Mukesh Chandra, Anil K. Rajak, and Sumit K. Sharma

Abstract Resistance welding is key to obtain light weight stronger structures and components for automotive and aerospace industry. Influence of heat input on microstructure and microhardness of resistance spot welded aluminum alloy AA6063 was investigated in depth in this research. Welding was carried out using different heat inputs of 10.59 J (high) and 6.62 J (low) respectively which was obtained by varying process parameters. Effect of heat input on weld zone surface roughness, weld morphology, microstructure, phase evaluation, and hardness were investigated in depth. Finally, complete microstructure-properties-process parameters correlation was carried out to create defect free resistance spot welds of aluminum alloy AA6063 with superior properties.

Keywords Resistance spot welding · Aluminum alloy · Heat input · Microstructure · Hardness · Defects

1 Introduction

Automobile industry is currently facing the challenge to reduce weight of automobile without compromising with strength and passenger safety, which is the major challenge currently [1]. The automobile industry is now developing lightweight, stronger, and energy-efficient automobiles to suit the competing goals of environmental rules and consumer demands for increased performance, luxury, and safety features. This has forced the automotive manufacturers to replace steel and other bulky materials with aluminum in body construction (the body accounts for 20–30%

P. Patel · A. K. Rajak · S. K. Sharma (✉)

Department of Metallurgical Engineering, BIT Sindri, Sindri, Jharkhand 828123, India
e-mail: sumit.met@bitsindri.ac.in

C. Sharma

Department of Mechanical Engineering, BIT Sindri, Sindri, Jharkhand 828123, India

M. Chandra

Department of Production Engineering, BIT Sindri, Sindri, Jharkhand 828123, India

of the overall vehicle weight) [2–4]. That's why, use of non-iron bearing light materials like aluminum, magnesium, polymers, rubber, and others alloys is increasing day by day to reduce overall weight of vehicle. Materials with mechanical properties equivalent to or greater than steel are ideal choice for use in place of steel [5]. Aluminum alloys are stronger, lighter, easy to process (i.e., forging, machining etc.) and possess excellent corrosion resistant than steel [6–8] hence their use has increased more than by 80% in recent years [9].

Joining is essential to fabricate body structure, parts or components for automotive and industrial application by combining two or more parts of similar and dissimilar composition. A variety of techniques, including, mechanical fastening, self-pierce riveting, resistance spot welding (RSW), friction stir spot welding, are available to join metal pieces [10, 11]. Selection of suitable welding technique is of prime importance as it influences weld properties, performance, and overall cost [12]. In RSW, prepared pieces are placed between electrodes (copper or tungsten) and applied axial force holds them together. The resistance to flow of current through the pieces being welded generates heat, melts them locally and creates a spot joint. Weld time, weld current, and power delivered during the process all influence heat generation. RSW is the most prevalent sheet metal joining technology, particularly in the automobile sector, due to its low cost, flexibility, high productivity, ease of automation, maintenance, and lack of specialist personnel requirements. The procedure is also frequently used in other sheet product manufacturing industries, such as transportation and culinary utensil manufacturing [10, 13–15]. Due to the high coefficient of thermal expansion of aluminum alloy, small melting point, and high thermal and electrical conductivity, RSW of aluminum alloy is not as straightforward as welding of steel. Despite these characteristics, the aluminum surface contains an oxide layer with a high melting temperature and high electrical resistance, which improved the specimens' contact resistance with the electrode. As a result, it claims that there is a weld defects in the resistance spot welded aluminum alloy [16–18]. Owing to small melting temperature of aluminum alloy, good combination of process parameters viz. electrode force, weld time, welding current, etc. is necessary. However, resistance spot welded aluminum shows the presence of several weld defects such as cracks, expulsion, porosity, etc. due to poor combination of process parameter for resistance spot welding. Hence, these welding defects greatly affect the weld surface and electrode life of resistance spot welding setup [8, 18–21]. The use of innovative techniques such as friction stir welding can eliminate defects occurring in aluminum welding and produces welds with superior microstructure, mechanical, fatigue, and corrosion properties [22–27]. Moreover, this technique is capable of producing dissimilar weld of good quality in different combination with ease [28, 29].

The goal of this research is to see how welding parameters like welding current, welding time, and electrode force (in terms of high and low heat input) will affect fabrication of defect free welds and morphology, microstructure, phase evolution, and microhardness of resistance spot welds of medium-strength AA6063 alloy.

AA6063 alloy is easy to work with, resistant to corrosion, and works admirably hence most prevalent extrusion alloy which is widely used for window sills, shocks,

door frames, scales, sign frames, roof, and store installation [30]. Therefore, present work aims to study the influence of optimization of welding parameters such as welding current condition, welding time, and electrode force (in terms of high and low heat input) to fabricate defects free welds and on morphology, microstructure, phase evolution and microhardness of resistance spot welded medium-strength AA6063 alloy. Moreover, a correlation between mechanical properties and microstructure of resistance spot welds of aluminum 6063 alloy was developed.

2 Experimental Methods

RSW of 1.6 mm thick sheets of aluminum alloy AA6063 was performed in lap configuration in this work. The composition of the alloys is as follows Si 0.51%, Fe 0.35%, Mn 0.01%, Cu 0.02%, Mg 0.67%, Zn 0.03%, Cr 0.02%, Ti 0.02%, Al Balance. Prior to RSW natural oxide layer was removed by abrading the surface with silicon carbide paper of grade P220 to get the desired results. Many pilot experiments were performed on pieces of size 250 mm × 25 mm, arranged in lap configuration with an overlap distance of 25 mm, to identify range of suitable parameters for RSW. Finally, RSW was performed successfully using process parameters listed in Table 1. All experiments used the identical squeeze time and forge times. Chromium copper electrode of end diameter of 7 mm, strength of 310 N/mm² and electrical conductivity of 0.4633 m/X mm² was utilized for RSW. Throat depth and nominal throat clearance was 220 mm. Highest short circuit current available was 8 kA (Fig. 1; Table 2).

All welds were cut from the middle of the nugget, vertical to the specimen’s longitudinal axis, using Wire EDM Machine. For microstructure analysis, specimens were polished using sandpapers, of grade 400, 600, 1000, 1200, and 1500. Finally, cloth polishing followed by diamond polishing was done to get a mirror finish surface. Specimens were cleaned with ethanol between each polishing steps. Keller’s etching agent (comprising hydrochloric acid, nitric acid, and hydrofluoric acid) was used for revealing the microstructural features. The cross section of each specimen is subjected to microstructural inspection, surface roughness assessment, and hardness testing. An optical microscope (Olympus BX51) and scanning electric microscope (Zeiss SMT AG, Germany) was used to conduct the microstructural examination. Surface roughness was measured in longitudinal direction on the top i.e., crown surface of each of the fabricated weld in as welded condition. Phases in

Table 1 Constant parameters for resistance spot welding of AA6063 alloy

S. No.	Parameters	Value
1	Squeeze time	5 cycles
2	Hold time	4 cycles
3	Current frequency	50 Hz
4	Sheet thickness	1.6 mm
5	Electrode diameter	7 mm

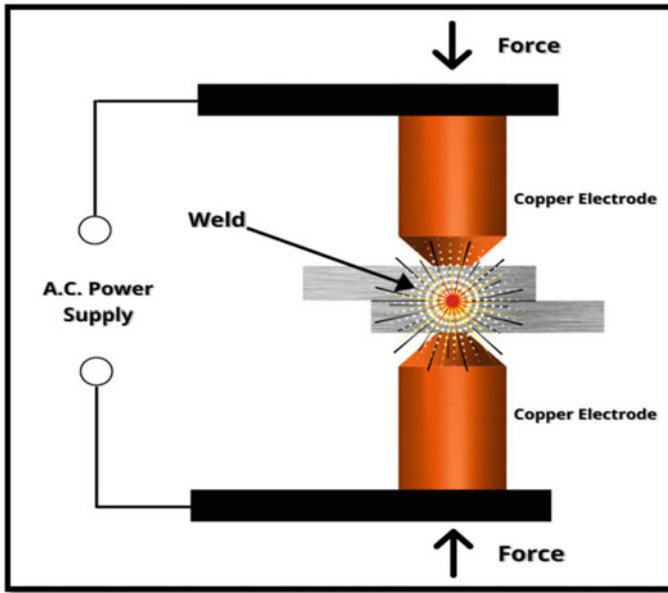


Fig. 1 Representation block diagram of resistance spot welding setup

Table 2 Variable process parameter for RSW of AA6063 alloy

Specimen ID	Welding time (cycle)	Welding current (kA)	Electrode force (kg/cm ³)	Heat (J)	No of spot
BM	Aluminum alloy AA 6063 (As received)				
LHW	5	9	8	6.62	3
HHW	9	8	10	10.59	3

welds were scrutinized by X-ray diffraction (Bruker AXS, Germany) analysis, while microhardness was obtained by Vicker’s microhardness tester (UHL-VHMT, Leica).

3 Results and Discussion

3.1 Weld Surface Morphology

Process parameters govern the heat input to welds during RSW hence is believed to change the morphology, microstructure, and mechanical properties of fabricated welds of AA6063. Variation of roughness of weld crown surface in as welded condition, measured across different weld region is shown in Fig. 2.

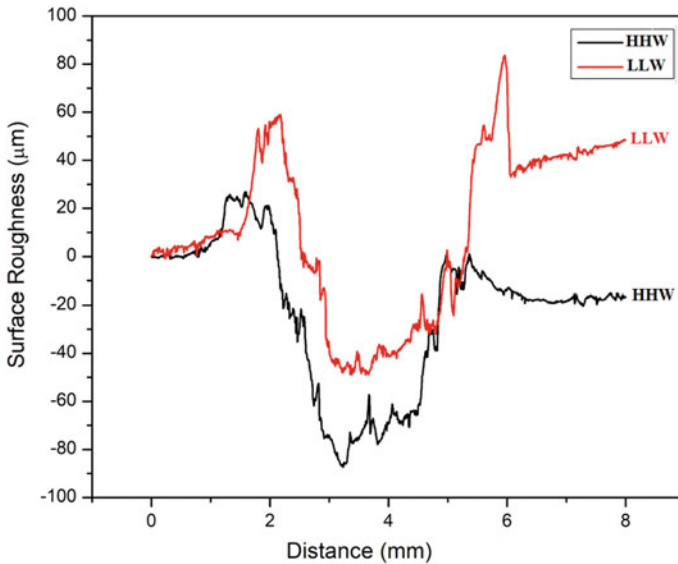


Fig. 2 Influence of heat input on weld surface roughness of RSW welds of AA6063 fabricated using high heat input (HHW) 10.59 J, and low heat input (LHW) 6.62 J

Trend of variation of surface roughness with increase in distance was identical up to first 5 mm beyond which gradual increment was observed after abrupt rise and fall up to 6 mm for low heat input welds while other welds exhibited relatively flat roughness after initial decrease between 5 and 7 mm. The roughness peaks can be associated to the edges of weld nugget which are raised than other region due to weld spattering. Average surface roughness was $24.4 \mu\text{m}$ and $29.7 \mu\text{m}$ for high heat input (HHW) and low heat input (LHW) welds, respectively and more or less same. Surface roughness is found to vary inversely with heat input to weld i.e., higher the heat input better (lower) the surface roughness.

3.2 Weld Defects

Resistance welding of aluminum alloys is challenging due to formation of defects owing to higher thermal conductivity and tendency of oxide formation. Figure 3 shows the several microstructural defects such as expulsion, porosity, cracks, etc. observed in welds of resistance spot welded aluminum alloy AA6063.

Microstructural weld defects are common in resistance spot welded aluminum alloys and occur at the point of contact between the electrode and the workpiece and interface of the workpiece surfaces. Expulsion defect occurred mainly owing to short time period and high welding current. The electrode force is another significant factor

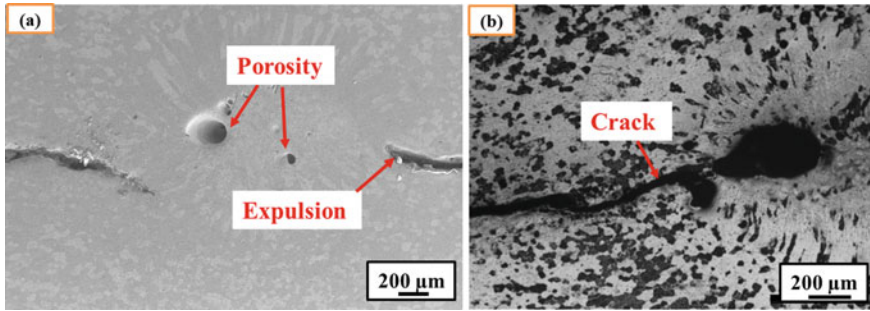


Fig. 3 Defects in resistance spot welds of AA6063 alloy

in causing expulsion [19]. Porosity in resistance spot welds is due to surface contamination, solidification shrinkages, and pre-existing holes in base metal. Porosity was also noticed in welds fabricated using low electrode force. Fraction of defects in RSW welds was found to decrease with increase in electrode force [31]. The defects such as weld cracks or liquation cracking, developed owing to large coefficient of thermal expansion and high solidification shrinkage of aluminum alloy [21]. In RSW, weld nugget size and area are so small and pressure is also applied therefore there is no possibility of large weld pool shrinkage to appear despite the presence of some tiny shrink spots.

3.3 Microstructure

Optical micrograph shown in Fig. 4 shows the microstructure of aluminum alloy AA6063 in as received condition, contains the aluminum matrix with the randomly dispersed tiny and large sized precipitates, aligned along the grain boundaries and within the grains. Different phases were detected along the grain boundary of the

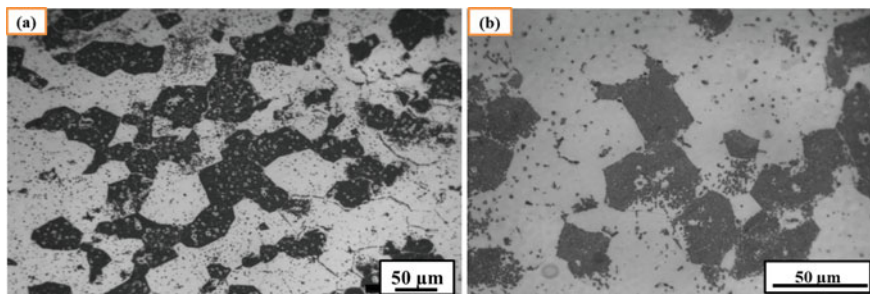


Fig. 4 Microstructure of aluminum alloy AA6063 in as received condition

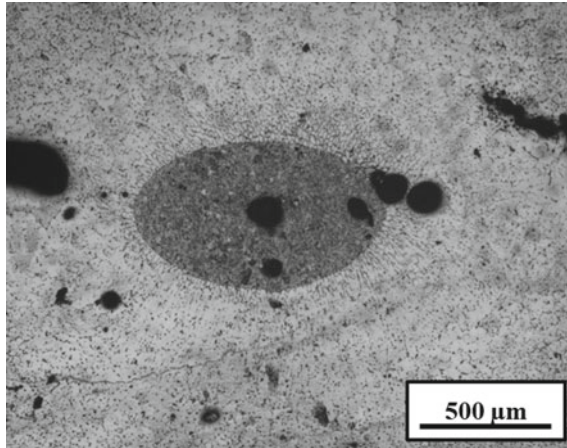


Fig. 5 Microstructure of resistance spot welds of AA6063 alloy fabricated by using high heat input (HHW) 10.59 J

aluminum matrix in the microstructure of aluminum 6063 alloy, and they can be readily seen in the dark shade of the microstructure.

Figure 5 shows microstructure evolution in weld region or spot area of resistance spot welds of AA6063 alloy fabricated using high (10.59 J) heat input. Well defined elliptical nugget is surrounded by heat affected zone, comprising coarsened grain. During the resistance spot welding the materials melt locally and hence results in spot feature as evident by dark appearance after etching. The density of spot features i.e., darkness decreased gradually outwards from the welding line. This can be attributed to variation in contact resistance hence in heat input to welds. Much higher contact resistance at sheet's interface beneath electrode tips results in the generation and dissipation of a highly concentrated heat than that in other areas of the sample. The intensive heating is responsible for 'spot features' exhibiting darkness or high density near welding line than sheet's surface.

Figure 6 shows the transition of microstructure from weld nugget to heat affected zone of (a) high heat input (10.59 J) and (b) low heat input welds (6.62 J), respectively.

Figure 6 demonstrates a columnar structure surrounding weld nugget with a segregation zone at the faying surface in the welded zone. Columnar structure of welded zone becomes significantly coarser in case of low heat input resistance spot welds of AA6063 than high heat input welds. Moreover, equiaxed grain formation in the weld nugget is also evident more prominently for low (6.62 J) heat input welds (Fig. 6a) than other welds. Extent of grain coarsening was severe in case of low heat input welds which had smaller temperature gradient so welds cool at a slower rate. Thus, greater post weld static grain growth and grain coarsening.

Grain growth during the cooling of welds of aluminum alloy has been restricted by alloying elements such as silicon and magnesium. Figure 7 shows scanning electron micrographs of high heat inputs (10.59 J) resistance spot welds. AlMg, AlFe, etc.

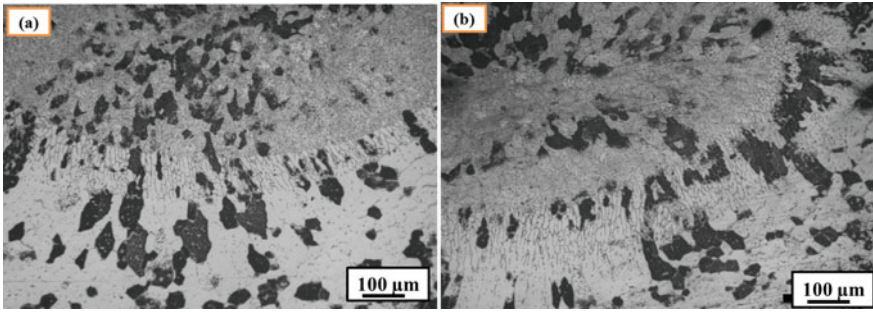


Fig. 6 Optical micrograph showing evolution of microstructure in nugget and surrounding region of resistance spot welds fabricated by using **a** high heat input 10.59 J, and **b** low heat input 6.62 J

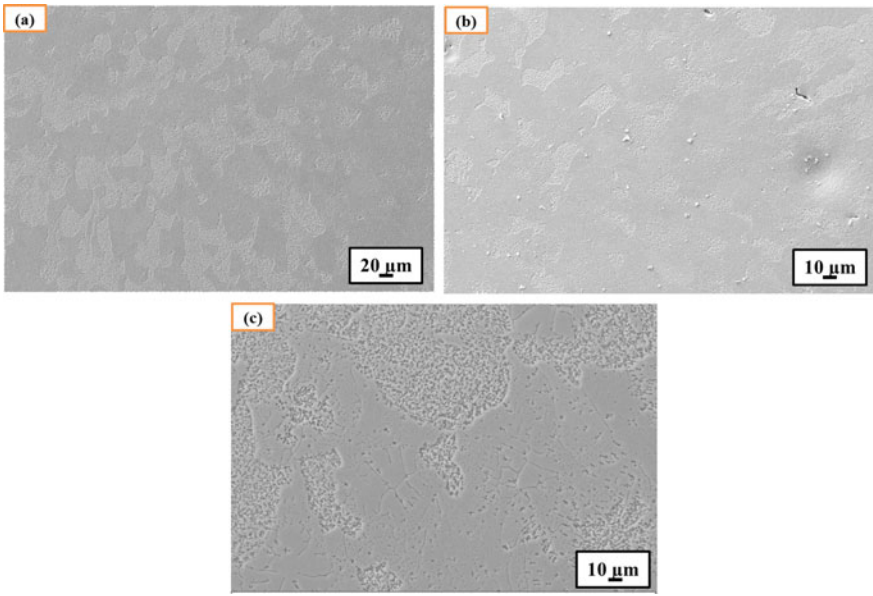


Fig. 7 Scanning electron micrographs of resistance spot welds of AA6063 fabricated using high heat input 10.59 J **(a)** equiaxed grain structure, **(b)** precipitates and void/porosity, and **(c)** high magnification micrographs showing different phases

precipitates (whitish particles) were present in welds as revealed and confirmed by scanning electron micrographs (Fig. 6b). Further, welding heat input was found to vary the fraction of precipitates along the grain boundaries.

3.4 Phase Analysis

Identification of phases present in aluminum alloy AA6063 in as received and after RSW was accomplished by x-ray diffraction and is shown in Fig. 8. Peak position in terms of 2θ value did not change much, however peak intensity changed with welding heat input and shows the existence of Al, AlFe, and AlMg, compounds. During welding, high heating followed by quick cooling has a complex thermal, metallurgical, and mechanical effects on the welded component, causing substantial stresses and strains. Remelting of old structure and re-precipitation of solutes is believed to cause lattice strain which in turn make initial matrix lattice strain free.

Lattice strain were calculated from the ‘Scherrer formula’ and are enlisted in Table 3. Both the welds showed lattice strain higher than as welded base metal. Further, lattice strain, decreased with increase in heat input. Lattice strain was 0.139 and 0.135% for high heat input (HHW) and low heat input (LHW) welds, respectively.

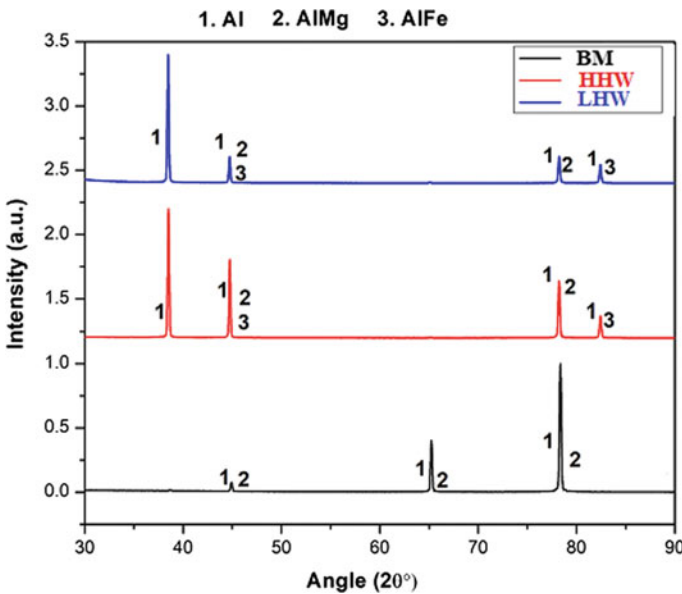


Fig. 8 X-ray diffraction of aluminum alloy AA6063 in as received and welded condition

Table 3 Lattice strain in aluminum 6063 alloy in as received and after resistance spot welding

Sample ID	Lattice strain (%)
Base metal (BM)	0.182
High heat input (HHW) welds	0.139
Low heat input (LHW) welds	0.135

Table 4 Variation of microhardness with heat input in resistance spot welds of AA6063 alloy

Sample ID	Heat input (Jules)	Nugget enter (HRB)	Nugget edge (HRB)	Base metal (HRB)
High heat input (HHW) welds	10.59	56	57	55
Low heat input (LHW) welds	6.62	59	58	55

3.5 Hardness Evaluation

The process parameters change the heat input which in turn influenced the weld hardness as evident from Table 4. Both the welds exhibited higher hardness in nugget edge and center region than unwelded base metal. Heat input had significant influence on hardness and with increase in heat input both nugget edge and center hardness were found to decrease however, difference in hardness values was insignificant. No specific trend was observed between heat input and nugget edge and center hardness. Low heat input welds exhibited highest nugget center hardness of 59 HRB and nugget edge hardness of 58 HRB respectively. The improvement in weld hardness may be attributed to re-precipitation of fine β phase strengthening precipitates after welding [32]

4 Conclusions

Defects free resistance spot welds were fabricated using optimized parameters i.e., high and low heat inputs. Following conclusion on the influence of variation of heat input on microstructure, morphology, phases, and mechanical properties of resistance spot welds can be drawn as follows:

1. Surface roughness of fabricated resistance spot welds lowered marginally when welding heat input was decreased from 10.59 to 6.62 J during RSW of AA6063.
2. Microstructural defects (such as expulsion, porosity, cracks, and so on) analysis of resistance spot welds was also performed considering numerous parameters, and process parameters were optimized to build defect-free resistance spot welds.
3. Microstructure of aluminum alloy AA6063 was found defect free for as received and both high and low heat input conditions during resistance spot welding. Different precipitates viz. AlFe, AlMg, and others were found along grain boundaries, resulting in the restrictions of grain growth in weld regions. Further, minor reduction in lattice strain was observed for fabricated welds than as received aluminum alloy AA6063 as confirmed by X-Ray diffraction analysis.
4. Percentage of precipitates varied with welding parameters i.e., heat input, resulting in changing weld strength/hardness and lattice strain. With higher

percentage of precipitates weld ductility decreases. Lattice strain was also found to decrease marginally with heat input. Both the welds exhibited hardness higher than base metal. Weld center hardness increased from 56 to 59 HRB with decrease in heat input.

References

1. Carle D, Blount G (1999) The suitability of aluminium as an alternative material for car bodies. *Mater Des* 20(5):267–272
2. Patrick E, Sharp M (1992) Joining aluminum auto body structure. SAE technical paper, 920282
3. Wan Z, Wang HP, Wang M et al (2016) Numerical simulation of resistance spot welding of Al to zinc-coated steel with improved representation of contact interactions. *Int J Heat Mass Transf* 101:749–763
4. Chantasri S, Poonnyom P, Kaewwicht J et al (2015) Effect of resistance spot welding parameters on AA1100 aluminum alloy and SGACD zinc coated lap joint properties. *Int J Adv Cult Technol* 3:153–160
5. Kawalla R, Lehmann G, Ullmann M et al (2008) Magnesium semi-finished products for vehicle construction. *Arch Civ Mech Eng* 8:93–101
6. Tisza M, Lukács Z, Kovács P et al (2017) Some recent developments in sheet metal forming for production of lightweight automotive parts. *J Phys Conf Ser* 896
7. Taban E, Gould JE, Lippold JC (2010) Characterization of 6061–T6 aluminum alloy to AISI 1018 steel interfaces during joining and thermo-mechanical conditioning. *Mater Sci Eng A* 527:1704–1708
8. Florea RS, Solanki KN, Bammann DJ et al (2012) Resistance spot welding of 6061–T6 aluminum: failure loads and deformation. *Mater Des* 34:624–630
9. Fentahun MA, Savas MA (2018) Materials used in automotive manufacture and material selection using ashby charts. *Int J Mater Eng (Internet)* 8:40–54
10. Sharma C, Tripathi A, Upadhyay V et al (2021) Friction stir spot welding-process and weld properties: review. *J Inst Eng India Ser D* 102:549–565. <https://doi.org/10.1007/s40033-021-00276-z>
11. Jaiswal S, Verma V, Sharma C (2021) Dissimilar friction stir spot welding of AA2014 and AA7075 aluminum alloys. In: Muzammil M, Chandra A, Kankar PK, Kumar H (eds) *Recent advances in mechanical engineering*. Lecture notes in mechanical engineering. Springer, Singapore, pp 567–573
12. Sharma C, Upadhyay V, Tripathi A (2015) Effect of welding processes on tensile behaviour of aluminium alloy joints. *Int J Mech Mechatron* 9(12):2051–2054
13. Brown DJ, Newton CJ, Boomer D (1995) Optimization and validation of a model to predict the spot weldability parameter lobes for aluminum automotive body sheet. *Adv Technol Process*, 100–106
14. Cho Y, Li W, Hu SJ (2006) Design of experiment analysis and weld lobe estimation for aluminum resistance spot welding. *AWS Weld J* 85:45–51
15. Spinella DJ, Brockenbrough JR, Fridy JM (2005) Trends in aluminum resistance spot welding for the auto industry. *AWS Weld J* 84:34–41
16. Boomer DR, Hunter JA, Castle DR (2003) A new approach for robust high-productivity resistance spot welding of aluminum. SAE Technical Paper -01-0575
17. Kim DC, Park HJ, Hwang IS, Kang MJRSW (2009) of aluminum alloy sheet 5J32 using SCR type and inverter type power supplies. *Int Sci J* 38:55–60
18. Mathers G (2002) *The welding of aluminum and its alloys*. Woodhead, Cambridge, 9781855737631

19. Senkara J, Zhang H, Hu SJ (2004) Expulsion prediction in resistance spot welding. *Weld J* (Miami, Fla) 83
20. Zhang H, Senkara J (2012) *Resistance welding—fundamentals and applications*, 2nd edn. Taylor & Francis Group, LLC, Boca Raton
21. Senkara J, Zhang H (2000) Cracking in spot welding aluminum alloy AA5754. *Weld J* (Miami, Fla) 79
22. Sharma C, Dwivedi DK, Kumar P (2012) Friction stir welding of Al-Zn-Mg alloy AA7039. In: Suarez CE (ed) *Light metals, aluminium alloys: fabrication, characterization and applications*, pp 503–507
23. Sharma C, Upadhyay V, Verma V, Tripathi A, Sharma SK (2021) Tensile behavior of friction stir welded joints of different aluminum alloys. *J Eng Res* 10 (Special Issue). <https://doi.org/10.36909/jer.ICCEMME.15693>
24. Sharma C, Dwivedi DK, Kumar P (2014) Investigating the microstructure and mechanical properties of friction stir weld joints of solution hardening aluminium alloy AA5086. *Indian Weld J* 47(4):65–74
25. Sharma C, Dwivedi DK, Kumar P (2014) Fatigue behaviour of friction stir weld joints of Al-Zn-Mg alloy AA7039 developed using base metal in different temper condition. *Mater Des* 64(12):334–344
26. Sharma C, Upadhyay V (2019) Investigating the effect of friction stir welding on microstructure and corrosion behaviour of Al-Zn-Mg Alloy. *Mater Sci Forum* 969:517–523
27. Sharma C, Upadhyay V (2021) Microstructure and mechanical behaviour of similar and dissimilar AA2024 and AA7039 friction stir welds. *Eng Rev* 41(1):21–33
28. Kumar R, Upadhyay V, Sharma C (2022) Microstructure and mechanical properties of dissimilar friction stir welds of AA2014 and AA7075. In: *Proceedings of Institution of Mechanical Engineers part E. J Process Mech Eng* 236(3):1083–1095. <https://doi.org/10.1177/09544089211058113>
29. Sharma C, Tripathi A, Verma V, Upadhyay V (2022) Material flow behaviour in dissimilar friction stir welds of AA2024 and AA5086 aluminium alloys. *J Eng Res* (Special Issue): 153–159
30. Pradeep S, Sharma SK, Pancholi V (2012) Microstructural and mechanical characterization of friction stir processed 5086 aluminum alloy. *Mater Sci Forum* 710:253–257
31. Kang J, McDermid JR, Bruhis M (2013) Determination of the constitutive behaviour of AA6022-T4 aluminium alloy spot welds at large strains. *Mater Sci Eng A* 567:95–100
32. Sharma S K, Patel P, Chandra M, Rajak AK, Sharma C (2022) Resistance spot welding of aluminium 6063 alloy for aerospace application: improvement of microstructural and mechanical properties. *J Inst Eng India Ser D* 103:311–318. <https://doi.org/10.1007/s40033-021-00324-8>

Cryogenic Behavior of TIG Welded Ni-Based Superalloy (IN617)



P. K. Mandal, Akash Kurian Lalu, Amal Michael Saji, and Manu M. Jacob

Abstract Inconel 617 is a solid-solution strengthening Ni–22Cr–13Co–9Mo based superalloy with excellent mechanical properties. It has been extensively used in aerospace, chemical, and power plants due to its excellent oxidation resistance, and good creep-rupture properties above 800 °C. At high temperature applications, it has been usually subjected to precipitation hardening because formation of γ' (Ni₃Al), M₂₃C₆, δ (Ni₃Mo) precipitates in matrix. Several characterizations were done through OM, Vicker's hardness, CVN impact and tensile testing, and examined fractography for WZ of TIG welded samples. The impact strength was investigated in CT ranges between –50 and –196 °C, and RT by CVN impact test. The results show that reasonable good impact and tensile properties had been achieved after PWHT at 950 °C for 4 h of TIG welded samples. The optimum Vicker's hardness values were evaluated for AR sample of 284 HV and 459.4 HV for AW in CT. The impact test was conducted on CVN impact samples while dipping in CT by varying the times. The impact strength is obtained in WZ after PWHT likely 1.81 J/mm² at RT, 1.25 J/mm² at –150 °C, and 1.13 J/mm² at –196 °C with variable CT times likely 30 s, and 120 s, respectively. Thus AW with similar PWHT samples have exhibited good tensile properties likely UTS of 391.66 MPa, YS of 344.33 MPa, ductility of 8.94%, and RA of 7.90%, respectively. The AR samples with similar PWHT exhibited excellent UTS of 846.33 MPa, YS of 358.33 MPa, ductility of 53.91%, and RA of 55.43%, respectively.

Keywords IN617 superalloy · Impact toughness · CT and high UTS

1 Introduction

Nickel-based (IN617) superalloy has been broadly used in the structural and aerospace industry due to its good weldability, good tensile strength, and ductility at cryogenic treatment (CT). CT is a complementary low temperature process that

P. K. Mandal (✉) · A. K. Lalu · A. M. Saji · M. M. Jacob
Department of Metallurgical and Materials Engineering, Amal Jyothi College of Engineering,
Kanjirappally, Kerala 686518, India
e-mail: pareshkmandal@amaljyothi.ac.in

has been recognized for several decades, since 1930s. Generally, the perception of cryogenic designates the science and technology that deals with extremely low temperature environment or subzero treatment, it was started to be employed as a part of the late sixteenth century to upgrade the mechanical properties of materials [1]. The CT increases strength and ductility, and the research about the effect of CT on the mechanical properties of superalloy is rare [2]. The TIG welded nickel-based superalloy is always preferable to induce low heat input, greater precision, better quality as possible to inhibit welding incompatibilities, as cracking, and distortion etc. [3, 4]. The CT entails the improvement of material properties and strength through microstructural changes incorporating phase transformation, particle size and homogeneous distribution, as well as it is exhibited as an ecologically viable, nontoxic, and nonexplosive process. It boosts microstructural refinement and material properties such as toughness, thermal conductivity, fracture resistance, dimensional stability, and chemical degradation [5]. It also implies the material modification of grains, changes in solubility of atoms, movement of dislocations, and creation of new strain free crystals in the matrix. During tensile deformation, the carbide particles (M_6C) can restrict the dislocations movement and also grain boundary sliding efficiently. It is noted that the weld zone (WZ) exhibits a complex heterogeneous nature both in terms of chemical composition and its structure. Specially, the impact toughness is an important mechanical assessment of the high strength superalloy, and it can be expressed as a measure of energy needed to be absorbed to cause fracture of the WZ or heat affected zone (HAZ) [6]. To optimization of the metallurgical properties by the superalloys to be treated under the subzero or CT (-50 to -196 °C) for a predetermined time to obtain the beneficial metallurgical crystalline structures to improve the mechanical properties and to decrease residual stresses, improves the deformation stability [7]. In addition, the principal measurement from the Charpy V Notch (CVN) impact test is the energy absorbed in fracturing the sample usually known as notch toughness. Another common feature of fracture surface is whether the surface is cleavage fracture or ductile fracture, or a mixture of both. The present results showed that CT had an outstanding effect on the improvement of impact strength and hardness of nickel-based superalloy. This research paper inclusively analyzed TIG welded nickel-based superalloy under CT and displays the far greater extent of mechanical properties such as hardness, impact toughness, and tensile properties.

2 Experimental Procedure

The nominal chemical compositions of the base material and filler wire are given in Table 1. The AR alloy plate ($200 \times 50 \times 10$ mm³) was pre-heated at 650 °C for 2 h then subsequently preferred for manual TIG welding (KEMPPi MinarcTig, 180MLP) with ErNiCrMo-3 filler wire continuing through optimized process parameters. In TIG welding, W-2wt% The electrode of 2.2 mm diameter for a single-sided 60° V-groove butt joint and 2 mm root gap and 2 mm root height with shielding gas of argon was used to join the similar plates for different steps as shown in Fig. 1a–c. The

Table 1 Chemical composition (wt%) of IN617 superalloy and the filler wire

Elements (wt%)												
IN617 alloy												
C	Si	Mn	Cr	Mo	Al	Co	Cu	S	P	Fe	Ni	
0.05-0.08	0.5-1.0	0.5-1.0	20-24	8-10	0.8-1.5	10-15	0.5	0.02	0.02	2.9	Bal	
[N.B: Ti-0.211 wt%, B-0.006 wt%]												
Filler wire (ErNiCrMo-3)												
0.1	0.5	9	21.5	-	0.4	8	0.5	0.01	0.2	Bal	50	
[N.B: Ti-0.40 wt%, Nb-3.57 wt%]												

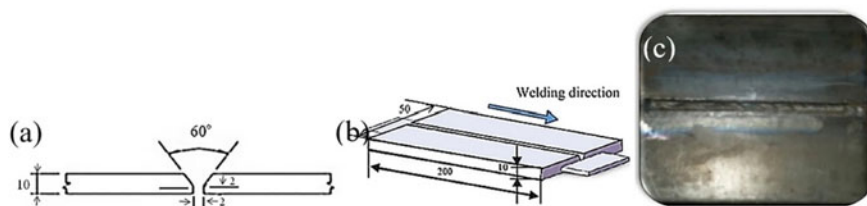


Fig. 1 a, b A single sided V-groove butt type similar joint with narrow gap and indicating welding direction for Inconel 617 alloy, c TIG welded plate ($200 \times 50 \times 10 \text{ mm}^3$)

Table 2 Calculation of heat input in each pass during manual TIG welding

No. of passes	Current (I)	Voltage (V)	Time for each pass (min)	Speed (S) (mm/min)	Ar gas flow rate (L/min)	Heat input = $(V \times I \times 60)/S$ (kJ/mm)
1	130	16.25	3.53	42.49	10	2.98
2	130	17.18	3.38	44.38	10	3.02
3	130	18.10	3.32	45.18	10	3.12

welding procedure was performed in three passes by the TIG welding with manually fitted a filler wire using DC electrode negative and 130 A current in argon gas flow rate at 10 lit./min. While welding was finished each pass, the surface conditions of the weld bead were carefully observed in interpass temperature ($>100 \text{ }^\circ\text{C}$), and the plate was allowed to cool in room temperature between two passes. The manual TIG welding voltage (V), current (I), and speed (S) were instantaneously noted down during welding. The heat input was considered as $V \times I/S$ in kJ/mm with 70% efficiency (η). As well, estimated heat input after each pass of manual TIG welding are given in Table 2. Welding parameters and thermal properties are given in Table 3. The welded plate was subjected to post weld heat treatment (PWHT) at $950 \text{ }^\circ\text{C}$ for 4 h then sectioned into small pieces across the WZ.

All samples were manually polished by using 800, 1000, 1200, and 1500 grade emery papers sequentially then finally used diamond paste ($1\text{--}2 \text{ }\mu\text{m}$) by applying mechanical wheel polisher to obtain mirror like surface finish. The polished samples were etched in aqua regia is a mixture of ($\text{HCl}:\text{HNO}_3 = 3:1$) for optical microscopy (OM) using standard metallographic techniques. The PWHT samples were subjected to OM, Vicker's hardness measurement, CVN impact testing, and tensile testing. These plates were designated for tensile testing and CVN impact testing usually prepared by EDM wire cutting machine as per ASTM E8 standard and ASTM A370 standard, respectively. But impact testing was carried out at room temperature (RT) after PWHT as well as in CT with a controlled manner from -50 to $-196 \text{ }^\circ\text{C}$. The samples were cooled down in the liquid nitrogen bath when dipped into several times for the 20 s, 30 s, and 120 s, respectively as shown in Fig. 2a. After specified cooling time, the sample was quickly inserted into the impact testing machine and tested as

Table 3 TIG welding parameters and thermal properties [8]

Material	No. of passes	Current (<i>I</i>)	Ar gas flow rate (L/min)	Avg. time for welding passes	Used filler wire and diameter (mm)	Density (g/cc)	Melting point (°C)	Thermal conductivity at 500 °C (W/m °C)	Activation energy (E_a) for oxidation (kJ/mole)
IN 617alloy	3	130	10	3.4 min	ErNiCrMo-3 & 2.2	8.4	1332-1380	20.9	374

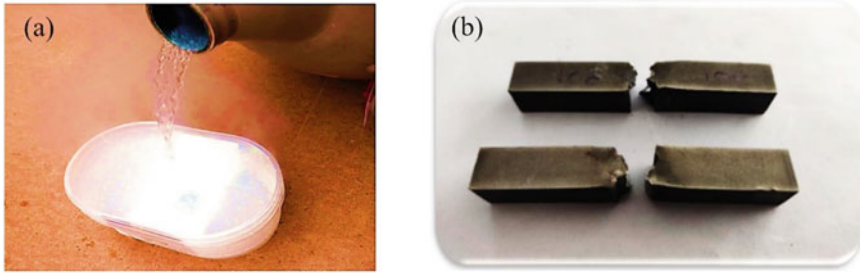


Fig. 2 a Pouring liquid nitrogen into a pan for immersion of impact samples with variable dipping times, b tested CNV impact samples

shown in Fig. 2b. During testing a hammer hit the notched specimen ($55 \times 10 \times 10 \text{ mm}^3$) then the absorbed energy by each sample was recorded. A series of three samples were tested in each condition and the average values were tabulated in Table 4. The Vicker's hardness measurements were taken across the weldment at a load of 30 kg, by using a VM 50 tester. The tensile testing was performed on electro-mechanically controlled Universal Testing Machine (Model no.: UNITEK-94100) with the crosshead speed at 5 mm/min and results are shown at bar diagrams in Fig. 6. The fracture surfaces were cleaned properly and evaluated by macroscopic examination at 10X as shown in Fig. 7c, d.

Table 4 Results of CVN impact test and hardness test as AR/AW IN617 alloy after PWHT at $950 \text{ }^\circ\text{C}$ for 4 h condition

CVN impact sample no	AR/AW impact test in PWHT condition	Various temperatures in RT and CT ($^\circ\text{C}$)	Dipping time in CT (s)	HV after dipping in CT	Impact strength in CT (J/mm^2)
Sample 1	AR/AW	RT	–	$279.6 \pm 13.24/284.0 \pm 12.25$	2.08/1.81
Sample 2	AR/AW	–100	20	$283.5 \pm 16.55/459.4 \pm 18.90$	2.00/1.28
Sample 3	AR/AW	–150	30	$283.0 \pm 18.80/412.4 \pm 17.81$	1.85/1.25
Sample 4	AR/AW	–196	120	$264.0 \pm 18.83/452.6 \pm 20.23$	1.69/1.13

3 Results and Discussion

3.1 Microstructural Analysis

The IN617 superalloy was welded by the TIG welding process and subsequently subjected to PWHT to reach the suitable microstructure with uniform distribution of the accurate size of intermetallic phases likely to γ' and carbides in the matrix and it may enhance mechanical properties at elevated temperatures. It is also expected that the best heat treatment conditions the most proper microstructural characteristics and precipitation of stable phases by the TIG welding process. Moreover, the microstructure of superalloy as heat treated condition is usually metastable, and when exposed to higher temperatures it will transfer to equilibrium condition [9]. The vulnerability of strain cracking is encouraged by high Ti and Al contents as these generate $L1_2$ -ordered γ' ($\text{Ni}_3(\text{Al}, \text{Ti})$) precipitates, and also sulfur, boron, and carbon show similar effects. This problem is overcome to achieve better weldability by controlling the Ti + Al contents (~4wt%) which need to be treated cautiously in terms of grain size, heat treatment, and cooling rate [10]. The metallurgical microstructures of similar plates at base metal (BM), interface, and WZ are exhibited mostly preheat treatment and PWHT effects in Figs. 3, 4 and 5. In addition, the grain boundary in HAZ is induced by the segregation of the solute elements of S, P, and B etc., while liquid film forms in the grain boundary due to low melting point of constitutional liquation [11]. But this problem can be minimized with the high input (9.12 kJ/mm) and preheating condition [12]. The purpose of preheat treatment and heat input affected the microstructure, grain sizes, and γ' precipitates in the HAZ, as well as PWHT which is usually applied to modify the AW microstructures for enhancing their properties due to precipitation of intergranular carbides, γ' ($\text{Ni}_3(\text{Al}, \text{Ti})$) particles in WZ [13]. The BM and interface zone microstructures consist of coarse and fine grains of γ with carbide precipitation along the grain boundaries and numerous secondary phases appear similarly in the matrix. The observation of HAZ exhibits grain growth

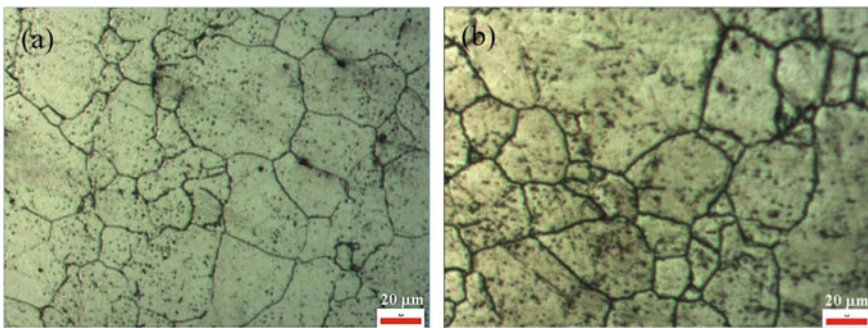


Fig. 3 Illustration of optical microstructures of the base metal (BM): **a** with preheat treatment at 650 °C for 2 h, **b** with PWHT at 950 °C for 4 h

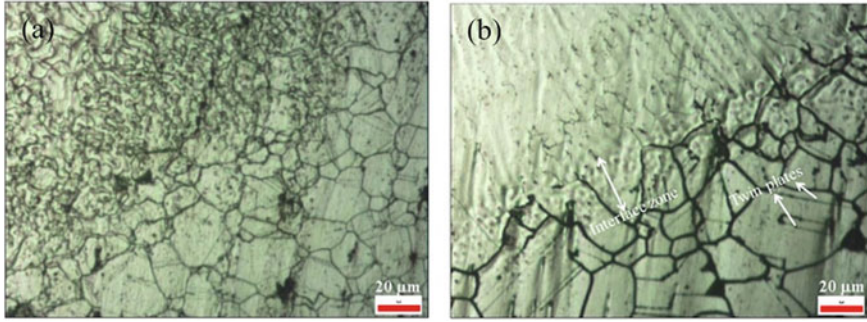


Fig. 4 Illustration of optical microstructures of WZ/HAZ interface: **a** with preheat treatment at 650 °C for 2 h, **b** with PWHT at 950 °C for 4 h

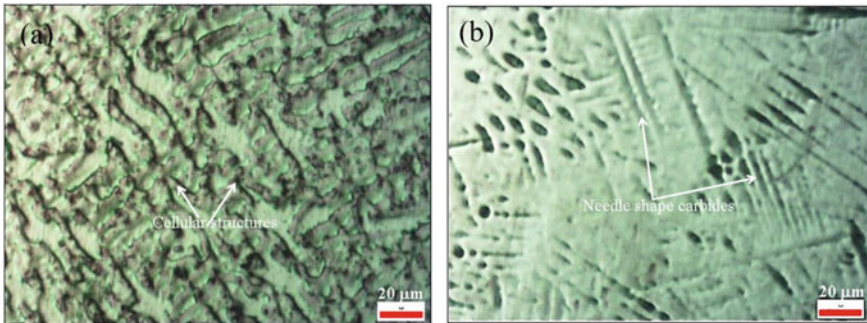


Fig. 5 Illustration of optical microstructures of WZ: **a** with preheat treatment at 650 °C for 2 h, **b** with PWHT at 950 °C for 4 h

is occurred due to high temperature during welding as γ phase has high heat capacity, low heat transfer coefficient, and low cooling rate. Some of the micrographs (Fig. 4) shows twin structure especially at interface to HAZ and BM in the superalloy. These twin structures have typical effects to prevent dislocation movements during the deformation usually enhancing the strength of cubic materials [14]. Figure 5a shows the equiaxed dendritic micrograph of WZ. The occurrence of cellular type structure in the WZ and columnar dendrite structures appear in the matrix and it may happen due to predominant thermal gradient. The steeper thermal gradients in WZ encourage the formation of columnar dendritic growth in a direction opposite to that of heat extraction. Figure 5b shows the elimination of dendritic structure but several black precipitates appear perhaps for coarse or needle shape carbide phases existence in discontinuous manner or may be lamellar structures present in discrete manner that weaken the grain boundary and reduce the mechanical properties and as a result of dominant effects of PWHT for nickel-based superalloy [15–17]. Moreover, the optical micrograph revealed several precipitates can be classified into carbides ($M_{23}C_6$, M_6C , TiC) with a high concentration of Cr, Mo, Ni and borides ($M_{23}(C, B)_6$)

in the matrix. Although most carbides are found at the grain boundaries and inside the grains, while borides are found at the grain boundaries. The carbides have plate-like morphology or blocky particles also observed in these cases (Figs. 4 and 5) [18]. Figure 6 shows the tensile properties are exhibited at RT in the PWHT condition.

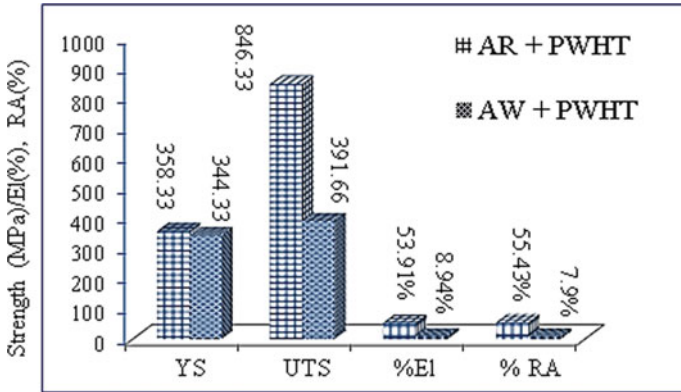


Fig. 6 Results of tensile properties of IN617 alloy after PWHT at 950 °C for 4 h condition

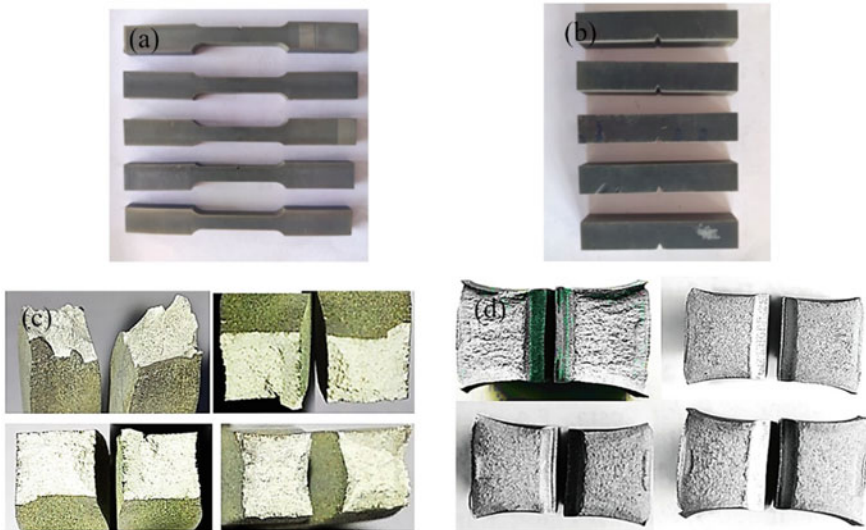


Fig. 7 a, b The tensile samples and CVN impact samples had been prepared according to ASTM standard by EDM wire cutting machine, c the tensile macro-fractography (10×), d the impact macro-fractography (10×)

3.2 Tensile Properties and Hardness, Impact Properties

The carbide particles (M_6C) could restrict the dislocation movement and also grain boundary sliding efficiently during tensile deformation. The tensile properties are influenced by the $M_{23}C_6$, while precipitated at grain boundaries enhance strengthening a significant effect on the mechanical properties of superalloy. In addition, twin boundaries are exhibited in the optical microscopy that acts as obstacles to dislocation motion, which enhances the alloy strengthening with γ' phase during heat treatments. The strengthening of superalloy is mostly accomplished by a large number of coherent precipitates γ' (Ni_3Al) in the γ matrix. Secondary carbides (Mo, Cr) $_{23}C_6$ boost the mechanical properties, particularly its creep resistance inhibiting grain boundary sliding. They are situated in the vicinity of grain boundary in the form of globular precipitates and vastly microstructural stability at high temperatures. The high temperature (>800 °C) creep properties are attributed to solid solution strengthening by the presence of Mo and Co elements and consequently carbide precipitates ($M_{23}C_6$) contributed to precipitation strengthening [19, 20]. Aluminium (~ 1 wt%) also increases mechanical properties by forming γ' intermetallic compound. The tensile properties are reasonably lower to as-welded (AW) in the PWHT condition because of the reduction of brittle phases, caused by solid solution strengthening of the solute atoms and the precipitation of carbides. The comparative study shows that the tensile properties are increased as ultimate tensile properties (UTS) of 116.10%, yield strength (YS) of 4.10%, elongation (EI) of 503.0%, reduction area (RA) of 601.65%, and YS/UTS ratio varies 0.89–0.42 in the AR alloy [21–23]. The impact strength acts as a function of variable temperatures. As the temperature gradually decreases from RT to CT (-50 to -196 °C) the impact strength is also reduced marginally in AR and AW both of the conditions. It should be noted that the impact strength of CT samples is conspicuously lower than the RT condition. There is also a linear relationship with liquid nitrogen dipping times in CT, if dipping time gradually increases also to impact strength decreases marginally and exhibited lowest values of 1.69 and 1.13 J/mm² in AR and AW conditions, respectively as shown in Table 4. In fact, lower impact strength spontaneously imposed in CT due to lower fracture initiation energy restricted for high strain rate impact loading process, and another important aspect of hardening effects augmented due to carbides and nitrides precipitate at -196 °C The macro-fractography indicates the brittle mode of grainy surface and brittle coarse carbides ($M_{23}C_6$) accumulation at the grain boundaries, intermetallic phases (Ni_3Mo , γ' ($Ni_3(Al, Ti)$) mainly differs at different dipping times in CT. The hardening mechanism is favorable in CT as indicates hardness rising sharply in AW alloy than AR alloy in a similar PWHT condition. This relationship can also be correlated with impact strength and hardness [24, 25]. The impact strength indicates inversely proportional to the hardness in AR and AW in both conditions, but in the case of AW condition is more conspicuous after CT and vice versa. In nickel-based superalloy usually, hardness is achieved through solid solution strengthening elements such as Cr, Co, and Mo etc. In addition, discontinuous carbide precipitates at the grain boundaries, γ' precipitates inside the grains that causes pinning of the

grain boundary and diminishes grain boundary sliding, and also recrystallized zone exhibits high hardness, and microstructural heterogeneity could influence the drastic changes in the high hardness of AW alloy. Notably, the solid solution and carbide precipitates provide higher hardness that is accelerated with dipping time in CT, as well as in comparison with RT hardness (i.e., $284.0 \pm 12.25\text{HV}$) for CT hardness increases sharply such as 61.53%, 52.95%, and 59.14% while dipping times varying with 20 s, 30 s, and 120 s, respectively [26, 27]. Figure 7a, b shows the AW and AR plates were sliced using the power hacksaw and then prepared by EDM wire cutting machined to the correct dimensions for preparing tensile test samples and CVN impact test samples as per ASTM standards. The tensile fracture surfaces are observed through macroscopic analysis as shown in Fig. 7c. The fracture surfaces reveal a cup-and-cone type of appearance with slanted fracture surfaces at RT tensile testing. It is also indicated the ductile mode of fracture lips on the tip of surfaces and shiny appearance and uneven fracture surfaces. Hence, the ductility may be connected with the reduction of active stress during tensile loading.

3.3 Macro-fractography Analysis

It is to note that the tips of fractures are highly elongated owing to ductile nature, and also tensile results indicated RA of 55.43% and ductility of 53.91% in the case of AR alloy in the PWHT condition. The appearance of impact fracture surfaces showing a continual character of fracture reveals entirely brittle mode with grainy surface and high reflectivity and mostly cracks originated from the notch edge surface and propagates quickly due to high strain rate impact loading process as shown in Fig. 7d.

4 Conclusions

Nowadays nickel-based superalloy has become an auspicious material through manufacturing desired properties obtained by CT due to their high structure stability, high toughness and ductility, high corrosion resistance, and high elastic modulus under cryogenic environments. Although improved many important properties such as toughness, ductility and fatigue resistance at CT found to be critical applications such as aerospace, superconducting magnet system usually applicable in international thermonuclear energy reactor. In this work, the tensile strength and CT behavior through CVN impact strength of IN617 superalloy was investigated for different conditions and the following conclusions can be summarized below:

1. The nickel-based superalloy is easily weldable, better resistance to cracking and corrosion resistance usually possess the mechanical properties preferably by TIG welding. The strengthening of superalloy is mostly accomplished by a large number of coherent precipitates $\gamma'(\text{Ni}_3\text{Al})$ in the γ matrix. Secondary

carbides $(\text{Mo, Cr})_{23}\text{C}_6$ boost the mechanical properties, particularly its creep resistance inhibiting grain boundary sliding.

2. The optical microstructures of BM and interface zone consists of coarse and fine grains of γ with carbide precipitation along the grain boundaries and numerous secondary phases appear similarly in the matrix. The HAZ exhibits grain growth is occurred due to high temperature during welding as γ phase has high heat capacity, low heat transfer coefficient, and low cooling rate in the matrix.
3. It is noted that after CT materials must be wisely designated because typically changes properties when they are exposed to extremely low temperatures, as well as materials normally ductile at atmospheric temperatures but properties are drastic changes to brittleness due to very low temperature treatments.
4. There is also a linear relationship with liquid nitrogen dipping times in CT, if dipping time gradually increases also decreases to impact strength marginally and exhibited lowest values of 1.69 and 1.13 J/mm² in AR and AW conditions. Notably, in comparison with RT hardness (i.e., 284.0 HV) for CT hardness increases sharply such as 61.53%, 52.95%, and 59.14% while dipping times varying with 20 s, 30 s, and 120 s in AW condition, respectively.
5. The CVN impact macro-fractography revealed an entirely brittle mode with grainy surface and high reflectivity and mostly cracks originated from the notch edge surface and propagated quickly due to the high strain rate impact loading process.
6. The tensile properties are reasonably lower for AW in PWHT condition because of the reduction of brittle phases, caused by solid solution strengthening of the solute atoms and the precipitation of carbides. The comparative study shows that the tensile properties are increased to UTS of 116.10%, YS of 4.10%, El of 503.0%, RA of 601.65%, and YS/UTS ratio varies 0.89 to 0.42 in AR condition.

References

1. Manjunath S, Ajay Kumar BS (2016) An extensive review on the effects of deep cryogenic treatment on cutting tools. *J Eng Sci Technol Rev* 9(3):49–59
2. Jaladurgam NR, Kabra S, Colliander MH (2021) Macro- and micro-mechanical behaviour of a γ' strengthened Ni-based superalloy at cryogenic temperatures. *Mater Des* 209:1–9
3. Hosseini HS, Shamanian, Kermanpur A (2011) Characterization of microstructures and mechanical properties of Inconel 617/310 stainless steel dissimilar welds. *Mater Charact* 62:425–431
4. Yang Z, Debapriya PM, Philipp S, Thomas S, Jamie JK, Vikas T (2017) High temperature indentation based property measurements of Inconel IN-617. *Int J Plast* 96:264–281
5. Abbas R, Cristiana D, Paolo B (2019) Correlation between microstructural alteration, mechanical properties and manufacturability after cryogenic treatment: a review. *Materials* 12(3302):1–36
6. Esmaeili H, Mirsalehi SE, Farzadi A (2018) Vacuum TLP bonding of Inconel 617 superalloy using Ni-Cr-Si-Fe-B filler metal: metallurgical structure and mechanical properties. *Vacuum* 152:305–311

7. Joseph JDJ, Aravindh C, Kannan PD, Dineshmuthu M, Kumar JJJ (2018) Analysis of dissimilar metal welding under cryogenic treatment. *Int J Eng Res Technol (IJERT)* 6(04):1–3
8. Park SY, Ham SH, Cho MS, Bae HD (2011) An assessment of the mechanical characteristics and optimum welding condition of Ni-based super alloy. *Procedia Eng* 10:2645–2650
9. Seksak A, Weerasak H, Panyawat W (2010) Strain-age cracking after Postweld heat treatments in Inconel 738 superalloy. *High Temp Mater Processes (London)* 29(1–2):61–67
10. Hisazawa H, Terada Y, Adziman F, Crudden DJ, Collins DM, Armstrong EJ, Reed RC (2017) The effect of Nb/Ti ratio on hardness in high-strength Ni-based superalloys. *Metals* 7(71):1–11
11. Xu H, Liu W, Lu F, Wang P, Ding Y (2017) Evaluation of carbides and its characterization in HAZ during NG-TIG welding of Alloy 617B. *Mater Charact* 130:270–277
12. Sun J, Ren W, Nie P, Huang J, Zhang K, Li Z (2019) Study on weldability, microstructure and mechanical properties of thick Inconel 617 plate using narrow gap laser welding method. *Mater Des* 175:1–13
13. Kim JK, Park HJ, Shim DN, Kim JK (2016) Effects of PWHT on microstructure and mechanical properties of weld metals of Ni-based superalloy 617 and 263 for hyper-supercritical power plants. *Acta Metall Sin (Engl Lett)* 29(12):1107–1118
14. Farahani E, Shamanian M, Ashrafizadeh (2012) A comparative study on direct and pulsed current gas tungsten arc welding of alloy 617. *AMAE Int J Manuf Mater Sci* 02(01):1–6
15. Liu W, Lu F, Yang R, Tang R, Tang X, Cui H (2015) Gleeble simulation of the HAZ in Inconel 617 welding. *J Mater Process Technol* 225:221–228
16. Tongjiao C, Huali X, Zhuguo L, Fenggui L (2019) Investigation of intrinsic correlation between microstructure evolution and mechanical properties for nickel-based weld metal. *Mater Des* 165:1–11
17. Vemanaboina H, Edison G, Suresh A, Reddy LS, Ramesh KB (2017) Multipass welding on Inconel material with pulsed current gas tungsten arc welding. *Mater Today Proc* 4:1452–1458
18. Jalilian F, Jahazi M, Drew RAL (2006) Microstructural evolution during transient liquid phase bonding of Inconel 617 using Ni-Si-B filler metal. *Mater Sci Eng A* 423:269–281
19. Pavan AHV, Vikrant KSN, Ravibharath R, Kulvir S (2015) Development and evolution of SUS 304H-IN 617 welds for advanced ultra supercritical boiler applications. *Mater Sci Eng A* 642:32–41
20. Panyawat W, Weerasak H, Seksak A (2009) Effect of Post weld heat treatments on Tig-welded microstructures of superalloy IN-738. *Chiang Mai J Sci* 36(3):320–330
21. Mashhuriazar A, Omidvar H, Sajuri Z, Gur H (2020) Effects of pre-weld heat treatment and heat input on metallurgical and mechanical behaviour in HAZ of multi-pass welded IN-939 superalloy. *Metals* 10(1453):1–17
22. Ahmad HW, Hwang JH, Lee JH, Bae DH (2016) An Assessment of the mechanical properties and microstructural analysis of dissimilar material welded joint between alloy 617 and 12Cr steel. *Metals* 6(242):1–11
23. Bassford TH, Hosier JC (1984) Production and welding technology of some high-temperature nickel alloys in relation to their properties. *Nucl Technol* 66:35–43
24. El-Bagoury N (2011) Microstructure and mechanical properties of aged nickel base superalloy. *Arch Appl Sci Res* 3(2):266–276
25. Jamrozik W, Gorka J, Kik T (2021) Temperature-based prediction of joint hardness in TIG welding of Inconel 600, 625 and 718 nickel superalloys. *Materials* 14(442):1–13
26. Yoshinori O, Tetsumi Y, Sumiyoshi H, Takeuchi E, Matsuoka S, Ogata T (2004) High-cycles fatigue properties at cryogenic temperatures in INCONEL 718 Nickel-based superalloy. *Mater Trans* 45(2):342–345
27. Yang YH, Yu JJ, Sun XF, Jin T, Guan HR, Hu ZQ (2012) Investigation of impact toughness of a Ni-based superalloy at elevated temperature. *Mater Des* 36:699–704

Additive Manufacturing

Thermal Modeling of Wire Arc Additive Manufacturing Process Using COMSOL Multiphysics



Vishal Kumar, Biplab Kumar Roy , and Amitava Mandal

Abstract Wire arc additive manufacturing (WAAM) is one of the emerging AM processes used to fabricate medium to large size components based on the principle of direct energy deposition (DED). Despite having several benefits of the WAAM process, few limitations such as parts distortion and induced residual stress have been a cause of concern in this area. Therefore, the work focuses on finite element process simulation and modeling of thermal cycle prevailed during the fabrication of multi-layered stainless steel (SS316L) wall using WAAM. The model is developed using the COMSOL Multiphysics® software. The simulation results predict the thermal history of the wall fabricated at the selected process parameters. Thus, the model helps in controlling the thermal gradient and the residual stress induced due to non-uniform cooling cycle developed during the manufacturing process. The effective study and altering the process input parameters cutoff a large number of trial experiments and save the production time and associated material loss.

Keywords Additive manufacturing (AM) · Wire arc additive manufacturing (WAAM) · Heat transfer · COMSOL

1 Introduction

The basic principle of additive manufacturing (AM) is the direct deposition of material layer-upon-layer to fabricate a three-dimensional complex object with the use of a CAD-generated 3-D model [1]. One of the branches of AM includes direct energy deposition (DED) that focuses on the thermal source of energy such as laser beam, electron beam, or electric arc and the feedstock material as a metallic wire or powder [2]. The wire arc additive manufacturing process (WAAM) works on the concept of DED that involves the simultaneously melting and fusing of metallic wire layer by layer over the substrate to build the desired component. The process is steadily getting popular as an energy-efficient process to build medium to large

V. Kumar (✉) · B. K. Roy · A. Mandal
Department of Mechanical Engineering, Indian Institute of Technology (ISM), Dhanbad 826004, India
e-mail: vishal0101kumar@gmail.com

size structures. The WAAM process is characterized as relatively lower equipment cost, higher deposition rate (3 kg/h), and power-efficient (around 90%) process in comparison with laser and electron beam-based DED [3]. However, the limitation to this process mainly includes part distortion and residual stress induced in the built part [4]. The pattern of uneven and uncontrolled heating and cooling cycle during the fabrication process is the major part of the concern that obstructs its applicability to a larger section. Therefore, many researchers have been working in this part of the area to acknowledge and closely regulate the thermal cycle during the process within some extent. In that area, many of the simulation work has been done using ANSYS, Abaqus FEA, and some with SIMUFACT welding software; however, least modeling work in this domain has been carried out using COMSOL Multiphysics software. The heat cycle during the part fabrication along with the effect of interlayer dwell time on thin-walled components built by GMAW-based WAAM process has been studied by Yang et al. [5]. Mughal et al. (2006) established a 3D finite element (FE) model to examine the induced residual stress and deformations in the parts fabricated by multi-pass single-layer bead deposition. An unexpected deformation has been observed during the deposition process caused mainly because complicated temperature cycle exists [6]. Similarly in other studies, Bai et al. (2013) examine the thermal cycle of multi-layer bead depositions to fabricate the part using by electric arc-based WAAM technique. A new approach has been proposed to calibrate the input process parameters based on the use of IR imaging and inverse analysis. The experimental results adopting the new approach show an error of less than 30 °C to that of the predicted temperature value. Also, results from the simulation discovered that both induction pre and post-heating cycles lead to a more homogeneous heat source and minimize the temperature gradients during the process [7, 8]. A numerical model has been developed by Kostin et al. (2017) based on the evolution of thermal cycle in a WoW built of 09G2S steel grade fabricated using GMAW-based WAAM process. The results obtained from the model observed that increasing multiple numbers of layers deposited during the WAAM, a significant decrease in the thermal gradient within the fabricated part especially in the region of the molten pool has been observed [9]. Zhao et al. (2011) develop a 3D heat transfer model together with temperature-dependent material properties to investigate the effect of heat cycle during WAAM. The result concluded that an increase in deposition height of the WAAM fabricated part deteriorates the heat transfer (diffusion) condition [10]. The present work is concentrated on the modeling of the GMAW-based WAAM process using COMSOL Multiphysics software. A model of thermal behavior is developed to establish the evolution of the thermal field during the bead deposition process and analyze the thermal cycle developed during fabrication of wall layer upon layer.

2 Simulation Procedure

2.1 Material Properties

The geometry of the base plate, substrate, C clamp, and the WAAM fabricated wall model has been shown in Fig. 1. The base plate of the mild steel with a dimension of $650 \times 650 \times 15 \text{ mm}^3$ has been used along with the four C clamped to support and hold the substrate plate rigidly. The substrate plate of material AISI1018 with a dimension of $500 \times 500 \times 5 \text{ mm}^3$ has been used over which the wall is built using SS316L filler MIG wire. The chemical composition of both the deposited MIG wire material and the substrate plate has been tabulated in Tables 1 and 2. The seven-layer wall is fabricated on the center of the substrate plate that is defined by the width and height of the deposits. The geometry of fabricated weld bead lines is modeled by a rectangular section to simplify the problems. Also, to avoid the complexity in model solving and to reduce the computational time, several assumptions were also made. The system was modeled as a rigid solid without considering the fluid flow in the weld pool zone, thus not considering the metallurgical transformations during the deposition process [11]. The material properties of the substrate plate and deposited bead material are assumed to be isotropic.

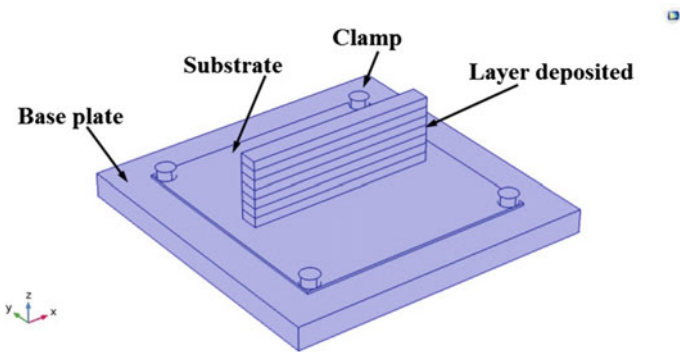


Fig. 1 Geometrical model of WAAM fabricated wall

Table 1 Chemical composition of the AISI1018 substrate (in wt.%)

C	Mn	S	P	Fe
0.15	0.60	≤ 0.05	≤ 0.040	Balance

Table 2 Chemical composition of the SS316L consumable electrode (in wt.%)

C	Mn	Si	S	P	Cr	Mo	Ni	Cu	Fe
0.01	1.53	0.59	0.001	0.027	18.56	2.53	11.55	0.17	Bal

2.2 Model Parameters

The simulation model is based on GMAW-based WAAM process that has been utilized to fabricate the wall by layer upon layer deposition. The standoff distance of 10 mm is maintained after every layer is deposited. The cooling time has been allocated to cool down the heated weld bead before the next layer is deposited. This also insures to minimize the residual stress induced in the fabricated part. The experimental setup of the MIG-based WAAM technique has been shown in Fig. 2. The experimental data for the simulation has been taken from the previous experimental work [1]. The detailed process parameters have been tabulated in Table 3.

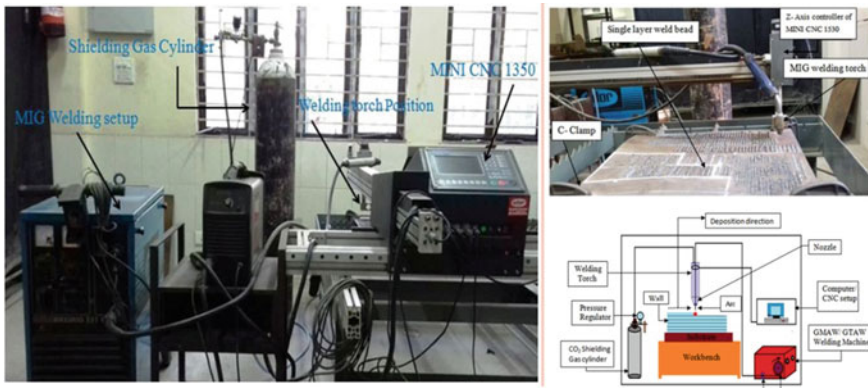


Fig. 2 Experimental setup of GMAW-based WAAM technique [1]

Table 3 Global process parameters for bead deposition [1]

S. No.	Process parameters	Values
1	Welding current (I)	110 A
2	Open circuit voltage (V)	16 V
3	Welding speed (TS)	95 mm/min
4	Shielding gas flow rate (f)	21Lit/min
5	Wire diameter (d)	0.8 mm
6	Dwell time (t)	10 s
7	Wire feed rate (r)	1.5 m/min
8	Stand-off distance (l)	10 mm

2.3 Boundary Conditions for Heat Transfer in Solid

The transient heat conduction equation is used as the governing equation for the temperature distribution and heat transfer in the entire volume of the material represented by Eq. (1).

$$\rho C_p \frac{\partial T}{\partial t} = \frac{\partial}{\partial x} \left[K \frac{\partial T}{\partial x} \right] + \frac{\partial}{\partial y} \left[K \frac{\partial T}{\partial y} \right] + \frac{\partial}{\partial z} \left[K \frac{\partial T}{\partial z} \right] + Q \quad (1)$$

where K and C_p represent the temperature-dependent thermal conductivity and specific heat capacity of material, respectively. Q denotes the heat source or sink, t is the time, ρ is the material density, and x, y, z are Cartesian coordinates in the reference system.

The widely acceptable Goldak double ellipsoidal arc heat source model that follows Gaussian heat distribution has been applied to the WAAM deposited bead [12]. The x -axis and z -axis were positioned toward the wire feeding direction and the arc aiming direction, respectively. The power density is separately defined in the front region of the arc center and the region behind the arc center represented by the Eqs. (2) and (3).

$$Q_f = \frac{6\sqrt{3}Qf_f}{\pi\sqrt{\pi}p_fqs} e^{-3\left(\frac{x^2}{p_f^2} + \frac{y^2}{q^2} + \frac{z^2}{s^2}\right)} \quad (2)$$

$$Q_r = \frac{6\sqrt{3}Qf_r}{\pi\sqrt{\pi}p_rqs} e^{-3\left(\frac{x^2}{p_r^2} + \frac{y^2}{q^2} + \frac{z^2}{s^2}\right)} \quad (3)$$

where coefficient q and s are the width and depth of the heat source. p_f and p_r are the frontal and rear length of the ellipsoid, respectively. Q denotes the energy heat input considering the factor of process efficiency. Factors representing the power distribution to the front and rear portion of the heat source are f_f and f_r . And, the process efficiency is represented as η . The complete parametric settings for the used Goldak heat source model in this paper are presented in Table 4.

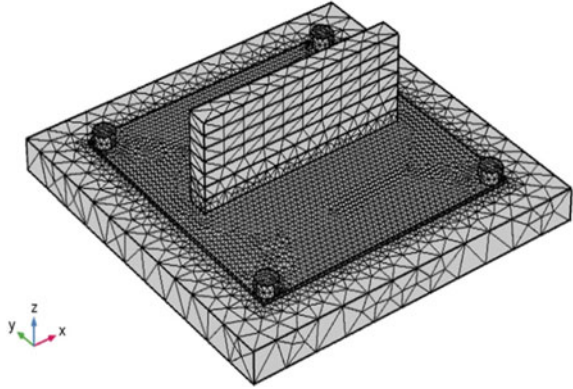
$$Q = \eta(V * I) \quad (4)$$

$$F = (f_f + f_r) = 2 \quad (5)$$

Table 4 Heat source parameters [13]

Parameters	p_f (mm)	q (mm)	s (mm)	p_r (mm)	f_f	f_r	Q (W)	T_a	η
Value	2	2.5	3	6	0.6	1.4	1408	300 K	0.8

Fig. 3 Physically controlled mesh of developed model



The substrate and base plate surfaces that are exposed to the ambient condition are assumed to undergo heat loss because of free convection. The initial temperatures of the setup model were assumed as 300 K. The following boundary conditions (BC) imposed on the fabricated thin wall component are represented by Eqs. 6 and 7.

$$q^* = h(T - T_0) \quad (6)$$

$$q^* = \sigma(T^4 - T_0^4) \quad (7)$$

where q^* represents heat flux per unit surface area, (σ) as the Stephane Boltzmann constant, (ϵ) and (h) as the material emissivity and the coefficient of convective heat transfer, respectively, and (T_0) as the environmental temperature. Thus, heat losses by convection and radiation mode of heat transfer have been considered in this model and so 15 W/m²K as convection heat transfer coefficient, 5.67×10^{-8} Wm⁻² K⁻⁴ as the Stefan-Boltzmann constant, and material emissivity of 0.3 were applied to external parts of the substrate, base plate, and the deposited layers for the FE analysis.

The number of mesh element 44,379 has been generated on the substrate and additively deposit 7th layers wall after performing mesh convergence tests with a mesh volume of 2.471×10^7 mm³. The element family is constituted of tetrahedral and triangular shapes with element sizes between 0.13 and 13 mm that ensure sufficiently accurate results (Fig. 3).

2.4 Results and Discussion

COMSOL Multiphysics simulation software has been used to study the thermal behavior and the cooling status of the process during layer depositions. The complete work step followed during the simulation has been mentioned in the form of a

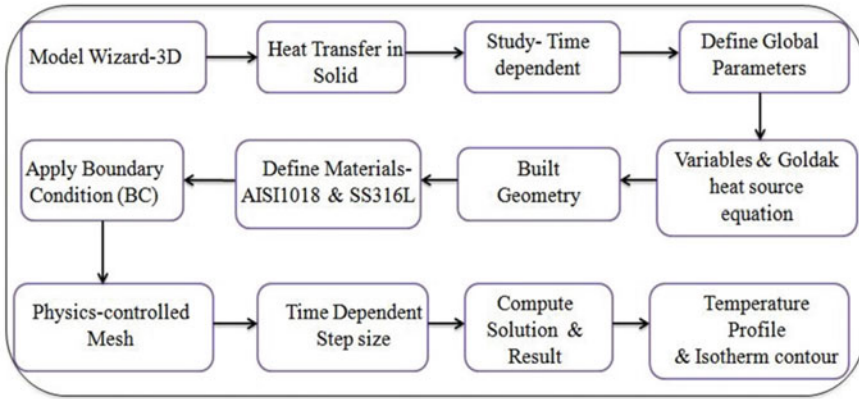


Fig. 4 Process flowchart for simulation using COMSOL

flowchart in Fig. 4. The observation of the simulation has been made over layer 1st, layer 4th, and layer 7th of the deposited wall at 15 s, 95 s, and 200 s, respectively. The maximum temperature prevailed during the deposition of the first layer was 1210 K that goes on to increase for layer fourth as 2110 K and finally increased to 2400 K for the seventh layer deposition. The cooling profile has been shown in Fig. 5. The increase in the value of maximum temperature with the layers is because of preheating of sub-layers that leads to non-uniform cooling during the complete deposition process. This is a serious issue in the WAAM fabrication process that can be reduced to some extent using air/water cooling channels below the base plates or by pre-heating the base plate before the deposition starts that ultimately reducing the temperature gradient during the process, and in this way, residual stress induced in the built part can be minimized.

A comparison has also been made by obtaining the temperature distribution profile during the deposition of weld bead at 1st, 4th, and 7th layers for a time interval of 50 s as dwell time. The result shows a marginal decrease in the maximum temperature from 1830 K for layer 1 to 1800 K for layer 4 and finally to 1780 K for layer 7. This observation has been shown in Fig. 6. As the number of layers deposited increases, the conductive mode of heat transfer also gets predominant in comparison with convective heat transfer. Thus, for the final deposited layer, three modes of heat loss take place that includes conduction heat transfer through the deposited wall and baseplate, convective heat transfer through the surrounding air, and radiative heat losses.

The result from isothermal contours obtained from the simulation results for the seventh layer deposition shows the penetration of heat source to the bead layers deposited. The isothermal plot has been shown in Fig. 7. It can be clearly seen that heat impact is more crucial in the pre-deposited layer during the fabrication process and mostly affects the 6th and 5th layer. This effect can be minimized using a combined

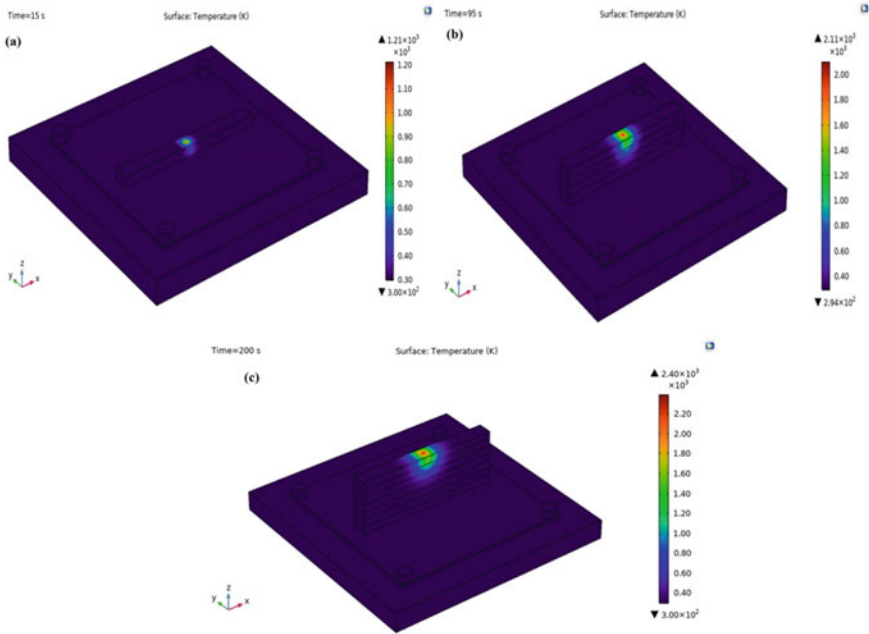


Fig. 5 Temperature distribution of a layer 1st at 15 s, b layer 4th at 45, c layer 7th at 200 s

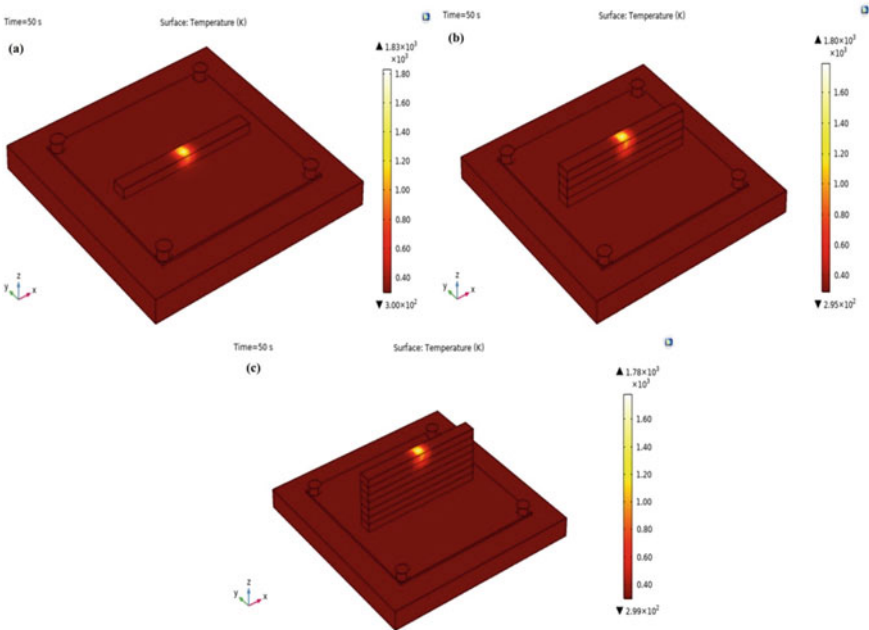


Fig. 6 Temperature distribution of a layer 1st at 50 s, b layer 4th at 50 s, c layer 7th at 50 s

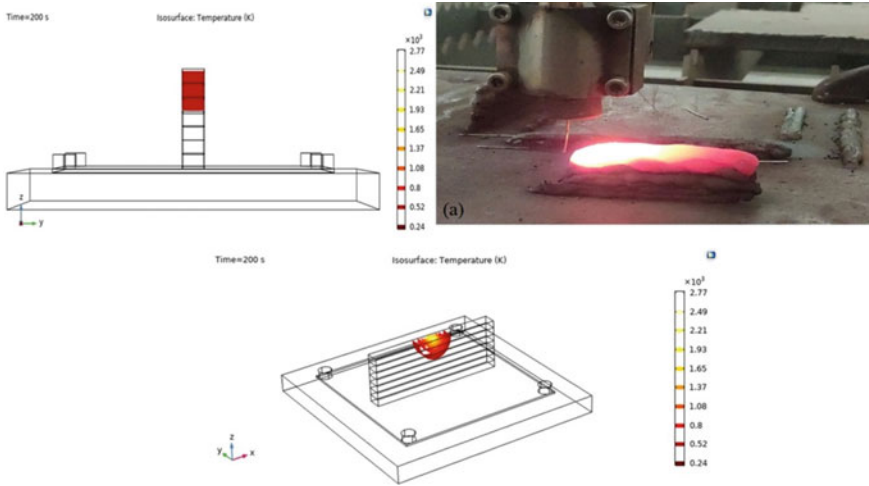


Fig. 7 Isothermal contours (ht) plot for the 7th layer deposited wall model, **a** experimental validation

factor of interlayer dwell time for cooling and optimized value of shielding gas flow to enhance the heat transfer through the forced convective mode of heat transfer.

3 Conclusion

In this study, FEM is employed through COMSOL Multiphysics to simulate the thermal behavior of single and multi-layered walls fabricated using the WAAM process.

A novel Goldak heat source model with a Gaussian distribution model has been developed and applied to the proposed model. The COMSOL software provides a wider scope and a user-friendly interface to be work-on. The obtained temperature profile during the deposition process allows us to understand the cooling cycle exits and their impact on the process performance. The study shows that during the deposition of a layer, the next two sub-layers are the most affected part of the fabricated wall that leads to re-solidification of the layer and induces thermal stress. The optimized value for the MIG torch travel speed and the shielding gas flow rate can be able to control the heating effect of the power source, and effective cooling will allow to minimize the thermal gradient prevailed during the process.

References

1. Kumar V et al (2021) Parametric study and characterization of wire arc additive manufactured steel structures. *Int J Adv Manuf Technol*, 1–11
2. Dutta B (2020) Directed energy deposition (DED) technology
3. Panchenko OV et al (2019) Macrostructure and mechanical properties of Al–Si, Al–Mg–Si, and Al–Mg–Mn aluminum alloys produced by electric arc additive growth. *Met Sci Heat Treat* 60(11):749–754
4. Colegrove P, Ganguly S (2016) Residual stress characterization and control in the additive manufacture of large scale metal structures. *Residual Stresses* 2017:455
5. Yang D, Wang G, Zhang G (2017) Thermal analysis for single-pass multi-layer GMAW based additive manufacturing using infrared thermography. *J Mater Process Technol* 244:215–224
6. Mughal MP, Fawad H, Mufti RA (2006) Three-dimensional finite-element modelling of deformation in weld-based rapid prototyping. *Proc Inst Mech Eng C J Mech Eng Sci* 220(6):875–885
7. Bai X, Zhang H, Wang G (2013) Improving prediction accuracy of thermal analysis for weld-based additive manufacturing by calibrating input parameters using IR imaging. *Int J Adv Manuf Technol* 69(5):1087–1095
8. Bai X, Zhang H, Wang G (2015) Modeling of the moving induction heating used as secondary heat source in weld-based additive manufacturing. *Int J Adv Manuf Technol* 77(1–4):717–727
9. Kostin VA, Grygorenko GM (2017) Simulation of the additive process of forming 3D products from HSLA Steel 09G2S. In: *COMSOL conference in Rotterdam*
10. Zhao H et al (2011) A 3D dynamic analysis of thermal behavior during single-pass multi-layer weld-based rapid prototyping. *J Mater Process Technol* 211(3):488–495
11. Abusalma HKJ (2020) Parametric study of residual stresses in wire and arc additive manufactured parts. Old Dominion University Dissertation
12. Goldak J, Chakravarti A, Bibby M (1984) A new finite element model for welding heat sources. *Metall Trans B* 15(2):299–305
13. Ding J et al (2011) Thermo-mechanical analysis of wire and arc additive layer manufacturing process on large multi-layer parts. *Comput Mater Sci* 50(12):3315–3322

Experimental Optimization of Green FDM Process Parameters: An Integrated MCDM Approach



Surajit Barad, Jagadish , Sathish Kumar Adapa , and Sagar Yanda

Abstract The 3D printing, also known as Additive Manufacturing (AM), is an emerging manufacturing technology in various industries like in automotive, aerospace, space applications, etc. Among the various AM process, fused deposition modeling (FDM) process is well known and widely used in developing the models. In spite of its advantages, few disadvantages of FDM process namely high energy consumption, production time and emission concentration, and rates of Fine Particles (FP), Ultra-Fine Particles (UFPs) as well as Volatile Organic Compounds (VOCs). Selection of optimum parameters for any FDM process to optimize the environmental effects is a cumbersome and difficult task and is a multi-criteria decision-making (MCDM) problem. In this paper, an attempt is made to optimize the green (i.e., environmental parameter into account) FDM process parameters using an integrated MCDM method, i.e., Entropy with VIKOR methods considering two inputs like print temperature (PT) and bed temperature (BT) and three outputs such as particle number concentration (PNC_{0.3–10 μm}), particle number concentration (PNC_{5.6–560 μm}) and specific emission rate (SER). Here, entropy method is used for extraction of precise priority weight while optimal selection of green FDM parameters using VIKOR method. In addition, most significant parameter is determined through parametric analysis. Results shows that, optimal conditions, i.e., PT as 254 °C and PBT as 30 °C and corresponding output as PNC_{0.3–10 μm} = 14 #/cm³, PNC_{5.6–560 μm} = 2.1 × 10⁵ #/cm³ and SER's = 2.0 × 10⁹ are obtained. The parameter SER is shown significant effect on the green FDM process parameter among other parameters.

Keywords Green FDM · Entropy · VIKOR · Optimization · Parametric analysis

S. Barad · Jagadish (✉)

Department of Mechanical Engineering, National Institute of Technology Raipur, Raipur, India
e-mail: jagadish.mech@nitrr.ac.in

S. K. Adapa · S. Yanda

Department of Mechanical Engineering, Aditya Institute of Technology and Management, Tekkali, India

1 Introductions

The additive manufacturing technology is an alternative to the conventional way of making 3D solid products. It allows the construction, using a variety of additive or layered development structures, of physical 3D models of objects, where layers are successively laid out to generate a full 3D structure [1]. At present, the 3D printing industry is at an early stage of its development. There are currently just over ten types of printing technology, using one material or another according to the process used. However, three-dimensional (3D), or additive manufacturing (AM), has been built such that complex 3D structures are produced without costly molds based on computer-assisted (CAD) models, layer-by-layer manufacturing. This technology has flourished over the past few decades in a variety of industries including aerospace, military, biomedical, food, and other fields. Bringing the flexibility of design, efficiency of composite material systems, and multi-axis movement controls of industrial robotics together, the future of AM in the composites industry shows promising results. Hence, additive manufacturing technologies have tremendous potential and advantages for a new age of lightweight structures that are not possible previously, such as degrees of geometric sophistication, component reduction, and design optimization. It is expected that the advanced composites manufacturing market will rise at a remarkable 22.1% CAGR to an approximate value of US\$ 7,676 billion by 2026 [2]. Moreover, in 1980, Scott Crump, founder of Stratasys Ltd., invented Fused Deposition Modeling (FDM) Technology at first. FDM is a technique widely used for components to obtain some mechanical response. In FDM, a thermoplastic printing material filament is melted through a printer extrusion nozzle and is mounted line by line, and layer by layer in order to create a 3D structure of the designed part. It is suitable for building robust components in almost all shapes and sizes with complex geometries.

The natural fibers are considered to be an eco-friendly commodity and is available in large quantities [3]. The world's production of natural fibers such as bamboo is around 30,000,000 tons, the sugarcane bagasse around 75,000,000 tons, and jute around 2,300,000 tons [3]. In contrast with synthetic fibers, natural fibers have their advantages of relatively small weights, low cost, reduced processing equipment damage, good relative mechanical properties, such as a tensile modulus and flexural module, improved composite surface finish, and renewable materials [4]. Many natural products with ample ssfibers, including palm-oil oils, bananas, sisal, jute, wheat, flax straw, sugar cane, cotton, silk, bamboo and coconut, have been shown powerful and effective thermoplastic and thermoset refurbishments [5]. Since natural fiber composites have a high specific strength and modulus [6], natural composites are used for a variety of structural applications. This involves households in sensitive and specialized fields such as spacecraft and aviation [7]. A development area is expected to be the use of natural fibers in composite materials The use of natural fibers has increased considerably with respect to composites. Six types of natural fibers are described below. This comprises: jute, flax, ramie, and kenaf (cotton, kapok), leaf fiber, and core (kenaf, hemp, jute) [8]. For additional applications for the generated

nonwovens, acoustic walls were recommended for halls, theaters, generator rooms, and floor mats [1]. However, emissions from green FDM processes like PNC and SER need to be evaluated to avoid health issues and environmental pollution.

From the literature, it is clear that analysis of environmental factors like particle emission and energy consumption plays a vital role along with other performance factors to shift the additive manufacturing toward Green Additive Manufacturing process. But adding an environmental dimension makes the process more complex as we need to study the effect of different input parameter setting to Green Additive Manufacturing process and optimize the process.

In some earlier studies, researchers have optimized the performance parameter of Additive Manufacturing using several optimization techniques. Alva [9] carried out experiment on PLA 3Dprinting process to optimize the process parameters by using Taguchi and response surface model. The results showed that the optimal process parameters setting is obtained at layer thickness of 0.05 mm, bed temperature of 199.8 °C, and raster angle of 45.10. Dey [10] reported FDM process parameters optimization and their effects on part characteristics. The results revealed that multi-objective process parameters optimization is still bottleneck issue. Shi Mohammadi [11] Studied and investigation of 3D printing process parameters optimization by using hybrid approach (combination of ANN and PSO). The investigation discloses that the surface morphology is significantly improved at an optimal process parameters setting. Suma latha [12] investigated optimal process parameters setting in FDM process parameters by using Taguchi design of experiment. The result shows that the optimal process parameters setting provides high-quality products with minimum energy consumption. Lyu [13] explored optimization of FDM process parameters by using response surface model. The results revealed that the obtained optimal process parameters setting improves the interlayer adhesion and mechanical properties of FDM parts. However, there is limited research has been carried out on green FDM emissions such as PNC and SER. A lot of research opportunities are available on green FDM emissions control and optimization.

In this article, optimization of process parameters such as print temperature (PT) and printing bed temperature (PBT) has been carried out taking the environmental factors into consideration. Here integrated MCDM approach viz. entropy with VIKOR method is described and used to optimize the process parameters of green FDM process. In addition, parametric analysis is adopted to determine the impact of process parameters on green FDM.

2 Methodology

An integrated MCDM method consisting of entropy [14, 15] coupled with VIKOR is illustrated for optimization of green FDM process parameters like PT and PBT and the response parameters such as PNC0.3–10 μm , PNC5.6–560 μm , and SER. The detailed steps of entropy and VIKOR method are as follows:

Step 1: Decision matrix formulation

Decision matrix is denoted by M , it is formed by combination of number of alternatives and criteria. An MCDM problem can be evaluated based on the following matrix [15].

$$M = \begin{bmatrix} & C_1 & C_2 & \dots & C_{1n} \\ A_1 & a_{11} & a_{12} & \dots & a_{1n} \\ A_2 & a_{21} & a_{22} & \dots & a_{2n} \\ \dots & \dots & \dots & \dots & \dots \\ A_{m1} & a_{m1} & a_{m2} & \dots & a_{mn} \end{bmatrix} \tag{1}$$

where M represents decision-maker value with respect to corresponding alternatives and criteria.

$A_1, A_2, A_3, \dots A_m$ are the alternatives; $C_1, C_2, C_3, \dots C_m$ are the criteria with respect to corresponding alternatives. a_{ij} is the performance of value of alternative A_i on the basis of criterion C_j .

Step 2: Calculate accurate weights by entropy method

To calculate the proper weights by entropy method for decision matrix M , the following equations are to be used [14].

$$F_{ij} = \frac{a_{ij}}{\sum_{i=1}^m a_{ij}^2} \tag{2}$$

where F_{ij} is represents feature weight of i th alternative of j th criteria

$$E_j = -k \sum_{i=1}^m F_{ij} \ln(F_{ij}) \text{ where } j = 1, 2, 3, 4 \dots n \tag{3}$$

Where E_j indicates entropy output factor of the j th criteria, [$k = 1/\ln m$]

$$g_i = |1 - E_j| \tag{4}$$

where g_j represents coefficient of variation of j th criteria

$$W_j = \frac{g_i}{\sum_{j=1}^m g_i} \tag{5}$$

where w_j represents the entropy weight.

Step 3: Identification of best (A^+), worst (A^-) values, and values of E_i and F_i

After the entropy weight calculation, best and worst values calculated by using the following equations.

$$A^+ = \text{Max}(a_{ij}) \tag{6}$$

$$A^- = \text{Min}(a_{ij}) \tag{7}$$

$$E_i = \sum_{j=1}^n W_j \times \frac{(a_{ij})_{\text{Max}} - (a_{ij})}{(a_{ij})_{\text{Max}} - (a_{ij})_{\text{Min}}} \tag{8}$$

$$F_i = \text{Max}^n \sum_{j=1}^n W_j \times \frac{(a_{ij})_{\text{Max}} - (a_{ij})}{(a_{ij})_{\text{Max}} - (a_{ij})_{\text{Min}}} \tag{9}$$

Step 4: Calculate the performance index (PI) values

In order to analyze the ideal criterion, the overall performance index (PI) values for each of the possibilities are determined. The single objective value is converted into multi-objective with considering beneficial parameters and non-beneficial (best and worst) parameters. The PI value is determined by using the following equation.

$$PI_i = u \times \frac{(E_i - \text{Min}(E_i))}{(\text{Max}(E_i) - \text{Min}(E_i))} + (1 - u) \frac{(F_i - \text{Min}(F_i))}{\text{Max}(F_i - \text{Min}(F_i))} \tag{10}$$

For the most part, u is employed as a weighting strategy and its value is set to 0.5. However, its value is typically between 0 and 1.

Finally, using the PI_i values, a constrained ranking of the options is performed. The best options are those with the lowest PI_i value in the ranking. The values of the related criteria are regarded as ideal criteria, relating to the system’s best options [14, 15].

3 Result and Discussion

3.1 Optimization of Green FDM Process Parameters

Optimization of green FDM process parameters is done using Entropy-VIKOR method. Work considered two input parameters like printing temperature (PT) and printing build temperature (PBT) while three output conditions/parameters like particle number concentration (PNC) of size 0.3–10 μm and particle number concentration (PNC) of size 5.6–560 nm and Specific Emission Rates (SERs). The experimentation on FDM process [desktop 3D printing] is performed and experimental data is taken directly from [16]. Two output parameters namely, emission particles in terms of Particle Number Concentration (PNC) and Specific Emission Rates (SERs) were measured in a standardized test chamber. They had obtained the results for Particle Number Concentration (PNC) during the printing process for particulate

Table 1 Experimental data obtained [16]

Exp. No	Input parameters		Output parameters		
	printing temp (PT) in °C	Printing bed temp (PBT) in °C	PNC 0.3–10 μm (#/cm ³)	PNC 5.6–560 nm (#/cm ³)	SER(#/min)
1	275	80	16	3.4×10^5	3.8×10^{10}
2	275	80	17	3.4×10^5	4.3×10^{10}
3	275	80	18	4.4×10^5	6.5×10^{10}
4	275	80	20	2.3×10^5	4.1×10^{10}
5	275	80	22	2.7×10^5	4.5×10^{10}
6	230	80	1	3.3×10^4	4.2×10^9
7	240	80	1	5.0×10^4	8.3×10^9
8	250	80	2	8.7×10^4	2.3×10^{10}
9	260	80	5	7.3×10^5	1.3×10^{11}
10	275	80	15	2.5×10^5	2.9×10^{10}
11	260	80	14	9.9×10^5	1.4×10^{11}
12	254	90	45	7.3×10^5	1.7×10^{11}
13	254	30	27	1.2×10^5	9.7×10^9
14	280	70	1	2.4×10^5	6.5×10^{10}
15	254	30	14	2.1×10^5	2.0×10^9
16	255	80	61	2.4×10^5	3.3×10^9
17	290	105	56	7.0×10^5	7.3×10^{10}

matters of size 0.3–10 μm and 5.6–560 nm and Specific Emission Rates (SERs). The obtained results have been tabulated in Table 1.

During the optimization, the input parameter like printing temperature (PT) and printing build temperature (PBT) with its experimental runs are considered as alternatives while output condition/parameters like particle number concentration (PNC) of size 0.3–10 μm and particle number concentration (PNC) of size 5.6–560 nm and Specific Emission Rates (SERs) are considered as criteria's. First, design of decision matrix is developed using Eq. (1). Here, total 17 experimental runs varying the PT & PBT and corresponding PNC & SER's values are calculated and the results are tabulated in Table 1.

Second, the precise priority weights of each criterion are calculated using entropy method using the Eqs. (2–5). Here, coefficient of variation (g_j) for each of the criteria is first determined using Eqs. (2–4) and this measures the distance of each FDM output parameter in to comparable sequence. Larger the divergence least impact on the performance of FDM process. Later, priority weights of each green FDM parameter or criteria are determined using Eq. (4) and the priority weights (Table 2) obtained are 0.620 for SER, 0.150 for PNC0.3–10 μm, and 0.120 for PNC5.6–560 μm. The results show that priority weight for SER is found to be higher and has greater

Table 2 Priority weight of green FDM criteria/parameters

Criteria's	PNC0.3–10 μm	PNC5.6–560 μm	SER's
Priority weights (w_j)	0.150	0.120	0.620

impact on the green FDM process performance compared to the PNC0.3–10 μm and PNC5.6–560 μm.

Third, calculation of best (A^+), worst (A^-) values followed by E_i and F_i values for each of the green FDM parameters/criteria are done using Eqs. (5–7) and measured the separation distance of each of the FDM parameters/criteria from the comparable values. The results of E_i and F_i values for each of the FDM process parameters are tabulated in Table 3. Fourth, overall preference index (PI_i) for each of the alternatives of green FDM process is calculated using Eq. (8). The single objective value is converted into multi-objective with considering beneficial parameters and non-beneficial (best and worst) parameters of the green FDM parameters and results of the same is tabulated in Table 3.

Lastly, ranking of best alternative for green FDM process is performed based on the values of PI_i . The raking result shows that alternative no or exp. No- 15 is yields least values of PI as 0.203 among the other and exp. No-15 is considered as optimal setting for green FDM process. The optimal setting obtains as PT as 254 °C & PBT as 30 °C and corresponding criteria are PNC0.3–10 μm = 14 #/cm³, PNC5.6–560 μm

Table 3 Ranking of PI_i values of green FDM process

Exp. No.	E_i values	F_i values	PI_i values	Rank
1	0.750	0.738	0.613	11
2	0.733	0.721	0.412	4
3	0.717	0.705	0.712	14
4	0.683	0.672	0.511	5
5	0.650	0.639	0.611	10
6	0.895	0.880	0.715	15
7	0.675	0.664	0.411	3
8	0.983	0.967	0.316	2
9	0.933	0.918	0.516	6
10	0.767	0.754	0.613	12
11	0.783	0.770	0.913	17
12	0.267	0.262	0.604	8
13	0.567	0.557	0.609	9
14	0.894	0.879	0.615	13
15	0.150	0.147	0.203	1
16	0.085	0.084	0.601	7
17	0.083	0.082	0.801	16

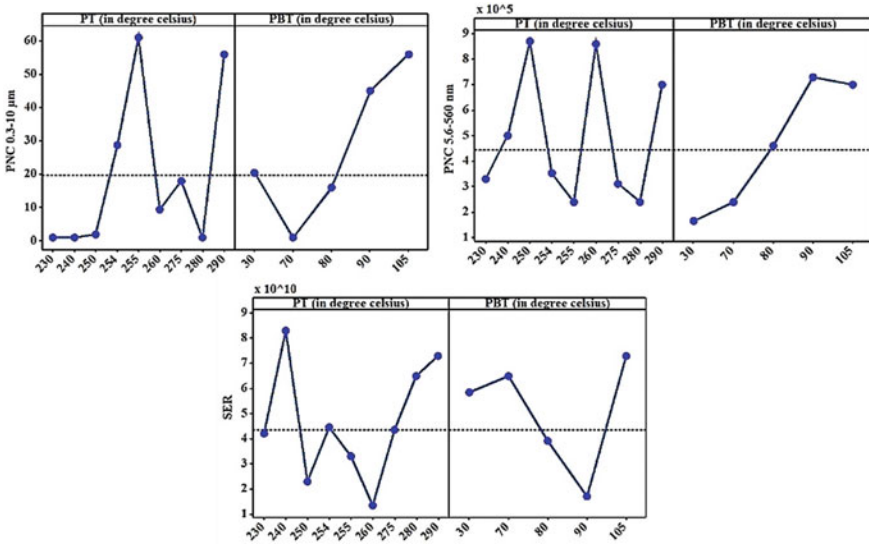


Fig. 1 Main effect plot of PNC and SER

= $2.1 \times 10^9 \text{ \#/cm}^3$ and SER's = 2.0×10^9 . The optimal setting obtained through Entropy-VIKOR provides most optimal output parameters for green FDM process and provides lesser PNC and SER during the printing of parts.

3.2 Parametric Analysis

The influence of input parameters PT and PBT on responses PNC and SER of green FDM process as observed in Fig. 1. The parameter PT increases from 230 to 255 °C then the response variable PNC significantly increases in cases of PNC range of 0.3–10 μm. And also, similar pattern is observed in case of PNC range of 5.6–560 nm. This is due to fact that the un-consumed filament presents in the extruded nozzle. Further, the PNC values are fluctuating in both the cases in between the temperature range of 250–290 °C. This trend occurs due to improper melting temperature of the filament. Moreover, the response PNC in case of range 0.3–10 μm slightly decreases at the PBT temperature increases from 30 to 700 °C, further PNC value significantly increases with increasing the PBT temperature gradually. This phenomenon occurs due to increasing the occupancy of the layers on the bed. In case of response SER increases at the PT rise from 230 to 2400 °C, further SER is drastically decreased at 250 °C and then fluctuates up to 260 °C after that gradually increases up to 290 °C. This is due to fact that, the improper melting of the filament in the extruder nozzle results in higher SER. Moreover, the parameter SER increases slightly at the PBT increases from 30 to 700 °C, then after SER drastically decreases with increasing

the PBT from 70 to 900 °C further increases significantly up 290 °C. This trend may expect due to proper melting of filament at lower and higher temperatures of PBT [17].

4 Conclusions

In this work, environmental factors such as Specific Emission Rates (SER), Particle Number Concentration (PNC) (for 0.3–10 μm and 5.6–560 nm) has been taken into consideration to shift the paradigm of additive manufacturing to green additive manufacturing. Optimization of process parameters of Green FDM process is done using integrated MCDM method, i.e., Entropy coupled with VIKOR methods. Work considered two input parameters like PT, PBT while SER, PNC_{0.3–10 μm}, and PNC_{5.6–560 μm} is considered as output parameters. The optimal setting obtained is exp. No-15 with optimal conditions is PT as 254 °C and PBT as 30 °C and corresponding output conditions are obtained as PNC_{0.3–10 μm} = 14 #/cm³, PNC_{5.6–560 μm} = 2.1×10^5 #/cm³ and SER's = 2.0×10^9 . Additionally, parametric analysis is also performed to find the significant process parameter and found that parameter SER has significant effect on the green FDM process parameter among other parameters. The study suggested that both print temperature and bed temperature play significant role in the emission of particles in additive manufacturing. Also, the proposed integrated method, i.e., Entropy-VIKOR is found feasible and significant in optimizing the green FDM process and can be used as systematic framework model for optimization of another additive manufacturing process.

References

1. Lindemann C, Jahnke U (2017) 11- Modelling of laser additive manufactured product lifecycle costs. Woodhead Publishing Series in Electronic and Optical Materials 281–316
2. Lezak E, Kulinski Z, Masirek R, Piorkowska E, Pracella M, Gadzinowska K (2008) Mechanical and thermal properties of green polylactide composites with natural fillers. *Macromol Biosci* 8:1190–1200
3. Shalwan A, Yousif BF (2013) In state of art: mechanical and tribological behaviour of polymeric composites based on natural fibres. *Mater Des* 48:14–24
4. Kaczmar JW (2007) Pach, J, Kozłowski, R: Use of natural fibres as fillers for polymer composites. *Int Polym Sci Technol* 34(6):45–50
5. Subramaniam SR, Samykano M, Selvamani SK, Ngui WK, Kadigama K, Sudhakar K, Idris MS (2019) Preliminary investigations of polylactic acid (PLA) properties. *AIP Conf Proc* 2059:1–9
6. Liu Z, Lei Q, Xing S (2019) Mechanical characteristics of wood, ceramic, metal and carbon fiber-based PLA composites fabricated by FDM. *J Mater Res Technol* 8:1–11
7. Rao VDP, Rajiv P, Geethika VN (2019) Effect of fused deposition modelling (FDM) process parameters on tensile strength of carbon fibre PLA. *Mater Today Proc* 18:2012–2018
8. Sindhuphak A (2007) Bioproducts of automotive accessories: rethinking design materials through cornstarch, sugarcane and hemp. *KMITL Sci Technol J* 7:160–170

9. Alva ET, Ramdan L, Erdizon RV, Baroroh DK (2017) Optimization of 3D-printer process parameters for improving quality of polylactic acid printed part. *Int J Eng Technol* 9:589–600
10. Dey A, Yodo N (2019) A systematic survey of FDM process parameter optimization and their influence on part characteristics. *J Manuf Mater Process* 3(64):1–30
11. Shirmohammadi M, Goushchi SJ, Keshtiban PM (2021) Optimization of 3D printing process parameters to minimize surface roughness with hybrid artificial neural network model and particle swarm algorithm. *Prog Addit Manuf* 6:199–215
12. Sumalatha M, Malleswara Rao JN, Supraja Reddy B (2021) Optimization of process parameters in 3D printing-fused deposition modeling using taguchi method. *IOP Conf Ser Mater Sci Eng* 1112:1–15
13. Lyu Y, Zhao H, Wen X, Lin L, Schlarb AK, Shi X (2021) Optimization of 3D printing parameters for high-performance biodegradable materials. *J Appl Polym Sci* 138:1–13
14. Çalışkan H, Kursuncu B, Kurbanog C, Güven ŞY (2013) Material selection for the tool holder working under hard milling conditions using different multi criteria decision making methods. *Mater Desi J* 45:473–479
15. El-Santawy MF, El-Dean RA (2012) On using VIKOR for ranking personnel problem mohamed. *Life Sci J* 9:9–11
16. Gu J, Wensing M, Uhde E, Salthammer T (2019) Characterization of particulate and gaseous pollutants emitted during operation of a desktop 3D printer. *Environ Int* 123:476–485
17. Zaman UK, Boesch E, Siadat A, Rivette M, Baqai AA (2019) Impact of fused deposition modeling (FDM) process parameters on strength of built parts using Taguchi's design of experiments. *Int J Adv Manuf Technol* 101:1215–1226

3-D Printing: A Review of Manufacturing Methods, Materials, Scope and Challenges, and Applications



Hiral H. Parikh, Rivaan Jadav, and Praas Joshi

Abstract 3D printing manufacturing technology has garnered a lot of interest in recent years to simplify the fabrication of complex geometries and for its ability to work with a wide range of materials including but not limited to metals, ceramics, polymers, and composites. It also reduces the amount of material required and opens up the scope to print composites that are highly specific to the desired mechanical properties. This review article gives an overview of the common 3D printing methods such as fused deposition modeling, selective laser sintering, stereolithography, and digital light processing. Additionally, it focuses on the 3-D printer materials, the scope of the 3D printed parts and discusses the limitations of each technique in order to encourage further research in this field.

Keywords Selective Laser Sintering (SLS) · Stereolithography (SLA) · Fused Deposition Modeling (FDM) · Digital Light Processing (DLP) · Acrylonitrile Butadiene Styrene (ABS) · Poly Lactic Acid (PLA)

1 Introduction

The additive manufacturing technique started in the late 80s with stereo lithography, which prints layer by layer using a photopolymer that hardens on contact with a laser. Since then, many patents for innovative and distinct techniques have been filed and the subsequent advancement in the technologies have been developed and commercialized [1]. 3D printing uses the STL (Surface Tessellation Language) file prepared by a CAD software to instruct the 3D printer to print the commodity normally layer by layer [2]. Thermoplastic polymers like polylactic acid (PLA), acrylonitrile butadiene styrene (ABS), polyamide (PA), polycarbonate (PC), tetraethyl orthosilicate (TEOS), and polyphenylsulfone (PPSF) [3–5] are commonly used polymer materials in 3D printing. These materials have their applications in various sectors including medical, automobile, and manufacturing industries. Although these materials have

H. H. Parikh (✉) · R. Jadav · P. Joshi
Department of Mechanical Engineering, School of Engineering and Technology, Navrachana University, Vadodara 391410, India
e-mail: dollyshah_3@yahoo.com

limited mechanical properties and less sustainability which pave the way for 3D printed composites, which take advantage of combining several materials to tailor highly specific desired mechanical properties which are normally not found in a single material. Additionally, reducing wastage while fabricating the same. In the past several years there has been significant work noted in the 3D printing of composites. This research article summarizes the different 3D manufacturing processes, working with various materials and their composites in terms of their advantages, limitations, and applications.

2 Types of 3 D Printing

Various types of expertise in 3D printing methods have been invented since 1970. Earlier, the printers were very huge and costly in terms of production, but over time and with significant technological advancement, a large number of additive manufacturing processes are now in use like stereolithography (SLA), selective laser sintering (SLS), fused deposition modeling (FDM), Digital light processing (DLP), etc.

2.1 Selective Laser Sintering (SLS)

The selective laser sintering is an additive manufacturing process (shown in Fig. 1) wherein which minute particles of polymers, metals, ceramics, and a large variety of

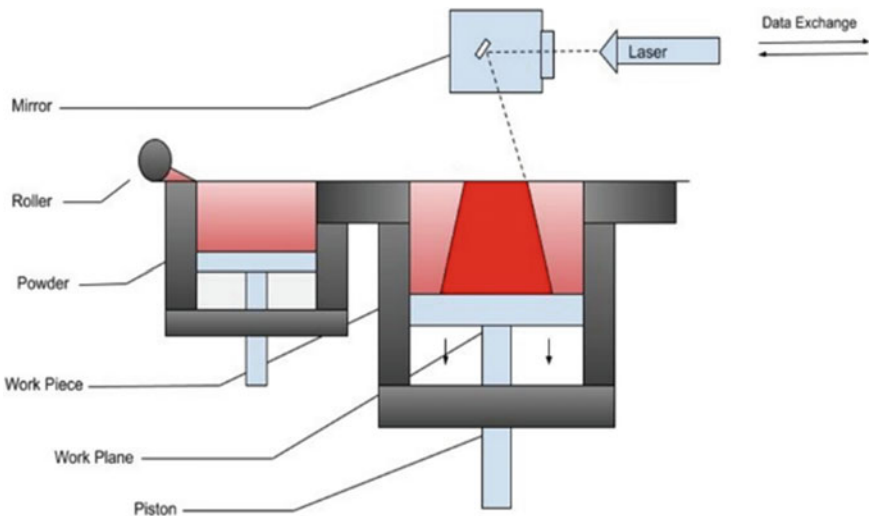


Fig. 1 Working of selective laser sintering process

composites are heated to just below its melting temperature and then sintered by a powerful CO₂ laser. The material is supplied in the form of a powder by a roller and occasionally contains a sacrificial binder polymer that has to be deboned afterward. The laser traces the cross-section of the final product to be formed on the powdered layer, immediately fusing the powdered particles together forming a hard layer. Once the layer is produced, the roller supplies another layer with powder and the process is continued until the final product is formed [6].

2.2 Stereolithography (SLA)

Stereolithography is a versatile additive manufacturing process belonging to the vat polymerization family wherein the photopolymer in a liquid state is subjected to point ultraviolet (UV) radiation. The working of SLA is illustrated in Fig. 2. The material is kept at a distance of one-layer height. The point source UV light from the laser traces the cross-sectional area of the workpiece and selectively cures and solidifies the layer by predetermined path using Galvos. Once the first layer is formed the elevator creates space for another layer and the sweeper blade recoats the surface. This is repeated till the final product is formed.

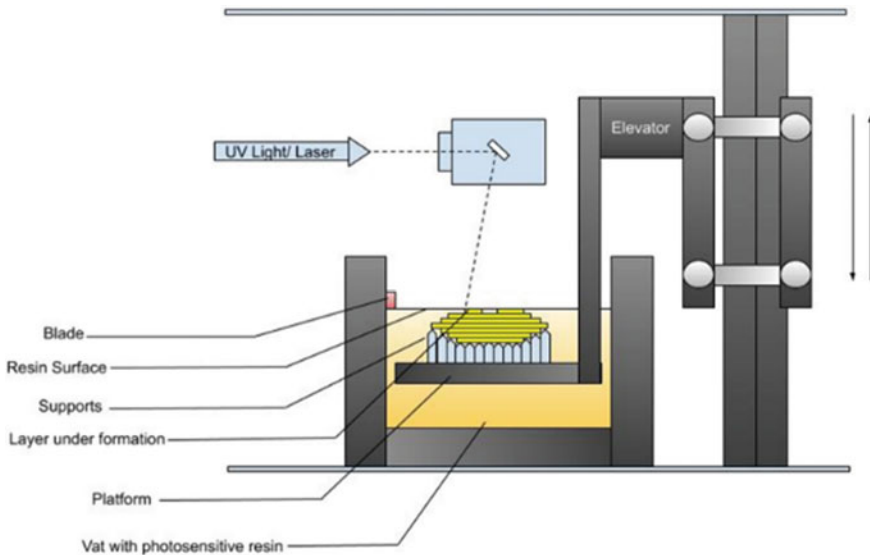


Fig. 2 Working of stereolithography

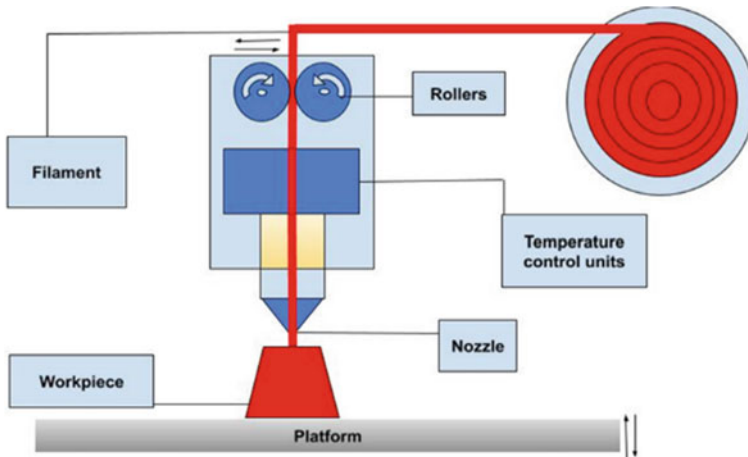


Fig. 3 Working of fused deposition modeling

2.3 Fused Deposition Modeling (FDM)

In the Fused Deposition Modeling (FDM) technique the material is added layer by layer to form a specified model. The most commonly used materials in fused deposition modeling are Acrylonitrile Butadiene Styrene (ABS) and Polylactic Acid (PLA). This process is also called Fused Filament Fabrication (FFF). The 3D printer that works in FDM consists of a platform, nozzle, and raw materials in filament form as shown in Fig. 3. The continuous filament of thermoplastic material is passed with the help of rollers to the extruder where the temperature is just enough to melt the filament. It is then passed through a nozzle to be deposited precisely layer by layer on the preheated platform.

2.4 Digital Light Processing (DLP)

Digital Light Processing uses the digital mirror device to reflect the emitted light onto the platform submerged in photopolymer resin. DLP uses a digital light projector to flash the figure of each layer at once. The 3D printer which works on the DLP consists of a light source, lens, reservoir, photopolymer resin, platform, and digital mirror device as shown in Fig. 4. In this technique, the material is used in resin form. Initially, light is emitted from the light source and passes to the digital mirror device (DMD) which reflects the emitted light to the lens. Through the lens, the emitted light falls on the reservoir which contains the photopolymer resin. As the light touches the photopolymer it hardens and solidifies. Once one layer has hardened, the platform rises up, creating space for the liquid resin to flow in that area and prepare it for another layer. The process continues until the model is fabricated.

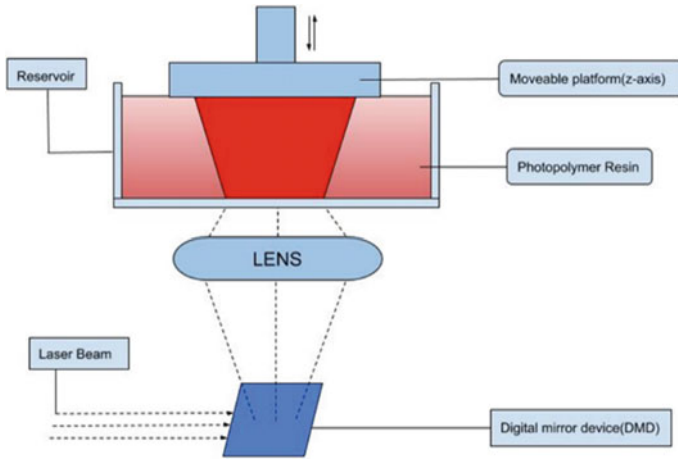


Fig. 4 Working of digital light processing

3 Survey on Materials and Its Mechanical Characterization

3D printing techniques require high-quality materials that can manufacture a high-quality product. Impurities in the material can affect the mechanical characteristics of final product drastically. A wide range of materials has been tested for their compatibility to be used in 3D printing. Different 3D printing methods are capable to develop fully functional parts in a wide range of materials: metal, ceramic, polymer, or composites. This section covers the material used and its mechanical parameters identified by different researchers for different 3D printing techniques.

3.1 Research Survey on SLS Technique

Since Carl Deckard invented the method, many researchers have worked on the SLS technique using metals, ceramics, polymers, and composites as base material. Some of the detailed work done on the SLS process is listed:

In the late 90s Subramanian et al. [7] used Al₂O₃ & Polymer Binder and conducted density, porosity, and internal strength tests and the author found that 3D printed Alumina bars with 50% relative densities had interconnected porosity, and strengths between 2 and 8 MPa. In the early twentieth century Tolochko et al. [8], Tan et al. [9], Kruth et al. [10], and Tang et al. [11] used materials like Ti Powder, PEEK and HA, Polymers, and Silica sand, respectively to analyze the microstructure and mechanical strength of the printed materials. All the studies came to the same conclusion that the SLS is an effective way to manufacture the materials for a specific application. Cormier et al. [12] and Childs et al. [13] have used steel material for the SLS technique to analyze the microstructural properties. Fan et al [14] have used

Bisphenol polycarbonate (PC) powder to study the material movement mechanism. Many researchers have worked on metal particles like Ti–6Al–4V; Co–Cr–Mo, Ti–6Al–7Nb, Inconel 625 [15–21] and conducted studies on the surface roughness, microstructure, porosity, and mechanical strength of the material. These studies revealed that the material properties depend on the powder morphology and SLS can be used for high-temperature application parts. Zarringhalam et al. [22] have worked on Nylon—12 and checked the amount of energy input in the SLS process affects the degree of melting with Differential scanning calorimeter and optical microscopy images. Dotchev and Yusoff [23] used Polyamide -12 material and artificially aged powder tested using the melt flow rate indexer for Consistent quality and efficiency. Khan and Dickens [24] has worked on Gold Powder. The author has checked for Tap density, Particle Size Distribution (PSD), and reflectance tests and concluded that reduced layer thickness had a small effect on density with less porosity at optimal scan speed. Thijs L et al. [25] have used Ti–6Al–4V in the SLS technique and observed the microstructure of the material using optical microscopy by varying the parameters.

Many researchers have used steel powder [26–30], Nylon [31], Titanium [32–34], Ceramic and Al oxide [35, 36], and composite materials [37] for the SLS technique and observed the microstructure of the final product and various properties of the same.

3.2 Research Survey on SLA Technique

This technique gained focus in the early twentieth century. Many researchers have worked on the SLA technique. They mainly used ceramic and polymer compounds to produce the parts.

Kataria and Rosen [38], Sá Ribeiro et al. [39], Chockalinga et al. [40] have used Photopolymer Resin and conducted tensile, yield, and impact tests on the material and developed Empirical relationships between the process parameters and the part strength through their design of experiments. The studies showed new applications in stereolithography. Esposito Corcione et al. [41] have used silica and evaluated the tensile strength of the material. The author revealed the average tensile strength was 55.2 MPa. Chockalingam K et al. [42] has performed tensile, yield, and impact strength test on Photopolymer Resin-based developed material and concluded that the strength is more when the layer is smaller. Xu et al. [43] have Experimentally determined to cure length and width with a ratio of laser power and scanning speed for the Photopolymer resin material. Bens et al. [44] have performed a strength test on Polyester (meth) acrylate-based resin material and concluded low young's modulus opening doors for novel soft engineering material in rapid prototyping. Many other researchers have worked on the Photopolymer resin SLS process [45–48] to check for Tradeoff between accuracy and process time, the force required to remove workpiece, and Electronics Structure Manufacturing. Zhou et al. [49] created different parts using ceramic material and concluded that Novel ceramic SLA uses aqueous ceramic suspension.

3.3 *Research Survey on FDM Technique*

Many researchers have worked on the FDM technique and evaluated the properties of the final product by varying various operating and material parameters. The exclusive research done by researchers has been summarized in this section:

Li et al. [50], Ahn et al. [51] have produced 3D printed material from ABS and conducted a tensile and compressive test on the material and noted that the tensile strength of the ABS was found in the range of 65–72, and the compressive strength was noted higher than the tensile strength. Li et al. [52], Ahn et al. [53] manufactured 3D printed material and observed dimensional stability of the material. Wang et al. [54] have done mechanical and structural analysis on Poly- ϵ -Caprolactone (PCL). El-Katatny et al. [55], Bagsik et al. [56] have worked on ABS and observed that fabrication accuracy is affected by the part dimensions. Many researchers have worked on Acrylonitrile butadiene styrene (ABS) polymers and produced 3D printed material from ABS filament by varying the different operating parameters. Tensile, compressive, dimensional analysis, and structural analysis test was conducted and properties of the material were observed and noted [57–73]. To take the advantage of combining a few properties which normally are not found in one single material, composites are being researched heavily in the present day. Many studies revealed the use of composite filament in 3D printing [74–79]. Many researchers also used PLA material for 3D printing and tested material for tensile tests, dynamic response, flexural tests, and electrical conductivity tests [80–85]

3.4 *Digital Light Processing (DLP)*

Many researchers have worked on the digital light processing method with a photopolymer resin material and evaluated its performance by conducting resolution tests, image quality tests, and lighting conditions [86–92] for various applications like estimated values of the crop, soil cover unaffected by lightning conditions, evaluation of local sharpness in an image, etc. Dean et al [93] used Propylene fumarate (PPF) and titanium dioxide (TiO₂) as a dye to produce a highly accurate product. ABS & PLA were used by Leigh et al. [94] and performed an electrical conductivity test on the material. Huang et al. [95] used photopolymer resin and performed a meta-analysis, Boyat and Joshi [96] worked on Photopolymer resin and analyzed the noise model using Probability Density Function (PDF). Patel et al. [97] used Elastomer polymer resin and conducted a mechanical characterization test, Ansari Moin et al. [98] used Zirconium and analyzed the tooth model using optical scanning technology. Mu et al. [99] worked on multi-walled carbon nanotubes (MWCNTs) and performed electrical conductivity tests and strength tests. Zhao et al. [100] used Grayscale printed polymer sheets and performed self-holding and recovery tests.

Kim et al. [101] worked on Sil-MA hydrogel and checked mechanical and rheological properties. All the researches show the scope of many different materials for digital light processing technique.

4 Scope and Challenges of 3D Printing Techniques

Stereolithography is a very versatile fabrication technique. Since it can produce parts with high accuracy and intricate details there is the liberty of designing and printing custom highly specific arrangements which indicate its strong scope in biomedical applications. It can produce smooth, clear, and flexible parts with good mechanical properties; however, the visual appearance and properties may degrade over time if the parts are exposed to sunlight. Further post-processing and support structures are a necessity for this process which often imparts to comparatively higher cost and processing time.

Selective Laser Sintering holds an important place among other rapid prototyping techniques due to its ability to 3D print about any material that is in the form of powder, be it metals, alloys, ceramics, polymers, composites, and even sand. SLS does not require any support and hence complex geometries can be easily produced, it also has good near-isotropic mechanical properties, making it the most preferred method to produce functional parts and prototypes. The quality of laser-sintered parts, however, depends greatly on the process parameters, even including the type of laser and powder composition. This is due to its dependence on the laser-material interaction. The SLS parts have a coarse finish and porosity despite higher lead times and hence usually require post-processing methods.

Fused Deposition Modeling (FDM) is the most widely used 3D printing technique among them all due to its low production cost of complex end-use parts and ease and speed of making a prototype. This technique is widely used for rapid prototyping and has been widely commercialized. This technique has few but drawbacks in terms of lower dimensional accuracy and poor finishing of the end product. Post-processing is required for a smooth surface finish.

Since DLP-based projectors produce intricate details of the product with high accuracy and clearly structured geometry, Jewelry, medical and dentistry industries were one of the first industries to adopt this technology to easily build wax molds for highly complex designs. The major drawback of this method is the final product cannot be subjected to sunlight and have a risk of deteriorating over time, also it is quite expensive and is not feasible for general purposes.

5 Applications of 3D Printing Techniques

The use of 3D printing, manufacturing techniques has gained a lot of interest in the present days, due to the ease of manufacturing complex geometry, economical energy requirement, less wastage of resources [102], and lightweight output. 3D printing is widely used in the aerospace industry, automotive industry, health sectors, medical industry, structural industry, and electrical and electronic industry due to the manufacturing flexibility in terms of variety of materials, including metals, alloys,

ceramics, polymers, and composites. The lightweight 3D printed parts have high replicability and accuracy of the parts making it highly convenient to change 1 parameter and test for performance, this makes it more preferable for aerospace applications as rapid prototyping is an integral part in such an industry. The first 3D printed car was produced by local motor in 2014, and it is extended to produce a 3D printed bus called OLLI. Big automobile companies like Ford, BMW, AUDI also apply 3D printing technology to manufacture various complex engine parts to improve the engine performance and eliminate even minute vibrations cause due to slightly dissimilar engine components. 3D printing technique is also used widely in health sectors and medical industry to print dentures, skin, bones, cartilage, and even functional organs. Additionally, 3D printing is used for cancer research, drug, and pharmaceutical research as well. [103]. 3D printing technology has also recently been used to print an entire building and a bridge, this technique can transform the idea into reality at highly economical rates and without a lot of manpower. Examples of 3D-printed buildings are Apis Cor Printed House in Russia [104] and Canal House in Amsterdam [105].

Nowadays, due to the expansion of green electronic devices and more emphasis on reducing the carbon footprint, reducing/recycling waste relatively less production cost, 3D printers and the technology behind it is instantly in demand to address the environmental concerns in today's society [106]. Lately different 3D printing technologies have been even used to produce electronic devices like active electronic materials, electrodes, and devices with mass customization and adaptive designs by embedding the conductors into 3D printed devices [107].

6 Summary

3D printed objects are fabricated using additive processes which are opposite of subtractive manufacturing where the object is cut down to achieve the final product. In an additive process, the object is manufactured layer by layer until the object is created, and hence is a really effective, economical, and precise way to manufacture. There are a variety of additive manufacturing techniques, which were explored in this review paper which have a promising future ahead. Various advances and existing developments were also looked into with an aim to contribute and help readers have a better understanding about 3D printing, predict tangible possibilities, help generate innovative ideas from the listed limitations, and promote more research in this field.

- **Cost Limitation:** To commercialize the 3D printers, the cost factor has to be reduced so that rapid prototyping and manufacturing can be done extensively, currently the 3D printers commercially available and affordable are majorly FDM type printers and lack variety according to the functionality requirements. Functional parts manufactured cost a lot and hence other methods apart from additive manufacturing are used. Further, due to higher lead times, the power needed to run the machine is more, and hence more cost is inhibited. If these costs are

reduced during future research, additive manufacturing will revolutionize the manufacturing industry.

- **Performance Limitation:** The stringent process parameters for optimal performance is a necessary evil in additive manufacturing, which leads to higher manufacturing time, resulting in inefficient bulk production. Adding to the problem post-processing of these manufactured products due to poor surface finish, etc. takes additional techniques, time, and cost, further slowing down the process. The need for support during manufacturing is inevitable, which consumes additional material, energy, and time. Scope in reducing these factors can have a drastic effect to promote and recognize the true potential of additive manufacturing.

References

1. Levy GN, Schindel R, Kruth JP (2003) Rapid manufacturing and rapid tooling with layer manufacturing (LM) technologies, state of the art and future perspectives. *CIRP Ann Manuf Technol* 52(2):589–609
2. Standard A (2012) Standard terminology for additive manufacturing technologies. West Conshohocken, Pa, USA: ASTM Int
3. Ahn SH, MonteroM, Odell D et al (2002) Anisotropic material properties of fused deposition modeling ABS. *Rapid Prototyping J* 8:248–257
4. Tymrak B, Kreiger M, Pearce J (2014) Mechanical properties of components fabricated with open-source 3-D printers under realistic environmental conditions. *Mater Des* 58:242–246
5. Caulfield B, McHugh P, Lohfeld S (2007) Dependence of mechanical properties of polyamide components on build parameters in the SLS process. *J Mater Process Technol* 182(1):477–488
6. Goodridge R, Shofner M, Hague R, McClelland et al (2011) Processing of a Polyamide-12/carbon nanofibre composite by laser sintering. *Polym Test* 30(1):94–100
7. Subramanian K, Vail N, Barlow J, Marcus H (1995) Selective laser sintering of alumina with polymer binders. *Rapid Prototyping J* 1(2):24–35
8. Tolochko NK, Arshinov MK, Gusarov AV et al (2003) Mechanisms of selective laser sintering and heat transfer in Ti powder. *Rapid Prototyping J* 9(5):314–326
9. Tan KH, Chua CK, Leong KF et al (2003) Scaffold development using selective laser sintering of poly(etheretherketone)-hydroxyapatite biocomposite blends. *Biomaterials* 24(18):3115–3123
10. Kruth JP, Wang X, Laoui T et al (2003) Lasers and materials in selective laser sintering. *Assem Autom* 23(4):357–371
11. Tang Y, Fuh JYH, Loh HT et al (2003) Direct laser sintering of a silica sand. *Mater Des* 24(8):623–629
12. Cormier D, Harrysson O, West H (2004) Characterization of H13 steel produced via electron beam melting. *Rapid Prototyping J* 10(1):35–41
13. Childs THC, Hauser C, Badrossamay M (2005) Selective laser sintering (melting) of stainless and tool steel powders: experiments and modelling. *Proc Inst Mech Eng Part B J Eng Manuf* 219(4):339–357
14. Fan KM, Cheung WL, Gibson I (2005) Movement of powder bed material during the selective laser sintering of bisphenol-A polycarbonate. *Rapid Prototyping J* 11(4):188–198
15. Liao HT, Shie JR (2007) Optimization on selective laser sintering of metallic powder via design of experiments method. *Rapid Prototyping J* 13(3):156–162
16. Lamikiz A, Sanchez JA, de Lacalle LL et al (2007) Laser polishing of parts built up by selective laser sintering. *Int J Mach Tools Manuf* 47(12–13):2040–2050

17. Vandenbroucke B, Kruth JP (2007) Selective laser melting of biocompatible metals for rapid manufacturing of medical parts. *Rapid Prototyping J* 13(4):196–203
18. Mumtaz KA, Erasenthiran P, Hopkinson N (2008) High density selective laser melting of Waspaloy. *J Mater Process Technol* 195(1–3):77–87
19. Sercombe T, Jones N, Day R, Kop A (2008) Heat treatment of Ti-6Al-7Nb components produced by selective laser melting. *Rapid Prototyping J* 14(5):300–304
20. Fan KM, Cheung WL, Gibson I (2008) Fusion behavior of TrueFormTM/SiO₂ composite powders during selective laser sintering. *Rapid Prototyping J* 14(2):87–94
21. Mumtaz K, Hopkinson N (2009) Top surface and side roughness of Inconel 625 parts processed using selective laser melting. *Rapid Prototyping J* 15(2):96–103
22. Zarringhalam H, Majewski C, Hopkinson N (2009) Degree of particle melt in Nylon-12 selective laser-sintered parts. *Rapid Prototyping J* 15(2):126–132
23. Dotchev K, Yusoff W (2009) Recycling of polyamide 12 based powders in the laser sintering process. *Rapid Prototyping J* 15(3):192–203
24. Khan M, Dickens P (2010) Selective Laser Melting (SLM) of pure gold. *Gold bulletin* 43(2):114–121
25. Thijs L, Verhaeghe F, Craeghs T et al (2010) A study of the micro structural evolution during selective laser melting of Ti-6Al-4V. *Acta Mater* 58(9):3303–3312
26. Yasa E, Kruth J (2011) Application of laser re-melting on Selective laser melting parts. *Adv Prod Eng Manage* 6(4):259–270
27. Yan C, Hao L, Hussein A, Raymont D (2012) Evaluations of cellular lattice structures manufactured using selective laser melting. *Int J Mach Tools Manuf* 62:32–38
28. Abd-Elghany K, Bourell DL (2012) Property evaluation of 304L stainless steel fabricated by selective laser melting. *Rapid Prototyping J* 18(5):420–428
29. Dadbakhsh S, Hao L, Sewell N (2012) Effect of selective laser melting layout on the quality of stainless steel parts. *Rapid Prototyping J* 18(3):241–249
30. Averyanova M, Cicala E, Bertrand P, Grevey D (2012) Experimental design approach to optimize selective laser melting of martensitic 17–4 PH powder: part I—single laser tracks and first layer. *Rapid Prototyping J* 18(1):28–37
31. Telenko C, Conner Seepersad C (2012) A comparison of the energy efficiency of selective laser sintering and injection molding of nylon parts. *Rapid Prototyping J* 18(6):472–481
32. Van der Stok J, Van der Jagt OP, Amin Yavari S et al (2013) Selective laser melting-produced porous titanium scaffolds regenerate bone in critical size cortical bone defects. *J Orthop Res* 31(5):792–799
33. Rickenbacher L, Etter T, Hövel S, Wegener K (2013) High temperature material properties of IN738LC processed by selective laser melting (SLM) technology. *Rapid Prototyping J* 19(4):282–290
34. Fu CH, Guo YB (2014) Three-dimensional temperature gradient mechanism in selective laser melting of Ti-6Al-4V. *J Manuf Sci Eng* 136(6):0610041–0610047
35. Wilkes J, Hagedorn YC, Meiners W, Wissenbach K (2013) Additive manufacturing of ZrO₂-Al₂O₃ ceramic components by selective laser melting. *Rapid Prototyping J* 19(1):51–57
36. Weingarten C, Buchbinder D, Pirch N, Meiners W et al (2015) Formation and reduction of hydrogen porosity during selective laser melting of AlSi10Mg. *J Mater Process Technol* 221:112–120
37. Yap CY, Chua CK, Dong ZL et al (2015) Review of selective laser melting: materials and applications. *Appl Phys Rev* 2(4):041101
38. Kataria A, Rosen DW (2001) Building around inserts: methods for fabricating complex devices in stereolithography. *Rapid Prototyping J* 7(5):253–262
39. Sá Ribeiro Jr, A., Hopkinson, N., & Henrique Ahrens, C.: Thermal effects on SAL tools during injection moulding. *Rapid Prototyping Journal* 10(3), 176–180 (2004).
40. Chockalingam K, Jawahar N, Ramanathan KN, Banerjee PS (2006) Optimization of stereolithography process parameters for part strength using design of experiments. *Int J Adv Manuf Technol* 29(1–2):79–88

41. Esposito Corcione C, Montagna F, Greco A, Licciulli A et al (2006) Free form fabrication of silica moulds for aluminium casting by stereolithography. *Rapid Prototyping J* 12(4):184–188
42. Chockalingam K, Jawahar N, Chandrasekhar U (2006) Influence of layer thickness on mechanical properties in stereolithographic. *Rapid Prototyping J* 12(2):106–113
43. Xu G, Zhao W, Tang Y, Lu B (2006) Novel stereolithographic system for small size objects. *Rapid Prototyping J* 12(1):12–17
44. Bens A, Seitz H, Bermes G et al (2007) Non-toxic flexible photopolymers for medical stereolithography technology. *Rapid Prototyping J* 13(1):38–47
45. Limaye AS, Rosen DW (2007) Process planning method for mask projection micro-stereolithography. *Rapid Prototyping J* 13(2):76–84
46. Campbell I, Combrinck J, de Beer D, Barnard L (2008) Stereolithography build time estimation based on volumetric calculations. *Rapid Prototyping J* 14(5):271–279
47. Joe Lopes A, MacDonald E, Wicker RB (2012) Integrating stereolithography and direct print technologies for 3D structural electronics fabrication. *Rapid Prototyping J* 18(2):129–143
48. Zhou C, Chen Y, Yang Z, Khoshnevis B (2013) Digital material fabrication using mask-image-projection-based stereolithography. *Rapid Prototyping J* 19(3):153–165
49. Zhou W, Li D, Wang H (2010) A novel aqueous ceramic suspension for ceramic stereolithography. *Rapid Prototyping J* 16(1):29–35
50. Li L, Sun Q, Bellehumeur C, Gu, P (2001) Composite modeling and analysis of FDM prototypes for design and fabrication of functionally graded parts. In: *Solid freeform fabrication symposium*, pp 187–194
51. Ahn SH, Montero M, Odell D, Roundy S et al (2002) Anisotropic material properties of fused deposition modeling ABS. *Rapid Prototyping J* 8(4):248–257
52. Li L, Sun Q, Bellehumeur C, Gu P (2002) Composite modeling and analysis for fabrication of FDM prototypes with locally controlled properties. *J Manuf Process* 4(2):129–141
53. Ahn SH, Lee CS, Jeong W (2004) Development of translucent FDM parts by post-processing. *Rapid Prototyping J* 10(4):218–224
54. Wang F, Shor L, Darling A, Khalil S et al (2004) Precision extruding deposition and characterization of cellular poly- ϵ -caprolactone tissue scaffolds. *Rapid Prototyping J* 10(1):42–49
55. El-Katatny I, Masood SH, Morsi YS (2010) Error analysis of FDM fabricated medical replicas. *Rapid Prototyping J* 16(1):36–43
56. Bagsik A, Schöppner V, Klemp, E (2010) FDM part quality manufactured with Ultem® 9085. In: *14th international scientific conference on polymeric materials 15*, pp 307–315
57. Mireles J, Adame A, Espalin D, Medina F et al (2011) Analysis of sealing methods for FDM-fabricated parts. In: *Proceeding from solid free-form fabrication symposium*, pp 185–196
58. Dudek P (2013) FDM 3D printing technology in manufacturing composite elements. *Arch Metall Mater* 58(4):1415–1418
59. Gajdoš I, Slota J (2013) Influence of printing conditions on structure in FDM prototypes. *Tehnički vjesnik* 20(2):231–236
60. Jami H, Masood SH, Song WQ (2013) Dynamic response of FDM made ABS parts in different part orientations. *Adv Mater Res* 748:291–294
61. Sa'ude N, Masood SH, Nikzad M, Ibrahim M et al (2013) Dynamic mechanical properties of copper-ABS composites for FDM feedstock. *Int J Eng Res Appl* 3(3):257–1263
62. Raut JY, Pfahnl AC (2014) 3D printing of surgical instruments for long-duration space missions. *Aviat Space Environ Med* 85(7):758–763
63. Raut S, Jatti VS, Khedkar NK et al (2014) Investigation of the effect of built orientation on mechanical properties and total cost of FDM parts. *Proc Mater Sci* 1625–1630
64. Jumani MS, Shaikh S, Shah SA (2014) Fused deposition modelling technique (Fdm) for fabrication of custom-made foot orthoses: a cost and benefit analysis. *Sci Int* 26(5)
65. Mishra SB, Mahapatra SS (2014) Improvement in tensile strength of FDM built parts by parametric control. *Appl Mech Mater* 592:1075–1079
66. Oskui SM, Diamante G, Liao C (2015) Assessing and reducing the toxicity of 3D-printed parts. *Environ Sci Technol Lett* 3(1):1–6

67. Satyanarayana B, Prakash KJ (2015) Component replication using 3D Printing technology. *Proc Mater Sci* 10:263–269
68. Belter JT, Dollar AM (2015) Strengthening of 3D printed fused deposition manufactured parts using the fill compositing technique. *PLoS ONE* 10(4):0122915
69. Ambrosi A, Pumera M (2016) 3D-printing technologies for electrochemical applications. *Chem Soc Rev* 45(10):2740–2755
70. Melenka GW, Cheung BK, Schofield JS (2016) Evaluation and prediction of the tensile properties of continuous fiber-reinforced 3D printed structures. *Compos Struct* 153:866–875
71. Witowski JS, Coles-Black J, Zuzak et al (2016) 3D printing in liver surgery: a systematic review. *Telemedicine e-Health* 23(12):943–947
72. Singh R, Singh S, Singh IP et al (2017) Investigation for surface finish improvement of FDM parts by vapor smoothing process. *Compos B Eng* 111:228–234
73. Sharma R, Singh R, Penna R (2018) Investigations for mechanical properties of Hap, PVC and PP based 3D porous structures obtained through biocompatible FDM filaments. *Compos B Eng* 132:237–243
74. Cerneels J, Voet A, Ivens J et al (2013) Additive manufacturing of thermoplastic composites. *Composites Week Leuven*, 1–7
75. Matsuzaki R, Ueda M, Namiki M, Jeong TK et al (2016) Three-dimensional printing of continuous-fiber composites by in-nozzle impregnation. *Sci Rep* 6:23058
76. Chai X, Chai H, Wang X, Yang J et al (2017) Fused deposition modeling (FDM) 3D printed tablets for intragastric floating delivery of domperidone. *Sci Rep* 7(1):2829
77. Gnanasekaran K, Heijmans T, Van Bennekom S et al (2017) 3D printing of CNT-and graphene-based conductive polymer nano composites by fused deposition modeling. *Appl Mater Today* 9:21–28
78. Yang C, Tian X, Liu T et al (2017) 3D printing for continuous fiber reinforced thermoplastic composites: mechanism and perf. *Rapid Prototyping J* 23(1):209–215
79. Ning F, Cong W, Hu Y et al (2017) Additive manufacturing of carbon fiber-reinforced plastic composites using fused deposition modeling: Effects of process parameters on tensile properties. *J Compos Mater* 51(4):451–462
80. Lužanin O, Movrin D, Plančak M (2014) Effect of layer thickness, deposition angle, and infill on maximum flexural force in FDM-built specimens. *J Technol Plast* 39(1):49–58
81. Jiang C, Zhao GF (2015) A preliminary study of 3D printing on rock mechanics. *Rock Mech Rock Eng* 48(3):1041–1050
82. Okwuosa TC, Stefaniak D, Arafat B et al (2016) A lower temperature FDM 3D printing for the manufacture of patient-specific immediate release tablets. *Pharm Res* 33(11):2704–2712
83. Afrose MF, Masood SH, Iovenitti P et al (2016) Effects of part build orientations on fatigue behaviour of FDM-processed PLA material. *Prog Addit Manuf* 1(1–2):21–28
84. Zhang J, Feng X, Patil H et al (2017) Coupling 3D printing with hot-melt extrusion to produce controlled-release tablets. *Int J Pharm* 519(1–2):186–197
85. Okwuosa TC, Pereira BC, Arafat B (2017) Fabricating a shell-core delayed release tablet using dual FDM 3D printing for patient-centred therapy. *Pharm Res* 34(2):427–437
86. Hornbeck LJ (1997) Digital light processing for high-brightness high-resolution applications. *Int Soc Opt Photonics* 3013:27–41
87. Nesbitt RS, Smith SL, Molnar RA (1999) Holographic recording using a digital micromirror device. *Int Soc Opt Photonics* 3637:12–21
88. Yokoyama R, Shirasawa M, Pike RJ (2002) Visualizing topography by openness: a new application of image processing to digital elevation models. *Photogramm Eng Remote Sens* 68(3):257–266
89. Rasmussen J, Nørremark M, Bibby (2007) Assessment of leaf cover and crop soil cover in weed harrowing research using digital images. *Weed Res* 47(4):299–310
90. Winder RJ, Morrow PJ, McRitchie IN (2009) Algorithms for digital image processing in diabetic retinopathy. *Comput Med Imaging Graph* 33(8):608–622
91. Goldsmith NT (2011) Deep focus; a digital image processing technique to produce improved focal depth in light microscopy. *Image Anal Stereology* 19(3):163–167

92. Chow CW, Yeh CH, Liu Y (2012) Digital signal processing for light emitting diode based visible light communication. *IEEE Photon Soc Newslett* 26(5):9–13
93. Dean D, Wallace J, Siblani A et al (2012) Continuous digital light processing (cDLP): highly accurate additive manufacturing of tissue engineered bone scaffolds: *Virtual Phys Prototyping* 7(1):13–24
94. Leigh SJ, Bradley RJ, Purssell CP (2012) A simple, low-cost conductive composite material for 3D printing of electronic sensors. *PLoS ONE* 7(11):49365
95. Huang Q, Yang X, Gao B et al (2014) Application of DMSP/OLS nighttime light images: a meta-analysis and a systematic literature review. *Remote Sens* 6(8):6844–6866
96. Boyat AK, Joshi BK (2015) A review paper: Noise models in digital image processing. *Int J (SIPIJ)* 6(2):63–75
97. Patel DK, Sakhaei AH, Layani M (2017) Highly stretchable and UV curable elastomers for digital light processing based 3D printing. *Adv Mater* 29(15):1606000
98. Anssari Moin D, Hassan B, Wismeijer D A novel approach for custom three-dimensional printing of a zirconia root analogue implant by digital light processing. *Clin Oral Implants Res* 28(6):668–670
99. Mu Q, Wang L, Dunn CK (2017) Digital light processing 3D printing of conductive complex structures. *Addit Manuf* 18:74–83
100. Zhao Z, Wu J, Mu X (2017) Desolvation induced origami of photocurable polymers by digit light processing. *Macromol Rapid Commun* 38(13):1600625
101. Kim SH, Yeon YK, Lee JM et al (2018) Precisely printable and biocompatible silk fibroin bioink for digital light processing 3D printing. *Nat Commun* 9(1):1620
102. Joshi SC, Sheikh (2015) 3D-printing in aerospace and its long-term sustainability. *Virtual Phys Prototyping* 10(4):175–185
103. Bogue R (2013) 3D printing: the dawn of a new era in manufacturing? *Assem Autom* 33(4):307–311
104. Sakin M, Kiroglu YC (2017) 3D printing of buildinga: construction of the sustainable houses of the future by BIM. *Energy Proc* 134:702–711
105. Hager I, Golonka A, Putanowicz R (2016) 3D printing of building components as the future of sustainable construction?. *Proc Eng* 151:292–299
106. Foo CY, Lim HL, Mahdi MA., Wahid MH, Huang NM (2018) Three-dimensional printed electrode and its novel applications in electronic devices. *Scientific Report* (1), 1–11
107. Jeongwoo L, Kim HC, Choi JW, Lee IH (2018) A review on 3D printed smart devices for 4D printing. *Int J Precis Eng Manuf Green Technol* 4(3):373–383

Influence of Infill Parameters on Flexural Properties of Bio-inspired Additively Manufactured Specimen



Mahesh Naik , M. C. Abhilash, and D. G. Thakur

Abstract In the recent period, FDM is selected as an efficient additive manufacturing technique to build 3D objects with complex geometries. The flexural properties of bio-inspired additively manufactured parts are examined in this study. Flexural properties such as specific flexural rigidity and flexural rigidity are evaluated. In this investigation, the infill parameters viz. infill density (20, 50 and 80%) and infill pattern (Grid, honeycomb & triangular) is considered for additive manufacturing of specimen. Two types of specimens, i.e. constant density specimen (CDS) and bio-inspired specimen (BiS) are 3D printed. The specimens are fabricated based on ASTM D790 standard. The flexural properties of the specimens are measured through three-point bending test and smartphone-based free vibration test. The results from both the test are compared. The results from smartphone-based free vibration test are in good agreement with three-point bending test. It is observed that the H80 pattern specimen among the CDS is having the highest specific flexural rigidity. Also, the H80T20 pattern specimen from the BiS category is having the highest specific flexural rigidity among all the 3D printed specimens.

Keywords AM · FDM · PLA · Bio-inspired structure · Three-point bending test · Smartphone-based free vibration test

1 Introduction

In the mid to late 1980s, additive manufacturing has begun to build prototypes as a basic process. Recently, almost in every industry, has spread its roots. Due to its advantages, it is normally used manufacturing techniques. Fused deposition modelling (FDM) process is mostly selected for fabricating prototypes. In this process, the polymer material in semi-molten form is extruded from nozzle and layered on print bed.

M. Naik (✉) · M. C. Abhilash · D. G. Thakur
Department of Mechanical Engineering, Defence Institute of Advanced Technology(DU), Pune
411025, India
e-mail: mahesh.naik4144@gmail.com

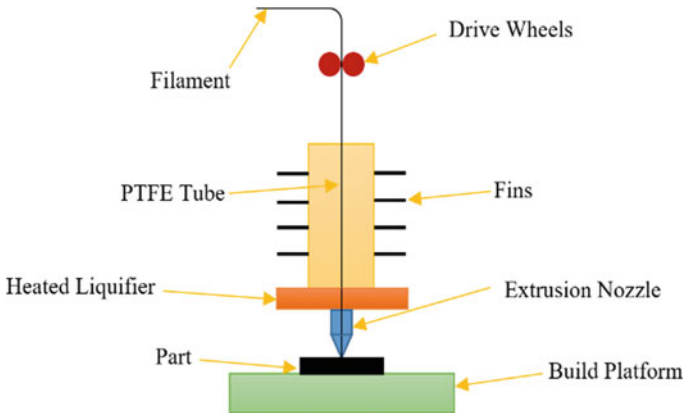


Fig. 1 FDM Process

In this process, the 3D model of parts is build in modelling software and is saved in STL format. The STL file is then transferred to slicer where the printing factors are assigned and the model is sliced to defined layer height. The file is then stored in G-code format. The file is then transferred to 3D printer where the printer starts printing the part layer-by-layer as per the G-code. The extruder head along with nozzle moves along x -axis and y -axis depositing the molten material. The print bed moves along z -axis to defined layer height after depositing one layer. Figure 1 represents the FDM process.

Based on the previous research, most of the studies were focused on investigating the effect of printing variables on mechanical properties. Lanzotti et al. [1] examined the influence of printing parameters on the tensile properties of 3D printed PLA samples. They reported that the tensile strength decreases as the raster angle increases towards 90° and the tensile strength increases as the layer height decreases. Motaparti et al. [2] investigated the bending properties of the FDM components. They concluded that at $0^\circ/90^\circ$ raster angle along with negative air gap, flexural strength increases. Luzanin et al. [3] studied the effect of printing parameters on flexural properties of FDM build components. They observed that flexural properties are highly affected by layer thickness and interaction between raster angle and infill density. Huang et al. [4] investigated that the build orientation and layer height affect the bending strength of the ABS printed parts. Garg et al. [5] reported that at low value of raster angle higher flexural strength is obtained because the deposited layer is almost parallel to the loading plane which offers resistance to bending. Ahn et al. [6] found that the air gap and raster orientation have a considerable influence on the mechanical strength, whereas other factors have less influence. Rajpurohit and Dave [7] reported that the maximum tensile strength is obtained at 0° raster angle and higher raster width. Also, due to strong bond between layers at minimum layer height, higher tensile strength is obtained. Vasudevarao et al. [8] stated that surface finish is more affected by part orientation, and the air gap has less influence on surface quality.

Dave et al. [9] investigated the tensile properties of multi-infill pattern specimens fabricated by FDM process. They reported that the multi-infill pattern of rectilinear and grid pattern with 45° raster orientation increases the tensile strength and 0° raster orientation decreases the tensile strength as compared to a single pattern. Porter et al. [10] investigated the influence of infill properties on flexural rigidity of 3D-printed parts by three-point bending, free vibration, and buckling test. It was observed that the optimal infill percentage that maximised specific flexural rigidity was determined to be between 10 and 20%.

The literature primarily focuses on studying the effects of process variables on flexural properties of additively manufactured specimens and significantly less research has been found on printing parameters like infill density and pattern and their effects on flexural strength. Therefore, in this research, an attempt is made in investigating the flexural properties of the bio-inspired additively manufactured parts inspired from turtle shell cross-section and the structure of flat bone [11, 12]. FDM can build complex parts, which make it one of the sought technology to fabricate bio-inspired structures. The aim of this research is to develop a suitable configuration and to find the optimum configuration of bio-inspired additively manufactured parts.

2 Materials and Methods

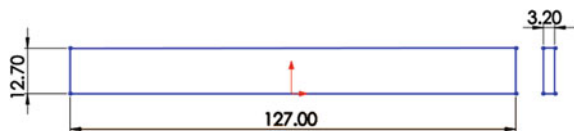
2.1 3D Printer and Material

FDM technique-based 3D printer is used to fabricate the specimens in this study. The 3D printer is having a print volume of $300 \times 300 \times 300 \text{ mm}^3$ along with dual extruder. One extruder is used for depositing the selected component material and the other is used for depositing the support material. Multiple thermoplastic materials can be used in this 3D printer. PLA is selected due to its high strength. The diameter of nozzle is 0.4 mm and is used along with the filament of PLA having 1.75 mm diameter.

2.2 Specimen Fabrication

The 3D model of specimen is created in Solidworks as per the ASTM D790 [13] standard. The 2D geometry is shown in Fig. 2. In present study, the infill density and

Fig. 2 Geometry of the flexural test specimen (ASTM D790)



infill pattern are selected to examine the flexural strength of bio-inspired 3D printed parts. For infill density, 20, 50 and 80% are selected whereas, for infill pattern grid (*G*), honeycomb (*H*) and triangular (*T*) patterns are selected. In this research two types of specimens are printed: the constant density specimens (CDS) where the specimens contain the single pattern and density and the bio-inspired specimens (BiS) where the infill pattern and density changes along with the thickness as shown in Figs. 3 and 4, respectively. An example of BiS terminology G80G50 tells us that the high-density region at top and bottom has 80% density grid pattern and the core has a 50% density grid pattern. Figure 5 shows that the high-density region in the top and bottom having a thickness of 1 mm each and the core portion has 1.2 mm. Full factorial experiments are designed for both CDS and BiS, as shown in Tables 1 and

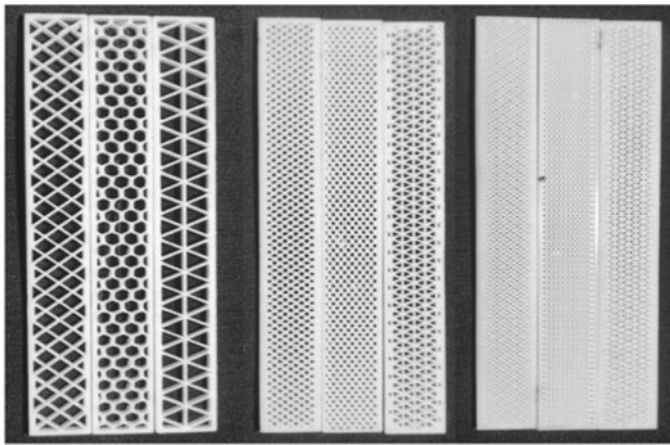


Fig. 3 CDS with 20%, 50% and 80% infill density, respectively

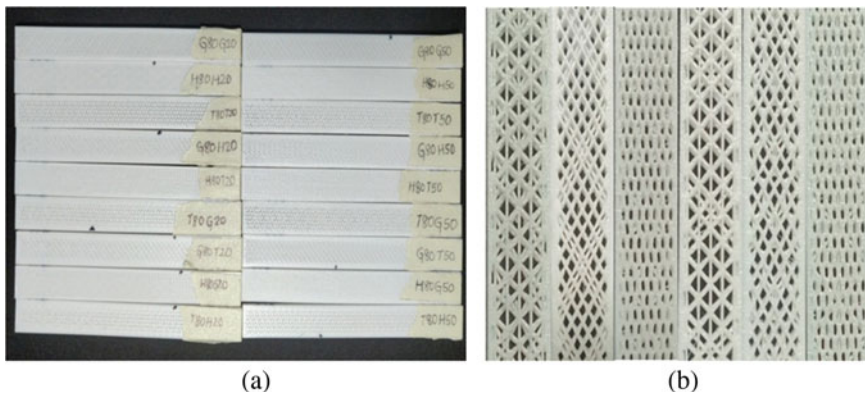


Fig. 4 a BiS b See-through images of BiS T50G20, G50T20, H50H20, T50T20, G50H20 and H50T20, respectively



Fig. 5 Density configuration of the BiS along its cross-section

Table 1 Design of experiment for CDS

Sr. No	Specimen
1	G20
2	H20
3	T20
4	G50
5	H50
6	T50
7	G80
8	H80
9	T80

Table 2 Design of experiment for BiS

Sr. No	Specimen	Sr. No	Specimen	Sr. No	Specimen
1	G80 G50	10	G80 G20	19	G50 G20
2	H80 H50	11	H80 H20	20	H50 H20
3	T80 T50	12	T80 T20	21	T50 T20
4	G80 H50	13	G80 H20	22	G50 H20
5	H80 T50	14	H80 T20	23	H50 T20
6	T80 G50	15	T80 G20	24	T50 G20
7	G80 T50	16	G80 T20	25	G50 T20
8	H80 G50	17	H80 G20	26	H50 G20
9	T80 H50	18	T80 H20	27	T50 H20

2. A full factorial experimental design was selected because it consists of all possible combinations of levels for all factors.

2.3 Three-Point Bending Test

The bending behaviour of a structure is due to the application of external load along the axis perpendicular to longitudinal axis. The highest deflection at the centre of a

simply supported beam due to the applied load (F) is given by Eq. (1).

$$\delta_{\max} = \frac{FL^3}{48EI} \quad (1)$$

where, L = support length of the beam, EI = flexural rigidity.

The highest deflection is dependent on flexural rigidity of the beam. The stiffness of the specimens in the lateral direction was found out using three-point bending test as per ASTM D790 standard. The testing is done in ARDE (Armament research and development establishment), DRDO with standard procedures. The support span (L) is 102 mm. The speed of the head is maintained 5 mm/min for all the specimens. The samples are deflected till the fracture. Peak flexural load (N) is noted for all the samples. Equation (1) is used to determine the flexural rigidity (EI), and the value of mass per unit length is divided to get specific flexural rigidity (EI/m).

2.4 Smartphone-Based Free Vibration Test

The fundamental frequency of the samples is found using the smartphone-based free vibration of the cantilever beam (ASTM E1876) [14]. The natural frequencies of the cantilever beam can be calculated as per the material and geometrical feature of beam. The equation of the fundamental frequency is given by, [10, 15].

$$f = \frac{1.875^2}{(2\pi)L_f^2} \sqrt{\frac{EI}{m}} \quad (2)$$

where, L_f = unclamped length (free length) of the beam, EI/m = specific flexural rigidity and m = mass per unit length of the specimen.

In order to find out the natural frequency, slow-motion video recordings are captured using smartphone having a sampling rate of 480 frames per second in slow-motion video recording, whereas the camera used in the reference paper [16] has 240 frames per second. A microsecond timer is used during the video recordings so that the time differences can be noted down for a particular number of oscillations. Here the number of oscillations counted are 50 and the time difference is noted down, and frequency is calculated. The damping of the beam is very negligible, and hence there will be no difference between damped frequency and undamped frequency (Natural frequency). Five readings are taken for each type of specimen, and the frequency is averaged. The clamped length of the specimens is 25 mm, and unclamped length is 102 mm. The experimental setup is, as shown in Fig. 6. The cantilever beams are displaced initially at their free end and released, and the free vibration data is noted. Figure 7 shows the mode shapes captured by the video recordings. The value of EI/m is obtained from Eq. (2) by substituting the value of natural frequency. The value of

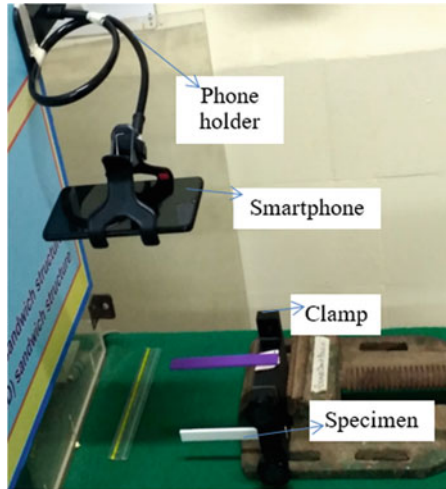


Fig. 6 Smartphone-based free vibration test setup

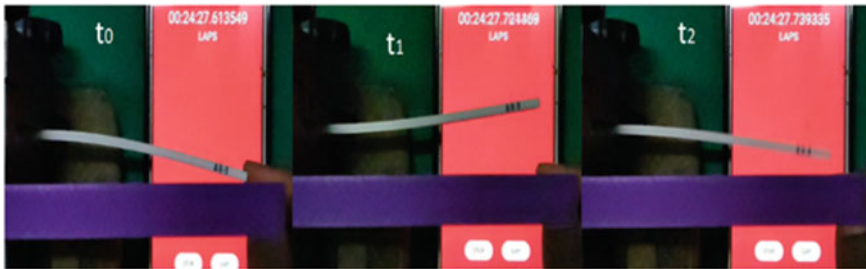


Fig. 7 Images from the recorded video depicting the mode shapes, at $t = 0$ s the initial displacement can be seen and the microsecond timer in the background

EI was determined by multiplying the EI/m by length density, which is the ratio of total mass to length of beam.

3 Results and Discussion

3.1 Mass

The mass of each of the specimens is measured using a weighing scale which has a resolution of 0.1 mg. Masses of Constant density specimens showing linear variation with respect to density in a particular pattern, for example, the red dot represents honeycomb pattern and the sample 2, 5 and 8 has 20%, 50% and 80% density,

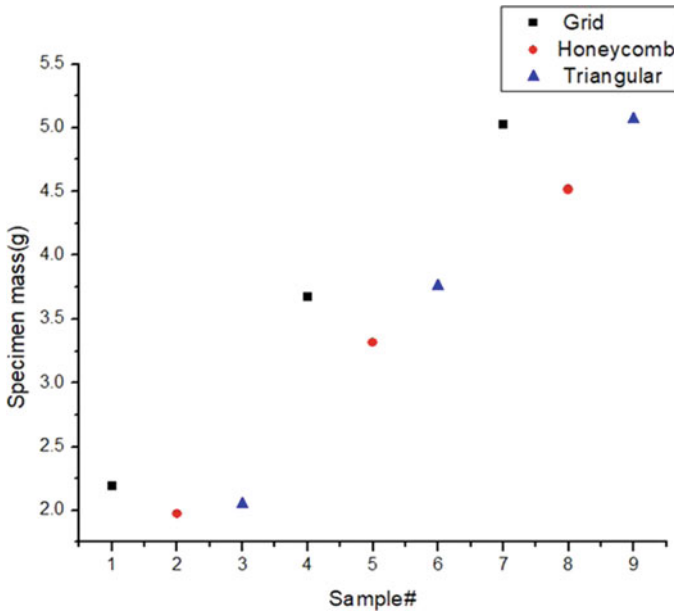


Fig. 8 Masses of CDSs

respectively (Fig. 8). In CDS, the honeycomb pattern has the less mass in all three infill densities compared to triangular and grid patterns. The masses of the BiS are showing grouping characteristics (Fig. 9). The first nine specimens have mass in the range 4–4.6 g (having 80% density at the extreme and 50% density in the core), the specimens from 10 to 18 has the mass in the range 3.5–4 g (having 80% density at the extreme and 20% density in the core). The last nine specimens have their masses in the range 2.7 g–3.1 g (having 50% density at the extreme and 20% density in the core).

3.2 Flexural Rigidity (EI) and Specific Flexural Rigidity (EI/m)

The values of EI and EI/m for CDS and BiS obtained from smartphone-based free vibration test and three-point bending test are shown in Tables 3 and 4. To verify and compare the result between two tests, the values of EI for both the specimen are plotted as shown in Figs. 10 and 11. The values (both EI and EI/m) from both the test are almost comparable and are in good agreement with each other. Quantitatively the discrepancy error in percentage for EI values between the three-point bending test and smartphone-based free vibration tests is below 5% for CDS and it is well below

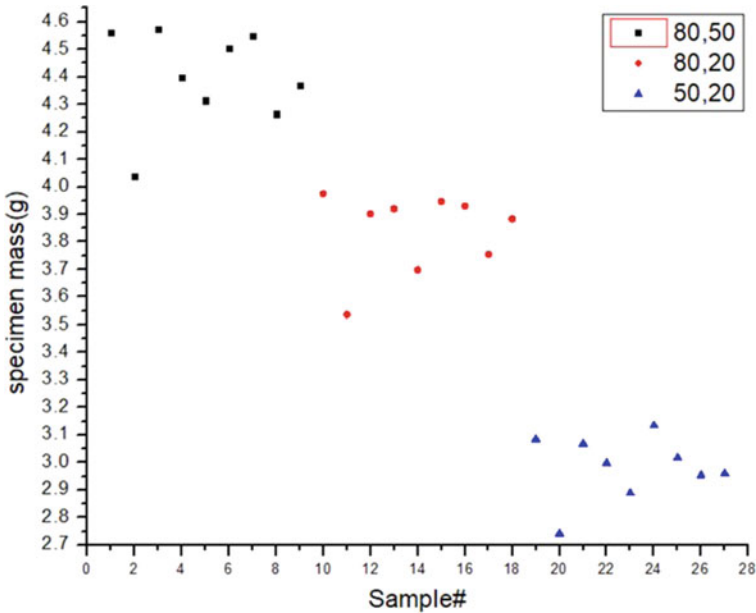


Fig. 9 Masses of BiS

Table 3 Experimental results for CDS

Sr. No.	Specimen	Mass (g)	Peak load (N)	Vibration test			Three-point bending test	
				Natural freq. (Hz)	EI (KNmm ²)	EI/m (m ⁴ /s ²)	EI (KN mm ²)	EI/m (m ⁴ /s ²)
1	G20	2.18	10.01	55	18.03	1.04	17.36	1.00
2	H20	1.97	9.84	37	17.43	1.12	17.22	1.11
3	T20	2.05	10.55	61	20.79	1.28	21.51	1.33
4	G50	3.67	13.95	53	23.08	0.97	27.86	0.96
5	H50	3.31	17.80	61	33.58	1.28	32.66	1.25
6	T50	3.76	18.66	60	36.86	1.24	38.74	1.30
7	G80	5.02	26.84	59	47.66	1.20	48.75	1.23
8	H80	4.51	29.37	67	55.18	1.55	55.53	1.56
9	T80	5.06	28.26	65	58.28	1.46	57.77	1.44

9% for BiS. It was noted that the discrepancy of EI values and EI/m values are also equal.

The EI value linearly increases for the given pattern of CDS when its infill density is increased. In CDS, the triangular pattern has the highest EI value in all three infill densities compared to honeycomb and grid patterns. It is observed that the

Table 4 Data set of the BiS

Sr. No	Specimen	Wt (gm)	Peak load (N)	Vibration test			Three-point bending test	
				Natural freq. (Hz)	EI (KNmm ²)	EI/m (m ⁴ /s ²)	EI (KNmm ²)	EI/m (m ⁴ /s ²)
1	G80G50	4.56	23.17	63	49.27	1.37	49.15	1.36
2	H80H50	4.03	26.00	70	53.88	1.69	55.93	1.75
3	T80T50	4.57	22.97	69	59.26	1.64	61.96	1.72
4	G80H50	4.39	22.55	63	47.52	1.37	50.01	1.44
5	H80T50	4.31	29.33	73	62.58	1.84	65.79	1.93
6	T80G50	4.50	22.68	69	58.35	1.64	60.84	1.79
7	G80T50	4.54	24.61	63	49.13	1.37	51.21	1.43
8	H80G50	4.26	28.07	72	60.19	1.79	65.7	1.95
9	T80H50	4.36	20.95	69	56.61	1.64	60.56	1.76
10	G80G20	3.97	22.76	68	50.03	1.59	51.51	1.64
11	H80H20	3.53	23.23	74	52.73	1.89	55.34	1.98
12	T80T20	3.90	20.00	73	56.62	1.84	59.32	1.93
13	G80H20	3.91	22.72	68	49.35	1.59	51.59	1.67
14	H80T20	3.69	26.84	78	61.26	2.10	63.5	1.18
15	T80G20	3.94	22.64	73	57.26	1.84	61.9	1.99
16	G80T20	3.93	23.05	69	50.94	1.64	52.66	1.70
17	H80G20	3.75	26.18	79	63.78	2.15	64.11	2.16
18	T80H20	3.88	22.33	74	57.89	1.89	60.91	1.99
19	G50G20	3.08	12.15	58	28.25	1.16	29.09	1.19
20	H50H20	2.74	16.06	66	32.25	1.50	32.04	1.57
21	T50T20	3.06	15.62	67	37.51	1.55	40.88	1.69
22	G50H20	2.99	13.06	59	28.41	1.20	29.43	1.24
23	H50T20	2.88	17.95	68	36.38	1.59	37.56	1.65
24	T50G20	3.13	16.07	67	38.31	1.55	39.33	1.53
25	G50T20	3.01	12.31	59	28.59	1.20	30.05	1.26
26	H50G20	2.95	17.73	68	37.19	1.59	38.58	1.65
27	T50H20	1.96	14.11	67	36.18	1.55	38.07	1.63

T20, H50 and H80 have the highest EI/m value in 20%, 50% and 80% infill density, respectively among the CDS. The T20 and H50 configuration have equal EI/m values making T20 more reliable owing to its less fabrication time. Among CDS specimens, H80 pattern specimen has the highest EI/m value and T80 pattern specimen has the highest EI value. The BiS from 1 to 9 and 10 to 18 with 50% and 20% infill density at core are having EI values in the range of 45 KNmm² and 65 KNmm². It is observed that the value of mass for the samples 10–18 is less compared to mass of

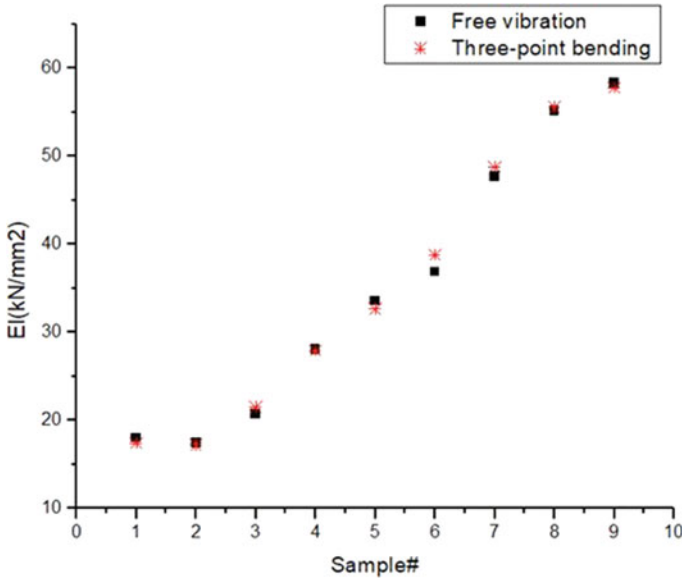


Fig. 10 EI values obtained from smartphone-based free vibration and three-point bending tests for CDS

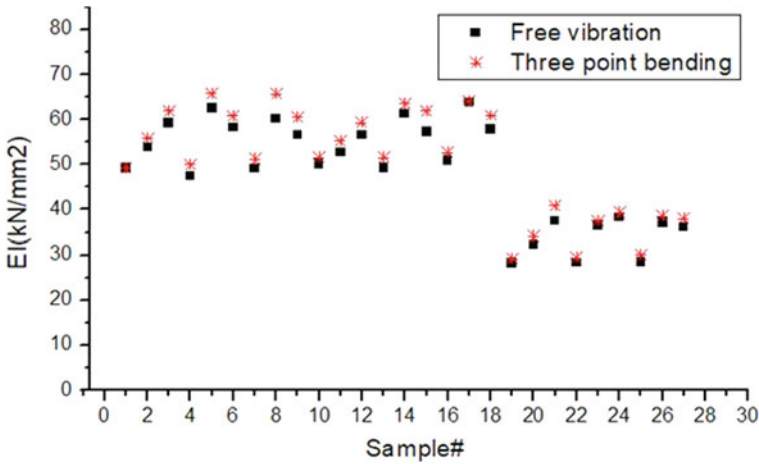


Fig. 11 EI values obtained from smartphone-based free vibration and three-point bending tests for BiS

samples 1–9. Indicating that samples 10–18 will have a better EI/m value. Among BiS, H80G20 specimen has the highest EI value and EI/m value. It is observed that specimens having H80 and H50 configurations in the periphery outperform the other specimens, showing that honeycomb structure is the best pattern among the

other patterns because the honeycomb pattern has low density and high mechanical properties together with high stiffness. It requires less material to fabricate and has high strength. The specimens with G80 and G50 configurations in the periphery have the lowest EI/m values. It is reported in [17], that the honeycomb pattern has minimum weight compared to triangular and grid patterns and also, the strength/weight ratio of honeycomb pattern is maximum.

4 Conclusion

The smartphone-based free vibration test and three-point bending test were conducted for both the CDS and BiS. The stiffness to mass ratio was used to determine the optimum configuration that provides the best flexural properties. Among CDS, the H80 pattern outperformed other CDS specimens. The H80G20 configuration of BiS had the highest natural frequency and hence specific flexural rigidity among all the printed specimens. The use of a smartphone as an economical alternative to high-speed cameras and accelerometers is reliable. The bio-inspired design strategy proved to be highly desirable in flexural structures. Finally, the honeycomb pattern, which is bio-inspired structure, is verified to be one of the best infill structures for enhancement of flexural properties. Also, lightweight structures with high flexural strength are required in applications such as automotive, medical and aerospace fields. The weight reduction of the structure can be done by considering the bio-inspired structure.

References

1. Lanzotti A, Grasso M, Staiano G, Martorelli M (2015) The impact of process parameters on mechanical properties of parts fabricated in PLA with an open-source 3-D printer. *Rapid Prototyping Journal* 21(5):604–617
2. Motaparti KP, Taylor G, Leu MC, Chandrashekhara K, Castle J, Matlack M (2017) Experimental investigation of effects of build parameters on flexural properties in fused deposition modelling parts. *Virtual Phys Prototyping* 12(3):207–220
3. Luzanin O, Movrin D, Plancak M (2014) Effect of layer thickness, deposition angle, and infill on maximum flexural force in FDM built specimens. *J Technol Plast* 39(1):49–58
4. Huang B, Meng S, He H, Jia Y, Xu Y, Huang H (2019) Study of processing parameters in fused deposition modeling based on mechanical properties of the acrylonitrile-butadiene-styrene filament. *Polym Eng Sci* 59(1):120–128
5. Garg A, Bhattacharya A, Batish A (2017) Failure investigation of fused deposition modelling parts fabricated at different raster angles under tensile and flexural loading. *Proc Inst Mech Eng Part B J Eng Manuf* 231(11):2031–2039
6. Ahn SH, Montero M, Odell D, Roundy S, Wright PK (2002) Anisotropic material properties of fused deposition modelling ABS. *Rapid Prototyping J* 8(4):248–257
7. Rajpurohit SR, Dave HK (2018) Effect of process parameters on tensile strength of FDM printed PLA part. *Rapid Prototyping J* 24(8):1317–1324

8. Vasudevarao B, Natarajan DP, Henderson M, Razdan A (2002) Sensitivity of RP surface finish processing parameter variation. In Solid freeform fabrication proceedings. Austin, TX: The University of Texas, p 251–258
9. Dave HK, Patel BH, Rajpurohit SR, Prajapati AR, Nedelcu D (2021) Effect of multi-infill patterns on tensile behaviour of FDM printed parts. *J Braz Soc Mech Sci Eng* 43(1):1–15
10. Porter JH, Cain TM, Fox SL, Harvey PS (2019) Influence of infill properties on flexural rigidity of 3D-printed structural members. *Virtual Phys Prototyping* 14(2):148–159
11. Ding XF, Jiang L, Liang Y, Wu CW (2011) The structure and mechanical properties of turtle shell and biomimetic. *Adv Mater Res* 189:3419–3422
12. Gu P, Li L (2002) Fabrication of biomedical prototypes with locally controlled properties using FDM. *CIRP Ann* 51(1):181–184
13. ASTM International—D790–10 (2010) Standard test methods for flexural properties of unreinforced and reinforced plastics and electrical insulating materials
14. ASTM E1876 (2015) Standard test method for dynamic young's modulus, shear modulus and poisson's ratio by impulse excitation
15. Virgin L (2017) On the flexural stiffness of 3D printer thermoplastic. *Int J Mech Eng Educ* 45(1):59–75
16. Baker JR, Capece V (2013) Use of an affordable high speed video camera for visualization in mechanical engineering courses. In: 120th ASEE annual conference and exposition
17. Chadha A, Haq MIU, Raina A, Singh RR, Penumarti NB, Bishnoi MS (2019) Effect of fused deposition modelling process parameters on mechanical properties of 3D printed parts. *World J Eng* 16(4):550–559

3D Printable Gearbox Casing



**T. N. Nikhil, Mayank Chutani, Gautam Mahesh,
and Lokavarapu Bhaskara Rao**

Abstract This paper discusses the materials suitable for the manufacturing of gearbox casing using 3D printing technology. Based on the research of different materials that can be used for 3D printing manufacturing, materials based on strength and availability for manufacturing were considered. Using Ansys 2020 static structural analysis, stress analysis, vibrational, and harmonic analysis were performed. Based on the results, comparison of the different materials based on maximum deformation, maximum stress, and vibrations frequencies with the conventionally used material. The basic aim of this research was to reduce the weight of the existing gearbox casing and find a suitable material that is lightweight as well as suitable for mass production for casing using 3D printing.

Keywords Gearbox · Casing · 3D printing · Modal analysis · Structural analysis · Harmonic analysis

Notation

P	Power
N_1	Rotations per minute of pinion
T_1	Torque of pinion
T_2	Torque of gear
F_T	Tangential force
F_R	Radial force
Φ	Pressure angle
F_V	Forces in vertical direction
$R_{V(B)}$	Reaction force to vertical force by bearing 1
$R_{V(D)}$	Reaction force to vertical force by bearing 2
F_H	Forces in horizontal direction

T. N. Nikhil (✉) · M. Chutani · G. Mahesh · L. Bhaskara Rao
School of Mechanical Engineering, Vellore Institute of Technology, Chennai,
Vandalur-Kelambakkam Road, Chennai, Tamil Nadu 600127, India
e-mail: nikhilnatarajan.t2018@vitstudent.ac.in

$R_{H(B)}$	Reaction force to horizontal force by bearing 1
$R_{H(D)}$	Reaction force to horizontal force by bearing 2
R_B	Radial load on bearing 1
R_D	Tangential load on bearing 2
δ	Thickness of housing

1 Introduction

The gearbox casing is a housing encompassing gears that protect against dust and moisture and at the same time serves as a platform for gear transmission. In addition, it accommodates the lubricant, holds the shaft, and helps in dissipating the heat generated during the process of gear transmission. One of the major parameters to be taken into consideration while designing the gearbox is the strength of the overall structure. In most of the researches going on the manufacturing of gearbox casing is done by sand casting for mass production and current designs are heavyweight and increase the weight of the overall system [1]. Shrenik and Pise [2] optimized a differential gearbox casing using Modal and Stress Analysis. They designed a gearbox casing and carried out the analysis for the material die-cast ALSi132. Himanshu et al. [3] researched the influence of mechanical properties on natural frequency and mode shapes of heavy vehicle gearbox transmission casing. Sagar and Kharde [4] completed a study on Vibration Analysis for Two Wheeler Gearbox Casing using FEA. Modal analysis of gearbox casing is solved using CATIA software and Hyper-mesh software was used for meshing. Neeta and Gunchita [5] through FEA analysis found out various factors for gearbox failures such as design and manufacturing defects.

In the research conducted by Xiaohan Tang [6], the gearbox casing is made using Solidworks software and FEA analysis in ABAQUS software is explained. Another research conducted in the year 2019 by Yogesh et al. [7] on Design and Analysis of Gearbox Casing is to determine the natural vibration modes and to find natural frequency and analysis to show the maximum amplitude. Research by Shekhar et al. [8] focuses on the design and optimization of a two-stage reduction gearbox for the BAJA All-Terrain Vehicle. Based on the CVT's high- and low-end ratios and different road resistances, the required reduction ratio of the gearbox is calculated. Anand et al [9] carried out an analysis for both the harmonic drive models for the three different force values obtained from torque values. The maximum values of equivalent von-Mises stress, deformation, and von-Mises elastic strain values for helical teeth harmonic drive and the straight teeth harmonic drive were obtained.

In a research paper by Neeta et al. [10] static and perturbation analysis has been performed on gearbox casing. Gearbox casing was designed in ABAQUS and Finite element analysis was performed for static and dynamic analysis. Namankumar et al. [11] researched gearbox casing in which they performed static and dynamic analysis using finite element analysis to find a total load, displacement, and natural frequency.

Timir and Ashutosh [12] designed and analyzed a planetary gearbox for an FSAE formula electric car and determined the materials of the gearbox by an iterative process.

Our focus is to make a 3D printable gearbox and use 3D printing for manufacturing instead of using the traditional sand casting methods used for mass production. Through research studies, we found that the existing designs made were very heavy which makes the overall powertrain heavier, so we aim to reduce the weight of the gearbox casing and to find a suitable material for 3D printing gearbox casing. A single-stage gearbox is chosen for study. This analysis aims to find different materials which are lightweight and are compatible with manufacturing by additive techniques.

2 Modelling

2.1 Materials

Material is important parameter for the any gearbox component. The material selection is based on the factors of the strength, rigidity, cost etc. Gearbox casing is traditionally made using casting process; but for it to be made using 3D printing, certain materials which are suitable for 3D printing as well as possessing desirable properties are chosen. Details of additive manufacturing materials are mentioned in Table 1.

Table 1 Additive manufacturing material details

Materials	Description
Polycarbonate	Polycarbonate is known for its strength and durability. It has very high heat and impact resistance making it an ideal choice for tough environments
Nylon	Nylon is a tough and semi-flexible material that offers high impact and abrasion resistance. It is an ideal choice for printing durable parts
Epoxy with carbon fibre	Carbon fibre filaments contain short fibres that are infused into a PLA or ABS base material to help increase strength and stiffness
Polyamide	With its strength and flexibility, polyamide allows for high levels of detail on a 3D-printed product. The material is especially suited for joining pieces and interlocking parts in a 3D-printed model. Polyamide is used to print everything from fasteners and handles to toy cars and figures
Carbon fibre	Composites such as carbon fibre are used in 3D printers as a top-coat over plastic materials. The purpose is to make the plastic stronger. The combination of carbon fibre over plastic has been used in the 3D printing industry as a fast, convenient alternative to metal

2.2 Parameters for Modelling

Input parameters for calculation of forces are given in Table 2 and pinion and gear data [13] is mentioned in Table 3.

$$P = \frac{2\pi N_1 T_1}{60} \tag{1}$$

$\therefore T_1 = 117.8 \text{ Nm}$ and $T_2 = \frac{Z_2 T_1}{Z_1} = 405.76 \text{ Nm}$

Tangential force: [14]

$$F_T = \frac{2T}{d} = 5235.56 \text{ N} \tag{2}$$

Radial force:

$$F_R = F_T * \tan \phi = 1905.59 \text{ N} \quad (\phi = 20^\circ) \tag{3}$$

Bearing Loads:

$$\sum F_{iH} =_{(B)} + R_{H(D)} - F_R = 0 \tag{4}$$

$R_{H(B)} = 0.952795 \text{ kN}$ and $R_{H(D)} = 0.952795 \text{ kN}$

$$\sum F_{iV} =_{(B)} + R_{V(D)} - F_T = 0 \tag{5}$$

$R_{V(B)} = 2.61778 \text{ kN}$ and $R_{V(D)} = 2.61778 \text{ kN}$

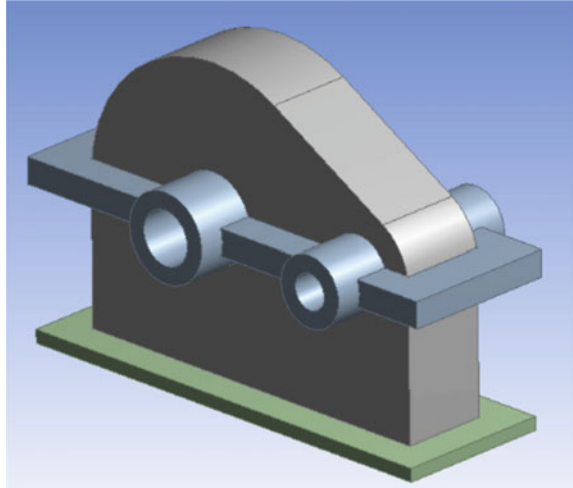
$$R_B = \sqrt{R_{H(B)}^2 + R_{V(B)}^2} = 1.34745561 \text{ kN} \sim 1347.46 \text{ N} \tag{6}$$

Table 2 Input parameters [9]

Parameter	Value
Power	18.5 kW
Input speed	1500 rpm
Overall gearbox ratio	4.5:1

Table 3 Pinion and gear data

	Module	No. of teeth	Face width	Diameter
Pinion	2.5	18	40	45
Gear	2.5	62	40	155

Fig. 2 CAD model

Accordingly, $d_1 = M18$, $K_1 = 46$ mm, $t_1 = 25$ mm, $d_{01} = 20$ mm and $D_{01} = 34$ mm

Notice that the thickness of this flange is

$$\text{thickness} = 2.35 \cdot \delta = 2.35 \cdot 8 = 18.8 \approx 20 \text{ mm} \quad (9)$$

and its bottom width is

$$\text{width} = K_1 + 1.5 \cdot \delta = 46 + 1.5 \cdot 8 = 58 \text{ mm} \quad (10)$$

As to bolts of the housing, their size is evaluated with

$$d_2 = 0.75 \cdot d_1 = 0.75 \cdot (19.2) = 14.4 \text{ mm} \quad (11)$$

Accordingly, the other parameters were chosen [15].

$d_2 = M14.2 = 33$ mm, $C_2 = 18$ mm, $d_{02} = 15$ mm and $D_{02} = 28$ mm

According to the aforementioned design dimensions a CAD model was developed as shown in Fig. 2.

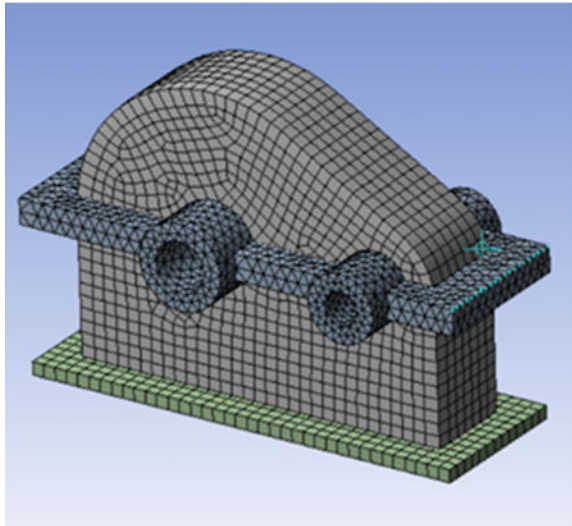
4 Mesh Convergence

Mesh convergence: As shown from the results obtained in Table 5, the mesh size for the analysis was taken as 14 mm and a meshing model was created in ANSYS as depicted in Fig. 3.

Table 5 Mesh convergence

Mesh size (mm)	Frequency (Hz) 1st mode
15	326.26
14.9	326.17
14.8	326.04
14.7	325.97
14.6	326.09
14.5	326.12
14.4	325.69
14.3	325.63
14.2	325.08
14.1	325.08
14	325.08

Fig. 3 Meshing of model



5 Validation

The 10 natural frequencies obtained were compared with Vijaykumar et al. [16] and percentage difference between them are tabulated in Table 6.

Table 6 Comparison of 10 natural frequencies with Vijaykumar et al. [16]

Mode	Frequency (Hz)	Frequency (Hz) Vijaykumar et al. [16]	(%) difference
1	118.56	120.93	1.96
2	245.42	256.71	4.40
3	288.18	295.27	2.40
4	419.07	434.45	3.54
5	433.19	464.22	6.68
6	544.39	545.23	0.15
7	597.21	598.62	0.24
8	658.26	627.11	-4.97
9	682.01	683.95	0.28
10	795.81	743.52	-7.03

Table 7 Load applied on each bearing

		X	Y	Z
Shaft 1	Bearing 1	0	0	-1347.46
	Bearing 2	0	0	-3702.1
Shaft 2	Bearing 1	0	0	-1347.46
	Bearing 2	0	0	-3702.1

6 Analysis Using Gray Cast Iron

6.1 Static Analysis for Gray Cast Iron

Boundary Condition: For the static analysis, forces acting on the each bearing was found from the above torque value. The load to be applied on each bearing is specified in Table 7. The boundary conditions can be seen in Fig. 4.

6.2 Modal Analysis for Gray Cast Iron

An analysis of measured data is a process in which the measured frequency response functions are analysed in order to find a theoretical model that closely resembles the dynamic behaviour of the structure under test. This part of the model test is called experimental modal analysis. Boundary Conditions, Total Deformation, Stress Analysis, Modal Analysis and first 10 Natural frequencies with Gray Cast Iron as material is shown in Figs. 4, 5, 6, 7 and 8 respectively.

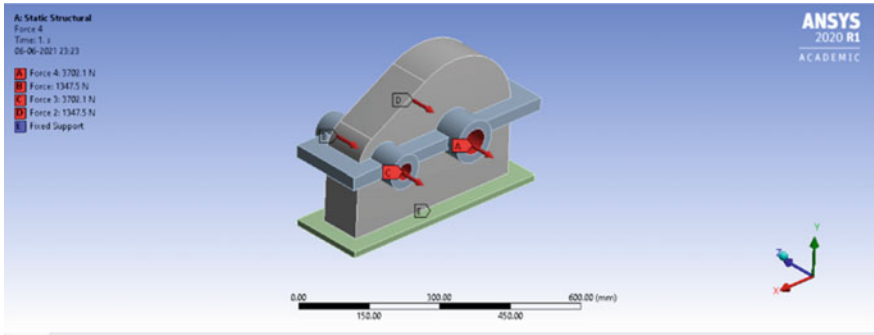


Fig. 4 Static analysis boundary conditions [11]

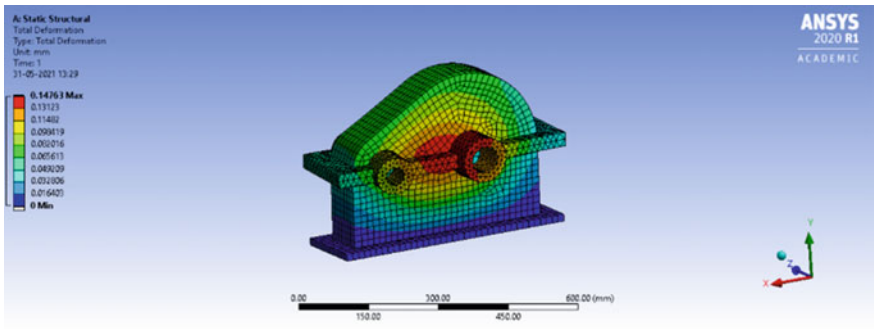


Fig. 5 Total deformation with gray cast iron as material

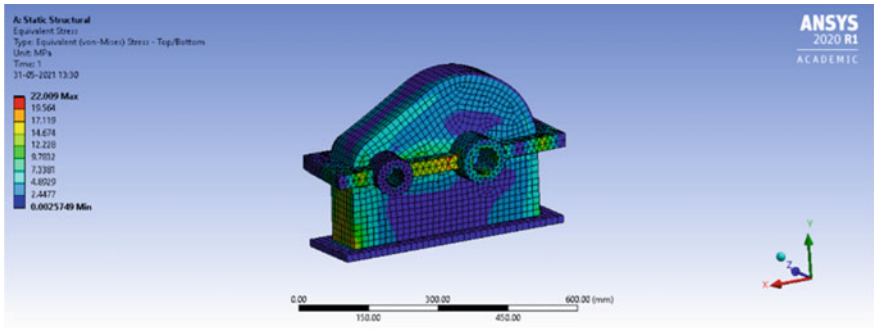


Fig. 6 Stress analysis with gray cast iron as material

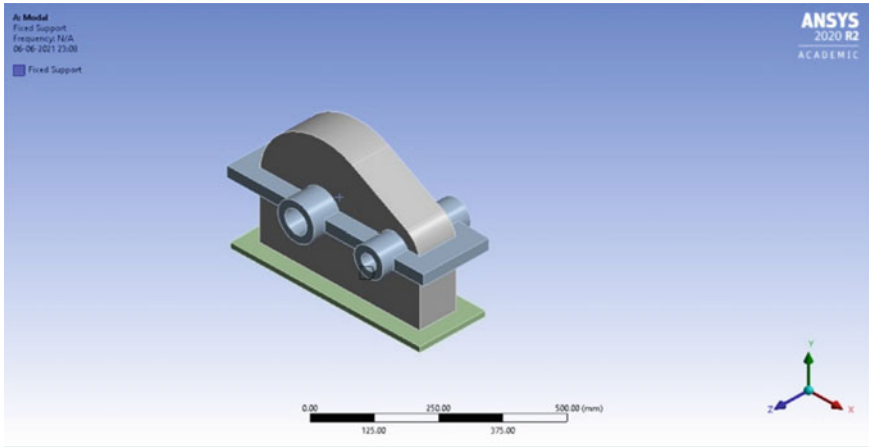


Fig. 7 Modal analysis boundary conditions [16]

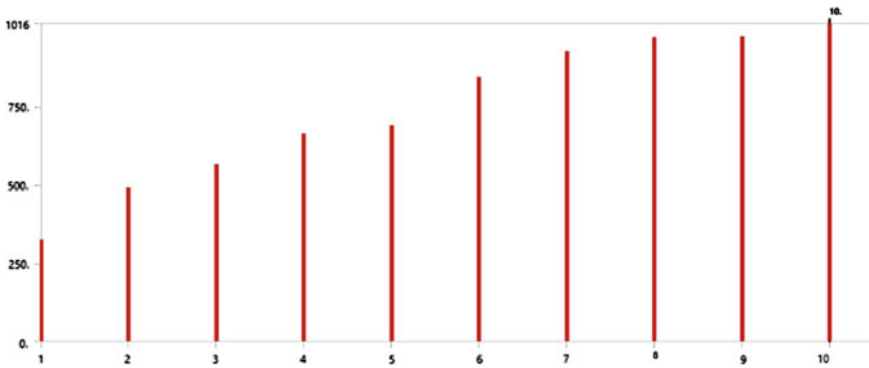


Fig. 8 First 10 natural frequencies with gray cast iron as material

6.3 Harmonic Analysis:

Boundary Condition: In the harmonic frequency response analysis, the fixed support is exactly same condition in Fig. 8. In this analysis, 1 MPa pressure is applied to the upper half of the bearings on one side of the gearbox and to the lower half of the other side for a frequency range from zero to 1.2 times the frequency of the tenth vibration mode [16]. This 1 MPa pressure is applied normal to the surface according to the Table 7. The analysis settings for Harmonic analysis are displayed on Table 8.

The Harmonic Analysis boundary conditions are applied on Gray Cast Iron Casing (Fig. 9). Deformation in harmonic analysis along X and Y axis are shown in Figs. 10 and 11. Normal Stress in harmonic analysis along X axis and Y axis are shown in Figs. 12 and 13.

Table 8 Details of analysis settings for harmonic analysis

Details of analysis settings	
Step controls	
Multiple RPMs	No
Options	
Frequency spacing	Linear
Range minimum	0. Hz
Range maximum	1219.3 Hz
Solution intervals	200
User defined frequencies	Off
Solution method	Mode superposition
Include residual vector	No
Cluster results	No
Modal frequency range	Program controlled
Skip expansion	No
Store results at all frequencies	Yes

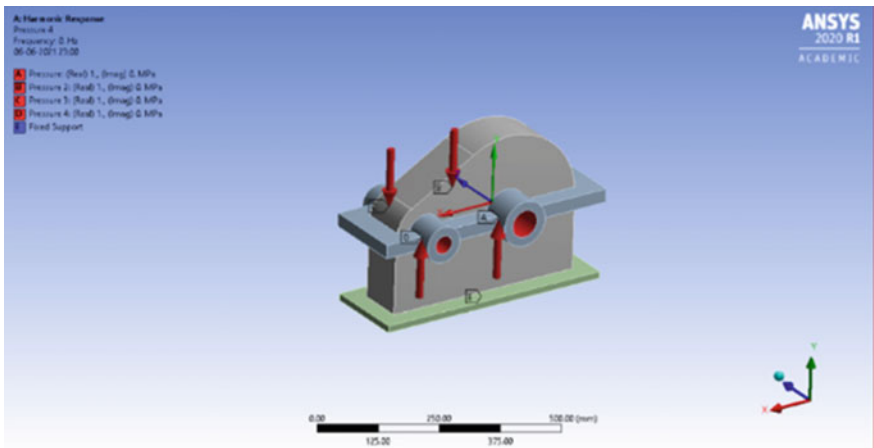


Fig. 9 Harmonic analysis boundary conditions [16]

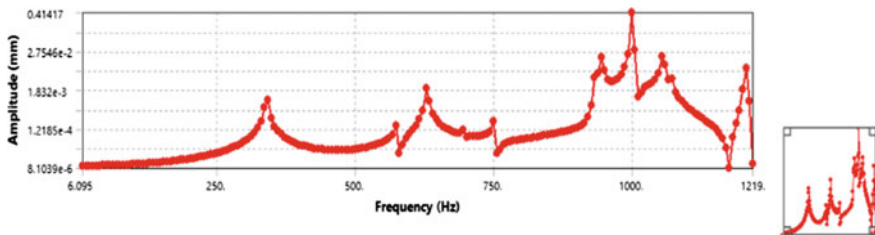


Fig. 10 Deformation in harmonic analysis (X-axis) with gray cast iron as material

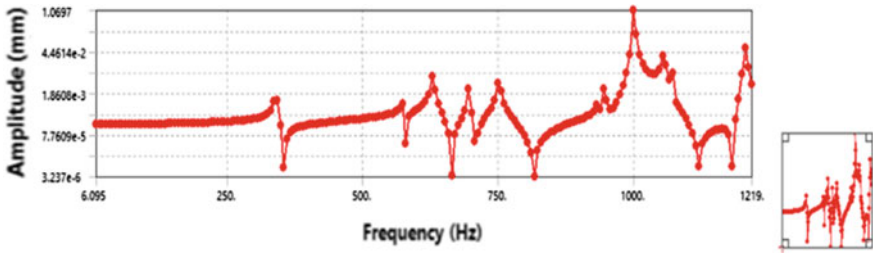


Fig. 11 Deformation in harmonic analysis (Y-axis) with gray cast iron as material

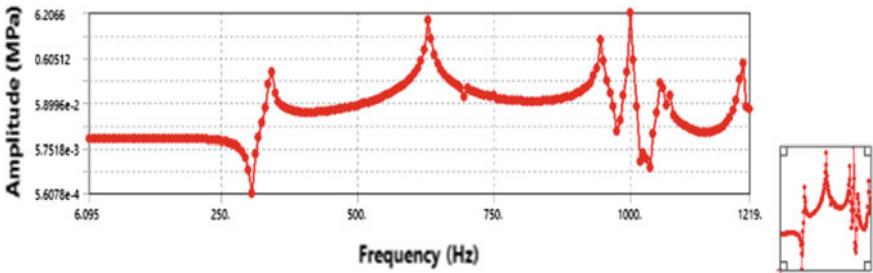


Fig. 12 Normal stress in harmonic analysis (X-axis) with gray cast iron as material

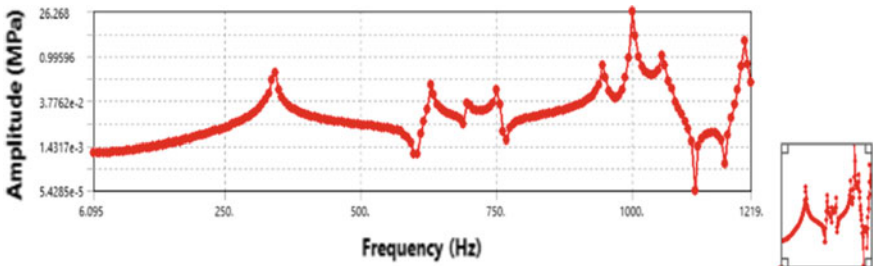


Fig. 13 Normal stress in harmonic analysis (Y-axis) with gray cast iron as material

7 Analysis With Additive Manufacturing Materials

7.1 Static Analysis

The deformation of the casing with Polycarbonate, Polyamide, and Carbon fibre Epoxy with carbon fibre and Nylon as material are shown in Figs. 14, 15, 16, 17 and 18 respectively. The stress analysis of the casing with Polycarbonate, Polyamide, Carbon Fibre, Epoxy with carbon fibre and Nylon as material are shown in Figs. 19,

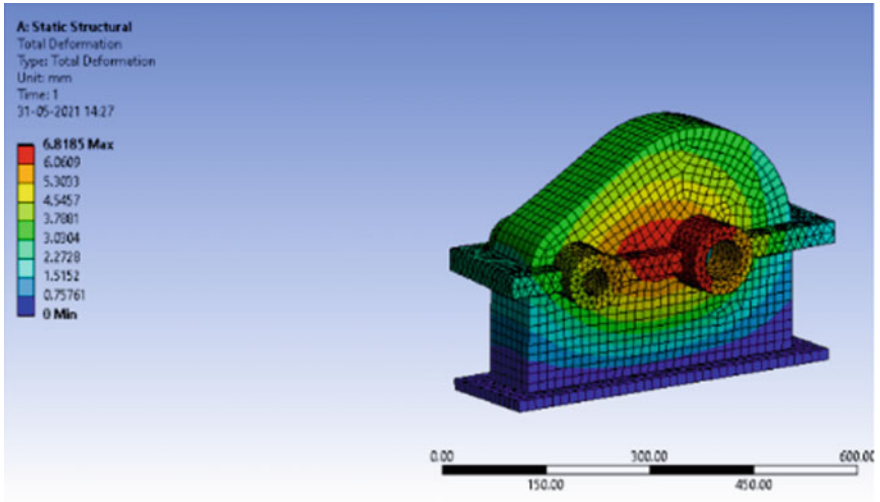


Fig. 14 Static analysis for polycarbonate material

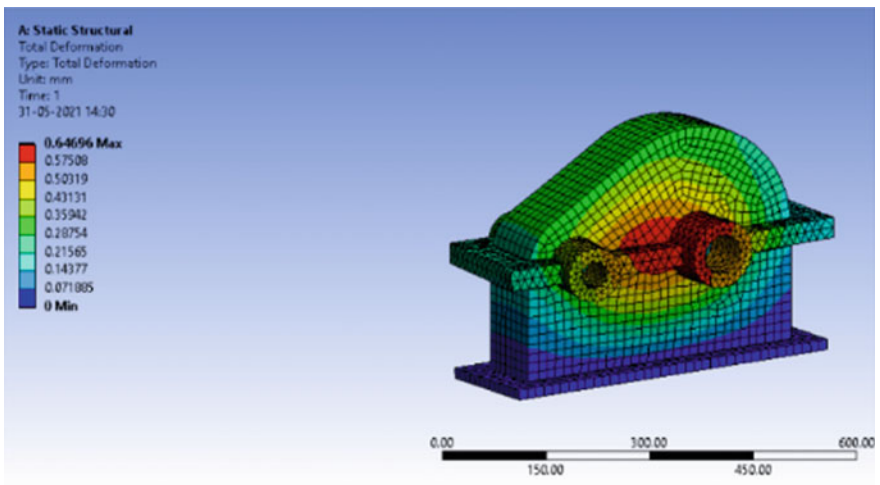


Fig. 15 Static analysis for polyamide material

20, 21, 22 and 23 respectively. The results from the analysis have been tabulated in Table 9.

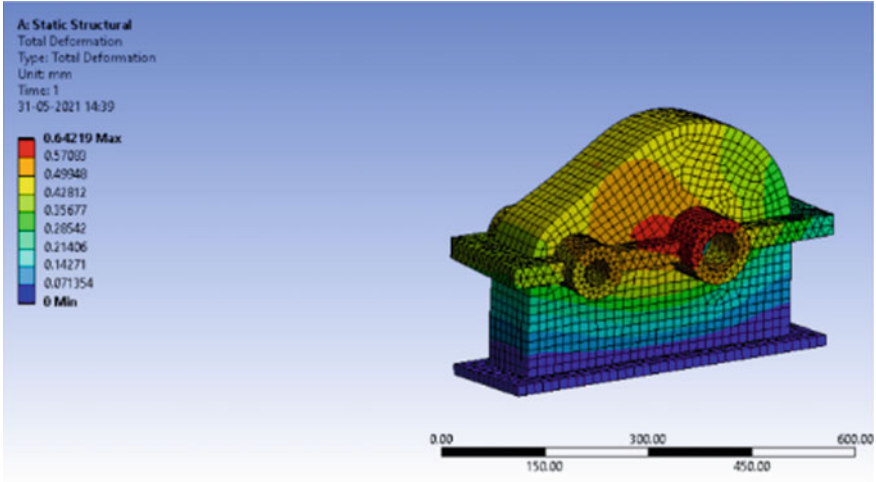


Fig. 16 Static analysis for carbon fibre material

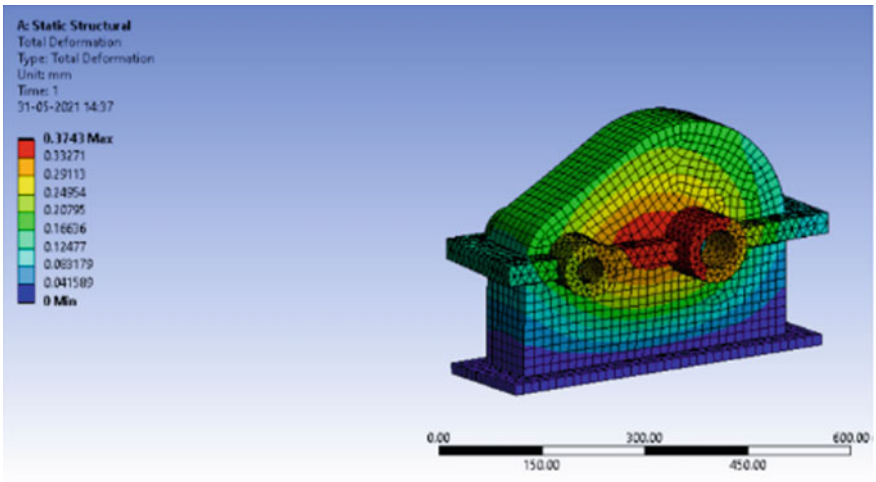


Fig. 17 Static analysis for epoxy with carbon fibre material

7.2 Modal Analysis

The First 10 Natural frequencies of the casing with Polycarbonate, Polyamide, Carbon Fibre, Epoxy with carbon fibre and Nylon as material are shown in Table 10.

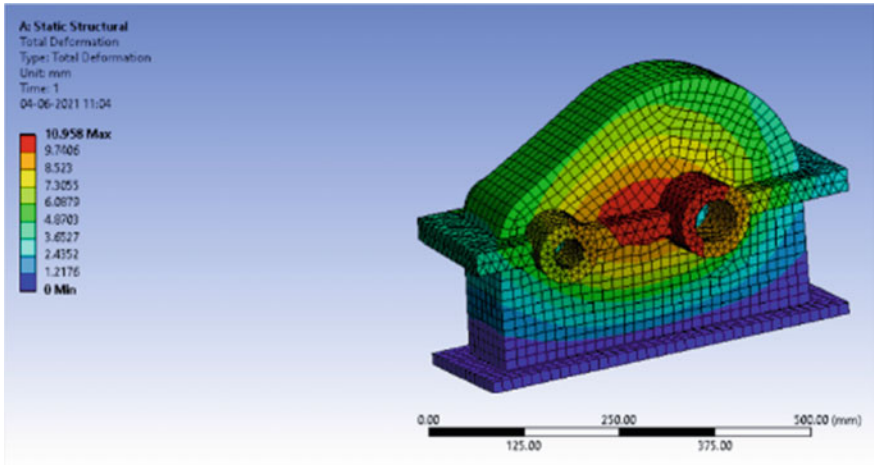


Fig. 18 Epoxy with nylon material

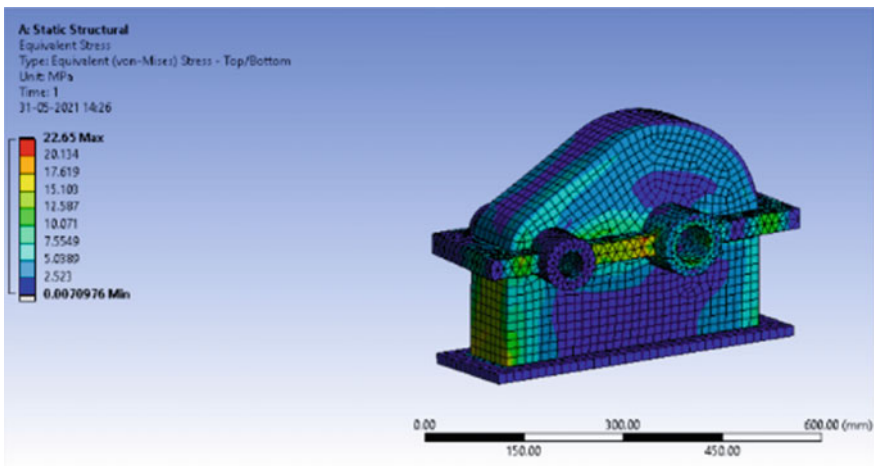


Fig. 19 Stress analysis with polycarbonate as material

7.3 Harmonic Analysis

The Deformation in harmonic analysis along X-axis of the casing with Polycarbonate, Polyamide, Carbon Fibre, Epoxy with carbon fibre and Nylon as material are shown in Figs. 24, 25, 26, 27 and 28 respectively. The Deformation in harmonic analysis along Y-axis of the casing with Polycarbonate, Polyamide, Carbon Fibre, Epoxy with carbon fibre and Nylon as material are shown in Figs. 29, 30, 31, 32 and 33 respectively.

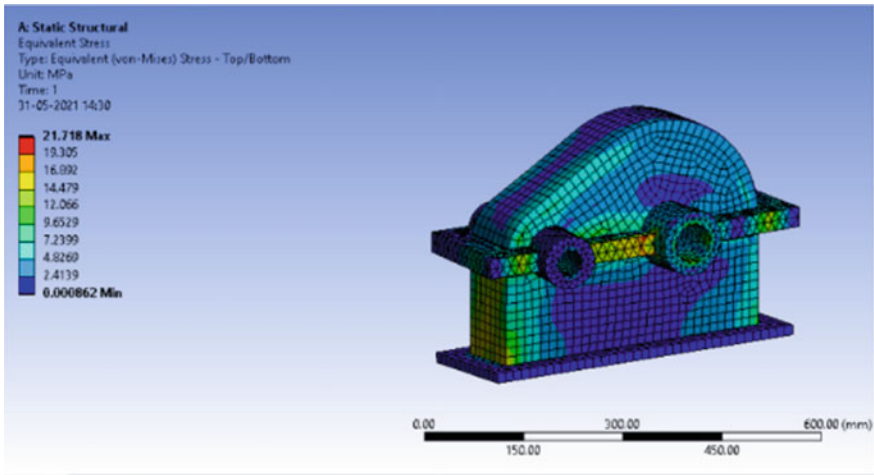


Fig. 20 Stress analysis with polyamide as material

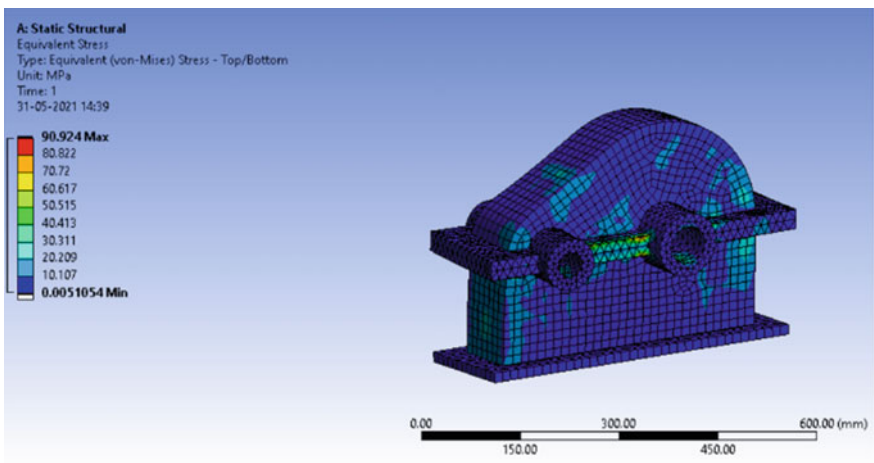


Fig. 21 Stress analysis with carbon fibre as material

The Normal Stress obtained in harmonic analysis along *X*-axis of the casing with Polycarbonate, Polyamide, Carbon Fibre, Epoxy with carbon fibre and Nylon as material are shown in Figs. 34, 35, 36, 37 and 38 respectively. The Normal Stress obtained in harmonic analysis along *Y*-axis of the casing with Polycarbonate, Polyamide, Carbon Fibre, Epoxy with carbon fibre and Nylon as material are shown in Figs. 39, 40, 41, 42 and 43 respectively.

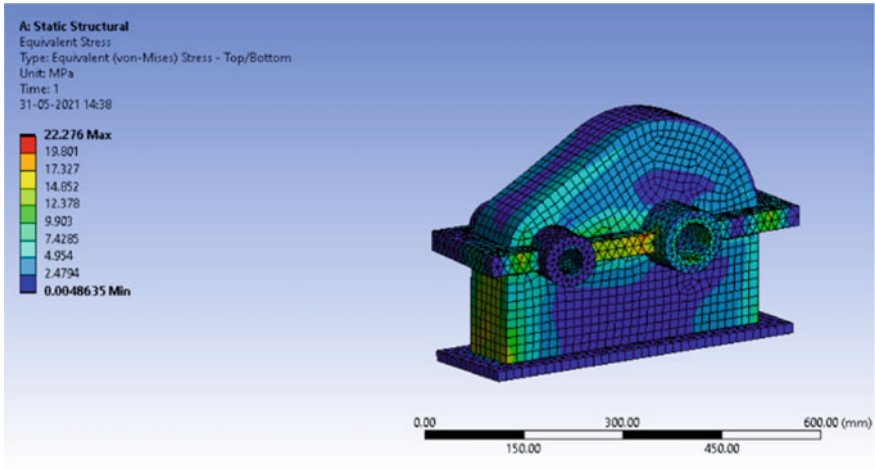


Fig. 22 Stress analysis with carbon fibre with epoxy as material

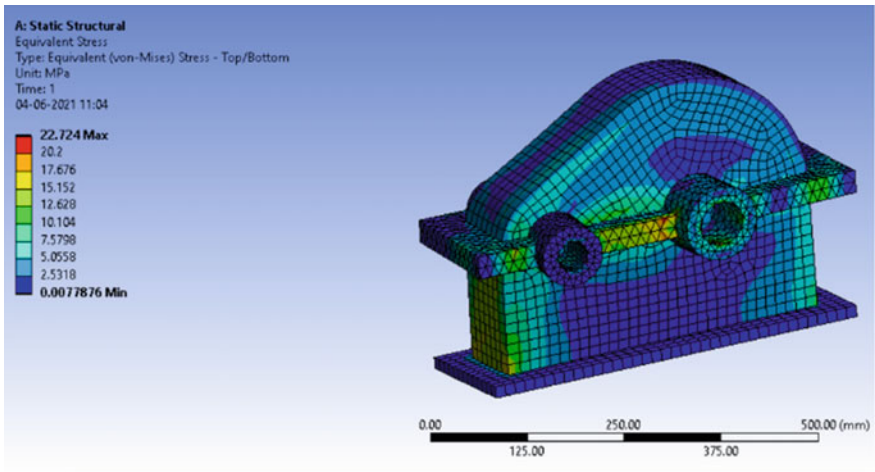


Fig. 23 Stress analysis with nylon as material

Table 9 von-Mises stress and maximum deformation for different materials

	Polycarbonate	Polyamide	Carbon fibre	Epoxy with carbon fibre	Nylon
von-Mises stress (MPa)	22.65	21.718	90.924	22.276	22.724
Max deformation (mm)	6.8185	0.64696	0.64219	0.3743	10.958

Table 10 The first 10 natural frequencies of the casing for different materials

Mode	Gray cast iron	Polycarbonate	Epoxy with carbon fibre	Carbon fibre	Polyamide	Nylon
1	325.08	7.5678	297.36	277.45	322.05	93.912
2	490.64	11.71	526.41	530.22	479.75	144.16
3	563.21	13.392	527.44	549.3	552.57	165.01
4	663.48	15.586	578.96	590.03	656.63	192.66
5	689.48	15.657	657.34	655.08	692.57	195.8
6	842.43	19.912	777.8	818.72	829.28	245.76
7	925.05	21.157	844.62	873.56	919.21	264.18
8	971.28	24.112	979.63	987.97	938.76	292.71
9	972.97	24.169	1022.5	1065.4	940.56	293.39
10	1016.1	25.058	1167.4	1187.9	982.62	305.12

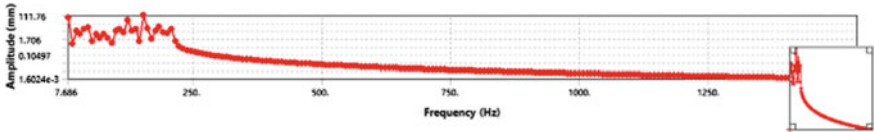


Fig. 24 Deformation in harmonic analysis (*X*-axis) with polycarbonate as material

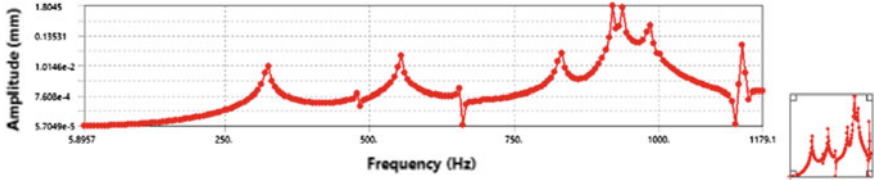


Fig. 25 Deformation in harmonic analysis (*X*-axis) with polyamide as material

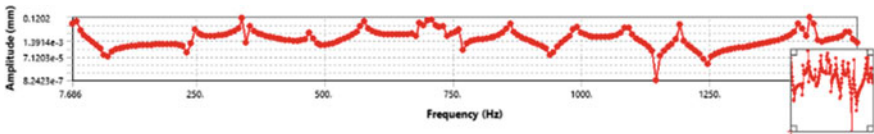


Fig. 26 Deformation in harmonic analysis (*X*-axis) with carbon fibre as material

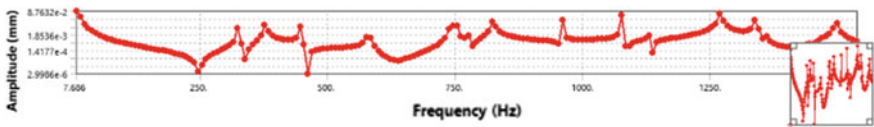


Fig. 27 Deformation in harmonic analysis (*X*-axis) with epoxy with carbon fibre as material

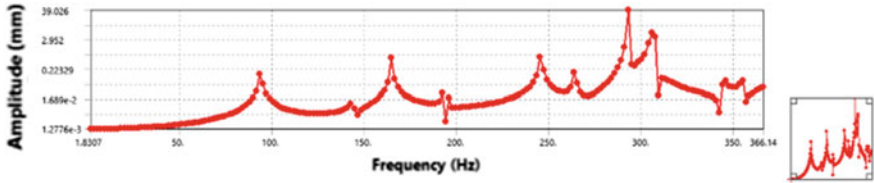


Fig. 28 Deformation in harmonic analysis (X-axis) with nylon as material

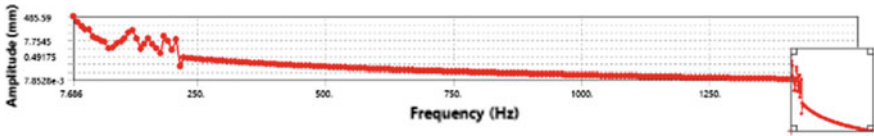


Fig. 29 Deformation in harmonic analysis (Y-axis) with polycarbonate as material

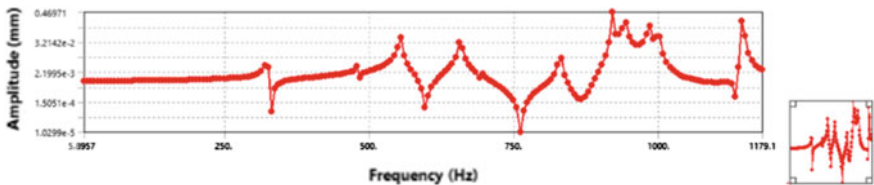


Fig. 30 Deformation in harmonic analysis (Y-axis) with polyamide as material

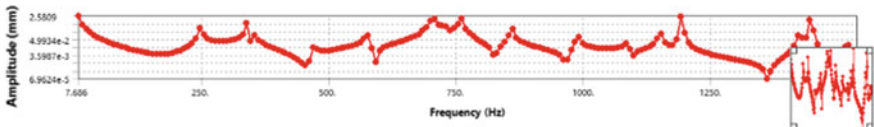


Fig. 31 Deformation in harmonic analysis (Y-axis) with carbon fibre as material

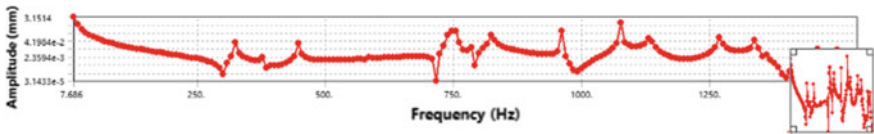


Fig. 32 Deformation in harmonic analysis (Y-axis) with epoxy with carbon fibre as material

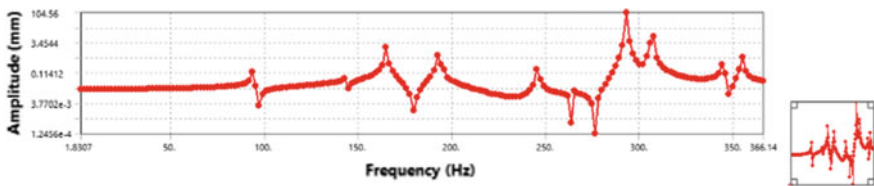


Fig. 33 Deformation in harmonic analysis (Y-axis) with nylon as material

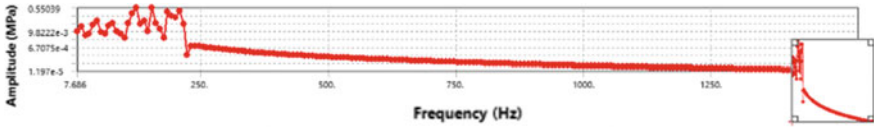


Fig. 34 Normal stress in harmonic analysis (X-axis) with polycarbonate as material

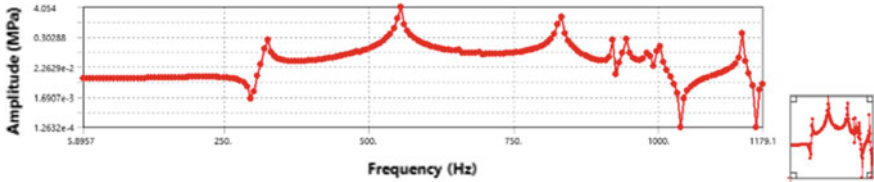


Fig. 35 Normal stress in harmonic analysis (X-axis) with polyamide as material

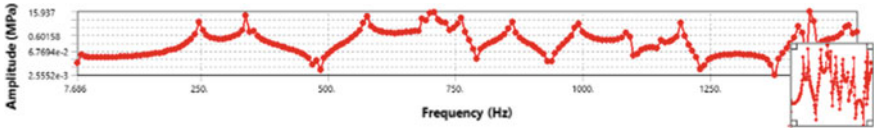


Fig. 36 Normal stress in harmonic analysis (X-axis) with carbon fibre as material

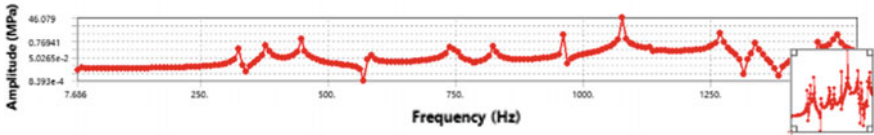


Fig. 37 Normal stress in harmonic analysis (X-axis) epoxy with carbon fibre as material

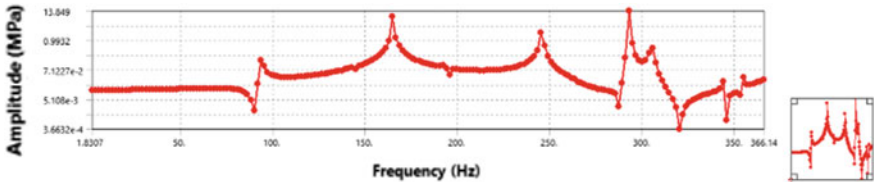


Fig. 38 Normal stress in harmonic analysis (X-axis) with nylon as material

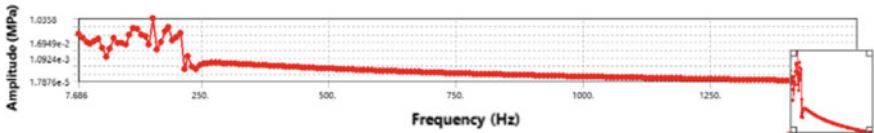


Fig. 39 Normal stress in harmonic analysis (Y-axis) with polycarbonate as material

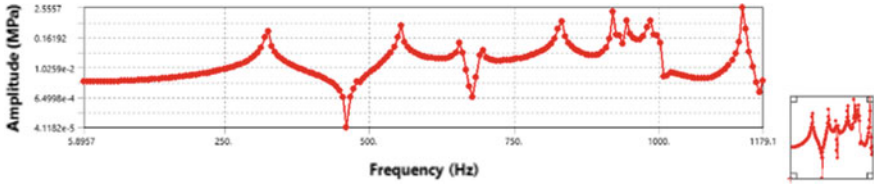


Fig. 40 Normal stress in harmonic analysis (Y-axis) with polyamide as material

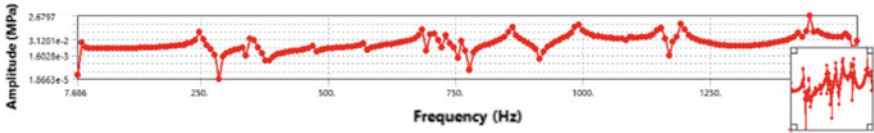


Fig. 41 Normal stress in harmonic analysis (Y-axis) with carbon fibre as material

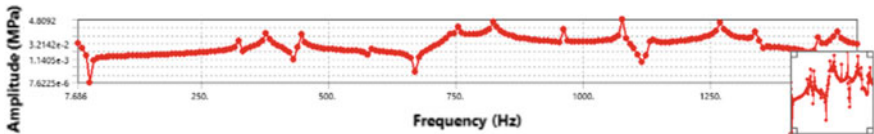


Fig. 42 Normal stress in harmonic analysis (Y-axis) epoxy with carbon fibre as material

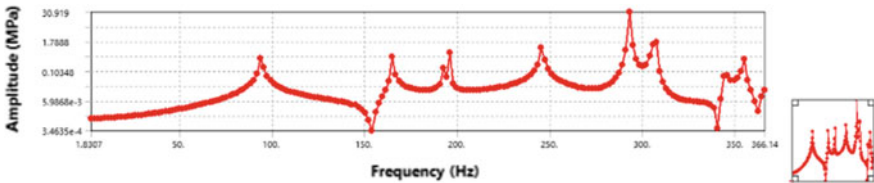


Fig. 43 Normal stress in harmonic analysis (Y-axis) with nylon as material

8 Results and Discussion

The comparison of maximum deformation of the gearbox with all the materials tells that the most deformation occurs for Nylon (10.96) and the least occurs in Epoxy with carbon fibre (0.37) among the additive manufacturing materials (Fig. 44).

The comparison of maximum stress of the gearbox with all the materials tells that the maximum stress occurs for Carbon fibre (90.92 MPa) and the least occurs in Polyamide (21.72 MPa) among the additive manufacturing materials (Fig. 45). The comparison of percentage decrease in weight as compared to Gray Cast Iron for each material as shown in Fig. 46 demonstrates that Polycarbonate is the lightest of all the other materials, that is it shows a 83.33% decrease in total weight as compared with

Fig. 44 Comparison of deformation of all the materials

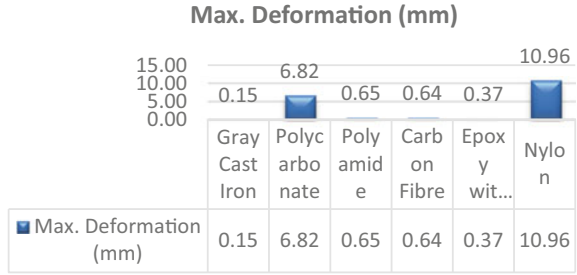


Fig. 45 Comparison of stress of all the materials

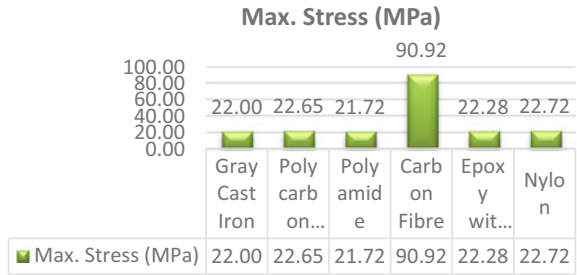
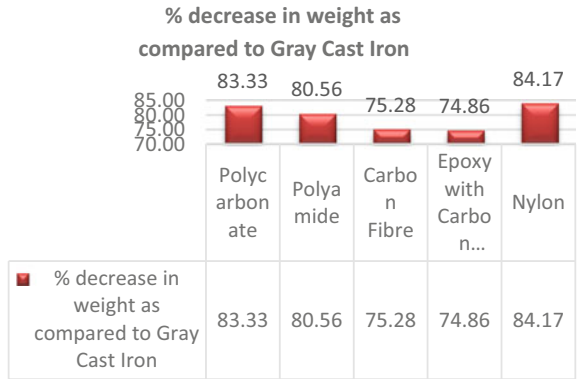


Fig. 46 The comparison of percentage decrease in weight as compared to gray cast iron for each material



Gray Cast Iron. Similarly, the material which shows the minimum weight reduction of the materials is Epoxy with Carbon Fibre which shows a 74.86% decrease in total weight as compared to Gray Cast Iron.

9 Conclusion

After conducting the static, modal, and harmonic analysis on Gray Cast Iron and 5 other additive manufacturing materials we find that Epoxy with carbon fibre produces the least deformation of 0.37. And maximum stress is obtained on carbon fibre with 90.92 MPa. Through cost analysis carbon fibre with epoxy is found to be the most expensive and Polycarbonate is the least expensive in comparison to the other materials. The decrease in weight as compared to the grey cast iron material for the casing is maximum in Nylon with 84.17%, in polyamide with 80.56% and in carbon fibre with 74.26%. So, on comparing all the materials with above mentioned parameters carbon fibre provides good material properties but is expensive in comparison to others. Polyamide has the maximum deformation of 0.65 which is at par with carbon fibre and has good material properties. Weight of the Polyamide casing is much lesser than carbon fibre. Through cost analysis it is found Polyamide is cheaper than Carbon fibre. Through this study and analysis, it is concluded that Polyamide provides the best results as an additive manufacturing material for the gear box casing.

References

1. Shigley J E (2011) Shigley's mechanical engineering design. Tata McGraw-Hill Education
2. Patil SM, Pise SM (2013) Modal and stress analysis of differential gearbox casing with optimization. *Int J Eng Res Appl* 3(6):188–193
3. Kumar A, Jaiswal H, Jain R, Patil PP (2014) Free vibration and material mechanical properties influence based frequency and mode shape analysis of transmission gearbox casing. *Procedia Eng* 97:1097–1106
4. Walhekar SP, Kharde RR (2015) Vibration analysis for two wheeler gearbox casing using FEA. *Int J Recent Technol Mech Electr Eng* 2(8):12–15
5. Basavaraj S, Panvel PIIT (2016) Analysis of gearbox casing using FEA. *Int J Eng Res Gen Sci* 4(5):215–219
6. Tang X (2019) Structural strength analysis of gearbox casing based on ABAQUS. *IOP Conf Ser Mater Sci Eng* 677(5):052067. IOP Publishing
7. Patil YV, Karanjka SV, Chavan HA, A review paper on design and analysis of gearbox casing. *Int J Innov Eng Sci* 4(10):175–179
8. Sekhar K, Dharmadhikari P, Panchal S, Rao LB (2021) Design and optimization of a two-stage gearbox using GearTrax. In: *Recent Trends in Mechanical Engineering*. Springer, Singapore, pp 445–477
9. Anand S, Sriekshav AD, Sharran B, Rao LB (2021) Design and analysis of helical teeth harmonic drive. *Recent Trends Mech Eng*. Springer, Singapore, pp 507–519
10. Chavan NT, Kaur-Wadhwa G, Talikoti BS (2016) Analysis of Gearbox Casing and Effect of Frequency on Stress and Strain using FEA. *Int J Res Eng Technol* 5(10):251–256
11. Patel N, Rokad V, Vora C (2014) Optimization of gearbox casing for multi-stage gearbox by using FEA approach. *J Appl Sci Comput*, 6(5):192–200
12. Patel T, Dubey A, Rao LB (2019) Design and analysis of an epicyclic gearbox for an electric drivetrain. *Int J Recent Technol Eng* 8(3):6834–6842
13. *Data Book of Engineers* by PSG College-Kalaikathir Achchagam
14. Gujaba KP, Parashar S, Rao LB (2021) Design and analysis of permanent magnetic gears. In *Recent Trends Mech Eng*. Springer, Singapore, pp 521–530

15. Maciejczyk A, Zdziennicki Z (2004) Design basic of industrial gear boxes. calculation and design case example. Technical U. o Lodz (April 2011)
16. Vijaykumar, Shivaraju, Srikanth (2014) Vibration analysis for gearbox casing using finite element analysis. *Int J Eng Sci* (2):18–36
17. Gupta A, Yashvanth VP, Rao LB (2021) Design of gears using aluminium 6061-T6 alloy for formula SAE steering system. *Recent Trends Mech Eng*. Springer, Singapore, pp 489–505

Design and Manufacturing

Design and Optimization of a 3-Stage Industrial Gearbox



Shubham Sunil Patil, Swaraj Chandraparkash Parate,
Hrushikesh Vishwas Kulkarni, and Lokavarapu Bhaskara Rao

Abstract Reduction Gearbox are widely used in many industrial applications like Conveyer belts in underground mines, Extruders, Cranes, Crushing Machine, etc. which require high power to function. This paper focuses on designing an optimized 3-stage gearbox. 3-Stage gearbox is chosen as it can work under high gear ratio very efficiently and effectively for speed reduction. The motive to develop a new gearbox is to improve in terms of safety, durability, and efficiency. Helical gears are chosen for gearbox design as they are extensively used in industrial operations for power transmission under heavy loads with smoother and noiseless operation. In this paper the gearbox is designed, considering the requirements of a mining conveyer belt. The gearbox is modeled using Solidworks and then analyzed based on finite element analysis method using Ansys workbench. FEA analysis is conducted to measure and analyze the safety factor, shear stress and total deformation. Finally, the optimal design of gearbox is achieved to meet functional as well as reliability requirements in the field.

Keywords Industrial gearbox · 3-stage gearbox · Helical gear · Gear analysis

S. S. Patil · S. C. Parate · H. V. Kulkarni · L. Bhaskara Rao (✉)
School of Mechanical Engineering, Vellore Institute of Technology Chennai,
Vandalur-Kelambakkam Road, Chennai, Tamil Nadu 600127, India
e-mail: bhaskarbabu_20@yahoo.com

S. S. Patil
e-mail: shubhamsunil.patil2018@vitstudent.ac.in

S. C. Parate
e-mail: swaraj.2018@vitstudent.ac.in

H. V. Kulkarni
e-mail: hrushikesh.vishwas2018@vitstudent.ac.in

Nomenclature of the code

Power	Operating power
N	Rpm
m	Module
alpha	Pressure angle
Psi	Helix angle
Zp	Number of pinion teeth
Zg	Number of gear teeth
i	Gear ratio
ha	Addendum height
hf	Dedendum height
t	Tooth thickness
dp	Pitch circle diameter of pinion
dg	Pitch circle diameter of gear
dap	Addendum circle diameter of pinion
dfp	Dedendum circle diameter of gear
dag	Addendum circle diameter of gear
dfg	Dedendum circle diameter of pinion
Mt	Transmitted torque
Pt	Tangential force
Pa	Axial force
Pr	Radial force

1 Introduction

An underground mine needs a 3-stage Industrial gearbox to facilitate the movement of a conveyor belt which carries coal from underground to the surface. The motive to develop a new gearbox is to improve in terms of safety, durability and efficiency. The aim of project is to design an optimized gearbox which could be later manufactured by the workshop. Helical gears are chosen for gearbox design as they are extensively used in industrial operations for power transmission under heavy loads with smoother and noiseless operation. In a gear, the surface strength, shear force and bending stress of the gear tooth majorly contribute to the failure of the gears. The gearbox is modelled using Solidworks and then analyzed by finite element analysis method using Ansys workbench. The static/transient motion analysis is conducted to measure and analyze the safety factor, shear stress, factor of safety and total deformation. Finally, the optimal design of gearbox is achieved to meet functional as well as reliability requirements in the field [1, 2].

Neeraj et al. [3] developed a robust and axiomatic design using a property-based approach to design applying functional requirements and design parameters. The different operating conditions of a gearbox are considered in the paper. The paper

presents a complex methodology for designing of the gearbox using CAD software, has followed a similar approach using functional requirements and design parameters using modern software. Sonali et al. [4] in their paper design and FEM analysis of helical gear have discussed the problem of gear breakdown in speed reduction gearbox that is resolved by changing the current material by steel with the help of AGMA and FEM analysis method on the Gear and Pinion. Module of the gear is calculated by the estimated stress which can withstand the loading conditions. We have used the modified Lewis beam strength method to perform Ansys analysis.

Ghewade et al. [5] in their work thermal analysis of helical and spiral gear train presented the study of thermal analysis of helical and spiral gears transmission gearbox. Firstly, the gearbox is designed using the known formulas. The 2D drawing of the gear is then converted into a 3D model by using CAD software. The temperature relation is tested for no load and full load condition. Venkatesh et al. [6] conducted a structural analysis on a helical gear in high speed operations like marine engines. The design parameters of the model were calculated by theoretical methods. Different materials were analyzed to find the stress and deflection of the tooth. The results of theoretical analysis and FEM analysis are compared to each other. The conclusion was to get the material which is suitable for the marine engines. We have followed a similar method for stress analysis and material selection.

May and New [7] in their work stress analysis on spur gears using Ansys workbench have explained that driving gear tooth meshes with the driven gear tooth to transmit power. Analysis of total deformation and bending stress of gear is the necessity of the gear design. In this paper, Hertz equation and ANSYS workbench is used for performing contact stress analysis on stainless-steel spur gear.

Niyamat and Bicha [8] in their project have researched about the design and analysis of helical gear having involutes profile. In this project the helical gear having involutes profile is modeled on the CATIA V5R16 software and ANSYS software is used to perform static structural and modal analysis. We decided to use a helical gear based on inference we got from the following and also followed a similar process to design helical gear with involutes using Solidworks.

Naresh and Chandrudhu [9] in the project titled designed and analysis of helical gear have discussed about helical gears which are widely used in industries. In this project they have designed the helical gear by using Solidworks software and Solidworks simulation is used for analysis of gear by applying different materials and different loads on it. We approached the designing of helical gear using Solidworks based on the guidelines followed in this paper. Many other projects related to gear designing and analysis were studied to find the best method to use for this work [10–17]. Many studies involve the use of alternative materials like plastics and aluminum for better performing gearbox. Also methods like the use of geartrax software for designing of gears were used in many studies, alternatively Solidworks and python is used for designing and calculations in this work.

The objective of this paper is to design a 3-stage industrial gearbox for operating a conveyor belt used to transport coal from beneath the surface to surface level in an underground mine conveyor belts are used. The motor used to facilitate the movement of the conveyor belt has an output of 1400 rpm, at that rpm, it is too high because at

that speed the conveyor belt wouldn't be able to retain coal as coal would spurt out of the conveyor belt, the fast motion of the conveyor also becomes a source of danger for the miners at work and also at that speed the chances of belt slippage is very high. To improve the efficiency, safety and durability of the conveyor an industrial gearbox is used for speed variation. The gearbox is designed assuming the length of the conveyor belt which is assumed to be 60 m, the required output speed is 1–1.5 m/s and the capacity of the conveyor belt is 200 ton/hr. This paper specifies the whole process of designing a safe and reliable industrial 3-stage gearbox for the application of conveyor belt used in coal mining.

2 Design and Force Calculations

2.1 Power Requirement for the Conveyor Belt

The power requirement for the belt is calculated using the formula in Eq. (1)

$$\text{Power} = \frac{F_c(L + T_f)(C + 3.6QS)}{367} \pm \frac{CH}{367} \quad (1)$$

where, F_c = Equipment friction factor = 0.0225, L = Horizontal center to center distance = 60 m, T_f = terminal friction constant = 60 m, C = capacity = 200 ton/hr, Q = mass of moving parts (assuming idler diameter = 152 mm and belt width = 2000 mm)

$$\therefore Q = 148$$

S = Belt speed

Size of head pulley = 500 mm, Circumference of head pulley = $2 \times \pi \times r = 1.57\text{m}$

$$\text{Output rpm} = 1400/30 = 48\text{rpm} = 0.8\text{rps}$$

$$\therefore S = 0.8 \times 1.57 = 1.256\text{m/s}$$

H = net change in elevation (assuming elevation of 15°).

$$\therefore H = 60 \times \tan 15 = 16.07\text{m}.$$

Substituting the values in above formula we get power (P) = 15.15 kW.

\therefore Power transmitted through the gearbox is 15.15 kW.

Table 1 Standard proportions of gear systems

Sr. no	Particulars	141/2° Composite full depth involute system	20° full depth involute system	20° stud involute system
1	Addendum	1 m	1 m	0.8 m
2	Dedendum	1.25 m	1.25 m	1 m
3	Working depth	2 m	2 m	1.60 m
4	Minimum total depth	2.25 m	2.25 m	1.80 m
5	Tooth thickness	1.57 m	1.57 m	1.57 m
6	Minimum clearance	0.25 m	0.25 m	0.2 m
7	Fillet radius at root	0.4 m	0.4 m	0.4 m

Standard proportions of gear:

Table 1 shows the standard proportions in module (m) for the gear systems [18].

For design and force calculations a standard model was considered for designing the helical tooth. All the calculations are done considering a 20° full depth involute system.

2.2 Formula for Calculating Gear Parameters

The formulas [1] used for calculating the torque and forces on the gears are presented in Eq. (2), (3), (4) and (5)

$$M_t = \frac{60 \times 10^6 (P)}{2\pi n_p} \quad (2)$$

$$P_t = \frac{2M}{d_p} \quad (3)$$

$$P_r = P_t \frac{\tan \alpha_n}{\cos \Psi} \quad (4)$$

$$P_a = P_t \tan \Psi \quad (5)$$

The formulas [1] used for calculating Addendum and dedendum Diameter are presented in Eqs. (6) and (7) respectively

$$d_a = m_n \frac{z}{\cos \Psi} + 2 \quad (6)$$

$$d_f = m_n \frac{z}{\cos \Psi} - 2.5 \quad (7)$$

The formulas [1] used for calculating Pitch circle diameter of pinion and gear are presented in Eqs. (8) and (9)

$$d_p = \frac{z_p \times m_n}{\cos \Psi} \quad (8)$$

$$d_g = \frac{z_g \times m_n}{\cos \Psi} \quad (9)$$

2.3 Python Code

The Python code has been implemented to compute gear design parameters and forces using the Eqs. 2, 3, 4, 5, 6, 7, 8 and 9, the code has been provided in Appendix.

2.4 Design parameters

For calculating the design parameters and forces standard modules were used like 3, 5 and 8 mm for first, second and third set of gears respectively. The numbers of teeth of each gear were calculated by iterative method for getting the desired gearbox ratio. The python code automatically calculates the diameters and forces after entering the required values like power, rpm, number of teeth, angles and module for each set of gear and pinion. The design parameters and forces for all set of pinion and gear are presented in Table 2.

2.5 Material Selection

Special attention has to be given to the material selection of the gearbox as it will decide the weight, life and cost of the product. In a gear box the gears are the main components as they are the one under wear and tear due to high loading conditions. So, material selection becomes a crucial stage in the designing process. Material is selected by analyzing its physical properties, manufacturing properties and cost. The four materials that are taken into consideration for the gears are Aluminum Alloy, Ductile Cast, Mild Steel and Iron Alloy Steel. The mechanical properties that will be used for evaluation are Tensile strength, Yield strength, Density and Hardness. The comparison of the metals based on mechanical properties is presented in Table 3.

Table 2 Design parameters for all set of gear and pinion

Description	Units	1st Set		2nd Set		3rd Set	
		Pinion value	Gear value	Pinion value	Gear value	Pinion value	Gear value
No. of teeth	–	37	89	27	88	20	76
Helix angle (ψ)	Degree	20		20		20	
Gear ratio	–	2.405	2.405	3.259		3.8	3.8
Pressure angle (φ)	Degree	20		20		20	
Module (m)	mm	3		5		8	
Addendum (h_a)	mm	3		5		8	
Dedendum (h_d)	mm	1.25 m = 3.75		6.25		10	
Pitch circle diameter (d_p)	mm	118.123	284.135	143.664	468.238	170.28	647.083
Pitch circle radius (r_p)	mm	59.1	142.065	71.835	234.142	85.14	323.541
Addendum circle diameter (d_a)	mm	124.1237	290.135	153.66	478.238	186.28	663.083
Dedendum circle diameter (d_f)	mm	110.6237	276.6355	131.164	455.73	150.28	627.083
Transmitted torque	N-mm	100,480		241,700		804,590	
Tangential force component	N	1701.3		3364.8		9450.8	
Axial force component	N	3806		7527.6		21,143	
Radial force component	N	9326.6		18,446		51,811	

Table 3 Material mechanical properties comparison

Material	Tensile strength (MPa)	Yield strength (MPa)	Density (g/cm^3)	Hardness (Brinell)
Ductile cast iron (GRADE 60–40-18)	414	40,000	7.1	200
Alloy steel	655	415	8.05	197
Mild steel	444	250	7.85	130
Al-alloy (6061)	310	276	2.7	95

2.6 CAD Model

CAD modeling of a pinion, gear and assembly of gearbox was done using Solidworks [18, 19]. A 3d model of the components is necessary for finite element method (FEM) analysis. Solidworks is solid modeling software used to design the components in 3 dimensions. There are a total of 5 components in the gearbox assembly as follows:

Input Shaft and Gear

Figure 1 represents the input shaft with the gear of the gear box. A high rpm motor will be attached on one end of this shaft.

1st Motion Shaft and Gear

As this is a three stage gearbox, there will be a total of 4 shafts with a total of 6 gears mounted on it. Figure 2 represents the 1st motion shaft. This shaft has two gears mounted on it. One of the gear will be linked with the input shaft gear to start the reduction process.

2nd Motion Shaft and Gear

The second motion shaft also has two gears on it. One of the gears will be linked to the gear of 1st motion shaft and the other gear will be linked to the gear of the output shaft gear. Figure 3 represents the 2nd motion shaft.

Fig. 1 Input shaft and gear

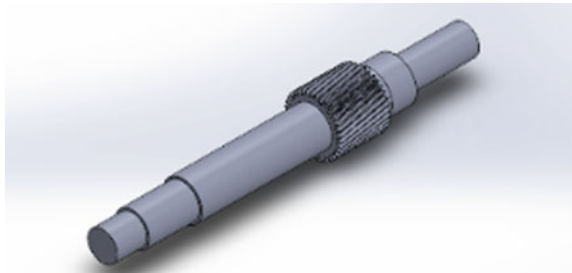


Fig. 2 1st motion shaft and gear

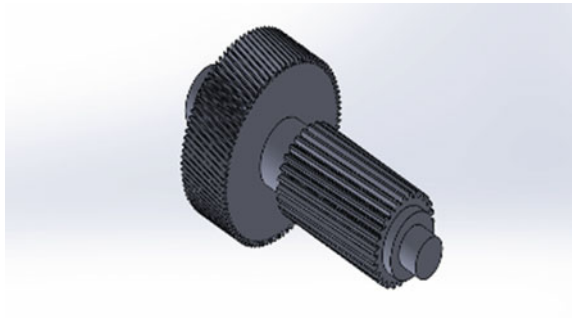


Fig. 3 2nd motion shaft and gear

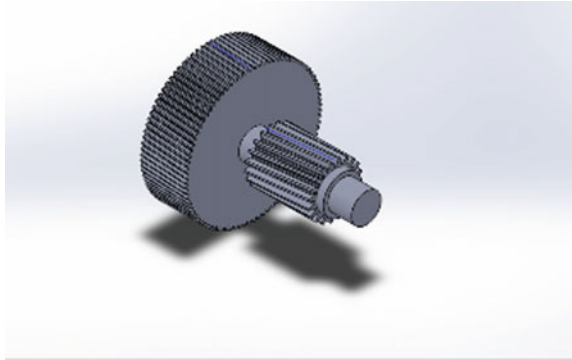
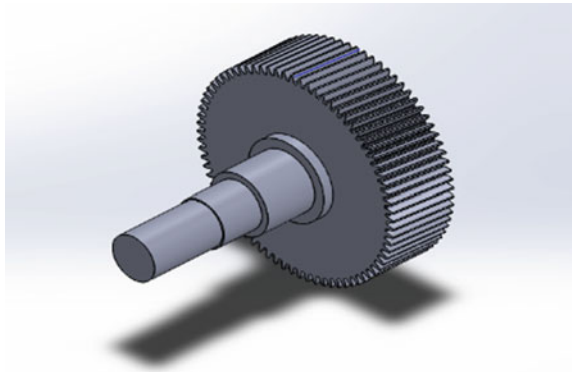


Fig. 4 Output shaft and gear



Output shaft and gear:

Figure 4 depicts the output shaft and gear.

Gearbox Casing

Figure 5 represents the gearbox casing. It is used to provide mechanical support to the shaft and gears.

Assembly

Figures 6, 7 and 8 represents the complete assembly of the gearbox in different views.

3 Meshing

Meshing is done to divide the whole component into a number of smaller discrete elements for computation of stresses, strains, deformation, etc. at a particular point. Tetrahedron elements were used for meshing the entire structure using mesh size as fine with smooth transition. Fine, smooth transition and tetrahedron mesh was chosen to get more accurate results.

Fig. 5 Outer casing

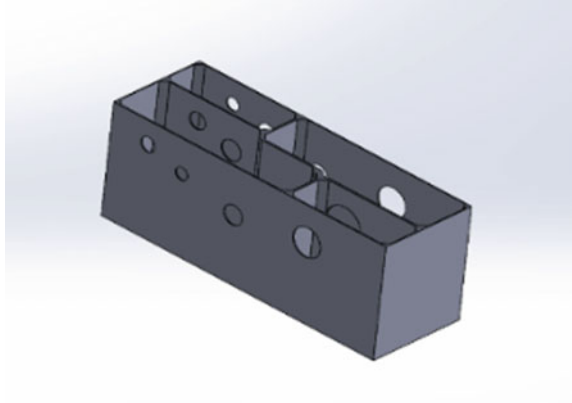


Fig. 6 Gear assembly (side view)

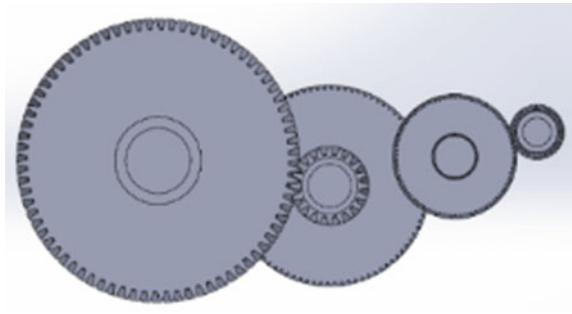


Fig. 7 Gear assembly (isometric view)

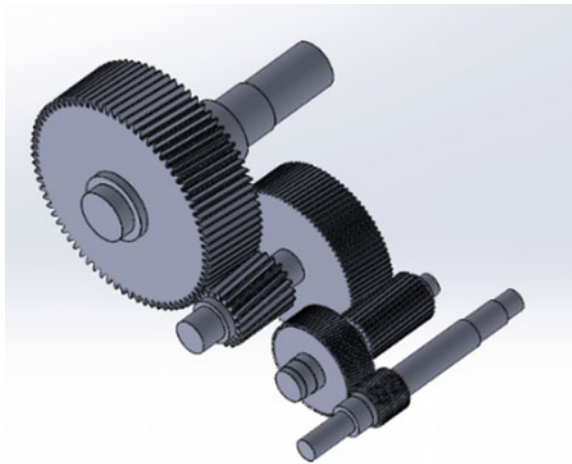
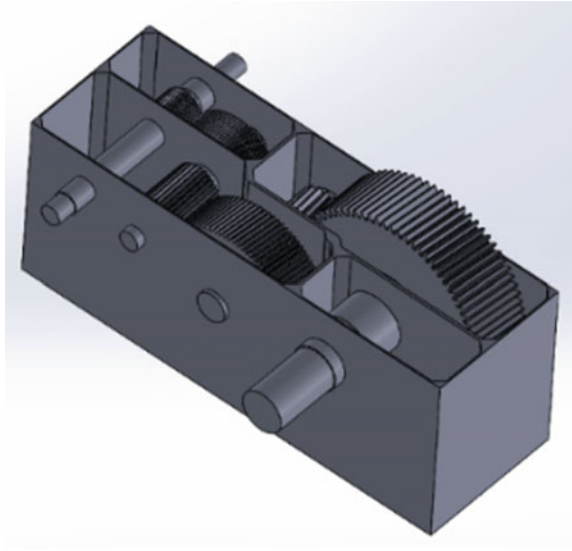


Fig. 8 Complete assembly
(isometric view)



4 Boundary Conditions

For finding the strength of the gears, the driven gear was made fixed and the driving gear that will transfer power to the driven gear was given a moment in the direction of motion which were calculated using formulas and python codes. The gear bigger in size were the driven gear and were made fixed by fixing the inner surface of the gear. Moment of the particular set of the gear was applied on the inner surface of the driven gear which is smaller in size. Frictionless support was added to the sides on the gear to maintain alignment of the gears.

5 Finite Element Analysis

Finite element analysis was performed on ANSYS workbench [19, 20]. The calculated tangential, radial and axial forces and moment were considered as inputs for the analysis. Output results were equivalent stress (von-Mises), total deformation and FOS (stress) for all set of gears.

5.1 Equivalent Stress (von-Mises)

Figures 9, 10 and 11 shows the total deformation of set 1, 2 and 3 respectively on applying all the necessary boundary conditions and forces on the gears. It is observed

Fig. 9 Equivalent stress (von-Mises) analysis of 1st set of gears

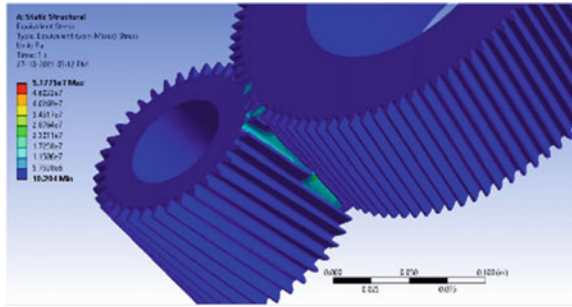


Fig. 10 Equivalent stress (von-Mises) analysis of 2nd set of gears

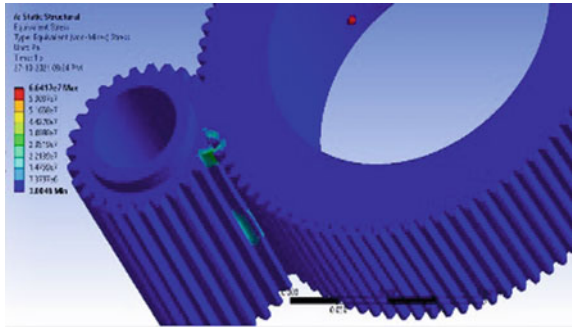
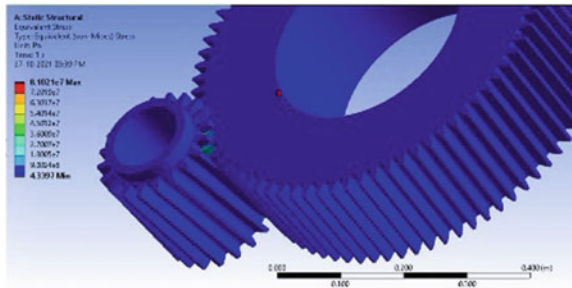


Fig. 11 Equivalent stress (von-Mises) analysis of 3rd set of gears



that the maximum equivalent stress value is under allowable limit. Thus the gears are safe.

5.2 Total Deformation

Figures 12, 13 and 14 shows the total deformation of set 1, 2 and 3 respectively on applying all the necessary boundary conditions and forces on the gears. The

Fig. 12 Total deformation of 1st set of gears

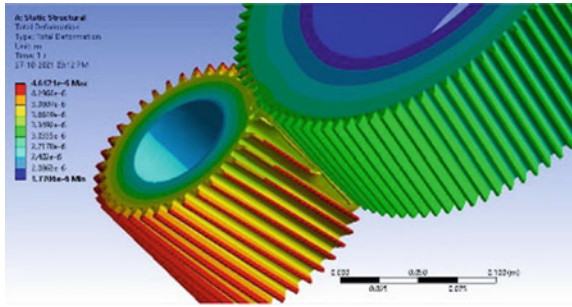


Fig. 13 Total deformation of 2nd set of gears

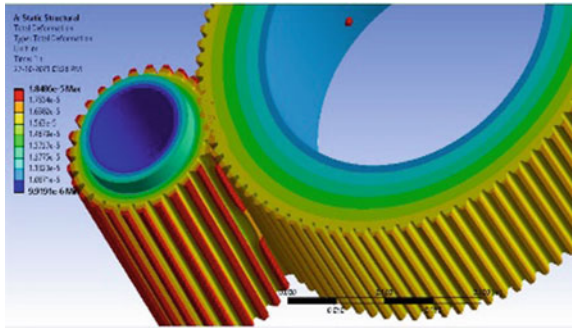
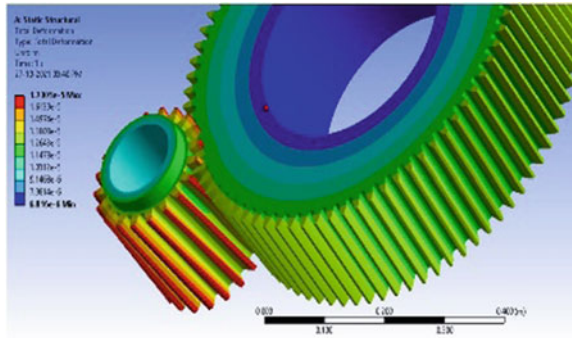


Fig. 14 Total deformation of 3rd set of gears



deformation in the gears is found to be in the figures of 10 raised to the power of -6 . Hence there is very less compliance.

5.3 Shear Stress

Figures 15, 16 and 17 shows the total deformation of set 1, 2 and 3 respectively on applying all the necessary boundary conditions and forces on the gears. The values of shear stresses are found to be under permissible limit. Hence the design is safe.

Fig. 15 Shear stress of 1st set of gears

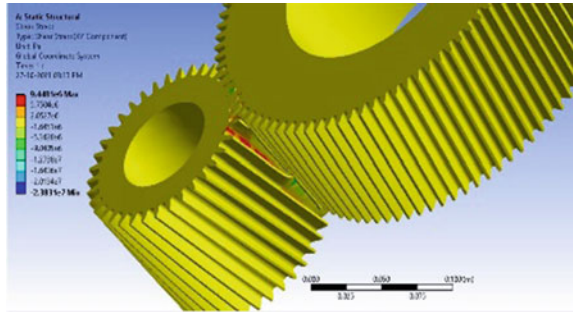


Fig. 16 Shear stress of 2nd set of gears

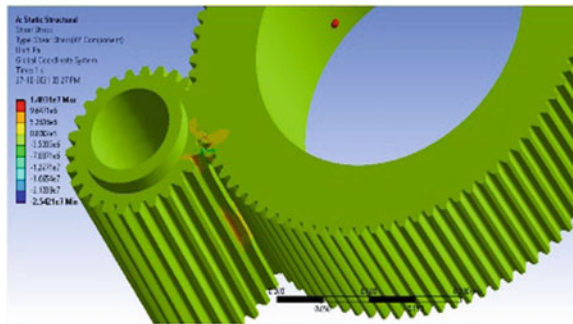
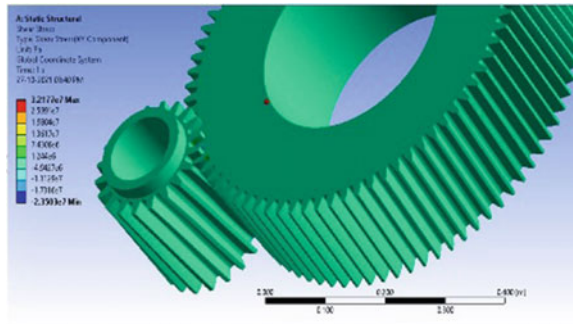


Fig. 17 Shear stress of 3rd set of gears



5.4 Stress Tool (Factor of Safety)

Figure 18, 19 and 20 shows the total deformation of set 1, 2 and 3 respectively on applying all the necessary boundary conditions and forces on the gears. The values of factor of safety are well above the required values. Thus, the design is safe.

Fig. 18 Stress FOS of 1st set of gears

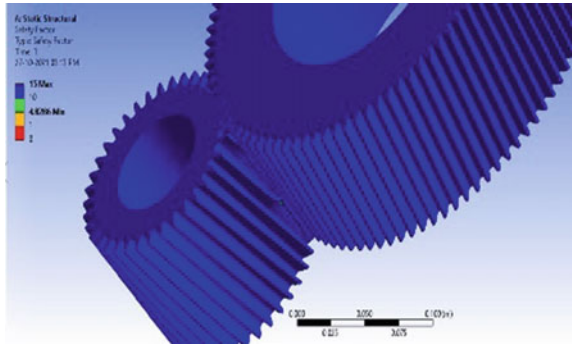


Fig. 19 Stress FOS of 2nd set of gears

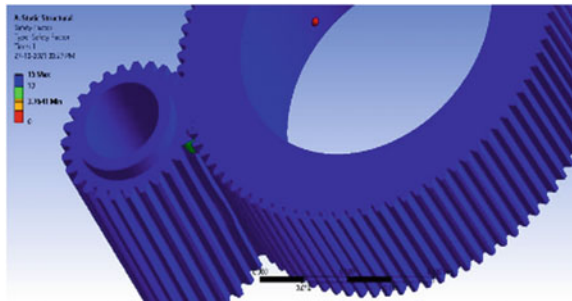
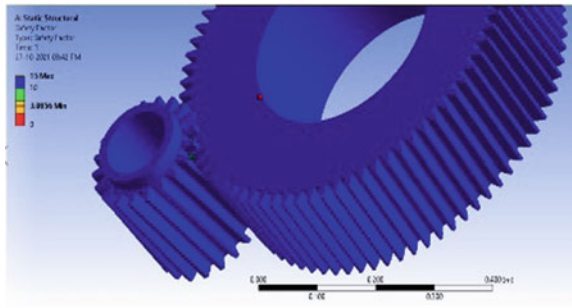


Fig. 20 Stress FOS of 3rd set of gears



5.5 Fatigue Tool (Factor of Safety)

Figures 21, 22 and 23 shows the total deformation of set 1, 2 and 3 respectively on applying all the necessary boundary conditions and forces on the gears. The values of factor of safety are observed to be a minimum of 2. Thus, the design is safe to handle at least twice the loads.

Fig. 21 Fatigue FOS of 1st set of gears

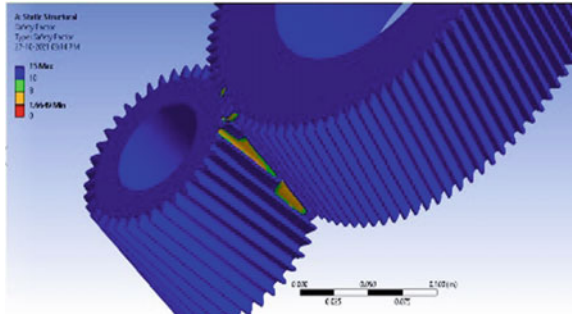


Fig. 22 Fatigue FOS of 2nd set of gears

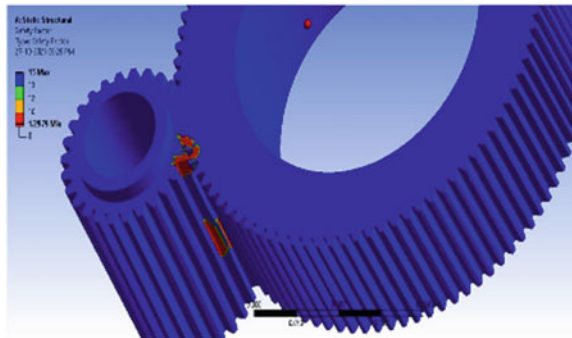


Fig. 23 Fatigue FOS of 3rd set of gears

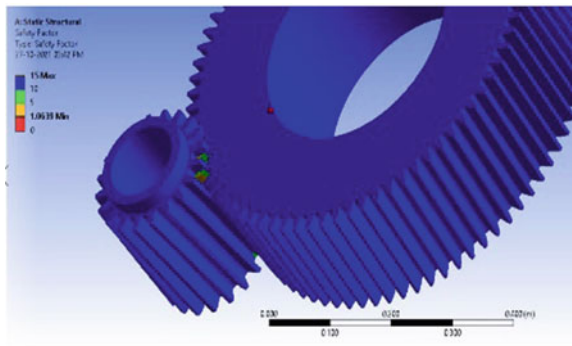


Table 4 Grid Independence study for 1st set of gears

Element size	Set 1		Set 2		Set 3	
	Equivalent stress	Stress FOS	Equivalent stress	Stress FOS	Equivalent stress	Stress FOS
0.06	1.9153	13.05	1.9059	13.11	2.0074	12.45
0.05	2.2341	11.19	2.1723	11.51	2.1429	11.66
0.04	2.5437	9.82	2.2363	11.18	2.1583	11.58
0.03	2.618	9.54	2.3591	10.59	3.6095	6.92
0.02	3.3525	7.45	3.6634	6.82	3.8697	6.46
0.01	3.4275	7.29	4.9698	5.03	5.4835	4.59
0.009	3.9101	6.31	5.1667	4.84	5.551	4.51
0.008	4.0655	6.15	5.7601	4.33	5.8805	4.25
0.007	4.2726	5.88	5.9305	4.21	6.1021	3.81
0.006	4.7078	5.31	6.3417	3.94	7.0031	3.55
0.005	4.8824	5.23	6.4253	3.76	7.0241	3.47

6 Result and Discussion

Grid Independence study was done for all the 3 set of gears. For all the three set of gears body sizing and face sizing functions were used to reduce the mesh size continuously till recurring values of stresses were obtained. The theoretical calculations using the python code gives the dimensions and other specifications of all the set of gears. The module for 3 set were considered to be 3, 5 and 8 mm and the gear parameters are calculated using the formulas and python code. After conducting FEA analysis on all the set of gears, the results were found and grid independence study is done to achieve mesh convergence of which the results are depicted in Table 4. From the grid independence study it can be seen that the minimum stress factor of safety for first set is 5.23, for second set is 3.76 and for third set is 3.47. As per the analysis it can be seen that the stress factor of safety is greater than 1 which specifies that all the gears are safe to use under the applied loads. Also the total deformation for the 3 set of gears is 4.6121e-6, 1.8486e-5 and 1.7305e-5 which is very less and cannot affect the performance of the gearbox. From the results it can be concluded that the gear box is safe for the applied loads and its further application.

7 Conclusion

From the research conducted, it can be concluded that the design of a 3-stage industrial gearbox was successfully completed. The calculations were performed considering all the loads on the gears to design a reliable system. The CAD model was

designed on Solidworks software and FEA analysis was done on ANSYS workbench. Finite element analysis was done on the CAD models using the calculated parameters to check the durability of the system. The gearbox has been properly analyzed considering many factors like stress, deformation, factor of safety, shear stress, fatigue damage and thus it can be concluded that the gearbox is safe and durable and can be used in the mining applications.

Appendix

Python Code

```
import math
pi = math.pi
power = float(input("Enter Power\t"))
N = float(input("Enter rpm\t"))
m = float(input("Enter module\t"))
alpha = float(input("Enter pressure angle\t"))
psi = float(input("Enter helix angle\t"))
zp = float(input("Enter Number of teeth of pinion\t"))
zg = float(input("Enter Number of teeth of gear\t"))
i = zg/zp
ha = m
hf = 1.25*m
t = 1.5808*m
dp = zp*m/(math.cos(psi*pi/180))
dap = m*(zp/(math.cos(psi*pi/180)) + 2)
dfp = m*(zp/(math.cos(psi*pi/180))-2.5)
dg = zg*m/(math.cos(psi*pi/180))
dag = m*(zg/(math.cos(psi*pi/180)) + 2)
dfg = m*(zg/(math.cos(psi*pi/180))-2.5)
Mt = (60,000,000*power)/(2*pi*N)
Pt = 2*Mt/dp
Pa = Pt*math.tan(psi)
Pr = Pt*(math.tan(psi)/math.cos(psi))
dict1
{'ha':ha,'hf':hf,'t':t,'dp':dp,'dap':dap,'dfp':dfp,'dg':dg,
'dag':dag,'dfg':dfg,'Mt':Mt,'Pt':Pt,'Pa':Pa,'Pr':Pr}
for i in dict1:
    print(i,dict1[i])
```

References

1. Bhandari VB (2010) Design of machine elements. Tata McGraw-Hill Education
2. Khurmi RS, Gupta JK (2005) A textbook of machine design. S. Chand publishing
3. Patel N, Gupta T, Wankhede A, Warudkar V (2017) Design and optimization of 2-stage reduction gearbox. *Int J Eng Develop Res* 5(2):541–552
4. Mote SA, Gaur AV, Gujale AB (2018) Design and FEM analysis of helical gear, *Int J Eng Res Adv Technol* 4(4):13–20
5. Ghewade DV, Nagarale SS, Pandav AN (2016) Thermal analysis of helical and spiral gear train. *Int J Ignited Mind* 3(1):1–5
6. Venkatesh B, Kamala V, Prasad AMK (2010) Design, modelling and manufacturing of helical gear. *Int J Appl Eng Res* 1(1):103–114
7. Thu MP, Min NL (2018) Stress analysis on spur gears using ANSYS Workbench 16.0. *Int J Sci Eng Appl* 7(8):208–213
8. Mulla, NA, Bicha K (2014) Design, modeling and structural analysis of helical gear for ceramic and steel material by using ANSYS. *Int J Eng Technol Sci* 1(2):28–32
9. Naresh K, Chandrudhu C (2016) Design and analysis of helical gear. *Int J Prof Eng Stud* 6(4):194–203
10. Gupta A, Yashvanth AP, Rao LB (2021) Design of gears using aluminium 6061-t6 alloy for formula sae steering system. In: *Recent trends in mechanical engineering*, pp 489–505. Springer, Singapore
11. Bardiya N, Karthik T, Rao LB (2014) Analysis and simulation of gearless transmission mechanism. *Int J Core Eng Manage* 1(6):136–143
12. Gopal VV, Rao LB (2017) Design and analysis of centrally mounted rotary fixture. *Int J of Comput Aided Eng Technol* 9(4):453–464
13. Patel T, Dubey A, Rao LB (2019) Design and analysis of an epicyclic gearbox for an electric drivetrain. *Int J Recent Technol Eng* 8(3):6834–6842
14. Cherian S, Azam AB, Rao LB (2021) Analysis of various cooling mechanisms for plastic gears using decision tree algorithms. In: *Recent trends in mechanical engineering*, pp 407–418. Springer, Singapore
15. Gujaba KP, Parashar S, Rao LB (2021) Design and analysis of permanent magnetic gears. In: *Recent trends in mechanical engineering*, pp 521–530. Springer, Singapore
16. Sekhar K, Dharmadhikari P, Panchal S, Rao LB (2021) Design and optimization of a two-stage gearbox using GearTrax. In: *Recent trends in mechanical engineering*, pp 445–477. Springer, Singapore
17. Anand S, Srikeshav AD, Sharran B, Rao LB (2021) Design and analysis of helical teeth harmonic drive. In: *Recent trends in mechanical engineering*, pp 507–519. Springer, Singapore
18. Damodaran GR (2018) PSG design data book (PSG College of Technology, Kalaikathir, Achchagam, Coimbatore)
19. Solidworks user manual, Version 18 (2020)
20. ANSYS user manual, Version 19.2 (2020)

Electric Mobility: Key Factors, Unresolved Issues and Significance for Foundry Industries



Himanshu Khandelwal and Sumeet Chavan

Abstract The automotive industries are enduring a technological transition, as the Internal Combustion Engine (ICE) technology is slowly being switched by electric engine technology. This transition will bring a drastic change in the automobile industry in many aspects. ‘Go electric’ has already started becoming the trend in the common public; simultaneously, the automakers are in full swing to fulfil the public demand. An Electric Vehicle (EV) has become the most prominent alternative for ICE vehicles, which utilizes a battery, electric motor and transmission system. EV being more environmental-friendly vehicles, offer low-cost maintenance, but the higher initial cost is driving potential buyers away. Keeping this in mind, the worldwide manufacturers are researching to make electric cars affordable for common people. The transition from ICE to EV will lead in reduction of part demand of the existing automotive. There may also be a social adverse effect as there may arise loss of jobs or closure of existing traditional automobile industries. This study aims to contribute in understanding the opportunities and consequences of EV transitions related to the metal casting industries. The paper also discusses the impacts of electric vehicle platforms on the metal casting industry and a life cycle analysis of ICE and EV technology to decide a better option for market sustainability in long run. An attempt is made to highlight unresolved issues for embracing EV’s.

Keywords Automotive · Internal combustion engine · Metalcasters · Charging · Electric vehicles

1 Introduction

In the early twentieth century, a survey was conducted by a leading magazine and the audience was requested to refer to a term that consisted of the progress of the

H. Khandelwal (✉)

National Institute of Foundry and Forge Technology, Ranchi 834003, India

e-mail: himanshuk@niamt.ac.in

S. Chavan

A3D Foundry Tech Pvt. Ltd, Mumbai 400080, India

nineteenth century. The word ‘Automobile’ got the maximum attention among the other compelling contenders like the internet, computers and phones [1]. In fact, the automobile can be considered as the highest invention of mankind. Presently, around 1.4 billion cars are moving on this planet, and the figure is projected to reach the mark of 2.8 billion by 2036 [2]. The automobile progress lies in its ability to travel around 500 km of distances with an speed of over 180 km per hour in single run without any refuelling [3]. The chronological growth of the global vehicles is represented in Fig. 1.

The worldwide automobile industry has come up as a prime mover of the economy for all the developed countries. The continuous growing automobile sector has registered an around 50% rise from the last decade (2009–2019). Manufacturing more than 91 million cars in a year (2019 statistics) involves around 12.4 million direct employment, which contributes significantly to the overall employment in manufacturing industries. Every direct employment in the automobile sector brings many indirect employments, translating to over 60 million employees. Every automobile manufacturing again depends on the supplies from many other supporting industries like metal, glass, rubber, plastic, textile, electronics and many more. The overall output from all the supportive industries makes it equivalent to a worldwide revenue of more than 2 T\$ (1.5 lac crore) [4].

Environmental pollution has also increased severely along with the growing automobile demand. The transport sector itself contributes around 25–30% of the total CO₂ emission, predominantly from personal road vehicles [5]. In order to control the carbon loading in the atmosphere, automobile manufacturers are aiming to produce vehicles that will go with any alternative energy source and battery-operated vehicles have appeared as a promising technology. Governments worldwide have started providing incentives and subsidies to plug in ‘Electric vehicles’ to boost the transition. These incentives include purchase rebates, tax exemption and other wavier in fees of charging, toll, parking, etc. [6].

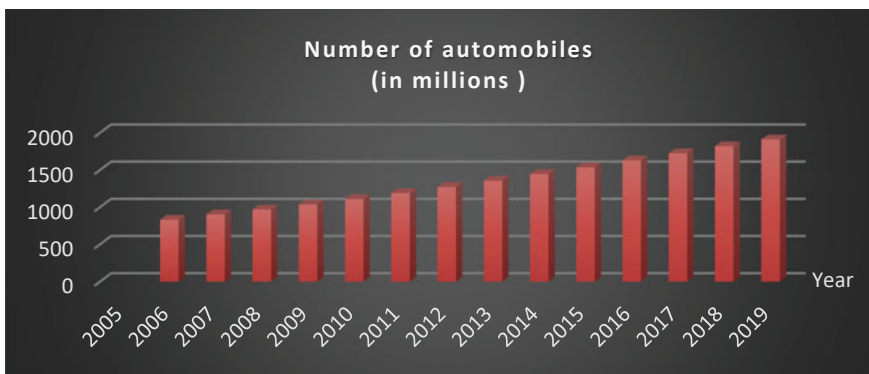


Fig. 1 Worldwide figure for total automobiles

Various factors support the vision for EV's. The cost of lithium-ion batteries has fallen to over 90% in the last decade (around 1000\$ per KWh to 100\$ per KWh) [7]. The battery capacity is increasing every year. Besides this, Tesla Motors has also unveiled a vehicle in 2020, which targets 1000 km run in just one charge [8]. The battery life has increased, and its capacity degrades by 1% in 30,000 km, which takes more than 2 years for regular working people to drive. The most important factor is the reliability of EV over ICE. An ICE vehicle drivetrain contains more than 2000 parts which are around 20 in an EV, and this reduces the possibility of faulty vehicles. Electric vehicles have reduced total moving parts, and their simplicity of design offers much higher overall efficiency. The other advantage with an EV is the operating cost, as EVs offers economical fuel cost. Being the future of automotive vehicles, the resale value of EVs will always be on the higher side compared to obsoleting ICE cars. This explores the consequences and the capability of electromobility on foundry industries. The rise of EV's has become the series topic of discussion among the classical metal automobile industries which beings opportunities with risk.

After a century of Internal Combustion Engine (ICE) ascendancy, now auto manufacturers have shown willingness to shift their manufacturing on the electric vehicle infrastructure. For many years, metal casters have produced metal components for automobile industries. There are about 2000 parts in the ICE powertrain and many of them are metal castings. With the advancements in electric vehicle technology, the total number of parts in an EV powertrain is brought down to 200 and many of them are not even metal. The average weight of an IC Engine car is nearly 1815 kg; 275 kg of those are castings [9].

Another vital aspect of moving vehicles is related to environmental constraints. In the automobile sector, emissions policy exclusively depends on tailpipe emissions, without considering the CO₂ generated during the vehicle manufacturing or gasoline use after the delivery. To guarantee that lawmakers make the greatest possible choices for society, the emissions for an entire life cycle must be quantified. The emphasis on tailpipe emissions poses two key obstacles for the cast iron foundry industry. To begin, several OEMs have replaced cast iron components with aluminium in the pursuit of lightweight castings and for good mileage. However, aluminium requires substantially higher energy to manufacture while comparing to cast iron manufacturing in foundries. Another, while battery electric vehicles do not emit tailpipe emissions, the creation of the batteries and power do generate CO₂. The sole distinction is in the position of the emissions [10].

Generally, common car buyers think about the emission of the gases produced during the car drive span, but they neglect gases emitted during the various process of their entire life. Nowadays, the government also supports electric vehicles through many framework conditions. The emerging electric vehicles have a lesser number of parts; because of this, foundry industries will be impacted. In battery vehicles, the main issue is weight; therefore, foundries should focus on lightweight materials using different casting processes. Still, there are some unresolved issues related to EVs like charging time, charging issues, emissions produced during electricity making, battery recycling, etc.

The growing EV demand has raised a few big questions in front of automakers. What if the customer's mood suddenly swings towards purchasing electric vehicles that require an only fraction of the total weight of casting compared to ICE vehicles? What will happen to the traditional foundry process when the demand for castings will decrease? How will production foundries behave in the long term as they traditionally belong to jobbing process? This paper tries to understand all the questions.

2 Key Factors Involved with EV

The manufacturing of electric vehicles cannot be neglected. There are a few aspects that need attention and balance to develop a sustainable EV.

2.1 *Environmental Balance*

Electric vehicles are in general referred to as 'zero-emission vehicles' because of tailpipe emission, which eliminates the CO₂ emitted during the vehicle run as it has a provision of electricity. However, Electric vehicles impact the environment by emissions associated with the EV and batteries production and electricity generation to support the battery charging facility. Then, the CO₂ footprint of battery production concerned with vehicle manufacture and assembly is four times that of the typical mid-size vehicle. Huge batteries need more precious metals, more electricity in manufacturing and offer a considerable weight in the car with more cost and a more complex CO₂ payback.

A general life cycle study for commuters with diesel engines, gasoline engines, hybrid engines, fuel cell engines and battery electric engines and CO₂ released for 200 thousand km life span is presented in Fig. 2. It is observed that the gasoline vehicle has the largest CO₂ emissions, whereas the BEV offers massive emissions during the production cycle [11].

The study also brings out the potential for other non-conventional energy sources like solar energy or biomass, which may satisfy the requirement of a lower emission rate and appeared as the perfect support system for internal combustion system. FEV performed a similar study in Germany in 2017, which also presented the life cycle research by including the renewal of the battery pack within the span of the BEV life cycle. The study also suggested that the availability of these natural carbon fuels will have less CO₂ release than the BEV or fuel cell [10].

So far, all the major automobile consumer countries are getting electric power from nonrenewable energy sources. The life cycle analysis suggests that it is not certain that the transition towards EV will improve the environmental condition by regulating emission rates.

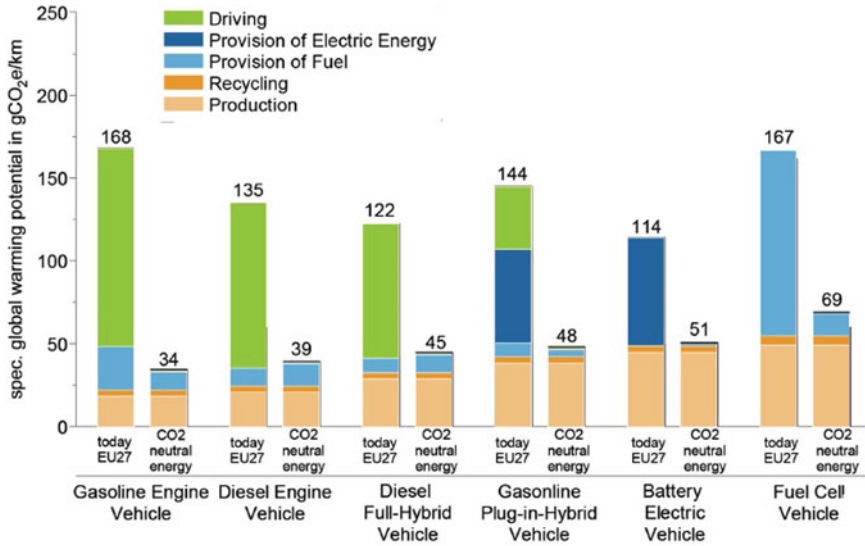


Fig. 2 Life cycle analysis for different vehicles [12]

2.2 Economic Impact

As discussed, the EV has appeared as the paradigm shift in the automobile industry, and this is being supported by all the major countries that drive the global economy. Countries like the USA, China, India and Japan have initiated many governments added policies like subsidies in registration costs, tax waivers, etc. These initiatives support and up drives the market demand for EVs.

Global sales of BEV’s and HEV’s have reached 3.5 million in 2021, showcasing an annual growth of 65% from the last year (published by <https://www.statista.com/>). The electric vehicles deployment industry encompasses various lighthouse projects to elevate the EVs development structure. The government is also offering subsidies for technological research in electric engine development and charging infrastructure for government fleets and private vehicles. Automotive companies like Tesla and Volkswagen are challenging the traditional brand’s outline plans to extend the EV collection rapidly. In this context, Volkswagen strategies to introduce around 30 new EV models by the next 5 years. Due to political support of electric mobility and limited fossil fuel, EVs will owe a major stack in the overall economy.

Simultaneously, the combustion engine vehicles will be slowly weeded out in the coming decades. And by 2030, markets will quietly differ depending on the newer policies, infrastructural development, customer preference, technological development and available resources. Estimably, light-duty electric vehicles are expected to share around 40% automobile market in the next 10 years [13]. The new launching of electric mobility will have fundamental implications on traditional automotive

Table 1 Summary of industrial survey on automotive suppliers [14]

Company	Product group	Clients	Impact on revenue by electromobility	Intensity of competition in current market
1	Iron cast product with and without coating	Automotive OEMs	0% (if product is adapted)	High and low, depending on product configuration
2	Iron cast products	Automotive OEMs	100%	Low
3	Aluminium and other non-ferrous products	Automotive OEMs and other industrial sectors	5–10%	Medium and low, depending on product
4	Steel components for drivetrain and engine	Automotive OEMs, system suppliers	98%	High
5	Steel components for drivetrain, engine and axis	Automotive OEMs, system suppliers, company internal	52%	High
6	Auto parts and -systems for engine, ventilation, drivetrain	Automotive OEMs	Not quantifiable, estimated medium risk	Medium
7	Auto parts and -systems for tubing and cooling	Automotive OEMs	Not quantifiable, estimated medium risk	Medium

suppliers like metal casting foundries and associated consumable supplier companies. Recently a study was published to assess the impact of EVs on automobile suppliers. For the assessment of impact, survey interviews were conducted with senior delegates of different automotive supplier companies [14]. The impression from the survey is outlined in Table 1. In general, all the companies accepted that their major revenue comes from ICE-based automotive vehicle production.

In India, the automobile industry plays an important role in propelling economic growth, making India dependent on overseas oil. Hence, EV growth is still considered a market dilemma as the government is set firmly to market India, a nation chiefly running on electric transportation by 2030.

2.3 Technological Impact

In regard to powertrain, electrification leads to a fundamental change. For engine manufacturing, it is essential to revise the entire supply chain. Unlike combustion engines, the EV does not need any intricate transmission system and can drive with

fewer components. As discussed, an electric motor has an engine and transmission consisting of 200 parts, while a conventional car has 1400 parts.

The 9th Foundry CEOs meet organized by The Institute of Indian Foundrymen (IIF) at New Delhi on 10th November 2017 discussed that the auto sector consumes 32% of total casting produced in India; and if the dynamics and future of casting need to be changed, the electric mobility needs to be propelled. The foundry industry may realize the consequences by eliminating IC engine components like cylinder heads, blocks, pistons and other elements which are not part of EV's. However, steel manufacturers will alleviate forged crankshafts and intricate transmission system manufacturing. The foundry industry will get relaxed about such developments. Initially, there is a need to manufacture the typical IC engines along with the new electric motors to increase in components. The scope for opportunities will be doubled as electric motors include forged and moulded steel parts and castings. It is very difficult for battery vehicles to move without the intricate metal casting parts.

Today, both the foundry and forge industries depend extremely on vehicle demands. The survey of few foundries forecasting revealed that with the growing EV demand in the market, the total production will observe a downtrend and may affect the production by 50%. The increasing demand for hybrid vehicles with lightweight metal structures has already started shifting the demand from ferrous castings to non-ferrous castings. Though the demand for IC engine parts will observe a sharp drop in the longer run, this shift towards the non-ferrous metals and non-metal carbon-reinforced composite will open up a new market for conventional foundries.

Batteries are one of the main important elements for EV's. The cost and range of the battery have appeared among the most researches domain in electric mobility. Batteries weighing between 200 and 300 kg are been introduced in average electric vehicles. Economic lightweight structures help raise the demand for electromobility regardless of higher battery cost and weight. Tesla had initiated with the titanium and steel blend of aluminium, whereas BMW chooses expensive lightweight steel materials. Demand for lighter structures in EV's encourages global foundries. Non-ferrous metals—aluminium and magnesium manufactures lightweight components that are becoming more important and being explored as the chassis material [15]. Even carbon-reinforced composites are recently being explored for body part manufacturing. Diecast aluminium is used to make struts and longitudinal bars [15].

Another critical technology requirement is the application of simulation tools. In the ongoing improvement of EV technology, simulation is the most important component. It helps engineers to discover new areas to bolster range. It also helps to determine the cause and effects by supplying precise results. The consolidated engineering simulation platform facilitates performance assessment by including different design modifications, material and battery considerations. The cost and weight are among the various challenges associated with battery technologies, but simulation assists to remedies all these issues.

3 Unresolved Issues for Embracing EVs

Any technological change comes along with many challenges that need to be addressed before society welcomes that open-handed. There are some unresolved issues that attribute to EVs that are beyond their advantages, which may impact the lives of human beings. A few significant issues are discussed regarding the jobs, EVs Range, emission and cost of fuel, EV cost and batteries.

3.1 *Jobs*

Unemployment creates obstacles for the economy at large for those who have to loosen their job. A heading was published in an article that Audi slashed 9500 auto manufacturing jobs to add new 2000 jobs for electric vehicle manufacturing. One interview from Morgan Stanley's representatives estimated that around 27% of employees have loosened jobs because of electrification. This unemployment will mainly affect the metal casters. Though there it is expected to have direct job cuts, but there are many instances that are creating direct and indirect jobs associated with EV industry.

In one of the recent events hosted by BlueGreen Alliance, an American foundation works to ensure clean and environmentally friendly jobs. Economic Policy Institute estimated that shifting to electric vehicles will create an additional 150 thousand new jobs in America by 2030. The theme of the event itself was 'EVs Are Coming: Strengthening Auto Manufacturing and Building Good Jobs in the Shift to Electric Vehicles'. The panel discussion on 'Next Era of Automotive Technology and associated jobs' estimated newer jobs associated with electric vehicle production, battery production, auto component manufacturing, EV manufacturing infrastructure creation, EV Charging and Maintenance Infrastructure Creation and research and development in many associated sectors [16].

3.2 *EVs Range*

The range of options in EV models and associated driving range to drive in a single charge are the prime concern for this technology, which is being researched extensively. However, as the leader in making electric vehicle technology, Tesla has recently refreshed its model S with around 600 km range, which is a significant improvement in this domain. The company is also researching towards the fast charging of EV's, say drive up to 570 km with 15 min of charge. To accommodate the limitations with the EV range, more focus is now being given to creating charging infrastructure.

Under the post covid recuperation strategy, many countries like Germany, China and India have proposed new independents in creating charging infrastructure [13]. Moreover, the focus is to utilize majorly renewable energy sources for this purpose. The EVgo is in the business of installing fast-charging station in USA which claims to be powered by 100% renewable energy. The forthcoming research to overcome the issues in the domain is bringing innovations focusing on the improvement of life.

3.3 EV Manufacturing Infrastructure Creation

Present infrastructure of conventional manufacturing industries like foundry and forge units are not compatible with manufacturing an electric vehicle. The infrastructure needs significant modernization with many new facility creations. Almost 98% of the EVs sold in China are being assembled there itself, whereas the USA is assembling around 70% of Evs in-house and the rest are imported from other countries. The assembly figure in the Indian context does not make much sense as it contributes only a 1% share in overall vehicle sales, based on the FY 20-21 figure [17]. Thus, most parts are being exported by China and other countries. However, the EV's needs to be manufactured in the regions where it has been consumed since this will help avoid the additional transportation cost and accommodate the localized geographical demands-based customization.

The NITI Aayog, Government of India has published a handbook on electric vehicle charging infrastructure that discusses the clear roadmap for implementing policies and projects for clearing and setting up the electric vehicle charging ecosystem [18]. In India, Tata Power has invested in offering EV charging facilities across the country. The charging station is being created for your fleet, offices/workplaces, malls, hotels, individual homes and housing societies.

3.4 Emission and Cost of Fuel

EVs are obviously better than ICEs concerning tailpipe emissions. The EVs are charged with the help of electricity produced by coal. Even the EVs are atmosphere suitable than ICEs. Also, EVs make use of cheap fuel. Figure 3 represents the source of power generation in all the major nations. It can be clearly observed that both India and China are majorly dependent on coal for their electricity production. Amidst the use of the EVs, which will use the electricity generated by these fossil fuel-based energy sources and thus will indirectly contribute to the higher emission of CO₂. Figure 4 represents the present and future region-wise carbon-intensive emissions in electricity generation, the data used for this study is based on the International Energy Agency. This is apparent from this figure that based on the 2008 data, India contributes heavily to carbon-intensive electricity generation whereas for the North American and European countries, the CO₂ intensive electricity uses is on the lower side. This

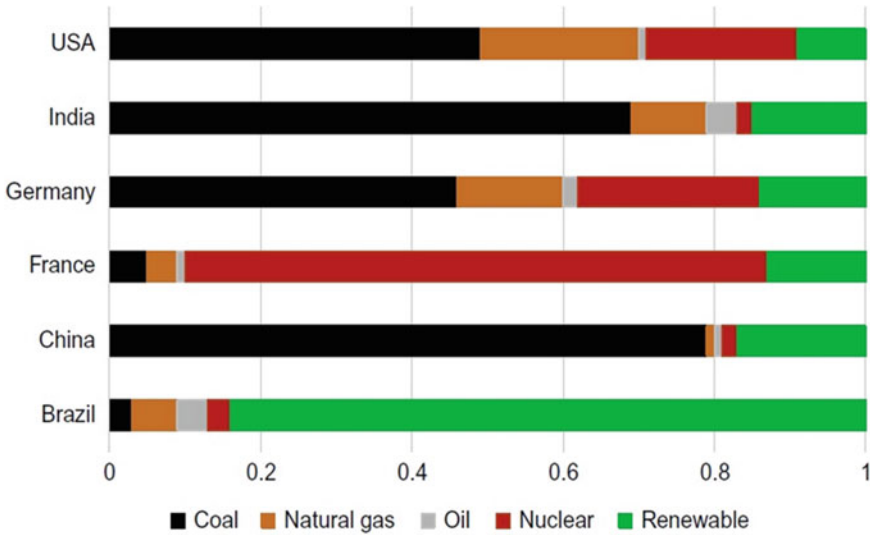


Fig. 3 Distribution of source for electricity generation in major countries [19]

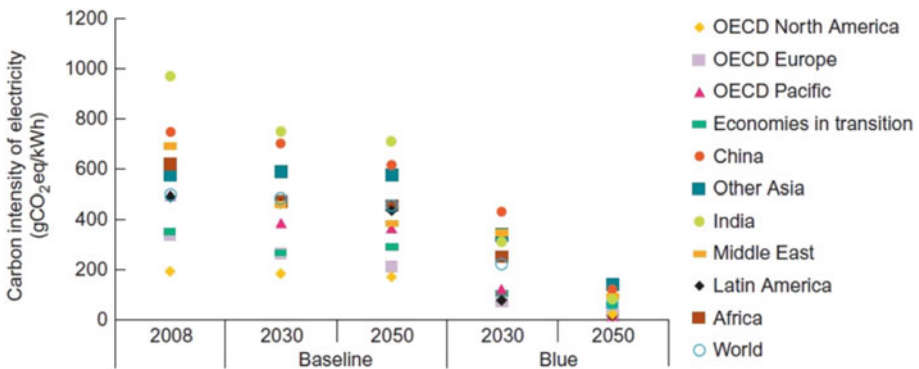


Fig. 4 Estimated CO₂ emission contribution of countries in electricity generation [1]

is because these countries have already started implementing carbon-neutral non-conventional energy sources in commercial power plants. Thus, the energy generated by renewable sources helps in facing the issue of climate change. However, an economic conundrum plays a crucial role in this. If millions of drivers fuel their vehicles quickly, its price will definitely reach the climax. Again, the price increases as the demand increases. Today, renewable sources have paced, yet it is not very easy to eradicate fossil fuels in producing electricity ultimately. Considering the case of India, where the very first Tidal Energy-based and Geo-Thermal Energy-based power plants are planned to regularize by 2030 only.

3.5 *EV Cost and Batteries*

The very known reason behind the slow acceptance rate for Electric vehicles is their price, which is costlier as compared to ICEs and the main reason for this is fuel storage limitation. The batteries are the most expensive component in EV's, which uses the rare metal lithium and its mining source is very limited. Though it is not certain when and how this problem will be addressed, but researchers globally are working to solve the overtightening requirement of low-cost batteries. The cost of batteries has reduced almost by 50% in the last decade. The sooner, the less all the emerging technologies will bring down the EV cost comparable to IC's.

The lead-acid based are cost-effective, but its recycling is quite challenging. The environmental laws do not allow the disposal of batteries. However, the main advantage of the use of the lithium-ion battery is that 95% of this is recyclable to other batteries. The technological advancement relevant to batteries will improve battery performance at lower cost and open up newer business opportunities for the automobile industry [9].

4 Conclusion

Electric mobility has taken its shape and now emerging with full potential. The technological advancement in the domain has brought a paradigm shift towards EV platforms. However, there are few technological and perception-based challenges regarding its acceptance to a wide population and the foundry-forge industry. The challenges are associated with the higher EV cost, reduced ICE production demand, job cutoff, CO₂ emission balancing and limited charging facilities in remote areas. The metal casters started accepting EV's as the future of automobile sector. The conventional foundries are upgrading their infrastructure to accommodate the EV's production. It is apparent that with reduced casting components, the market demand for ferrous casting will reduce, but the requirement of lightweight structure has opened a new domain for foundries to produce high-value-added components and rejuvenate the lost profit due to lower ICS-based component demand. Again the up-gradation of manufacturing infrastructure towards the EV platform will impact the direct employment in the automobile sector. However, in creating EV manufacturing infrastructure, charging facility creation and EV implementation bring newer employment opportunities in diverse domains. The past life cycle study challenges the perception that EVs will minimize the environmental impact by carbon emissions and benefit humanity. The ongoing research on lightweight non-metallic infrastructure, enhancing battery efficiency and range and the cost reduction efforts and adoption of non-conventional energy sources for electricity generation will bring the era of the automotive industry by incorporating all-around environmental and human resource

balance. The paper also discusses the strategic options for foundries and associated companies to come out from EV's possible implications and acknowledge the new opportunities.

References

1. Muneer T, García II (2017) The automobile. In: *Electric Vehicles Prospects Challenges* p 191. <https://doi.org/10.1016/B978-0-12-803021-9.00001-X>
2. Chesterton A (2021) How many cars are there in the world in 2021? CarsGuide. <https://www.carsguide.com.au/car-advice/how-many-cars-are-there-in-the-world-70629>, last Accessed 2021/12/23
3. Todd J, Chen J, Clogston F (2013) *Creating the clean energy economy analysis of the electric vehicle industry*. Int Econ Dev Coun Washington:1–101
4. IOMVMs, The design, manufacture and sales of automobiles drive economic growth around the world. International organization of motor vehicle manufacturers, production statistics. <https://www.oica.net/category/economic-contributions/>. Accessed 2020/06/04
5. Singh KV, Bansal HO, Singh D (2019) A comprehensive review on hybrid electric vehicles: architectures and components. *J Mod Transp* 27(2):77–107. <https://doi.org/10.1007/s40534-019-0184-3>
6. Global EV Outlook (2017). *Glob EV Outlook 2017*. <https://doi.org/10.1787/9789264278882-en>
7. Yamaguchi M et al (2021) Importance of developing photovoltaics-powered vehicles. *Energy Power Eng* 13(05):147–162. <https://doi.org/10.4236/epe.2021.135010>
8. Buchal C, Sinn HW (2019) Decarbonizing mobility: thoughts on an unresolved challenge. *Eur Phys J Plus* 134(12)<https://doi.org/10.1140/epjp/i2019-13020-6>
9. Jefferson R (2020) Electric cars & metalcasting. *Mod Cast* 110(Feb):18–22. <https://doi.org/10.1017/CBO9781107415324.004>
10. Dawson S (2018) Cast Iron : we just need to get better at telling our story. Sweden
11. Lenz HP (2017) 38th International Vienna Motor Symposium. In: *38th international vienna motor symposium* 22(S1):34–61. <https://doi.org/10.1007/s41491-017-0002-3>
12. Severin C et al (2017) Potential of highly integrated exhaust gas aftertreatment for future passenger car diesel engines. *Int Wiener Mot* 38
13. Hamilton J, Walton B, Ringrow J, Alberts G, Fullerton-Smith S, Day E (2020) *Electric vehicles—setting a course for 2030*. Deloitte Insights, pp 295–320
14. Schwabe J (2020) Risk and counter-strategies: the impact of electric mobility on German automotive suppliers. *Geoforum* 110(March 2019):157–167. <https://doi.org/10.1016/j.geoforum.2020.02.011>
15. Perzyk M, Dybowski B, Kozłowski J (2019) Introducing advanced data analytics in perspective of industry 4.0 in a die casting foundry. *Arch Foundry Eng* 19(1):53–57. <https://doi.org/10.24425/afe.2018.125191>
16. “The shift to all-electric vehicles could create over 150,000 jobs by 2030—if policymakers make smart investments to secure U.S. leadership in the auto sector,” Press Release: by EPI, Sep. 22, 2021
17. Singh B (2021) EVs Covers 1.3% of vehicle sales in India in FY 20–21. *Solar Energy Int*. <https://www.saurenergy.com/ev-storage/evs-covers-1-3-percent-of-vehicle-sales-in-india-in-fy-20-21>. Accessed 2021/12/25
18. Amitabh Kant CK, Singh R, Sanjeev Kumar Kassi, Sharma A, Mubashir S, Sharma A. *Handbook of electric vehicle charging infrastructure implementation*
19. “Global EV Outlook 2016 Beyond one million electric cars,” *Global EV Outlook 2018* (2016)

Response Surface Methodology to Establish Friction Model for Upset Forging



Karnam Thulasiram Vamsi Krishna, G. S. Amrith,
and Lokavarapu Bhaskara Rao

Abstract In the process forging, which is essentially a major process of processing the work piece in the industries have the higher chances of friction exposure which may not be necessary at times and this may cause a result of unwanted finishing which may affect the component and leads to both functional and cosmetic errors and mainly, these forging conditions can cause any undesirable physical changes like increase in the surface compressive residual stress and even resulting surface roughness many times and even during the operation, the tools may get deformed due to excessive surface roughness. So, the lubricants come into picture in all the time to decrease these effects, and the types of lubricants and also the change in the forging load can affect the surface roughness, and so the appropriate use of lubricants and forging load can enhance the tool life as well as the components quality of performance and reliability.

Keywords Response surface methodology · Friction · Lubrication · Forging · Minitab · Tool life

1 Introduction

In metal forming processes, forging is commonly used technique which simply uses the die of the required geometry and a simple mechanism to RAM the metal to the die and so is widely used technique for components of automobile and many more. There are several techniques used to understand the behavior of the metals that undergo these processes due to significant plastic deformation caused. Some techniques help

K. T. Vamsi Krishna · G. S. Amrith · L. Bhaskara Rao (✉)
School of Mechanical Engineering, Vellore Institute of Technology, Chennai Campus,
Vandalur-Kelambakkam Road, Chennai, Tamil Nadu 600127, India
e-mail: bhaskarbabu_20@yahoo.com

K. T. Vamsi Krishna
e-mail: vamsikrishna.t2020@vitstudent.ac.in

G. S. Amrith
e-mail: amrith.gs2020@vitstudent.ac.in

in finding the behavior of materials in the terms of flow stresses. Flow of material in die and its deformation behavior is affected by the frictional conditions during the forming process especially in upset forging process. Like, when the specimen is upset forged, the interfacial friction at the interaction surface resists the material flow, gradually, this leads to the heterogeneous deformation, and in this study, to minimize this, we use RSM to optimize the specific response influencing the variable which causes the heterogeneous deformation [1, 2].

The experiments were performed on the upset forging with the combinations of various uneven boundaries of the frictional conditions of dies and work pieces and with different surface conditions. A three-level full factorial experimental design is based on the experimental values, and a regression utilizing RSM established the experimental points. The regression model from a second-order model including interactive factors by using a pointer variable, and also, various other qualitative conditions are used to construct the regression model. Afterward, the regression model consisting of both frictional isotropy and anisotropy is also constructed that helps us in the prediction of plastic deformation of the materials, and their behavior after the upset forging process is accomplished [3, 4]. Based on these, the literatures have been collected and studied the required further implementations in the research in order to enhance the modeling of contact surface area which relates to the implementation of frictional conditions containing finite element codes used in analysis simulation of metal forming processes [5]. Now, the influence of the four different lubricants that causes variations of hardness and effective strain while the simple upsetting process has been studied by Narayanan et al. [6].

Here, the ring compression test is chosen and conducted on different metals and alloys which are frequently used in the industries for metal forming process which, this test is mainly chosen to determine the friction calibrations [7]. The tribological properties using the three commonly used friction tests, namely draw bead, strip drawing, and bending under tension test, using a particularly designed friction simulator were studied on a deep drawing quality steel sheet by Trzepiecinski [8]. A cold ring compression test on medium carbon steel is conducted to evaluate its friction conditions by Zhang et al. [9]. The ring compression test to evaluate the friction coefficient, friction factor in Coulomb, and Tresca friction model for plastic deformation of aluminum alloy AA5052 is conducted by micro–macro analysis method using both micro-texture and surface morphology to explore the friction behaviors in AA5052 cold forming process [10].

Ghassemali et al. [11] studied an upper bound model which evaluates the friction factor by two approaches, namely (i) localized friction factor and (ii) global friction factor. The different frictional conditions (grease, dry, and mineral oil) and their effect on barreling while performing the upset forging of aluminum 6082 solid cylinders in various aspect ratios were studied by Priyadarshini et al. [12]. A line of theoretical and experimental stresses, sliding length and geometry of interacting surfaces, and the properties of lubricants that are trapped between the interacting surfaces, etc., have been studied by Wanheim and Bay [13]. Ring compression test, i.e., low speed is introduced to evaluate the frictional property of lubricants used for hot forging of steel and also found that every lubricant concluded to have critical temperature of

less than 4500 °C and 10,000 °C to maintain the friction as desired between the billets and dies [14]. For FEM analysis, the updated calibration curves including the heat transfer in between the lubricant and die which is underestimated earlier including the press velocity and found that frictional coefficient between a die and to classify the tribological performances of lubricants, a low-speed hot-ring compression test has been suggested [15]. Box et al. [16] analyzed the results of studies concerning the effect of the amount, frequency, and application manner of the lubricating agent, as well as the use of a proprietary lubrication and cooling system, on the durability of the forging instrumentation in hot die forging processes.

From the above-stated literature review, it becomes clear that friction at the interference can be reduced by various factors like applying lubricants, optimal geometry of work piece, and temperature in the upset forging process. Keeping this perspective, the present work has been taken with the objective to minimize the friction effect on surface of the dies and work piece and to reduce friction at the interface by considering effective variables leading to friction.

2 Problem Definition

Surface compressive residual stresses are highly influenced by the forging conditions besides the surface roughness and even the tool deformation during the process. These parameters like surface roughness, forging load, compressive residual stresses, lubricants, and the effects like deformation of the tool altogether are interconnected and contribute a great influence on the material life and other important features of the component to be manufactured. In order to increase the tool life and reliability of the component, the appropriate amount, type of lubricants, and the forging load specified to the component requirement are to be chosen wisely. To avoid the adhesion phenomena between work piece and die interface and to reduce friction at the interface by considering effective factors leading to friction such as surface roughness of work piece, geometry, irregular temperature distribution over the job and many other to avoid these factors to cause undesirable effects on the process, it is recommended to use lubricants in almost all the metal forming process. We use the response surface methodology to establish experimental points obtained from the experimental results as a regression (least squares curve-fit) and establish friction model.

3 Experimental Procedure

The work carried out is completely based on varying the experimental setup, conditions, and the assumed parameters. The experimental values are taken from the ring compression test, and in this research, we took the values from the literature survey.

3.1 Experimental Conditions

Method of testing	hot-ring compression test
Material	0.45% carbon steel
Lubrication	L1-Mica, L2-Glass, L3-Graphite, L4-Dry
Temperature range	1100 °C–1700 °C
Presses	Mechanical press, Hydraulic press

3.2 Effect of Lubrication and Forging Load

However the forging load can be varied and can be stated in quantity or measurement, and the lubrication types have many individual factors to define a proper type of lubricant and their application for the appropriate material type. Basically, the typical results of the appropriate friction necessary are stated like the forging load in the appropriate force direction in the die, and the proper application of lubricant or sometimes even the coolant can lead to significant changes of the component in terms of surface finish, strength, and reliability of the component.

3.3 Response Surface Methodology

In statistics, response surface methodology introduced by George and Wilson in 1951 [17] explores the relations between considered variables and one or more response variables. The main task of RSM is to obtain an optimal response by using an appropriate sequence of designed experiments. Box and Wilson suggested using a second-degree polynomial model to do this also, they say this is only an approximation process for optimum results, and it is easy to perform with the method as it is easy to use with not much skills or experience needed to follow the process. RSM being a statistical approach can be applied to maximize the production or quality of a particular parameter or a component by optimization of operational factors. For the optimization of formulation, by using the proper design of experiments, the RSM has been extensively used, and here, we use RSM because it allows evaluating the effects and interaction of multiple factors or parameters we considered.

3.4 Basic Approach of Response Surface Methodology

By using the factorial experiment or a frictional design, a first-degree polynomial model can be easily estimated, and this clearly states which response variable(s) is affected by the particular explanatory variable, but the second-degree model can be used to optimize that is, whether to minimize, maximize, or to attain a specific target

for the chosen response variable(s). Here, we also proposed to use Taguchi method because RSM involves more experiments, and usually, Taguchi method reduces the experiments to be performed.

Factors to be considered: Number of forging cycles, initial height, with and without lubrication, forging load, surface roughness, forging temperature, and die geometry.

3.5 Experimental Setup

Ring compression test is adopted widely in order to get the experimental values of friction factor in metal forming processes as shown in Fig. 1.

Here, the lubrications (L1, L2, L3, and L4) are used at different temperature conditions ranging from 1100 to 1170 °C to get the diameter change and frictional factor. Here, our intention is to find at what conditions, the friction factor and coefficient of friction are minimum, so the life cycle of die increases as well as production rate besides fine grain structure of the manufactured component.

4 Results and Discussion

The experimental values are obtained from Minitab [18]. Here, the friction factor (m) is calculated by the experiment. Temperatures and the corresponding friction factor as different experimental conditions or parameters for the optimum design sequence generation is presented in the Table 1 and for the lubricant type and the respective coefficient of friction at two levels of temperature is presented in the Table 2 are used

Fig. 1 Ring compression test

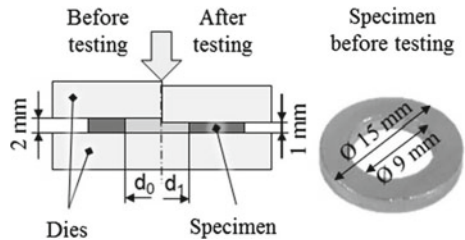


Table 1 Temperature (°C)—friction factor (m) readings

Temperature (°C)	Friction factor (m)		
	L1	L2	L3
1100	0.30	0.32	0.50
1170	0.32	0.38	0.60

Table 2 Lubricant—coefficient of friction μ

Lubricant	1100 °C	1170 °C
L1	0.44–0.13	0.45–0.29
L2	0.49–0.2	0.5–0.300
L3	0.61–0.25	0.75–0.41
L4	0.75–0.28	0.87–0.78

in Minitab as input parameters and the regression model of 2nd degree is generated as shown in the Eq. (1). Mainly here, RSM helps to optimize the parameters to be followed in order to achieve high production rate and to follow proper sequence for experiments. Whereas the contour plots generated tell the effect of different factors and their interaction on production rate and tool life.

$$\begin{aligned}
 Sa = & 1.90 + 0.00307 \text{ temp} + 1.32 m - 0.07\mu - 0.000001 \text{ temp} * \text{temp} \\
 & + 0129 m * m - 0.228\mu * \mu - 0.001587 \text{ temp} * m \\
 & + 0.00000 \text{ temp} * \mu + 0.397 m * \mu
 \end{aligned}
 \tag{1}$$

The run order is generated from the random input of the parameters that is the standard order, and Minitab recommends the sequence of experiments to obtain the optimum result as shown in Table 3 And it is then sorted as shown in Table 4 without any loss of considered parameters and their data.

Whereas the statistically significant result between the independent variables is in the ANOVA shown in Table 5, the factors and levels in the Taguchi experimental methodology are shown in Table 6, thus, the minimum number of experiments to

Table 3 St. run order

Std order	Run order	Pt type	Blocks	Temp	<i>m</i>
1	1	1	1	1100.00	0.30000
10	2	0	1	1135.00	0.59000
3	3	1	1	1100.00	0.88000
7	4	−1	1	1135.00	0.17988
6	5	−1	1	1184.50	0.59000
12	6	0	1	1135.00	0.59000
2	7	1	1	1170.00	0.30000
11	8	0	1	1135.00	0.59000
5	9	−1	1	1085.50	0.59000
4	10	1	1	1170.00	0.88000
13	11	0	1	1135.00	0.59000
8	12	−1	1	1135.00	1.00012
9	13	0	1	1135.00	0.59000

Table 4 Sorted St. run order

Sorted St. order	Run order	Pt. type	Pt. type	temp	<i>m</i>
1	1	1	1	1100.00	0.30000
2	7	1	1	1170.00	0.30000
3	3	1	1	1100.00	0.88000
4	10	1	1	1170.00	0.88000
5	9	-1	1	1085.50	0.59000
6	5	-1	1	1184.50	0.59000
7	4	-1	1	1135.00	0.17988
8	12	-1	1	1135.00	1.00012
9	13	0	1	1135.00	0.59000
10	2	0	1	1135.00	0.59000
11	8	0	1	1135.00	0.59000
12	6	0	1	1135.00	0.59000
13	11	0	1	1135.00	0.59000

Table 5 ANOVA

Source	OF	Adj. SS	Adj.MS	F-value	P-value
Model	5	0.195700	0.039140	0.88	0.540
Linear	2	0.101350	0.050675	1.14	0.373
Temp	1	0.017190	0.017190	0.39	0.554
<i>m</i>	1	0.084160	0.084160	1.89	0.211
Square	2	0.029325	0.014662	0.33	0.730
Temp * Temp	1	0.029053	0.029053	0.65	0.445
<i>m</i> * <i>m</i>	1	0.001488	0.001488	0.03	0.860
2-way interaction	1	0.065025	0.065025	1.46	0.266
Temp * <i>m</i>	1	0.065025	0.065025	1.46	0.266
Error	7	0.310993	0.044428		
Lack-of-fit	3	0.073113	0.024371	0.41	0.755
Pure error	4	0.237880	0.059470		
Total	12	0.506692			

Table 6 3 Factors and three levels

Temperature °C	<i>m</i>	μ
1100	0.52	0.61
1140	0.73	0.68
1170	0.88	0.76

Table 7 Taguchi (3³)

Temperature °C	m	μ	Sa
1100	0.52	0.61	0.16
1100	0.73	0.68	0.15
1100	0.88	0.75	0.17
1140	0.52	0.68	0.16
1140	0.73	0.75	0.17
1140	0.88	0.61	0.15
1170	0.52	0.75	0.2
1170	0.73	0.61	0.19
1170	0.88	0.68	0.18

For Taguchi

be conducted with factors and levels (3 × 3) is shown in Table 7, minimization of experiments with rank is given in Table 8, response table for means with different levels is given in Table 9 with three factors, whereas the regression analysis with F-value is shown in Table 10 which gives the variation between or within the samples. In Table 11 the interpretation that whether the means differences are statistically significant. In Table 12, response surface regression between surface roughness (Sa) and factors with coefficient of friction ANOVA and in Table 13 response surface regression of Sa versus factors are listed.

Figure 2 shows the Pareto chart of standard effects of different factors and their interaction by taking standard effects in horizontal axis and factors in vertical axis. In Fig. 3, residual plots of surface roughness can be seen with normal probability plot

Table 8 Minimization

Level	Temp	m	μ
1	15.93	15.27	15.61
2	15.93	15.43	15.76
3	14.43	15.59	14.92
Delta	1.50	0.32	0.84
Rank	1	3	2

Smaller is better

Table 9 Response table for means

Level	Temp	m	μ
1	0.16 0 0	0.1733	0.1667
2	0.1600	0.1700	0.1633
3	0.1900	0.1667	0.1800
Delta	0.0300	0.0 067	0.0167
Rank	1	3	2

Table 10 Regression analysis with F-value: Sa versus temp, m, μ

Source	DF	Adj SS	Adj MS	F-value	P-value
Temp	1	0.001216	0.001216	7.15	0.044
m	1	0.000066	0.000066	0.39	0.561
μ	1	0.000267	0.000267	1.57	0.266
Error	5	0.000851	0.000170		
Total	8	0.002400			

Table 11 Regression analysis: Sa versus temp, m, μ

Term	Co. ef.	SE Co. ef.	T-value	P-value	VIF
Constant	-0.343	0.181	-1.89	0.117	1.00
Temp	0.000405	0.000152	2.67	0.044	
m	-0.0183	0.0295	-0.62	0.561	1.00
μ	0.0952	0.0761	1.25	0.266	1.00

Table 12 Response surface regression: Sa versus temp, m, μ -ANOVA

Source	OF	Adj SS	Adj MS	F-value	P-value
Model	9	0.002622	0.000291	1.20	0.389
Linear	3	0.001306	0.000435	1.79	0.213
Temp	1	0.000211	0.000211	0.87	0.374
m	1	0.000363	0.000363	1.49	0.250
M	1	0.000732	0.000732	3.01	0.113
Square	3	0.000315	0.000105	0.43	0.735
temp*temp	1	0.000018	0.000018	0.07	0.791
m*m	1	0.000252	0.000252	1.04	0.333
μ * μ	1	0.000018	0.000018	0.07	0.791
2-way interaction	3	0.001000	0.000333	1.37	0.308
temp*m	1	0.000800	0.000800	3.29	0.100
temp* μ	1	0.000000	0.000000	0.00	1.000
m* μ	1	0.000200	0.000200	0.82	0.386
Error	10	0.002433	0.000243		
Lack-of-Fit	5	0.000833	0.000167	0.52	0.754
Pure error	5	0.001600	0.000320		
Total	19	0.005055			

Table 13 Response surface regression: Sa versus temp, m, μ

Term	Coef	SE coef	T-value	P-value	VIF
Constant	0.17017	0.00636	26 0.75	0.000	
temp	-0.00393	0.00422	-0.93	0.374	1.00
m	-0.00516	0.00422	-1.22	0.250	1.00
μ	-0.00732	0.00422	-1.73	0.113	1.00
temp*temp	-0.00112	0.00411	-0.27	0.791	1.02
m*m	0.00418	0.00411	1.02	0.333	1.02
μ * μ	-0.00112	0.00411	-0.27	0.791	1.02
temp*m	-0.01000	0.00552	-1.81	0.100	1.00
temp* μ	-0.00000	0.00552	-0.00	1.000	1.00
m* μ	0.00500	0.00552	0.91	0.386	1.00

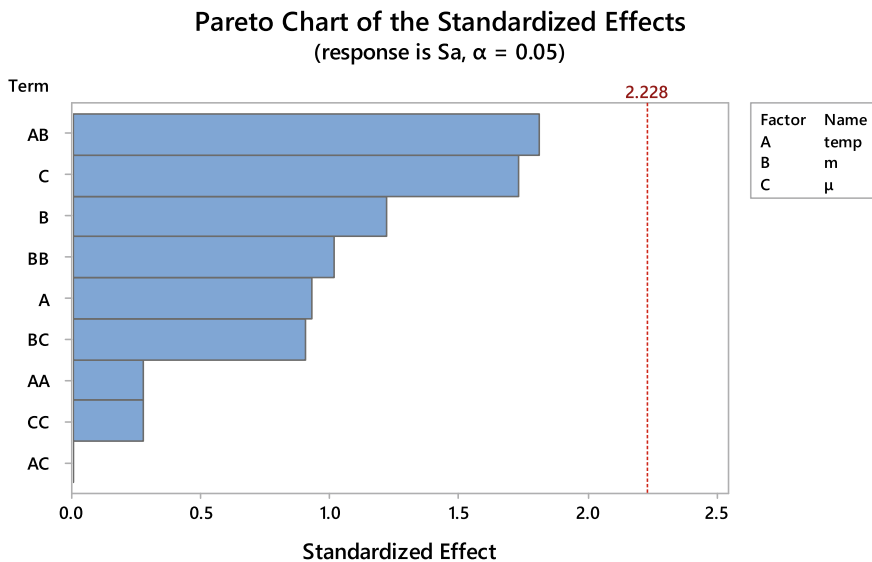


Fig. 2 Pareto chart of standardized effects

which is made of raw data which tells the normality in the graphical representation, and the figure also includes versus fits, order, and histogram. In Figs. 4 and 5, residual plots versus coefficient of friction and surface roughness, respectively, are included which represent the residuals on vertical axis and the different independent variables on horizontal axis. The effect of Sa and coefficient of friction variation with the temperature is shown in the above contour, i.e., in Fig. 6 with the combination of temperature more than 1180 °C and coefficient of friction 0.76 has less effect of friction effect in the process. Likewise, the effect of friction on Sa vs coefficient of friction and friction factor also varies as shown in contour Fig. 7; that is, it can

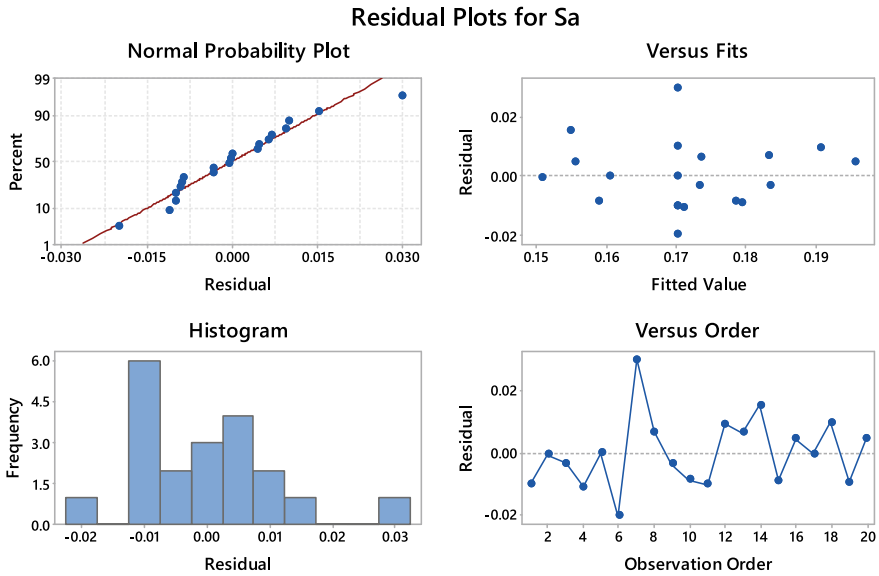


Fig. 3 Residual plots for Sa

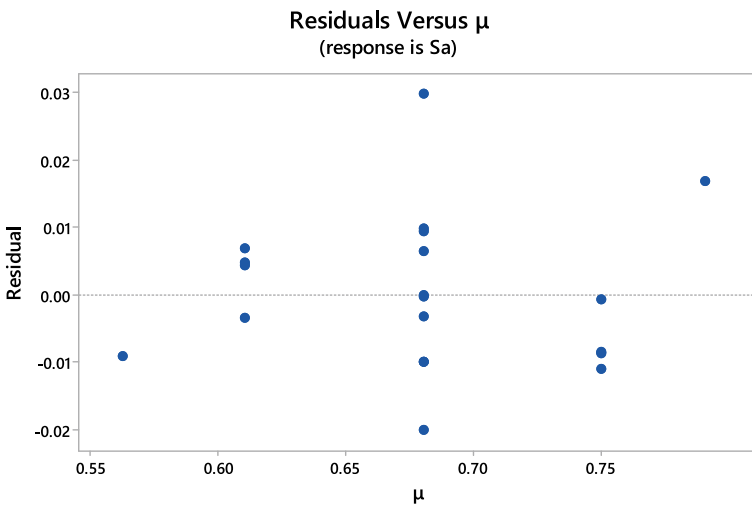


Fig. 4 Residual versus μ

be seen that the friction factor has no much significance friction effect with the Sa vs μ and the friction in the process. In Fig. 8 surface plot, the factors Sa, μ , temp, and their interaction that has significant effects on the friction of the upset forging process have the unfavorable conditions at low temperature high Sa factor and at the highest coefficient of friction, at these conditions, it is not recommended to operate

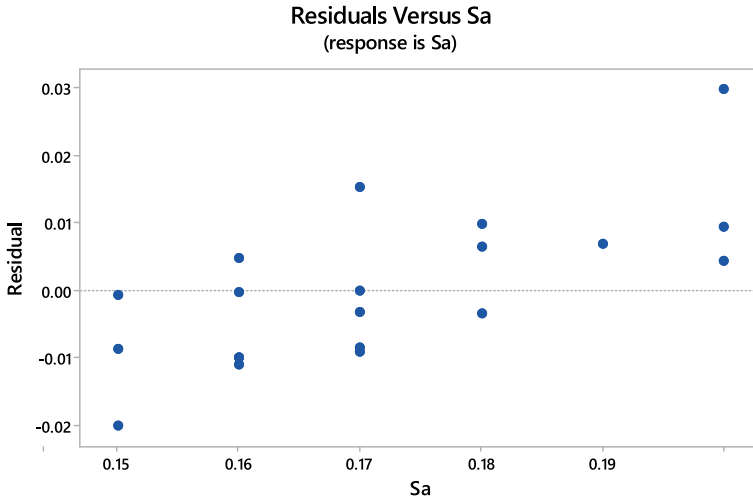
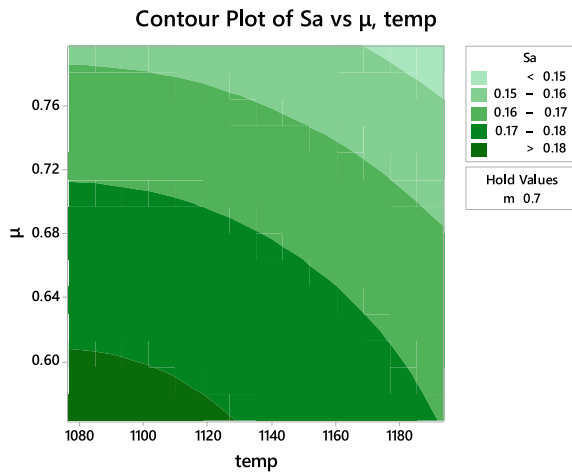


Fig. 5 Residuals versus Sa

Fig. 6 Contour plot of Sa versus μ , temp



the process as it may reflect on the surface finish and mechanical properties of the component processed, and likewise, in the Fig. 9, the surface plot contour of Sa with friction factor and temperature shows as the effect is significant at the highest value of Sa and at the friction factor and is independent of the temperature as per the plot.

Fig. 7 Contour plot of Sa versus μ , m

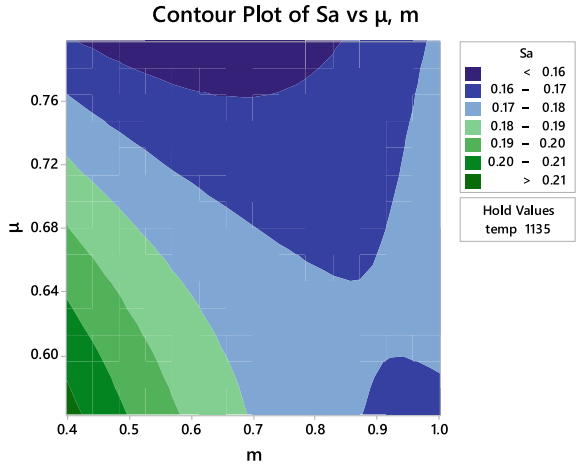


Fig.8 Surface plot of Sa versus μ , temp

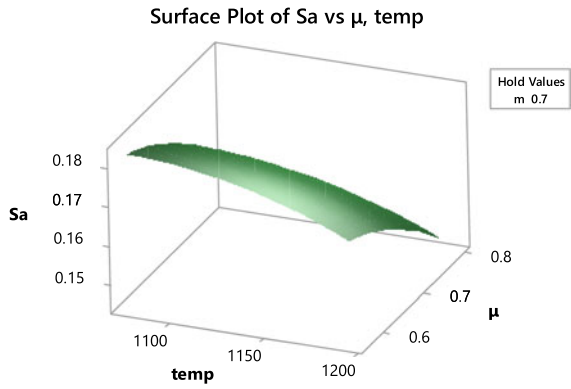
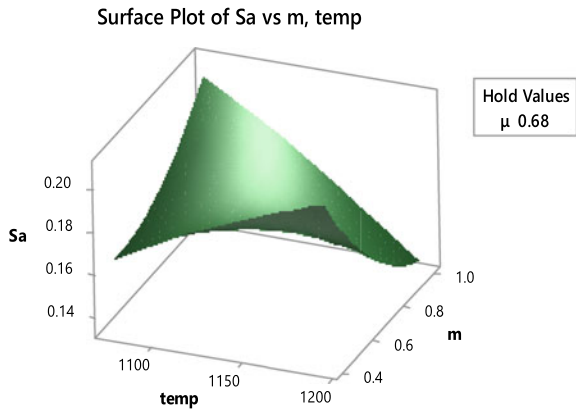


Fig. 9 Surface plot of Sa versus m, temp



5 Conclusion

5.1 Remarks

- In the surface roughness–coefficient of friction contour plot, it is clearly visible that the friction is higher at the low temperature, and there is a significant change on the coefficient of friction when the temperature is at maximum.
- From the contour plot of friction factor and temperature, the minimization of friction can be achieved at high temperature and low friction factor

5.2 Suggestions

We can minimize the friction by choosing.

- Temperature at 1200 °C
- Friction factor at 0.8
- Surface roughness at 0.17.

Acknowledgements We would like to express our special thanks of gratitude to our guide Dr. Lokavarapu Bhaskara Rao who gave us the wonderful opportunity to do this work titled “Response surface methodology to establish friction model of upset forging” which also helped us to do a lot of research, and we come to know so many new things that are essential for industrial needs.

References

1. Bolton W (2013) Production technology: processes materials and planning. Elsevier
2. Sharma, PCA (2007) Textbook of production technology (manufacturing processes): manufacturing processes. S. Chand Publishing
3. Montgomery DC (2017) Design and analysis of experiments. Wiley
4. Hicks CR (1964) Fundamental concepts in the design of experiments
5. Nielsen CV, Bay N (2017) Overview of friction modelling in metal forming processes. Proc Eng 207:2257–2262
6. Narayanan, R. Ganesh, M. Gopal, and A. Rajadurai. “Influence of friction in simple upsetting and prediction of hardness distribution in a cold forged product.” Journal of Testing and Evaluation 36(4), 371 (2008).
7. Camacho AM, Torralvo AI, Bernal C, Sevilla L (2013) Investigations on friction factors in metal forming of industrial alloys. Proc Eng 63:564–572
8. Trzepiecinski T (2019) A study of the coefficient of friction in steel sheets forming. Metals 9(9):988
9. Zhang D, Liu B, Li J, Cui M, Zhao S (2020) Variation of the friction conditions in cold ring compression tests of medium carbon steel. Friction 8(2):311–322
10. Zhang D, Guangcan YANG, Shengdun ZHAO (2021) Frictional behavior during cold ring compression process of aluminum alloy 5052. Chinese J Aeronaut 34(5):47–64

11. Ghassemali E, Tan MJ, Wah CB, Lim SC, Jarfors AE (2014) Friction effects during open-die micro-forging/extrusion processes: an upper bound approach. *Proc Eng* 81:1915–1920
12. Priyadarshini A, Kiran CP, Suresh K (2018) Effect of friction on barreling during cold upset forging of aluminium 6082 alloy solid cylinders. *IOP Conf Ser Mater Sci Eng* 330(1):012072
13. Wanheim T, Bay N (1978) A model for friction in metal forming processes. *CIRP Annals Manuf Technol* 27:189–194
14. Asai K, Kitamura K, Yukawa N, Hayashi N (2017) Estimation of friction by using improved calibration curves of ring compression test for hot forging of steel. *Proc Eng* 207:2280–2285
15. Hawryluk M, Ziemba J (2019) Lubrication in hot die forging processes. *Proc Inst Mech Eng, Part J: J Eng Tribol* 233(5):663–675
16. Box GEP, Draper NR (1987) *Empirical model-building and response surfaces*. Wiley
17. Alin A (2010) *Minitab*. *Wiley interdisciplinary reviews: computational statistics* 2(6):723–727
18. MINITAB user's guide 2: data analysis and quality tools, February 2000

Studies on Annealing Kinetics of Cold Forged AA6082



Ashutosh Ranjan, Ashvani Kumar, and Rahul Kulkarni

Abstract Aluminum alloys are popular for their lightweight applications. Usefulness of these alloys in the aerospace and automobile industries are well-known especially in structural parts. Among the many aluminum alloys, Al–Mg–Si alloys are having good forgeability. The mechanical properties of these alloys are depending on microstructural changes occurring during forging and heat treatment. AA6082 is one of the alloys belonging to the category of Al–Mg–Si alloys which is having medium strength. In the present work, annealing kinetics were studied in terms of hardness on cold forged material. AA6082 alloy was cold forged and after it was heated in the temperature range of 175–375 °C at different period in the range of 0.5–3 h. The annealing kinetics were studied with the help of JMAK equation in terms of hardness and compared with AA6063. The attempt was made to predict and discuss the microstructural changes during the annealing of cold forged material to relate with hardness of AA6082.

Keywords AA6082 · Annealing kinetics · JMAK equation

1 Introduction

Aluminum alloys are well known due to their light weight; high specific strength; especially in aerospace, automobile, ship building and food packaging and transportation industries [1–4]. Al–Mg–Si alloys are also known to be having better forgeability as compared to other aluminum alloys [2]. Due to this, these alloys are always of interest of the researcher. AA6082 is one of the alloys belonging to the category of Al–Mg–Si alloy. This alloy can be the potential material in automobile parts such as suspensions, chassis and engine etc. In addition, arms in flight control and brake body parts in aviation industry can be made of AA6082 alloy [5]. The previous study reported the presence of Mg₂Si as a second phase in this alloy. This is heat treatable alloy which means strengthening can be achieved using solutionizing and

A. Ranjan · A. Kumar · R. Kulkarni (✉)

Department of Forge Technology, National Institute of Foundry and Forge Technology, Hatia, Ranchi, Jharkhand 834003, India

e-mail: rahulkulkarni16122012@gmail.com

precipitation hardening heat treatment [6–9]. The microstructure features like grain sizes and size and distribution of second phase plays very important role to determine the deformability of the alloys. So also, the mechanical properties at the end of forming process are dependent on the microstructure evolved during the process. Although formability of this alloy is good with medium strength, due to higher cost of this alloys one can think of reducing the time and energy during forming such as forging. This could be achieved through microstructural changes in this alloy. This is further altered with thermomechanical processing which involves thermal treatment with mechanical work. In addition to this, the kinetics and transformation usually had been studied using Johnson–Mehl–Avrami–Kolmogorov (JMAK) equation [10]. The constants of this equation tell us about the behavior of the transformation. The phase transformation study using JMAK equation was reported previously [11, 12]. The very less work was reported with reference to the kinetics of deformation associated annealing treatment for AA6082 alloy. Such a kind of work was reported in case of AA6063 [13]. Further, it is well known that the driving force for the static recrystallization is the prior cold work done on the material. By considering above aspects, the aim of the present work is to study the annealing kinetics of cold forged 6082 aluminum alloy in terms of hardness in comparison of the behavior of 6063 aluminum alloy during annealing.

2 Experimental Methodology

The material selected for study is AA6082 in T6 heat treated condition whose chemical composition was determined using weight chemical analysis. Metallographic examination was carried out on the initial sample. For this, the specimens were prepared by polishing with 400, 600, 800, 1000, 1200 grit papers followed by wet polishing with alumina powder in water. After polishing, the samples were cleaned with water and alcohol, these were followed by drying with compressed air. To reveal the microstructure, the sample was further etched with etchant containing the solution 25 ml Methane, 25 ml HCL, 25 ml HNO₃, 1 drop of HF. The microstructure study was done using OLYMPUS metallurgical optical microscope. The grain size of initial material was calculated using line intercept method at 95% confidence level.

The block of 25 × 25 × 25 mm³ was cut from the plate. This material was solutionized at 400 °C for 4 h in muffle furnace. The material was further, cold forged using open dies to 70% deformation and using hydraulic press. The different specimens of equal dimensions were cut after deformation. The specimens were heated to 175, 280 and 375 °C for the period of 1800, 3600, 5400 and 10800 s followed by water quenching to give annealing treatment. The Vickers hardness test was carried out on all the annealed specimens with 5 Kg load for 10 s. The average of 5 readings are reported for the given study.

3 Result and Discussion

Initial characterization of the material

The material used for study was aluminum alloy 6082 with chemical composition Al–0.97 Mg–1.11 Si–0.5Mn. The initial material is in heat treated with T6 condition. The initial microstructure of this material is as shown in Fig. 1 which indicates the presence of uneven grains. The average grain size was found to be $270 \pm 23 \mu\text{m}$ with 95% confidence level.

Annealing kinetics

To study the annealing kinetics was done on the material which was solutionized at 400°C for 4 h and cold forged to 70% deformation. The hardness measured after 70% deformation was found to be 76.15 in VHN. Figure 2a shows the variation of hardness as a function of time at annealing temperatures 175, 280 and 375°C . It indicates that the disparity in trend of change in hardness values for the time period under study. At 175°C , the hardness first decreases from cold forged condition for the time period of 1800 s. It further shows the increase in the hardness for the time period of 3600 s. The decrease in hardness was observed for 5400 s with subsequently increase in hardness for the time period of 10,800 s. This variation of hardness could be attributed to the precipitation of second phase with variation in sizes and distribution in addition to GP zone (coherency in matrix and product phase interface) [6–9]. Such a kind of study was reported without prior deformation for normal T6 heat treated condition [6–9] which supports the same. At annealing temperature of 280°C , after decrease in hardness for initial period of annealing time, increase in hardness was observed (Fig. 2a). Subsequently, hardness decreases continuously for annealing period of 5400 s and 10,800 s. The annealing temperature could be the transition temperature from precipitation temperature to recovery, recrystallization temperature. This could be the reason to show the decrease in hardness at initial stage and increase in hardness with further decrease in hardness at the last stage of annealing time under study. This

Fig. 1 Initial microstructure of AA6082



variation of hardness may be because of tussle between precipitation, growth of precipitates and recrystallization. Interestingly, continuous decrease in hardness was observed at 375 °C for all annealing time. This indicates the recrystallization due to formation of new strain free grains and growth of the second phase particles. The rate of decrease is found to be decreased after annealing of 5400 s (Fig. 2a). Figure 2b shows the variation of hardness as function of temperature at all annealing time period. For the annealing time of 10,800 s, the hardness increases first at 175 °C and steep decrease in hardness is observed at 280 °C. This behavior is continued to be observed till 375 °C with reduced rate of decrease in hardness values. This also supports that at 175 °C for highest annealing time period, possibility of precipitation is associated with variation in size and distribution of second phase particle and further growth of grain and size of second phase particle. The similar variation was observed for all other annealing period. But the difference is that the variation has not that much drastically happened as observed for the annealing period 10,800 s (Fig. 2b). At annealing temperature of 375 °C of deformed specimen, the decrease in hardness shows the proper trend with equation of the curves as shown in Fig. 2c with R^2 value as 0.94 within available data points. From this curve fitting, it is observed that the decrease in hardness is a function of time. Further, it can be predicted that at the initial period of time there is a sharp decrease in hardness and at later period of time, there is decrease in rate of hardness. This could be attributed to decrease in rate of recrystallization or further grain growth at higher time of annealing at 375 °C.

The kinetics study was carried out using JMAK equation [Eq. (1)] [10]. For this purpose, the fraction transformed was calculated in terms of hardness by considering maximum hardness, minimum hardness and hardness at the time under consideration. The Eq. (2) was used to calculate the fraction transformed.

$$X_v = 1 - \exp[-Kt^n] \quad (1)$$

$$X_v = \frac{H_{\max} - H_{\text{time}}}{H_{\max} - H_{\min}} \quad (2)$$

where X_v = Fraction transformed; n and K are constants; H_{time} = Hardness at the particular time.

The fraction transformed was plotted as a function of time to calculate JMAK constants at all three temperatures 175, 280 and 375 °C as shown in Fig. 3a, (b) and (c) respectively. As depicted in Fig. 3, the variation of fraction transformed as a function of time is different for different temperatures. At 175 and 280 °C, the fraction transformed first decreases and then increases. But increase in fraction transformed observed to be larger at temperature 175 °C as compared to 280 °C. Interestingly, the fraction transformed is observed to be continuously increased at 375 °C. These variations can be attributed to the changes in the microstructure evolution during annealing. As stated earlier, these fractions transformed was calculated on the basis of hardness. The changes in the hardness can be related to the microstructure evolution at respective time and temperatures. The fraction transformed consists of two

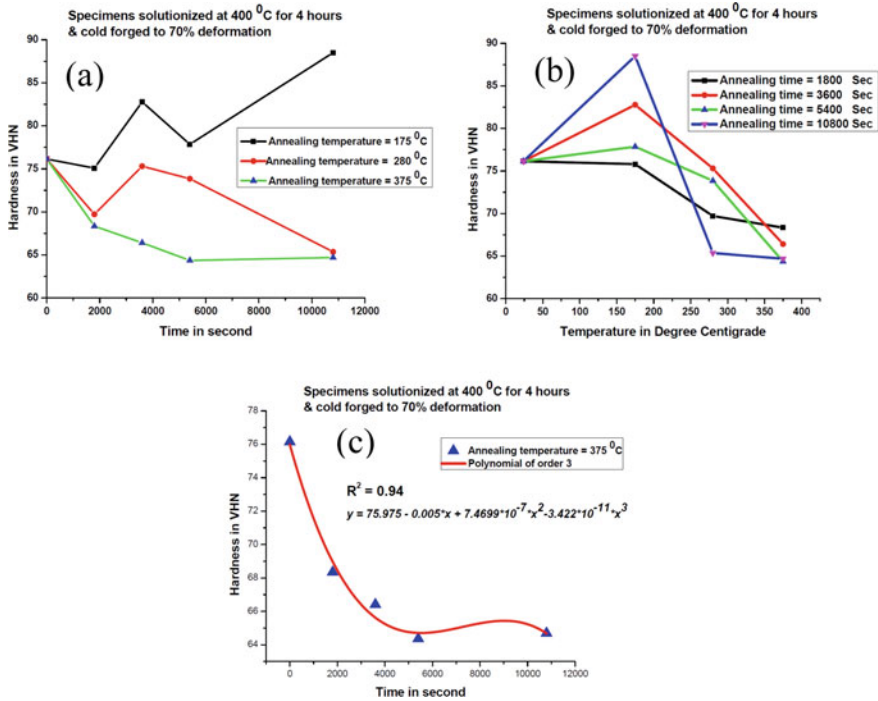


Fig. 2 Variation of hardness (VHN) as a function of **a** Time at temperatures of 175, 280 and 375 °C **b** Temperature for time period of 1800, 3600, 5400 and 10,800 s **c** Time at 375 °C showing proper trend of curve with equation fit within available data points

components. One is the changes in the grain size and other one is precipitation behavior of second phase. The decrease in the fraction transformed at temperature of 175 °C from initial condition at annealing time of 3600 s may be attributed to the rearrangement of coherency between parent and product phase with start of precipitation of second phase. Further, increase in transformation may indicate the large amount of precipitation. Similar trend was observed at 280 °C, but the decrease and increase in transformation is less as compared to that at 175 °C (Fig. 3a and b). This may be due to the start of recrystallization as well as continuation of precipitation. The continuous increase in transformation at 375 °C (Fig. 3c) may indicate the static recrystallization i.e., formation of strain-free grains on existing strained grains. Further analysis of these transformations used to calculate the JMAK constants n and K as depicted in Fig. 3. The values of rate constant n calculated to be 2.56, 2.4 and 0.66 at 175°, 280° and 375 °C respectively between two points. At first two temperatures, the values of n indicate the three-dimensional growth of product phase randomly [10]. The value of n at 375 °C indicate the rate of transformation decrease with time. But, more period of time may require to get the proper explanation about the phase transformation which further affects the mechanical properties.

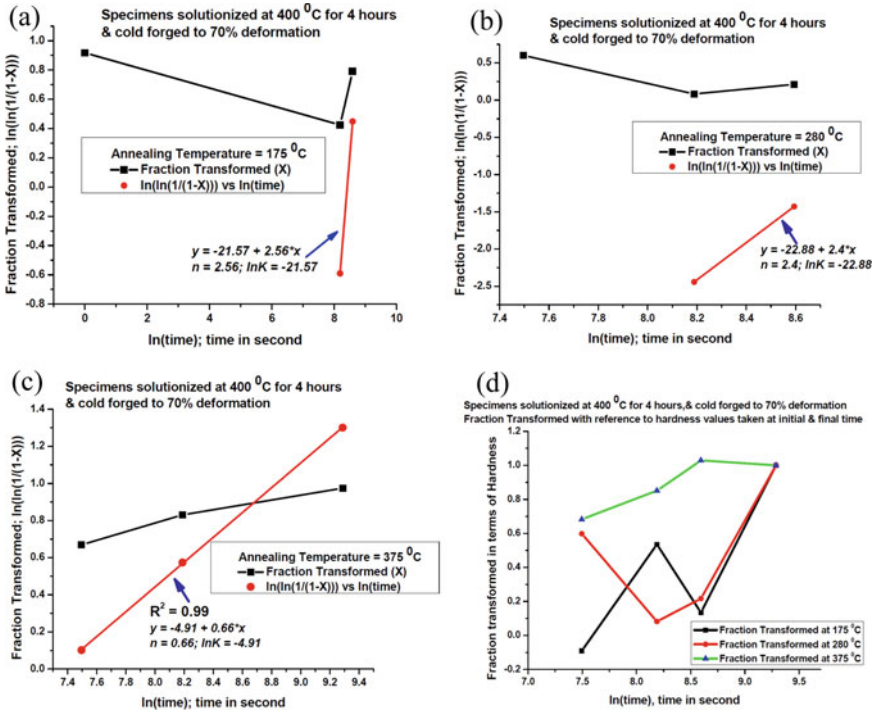


Fig. 3 Showing fraction transformed as function of time at **a** 175 °C **b** 280 °C **c** 375 °C by considering maximum hardness, minimum hardness and hardness at the time under consideration **d** by considering hardness at initial and final annealing time

The similar kind of analysis was carried out by considering the hardness at initial and final time at all temperatures which is shown in Fig. 3d. The trend of change of transformation is analogous to that of as shown in Fig. 3a, b and c. The similar kind of study was reported previously in case of 6063 aluminum alloy, which also said the change in grain size and sizes with distribution of second phase Mg₂Si occurred during annealing on existing deformed material [13]. But, hardness achieved is less as compared to the hardness observed in this study of 6082 alloy. This will be due to the content of manganese which leads to strengthening of the aluminum alloy [13].

4 Conclusions and Summary

The initial microstructure of AA6082 reveals the disparity in the grain sizes in heat treated T6 condition. Further, increase in hardness was observed after solutionizing at 400 °C for 4 h and 70 % cold forged. Hardness decreases as the annealing time and annealing temperature increase as compared to hardness at 70% cold forged material.

Annealing at different temperatures and time shows the variation in hardness which is further related to the predicted microstructural changes. Kinetic of annealing shows the variation of phase transformation in terms of hardness. Further, the values of rate constant n were found to be 2.56, 2.4 and 0.66 within limited data points of time period of 175°, 280° and 375 °C respectively. In addition, the hardness values were found to be more in AA6082 as compared to the hardness values reported in case of AA6063 for similar kind of study. The extended study in terms of more time period and microstructure evolution may require to get the more information and understanding about the transformation kinetics.

References

1. Lisa W, Kristin H, Thomas L (2018) High cycle fatigue behavior of the severely plastically deformed 6082 aluminum alloy with an anodic and plasma electrolytic oxide coating. *Surf Coat Tech* 349:576–583
2. El-Shennawy M, Abdel-Aziz A, Omar AA (2017) Metallurgical and mechanical properties of heat treatable aluminum alloy AA6082 welds. *Int J App Eng Res* 12(11):2832–2839
3. Anderson K, Weritz J, Kaufman JG (2018) *ASM Handbook. Alum Sci Technol 2A*. ASM International
4. Hu DC, Wang L, Wang HJ (2020) Dynamic recrystallization behavior and processing map of the 6082 aluminum alloy. *Mater* 13(1042):1–16
5. https://www.researchgate.net/publication/349997723_Investigation_of_Forging_Performance_for_AA6082/fulltext/604abe05299bf1f5d840dea3/Investigation-of-Forging-Performance-for-AA6082.pdf
6. Kumar N et al (2018) The influence of metallurgical factors on low cycle fatigue behavior of ultra-fine grained 6082 Al alloy. *Int J Fatig* 110:130–143
7. Prabhukhot AR, Prasad K (2015) Effect of heat treatment on hardness of 6082-t6 aluminum alloy. *Int J Sci Eng Res* 6 (12):38–42
8. Aditya R (2015) Prabhukhot: effect of heat treatment on hardness and corrosion behavior of 6082-t6 aluminum alloy in artificial sea water. *Int J Mat Sci Eng* 3(4):287–294
9. Chang Y-L, Hung F-Y, Lui T-S (2019) Study of microstructure and tensile properties of infrared-heat-treated cast-forged 6082 aluminum alloy. *J Mat Res Tech* 8(1):173–179
10. Jena AK, Chaturvedi MC (1991) *Phase transformation in materials*. Prentice Hall, Lebanon, Indiana, U.S.A.
11. Kulkarni RR, Prabhu N, Hodgson PD, Kashyap BP (2012) Phase dissolution of γ -Mg₁₇Al₁₂ during homogenization of as-cast AZ80 Magnesium alloy and its effect on room temperature mechanical properties. *Magnesium technology 2012*, Springer, Cham, pp 543–548
12. Moghadam MM, Pang EL, Philippe T, Voorhees PW (2016) Simulation of phase transformation kinetics in thin films under a constant nucleation rate. *Thin Solid Films* 612:437–444
13. Monteiro WA et al (2011) Microstructure and mechanical characterization after thermomechanical treatment in 6063 aluminum alloy. *Mat Sci App* 2:1529–1541

Evaluation of Maximum Bending Stiffness of Stranded Cables with Refined Kinematic Relations



Hadiya Pritesh Dulabhai , N. S. Parthasarthy ,
and Gurumoorthy S. Hebbar 

Abstract The mechanical response of a helically stranded cable depends on the effective stiffness offered by the collective assembly of its constituent wires. This can vary between two extreme conditions, namely a monolithic state, also known as the stick–slip state, wherein all the wires in the cable behave as a single unit with no relative movements among themselves, offering the maximum stiffness for the cable. In the other extreme condition, all the wires are free to move among themselves, with no frictional holding among them, thus offering the minimum stiffness. This paper reviews the various mathematical models that are available for the estimation of maximum bending stiffness and brings out the need for considering a vital parameter known as the ‘wire stretch effect’ that has been neglected by many authors till date. The consequent fundamental changes that occur in the basic kinematic relations are brought out and refined expressions for the internal wire forces and moments are established for the first time in the coupled axial-bending analysis. Further, the shear displacement of the wire due to the stretch has also been included in the wire normal and binormal shear forces. A single-layered cable with core-wire contact has been considered for analysis and the numerical results are evaluated with these new inclusions and are compared with the published results. It is hoped that the refined model suggested in this paper for the accurate estimation of the maximum stiffness, will pave way for more reasonable cable analysis in the subsequent slip stages.

Keywords Helical cable assembly · Kinematic relations · Effective stiffness

1 Introduction

Helically wound cable assemblies find extensive usage in structural, mechanical, and electrical power transmission applications. Since, a cable is a composite assembly of a central core & a few concentric layers of wires that are wrapped around helically, the development of a proper mathematical model to estimate its response is

H. P. Dulabhai (✉) · N. S. Parthasarthy · G. S. Hebbar
CHRIST (Deemed to be University), Bangalore 560074, India
e-mail: hadiyapriteshd@gmail.com

often challenging particularly when it is acted upon with bending loads. Accurate modeling of the interaction of the wires at the contact locations, interwire friction mechanics to define the movement and the slip in the wires will enable the realistic estimation of the bending stiffness. The bending stiffness of the cable varies between two extremes values—one corresponding to the monolithic state, wherein all the wires are locked with infinite friction and offering maximum stiffness, and the other corresponding to a complete loose wire assembly with no friction holding in the wire & offering the minimum stiffness. Even the prediction of the extreme values of stiffness demands a proper formulation that defines accurately the basic kinematic relations like the curvature and the twist of the helical wire and the associated internal forces & moments that are generated along the three axes of the wires. Since the cable is predominantly an axial load carrying application and the construction of the helical wire is also made with small lay angles, the force generated along the axial direction of the wire has a major contribution, compared to the forces in the other two directions. This constructional feature of the cable enabled many authors to consider the wire axial force primarily in their models and to neglect the influence of forces in the other directions, thereby resulting in different mathematical models with varied results.

Love [1] had established the basic kinematic relations and the equations of the equilibrium of a thin curved bent and twisted rod his book on “A treatise on the mathematical theory of elasticity”. These mathematical relations were fundamentally adopted partially or fully by all the cable researchers depending on the assumptions made by them. The cable research studies undertaken in the last seven decades are classified and the salient contributions are only presented here, with the significant changes in the research approach.

McConnell and Zemke [2] were one of the early authors to establish the extreme values of bending stiffness of the cables by conducting tests on few types of overhead electrical ACSR conductors. Basic mathematical relationships for the maximum and the minimum bending stiffnesses were presented with simple equations that did not consider the wire lay angle effects. However, this research paved a way for more analytical formulations.

Costello and Butson [3] improved the bending of cable with axial deformation but treated it as an assembly of loose wires. Lanteigne [4] studied the coupled effects of axial tension, torsion, and bending of a cable under static loading and derived expressions for the stiffness matrix of the cable. Knapp [5] studied the bent cables and derived expressions to include the wire binormal curvature and twist but limited his analysis with the wire axial strain only. LeClair and Costello [6] attempted to consider wire bending and twisting together with the wire axial force and obtained expressions for wire curvatures and twists. Costello [7] had summarized his research findings on axial-torsion models and coupled bending models in his book on “Theory of wire rope”.

When the cable is applied with a tensile load, all the helical wires experience tensile force along their axes initially. When the wire is subsequently bent and twisted to take a helical path, the influence of the basic axial force and its consequent stretch is also carried out in the bending and twisting phenomenon and this alters the expressions

of the wire curvatures and twists derived by Love [1] This is known as the ‘wire stretch effect’, a feature required to define the kinematic relations realistically as suggested by Wempner and Lardner [8] in his book. Wempner and Lardner [8] had also established expressions for the shear displacement of the wire due to stretch, along the normal and binormal directions. These shear displacements, though small, will also find their due share in the wire normal & binormal direction shear forces. The suggestions made by Wempner and Lardner [8] however had not been accounted in the research analysis till date.

Sathikh et al. [9] aptly included the wire stretch phenomenon as suggested by Wempner and Lardner [8] in the axial loading case and had derived the stiffness matrix for a cable which has yielded symmetry for the first time in the cable research studies. However, in Sathikh’s analysis, the second aspect of Wempner’s hypothesis on the shear stresses was assumed to be negligible and the expressions for the forces in the normal and binormal directions were analyzed as done by all the other researchers. Papailiou [10] had adopted Costello’s model and had extended it to provide useful insights on the bending behavior of multi-layered pre-tensioned spiral strands.

Sathikh et al. [11] included considered the wire stretch effect as suggested by Wempner and Lardner [8] for the first time in bending and obtained the expressions for the wire curvatures and twist. However, the shear influences were not adequately accounted for the net shear force in the strand cross-section, while estimating the cable stiffness.

Hong et al. [12] developed a mathematical model for the bending behavior of the helically wrapped cables by accounting the slippage of the wires under friction forces and proposed expressions for the bending stiffness under various slip stages. However, the expressions confined to the formulation of Love [1].

Spak et al. [13] reviewed the various cable models and studied the internal damping mechanisms due to interwire friction and variable bending stiffness as a function of cable curvature and certain wire parameters.

Khan et al. [14] formulated an analytical model to predict the bending stiffness of the multi-layered spiral strands in lines of Hong et al. [12]. The effect of slip and friction forces of helical wires were considered to include the fretting failures among them. The contact force and the strand deformation were found to vary significantly with the lay angles of the wire in different layers.

Zhang and Ostoja-Starzewski [15] proposed a Finite Element model to evaluate the bending stiffness of a single-layered cable. Two different FEM models were reported to obtain the bending stiffness of the strand. The cable was considered as a single entity in one model, where the friction is unlimited or infinite at the contact locations, resulting in higher bending stiffness. The mathematical formulation followed the basic works of Costello & other researchers. Loose wire assumption between the core & the wire was adopted in the second model, which yielded the minimum stiffness. However, the kinematic relations of the helical wire were in line with that of Love [1] and did not consider the effect of wire stretch.

The above literature survey indicates that all the researchers (except Sathikh et al. [11]) have retained the basic kinematic relations of the curvature and twist as maintained by Love [1] and have not improved them with the wire stretch phenomenon as suggested by Wempner and Lardner [8], till date. Though Sathikh et al. [11] have derived equations for refined curvatures and twists, the influence of wire stretch on the shear forces in the normal and binormal directions have not been considered.

Hence, this research paper attempts to bridge the fundamental gap in the existing basic kinematic relations of a helical strand with the inclusion of the wire stretch effect, a feature neglected till date in cable research. This has been considered essential, particularly when the cable is under significant axial pull and subsequently made to take up the bending mode, as encountered during overhead transmission line vibrations. Further, this paper considers for the first time the influence of the shear forces due to the wire stretch effect, a feature required to model the rolling of the wires during bending and enable the computation of bending stiffness realistically. Numerical computations are made for a single-layered cable as per the formulation of the recent Zhang model and are compared with the revised model suggested in this paper. It is hoped that the refinements for the fundamental kinematic relations suggested in this paper will enable the cable designers and the transmission line industry to predict the response of the cables effectively.

2 Mathematical Model

The cable is modeled as an assembly of thin rods which are pulled, bent, and twisted to form a helical structure around a central straight wire that forms the core. The wire deformations due to the externally applied axial tension, torsion, and bending loads and the consequent wire forces and moments in all the three directions of the wire are estimated based on the elastic theory of curved & bent thin rods adopted by Love and further improved in this paper by considering the wire stretch effect for the first time in coupled axial-bending analysis.

Figure 1a shows a cable subjected to an axial tension (F), axial twisting moment (M_T), and bending moment (M_B). The cable strand axes are indicated by X_1, X_2, X_3 (X_3 being along the length of the strand) in Fig. 1b Any point in the helical wire can be represented by a system of moving axes n, b , and t in the normal, binormal, and tangential directions, respectively with t being directed along the axial direction of the helical wire. Figure 1c illustrates the distribution of internal forces and moments generated on a helical wire due to the global cable loads shown in Fig. 1a. The internal wire end forces and moments along the normal, binormal, and axial directions are denoted by N, N', T and G, G', H , respectively. To maintain equilibrium, each helical wire is acted upon with distributed forces and moments X, Y, Z , and K, K', θ along the respective wire directions.

Love [1] had discussed the equilibrium of the helical wire under the above internal forces and moments and had derived the following equilibrium equations,

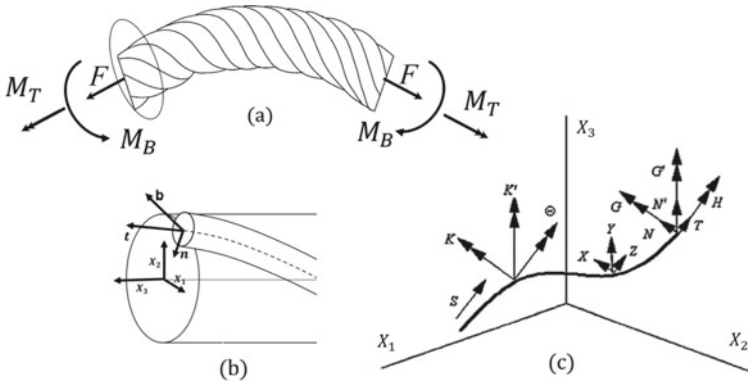


Fig. 1 Forces and moments acting on a wire element

$$\frac{\partial N}{\partial s} - N'\tau + T\kappa' + X = 0 \tag{1}$$

$$\frac{\partial N'}{\partial s} + N\tau - T\kappa + Y = 0 \tag{2}$$

$$\frac{\partial T}{\partial s} + N'\kappa - N\kappa' + Z = 0 \tag{3}$$

$$\frac{\partial G}{\partial s} - G'\tau + H\kappa' - N' + K = 0 \tag{4}$$

$$\frac{\partial G'}{\partial s} + G\tau - H\kappa + N + K' = 0 \tag{5}$$

$$\frac{\partial H}{\partial s} + G'\kappa - G\kappa' + \Theta = 0 \tag{6}$$

where κ, κ' are the curvatures of the helical wire in the normal and binormal directions and τ is the angular twist of the helical wire. The initial values of the wire curvatures and twist can be expressed in terms of helix angle (α) and the radius of the helix (r) as,

$$\left(\kappa_0, \kappa'_0, \tau_0\right) = \frac{1}{r}(0, \sin^2\alpha, \sin\alpha \cos\alpha) \tag{7}$$

The axial tensile force (T) generated in the helical wire can be related to the axial strain (ϵ_w), area of cross-section (A) and modulus of elasticity (E) as,

$$T = EA\epsilon_w \tag{8}$$

When, the cable is under the coupled effects of tension, torsion, and bending the axial strain in the wire at an orientation angle (ϕ) can be obtained from the basic elastic relations as,

$$\epsilon_w = \epsilon \sin^2(\alpha) + \gamma \cos^2(\alpha) + \frac{r \cos \phi \sin^2 \alpha}{\rho} \tag{9}$$

where, ϵ , γ and ρ are the axial strain, shear strain, and bending radius of the strand, respectively.

Hence, the axial force generated in the helical wire can be written as,

$$T = EA\epsilon_w = EA \left\{ [\epsilon \sin^2(\alpha) + \gamma \cos^2(\alpha)] + \frac{r \cos \phi \sin^2 \alpha}{\rho} \right\} \tag{10}$$

The wire flexural moment in the normal (G), binormal (G') directions and twisting moment (H) about the wire axis can be related with the respective wire strains ($\omega_n, \omega_b, \omega_t$) and the cross-sectional and material properties of the wire as,

$$(G, G', H) = (EI\omega_n, EI\omega_b, GJ\omega_t) \tag{11}$$

The shear forces in the normal (N) and binormal (N') directions of the wire as a result of bending and twisting moment, can be written as,

$$N = H\kappa - G\tau \tag{12}$$

$$N' = H\kappa' - G'\tau \tag{13}$$

2.1 Existing Kinematic Relations of the Helical Wire

The wire flexural strains about the normal (ω_n) and binormal (ω_b) axis are usually attributed to the change in the normal and binormal curvature of the wire. The change in the normal curvature ($\Delta\kappa$) of a helical wire in a strand under the coupled effects of tension, torsion and bending can be given by,

$$\omega_n = \Delta\kappa = \frac{\sin \alpha \sin \phi}{\rho} \tag{14}$$

The change in the binormal curvature ($\Delta\kappa'$) of a helical wire in a strand under the coupled effects of tension, torsion and bending can be given by,

$$\omega_b = \Delta\kappa' = \frac{-\sin 2\alpha \sin \alpha \cos \alpha (\varepsilon - \gamma)}{r} + \frac{\sin^2 \alpha \cos \phi}{\rho} \tag{15}$$

Similarly, the wire torsional strain about the wire axis (ω_t) can also be attributed to the change in a twist. The change in the twist ($\Delta\tau$) of a helical wire in a strand under the coupled effects of tension, torsion and bending can be given by,

$$\omega_t = \Delta\tau = \frac{\cos 2\alpha \sin \alpha \cos \alpha (\varepsilon - \gamma)}{r} + \frac{\sin \alpha \cos \alpha \cos \phi}{\rho} \tag{16}$$

2.2 Refined Kinematic Relations of the Helical Wire

When a cable is applied with a tensile load, all the helical wires experience tensile force along their axes. Initially, when the wire is subsequently bent and twisted to take a helical path the influence of the basic axial force and its consequent stretch is also carried out in the successive bending and twisting phenomenon. This is known as the ‘Wire Stretch effect’. As a result of this, the basic kinematic relations of the wire curvature and twist under are refined as below,

$$\omega_n = \Delta\kappa + \kappa_0 \in_w \tag{17}$$

$$\omega_b = \Delta\kappa' + \kappa'_0 \in_w \tag{18}$$

Similarly, the wire torsional strain about the wire axis (ω_t) can also be attributed to the change in the twist and a corresponding term to include the wire stretch effect as below,

$$\omega_t = \Delta\tau + \tau_0 \in_w \tag{19}$$

Combining the Eqs. 7, 9, 14, 15 and 16 the refined kinematic relations are presented as under,

$$\omega_n = (\sin \alpha (1 + \cos^2 \alpha) - a_1 \sin \alpha \cos \alpha + a_3 \cos^2 \alpha + a_2 \cos \alpha) \frac{\sin \phi}{\rho} \tag{20}$$

$$\begin{aligned} \omega_b = & -\frac{\sin^2 \alpha \cos^2 \alpha \varepsilon}{r} + \frac{\cos^2 \alpha (1 + \sin^2 \alpha) \gamma}{r} \\ & + (\sin^4 \alpha + a_1 \cos \alpha - a_2 \sin \alpha \cos \alpha) \frac{\cos \phi}{\rho} \end{aligned} \tag{21}$$

$$\omega_t = \frac{(\sin \alpha \cos^3 \alpha) \varepsilon}{r} + \frac{(\sin^3 \alpha \cos \alpha) \gamma}{r}$$

$$+ (-\cos \alpha \sin^3 \alpha + a_3 \cos \alpha + a_2 \cos^2 \alpha) \frac{\cos \phi}{\rho} \quad (22)$$

where, a_1 , a_2 and a_3 are the factors defining shear strains and twists based on Sathikh et al. [11] work.

2.3 Refined Wire Shear Force Expressions

The earlier authors have not accounted for the shear strains that arise in a wire cross-section and attributed the shear forces in the normal (N) and binormal (N') directions only due to the influence of bending moment and twisting moment, assuming the role of shear strains as negligible. Wempner and Lardner [8] has stressed the importance of shear strains and their corresponding contribution to shear forces. The shear strains induced in the cross-section of a helical wire in the normal and binormal directions are associated with the position angle of the wire (ϕ) and the radius of bending (ρ). In the case of coupled axial-bending loading, the net shear strain induced in a wire cross-section can be accounted for by the summation of the respective shear strains arising from the axial and bending deformations and are presented as under.

$$\gamma_{nt} = \frac{a_1 r \sin \phi}{\rho} \quad (23)$$

$$\gamma_{bt} = \varepsilon \sin \alpha \cos \alpha + \frac{a_2 r \cos \phi}{\rho} \quad (24)$$

The shear forces induced by the above shear strains can be readily obtained from the basic mechanic's relations as,

$$\tilde{N} = CA \gamma_{nt} = CA \frac{a_1 r \sin \phi}{\rho} \quad (25)$$

$$\tilde{N}' = CA \gamma_{bt} = CA \left(\varepsilon \sin \alpha \cos \alpha + \frac{a_2 r \cos \phi}{\rho} \right) \quad (26)$$

where C is the rigidity modulus of the wire.

Hence, the net shear force in a wire cross-section (N , N') can be expressed as the summation of shear forces induced due to shear strains (which had been neglected in the research so far) and that resulted from the bending and twisting of the helical wire, as under.

$$N = \tilde{N} + H\kappa - G\tau \quad (27)$$

$$N' = \tilde{N}' + H\kappa' - G'\tau \tag{28}$$

The refined expression for wire normal shear force (N) as in Eq. 29 is obtained by combing Eqs. 11 and 25 as below,

$$N = CA \frac{a_1 r \sin \phi}{\rho} + GJ\omega_t \kappa - EI\omega_n \tau \tag{29}$$

The refined expression for wire binormal shear force (N') is obtained by combing Eqs. 11 and 26 as below,

$$N' = CA \left(\varepsilon \sin \alpha \cos \alpha + \frac{a_2 r \cos \phi}{\rho} \right) + GJ\omega_t \kappa' - EI\omega_b \tau \tag{30}$$

It can be noted that the additional terms that are introduced with CA in Eqs. 29 and 30 are due to the consideration of shear strain in the present model.

2.4 Strand Equilibrium Equations

In a single-layered strand of *m* helical wires in a layer surrounding the core, the resultant axial force F, twisting moment (couple) *M_T* and Bending Moment *M_B* along the strand, axis can be obtained by the summation of respective forces and moments in all the helical wires and the central core as below,

$$F = \sum_{i=1}^m \left[T_i \sin \alpha + N'_i \cos \alpha \right] + E_c A_c \varepsilon \tag{31}$$

$$M_T = \sum_{i=1}^m \left[H_i \sin \alpha + G'_i \cos \alpha + T_i r \cos \alpha - N'_i r \sin \alpha \right] + \frac{G_c J_c}{r} \gamma \cot \alpha \tag{32}$$

$$M_B = \sum_{i=1}^m \left[r \cos \phi_i \times T_i \sin \alpha - r \sin \phi_i \times N'_i \cot \alpha + r \cos \phi_i \times N'_i \cos \alpha \right] + \frac{E_c I_c}{\rho} \tag{33}$$

where the suffix ‘*i*’ represents the *i*th wire in the layer and *m* is the number of helical wires in the layer of the strand and *E_c*, *G_c* are Young’s modulus and the rigidity modulus and *A_c*, *I_c*, *J_c* are the cross-sectional properties of the core wire. Substituting the values of wire forces and moments from Eqs. 10, 11, 20, 21, 22 and 30 in the strand equilibrium Eqs. 31–33 and arranging them in a matrix form, the following relation matrix can be obtained.

$$\begin{bmatrix} F \\ M_T \\ M_B \end{bmatrix} = \begin{bmatrix} F_{\in\in} & F_{\in\gamma} & F_{\in b} \\ M_{\gamma\in} & M_{\gamma\gamma} & M_{\gamma b} \\ M_{b\in} & M_{b\gamma} & M_{bb} \end{bmatrix} \begin{bmatrix} \in \\ \gamma \\ 1/\rho \end{bmatrix} \quad (34)$$

2.5 Elements of the Stiffness Matrix of the Cable Assembly

The elements of the stiffness matrix of the cable as mentioned in Eq. 34 are obtained by substituting the wire force, twisting moment, and bending moment expressions in the previous section with the refined kinematic relations and the shear strain considerations that are exclusively developed in this paper and then by summing them up for all the wires in the layer around the central core wire. The core axial, torsional, and bending stiffnesses are appropriately added to the layer stiffness elements in the principal diagonal.

$$F_{\in\in} = m \left(EA \sin^3 \alpha + \frac{GJ \sin \alpha \cos^6 \alpha}{r^2} + \frac{EI \sin^3 \alpha \cos^4 \alpha}{r^2} \right) + A_c E_c \quad (35)$$

$$F_{\in\gamma} = m \left(EA \sin \alpha \cos \alpha + \frac{GJ}{r^2} \sin^3 \alpha \cos^4 \alpha - \frac{EI}{r^2} (1 + \sin^2 \alpha) \cos^4 \alpha \sin \alpha \right) \quad (36)$$

$$F_{\in b} = \sum_{i=1}^m \cos \phi_i \left(\begin{array}{l} EA r \sin^3 \alpha + \zeta A r a_2 \cos \alpha \\ + GJ \cos^2 \alpha \frac{1}{r} (a_3 \cos^2 \alpha - \sin^3 \alpha + a_2 \cos^3 \alpha) \\ - \frac{GJ \cos^2 \phi_i}{r} + \frac{GJ}{r} - \frac{EI \sin \alpha \cos^3 \alpha}{r} (\cos^2 \alpha - a_1 \sin \alpha) \end{array} \right) \quad (37)$$

$$M_{\gamma\in} = m \sin^2 \alpha \cos \alpha \left(EA r + \frac{GJ \cos^2 \alpha \sin^2 \alpha}{r} - \frac{EI \cos^2 \alpha \sin^2 \alpha}{r^2} \right) \quad (38)$$

$$M_{\gamma\gamma} = \frac{\cos^3 \alpha}{r} m \left(EA r^2 + EI (1 + \sin^2 \alpha)^2 + GJ \sin^4 \alpha \tan^2 \alpha \right) + \frac{G_c J_c}{r} \cot \alpha \quad (39)$$

$$\begin{aligned} M_{\gamma b} = & \sum_{i=1}^m \frac{EA r^2}{\rho} \cos \alpha \sin^2 \alpha \cos \phi_i \\ & + \frac{EI \zeta A r^3 a_2 \cos \phi_i \sin^2 \alpha}{\cos \alpha \rho} \sin^4 \alpha \cos \alpha \cos \phi_i \\ & + a_1 \sin^2 \alpha \cos^2 \alpha \cos \phi_i + a_2 \sin^3 \alpha \cos^2 \alpha \cos \phi_i \\ & + \sin^2 \alpha \cos \phi_i \cos \alpha + a_1 \cos^2 \alpha \cos \phi_i - a_2 \sin \alpha \cos^2 \alpha \cos \phi_i \end{aligned}$$

$$\begin{aligned}
 &+ GJ(a_3 \cos \alpha \sin \alpha \cos \phi_i + a_2 \cos^2 \alpha \cos \phi_i \sin \alpha \\
 &- \cos \alpha \cos \phi_i \sin^4 \alpha - a_3 \sin \alpha \cos \phi_i \cos^3 \alpha \\
 &- a_2 \cos^2 \alpha \sin \alpha \cos^3 \phi_i)
 \end{aligned} \tag{40}$$

$$\begin{aligned}
 M_{b\epsilon} = &\sum_{i=1}^m EA r \cos \phi_i \sin^3 \alpha + \frac{EI}{r} \sin^2 \alpha \cos^4 \alpha \cos \phi_i \\
 &- \frac{EI}{r} \sin^3 \alpha \cos^2 \alpha \cos \phi_i + \frac{GJ}{r} \sin^2 \alpha \cos^5 \alpha \cos \phi_i \\
 &- \frac{GJ}{r} \sin \alpha \cos^4 \alpha \cos \phi_i
 \end{aligned} \tag{41}$$

$$\begin{aligned}
 M_{b\gamma} = &\sum_{i=1}^m EA r \cos^2 \alpha \sin \alpha \cos \phi_i + \frac{GJ}{r} \sin^3 \alpha \cos^4 \alpha \cos \phi_i \\
 &- \frac{GJ}{r^2} \cos^5 \alpha \cos \phi_i + \frac{EI}{r} \cos^2 \alpha \sin \alpha (1 + \sin^2 \alpha) \cos \phi_i \\
 &- \frac{EI}{r} \cos \phi_i \sin \alpha \cos^4 \alpha (1 + \sin^2 \alpha)
 \end{aligned} \tag{42}$$

$$\begin{aligned}
 M_{bb} = &\sum_{i=1}^m EA r^2 \cos^2 \phi_i \sin^3 \alpha + GA r^2 (a_2 \cos^2 \phi_i \cos \alpha + a_1 \sin^2 \phi_i \cot \alpha) \\
 &+ GJ(a_3 \cos^2 \phi_i \cos^4 \alpha - \sin^3 \alpha \cos^5 \alpha + a_2 \cos^2 \phi_i \cos^5 \alpha \\
 &+ \sin^3 \alpha \cos^2 \phi_i \cos^2 \alpha - a_3 \cos^2 \alpha \cos^2 \phi_i - \cos^2 \phi_i \cos^3 \alpha) \\
 &+ EI(\sin \alpha \cos^2 \alpha \sin^2 \phi_i (1 + \cos^2 \alpha) + a_1 \sin \alpha \cos^3 \alpha \sin^2 \phi_i \\
 &- a_3 \sin \alpha \cos^3 \alpha \cot \alpha - a_2 \sin^2 \phi_i \cos^3 \alpha - \sin^3 \alpha \cos^2 \alpha \cos^2 \phi_i \\
 &- a_1 \sin \alpha \cos^2 \phi_i + a_2 \sin^2 \alpha \cos^3 \alpha \cos^2 \phi_i + \sin \alpha \sin^2 \phi_i (1 + \cos^2 \alpha) \\
 &- a_1 \sin \alpha \cos \alpha \sin^2 \phi_i + a_3 \cos^2 \alpha \sin^2 \phi_i + a_2 \cos \alpha \sin^2 \phi_i + \cos^2 \phi_i \sin^3 \alpha \\
 &+ a_1 \sin \alpha \cos \alpha \cos^2 \phi_i - a_2 \cos \alpha \cos^2 \phi_i \sin^2 \alpha) + \frac{E_c I_c}{\rho}
 \end{aligned} \tag{43}$$

2.6 Numerical Results and Discussion

Numerical computations are carried out for a single-layered strand as per the specifications mentioned in Table 1.

Comparison of stiffness elements

Using the revised kinematic relations that are exclusively developed in this paper for the case of the combined axial and bending loads on a cable, the wire forces and moments in the normal, binormal, and axial direction (N, N', T and G, G', H) are evaluated as in Eqs. 10, 11, 29, 30. Numerical computations of the nine stiffness elements of the cable are carried out as in Eqs. 35–43 for a single-layered cable (whose specifications are shown in Table 1) as per the revised model that includes the ‘wire stretch effect’ and the shear strain considerations suggested in this paper. The stiffness elements for the Sathikh et al. [11] and Zhang and Ostoja-Starzewski [15] models are also calculated by making appropriate changes in the above equations as indicated in the previous section. It can be noted that the stiffness coefficients $F_{\epsilon b}, M_{\gamma b}, M_{b\epsilon}, M_{b\gamma}$ are observed to be zero in all the models, due to the symmetric orientation of the wires above and below the neutral axis. Hence, the results of the other five stiffness elements are presented in Table 2 for the Zhang and Ostoja-Starzewski [15] and Sathikh et al.[11], and fully refined present model suggested in this paper.

It can be observed from Table 2 that the stiffness coefficients ($F_{\epsilon\epsilon}, F_{\epsilon\gamma}, M_{\gamma\epsilon}, M_{\gamma\gamma}$) of the present model and Sathikh’s model agree very close to each other due to the common consideration of the wire stretch effect in these models. The stiffness coefficients of the Zhang model have been observed to

Table 1 Material and geometrical properties of the single-layered strand [15]

Parameter (unit)	Value
Diameter of core (mm)	3.94
Diameter of helical wire (mm)	3.73
Helix radius (mm)	3.835
Helix angle (α°)	72.97
Lay angle (β°)	17.03
Young’s modulus of core and helical wire (GPA)	188
Poisson’s ratio	0.3

Table 2 Comparison of stiffness elements of the strand

Model	$F_{\epsilon\epsilon}(N)$	$F_{\epsilon\gamma}(Nm)$	$M_{\gamma\epsilon}(N)$	$M_{\gamma\gamma}(Nm)$	$M_{bb}(N - m^2)$
Zhang [15]	10.78	12.85	11.97	25.11	90.3
Sathikh [11]	10.77	12.57	12.57	25.82	91.8
Present model	10.77	12.57	12.57	25.82	86.5

differ from Sathikh et al. [11] and the present model, due to the obvious reason of non-consideration of wire stretch effect.

The bending stiffness coefficient (M_{bb}) values have been tabulated for all the three models in the last column of Table 2. In the finite element model of Zhang and Ostoja-Starzewski [15], the cable assembly has been maintained as a single entity, where the wire-core and wire-wire movements are restricted as in Sathikh et al. [11] model. Hence, the bending stiffness coefficients of the two models are closer. The inclusion of wire stretch effect and the consideration of wire normal and binormal shear influence due to the shear strain consideration in the present model has permitted shear rotations as against the earlier models and hence has resulted in lesser bending stiffness.

3 Conclusion

In this paper, a mathematical model has been developed to evaluate the maximum stiffness of helically stranded cables under the simultaneous effect of axial, torsion, and bending load. The basic kinematic relations for the normal, binormal, and twist of a helical wire are refined by accounting the influence of wire stretch, a parameter neglected till date in the cable research.

In view of the above refinements in the basic kinematic relations, the following observations are noticed in the stiffness elements of a single-layered cable.

- The stiffness elements corresponding to the axial and torsional loads do not register a significant difference between the present model and the existing models that are used for analysis.
- The stiffness element due to the cable bending is however observed to show a reduction up to 5% in the present model from that of the existing analytical models. The wire stretch effect, which is additionally considered in this paper, has resulted in shear displacement, permitting rotations in the wire and thereby causing a reduction in stiffness.
- The impact of the wire stretch effect has become significant when the cable is subjected to bending loads in addition to its axial loads and hence will be of concern in applications like electrical overhead power transmission lines, where the cable is under an axial pull and experiencing bending during vibrations simultaneously.

It is hoped that the refined parameters considered in this paper will enable cable designers to arrive at a realistic estimation of the cable stiffness.

References

1. Love AEH (1940) A treatise on the mathematical theory of elasticity. *Nature* 105:511–512
2. McConnell KG, Zemke WP (1980) The measurement of flexural stiffness of multistranded electrical conductors while under tension. *Exp Mech* 20:198–204
3. Costello GA, Butson GJ (1982) Simplified bending theory for wire rope. *J Eng Mech Div* 108:219–227
4. Lanteigne J (1985) Theoretical estimation of the response of helically armored cables to tension, torsion, and bending. *J Appl Mech* 52:423–432
5. Knapp RH (1988) Helical wire stresses in bent cables. *J Offshore Mech Arct Eng* 110:55–61
6. Le Clair RA, Costello GA (1988) Axial, bending and torsional loading of a strand with friction. *J Offshore Mech Arct Eng* 110:38–42
7. Costello GA (1990) *Theory of wire rope*, Springer. Springer Science & Business Media
8. Wempner G, Lardner TJ (1983) Mechanics of solids with applications to thin bodies. *J Appl Mech* 50:701–701
9. Sathikh S, Moorthy MBKK, Krishnan M (1996) A symmetric linear elastic model for helical wire strands under axisymmetric loads. *J Strain Anal Eng Des* 31:389–399
10. Papailiou KO (1997) On the bending stiffness of transmission line conductors. *IEEE Trans Power Deliv* 12:1576–1588
11. Sathikh S, Rajasekaran S, Jayakumar Jebaraj C (2000) General thin rod model for preslip bending response of strand. *J Eng Mech* 126:132–139
12. Hong K-J, Der Kiureghian A, Sackman JL (2005) Bending behavior of helically wrapped cables. *J Eng Mech* 131:500–511
13. Spak K, Agnes G, Inman D (2013) Cable modeling and internal damping developments. *Appl Mech Rev* 65:010801
14. Khan SW, Gencturk B, Shahzada K, Ullah A (2018) Bending behavior of axially preloaded multilayered spiral strands. *J Eng Mech* 144:4018112
15. Zhang D, Ostoja-Starzewski M (2015) Finite element solutions to the bending stiffness of a single-layered helically wound cable with internal friction. *J Appl Mech* 83:031003

The Interest of the Longitudinal Friction Coefficient on the Slip Ratio of the Heavy Vehicle When Braking at 60 km/h



Luong Van Van and Nguyen Thanh Tung

Abstract During acceleration and braking, the tires often slip relative to the road surface, which affects the acceleration and braking efficiency of the heavy vehicle. This paper indicates the research results on the slip ratio of a heavy vehicle when braking on six types of road surfaces at the velocity of 60 km/h. This paper uses the Newton–Euler method to institute a dynamics model and the Matlab-Simulink software to dissect the consequence of the maximum longitudinal friction coefficient ($\varphi_{x\max}$) on the slip ratio when braking a heavy vehicle. The outcomes show at the heavy vehicle is braked on the road surface has $\varphi_{x\max} = [0.7, 0.8, 0.9, 1.0]$, the slip ratio is less than 10%, the heavy vehicle runs smoothly, the braking performance of the vehicle qualified for ECE-R13 standards; If the heavy vehicle is braked on the road surface has $\varphi_{x\max} = 0.6$, the slip ratio of the middle and rear tires are 100%, the heavy vehicle is unstable, the braking efficiency is only about 75%; If the heavy vehicle is braked on the road surface has $\varphi_{x\max} = 0.5$, the middle and rear tires slip completely, the heavy vehicle is unstable, the braking efficiency is only about 63%.

Keywords Longitudinal friction coefficient · Slip ratio · Heavy vehicle

1 Background

The slip ratio influences the acceleration and braking of the heavy vehicle. The longitudinal slip ratio of a driving tire is determined as formula 1 [1, 2].

$$s = 1 - \frac{V_x}{R_d\omega_w}; \quad R_d\omega_w > V_x; \quad 0 < s < 1 \quad (1)$$

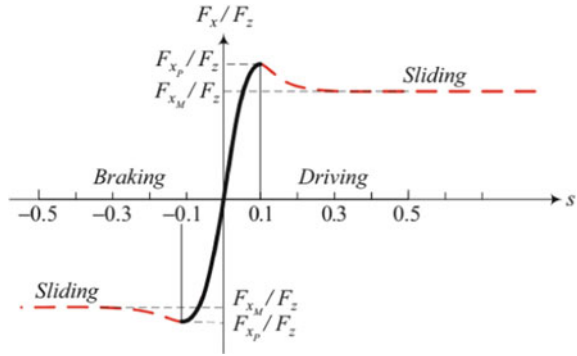
and a braking tire is determined as formula 2. [1, 2]

$$s = \frac{R_d\omega_w}{V_x} - 1; \quad R_d\omega_w < V_x; \quad -1 < s < 0 \quad (2)$$

L. V. Van · N. T. Tung (✉)

Vinh Long University of Technology Education, 73 Nguyen Hue street, Vinh Long City, Vietnam
e-mail: tungnt@vlute.edu.vn

Fig. 1 Function of slip ratio [1]



Slip ratio $s > 0$ for driving and $s < 0$ for braking. The longitudinal slip ratio $\varphi_x = \frac{F_x}{F_z}$ is a function of slip ratio s as depicted in Fig. 1. In driving, the longitudinal slip ratio has its maximum value at $s \approx 0.1$, before decreasing to a minimum and almost constant value. Tire longitudinal force F_x is proportional to the coefficient of slip when the coefficient of slip is small. The tire will rotate when the coefficient of slip is greater than 0.1 and the longitudinal tire force is assumed to be constant at F_{xM} . During braking, the phenomenon of slippage also occurs similar to the process of driving a heavy vehicle, but in the opposite direction. [1, 2]

2 The Heavy Vehicle Model

The heavy vehicle belongs to the multi-body system, it has a very complex structure, including the mass-spring-damper and the un-mass-spring-damper linked together by a suspension system. To build a three-dimensional dynamic model of the heavy vehicle in the coordinate system OXYZ, the authors use the method of structural separation of a multi-body system and Newton–Euler methods [3–5]. Based on the Newton–Euler equation system, with $i = [1-6]$ are the ordinal number of the axles, $j = 1$ is the left wheel, $j = 2$ is the right wheel, the dynamic equations of the heavy vehicle in the (OXZ) and (OXY) plane expressed in the Formula (3–12):

$$m_{ci}(\ddot{z}_{ci} - \dot{\varphi}_{ci}\dot{x}_{ci}) = F_{Cij} + F_{Kij} - F_{kz} \tag{3}$$

$$J_{yci}\ddot{\varphi}_{ci} = -(F_{Cij} + F_{Kij})l_i + F'_{xij}(h_{ci} - r_i) + F_{kxi}(h_{ci} - h_{ki}) + F_{kzi}l_{ki} + M_{ij} \tag{4}$$

$$\left(m_{c1} + \sum_1^3 m_{Ai} \right) (\ddot{x}_{c1} - \dot{\psi}_{c1}\dot{y}_{c1}) = F_{x11} + F_{x12} + F_{x21}$$

$$+ F_{x22} + F_{x31} + F_{x32} - F_{kx1} \tag{5}$$

$$\left(m_{c1} + \sum_1^3 m_{Ai} \right) (\ddot{y}_{c1} + \dot{\psi}_{c1} \dot{x}_{c1}) = F_{y11} + F_{y12} + F_{y21} + F_{y22} + F_{y31} + F_{y32} - F_{ky1} \tag{6}$$

$$J_{zc1} \ddot{\psi}_{c1} = (F_{x12} - F_{x11})b_1 + (F_{x22} - F_{x21})b_2 + (F_{x32} - F_{x31})b_3 - (F_{y11} + F_{y12})l_1 - (F_{y21} + F_{y22})l_2 - (F_{y31} + F_{y32})l_3 + F_{ky1}l_{k1} \tag{7}$$

$$\left(m_{c2} + \sum_4^6 m_{Ai} \right) (\ddot{x}_{c2} - \dot{\psi}_{c2} \dot{y}_{c2}) = F_{x4j} + F_{x5j} + F_{x6j} + F_{kx2} \tag{8}$$

$$\left(m_{c2} + \sum_4^6 m_{Ai} \right) (\ddot{y}_{c2} + \dot{\psi}_{c2} \dot{x}_{c2}) = F_{ky2} + F_{y4j} + F_{y5j} + F_{y6j} \tag{9}$$

$$J_{zc2} \ddot{\psi}_{c2} = (F_{x42} - F_{x41})b_4 + (F_{x52} - F_{x51})b_5 + (F_{x62} - F_{x61})b_6 + F_{ky2}l_{k2} - F_{y4j}l_4 - F_{y5j}l_5 - F_{y6j}l_6 \tag{10}$$

The lateral dynamic equations of the heavy vehicle in the (OYZ) plane and the tires dynamic equations are written as the formula (11–15) (Figs. 2 and 3; Table 1):

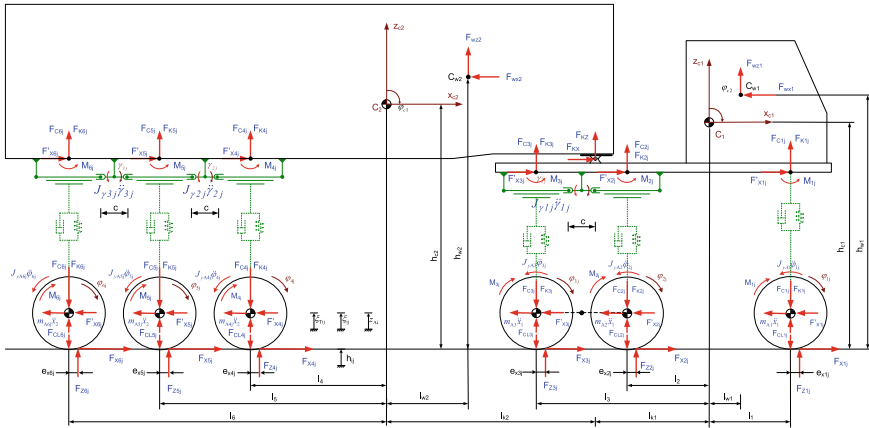


Fig. 2 The dynamics model of the heavy vehicle in the (OXZ) plane

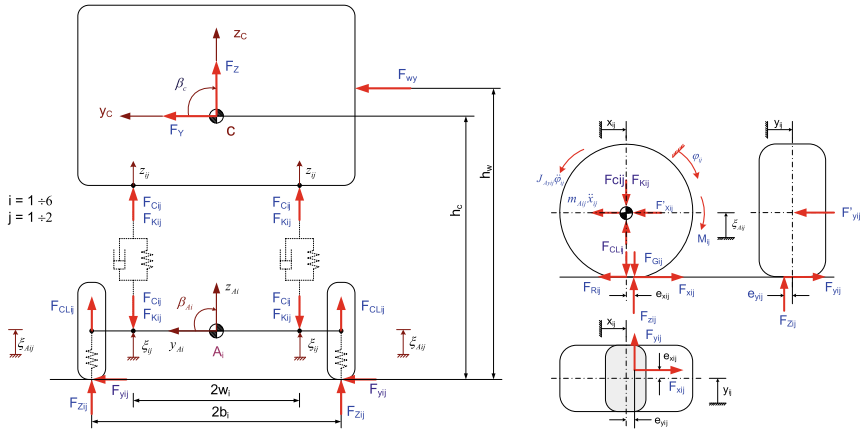


Fig. 3 The dynamics model in the (OYZ) plane and the tire dynamics model

$$J_{xci}\ddot{\beta}_{ci} = \sum_{i=1}^{i=6} (F_{C2i} + F_{K2i} - F_{C1i} - F_{K1i})w_i + \sum_{i=1}^{i=6} F_i(h_c - h_{Bi}) - M_{kx} \quad (11)$$

$$m_{Ai}(\ddot{z}_{Ai} + \dot{\beta}_{Ai}\dot{y}_{Ai}) = F_{CLij} - F_{Cij} - F_{Kij} \quad (12)$$

$$m_{Ai}(\ddot{y}_{Ai} - \dot{\beta}_{Ai}\dot{z}_{Ai}) = F_i + F_{yij} + F_{yij} \quad (13)$$

$$J_{Axi}\ddot{\beta}_{Ai} = (F_{C1i} + F_{K1i} - F_{C2i} - F_{K2i})w_i + (F_{CLi2} - F_{CLi1})b_i - F_{yij}(r_{ij} + \xi_{Aij}) + F_i(h_{Bi} - r_i) \quad (14)$$

$$J_{Ayij}\ddot{\phi}_{ij} = M_{Aij} - M_{Bij} - F_{xij}r_{dij} \quad (15)$$

3 Investigation on the Slip Ratio of the Heavy Vehicle

The authors used Matlab-Simulink software to investigate the influence of the longitudinal friction coefficient on the slip ratio when braking a heavy vehicle. The authors investigate the slip ratio of the heavy vehicle as follows:

- (i) The heavy vehicle is driven on a straight road at the velocity of 60 km/h and then is braked with a braking torque of $M_B = 0.8 M_{Bmax} = 0.8F_{G\varphi_{xmax}}r_d$.

Table 1 Table of symbols and abbreviations

Symbols	Names
i	Axle number of the heavy vehicle, $i = [1-6]$
j	$j = 1$ is left tire; $j = 2$ is right tire; $j = [1, 2]$
x_c, y_c, z_c	Displacement in the $B(x_c y_c z_c)$ coordinate system
R_d	Dynamic radius of a tire
R_g	Geometric radius
V_x	The longitudinal velocity of the vehicle
ω_w	The rotational velocity of the wheel
$\varphi_{x\max}$	The maximum longitudinal friction coefficient
S	The slip ratio
$l_1, l_2, l_3, l_4, l_5, l_6$	Distance from mass center to axle 1, 2, 3, 4, 5, 6
h_{c1}, h_{c2}	Height of mass center of the tractor and semi-trailer
B	Distance from the x -axis to a tire
φ_{ij}	The angle of rotation of an ij wheel
β, φ, ψ	Rotation of the vehicle body around the x, y, z axes
m, m_A	Mass-spring-damper and un-mass-spring-damper of the vehicle
J_x, J_y, J_z	Inertia moment of the vehicle about the x, y, z axes
J_{Ayij}	Inertia moment of the ij wheel about the y -axes
F_{Cij}	The elastic force of the suspension system of the ij tire
F_{Kij}	The damping force of the suspension system of the ij tire
F_{CLij}	The elastic force of the ij tire
F_{xij}	The longitudinal force of the ij tire
F_{yij}	The lateral force of the ij tire
F_{zij}	The vertical force of the ij tire
F_G	The static weight of the vehicle
M_{Aij}, M_{Bij}	Driving moment and braking moment of the ij tire

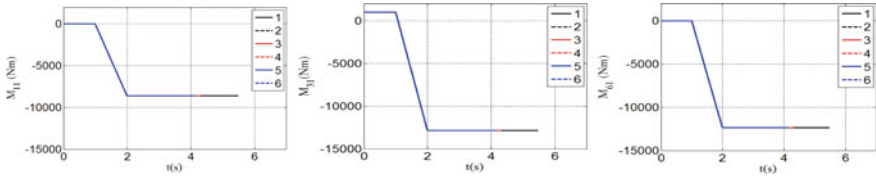


Fig. 4 The moment of the front, middle and rear axles

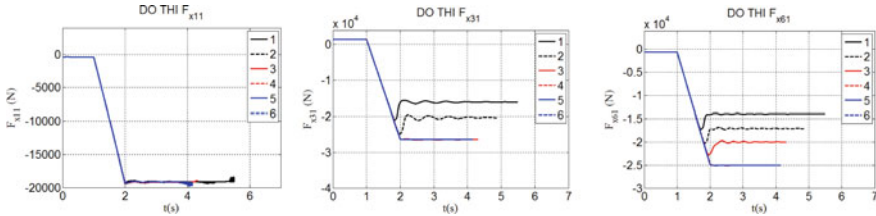


Fig. 5 Longitudinal force of the heavy vehicle

- (ii) The authors have surveyed 6 types of roads with different longitudinal friction coefficient $\varphi_{x\max} = [0.5, 0.6, 0.7, 0.8, 0.9, 1.0]$. Line 1, solid black line with $\varphi_{x\max} = 0.5$; Line 2, dash black line with $\varphi_{x\max} = 0.6$; Line 3, solid red line with $\varphi_{x\max} = 0.7$; Line 4, dash red line with $\varphi_{x\max} = 0.8$; Line 5, solid blue line with $\varphi_{x\max} = 0.9$; Line 6, dash blue line with $\varphi_{x\max} = 1.0$.

Driving moment and braking moment of the front, middle and rear axles of the heavy vehicle are shown in Fig. 4.

Figure 5 is the longitudinal force graph of the front, middle and rear tires of the heavy vehicle at the velocity of 60 km/h. Looking at Fig. 5, we can see that when the heavy vehicle is moving on six types of roads with different longitudinal friction coefficient $\varphi_{x\max} = [0.5, 0.6, 0.7, 0.8, 0.9, 1.0]$, the longitudinal force of the front tires F_{x11} is about 19 kN. Because slip occurs between the tire and the road, the longitudinal force of the middle tires $F_{x31} = 27$ kN, with $\varphi_{x\max} = [0.7, 0.8, 0.9, 1.0]$; $F_{x31} = 20$ kN, with $\varphi_{x\max} = 0.6$; $F_{x31} = 16$ kN, with $\varphi_{x\max} = 0.5$; the longitudinal force of the rear tires $F_{x61} = 25$ kN, with $\varphi_{x\max} = [0.9, 1.0]$; $F_{x61} = 20$ kN, with $\varphi_{x\max} = [0.7, 0.8]$; $F_{x61} = 17$ kN, with $\varphi_{x\max} = 0.6$; $F_{x61} = 14$ kN, with $\varphi_{x\max} = 0.5$.

The vertical force charts of the front, middle and rear tires of the heavy vehicle at the velocity of 60 km/h are shown in Fig. 6. Looking at Fig. 6, we can see that when the heavy vehicle is moving on six types of roads with different longitudinal friction coefficient $\varphi_{x\max} = [0.5, 0.6, 0.7, 0.8, 0.9, 1.0]$, the vertical force of the front tires F_{z11} is lifted from 28 to 51 kN equivalent to 80%; the vertical force of the middle tires F_{z31} decreases from 42 to 39 kN by about 8%; the vertical force of the rear tires F_{z61} decreases from 40 to 32 kN by about 20%.

Figure 7 are the slip ratio charts of the front, middle and rear tires of the heavy vehicle on six types of roads at the velocity of 60 km/h. Looking at Fig. 7, we can see that the front tires have a slip ratio of less than 10% when the heavy vehicle is

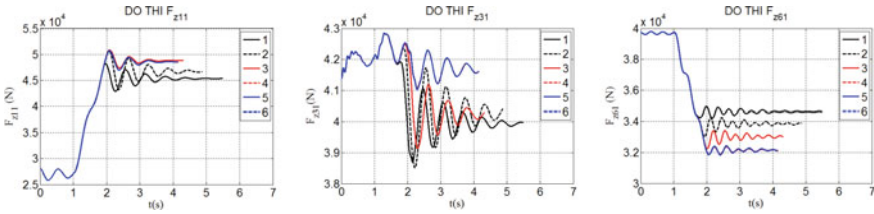


Fig. 6 Vertical force of the heavy vehicle

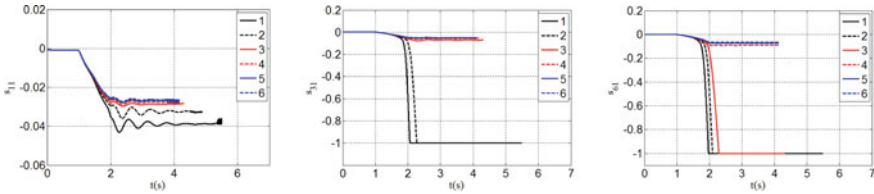


Fig. 7 Slip ratio of the front, middle and rear tires

braked on six types of roads with $\varphi_{xmax} = [0.5, 0.6, 0.7, 0.8, 0.9, 1.0]$, so the tires work in the linear elastic region. At this time, the transmission of force between the tire and the road is the transmission of joint-elastic force.

For the middle tires, when the heavy vehicle is braked on four types of roads with $\varphi_{xmax} = [0.7, 0.8, 0.9, 1.0]$, the slip ratio is less than 10%, the tires work stably; while the heavy vehicle is braked on two types of the road with $\varphi_{xmax} = [0.5, 0.6]$, the slip ratio increases rapidly to a maximum value of 100%, at this time the tires are completely locked, the force transmission between the tire and the road is the transmission of friction force, the tires slip on the road, the heavy vehicle loses its stability.

Similarly, for the rear tires, when the heavy vehicle is braked on the road with $\varphi_{xmax} = [0.8, 0.9, 1.0]$, the slip ratio is less than 10% and the tires work stably. When the heavy vehicle is braked on the road with $\varphi_{xmax} = [0.5, 0.6, 0.7]$, the slip ratio reaches the maximum value of 100%, the tires are locked and slip completely.

The braking distance and braking acceleration of the heavy vehicle at the velocity of 60 km/h are shown in Fig. 8. Looking at Fig. 8, we can see that when the heavy

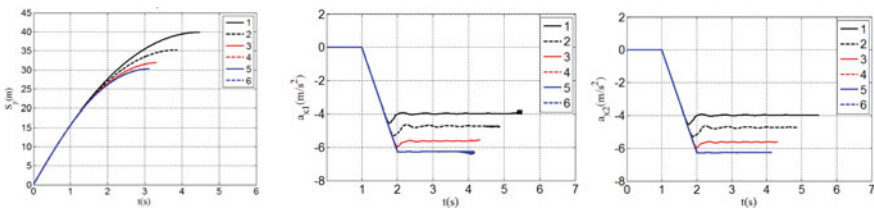


Fig. 8 Braking distance and braking acceleration

vehicle is braked on four types of roads with $\varphi_{x\max} = [0.7, 0.8, 0.9, 1.0]$, the braking performance of the vehicle qualified for ECE-R13 standards [6], and on two types of roads with $\varphi_{x\max} = [0.5, 0.6]$, the braking performance of the vehicle didn't qualify for ECE-R13 standards [6].

4 Conclusions

The heavy vehicle is braked at the velocity of 60 km/h on the road surface has $\varphi_{x\max} = [0.7, 0.8, 0.9, 1.0]$, the braking acceleration is greater than 5 m/s^2 , the slip ratio is less than 10%, the heavy vehicle runs smoothly, the braking performance of the vehicle qualified for ECE-R13 standards; If the heavy vehicle is braked on the road surface has $\varphi_{x\max} = 0.6$, the middle and rear tires slip completely, the heavy vehicle is unstable, the braking acceleration is about 4.7 m/s^2 , the braking efficiency is reduced about 25%; If the heavy vehicle is braked on the road surface has $\varphi_{x\max} = 0.5$, the middle and rear tires slip completely, the heavy vehicle is unstable, the braking acceleration is about 4 m/s^2 , the braking efficiency is reduced by 37%.

References

1. Jazar RN (2019) *Advanced vehicle dynamics*. Springer Nature Switzerland
2. Van Huong V (2014) *Vehicle dynamics*. Vietnamese Educational Publishing House
3. Tung NT (2017) *Research on braking efficiency on the roads with different grip coefficients of the tractor semi-trailer and proposed measures to reduce traffic accidents*, Doctoral thesis, Hanoi University of Science and Technology, Vietnam
4. Tung NT Van Huong V (2020) *The effect of the wheel rotation angle on the braking efficiency of the tractor semi-trailer on the wet roundabout route*, Switzerland Springer: *Lecture notes in networks and systems*, vol 178, pp 798–804
5. Tung NT, Van Huong V (2021) *Research on the dynamic load of the tractor semi-trailer when braking on the round road*, United States Springer Verlag: *Lecture notes in mechanical engineering*, pp 456–461
6. The international braking regulation of the Economic Commission for Europe in Geneva—ECE-Regulation No. 13, ECE-R13, *Vehicle Regulations* (2004)

Implementation of ISO 9001 in the Manufacturing Industry, a Literature Review



Prashant N. Shende, Aditya Kadao, and Adithyakrishna Palery

Abstract 22,027 International Standards have been produced by the International Organization for Standardization (ISO) (As of Feb 5, 2018). ISO 9000 is one of the most widely used ISO standards. ISO 9000 is a set of quality management system (QMS) standards that give companies and organizations direction and tools to ensure that their goods and services consistently satisfy client expectations, resulting in continuous quality improvement. ISO 9001 is a globally recognized standard for quality management systems. It is an important component of a well-rounded production management system. During a continuous improvement cycle, ISO 9001 helps to simplify the process, increase company performance, and boost efficiency. The case study shows how ISO 9001 was implemented in the manufacturing industry. To better understand the application and advantages of ISO 9001, we conducted a survey in a variety of ways to get input from various industries. Finally, the industry becomes more efficient as all of its processes are linked and understood by all parties involved. This boosts productivity and efficiency while lowering internal expenses. The industry will comply with all legal and regulatory standards. Because some industries and clientele demand ISO 9001 certification before conducting business, the industry can grow into new markets. In a few words, the abstract should describe the substance of the work.

Keywords ISO 9001 series · Management · Customer requirements · Feedback

1 Introduction

ISO 9001 is the most extensively utilized international standard. A quality system is a procedure that integrates with production or service supply to ensure high-quality goods and services. ISO is an abbreviation for the International Organization for Standardization. ISO originally issued the ISO 9000 series of general quality standards in 1987, and it has subsequently been amended in 1994, 2000, 2008, and 2015. The sixth

P. N. Shende (✉) · A. Kadao · A. Palery
Department of Mechanical Engineering, YCCE, Nagpur University, Nagpur, Maharashtra
441110, India
e-mail: prashant_sn1@yahoo.co.in

revised version was accepted by the international standards committee ISO/TC176 in September 2015. With over 500,000 registrations from registrants in over 100 countries across all continents, including the United States, the United Kingdom, European nations, India, Japan, Korea, Taiwan, Hong Kong, Singapore, and Malaysia, ISO 9000 is the most successful standard in ISO history. Obtaining ISO certification has various advantages, including lower quality and mistake costs, higher product quality and waste elimination, fewer failed delivery potentials, improved manufacturing, advertising opportunities, and lower return charges. This does not, however, ensure that a company will be able to enjoy all of the benefits. Standardization will aid in maintaining the expected quality of goods and amenities. The purpose of this article is to examine elements that will aid in the implementation of ISO 9001:2015. Many manufacturing organizations use a framework for identifying and prioritizing issues. ISO helps to properly account for the commercial benefits of the standard's excellent elements while avoiding dangers, defining roles within organizations using the standard, and stimulating new thinking and solutions. This document is also meant to educate others with the information they need to set quality targets. Businesses must create quality targets for nursing the performance of their eminence administration arrangement, according to ISO 9001. The recommended ISO 9001 implementation effectiveness measuring tool may be used to help companies meet and track their quality goals.

1.1 What Exactly Is ISO 9001

ISO 9001 defines the standards for a quality management system, and it is the only standard in the family that may be audited for voluntary compliance or third-party registration. In actuality, ISO 9001 certification is held by over one million firms and organizations in over 170 countries. All ISO 9001 criteria are generic and intended to apply to any firm, regardless of its type, magnitude, or goods and services offered. The standard is based on seven quality management principles, which include a strong customer focus, top management motivation and participation, a procedural approach, and continual improvement. ISO 9001:2015 standards are based on seven quality management concepts that senior management may use to strengthen the firm. • Customer focus • Leadership • Engagement of people • Process approach • Improvement • Evidence-based decision-making • Association management.

The standards provide guidance and tools for businesses and organizations seeking to guarantee that their goods and services consistently meet the demands of their consumers while enhancing quality and customer satisfaction. Compliance with ISO 9001 ensures that consumers obtain consistent, high-quality goods and services, resulting in a number of business advantages.

1.2 Why Implement ISO 9001

Implementing an ISO 9001 Quality Management System (QMS) that is active and comprehensive will permit you to focus on the most crucial elements of your firm and boost competence. The management strategies you use throughout your organization will provide a firm foundation for increased output and profit. As a consequence, your customer acquisition and retention will increase. Most importantly it benefits: Implementing an ISO 9001 Quality Management System (QMS) that is active and comprehensive will permit you to focus on the most crucial elements of your firm and boost competence. The management strategies you use throughout your organization will provide a firm foundation for increased output and profit. As a consequence, your customer acquisition and retention will increase. Most importantly it benefits:

1.3 Regarding Your Company

ISO 9001 strives to establish an accurate and functional QMS for developing and keeping track of every aspect of the organization. Obtaining the ISO 9001 standard does not infer building a set of sophisticated and difficult-to-manage procedures. The objective is to create a workable management system that is tailored to your company's needs. If you have the appropriate support and expertise from your personnel, you will end up with a system that will help all aspects of your firm. The following are some of the leading advantages of ISO 9001 certification:

- Suitable for every type of business, i.e., micro, small, medium, and large.
- Internal management has improved.
- Reduced waste.
- Enhancement of efficiency, production, and profit.
- Retention and acquisition of customers have both improved.
- Consistent, measured, and monitored outcomes.
- Internationally recognized standard.
- Other ISO standards are compatible.
- UKAS certification.

A legitimate ISO 9001 certificate will be a necessity for certain of your clients and a “nice to have” for others when it comes to providers. It gives your customers confidence that you are adhering to procedures and standards that will ensure they receive exceptional service.

1.4 To Your Clients

The ISO 9001:2008/ISO 9001:2015 standard is a set of guidelines for quality management systems globally recognized, and your clients will grasp the benefits of dealing with ISO 9001 certified organizations. About your customer's determination only do business with certified businesses since it ensures them that your management practices are being assessed and approved on a regular basis. They would know from past experience that collaborating with ISO 9001:2008/ISO 9001:2015 certified firms has various advantages:

- Mistakes are reduced.
- Enhances reporting and communication.
- Improved product and service quality.
- Increased dependability in production schedule and delivery.
- Annual evaluations ensure that standards are maintained.

2 Literature Review

2.1 Distinction Between ISO-Certified and Non-certified Businesses

Ilkay and Aslan [1] found that, in terms of performance, the difference between certified and non-certified organizations is not clinically meaningful. Certification had no distinct influence on performance. Furthermore, it has been stated that certified firms' quality procedures were greater than those of non-certified organizations, with data indicating a difference with a predictive value. However, better practice does not always imply better performance. Certification motivations have been found to influence performance; firms that are internally motivated for accreditation surpass those that are externally motivated.

2.2 Quality Improvement

Guchu and et al. [2] concluded that the document proposes steps that can be utilized to successfully certified ISO 9000. The plan may be used by SMEs that want to obtain ISO certification, which will lead to quality improvements and commercial success.

2.3 Customer Satisfaction

Nabavi and et al. [3] found that among the elements influencing a kitchen work-tops customer's happiness, the product's price and conditions of sale have changed considerable criteria have an impact on consumer satisfaction, and it is especially important in cheap situations plays a decisive role in the production usefulness for consumers. Within an 11-month research period, the ISO 9001 QMS was gifted to enhance the CSI.

2.4 Benefits in Construction Companies

Keng et al. [4] The study's objectives were to determine the advantages of implementing the ISO 9001 Quality Management System in Malaysian construction companies, as well as the challenges that construction companies face when implementing the ISO 9001 Quality Management System and the strategies used by ISO-certified construction companies to overcome or minimize enactment challenges. The most important benefit of adopting the system, according to the research findings, is improved corporate management and work productivity, while the most significant disadvantage is a lack of knowledge of the system among employees.

2.5 Management

Almeida et al. [5] concluded that according to the report, senior management commitment is the most important aspect in ensuring an efficient ISO 9001 implementation. Without it, the whole firm would be uninspired to participate in the quality management process, which could have negative consequences. To ensure that all procedures are performed effectively, top management must emphasize the role of ISO 9001 execution and provide necessary support and leadership.

2.6 Importance Throughout the World

Priede [6] concluded that quality is a critical and essential component of competitiveness. The ISO 9001 standard is among the most popular quality management systems across the globe. It has several advantages that make it so popular among enterprises. In 2010, there were over one million firms and organizations that had an ISO 9001 certified QMS.

3 The Purpose of the Research Study

- Toward progress the plant's overall effective efficiency.
- Making appropriate use of the industry's manufacturing capability.
- Designate how to put each quality management system concept into practice.
- Elucidate how visual control may be used to improve production.
- Regulate the paperwork and expenses associated with the installation of a quality management system.

4 Methodology

4.1 *Establishing Priorities and Outcomes*

Desired results should be established with the participation of employees from the relevant functional area. These people are in a good position to help with the formulation, strategy, and fulfillment of these objectives. People's involvement promotes dedication and positive administration.

- Obtain top management support for the quality objectives. This ensures that sufficient resources are assigned and the objectives are ranged with other corporate goals.
- When conveying objectives to employees, endeavor to relate the objectives to the actual quality improvements sought, such as lowering non-conformance and closing out corrective actions, since this will offer individuals something practical to work toward.
- The quality targets must be aligned with the overarching mission/plan and the important policy commitments.
- Be flexible with your aims, describe the intended outcome, and then, enjoy responsibility for determining how to reach the outcome.
- Objectives can be developed to maintain or increase present levels of performance.
- Share your progress in meeting objectives and targets with the rest of the organization. Consider providing regular updates on this progress during staff meetings.
- How many goals and objectives should a company have? Several QMS implementation studies for micro, small, and medium businesses show that it is ideal near start with a small number of objectives (say, two to five) and then gradually extend the list.
- Begin with minimal quality targets, achieve some early achievements, and then build on them.
- Preserve in attention that your suppliers (of services or materials) can assist you in attaining your goals and objectives (e.g., on-time delivery).

Ensure that your organization has identified significant internal and external challenges, as well as interested stakeholders, that support your business's strategic goal. The strategic direction must be used to inform policies, objectives, risk management, monitoring and measuring, and management review procedures.

4.2 *Gap Analysis*

This entails evaluating the current quality manual to define how things are done, demonstrate how things are done, demonstrate that things are done correctly, monitor what is being done, and improve. This examination, also known as a baseline audit, comprises audits of appropriateness and truce, which are characterized as follows:

- **Adequacy audit:** It is defined as an examination of how effectively the defined quality assurance system, as indicated by the specification document and related processes, fits the requirements of the applicable standard.
- **Compliance audit:** The compliance audit is defined as an evaluation of how the specified system is applied and monitored by the employees.

4.3 *Approach*

General approach

- i. The International Organization for standardization promotes something like a methodical approach for creating, implementing, and increasing the performance of a QMS in order to increase customer satisfaction by meeting customers' requirements.
- ii. Empathetic and controlling interrelated processes as a system increases an organization's efficiency and effectiveness in achieving its objectives. This approach allows the organization to regulate the interconnections and interrelated among the system's processes, hence increasing overall efficiency.
- iii. The system method incorporates the methodical development and control of processes and their connections in order to achieve the intended results in accordance with the quality strategy and program direction of the company.
- iv. The procedure technique, when used in a QMS, provides for:
 - Comprehension as well as reliability in satisfying standards,
 - Methods are assessed based on their extra value.
 - The attainment of design sense that is effective.
 - Process enhancement analysis of data and analysis techniques.

• **Group Approach**

Teamwork in any business is a vital component of total quality management implementation, as it is required to generate trust and increase communication, which fosters dependency. Quality improvement teams are people and groups who have the necessary knowledge, talents, and expertise who are put together to govern, specifically to oversee, and resolve a project-based issue. They are typically multidisciplinary and cross-functional. However, improving the team’s quality takes it a step beyond, and they are increasing. Squad selection and leadership, organization goals, team meetings, team tasks, group dynamics, methods utilized, and evaluation are all important aspects of quality improvement teams. The group leader is largely responsible for the team’s survival and direction, and his or her recruitment and training are vital to the team’s success. Team activity and member engagement are important to the achievement of any team. Quality circles are defined as a group of employees who conduct comparable jobs that convene and work on a consensual, regular, inside regular working hour schedule, under the observation of their manager, to discover and assess, solve effort issues, and give effective guided solutions.

• **Team Approach**

The PDCA cycle may be used in all processes as well as the overall QMS. The diagram below shows how Clauses 4 through 10 can be organized about the PDCA cycle (Fig. 1).

The PDCA cycle can be briefly described as follows:

- **Plan:** Establish the objectives of the systems and their processes, as well as the resources necessary to generate results that are in accordance with customer expectations and organizational standards, and identify and manage risks and opportunities.

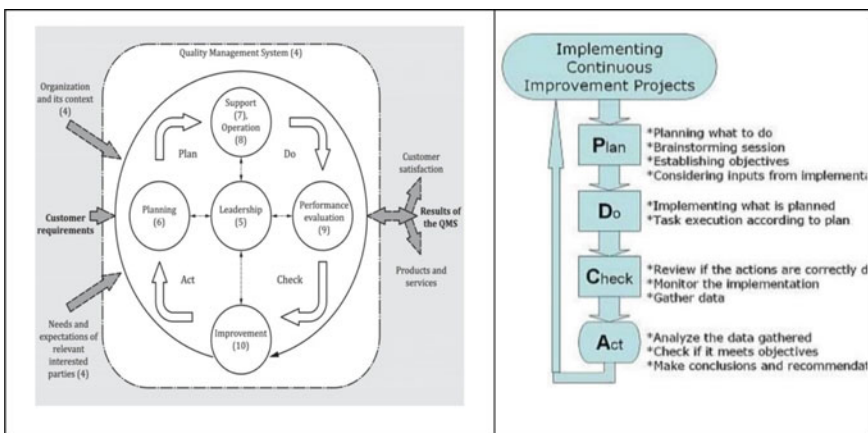


Fig. 1 PDCA

- **Do:** Carry forth what was intended.
- **Check:** Monitor and (where appropriate) measure progressions and resulting goods and services in accordance with principles, goals, needs, and scheduled activities, and report the results
- **Act:** As needed, yield measures to enhance recital.

- **Risk-based Thinking**

Implementing an efficient quality management system necessitates risk-based thinking. Earlier versions of this International Standard implicitly included the concept of risk-based thinking, like implementing preventive steps to eliminate possible nonconformities, analyzing any non-conformances that do occur and taking corrective measures to prevent the reoccurrence of the effects of the non-conformance.

- In order to achieve the standards of this International Standard, an organization must design and implement risk and opportunity management methods. Considering both opportunities and risks lays the groundwork for increasing the efficacy of the quality management system, creating good outcomes, and preventing adverse effects.
- Opportunities can arise as a result of a favorable environment for achieving the intended aim, such as a set of conditions that allow the company to attract customers, develop new products and services, reduce waste, or improve efficiency. Actions to handle opportunities may also entail consideration of corresponding dangers. Ambiguity causes risk, and any uncertainty might have positive or bad repercussions. Although not all health risk effects result in chances, a favorable deviation generated by risk may provide one.

4.4 Before Plant Layout

See Figs. 2, 3 and 4.

4.5 Before Using the Machine

1. You must have received formal training from Pravin Ghode related to machine safety and operation.
2. You must read and understand SOP and machine operating and manual.
3. You must use this machine under the direct supervision of Pravin Ghode.
4. You must have signed the agreement document with Tanmay Industries.
5. If you do NOT follow the above instructions, you will be held responsible for your own safety and damages.

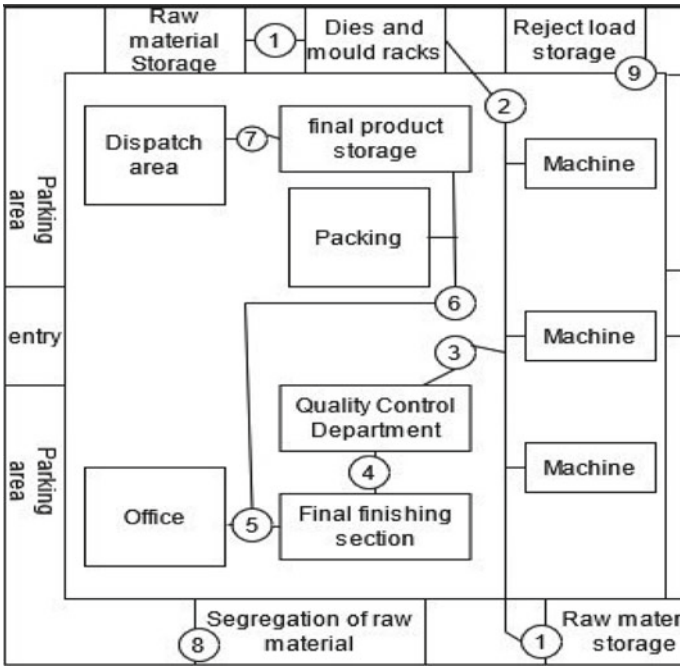
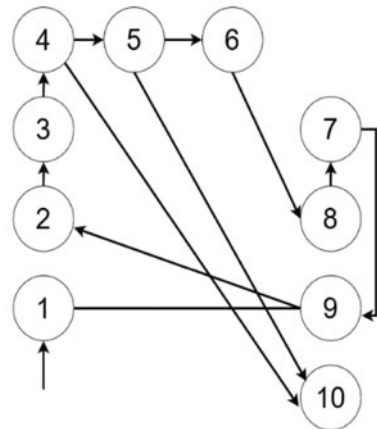


Fig. 2 Plant layout

Fig. 3 Material flow in existing layout



- **Location of Standard Operating Procedure (SOP) and Machine Operating & Safety**

Manual Emergency Contact

1. Call MIDC Fire Brigade.



Fig. 4 Location of SOP and machine operating and safety manual

2. Call MIDC Police Station.
3. Call MIDC Medical Services.
4. Call Management.
5. Call Supervisor.

• **Safety Precautions and Important Safeguards**

Safety precautions—Personal Protective Equipment: The following personal protective equipment must be obtained and ready for use prior to performing this procedure: safety goggles and insulated gloves.

Important Safeguards

1. When grinding waste materials, always use safety glasses because it protects the user throughout each grinding and molding cycle.
2. Never operate the machine when people are standing close to it.
3. Never reach into the machine while it is in the grinding process.
4. Before using the machine, ensure that your hands are not too close to the feeder.
5. When performing maintenance tasks, always turn off the machine’s power.
6. Do not attempt to extrude or try to open the safety covers of the grinding machine until the machine fully stops.
7. When removing safety covers for maintenance, turn off the power, unplug, and then work on the machine.
8. Do not put your fingers into the machine while it is running.

• **Emergency Situation and General Information Emergency Situation for Grinding.**

Grinding machine—A safe distance should be maintained. In the event of malfunctioning, the following emergency procedures should be executed.

1. Make sure to keep a safe distance from the machine.

2. Turn off the main power supply switch.
3. Ensure everyone is safe.
4. If the situation is severe, contact emergency contacts.

• **Emergency Situation for Injection Molding Machine.**

Injection Molding Machine

The die should be placed carefully in its position. In the event of improper die placement, the following emergency procedures should be executed.

1. Press the emergency shutdown button located on the control panel.
2. Make sure to keep a safe distance from malfunctioning.
3. Turn off the main power supply switch.
4. Ensure everyone is safe.
5. If the situation is severe, contact emergency contacts.

4.6 Problem Identification Due to Improper Plant Layout

1. More waiting time between straitening and grinding the beam.
2. More traveling distance and related time in material flow.
3. Material flow pattern is not standard.
4. Backtracking moves.

5 Result

See Fig. 5.

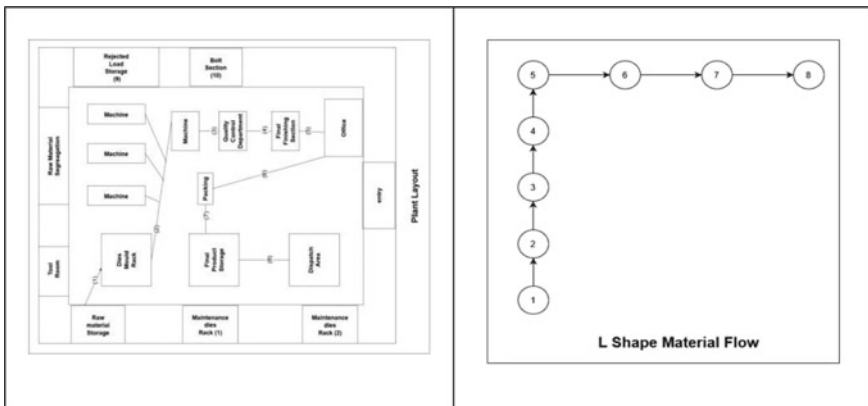


Fig. 5 Plant layout before and after implementation

2. After Implementation Improved Maintenance, Improved, Safety, More Committed Employees, Improved Quality

3. Before OEE = 83.24

After OEE = 91.83

6 We Found that in ISO 9001

ISO 9001:2015 requires ensuring the QMS accomplishes its goals and results, but in order to understand what these results are, we must first look at the big picture. So, to begin, let us define what we mean by business results. Productivity increased due to well-defined space and systematic arrangement at the workplace.

- Inventory costs for undesired goods are dramatically decreased, which saves a lot of money.
- More storage space for raw materials, bins, and completed items is now available. There is also a distinct and quite well walkway for mobility.
- Equal participation of officers, staff, and employees motivates them.

7 Conclusion

- Organizations may determine who is influenced by their work and what they anticipate by examining their context. This permits the establishment of clearly articulated corporate objectives as well as the discovery of new ventures prospects.
- Risks associated with organizations can be identified and mitigated.
- By prioritizing the consumer, businesses may ensure that they constantly satisfy their customers' expectations and improve their customer happiness. This might result in more repeat business, additional clients, and higher revenue for the organization.
- Organizations operate more efficiently because all of their procedures are coordinated and comprehended by everybody. This boosts performance and effectiveness while lowering internal expenses.
- Organizations shall comply with all applicable legislative and regulatory obligations.
- Because several sectors and customs need ISO 9001 accreditation while making deals, businesses can expand into new markets.

References

1. Ilkay MS, Aslan E (2012) The effect of the ISO 9001 quality management system on the performance of SMEs. *Int J Qual Reliab Manag* 29(7):753–778
2. Guchu G (2012) ISO quality management system implementation for small to medium manufacturing firms Kenya. In: *Proceedings of the 2012 mechanical engineering conference on sustainable research and innovation*, vol 4, pp 140–147
3. Nabavi V, Azizi M, Faezipour M (2013) Implementation of quality management system based on ISO9001:2008 and its effects on customer satisfaction case study. *Int J Qual Reliab Manag* 31(8):921–937
4. Keng TC, Kamal SZ (2016) Implementation of ISO quality management system in construction companies of Malaysia. *J Technol Manag Bus* 3(1):1–21
5. Almeida D, Pradhan N, Muniz J Jr (2018) Assessment of ISO 9001:2015 implementation factors based on AHP: case study in Brazilian automotive sector. *Int J Qual Reliab Manag* 35(7):1343–1359
6. Priede J (2012) Implementation of quality management system ISO 9001 in the world and its strategic necessity. In: *8th international strategic management conference, Procedia—social and behavioral sciences*, University of Latvia, Riga, LV-1050, Latvia, vol 58, pp 1466–1475

Improvised Model for Estimation of Cable Bending Stiffness Under Various Slip Regimes



Hadiya Pritesh Dulabhai , N. S. Parthasarthy ,
and Gurumoorthy S. Hebbar 

Abstract It is well known that the bending response of a stranded cable varies between two extremes, known as a monolithic stick–slip state and a completely frictionless loose wire state. While the monolithic state offers the maximum stiffness for the cable, the latter loose wire assembly results in minimum stiffness. The estimation of the actual behavior of the cable under any loading scenario demands a proper modeling that accounts for the interaction of the constituent wires in the intermittent slip stages. During loading, the wires are not only subjected to forces along their axes but are considerably acted upon with radial forces that cause clenching effect. Major research works have focused on the frictional resistance of these radial forces from the Coulomb hypothesis, which contributes to the macro slip phenomenon. As the effect of these radial clenching forces are also significant in causing high contact stresses between wires at the adjacent layers, the need for considering the micro slip at these locations is also vital in the evaluation of the net cable stiffness. In this paper, a novel model is proposed that considers the slip caused by the Coulomb friction hypothesis and the micro slip caused by the Hertzian contact friction for the evaluation of bending stiffness. The variation of the bending stiffness has been evaluated for a single-layered cable as a function of bending curvature at various locations by studying their slip regimes. The predicted results are compared with the published results to establish the refined combined slip hypothesis suggested in this paper. The suggested slip model in this paper has also been accounted with the improvised kinematic relations that consider the wire stretch effect, a parameter that has been neglected in this cable research till date.

Keywords Stranded cables · Bending stiffness · Coulomb friction force · Hertzian contact theory · Interwire slippage

H. P. Dulabhai (✉) · N. S. Parthasarthy · G. S. Hebbar
CHRIST (Deemed to be University), Bangalore 560074, India
e-mail: hadiyapriteshd@gmail.com
URL: <https://www.scopus.com/authid/detail.uri?authorId=57215723295>

1 Introduction

The use of helically wound cable is well known in various practical applications as taut cables & guyed ropes, and tethers in structural, marine, and ocean engineering. When used in material handling applications, they are subjected to bending loads also. The cables are used as electrical conducting elements in overhead power transmission. When the overhead taut cables are vibrating due to wind forces, they are also subjected to additional bending loads. Since the cable is an assembly of a central core and surrounding coaxial layers of helical wires, prediction of their response under external loads is a real challenge. Though many mathematical models are addressed to predict their response, the continuous challenge remains as some of the intricate parameters like the interfacial contact forces and deformations due to them, the coefficient of friction during its working and allied frictional movements, etc., are yet to be addressed appropriately to arrive at a realistic response estimation. The complexity increases when the cables are subjected to bending loads. The models used for bending studies vary between two extremes—a monolithic assembly with wires in infinite friction status and a completely loose wire assembly with no friction to hold them. The stiffnesses offered in these extreme cases often become guidelines within which the cable behavior is thought of in any realistic working scenario.

Since the order of the bending stiffnesses in these extreme limits is very large, a closer analysis of the cable behavior is mandatory. Hence, this paper presents an insight into the mechanics that decides the behavior of bent cables and proposes a combined slip model to estimate the stiffness.

Though more than 100 analytical publications have resulted in bending studies on cable as of date, the salient classified contribution of the researchers is reviewed in this paper. The experimental tests conducted by McConnell and Zemke [1] on different overhead conductor cables have become the early benchmark to understand the maximum & minimum stiffness values. Costello and Butson [2] included the wire twist in their modeling and addressed with Love's [3] analytical equations for the equilibrium of the helical wires. The predominant effect of wire axial force was found to influence the stiffness when the wires are not having relative motion. Sathikh and Parthasarathy [4] studied the response of bent cable under a sinusoidal transverse force. The thin rod model proposed by Papailiou [5] addressed the bending phenomenon with inter-layer friction forces and noticed a smooth transition from stick to slip state. All the existing cable models were nicely reviewed and presented by Jolicoeur [6] with their parametric limitations. Sathikh et al. [7] studied the pre-slip behavior of helical wires and stressed the importance of "wire stretch" a parameter influencing the basic curvature & twist relations of a helical wire. Papailiou's model was extended to multilayer cable and was studied by Hong et al. [8] with the inclusion of frictional forces transferred from one layer to another. The various cable modeling and their internal damping mechanisms were reviewed by Spak et al. [9] and this had opened the eyes of the researchers further, to explore the contact mechanics and the frictional behavior. The cable bending was studied by Foti and Martinelli [10] by accounting for the slip in the wires from Coulomb stick friction theory. Khan

et al. [11] studied the bending behavior of axially preloaded multilayered strands in similar lines of Hong et al. [8] but included the hoop contact force arising between wires in the same layer.

A quick review of the various bending models to date indicates that the interwire slip among the helical wires has been addressed with the Coulomb friction theory which considers the axial force in the wire as primarily responsible to overcome friction force caused by the radial clenching effect. This slip is known as the macro slip and has been considered by many authors. Few authors have addressed the contact forces that exist at the wire interfaces and have accounted for the slip or movement of the helical wires in the same layer to estimate the bending stiffness.

When a cable under a higher axial load is bent, the radial clenching forces introduced from the wires in one layer to that in the adjacent layer are significant enough to cause local deformation at the contact interfaces. This deformation has been addressed from the Hertzian contact phenomenon and its influence in the axial direction has to be estimated apart from the Coulomb friction theory. This additional deformation caused by the contact influence is known as the micro slip. As of date bending phenomenon has not been completely addressed with these two slip possibilities. This paper addresses the macro slip from Coulomb friction theory and micro slip from Hertzian contact theory and judiciously combines them with a series spring concept to estimate the bending stiffness of the cables. Further, when the cable is pulled and bent, the helical wires carry the initial influence of wire stretch in their subsequent bending and twisting phenomenon also. This parametrical inclusion of wire stretch alters the basic curvature and twist relations of a helical wire and also alters the wire moments in the normal, binormal directions, and axial directions. As a result of this fundamental change in the kinematic relations, the bending response of the cable also is varied. This paper also addresses the bending mechanics relations with the revised kinematic relations that account wire stretch effect.

The resulting loss of stiffness of the cable due to these combined slip theories has been studied as a function of axial load and the bending curvature at any location. Inclusion of all the wire forces and wire couples with refined expressions for the wire curvatures and twist are some of the specific features introduced in this work, probably for the first time in bending studies.

2 Mathematical Model

A helical strand of cable radius r is shown in Fig. 1. under a bent configuration. The forces acting on the helical wire along its axial (tangential), normal, and binormal directions T , N , and N' , respectively can be identified with the position angle (\emptyset). The strain generated along the strand axis ϵ , can be represented as refereed by Papailiou [5] in terms of its helix radius (r), position angle (\emptyset), and the bent curvature (κ_1) as

$$\epsilon = \kappa_1 r \cos \emptyset \tag{1}$$

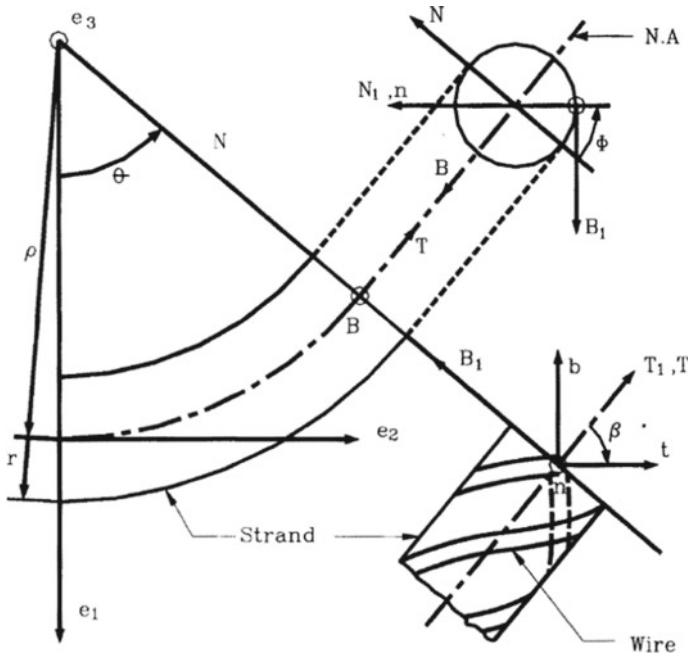


Fig. 1 Strand and wire under bent configuration

The axial strain in the helical wire at a lay angle (β), can then be written as,

$$\xi_w = \kappa_1 r \cos^2 \beta \cos \phi \tag{2}$$

The axial force generated in the helical wire can be readily obtained from,

$$T = EA\xi_w = EA\kappa_1 r \cos^2 \beta \cos \phi \tag{3}$$

where E and A are the elastic modulus and area of cross-section of the wire.

2.1 Kinematic Relations

2.1.1 Basic Kinematic Relations

The flexural strains in the normal (ω_n), binormal (ω_b) directions and the change in twist (ω_t) of a helical wire as considered by all the researchers [2, 4, 5, 8] and [11] till date are presented below.

$$(\omega_n, \omega_b, \omega_t) = (\Delta\kappa, \Delta\kappa', \Delta\tau) = \kappa(\cos\beta \sin\phi, \cos^2\beta \sin\phi, -\sin\beta \cos\beta \cos\phi) \tag{4}$$

where κ is the net curvature of the strand.

2.1.2 Revised Kinematic Relations

When a cable is applied with a tensile load, all the helical wires experience tensile force along their axes. When the wire is subsequently bent and twisted to take a helical path, the influence of the basic axial force and its consequent stretch is also carried out in the successive bending and twisting phenomenon. This is known as the “Wire Stretch effect”. This paper considers the wire stretch effect for the first time in the coupled axial-bending analysis and has derived the revised kinematic relations of the wire curvatures and twist as below, taking clue from Sathikh et al. [7].

$$\omega_{n'} = \kappa(\cos\beta(1 + \sin^2\beta) - a_1 \sin\beta \cos\beta + a_3 \sin^2\beta + a_2 \sin\beta) \sin\phi \tag{5}$$

$$\omega_{b'} = \kappa(\cos^4\beta + a_1 \sin\beta - a_2 \sin\beta \cos\beta) \cos\phi \tag{6}$$

$$\omega_{t'} = \kappa(-\sin\beta \cos^3\beta + a_3 \sin\beta + a_2 \sin^2\beta) \cos\phi \tag{7}$$

where, a_1, a_2 & a_3 are the factors defining shear strains and twist, keeping their value as zero will result in the kinematic relation proposed by Sathikh et al.[7].

2.2 Displacement as Per Coulomb Friction Stick Hypothesis

The displacement Δ_1 of the helical wire under an axial force can be obtained in similar lines of Papailiou [5], Hong et al. [8], Foti et al. [10] and Khan et al. [11] by performing the integration of the wire axial strain shown in Eq. 2.

$$\Delta_1 = \int \xi_w ds \tag{8}$$

The displacement (slip) of the helical wire along its axis will happen when the fiber axial force of the helical wire exceeds the limiting Coulomb friction force at the core-wire interface. The wire axial force X , that is responsible for this displacement can be obtained from the base wire equilibrium equation shown by Love [3] as under,

$$X = -\frac{dT}{ds} \tag{9}$$

Substituting T from Eq. 3 and combining with Eq. 8, the displacement of the wire can be obtained as below,

$$\Delta_1 = B\bar{X}\kappa_1 \sin \phi \quad (10)$$

where,

$$B = \left[\frac{(r/R)^2}{E\pi \sin^2 \beta} \right] \quad (11)$$

$$\bar{X} = EA \cos^2 \beta \sin \beta \quad (12)$$

This is referred to as the macro slip. The average value of the slip in the strand cross-section can be obtained by integrating it over its active domain range 0 to $\pi/2$ and accounting it with the “ m ” number of wires in the strand cross-section as

$$\bar{\Delta}_1 = \left(\frac{2}{\pi} \right) B\bar{X}\kappa_1 \quad (13)$$

2.3 Displacement of the Helical Wire as Per Hertzian Contact Hypothesis

This paper accounts for the additional displacement caused in the wire axial direction, due to the tangential compliance resulting from the radial contact force at the core-wire interface (X_0), which is obtained from the basic wire equilibrium equations of Love [3] as

$$X_0 = EA \in \frac{\cos^2 \beta \sin^2 \beta}{r} \quad (14)$$

where \in is the cable axial strain which can be obtained from the applied axial load and the stiffness matrix of the strand.

The contact force and the deformation in that direction are obtained from the Hertzian contact stress theory and are duly accounted in the wire axial direction using the tangential compliance relations which relate the contacting bodies (core and helical wire) along with their interface geometry as below,

$$S_{22} = \frac{C_e}{\pi} \left[-\frac{1}{3} + \ln \left((R_c + R) \frac{\pi}{X_o C_e} \right) \right] \quad (15)$$

where,

$$C_e = \frac{1 - \nu_c^2}{E_c} + \frac{1 - \nu^2}{E} \tag{16}$$

where, ν and ν_c are the Poisson’s ratio of the helical wire and core, respectively. The net displacement in the wire axial direction caused by the contact force can then be related as

$$\Delta_2 = \left\{ d \left[1 - \left(1 - \frac{X}{\mu X_0} \right)^{2/3} \right] \right\} \tag{17}$$

where,

$$d = \frac{3}{2} \left(\frac{\mu X_0 S_{22}}{1 - \nu} \right) \tag{18}$$

The average value of this micro slip also can be obtained in similar lines as in Sect. 2.2 and is presented as,

$$\bar{\Delta}_2 = d \left(\frac{2}{\pi} \right) \int_0^{\pi/2} \left[1 - \left(1 - \frac{\bar{Z} \kappa_1 \sin \phi}{\mu X_0} \right)^{2/3} \right] d\phi \tag{19}$$

2.4 The Improvised Slip Model

The macro and the micro slip concepts of the helical wire discussed in Sects. 2.2 and 2.3 are combined in this paper with a novel idea of an equivalent spring in series arrangement since the displacements are caused by the same wire axial force. Hence, the total displacement of the helical wire is given by,

$$\Delta = \Delta_1 + \Delta_2 \tag{20}$$

The total curvature of the strand can be obtained as

$$\kappa = \kappa_1 + \kappa_2 = \kappa_1 \left(1 + \left(\frac{\bar{\Delta}_2}{\Delta_1} \right) \right) \tag{21}$$

2.5 Evaluation of Bending Curvature at Various Slip Regimes

The helical wire will undergo three stages of slip namely—no-slip, partial slip, and full slip depending on the fiber axial force present in the helical wire (\bar{X}) and the resistive friction force caused by the radial clenching force (X_0). Which are related as,

$$\bar{X}\kappa_1 \sin \theta = \mu X_0 \quad (22)$$

where μ is the coefficient of friction between the contacting wires. From the above equation, the curvature at which a slip will be initiated can be given by

$$\kappa_o = \frac{\mu X_0}{\bar{X}} \quad (23)$$

The partial slip of the helical wire will be experienced when the position angle θ_b of the wire varies from 0° to 90° and the corresponding curvature can be related as

$$\kappa_b = \kappa_o \left(\frac{\frac{\pi}{2} - \phi_b}{\cos \phi_b} \right) \quad (24)$$

The full slip stage of the wire is identified when the wire crosses the neutral axis where its position angle is zero and the corresponding curvature is given by,

$$\kappa_f = \frac{\pi}{2} \kappa_o \quad (25)$$

2.6 Strand Bending Moment at Various Slip Regimes

The net bending moment developed in the strand at any bending radius is the resultant summation of moments caused by the three internal wire forces T , N and N' and the three internal wire moments G , G' and H .

While the moments caused by the wire forces depend on the interwire movements or slip along the respective axes, the moments caused by the wire couples are related to the wire rotation about the respective axes. Since the normal force N lies in the plane of bending it does not cause any moment. Since, the wire axial force T is the dominant internal force, the moment caused by that is evaluated by considering the relevant slip stage of the wire at any bending radius. As discussed in Sect. 2.5, each helical wire can undergo three stages of slip depending on their angular position and the bending curvature. The moments developed in the respective slip stages of each helical wire are identified and the resulting layer moment equations are presented below in lines of Papailiou [5].

2.6.1 Layer Bending Moment Due to Wire Movements

Stage 1: Monolithic stage or No gross slip stage ($\kappa_1 \leq \kappa_0$)

In a monolithic stage or no gross slip stage the limiting curvature (κ_0) is greater than the bending curvature (κ_1) and the layer bending moment (M_T) based on the axial force generated in the wire (T) can be written as,

$$M_T = m \left(\frac{2}{\pi} \right) \int_0^{\pi/2} T r \cos \beta \cos \phi \, d\phi \tag{26}$$

Substituting T from Eq. 3, the bending moment is obtained as,

$$M_T = \frac{m}{2} E A r^2 \kappa_1 \cos^3 \beta \tag{27}$$

Stage 2: Intermittent stage

In this stage, a helical wire can undergo two types of slip based on its position in the strand. When the position angle in the wire in any cross-section (ϑ_b) lies between 0 and $\pi/2$ partial slip occurs and the curvature κ_1 is evaluated as shown in Eq. 24. Using this curvature, the wire axial force, T in evaluated from Eq. 3 and corresponding layer bending moment (M_{T_p}) is envaulted by substituting in Eq. 26 with the integration limit from 0 to ϕ_b as below,

$$M_{T_p} = \frac{m}{\pi} E A \kappa r^2 \cos^3 \beta \left[\vartheta_b + \frac{\sin 2\vartheta_b}{2} \right] \tag{28}$$

When the position angle of the wire ϑ_b reaches beyond $\pi/2$ the wire undergoes the full slip and the wire axial force is obtained as,

$$T_s = \mu X_0 \left(\frac{\pi}{2} - \phi \right) \frac{r}{\sin \beta} \tag{29}$$

The layer bending moment for full slip is evaluated from Eq. 26 by substituting T with T_s as,

$$M_{T_s} = m \left(\frac{2}{\pi} \right) \int_0^{\pi/2} \mu X_0 \left(\frac{\pi}{2} - \phi \right) \frac{r}{\sin \beta} r \cos \beta \cos \phi \, d\phi \tag{30}$$

$$M_{T_s} = m r^2 \cot \beta \mu X_0 \left(\frac{2}{\pi} \right) \left[\cos \vartheta_b + \vartheta_b \sin \vartheta_b - \frac{\pi}{2} \sin \vartheta_b \right] \tag{31}$$

The layer bending moment from the wires that undergo partial and full slip in a cross-section can then be written as

$$M_T = M_{T_p} + M_{T_s} \tag{32}$$

Stage 3: Fully slipped (Loose) stage

In this stage the $\phi_b = 0$ and the curvature is (κ_1) is obtained from Eq. 25. Hence, the layer bending moment (M_{T_f}) is obtained similar to Eq. 31 by substituting $\theta_b = 0$.

$$M_{T_f} = m \left(\frac{2}{\pi} \right) \mu X_o r^2 \cot \beta \quad (33)$$

It can be noted that the layer bending moment due to the wire axial force T at any cross-section can be evaluated based on the position angle of the wires in that cross-section and depending on their stages of slip, namely no-slip, intermittent slip (partial and full slip) and full slip as given by the Eqs. 27, 28, 31 and 34.

2.6.2 Layer Bending Moment Due to the Rotation of the Wires

The moment generated within the layer due to the rotation of the wire in the normal (M_G), binormal ($M_{G'}$) and the axial directions (M_H) are expressed as below with their respective curvature Equations cited in 5–7.

$$M_G = m \left(\frac{2}{\pi} \right) \int_0^{\pi/2} EI \omega_n \sin \phi d\phi \quad (34)$$

$$M_{G'} = m \left(\frac{2}{\pi} \right) \int_0^{\pi/2} EI \omega_{b'} \cos \beta \cos \phi d\phi \quad (35)$$

$$M_H = -m \left(\frac{2}{\pi} \right) \int_0^{\pi/2} GJ \omega_t \sin \beta \cos \phi d\phi \quad (36)$$

The total layer bending moment due to the rotation of the wire in the three directions is given by

$$M_r = M_G + M_{G'} + M_H \quad (37)$$

2.6.3 Strand Bending Moment

The total bending moment in the strand is the summation of the bending moment experienced in all the layers and the core and is given by

$$M_b = M_T + M_r + E_C I_C \kappa \quad (38)$$

where, E_C and I_C are the modulus of elasticity and area moment of inertia of the core and κ is the total curvature of the strand.

2.7 Strand Bending Stiffness

The cable or strand stiffness can be evaluated from the bending moment (M_b) and bending curvature (κ) relations discussed in the previous sections, by plotting a graph and evaluating its slope at each curvature. The effective stiffness of the cable is given by

$$EI_{strand} = M_b/\kappa \tag{39}$$

3 Numerical Results and Discussion

The mathematical model reported has been worked out for a single-layered helical strand having geometrical parameters as shown in Table 1. The radial clenching contact force X_0 is calculated from Eq. 14 for a given axial load. The limiting curvature at which slip begins as per the Coulomb friction theory in a helical wire is evaluated from Eq. 23, (whose position angle corresponds to 90°) after estimating the fiber axial force (that resists the friction force) from Eq. 12 for the cable geometry cited in Table 1. The bending moment generated in the cable due to this curvature is evaluated from Eq. 27 which corresponds to the monolithic stage. The additional curvature caused by the micro slip phenomenon is evaluated based on the Hertzian contact hypothesis in Sect. 2.3 and the total curvature as per the improvised slip model is evaluated as in Eq. 21. The layer bending moment due to the rotation of the wires along its normal, binormal, and tangential axes is evaluated from Eqs. 34–36 and the total bending moment in the cable is obtained from Eq. 37. The overall strand bending moment is then evaluated from Eq. 38 after accounting for the contribution from the central core wire. The effective cable bending stiffness is evaluated from Eq. 39 for the total curvature of the cable.

The helical wire in a strand cross-section is evaluated for its slip status based on its position angle varying from 0 to 90° and the respective curvatures are evaluated

Table 1 Material and geometrical properties of the single-layered strand

Parameter (unit)	Value
Diameter of core (mm)	3.94
Diameter of helical wire (mm)	3.73
Helix radius (mm)	3.835
Lay angle (α°)	17.03
Young’s modulus of core and helical wire (GPA)	188
Poisson’s ratio	0.3
Coefficient of friction	0.12
No of wires in a layer	6

as per Eq. 24. The layer bending moment developed in this intermittent stage due to axial force involving partial and full slip is evaluated from Eqs. 28 and 31. The total bending moment in the cable is evaluated after accounting the due contributions from the rotation of the wires and that of the core in similar lines as cited above. The status of the helical wires in a strand cross-section that undergoes full slip is evaluated as per Eq. 25 and the bending moment caused due to the axial and rotational wire movements are evaluated as in Eqs. 33 and 37. The bending moment in the strand is evaluated as per Eq. 38 after accounting the core contribution.

The overall strand bending stiffness is evaluated from Eq. 39 by accounting the net bending moment caused in a strand cross-section as per the slip conditions defined above.

Figure 2a shows the variation of bending stiffness of the strand as a function of curvature for an axial load of 10 kN as per the formulations made in this paper. It can be noticed that the bending stiffness retains the constant value up to some curvature level in which the strand is behaving in a monolithic state. As the curvature increases the slip initiation has begun and has progressed and the bending stiffness reduces gradually, thereby explaining the phenomenon of a mixed slip status of wires in the strand. The fully slipped stage of all the wires in the strand is noticed at a curvature of $188(m^{-1})$ and thereafter the bending stiffness plot remains constant. It can be recalled that the bending stiffness plot explained above is the result of a combined slip behavior, depicting the simultaneous occurrence of Coulomb friction theory of macro slip and the Hertzian contact theory of micro slip. The curvature and twist relations which are basically used to define the wire moments are improvised in this paper to include the effect of the “wire stretch”, a phenomenon ignored by many researchers till date.

The numerical results of bending stiffness for the single-layered cable are also evaluated with the mathematical model adopted by Khan et al. [11] and are presented in Fig. 2a as a function of curvature as shown in Eq. 4. It can be observed that the

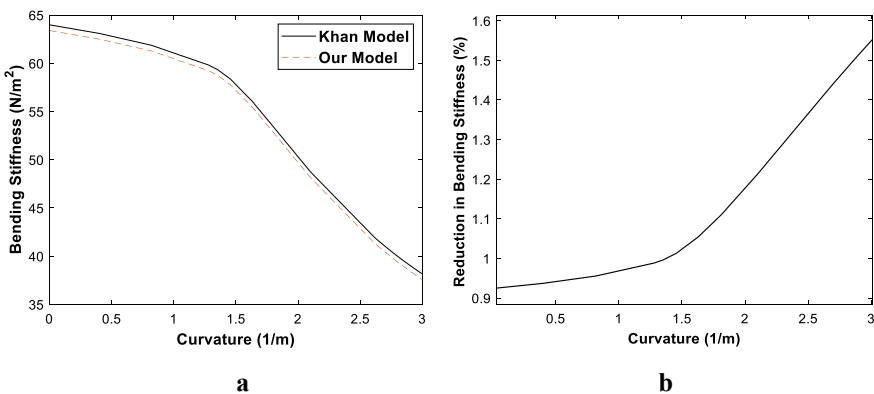


Fig. 2 **a** Comparison of strand stiffness versus curvature for our versus Khan model. **b** Difference in stiffness for a load of 10 KN

bending stiffness values of Khan et al. [11] register higher values than that of our model in the entire curvature range, due to the non-inclusion of wire stretch effect, a vital parameter required to distinguish the performance of cables subjected to axial and bending loads. It can be observed from Fig. 2a that the slip initiation has significantly commenced at a strand curvature of $1.5(m^{-1})$ and thereafter the cable stiffness drastically reduces as per the slip regimes discussed.

Figure 2b shows the percentage difference in the bending stiffness of our model with that of Khan et al. [11] for an axial cable load of 10 kN. It can be observed from Fig. 2b that the percentage reduction in stiffness remains constant up to a curvature of $1.5(m^{-1})$ due to the monolithic state of behavior. As the cable undergoes combination of slip stages beyond this curvature, the cable stiffness reduces. Since our model considers the macro slip & the micro slip phenomenon as against the macro slip phenomenon of Khan et al. [11], the percentage difference in Fig. 2b also increases beyond this critical curvature of $1.5(m^{-1})$. However, it remains constant in the fully slipped region. In the curvature range that is adopted in this study, a maximum reduction of bending stiffness has been noticed up to 4.34% due to the refined curvature expressions that take into account the wire stretch in this paper.

Figure 3a shows the variation of the bending stiffness as a function of curvature for five different axial loads as per the revised models suggested in this paper. It is observed from those plots that the slip initiation sets in earlier when the axial cable load is reduced. Figure 3b shows the percentage reduction of the bending stiffness between our and Khan’s model as a function of bending curvature for different cable axial loads.

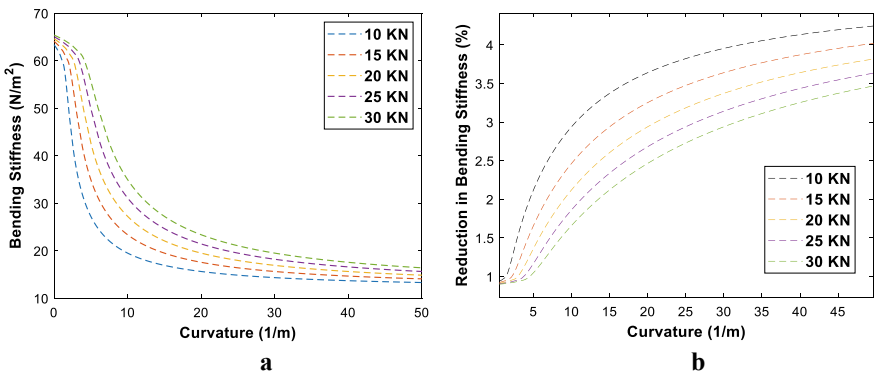


Fig. 3 **a** Strand stiffness versus curvature for various loading conditions. **b** Difference in strand stiffness for different loading conditions

4 Conclusions

The improvised model proposed in this paper considers the slip caused by the Coulomb friction hypothesis and the micro slip caused by Hertzian contact friction theory along with the wire stretch effect. The mathematical model proposed has been validated with the recent research works for the single-layered cable as a function of bending curvature and axial loads. It has been found that the proposed model tends to follow the trend set by the recent works of Khan wherein the wire stretch effect and curvature refinements are not considered. The refined model proposed in this paper registers reduction in stiffness values up to a maximum of 4.34% for a cable axial cable of 10 kN. It is further observed that the percentage reduction in bending stiffness substantially reduces as the cable axial load is increased. It is hoped that the combined slip theory taking into account the macro and the micro slip phenomenon will give a realistic estimation of the cable bending stiffness values which are vital for estimating the cable response accurately. It is further claimed that the inclusion of the wire stretch phenomenon in the estimation of basic kinematic relations will enable the accurate prediction of cable response.

References

1. McConnell KG, Zemke WP (1980) The measurement of flexural stiffness of multistranded electrical conductors while under tension. *Exp Mech* 20:198–204
2. Costello GA, Butson GJ (1982) Simplified bending theory for wire rope. *J Eng Mech Div* 108:219–227
3. Love AEH (1940) A treatise on the mathematical theory of elasticity. *Nature* 105:511–512
4. Sathikh S, Parthasarathy NS (1988) Discussion of: internal friction due to wire twist in bent cable. *J Eng Mech* 114:727–728
5. Papailiou KO (1997) On the bending stiffness of transmission line conductors. *IEEE Trans Power Deliv* 12:1576–1588
6. Jolicoeur C (1997) Comparative study of two semicontinuous models for wire strand analysis. *J Eng Mech* 123:792–799
7. Sathikh S, Rajasekaran S, Jayakumar, Jebaraj C (2000) General thin rod model for preslip bending response of strand. *J Eng Mech* 126:132–139
8. Hong K-J, Der Kiureghian A, Sackman JL (2005) Bending behavior of helically wrapped cables. *J Eng Mech* 131:500–511
9. Spak K, Agnes G, Inman D (2013) Cable modeling and internal damping developments. *Appl Mech Rev* 65:010801
10. Foti F, Martinelli L (2016) Mechanical modeling of metallic strands subjected to tension, torsion and bending. *Int J Solids Struct* 91:1–17
11. Khan SW, Gencturk B, Shahzada K, Ullah A (2018) Bending behavior of axially preloaded multilayered spiral strands. *J Eng Mech* 144:4018112

Green Manufacturing: Benefits, Implementation and Challenges



Ankit, Moti Lal Rinawa, and M. S. Karuna

Abstract Green manufacturing (GM) focuses on improving production methods rather than controlling technology to preserve natural resources for future generations and recycle materials. Various researches claims it is advantageous to use it for economic advancement by simultaneously lowering resource depletion, waste output, and pollution in any form. The study promotes the adoption of green technology over traditional methods due to its eco-friendly design, reduced waste, and increased customer pleasure. Using traditional methods wastes natural resources and pollutes the environment. However, in our fast-paced sector, implementing GM is a difficult undertaking. The article presented the state-of-the-art related to GM and Sustainable Development. In addition to this, this article also discussed how GM contributes to cost savings and improved product quality that is beneficial to both the environment and industry.

Keywords Green manufacturing (GM) · Resource depletion · Reusable · Sustainable development · Industrial standards

1 Introduction

There is a long-held desire for a biologically, economically, and socially healthy society—a community that addresses the needs of the present without undermining the capacity of future generations to fulfil their own needs. On our earth, there are few/limited resources for a large number of populations which becomes a global and critical challenge for the industry [1]. This limitation is very crucial for our environment and if not considered seriously then it will cause an imbalance. There are many Standardization Institutions like ISO that develop a framework for quality

Ankit · M. L. Rinawa

Mechanical Engineering Department, Government Engineering College Jhalawar, Jhalrapatan, Rajasthan, India

M. S. Karuna (✉)

Department of Chemical Engineering, M.J.P. Rohilkhand University, Uttar Pradesh, Bareilly, India

e-mail: m.karuna@mjpru.ac.in

management while considering products' effect on the environment [2]. To maintain the trade-off, industries must rethink/change their conventional methods. There is a need for a new manufacturing process, i.e., GM that is strategically suited for sustainable development. The cost of the product is mainly depending upon the availability of the resources if the resource is less then the cost of production increases. However, it is nearly impossible to predict the price of price trends, so industries should aim to successfully produce energy and resources in large price ranges [3]. One strategy to accommodate price fluctuations is to pass on the mark-up to the customer. However, a price mark-up can allow changes to be made to the commodity. Another solution is to increase/improve the output efficiency, it can be done, increased by rising resource consumption and by improving the core structure of the industry. Companies performing green production are mindful of the value of incorporating elements but have not been able to accomplish them in their entirety today [4].

This work consists of multiple sections. Section 2 provides a brief introduction to GM and its advantages. Section 3 discusses sustainable development. Section 4 discusses the usability of eco-efficiency and provides the benefits of GM. Section 5 discusses the implementation of GM. Section 6 discusses the challenges faced by the industries.

2 Green Manufacturing

GM (i.e., Green Manufacturing) is a term that describes industrial activities that do not damage the environment in any aspect of the manufacturing process [5]. It stresses the use of manufacturing practice that does not cause environmental pollution or damage parties like customers, an employee of the industry or other habitats. GM terms consist of two words. The term "green" refers to reducing pollution/waste by minimizing the use of natural resources and by recycling/reusing [6]. The word "manufacturing" refers to the complete life cycle of creating the product. So many relevant concepts such as green design, ecological process planning, green manufacture, and so on are brought out (see Fig. 1). GM is a sophisticated machine engineering problem. Finally, the purpose of GM is a kind of sustainable development in the field of module manufacturing. GM is, therefore, the only solution to sustainable development and is also the company's responsibility to society. GM is emphasizing the reduction of parts, the rationalization of materials and the reduction of components to help make vehicles more effective. GM illustrates the path map of companies to enhance efficiency through economic growth and the effect of successful operational outcomes [7]. It also illustrates the benefits and drawbacks of sustainable development activities and overall successful operational results through the creation of the research instrument. The following are some advantages of GM [8]:

- Checks and decreases waste material in production cycles.
- Saves money and protects capital.
- Increased efficiency and cost savings.

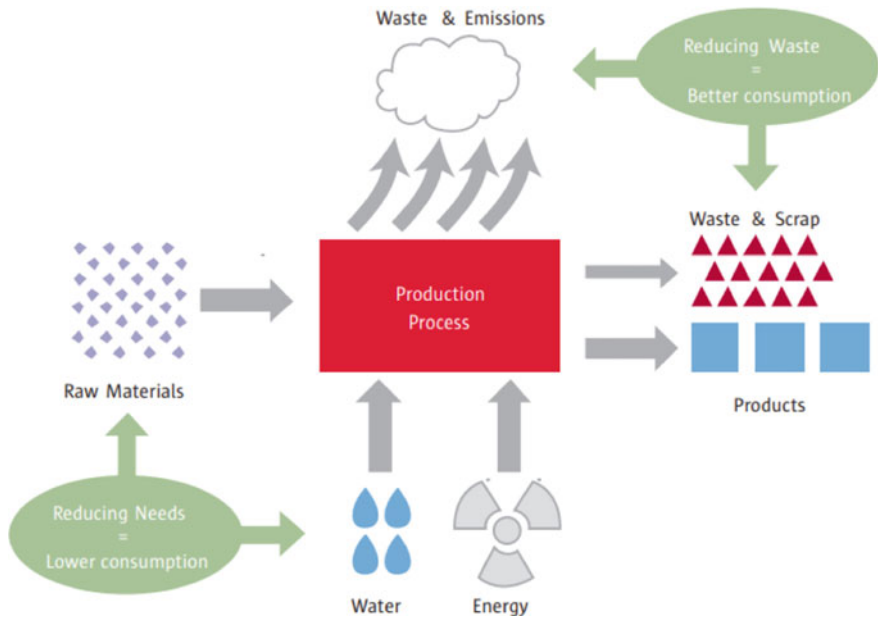


Fig. 1 Process of GM [9]

- Encouraging and influencing both internal and external corporate behaviours to ensure sustainability.
- Simple environmental adaptability to shifting laws.

3 Sustainable Development

The term “sustainable” is derived from the word “sustainability” and is described as “growth that meets the needs of the present without jeopardizing the ability of future generations to adapt to their own need” as set out in the report of the United Nations World Commissioner on Environment and Development [10]. The question of sustainability is growing in concern for manufacturers [11]. If a society uses resources and produces waste in a region which goes beyond the capacity of nature to turn industrial and societal waste into environmental nutrients and energy, one should consider a system unsustainable. Sustainable development is therefore a concept that includes social, ecological, and economic goals and requires the integrity of resource use, the direction of investments, the focus on technological development and institutional change to be maintained (see Fig. 2).

Fig. 2 Goals or pillars of sustainable development [12]



4 Eco-Efficiency and the Benefits of Green Manufacturing

The World Business Council for Sustainable Development (WBCSD) coined the word “eco-efficiency”. The idea is that more goods and services will be created using fewer resources, less pollution, and less waste [13]. This definition represents a vision for the creation of products and services with economic importance while reducing the environmental impacts of manufacturing. Eco-efficiency means, in other words, more and less efficient. According to the WBCSD, eco-efficiency vital considerations are [14]:

- Reduction of products or services’ content intensity.
- Reduce the energy cost of products or services.
- Reduced toxic material dispersal.
- Enhanced recycling.
- Maximum utilization of renewables.
- Increased drug durability.
- Increased goods and services market volume.

4.1 Environmental Benefits

Green development would have a major environmental impact. About 80% of hazardous waste belongs to the electrical and electronic sectors [15]. Green development aims to reduce waste to zero. It certainly would boost the natural atmosphere

and avoid emissions, in particular the greenhouse effect which has had an impact on Earthbound for more than 50 years without concern for the climate [16].

4.2 Company Benefits

A GM company gives the public a perfect image. With the public becoming increasingly aware of the greenhouse effects, greens are an action that is appreciated by the public and promoted byte. It is said that in the eyes of the viewers, the company has a social responsibility. The business is now more environmentally conscious. A corporation that might grow a comparable greener commodity is likely to have a competitive advantage [17]. For starters, car consumers are more interested in scientifically buying electricity than in driving high-speed cars, with less carbon monoxide. The firm that makes the greener car thus reports greater sales. While it is costly to move from the traditional model of manufacturing to greener processes, GM's practice will help save money. The zero-waste strategy ensures that firms can maximize their assets and then save resources in micro-management. The cost savings would also be brought on by improved energy management and greater technical opportunities to manage processes.

A lot of research and technology projects are distributed by Green Manufacturing [18]. Through project enhances our technology. The car industry, for instance. It is required to replace all vehicles with hydrogen by gradually creating electric cars. A more modern development is generated by the need for a greener environment. The mother of all inventions, as the saying goes, is a necessity [19].

5 Implementation

5.1 Production Process

Product design and process management are part of the development cycle. In the introduction of GM, both play an important function. Shave from manufacturers designing greener products. This means that the production companies must consider the product life cycle and the virgin material used. Biodegradable and recyclable materials are required to minimize waste. Only non-toxic products need to be. Therefore, the component will be produced and remanufactured for disassembly, instead of glue and screws, the modular design and the snap-fit or push-fit. The producers will switch from conventional pipe controls to emerging technology, for example, emissions reduction, automation of manufacturing processes, and material substitution in the process design. To minimize waste and losses to energy and materials throughout the manufacturing process, process optimization should be carried out. The process

of distillation and filtering allows the recycling of virgin materials. Where new materials are not required, refined, or recycled materials may be reintroduced into the life cycle. On the spot, waste is reduced [3, 10, 11, 19].

5.2 International Organization for Standardization

ISO 14000 requirements exist to help companies mitigate whether their activities have a detrimental effect on their climate, comply with and continue to strengthen the aforementioned laws (because of adverse improvements to air, water or land) and conform with relevant laws and regulations [20]. ISO14000 is unlike ISO 9000 quality control as they contribute not only to production but also to the process (the complete outcome of how a product is produced) [21]. The overall idea is to devise an organized approach to systematically reduce the impact that an organization can control on environmental aspects. The definition of Sustainable Development 14001 is a globally recognized environmental management system (EMS) standard that offers useful tools for evaluating environmental aspects of an enterprise as well as identifying enhancement choices. It sets out environmental policy requirements, determines the sand impact of products/activities/services, plans environmental goals and measurable targets, implements, and runs programmes to achieve goals, controls and corrections, and management reviews. The following criteria are required to achieve ISO 14001 certification: lower releases of contaminants, energy efficiency saving, saving resources, such as saving water and paper recycling and prevention of potential environmental hazards.

5.3 Regulations

The United States is not alone in its interest in greener production. Many new industries have started to enact environmental laws covering waste processing practices and waste management within their boundaries [22]. As an example, China once generated about 70 per cent of its electricity consumption using coal, leading to extremely poor air quality. To mitigate the smog problem, China had ambitious government plans to turn to nuclear power, but it was not as effective as expected [23]. Now China is the second-largest wind power producer and consumer in the world. China now has solar water heating and wastewater treatment regulations to make production processes safer and cleaner. Since 2012, India has enacted strict recycling laws covering recycling standards, reduction in the use of hazardous materials, and safe storage and disposal centres for toxic substances [24]. Countries have taken similar collective steps to keep the environment safer. The global automotive sector needed to collaborate more closely with some of the various national governments to ensure a healthier atmosphere from the management of greenhouse emissions to the regulation of hazardous chemical materials. The Kyoto Protocol

contains legally binding commitments for industrialized countries to reduce their emissions of greenhouse gases by a total of at least five per cent [25]. Effective as of June 2012, the Environmental Protection Agency (EPA) has adopted the Toxic Substances Control Act, which governs 119 toxic substances to be manufactured, distributed, sold, and substantially newly used [26]. This act defines the protocols required for the use of four highly toxic substances requiring consent. In the Federal Register, the substances covered are defined.

6 Challenges

6.1 Investment

Companies are required to invest a great deal of cash in water, waste, and emission control treatment. As production costs in this field increase, a higher allocation could lead to a lower profit margin for them. Furthermore, Green Production needs testing, equipment, and ISO 14020 certification [27].

6.2 Engineers

The engineers face a real challenge. During product creation, they must balance between product durability and disassembly/assembly. In addition, methods to increase the component twice to improve their life cycle must be determined. In line with the Green Production Strategy, engineers must undergo strict process control and will track the supply chain. Engineers are responsible not only for their business but also for social justice. To speed up the process companies may opt for advanced Artificial Intelligence and Data Mining techniques, especially in the chemical and health industries [28–30].

6.3 Increase in Production Cost

For all investments in the above sector, output costs will undoubtedly increase. Furthermore, as green materials are still not widely accepted by the industry, there is less choice and few suppliers to choose from. This translates to higher manufacturing prices, thereby increasing the cost of supply [31].

6.4 Long-Term Effort

When it comes to green growth, the producer wants a lot of commitment. Green production is not only an effort for a short time, as results will not be present in a short period. To ensure the success of green production, essential and appropriate education and training must be provided [32, 33].

7 Conclusion

This work provided the state-of-the-art related to GM, sustainable development, implementation of GM and challenges faced by industries while implementation. Protection of our natural resources for future generations is vital to green growth. It can be pricey and takes a lot of commitment, but several businesses have embraced the green programme. GM will show the power, capability, and efficiency of truly renewable businesses. Green manufacturing has the potential to provide sustainable & long-term development on a massive scale with unparalleled speed and efficacy. It is recommended to use this work as a blueprint and extend this work by including the latest technologies and ISO standards.

References

1. Paul ID, Bhole GP, Chaudhari JR (2014) A Review on Green Manufacturing: It's Important, Methodology and its Application. *Procedia Mater. Sci.* 6:1644–1649. <https://doi.org/10.1016/j.mspro.2014.07.149>
2. Business & Sustainable Development Commission: Better Business Better World. Better Bus. Better World. (2017).
3. Vardia, J., Soni, D., Ameta, R.: Green manufacturing processes. In: *Green Chemistry: Fundamentals and Applications* (2013). <https://doi.org/10.1201/b15500>.
4. Lin R, Sheu C (2012) Why Do Firms Adopt/Implement Green Practices?—An Institutional Theory Perspective. *Procedia - Soc. Behav. Sci.* 57:533–540. <https://doi.org/10.1016/j.sbspro.2012.09.1221>
5. Pang R, Zhang X (2019) Achieving environmental sustainability in manufacture: A 28-year bibliometric cartography of green manufacturing research. *J Clean Prod* 233:84–99. <https://doi.org/10.1016/j.jclepro.2019.05.303>
6. Dornfeld, D., Yuan, C., Diaz, N., Zhang, T., Vijayaraghavan, A.: Introduction to Green Manufacturing. In: Dornfeld, D.A. (ed.) *Green Manufacturing*. pp. 1–23. Springer US, Boston, MA (2013). https://doi.org/10.1007/978-1-4419-6016-0_1.
7. Rehman MAA, Shrivastava RL (2013) Green manufacturing (GM): past, present and future (a state of art review). *World Rev. Sci. Technol. Sustain. Dev.* 10:17. <https://doi.org/10.1504/WRSTSD.2013.050784>
8. Willis, K.: The Sustainable Development Goals. In: Cupples, J., Palomino-Schalscha, M., and Prieto, M. (eds.) *The Routledge Handbook of Latin American Development*. pp. 121–131. Routledge, London ; New York : Routledge, 2019. (2018). <https://doi.org/10.4324/9781315162935-11>.
9. 2008 Supply Chain Monitor “ How mature is the Green Supply Chain ?” Context. (2008).

10. Girardon, P.: Sustainable Development. In: *Gases in Agro-Food Processes*. pp. 669–673. Elsevier (2019). <https://doi.org/10.1016/B978-0-12-812465-9.00028-1>.
11. Schrettle, S., Hinz, A., Scherrer -Rathje, M., Friedli, T.: Turning sustainability into action: Explaining firms' sustainability efforts and their impact on firm performance. *Int. J. Prod. Econ.* 147, 73–84 (2014). <https://doi.org/10.1016/j.ijpe.2013.02.030>.
12. Expert working Groups | The Department of Economic Affairs, Commerce and Industry of Aruba, <https://www.deaci.aw/sustainable-development/expert-working-groups/>, last accessed 2021/07/26.
13. Huppés G, Ishikawa M (2005) Eco-efficiency and Its Terminology. *J Ind Ecol* 9:43–46. <https://doi.org/10.1162/108819805775247891>
14. Nelson, J., Grayson, D.: World Business Council for Sustainable Development (WBCSD). In: *Corporate Responsibility Coalitions*. pp. 300–317. Routledge (2017). <https://doi.org/10.4324/9781351277525-29>.
15. Defining Hazardous Waste: Listed, Characteristic and Mixed Radiological Wastes | US EPA, <https://www.epa.gov/hw/defining-hazardous-waste-listed-characteristic-and-mixed-radiological-wastes>, last accessed 2021/07/26.
16. Ries R, Bilec MM, Gokhan NM, Needy KL (2006) The Economic Benefits of Green Buildings: A Comprehensive Case Study. *Eng Econ* 51:259–295. <https://doi.org/10.1080/00137910600865469>
17. Soni, G.D.: ADVANTAGES OF GREEN TECHNOLOGY. *Int. J. Res. -GRANTHAALAYAH.* 3, 1–5 (2015). <https://doi.org/10.29121/granthaalayah.v3.i9SE.2015.3121>.
18. Deif AM (2011) A system model for green manufacturing. *J Clean Prod* 19:1553–1559. <https://doi.org/10.1016/j.jclepro.2011.05.022>
19. Li C, Liu F, Tan X, Du Y (2010) A methodology for selecting a green technology portfolio based on synergy. *Int J Prod Res* 48:7289–7302. <https://doi.org/10.1080/00207540903382857>
20. Gillum, D.R.: ISO 14000. In: *Environmental Compliance: A Web-Enhanced Resource* (2000). <https://doi.org/10.1201/b12446-29>.
21. Ziegel ER, Lamprecht J (1993) ISO 9000. *Technometrics* 35:240. <https://doi.org/10.2307/1269696>
22. Gabaldón-Estevan D, Criado E, Monfort E (2014) The green factor in European manufacturing: a case study of the Spanish ceramic tile industry. *J Clean Prod* 70:242–250. <https://doi.org/10.1016/j.jclepro.2014.02.018>
23. Zhu Q, Sarkis J, Geng Y (2005) Green supply chain management in China: pressures, practices and performance. *Int J Oper Prod Manag* 25:449–468. <https://doi.org/10.1108/01443570510593148>
24. Rud JP (2012) Electricity provision and industrial development: Evidence from India. *J Dev Econ* 97:352–367. <https://doi.org/10.1016/j.jdeveco.2011.06.010>
25. Wang C-H, Ko M-H, Chen W-J (2019) Effects of Kyoto Protocol on CO2 Emissions: A Five-Country Rolling Regression Analysis. *Sustainability* 11:744. <https://doi.org/10.3390/su11030744>
26. Judson, R.S., Martin, M.T., Egeghy, P., Gangwal, S., Reif, D.M., Kothiya, P., Wolf, M., Cathey, T., Transue, T., Smith, D., Vail, J., Frame, A., Mosher, S., Hubal, E.A.C., Richard, A.M.: Aggregating Data for Computational Toxicology Applications: The U.S. Environmental Protection Agency (EPA) Aggregated Computational Toxicology Resource (ACToR) System. *Int. J. Mol. Sci.* 13, 1805–1831 (2012). <https://doi.org/10.3390/ijms13021805>.
27. Minkov N, Lehmann A, Winter L, Finkbeiner M (2020) Characterization of environmental labels beyond the criteria of ISO 14020 series. *Int J Life Cycle Assess* 25:840–855. <https://doi.org/10.1007/s11367-019-01596-9>
28. Giraud RJ, Williams PA, Sehgal A, Ponnusamy E, Phillips AK, Manley JB (2014) Implementing Green Chemistry in Chemical Manufacturing: A Survey Report. *ACS Sustain. Chem. Eng.* 2:2237–2242. <https://doi.org/10.1021/sc500427d>
29. Aman, Chhillar, R.S.: Disease predictive models for healthcare by using data mining techniques: State of the art. *SSRG Int. J. Eng. Trends Technol.* 68, 52–57 (2020). <https://doi.org/10.14445/22315381/IJETT-V68I10P209>.

30. Aman, Chhillar, R.S.: Analyzing Predictive Algorithms in Data Mining for Cardiovascular Disease using WEKA Tool. *Int. J. Adv. Comput. Sci. Appl.* 12, 2021 (2021).
31. Zhang J, Ouyang Y, Philbin SP, Zhao X, Ballesteros-Pérez P, Li H (2020) Green dynamic capability of construction enterprises: Role of the business model and green production. *Corp Soc Responsib Environ Manag* 27:2920–2940. <https://doi.org/10.1002/csr.2012>
32. Ankit, Rinawa, M.L.: Sustainable Natural Bio-composites and its Applications. In: Agrawal, R., Jain, J.K., Yadav, V.S., Manupati, V.K., and Varela, L. (eds.) *Recent Advances in Smart Manufacturing and Materials*. pp. 433–439. Springer, Singapore (2021). https://doi.org/10.1007/978-981-16-3033-0_41.
33. Ankit, Rinawa, M., Chauhan, P., D.Suresh, Kumar, S., Santhosh Kumar, R.: A review on mechanical properties of natural fiber reinforced polymer (NFRP) composites. *Mater. Today Proc.* S2214785321051348 (2021). <https://doi.org/10.1016/j.matpr.2021.07.275>.

Crack Propagation Analysis of Spur Gear



Mahendra Singh Raghav, Amandeep Singh, and Shivdayal Patel

Abstract Spur gears, the extensively used and simplest in geometry, are used for transmitting motion and torque from point to another. Gears are subjected to high loading conditions for longer period. The high loading conditions coupled with longer duration of operation, make gear tooth subjected to crack fault at the root. The stresses induced at the tooth root are determined using FEM and validated analytically using Lewis Theory. In the present study, a detailed analysis of behavior of crack path has been conducted for a backup ratio of 0.6. The cracks with initial lengths of 0.1, 0.3, 0.6 and 0.8 mm are placed at 180° and 225° orientation from the positive X-axis. The propagation path of cracks along with gear's fatigue life is studied. The crack propagation paths and fatigue life of gear is studied for both orientation angle. In this numerical study, it is found that the initial length of cracks affects both crack initiation and fracture life of gear. It is also noted that spur gears with cracks at 180° initial orientation has higher life expectancy as compared to 225° crack orientation.

Keywords Gears · Finite element analysis · Faults · Crack initiation · Crack propagation · Backup ratio

1 Introduction

The most common types of faults in a gear are wear, pitting and scuffing. These faults are responsible for the reduced efficiency of the whole transmission system. However, a crack, at the root, may result in breakage of tooth or rim and hence, failure of transmission system. In industries, transmission failure leads to unscheduled maintenance and loss of productivity. There are some machineries such as rotor craft or a helicopter where the failure of transmission system may lead to loss of human life also. This makes the study of this gear fault very significant. This paper also intends to add some more insights in to this area of research.

M. S. Raghav (✉) · A. Singh · S. Patel
Department of Mechanical Engineering, Indian Institute of Information Technology, Design and Manufacturing, Jabalpur, India
e-mail: 20pmee09@iiitdmj.ac.in

In last two decades a good quality of research work has been done on this gear fault and some important results have been obtained. Lewicki et al. [1–3] studied the factors like rim thickness, location of initial crack and backup ratio and observed the variations in crack propagation paths with these factors in gear tooth. Their analysis concluded that the gear with 25° pressure angle is more likely to get tooth crack fault in comparison to gears with 20° pressure angle. Another finding was that backup ratio has an important role in the propagation nature of gear tooth crack. Belsak and Flasker [4] concluded in their crack propagation study that crack propagates through a smooth, continuous and straight path with a slight curvature only. Kramberger et al. [5] found that the initiation of crack occurs in the gear tooth at a point where principal stresses are maximum. The research studies in [6, 7] modeled the gear tooth crack as a slight curve or a straight line. A similar model was used by Mohammed et al. [8] to study crack propagation and investigated the same using time–frequency analysis. Chen et al. [9] in his cracked gear model allowed the crack to propagate along width as well as depth of the teeth. Faults at tooth surface, broken teeth and cracks at the root was analyzed by Dadon et al. [10] using dynamic modeling and experimental data.

Wu et al. [11] in his model varies crack levels from 0–80% and studied the crack propagation effect on the dynamic response of the gear box. Gear mesh stiffness reduction due to crack progression was calculated in [12] using an analytical approach. Results were verified using an FEM model. Zhou et al. [13] modeled crack growth at the tooth root using a modified mathematical model. The time varying mesh stiffness (TVMS) was calculated using a potential energy method. While investigating the tooth profile error, Mark et al. [14] found a significant role of increment in crack size while detecting errors in tooth profile caused due to plastic deformation. In [15], Saxena et al. while studying various tooth crack cases found that model characteristics and frequency response of the system are affected by the tooth cracks.

Chen et al. [16] used lumped parameter model to study the effects of crack at the tooth root distributed non-uniformly along its width.

This paper studies the crack propagation behavior for varying initial crack lengths for two different crack orientation angles. This study further calculates fatigue life and crack propagation rate for varying initial crack lengths and orientation angles. The maximum principal stress criteria and Paris law is implemented in the FEM model for damage initiation and fatigue life calculation respectively.

2 Research Methods

2.1 Bending Stress Calculation Using Lewis Criteria

The bending stresses in gears are most commonly calculated by Lewis Method. The method mainly focuses on a single gear tooth and assumes it as cantilever beam

under loading. The bending stress distribution can be related mathematically and is given below.

By neglecting the effect of radial force, the tangential force using Lewis Method can be calculated as,

$$M = Ft \times R \quad (1)$$

Bending stress is given by,

$$\sigma_b = \frac{F_t \cdot P}{W \cdot Y} \quad (2)$$

2.2 *Extended FEM or XFEM*

Refined meshing is needed around the tip of the crack to obtain better results. As the crack progresses deeper in to the body, in FEM a continuous refinement is needed around the crack for crack to grow properly. XFEM helps in overcoming these difficulties. It is used for analysis of the models having discontinuities in such notches, cracks etc. XFEM is a numerical method that enriches or extends the approximation space. It reproduces the space and overcomes difficulties that arise due to discontinuities such as cracks. XFEM helps in improving accuracy and reduction in the computational rates.

In many researches this method proved very helpful in predicting the fatigue cracks. In [17, 18], researchers used XFEM for determining crack growth in gears and in [19] for analysis of cracks generated in railway axles due to extensive loading. Mathematically, partition of unity method forms the basis of XFEM method as shown below.

$$\sum_{i=1}^n N_i(X) = 1 \text{ and } \sum_{i=1}^n N_i(X) f(X) = f(X) \quad (3)$$

2.3 *Maximum Principal Stress Criteria (MPSC)*

Maxps or Maximum Principal Stress criteria is a prediction model used in XFEM enriched region in determining initial damage due to discontinuity in the model.

It is given as,

$$\left\{ \begin{array}{l} \sigma_{\max} \\ \sigma_{\max}^{\circ} \end{array} \right\} = 1 \quad (4)$$

where, σ_{\max} = current maximum principal stress.

σ_{\max}° = allowable maximum principal stress.

2.4 Fatigue Life Estimation Using Paris Law

The crack growth life due to fatigue is estimated using Paris law. The law is given by [20],

$$\frac{d\alpha}{dN} = c(\Delta K)^n \quad (5)$$

where $d\alpha$ and dN are increment in crack growth and the increment in crack propagation fatigue life respectively.

$$\Delta K_{\text{eq}} = \frac{\Delta K_{\text{I}}}{2} + \frac{1}{2}\sqrt{\Delta K_{\text{I}}^2 + 4(\alpha_1 \Delta K_{\text{II}})^2 + 4(\alpha_2 \Delta K_{\text{III}})^2} \quad (6)$$

where, K_{I} , K_{II} and K_{III} are the three modes SIFs (Stress Intensity Factors) respectively.

3 Computational Study

This computational study uses a single tooth sector model to reduce computational time as compared to a full gear model. The variation in the path of crack propagation has been studied at gradually varied initial crack lengths placed at root of the tooth at orientation of 180° and 225° from the positive X -axis. The initial crack lengths are varied as 0.1, 0.3, 0.6 and 0.8 mm.

3.1 Finite Element Modeling

The planar single tooth model used here is meshed with linear quad dominated elements with enhanced hourglass control. The size of element is kept at 0.15 with a plain stress condition and a backup ratio of 0.8. The tooth flank is loaded with a static tangential load equivalent to 35 Nm while keeping the shaft hole fixed. A symmetric boundary condition is been applied on side edges of the rim of the gear tooth. The meshed gear tooth and its boundary conditions are shown in Fig. 1.

Fig. 1 a Meshing b boundary condition

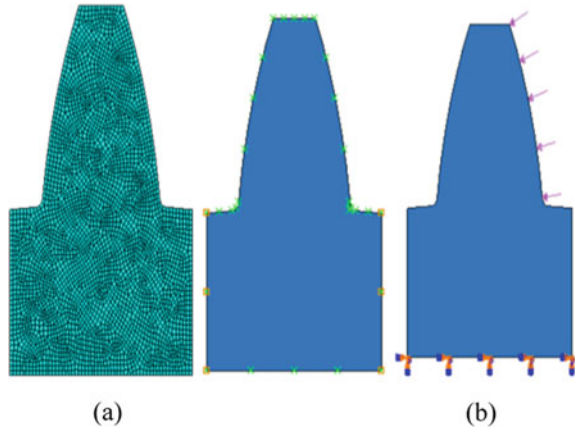


Table 1 Comparison of Von-Mises stress and maximum principal stress

Lewis theory		FEM method		FEM method	
Von-Mises stress	591.897 MPa	Von Mises stress	586.4 MPa	Maximum principal stress	558.9 MPa

3.2 Numerical Validation Using Bending Stress

The bending stresses generated in the single teeth sector model loaded with the static tangential force equivalent to 35 Nm as shown in Fig. 1 and validation is done analytically using Lewis theory as given in Table 1. Figure 2 shows the Von Mises and bending stress results obtained through FEM model.

3.3 Experimental Validation

The experimental validation of the Numerical Analysis has been done by comparing the FEM results with experimental results [1]. For gear with a backup ratio of 0.3, it was found in the experiments that the crack generated in the root of the tooth follows a path into the rim of the gear. Ultimately, fracturing the rim of the gear. While in case of backup ratio of 3.3, the crack originated in the root follows a path, tangential to the rim, into the tooth body which ultimately leads to the fracture of the tooth. Similar results are also obtained through the single tooth model. The experimental and FEM results for back up ratio 0.3 and 3.3 are shown in Figs. 3 and 4 respectively.

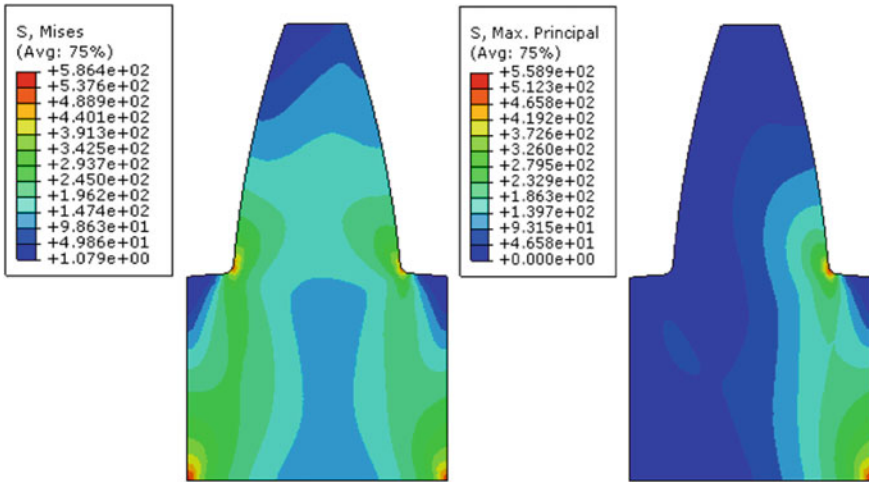


Fig. 2 Numerical results of Von Mises and bending stress respectively

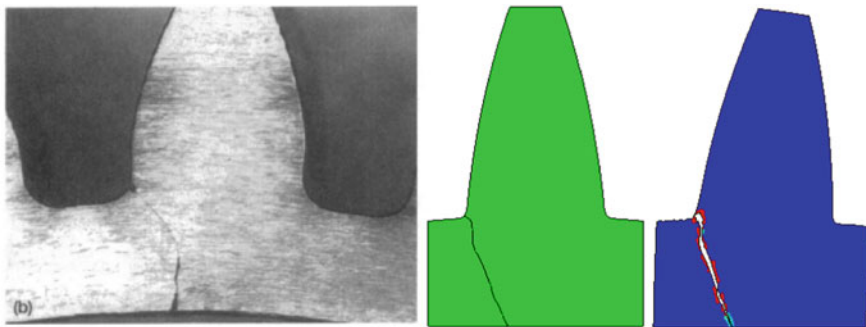


Fig. 3 Experimental [1] and numerical result for backup ratio 0.3

3.4 Path of Crack Propagation in Gear Tooth

Figure 5 shows the path of crack propagation and final fracture status for the initial crack lengths of 0.1, 0.3, 0.6 and 0.8 mm with initial orientation of 180°. The backup ratio taken in this study is 0.6.

Figure 6 shows the crack propagation path and final fracture status for the same initial crack lengths of 0.1, 0.3, 0.6, and 0.8 mm for 225° crack orientation.

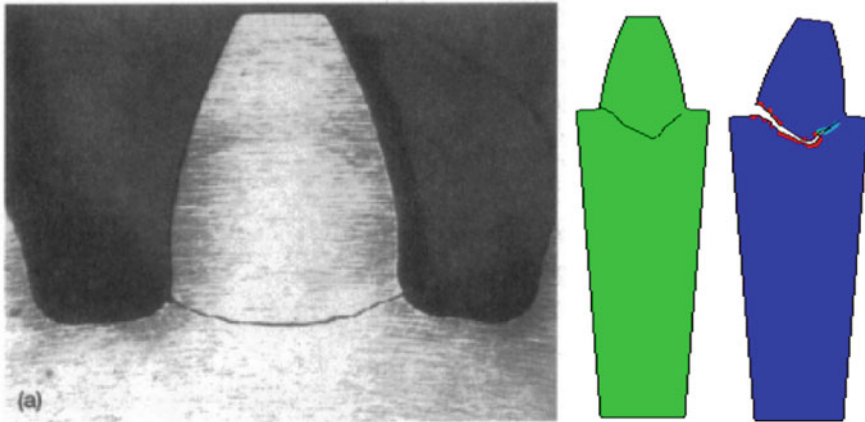


Fig. 4 Experimental and FEM result respectively for back up ratio 3.3

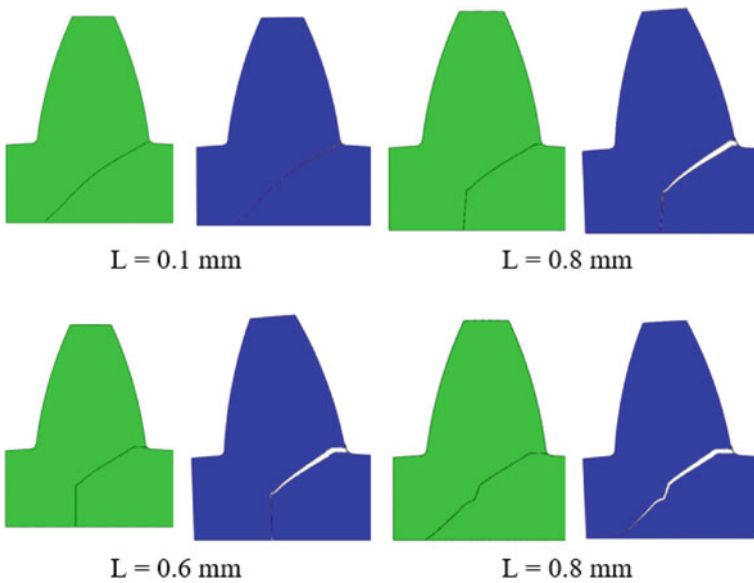


Fig. 5 FE result of different crack lengths with initial orientation 180°

4 Computational Results

4.1 Fault Analysis of Spur Gear

The gears are subjected to higher loads for a very long duration. The generation of higher stresses at the tooth root causes the initiation of the crack. The spur gear

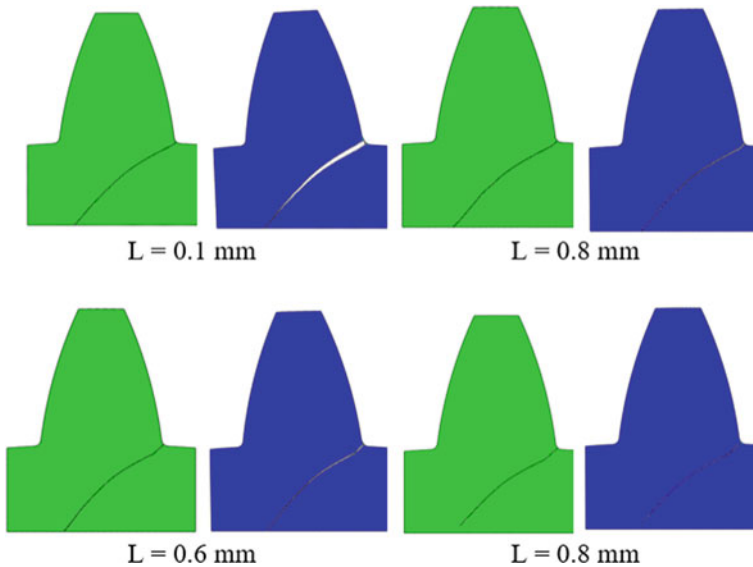


Fig. 6 FE result of different crack lengths with initial orientation 225°

significant induced the high bending stresses. Hence, in this work, the crack was placed at 180° and at 225° in the tooth root along the tooth thickness where the tensile bending stress is maximum. The crack propagation angles for these two orientation angles has been compared.

Figure 5 shows the path of crack progression when the initial orientation angle is kept at 180° . The results shows that for the backup ratio of 0.6 the chances for rim fracture are higher. The crack propagates toward the tooth width for half of its path. As the crack propagates, it starts penetrating deeper into the rim of the gear. It is found that as the length of initial crack is increased, the propagation path starts shifting closer to the tooth body, causing less penetration into the rim. For 0.3 and 0.6 mm initial crack lengths, the crack path shows a sudden shift toward rim, following a straight path and causing rim fracture.

When the initial crack angle is increased to 225° , the crack proceeds through a similar path for all initial crack length. It is found that initial crack length does not affect the propagation path for cracks with initial angle of 225° .

It has been stated by Lewicki et al. [1–3] path of crack propagation and its behavior is determined by backup ratio. It can be included further into this conclusion that initial length and angle of crack will also determine direction of crack propagation. In case of backup ratio 0.6, it is found that crack may propagate into both tooth and rim. It may lead to fracture of both tooth and rim and depends on the length of initial crack. Increase in length of initial crack increases the tooth damage.

4.2 Fatigue Life Analysis

Along with crack propagation path analysis, the effect of length and orientation angle of initial crack on the fatigue life of gear has also been studied. Figures 7, 8 and 9 shows the results for fatigue life analysis of gear for initial orientation angle of 180°. For 0.1 mm of initial crack length, the crack starts propagating around 164,000 cycles and fracture occurred after 375,000 cycles. When initial crack length is increased to 0.3 mm, significant decrease in cycles is observed. For 0.3 mm crack length, the crack start propagating around 30,000 cycles and fracture occurred after 115,000 cycles. Further reduction in gear fatigue life is observed for the crack length of 0.6 and 0.8 mm.

When the crack is placed at initial angle of 225°, the crack starts propagating around 51,000 load cycles and final fracture occurred after 176,000 cycles for 0.1 mm length of initial crack. Similar trend of decrease in load cycles for crack initiation and final fracture is observed for 0.3, 0.6 and 0.8 mm crack lengths. The results for fatigue life of gear with initial orientation of 225° is shown in Figs. 10, 11 and 12. The fatigue life of gear decreased with the increase in length of initial crack. However, it is higher for the orientation angle of 180° as compared to 225° orientation for all crack lengths.

The decrease in fatigue life with increase in length of initial crack can be attributed to the increase in SIF. The value of SIF increased with the increase in length of initial crack which lead to the fast propagation of crack. Also SIF value is higher for orientation angle of 225° as compared to 180° as shown in Figs. 8 and 11. It leads

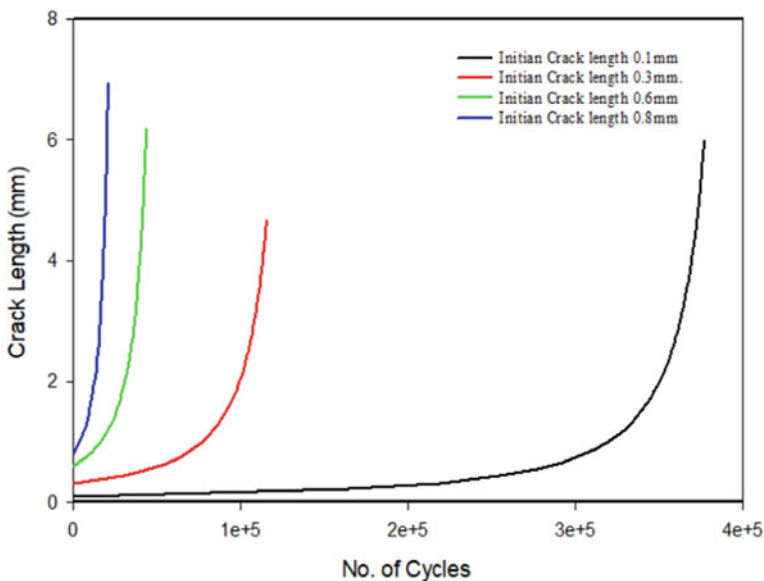


Fig. 7 Crack length versus number of cycles for 180° orientation

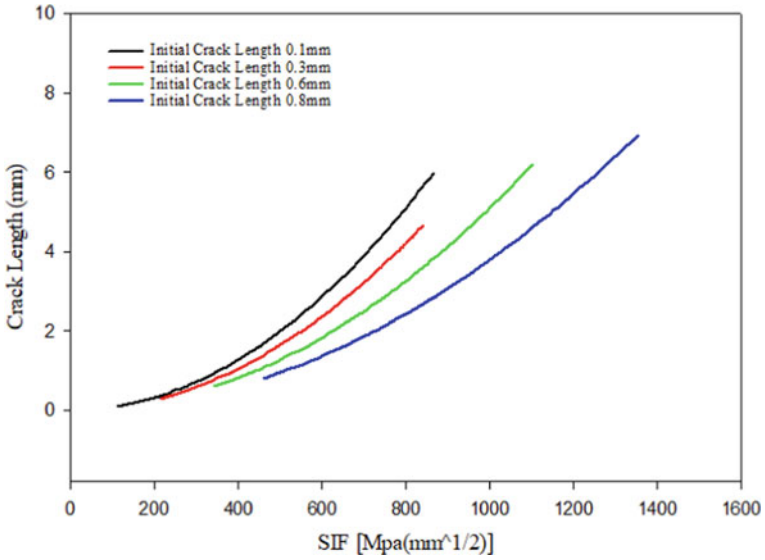


Fig. 8 Crack length versus stress intensity factor (SIF) for 180° orientation

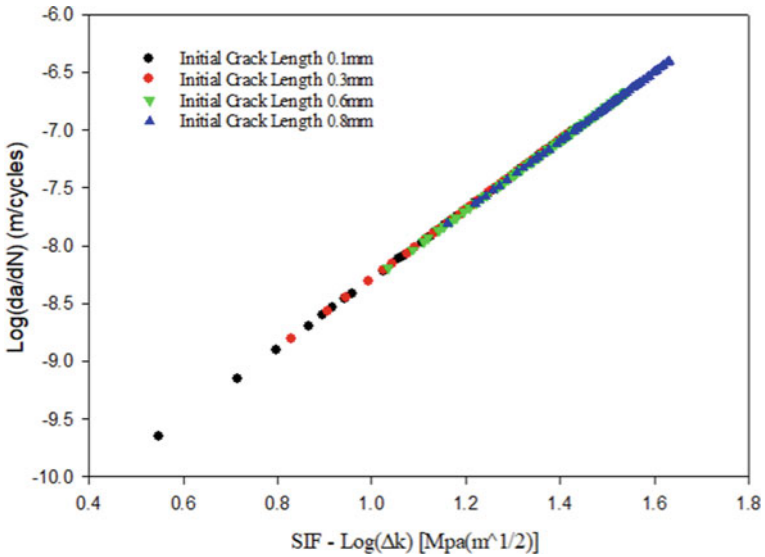


Fig. 9 Crack propagation rate (da/dN) versus SIF for orientation 180°

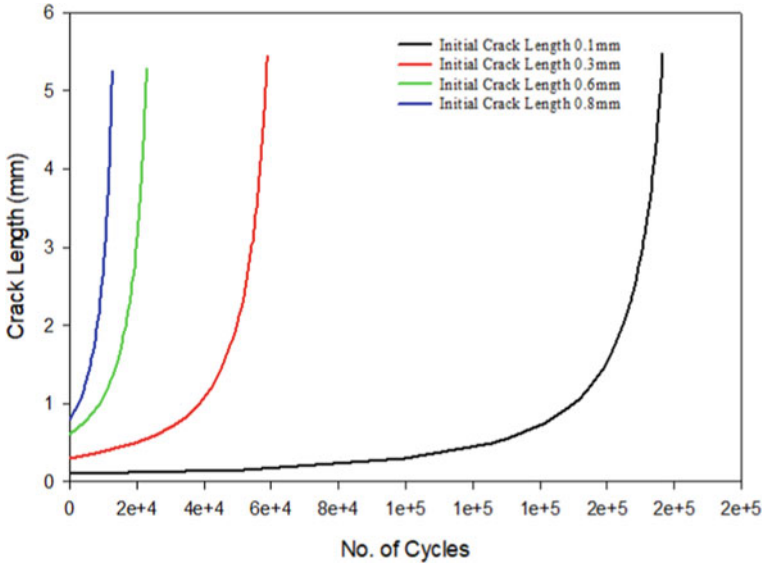


Fig. 10 Crack length versus number of cycles for 225° orientation

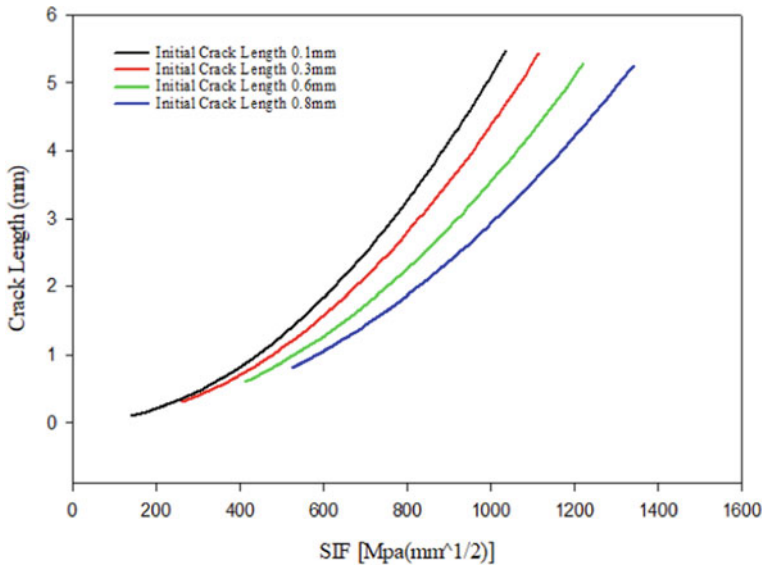


Fig. 11 Crack length versus stress intensity factor (SIF) for 225° orientation

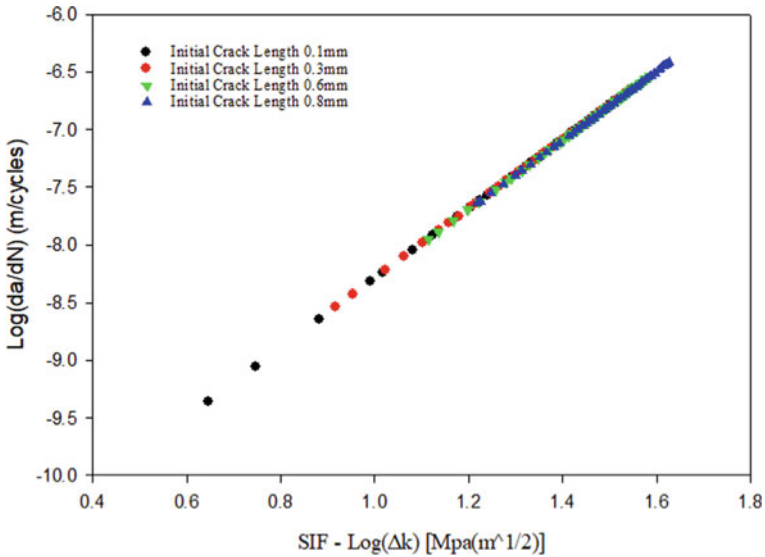


Fig. 12 Crack propagation rate (da/dN) versus SIF for orientation 225°

to the failure of gear at relatively low fatigue cycles. The crack propagation rate is shown in Figs. 9 and 12 for orientation angle 180° and 225° respectively.

5 Conclusions

The obtained results proves the efficiency of the FEM models to examine the crack propagation behavior for static loading. It is also not necessary to model complete gear. A single tooth model or a part of gear can be used for simulation and it will give the necessary insights.

Tooth root crack has been analyzed for two orientation angles with varying initial crack lengths. It can be noted that the crack propagation path damages tooth body in case of 180° orientation as compared to 225° . The crack placed at 180° orientation shows more variation in its path as compared to 225° orientation.

Apart from crack propagation path, gear fatigue life is also studied. It is found that the length of initial crack affects the crack initiation and fracture life as well. The fatigue life of gear depends on the orientation angle of the initial crack also. The gear in this study showed higher fatigue life with crack at 180° as compared to the 225° orientation for all crack lengths.

References

1. Lewicki DG, Gear crack propagation path studies-guidelines for ultra-safe design. *J Am Helicopter Soc* 64–72
2. Lewicki DG, Ballarini R (1997) Effect of rim thickness on gear crack propagation path. *J Mech Des* 119
3. Lewicki DG, Ballarini R (1997) Rim thickness effects on gear crack propagation life. *Int J Fract* 87:59–86
4. Belsak A, Flasker J (2007) Detecting cracks in the tooth root of gears. *Eng Fail Anal* 14:1466–1475
5. Kramberger J, Šraml M, Glodež S, Flašker J, Potrc I (2004) Computational model for the analysis of bending fatigue in gears. *Comput Struct* 82:2261–2269
6. Liang X, Zuo MJ, Pandey M (2014) Analytically evaluating the influence of crack on the mesh stiffness of a planetary gear set. *Mech Mach Theory* 76:20–38
7. Ma H, Song R, Pang X, Wen B (2014) Time-varying mesh stiffness calculation of cracked spur gears. *Eng Fail Anal* 44:179–194
8. Mohammed OD, Rantatalo M (2016) Dynamic response and time-frequency analysis for gear tooth crack detection. *Mech Syst Signal Process* 66:612–624
9. Chen Z, Shao Y (2011) Dynamic simulation of spur gear with tooth root crack propagating along tooth width and crack depth. *Eng Fail Anal* 18:2149–2164
10. Dadon I, Koren N, Klein R, Bortman J (2019) A step toward fault type and severity characterization in spur gears. *J Mech Des* 141(8)
11. Wu S, Zuo MJ, Parey A (2008) Simulation of spur gear dynamics and estimation of fault growth. *J Sound Vib* 317:608–624
12. Chaari F, Fakhfakh T, Haddar M (2009) Analytical modeling of spur gear tooth crack and influence on gearmesh stiffness. *Eur J Mech A Solids* 28(3):461–468
13. Zhou X, Shao Y, Lei Y, Zuo M (2012) Time-varying meshing stiffness calculation and vibration analysis for a 16 DOF dynamic model with linear crack growth in a pinion. *J Vib Acoust* 134
14. Mark WD, Reagor CP, McPherson DR (2007) Assessing the role of plastic deformation in gear-health monitoring by precision measurement of failed gears. *Mech Syst Sig Process* 21(1):177–192
15. Saxena A, Chouksey M, Parey A (2017) Effect of mesh stiffness of healthy and cracked gear tooth on modal and frequency response characteristics of geared rotor system. *Mech Mach Theory* 107:261–273
16. Chen Z, Zhai W, Shao Y, Wang K, Sun G (2016) Analytical model for mesh stiffness calculation of spur gear pair with non-uniformly distributed tooth root crack. *Eng Fail Anal* 66:502–514
17. Amiri Rad A, Forouzan MR, Sadeghi Dolatabadi A (2014) Three-dimensional fatigue crack growth modelling in a helical gear using extended finite element method. *Fatigue Fract Eng Mater Struct* 37(6):581–591
18. Raghav MS, Singh A, Patel S (2022) Fault analysis of spur gear using XFEM. *Eng Fail Anal* p 106060
19. Martínez JC, Useche LVV, Wahab MA (2017) Numerical prediction of fretting fatigue crack trajectory in a railway axle using XFEM. *Int J Fatigue* 100:32–49
20. Ghaffari MA, Pahl E et al (2015) Three dimensional fatigue crack initiation and propagation analysis of a gear tooth under various load conditions and fatigue life extension with boron/epoxy patches. *Eng Fract Mech* 135:126–146

Minimization of Structural Error of the Steering Mechanism of an Agricultural Harvesting Machine



Santiranjana Pramanik 

Abstract Kinematic synthesis has been carried out for a four-wheel vehicle named as power-frame to be used in orchard for harvesting fruits. The vehicle is collapsible to half size along its width. The steering mechanism is such that the vehicle can be steered both on the road and on the field with little modification. Precision point synthesis method has been used to minimize the steering error for seventy degree rotation of the inner wheel. We study this compound mechanism as addition of two as well as four identical crossed four-bar mechanisms (CFBM) in series. At first the kinematic synthesis has been carried out for one CFBM only and not entire mechanism. The maximum steering error of the proposed mechanism has been found to be small and the maximum value of pressure angle is within an acceptable limit. Then kinematic synthesis has been carried out by Hooke and Jeeves optimization method for the entire mechanism having four CFBMs. The steering error is again very small and five precision points have been found for steering on the road as well as on the field.

Keywords Four-wheel power-frame · Steering mechanism · Optimization

1 Introduction

Steering mechanisms play an important role in automobiles whenever there is need to change the direction of its motion. Several types of steering mechanisms are available for four-wheel vehicles. These are Ackermann steering mechanism, center-lever steering mechanism and rack-and-pinion steering mechanism. Ackermann steering mechanism is the most simple in construction. But this mechanism has a drawback that the steering error gradually increases while the inner wheel approaches the end of range of rotation. Even then it is used in buses and trucks for its simple construction. A large extent of research has already been carried out by researchers and few of these researches are mentioned below.

S. Pramanik (✉)

College of Military Engineering, Pune, Maharashtra 411031, India

e-mail: santiranjana_pramanik@rediffmail.com

Simionescu and Smith [1] considered both leading and trailing types of center-lever steering linkages and found the initial estimates for the design parameters. A mechanism is called a leading mechanism when all links are placed ahead of the front axle. On the other hand a mechanism is called a trailing mechanism when all links are placed behind the front axle. These authors developed design charts for both leading and trailing type center-lever steering mechanisms. These charts were helpful for the automobile engineers who carried out the research and development activities on steering mechanisms.

De-Juan et al. [2] synthesized central-lever steering mechanisms which were both leading and trailing types. It has been observed from their research that five precision points can be achieved in the steering error curve for leading mechanism only.

De-Juan et al. [3] investigated various types of leading steering linkages like four-bar, center-lever type and rack-and-pinion type steering. They compared these mechanisms after optimizing the steering errors by including the transmission angles.

Peterson and Kornecki [4] considered a steering mechanism of a vehicle used for agricultural harvesting. This vehicle was used for harvesting fruits from the orchards. This was called as power-frame which needed track to wheelbase ratios 0.775 and 1.55 both. The vehicle could be collapsed to half the width while it was to be transported on the road. The track to wheelbase ratio was 1.55 while the power-frame was used to harvest fruits from the orchard and 0.775 while the collapsed power-frame was to move on the road. They used a five-bar linkage which used a guide plate having a curved groove. One hinge joint had to move along the curved groove which was symmetrical in nature. The steering accuracy was exactly maintained up to sixty degree rotation of the inner wheel. However after that amount of rotation the error increased sharply.

Pramanik and Thipse [5] carried out kinematic synthesis of a CFBM using precision point method and optimization method both. In precision point method they considered two precision points and two design parameters. Two non-linear equations were framed and the solution of this set of equations was found out using Newton-Raphson method. In optimization method they minimized the steering error by application of Hooke and Jeeves method. The objective function comprising of squares of steering errors was minimized by direct method. Both the methods gave good results.

Pramanik and Thipse [6] considered a compound mechanism which can be used for steering of automobiles. This compound mechanism comprises of two CFBMs connected in series. They showed that their method simplified the method of kinematic synthesis and explained that four such CFBMs can also be added serially to achieve higher value of wheel track by wheelbase ratio.

The aim of steering mechanism design is to provide such a mechanism that has low steering error, high mechanical advantage and simple construction. The accuracy of the steering mechanism has to be increased in order to ensure smooth turning at the corner and to increase the life of tyres by reducing wear on the surfaces of the wheels.

The aim of the present study is to find out a mechanism which can be suitable for two different values of track to wheelbase ratios. This is required for an agricultural

harvesting machine which is foldable. That means the track to wheelbase ratio has two values, one value is twice the other. The present work considers a mechanism consisting of two as well as four crossed four-bar mechanisms (CFBM) according to the requirement. Kinematic synthesis of the steering linkage has been carried out using two design parameters and steering error has been minimized for both cases. This paper has demonstrated that a CFBM can become a simple chain which can be added in even numbers to form a compound mechanism with large value of track to wheelbase ratio of a power-frame to be used for agricultural harvesting.

The mechanism used earlier for steering such a vehicle has been explained in Ref. [4]. The performance of this steering mechanism depends on the accuracy of cutting a groove on flat plate that guides the movement of a hinge joint. That is why a different type mechanism has been suggested in this study after examination of steering accuracy and pressure angles.

The track to wheelbase ratio is 1.55 which is very high for this vehicle and this value is adjustable for two different places like roads and field. The compound mechanism suggested in Ref. [6] is particularly suitable for such requirements. This is the motivation for the present study.

2 Ackermann Condition of Steering

A steering mechanism is theoretically correct if all wheels rotate about a common center called the instantaneous center of rotation. Figure 1 indicates that the inner and outer wheels are rotated by angle γ and α respectively so that the steering action is correct by making all four wheels to rotate about a common center O.

From this geometry one can write the following equation:

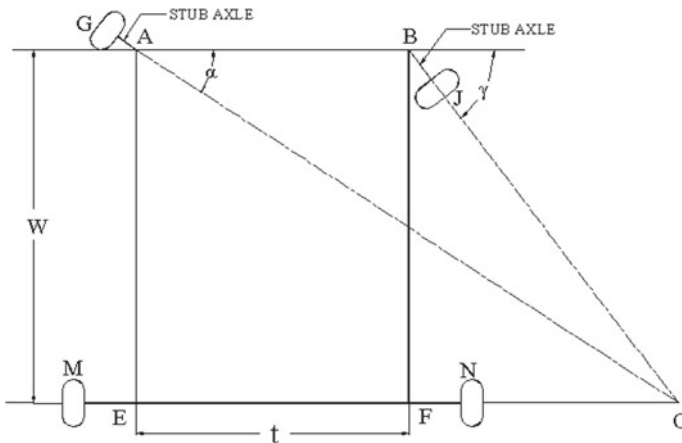


Fig. 1 Wheel positions for correct steering

$$\cot \alpha - \cot \gamma = \frac{t}{w} \tag{1}$$

where, 't' is the wheel track and 'w' is the wheelbase.

In Fig. 2, AGFB is a CFBM which is the basic kinematic chain that has been repeated to make the final steering mechanism to be used in the field as well as on the roads. Two such kinematic chains are to be used on the roads to make a track to wheel base ratio 0.775. But four such kinematic chains are to be used in the field to make track to wheelbase ratio 1.55. In this mechanism links AG and BF are equal in length. These two links make equal angle with the vehicle longitudinal axis while the vehicle moves along a straight path. This means that the angles KAG and FBH are equal. These angles are denoted by β which is one design parameter k_2 . The distance AB is taken as d . The steering arm AG and BF are equal to r and the ratio r/d is k_1 which is another design parameter. When the arm AG rotates by angle GAD (α), then the arm BF rotates by angle FBE (ϕ).

The co-ordinates of the points D and E are as under.

$$D = \{r \sin(\beta + \alpha), -r \cos(\beta + \alpha)\} \text{ and } E = \{d + r \sin(\phi - \beta), r \cos(\phi - \beta)\}$$

Now $DE^2 = GF^2$ gives the following relation.

$$\begin{aligned} \{d + r \sin(\phi - \beta) - r \sin(\beta + \alpha)\}^2 + \{r \cos(\phi - \beta) + r \cos(\beta + \alpha)\}^2 \\ = (d - 2r \sin \beta)^2 + (2r \cos \beta)^2 \end{aligned}$$

Writing $r/d = k_1$ and $\beta = k_2$ we get

$$\{1 + k_1 \sin(\phi - k_2) - k_1 \sin(k_2 + \alpha)\}^2 + k_1^2 \{\cos(\phi - k_2) + \cos(k_2 + \alpha)\}^2$$

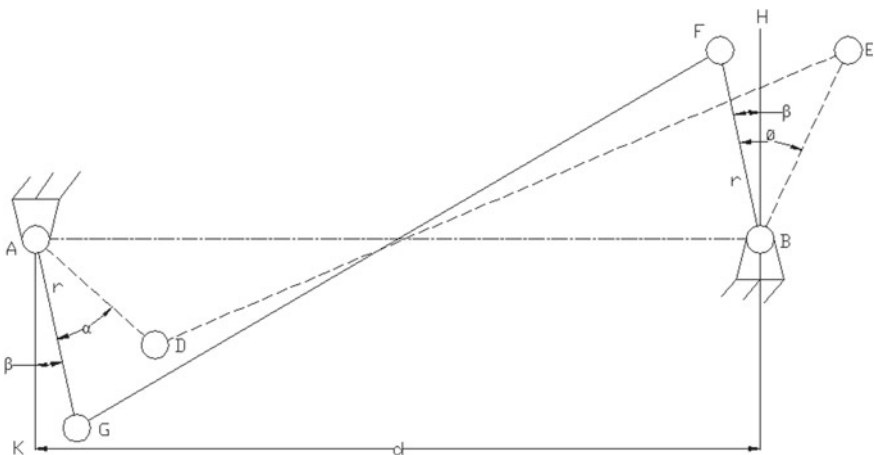


Fig. 2 Crossed four-bar mechanism

$$= \{1 - 2k_1 \sin(k_2)\}^2 + 4k_1^2 \cos^2(k_2)$$

Finally this equation was reduced to the following equation which had been shown in detail in Ref. [5].

$$k_1\{\cos(\alpha + \theta) - 1\} - \sin(k_2 - \theta) - \sin(k_2 + \alpha) + 2 \sin(k_2) = 0 \tag{2}$$

3 Numerical Analysis

Equation (2) has two unknown design parameters k_1 and k_2 . There are two precision points $\theta = 42^\circ$ and 70° . These two non-linear equations are solved by using Newton–Raphson method which has been explained in Ref. [5].

The combination (α_i, θ_i) in Eq. (2) are written below where $i = 1, 2$.

$$\alpha_1 = 33.72^\circ, \theta_1 = 42^\circ \text{ and } \alpha_2 = 53.08^\circ, \theta_2 = 70^\circ$$

The following initial estimate for the root of the system of Eq. (2) has become suitable to arrive at the final solution.

$$r = 0; k_{10} = 0$$

$$\beta = 0; k_{20} = 0$$

The wheel track to wheel base ratio has been taken as 1.55 for the power-frame as in Ref. [4]. Since there are four CFBMs, the wheel-track by wheel base ratio should be $1.55 \div 4 = 0.3875$ for each CFBM. The precision points for the last CFBM are taken as 42° and 70° rotations of the inner wheel. The maximum rotation of 70° has been taken from the example of Ref. [4]. However, this value can be taken arbitrarily.

The solution to the non-linear equations is found as under:

$$k_1 = 0.38949; k_2 = 0.467916 \text{ radian} = 26.80962^\circ$$

The dimensions of various links are $d = 10$ unit; $r = 3.8949$ unit; $\beta = 26.80962^\circ$.

The vehicle has track to wheelbase ratio 0.775 and 1.55 for transporting on roads and harvesting on the field respectively. Utilizing the conception of compound mechanisms, the track to wheelbase ratio for one CFBM has been taken as 0.3875.

4 Result

The steering error of the vehicle has been calculated for 70° rotation of the inner wheel for moving on the road and harvesting on the field also. Figure 3 shows the steering error. The maximum steering error is about 0.27°.

The variation of the pressure angles has been shown in Fig. 4. The pressure angles shall be different for different CFBM of the compound mechanism and it will be crucial for the last CFBM in which rotation of the arm is a maximum. The maximum values of the pressure angle at joint D and E in Fig. 4 are high and one should reduce the maximum rotation of the inner wheel so that the maximum value of pressure angle remains within acceptable limit.

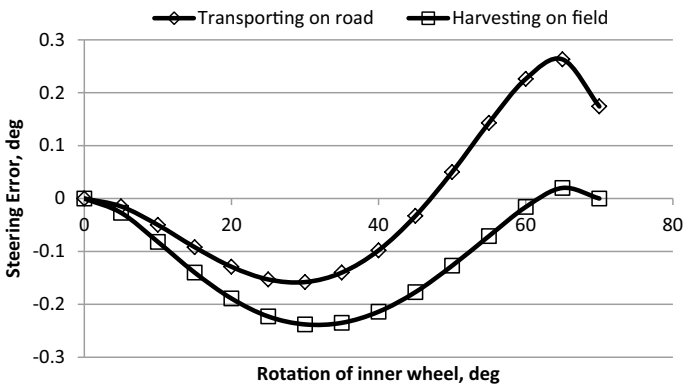


Fig. 3 Steering error curve

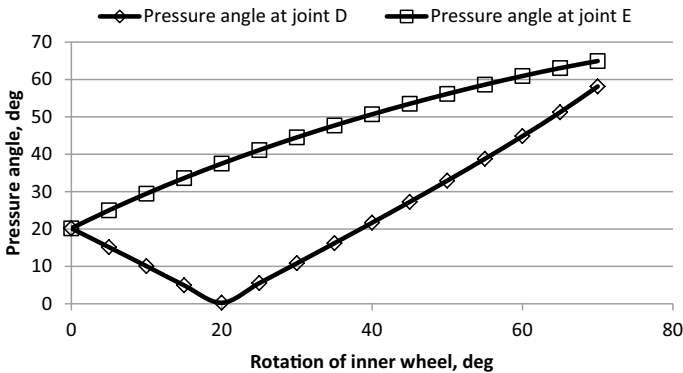


Fig. 4 Variation in pressure angles in the steering mechanism

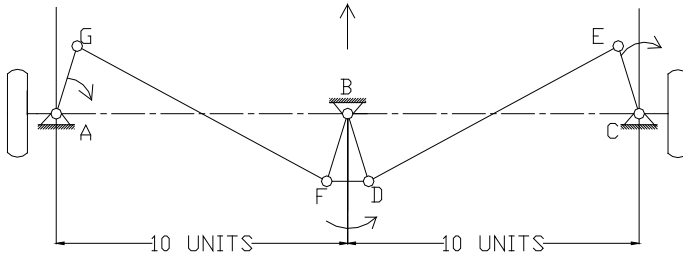


Fig. 5 Compound steering mechanism while transporting on road

4.1 Compound Mechanism for Use on Road

This compound mechanism comprises of two mirrored CFBMs as shown in Fig. 5. The track to wheelbase ratio of this is 0.775 which is required for this vehicle in collapsed condition for transportation on the road. The wheel track AC of this vehicle 2165 mm is represented as 20 units. Hence one unit represents 108.25 mm in this figure. The wheelbase of the vehicle is 2794 mm. The length of the arms CE, BD, BF and AG is 3.8949 units which is equal to 421.6 mm. The length of the coupler GF and DE is 1029.3 mm.

4.2 Compound Mechanism for Use on Field

This compound mechanism comprises of four CFBMs as shown in Fig. 6. The track to wheelbase ratio of this is 1.55 which is required for this vehicle while harvesting on the field. The wheel track AE of this vehicle is 4330 mm which is represented as 40 units. Hence one unit represents 108.25 mm in this figure. The wheelbase of the vehicle is 2794 mm. The length of the arms AM, BL etc. is 3.8949 units which represents 421.6 mm. The length of the coupler ML, KJ etc. is 1029.3 mm.

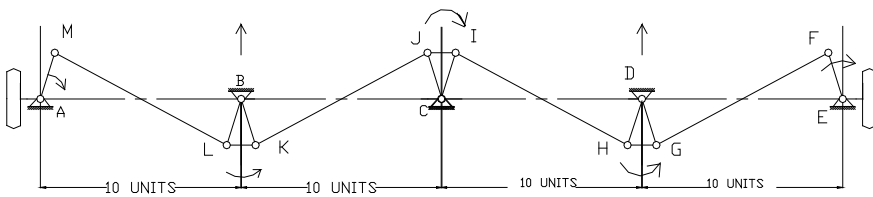


Fig. 6 Compound steering mechanism while harvesting on field

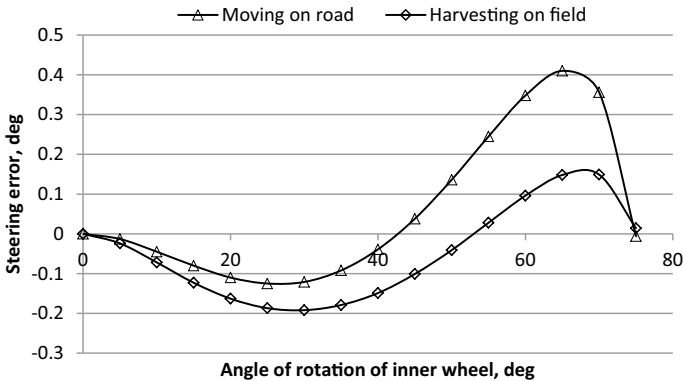


Fig. 7 Steering error curves for synthesis of entire mechanism

4.3 Result of Kinematic Synthesis for Entire Mechanism

Kinematic synthesis has been made for the entire mechanism comprising of four CFBMs by using Hooke and Jeeves optimization method [6]. The initial estimate is as under.

$$r = 3.8949 \text{ units and } \beta = 26.8^\circ$$

The final estimate is given below.

$$r = 3.9049 \text{ units and } \beta = 26.8175^\circ$$

The steering error curves for fully expanded vehicle and folded vehicle are shown in Fig. 7. The steering error is very low and three precision points are obtained in each curve.

5 Conclusion

It has been shown that we have to add two CFBMs in series when we want to steer the vehicle in collapsed condition while transporting on the roads. Again we have to add four CFBMs in series when we want to use the steering mechanism for the expanded condition of the vehicle in the field. This proposed mechanism is better than the mechanism suggested by Peterson and Kornecki in the following ways.

- (1) In the presently suggested mechanism the basic CFBM is same for both places—the road and the field. Therefore, it is easier to convert from one configuration to the other configuration. Whereas for the mechanism suggested by

Peterson and Kornecki [4] when one wants to change the place of work from road to the field, he has to use different size of the steering arm and the coupler.

- (2) In the presently suggested mechanism the steering error is less than that of the previous mechanism in the extreme end rotations like 60° to 70° rotation of the inner wheel. In case of the mechanism by Peterson and Kornecki this error is 2.1° , while in the presently suggested mechanism this error is 0.27° .

The major findings are listed below.

- (1) Kinematic synthesis of a single CFBM using precision point method has given a low steering error of 0.24° over a range of rotation of 70° of the inner wheel of the compound mechanism comprising of four CFBMs. The design parameters for this case are $r = 3.8949$ and $\beta = 26.80962^\circ$. Using these same design parameters the compound mechanism comprising of two CFBMs is used for transportation on roads. However the maximum steering error for this configuration is 0.26° for a range of rotation of 70° of the inner wheel.
- (2) Application of direct method using Hooke and Jeeves optimization has also become successful to minimize the steering error to 0.19° for the compound mechanism comprising of four CFBMs. The design parameters for this case are $r = 3.9049$ and $\beta = 26.8175^\circ$. Using these same design parameters the compound mechanism comprising of two CFBMs is used for transportation on roads. However the maximum steering error for this configuration is 0.41° for a range of rotation of 70° of the inner wheel.

Thus the steering error of the entire mechanism comprising of four CFBMs and of two CFBMs has been minimized by Hooke and Jeeves optimization method as well as precision point method.

References

1. Simionescu PA, Smith MR (2002) Initial estimate in the design of central-lever steering linkages. *ASME J Mech Des* 124:646–651
2. De-Juan A, Sancibrian R, Viadero F (2012) Optimal synthesis of function generation in steering linkages. *Int J Automot Technol* 13(7):1033–1046
3. De-Juan A, Sancibrian R, Viadero F (2009) Optimal synthesis of steering mechanism including transmission angles. In: Ceccarelli M (ed) *The second European conference on mechanism science 2008*. Springer, Netherlands, pp 177–183
4. Peterson DL, Kornecki TS (1986) Steering mechanism for wide-track vehicles. *Appl Eng Agric* 2(1):16–17
5. Pramanik S, Thipse SS (2019) Kinematic synthesis of a crossed four-bar steering linkage for automobiles. In: Prasad A, Gupta SS, Tyagi RK (eds) *1st International conference on future learning aspects of mechanical engineering 2018, LNME*, Springer, Singapore, pp 503–508
6. Pramanik S, Thipse SS (2020) Kinematic synthesis of central-lever steering mechanism for four wheel vehicle. *Acta Polytech* 60(3):252–258

Design of Differential Mounts and Rear Inboard Braking for an FSAE Vehicle



Shubhayu Das, Pragma Gogoi, Mihir Agrawal, Rounak Deswal,
and Lokavarapu Bhaskara Rao

Abstract The paper depicts the design and optimization of differential mounts of an FSAE vehicle along with the effects of rear inboard braking on it to produce an efficient and performance-based output. With increasing competition in the motorsport world, the application of mechanisms like inboard braking can be a difference in outcomes. The paper also depicts the applicability of the same in the real world and its benefits like reduction of unsprung mass, relieving the designer from usual problems like clearance measurements, wheel fitting, etc. The difference and advantage of the system are prominent as we use a single rotor and caliper mount along with the calipers, whereas if the vehicle would have undergone a conventional outboard braking assembly it would comprise twice the number of these parts and an increased wheel hub mass due to the rotor mounts required. Drexler's limited slip differential has been chosen as the differential for the research considering its properties, and the differential mounts are designed to be able to withstand the rotational moment of the sprocket and frictional force induced between the rotor and brake pads.

Keywords Braking system · Rotor · Analysis · Differential · Differential mounts · Simulation

S. Das · P. Gogoi · M. Agrawal · R. Deswal · L. Bhaskara Rao (✉)
School of Mechanical Engineering, Vellore Institute of Technology, Chennai Campus,
Vandalur-Kelambakkam Road, Chennai, Tamil Nadu 600127, India
e-mail: bhaskarbabu_20@yahoo.com

S. Das
e-mail: shubhayu.das2018@vitstudent.ac.in

P. Gogoi
e-mail: pragya.gogoi2018@vitstudent.ac.in

M. Agrawal
e-mail: mihirrajesh.agrawal2018@vitstudent.ac.in

R. Deswal
e-mail: rounak.deswal2018@vitstudent.ac.in

Nomenclature

FSAE	Formula society of automotive engineers
ABS	Antilock braking system
ATV	All-terrain vehicle
CAE	Computer-aided engineering
MIT	Massachusetts Institute of Technology
FEA	Finite element analysis
OEM	Original equipment manufacturer
AISI	American Iron and Steel Institute
CAD	Computer-aided designing
PCD	Pitch circle diameter
FOS	Factor of safety

1 Introduction

A braking system not only provides the vehicle the ability to stop or slow down but also plays a vital role in the handling and maneuvering of the vehicle. For this research, antilock braking system (ABS) is not used. Inboard braking for the rear wheels (driven wheels) is being used to exploit the advantages coming with it like reduction of the unsprung mass of the vehicle, as in this case, a single rotor is to be mounted on the differential along with the calipers, whereas in the case of an outboard system, we would require twice the number of rotors and calipers fitted on the hubs and uprights, respectively. Besides this, it also allows choosing a greater wheel, giving more flexibility in choosing tire diameters. To accommodate the inboard braking system, the differential mounts have been made to carry the rear brake caliper. The calculations of the differential mounts along with optimization of part were carried out as per requirements.

Study of existing literature on related topics was done to optimize the research and its results. Sharma et al. [1] carried out a study for the design, analysis, and fabrication of a braking system with the rear inboard brakes in BAJA ATV, exhibiting the performance of disk brakes with rear inboard braking system along with its utility. Rana et al. [2] optimized the design of a braking system for a Formula 3 race car with numeric computations and thermal analysis that primarily focused on weight reduction of brake system with the usage of disk rotor and bike calipers. James [3] worked on the design of an aluminum differential housing and driveline components to be used in an MIT Formula SAE 2004 vehicle to come up with a high performance generating, lightweight, limited slip differential and to replace cast iron housing in Torsen® T-1.

Scelfo [4] also worked on optimization for MIT Formula SAE 2006 race car with the design of a complete driveline package and aluminum limited slip differential housing for saving weight and modular integration implementation. Mora

[5] designed a braking system for the MIT motorsports team that focused on the consistent and reliable deceleration of the vehicle by the driver with a maximum deceleration rate that the traction limit of the tires allows. Galbincea [6] came up with a hydraulics-based braking system that implemented the concept of single man performance with the goal of converting kinetic energy to thermal energy in the vehicle so that it can have a safe, optimal deceleration. Casella et al. [7] worked on an optimized design of an FSAE car with the main goals focused on weight reduction and improved robustness and competition performance. Zankat [8] worked on reduction gearbox with an inboard braking system for an all-terrain vehicle (ATV) aiming at gear ratio reduction so that the torque requirements of ATV are effectively met and also for rear compartment inboard braking system implementation. Chavan et al. [9] worked on the design and manufacturing of the braking system of an ATV, and it was found that significant weight reduction and braking efficiency were achieved with the usage of inboard braking system design, and the system was able to fulfill the ATV braking system objectives.

Bulsara et al. [10] designed and tested for performance and reliability in an FSAE car that yielded that 40 kg pedal force is required to be applied by the driver for gaining the system's maximum potential which was quite lesser than an average person's average panic braking force, verified using track testing.

After studying the available research papers on the topic concerned, the following literature gaps were identified:

- Literature for use of the inboard braking system in FSAE events.
- The study of forces experienced by the differential during differential locking during rear inboard braking.
- Material study and optimization of the differential housing to facilitate weight reduction and easy integration into the FSAE cars.

Hence, in light of the above, this paper discusses the design of an FSAE vehicle with the implementation and study of the effects of the inboard braking system. An optimized, effective model has been designed with the material study of differential mounts and rear brake rotor. Part consolidation has been considered too.

2 Braking System

The braking system has been designed to perform using dual independent hydraulic systems for both the front and the rear brakes [11]. The properties of the master cylinders and the calipers have been depicted in Table 1 [12].

Table 1 Master cylinder and caliper properties

Master cylinder			Caliper (front and rear)	
Location	Front	Rear	Model	Wilwood GP200
Model	Tilton SKU-76XXX		Piston dia. (in)	1.25
Bore dia. (in)	0.750	0.625	No. of pistons	2
Stroke (mm)	27	27	Pad volume (in ³)	0.34

3 Brake Calculations

The calculations for the braking system were done for both static and dynamic conditions using the required data from a similar standard vehicle. The vehicle dimensions and weights have been based on Zuura Formula Racing’s vehicle for 2019 season.

3.1 Static Loading

Mass of the vehicle (W) = 273 kg = 273 * 9.81 N = 2678.13 N \approx 2680 N.

Weight ratio (front: rear) = 45:55 (weights at the touchpoints for individual wheels).

Wheelbase (L) = 1545 mm = 1.545 m.

L_1 = Distance of center of gravity from front axle = 0.850 m.

L_2 = Distance of center of gravity from rear axle = 0.695 m

$$\text{Front axle static load} = \frac{W * L_2}{L} = \frac{2680 * 0.695}{1.545} = 1205.566N \tag{1}$$

$$\text{Rear axle static load} = \frac{W * L_1}{L} = \frac{2680 * 0.850}{1.545} = 1474.434N \tag{2}$$

3.2 Dynamic Loading

Height of center of gravity (h) = 513 mm = 0.513 m.

Radius of tire (R) = 0.229 m.

Coefficient of friction between road and tire (μ_r) = 0.6 [1]

$$\begin{aligned} \text{Frictional force on wheels} &= F_f = \mu_r N = \mu_r mg \\ &= 0.6 * 273 * 9.81 = 1606.87N \end{aligned} \tag{3}$$

$$\text{Force due to deceleration(d)} = F_i = md = 273 * d \tag{4}$$

$$F_f = F_i \quad (5)$$

$$1606.878 = 273 * d$$

$$d = 5.886 \text{ m/s}^2$$

$$\frac{d}{g} = 0.6$$

Dynamic Load Transfers

$$\begin{aligned} \text{Front axle dynamic load} &= W_{fd} = \frac{W[L_1 + (d/g)h]}{L} \\ &= \frac{2680[0.850 + (0.6)0.513]}{1.545} = 2008.352 \text{ N} \end{aligned} \quad (6)$$

$$\begin{aligned} \text{Rear axle dynamic load} &= W_{rd} = \frac{W[L_2 + (d/g)h]}{L} \\ &= \frac{2680[0.695 + (0.6)0.513]}{1.545} = 1739.488 \text{ N} \end{aligned} \quad (7)$$

$$\begin{aligned} \text{Frictional torque required at front}(T_f) \\ &= \mu_r * W_{fd} * R = 0.6 * 2008.352 * 0.229 = 275.947 \text{ Nm} \end{aligned} \quad (8)$$

$$\begin{aligned} \text{Frictional torque required at rear}(T_r) \\ &= \mu_r * W_{rd} * R = 0.6 * 1739.488 * 0.229 = 239.006 \text{ Nm} \end{aligned} \quad (9)$$

Brake Rotor Diameters

Brake biasing = front: rear = 70: 30.

Diameter of front master cylinder piston = 0.01905 m [12]

$$\begin{aligned} \text{Area of front master cylinder piston } A_{mc(f)} \\ &= \pi \left(\frac{0.01905}{2} \right)^2 = 0.000285 \text{ m}^2 \end{aligned} \quad (10)$$

Diameter of rear master cylinder piston = 0.015875 m [12]

$$\begin{aligned} \text{Area of rear master cylinder piston } A_{mc(r)} \\ &= \pi \left(\frac{0.015875}{2} \right)^2 = 0.000198 \text{ m}^2 \end{aligned} \quad (11)$$

Area of caliper piston (A_c) = 0.000793 m².

Pedal ratio = $p = 4$.

Pedal force by driver = 250 N.

Force on balance bar = $4 * 250 = 1000$ N.

Coefficient of friction between brake pad and rotor (μ_d) = 0.4

For Front Wheels (Outboard)

Actuation force at master cylinder (front) = $0.70 * 1000 = 700$ N.

Pressure inside master cylinder = Force/Area = $700/0.000285 = 2.46$ MPa.

Force at caliper = $2.46 \times 10^6 * 0.000793 = 1950.78$ N.

Clamping Force = $2 * 1950.78 = 3901.56$ N

$$\text{Frictional force by brake pads on rotor} = 3901.56 * \mu_d = 1560.624 \text{ N} \quad (12)$$

$$\text{Braking Torque} = \text{Frictional force} * \text{Effective Radius} \quad (13)$$

$$137.973 = 1560.624 * R_{ef}$$

Effective radius (R_{ef}) = 0.088 m = 88 mm.

Rotor radius considering clearance of 5 mm (R_f) = $88 + 5 = 93$ mm.

Final rotor diameter = 186 mm.

For Rear Wheels (Inboard)

Actuation force at master cylinder (rear) = $0.30 * 1000 = 300$ N.

Pressure in master cylinder (rear) = Force/Area = $300/0.000198 = 1.5$ MPa.

Force at caliper = $2 * \text{Pressure} * \text{Area} = 2 * 1.5 \times 10^6 * 0.000793 = 2379$ N

$$\text{Frictional force by brake pads} = 2379 * \mu_d = 2379 * 0.4 = 951.6 \text{ N} \quad (14)$$

Braking Torque = Frictional force * Effective Radius of braking

$$119.503 = 951.6 * R_{er} \quad (15)$$

Effective radius (R_{er}) = 0.125 m = 125 mm.

Rotor diameter considering clearance of 5 mm (R_r) = $2(125 + 5) = 260$ mm.

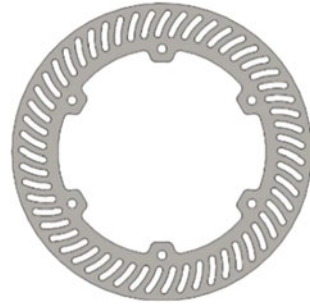
4 Material Selection of the Rear Rotor

The material of the rotor was selected majorly based on the thermal properties because the material must not show a very high rise in temperatures as the rear rotor is not expected to receive adequate fresh cooling air for being placed just behind the engine.

Table 2 Comparison of materials for rear brake rotor

Material	Mild steel	AISI-304	AISI-430	Cast iron
Mass of rotor (g)	568.100	578.900	560.800	497.100
Specific heat capacity (C_p)(J/kg-K)	510.796	502.416	460.550	468.532
Rise in temperature ($^{\circ}$ C)	47.886	47.772	53.796	57.445

Fig. 1 CAD model of the rear brake rotor



For comparison, the heat distribution was taken to be even overall although it is not the real-case scenario. Equation (16) was used to compare the materials.

Kinetic Energy of the Vehicle = Heat Energy Generated.
 thus,

$$\frac{1}{2}Mv^2 = m * C_p * dT * n \tag{16}$$

where

- M = mass of the vehicle = 273 kg.
- v = velocity of the vehicle = 16.67 m/s.
- m = mass of the rotor.
- n = total number of rotors in the vehicle = 3.
- dT = rise in temperature.
- C_p = specific heat capacity of the material.

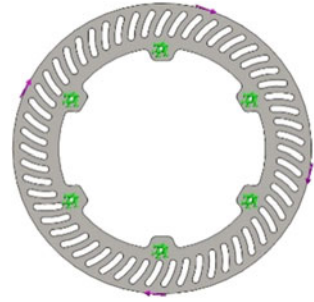
Table 2 depicts the material comparison for the rear rotor.

Material showing the lowest change in temperature was considered for the rotor, and hence, AISI-304 was chosen. Figure 1 shows the rotor design done on solidworks [13].

5 Static Analysis of the Rear Rotor

The static analysis of the rotor was done using the solidworks simulation tool [13]. The target was to achieve working stress below the yield stress of the material and

Fig. 2 Input parameters for the stress analysis of the rear rotor



factor of safety (FOS) of above 2 so that the part can withstand any sudden forces in dynamic conditions. The force calculations were used to determine the input parameters of the simulation for which the output was targeted. The bolting points of the rotor with the rotor mount were fixed using fixed geometry, and torque was applied on the outer diameter of the rotor. The torque was taken as the sum of the differential torque (592.356 Nm) and the braking torque (119.503 Nm). Figure 2 shows how the input parameters were given.

Meshing was done using the default fine mesh setting of the software and the simulation was performed to get the results. Figure 3 depicts the results obtained from the simulation.

From the simulation results, the maximum induced stress in the rotor ($9.317 \times 10^7 \text{ N/m}^2$) is found to be less than the yield stress of the material ($2.068 \times 10^8 \text{ N/m}^2$) and the minimum FOS is 2.2. Thus, the design is taken to be safe for performing under the calculated loads.

6 Thermal Analysis of the Rear Rotor

Along with the stress analysis, the thermal analysis was also important for the rotor as the brake pads are expected to create a considerable amount of frictional force. The stopping time of the vehicle is calculated to find out the duration for which the force acts on the rotor.

$$\text{Deceleration } (d) = 5.886 \text{ m/s}^2.$$

$$\text{Initial velocity } (u) = 16.67 \text{ m/s.}$$

$$\text{Final velocity } (v) = 0 \text{ m/s.}$$

$$\text{Time to stop} = t$$

$$v = u - dt \tag{17}$$

$$0 = 16.67 - (5.886)t$$

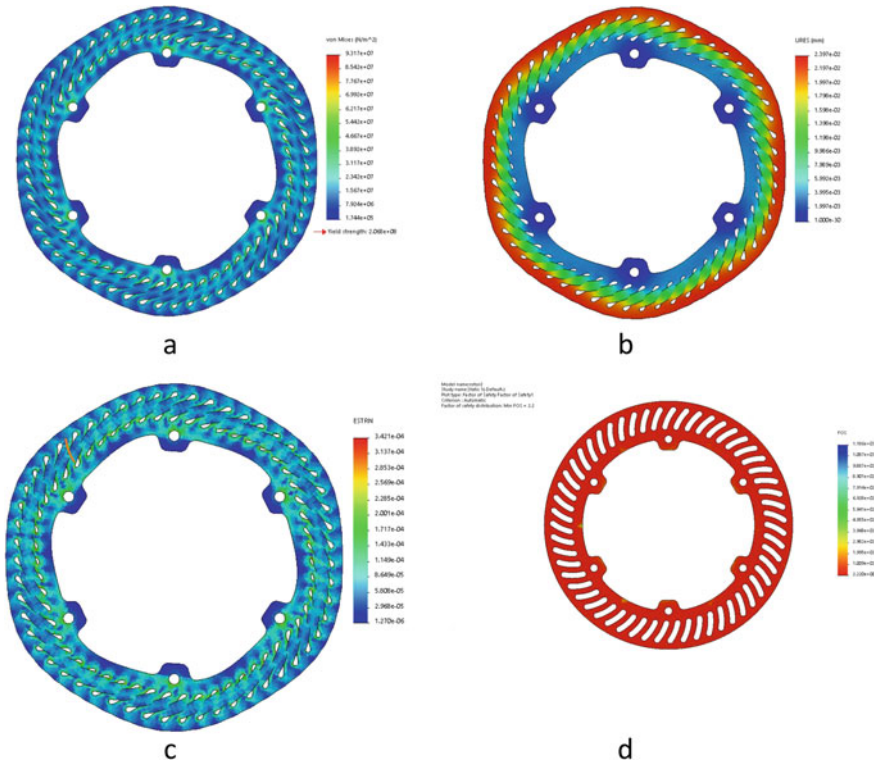


Fig. 3 a Stress; b Displacement; c Strain; d FOS simulation results

$$t = \frac{16.67}{5.886} = 2.832 \text{ s} \approx 3 \text{ s (approx.)}$$

Solidworks simulation tool [13] was used to conduct the thermal analysis. The heat load was calculated using the energy conservation theorem.

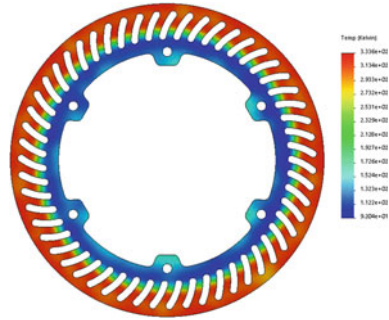
$$\begin{aligned} \text{Kinetic energy of the vehicle (K.E.)} &= \frac{1}{2}mv^2 \\ &= \frac{1}{2}(273)(16.67)^2 = 37931.835 \text{ J} \end{aligned} \tag{18}$$

where

- m = mass of vehicle = 273 kg.
- v = velocity of the vehicle = 16.67 m/s

$$\text{Heat Power}_{\text{total}} = \frac{K.E.}{t} = \frac{37,931.835}{2.832} = 13,394.009 \text{ W} \tag{19}$$

Fig. 4 Heat distribution pattern of the rear rotor



$$\text{Heat Power}_{\text{each pad}} = \frac{\mu_d(\text{Heat Power}_{\text{total}})}{2} = \frac{(0.4)(13,394.009)}{2} = 2678.801 \text{ W} \tag{20}$$

where

μ_d = coefficient of friction of brake pad = 0.4

The calculated heat load was used as the input on each of the faces, where the brake pads contact the rotor for 3 s, and the convection coefficient was taken as 90 W/m²K. The ambient room temperature was taken as 25 °C to conduct the analysis. After entering the inputs, the simulation was conducted to get the results. Figure 4 shows the heat distribution over the surface area of the rotor.

The heat distribution pattern shows that the maximum temperature reached by the rotor while braking is 63 °C which is lower than the melting point of both the rotor (1450 °C) and the brake pad (655 °C). Thus, the heat dissipation of the rotor is sufficient for the safe operation of the system and the temperature of the mounting points does not reach above 40°C for the rotor mount to face any thermal operational problems.

7 Rotor Mount for the Rear Rotor

The rotor mount was designed to connect the rotor to the differential and transmit the braking torque from the rotor to the differential. The mounting point was chosen as the end opposite to the mounting point of the sprocket to accommodate the sprocket adapter and the scatter shield for the chain. The main criteria for the mount design were its static strength and the minimum FOS achieved during the loading conditions. Al-7075 was considered for its material as it gives a good weight to strength ratio. For the design, the PCD of the bolting holes was chosen as the PCD for the bolting points of the mount to the differential. Material removal was done to optimize the mount and the simulation of loading conditions was done for the mount. The final

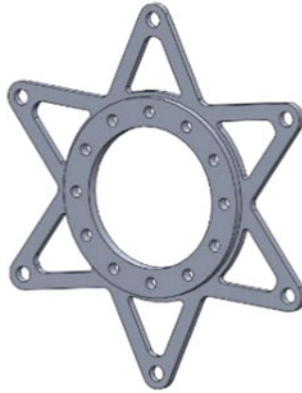


Fig. 5 CAD model of the rear rotor mount

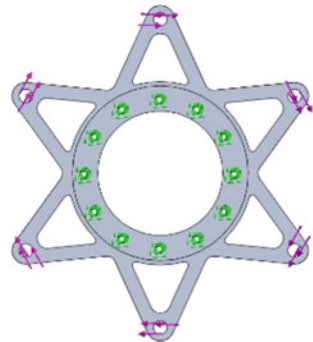
mass of the mount came to be 0.267543 kg. Figure 5 shows the design of the rotor mount [13].

8 Static Analysis of the Rear Rotor Mount

The stress analysis was done using the solidworks simulation tool [13]. The main objective of the simulation was to depict the maximum induced stress in the mount and to achieve a target FOS of above 2. The fixed points of the mount were chosen as the bolting points of the mount to the differential and the sum of the braking torque (119.503 Nm), and the differential torque (592.356 Nm) was applied on the bolting points of the mount to the rotor. Figure 6 depicts the input parameters for the simulation.

After providing the input values, the simulation was performed to obtain the results. Figure 7 depicts the results of the simulation.

Fig. 6 Input parameters for the static analysis of the rotor mount



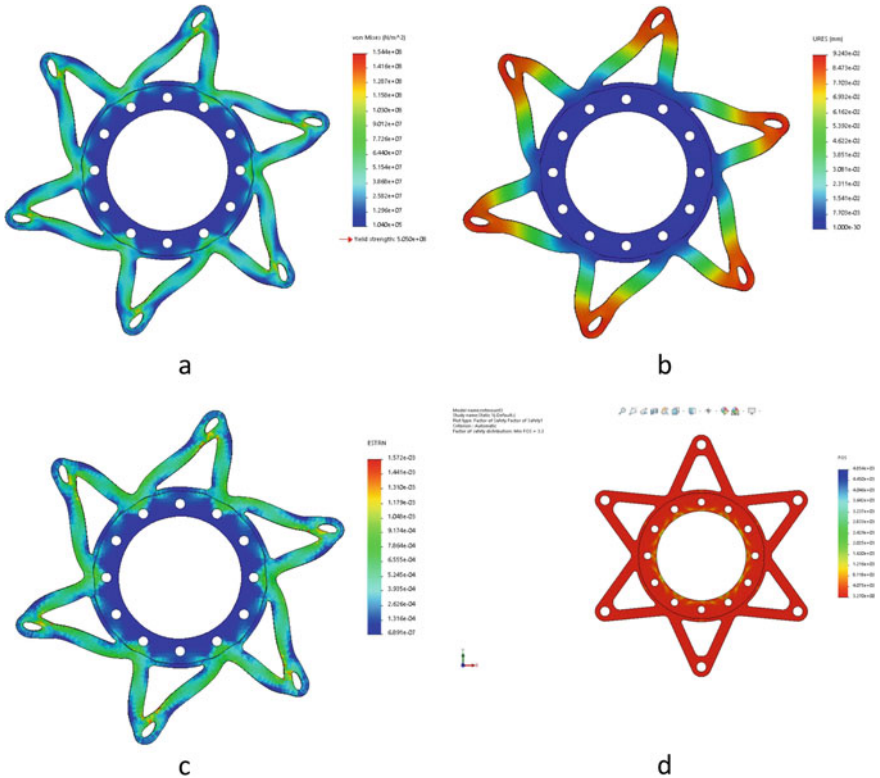


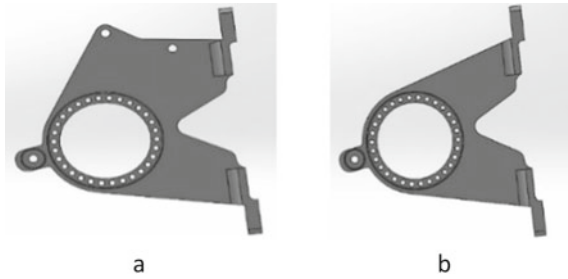
Fig. 7 a Stress; b Displacement; c Strain; d FOS simulation results

From the results obtained, we can see that the maximum induced stress ($1.544 \times 10^8 \text{ N/m}^2$) in the mount is less than its yield stress ($5.05 \times 10^8 \text{ N/m}^2$) and the minimum FOS achieved is 3.3. Thus, the part is taken to be safe to perform in the calculated loading conditions.

9 Differential

The differential is a gear arrangement that transmits power from an engine to a pair of driving wheels. It distributes the force equally but allows them to follow paths of unequal length during turning or traversing an uneven road. Drexler’s limited slip differential was chosen as it gave utmost advantages over the Torsen differential. It is lightweight. The differential is mounted eccentrically to the center (left) that runs through the sprocket by a chain with two shafts on either side of it.

Fig. 8 **a** Initial solid design of the right differential mount; **b** Initial solid design of the left differential mount



10 Differential Mounts

Differential mounts are a mounting system for the differential to hold it in a fixed position. As for the differential mount, it has been designed using solidworks [13] in a way that it can effectively withstand the results from the rotational motion of the sprocket and frictional force induced between rotor and brake pads due to the braking torque. The rear brake caliper mounts have also been included in the right differential mount to achieve part consolidation. Figure 8 shows the initial solid design for differential mounts. Bearing used for mounts is SKF 6010 with an outer diameter of 80 mm and an inner diameter of 55 mm [14].

11 Differential Mount Calculations

For the study, the engine used is KTM 390. The maximum torque achieved by this test engine is 24.5 Nm. It has a total of 6 gears as depicted in Table 3 with an initial reduction between the crank shaft and primary shaft of the gearbox of 80/30. OEM drive sprocket has 15 teeth and customized driven sprocket has 51 teeth. This gives a secondary reduction value of 51/15. The maximum torque that can be produced is calculated by Eq. (19) [15, 16].

$$T_{\max} = \text{Engine torque} * \text{initial reduction} * \text{1st gear ratio} * \text{secondary gear ratio}$$

$$T_{\max} = 24.5 * \left(\frac{80}{30}\right) * \left(\frac{32}{12}\right) * \left(\frac{51}{15}\right) = 592.356 \text{ Nm} \tag{21}$$

$$\text{Maximum force on rear sprocket, } F_{\max} = \frac{T_{\max}}{r} \tag{22}$$

Table 3 Gear ratios for the gears in the engine [14]

Gear	1st	2nd	3rd	4th	5th	6th
Gear ratio	32/12	26/14	27/19	24/21	22/23	21/25

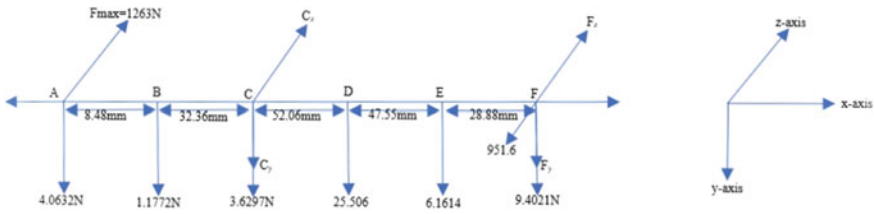


Fig. 9 Magnitude and direction of forces in the differential axis. **a** Sprocket; **b** Adapter; **c** Left differential mount; **d** Differential; **e** Rotor mount and rotor; **f** Caliper and right differential mount

$r = \text{pitch radius of driven sprocket} = 0.134 \text{ m}$

$$F_{\max} = \frac{592.357}{0.134} = 4420.52\text{N};$$

For designing 1/3.5th of maximum force, F_{\max} is used.

$$F_{\max} = 4420.52/3.5 = 1263.00 \text{ N.}$$

Figure 9 represents direction and magnitude along with the distance between forces. Assuming forces acting from the center of mass, it has been resolved on the y-axis and z-axis. Y-axis depicts the weight of all components and also the resulting reaction force on the left differential mount (C) and right differential mount (F). Z-axis consists of maximum force due to torque on sprocket (A), frictional force acting on caliper (F), the reaction force on the left differential mount (C), and right differential mount (F).

$$\text{Sum of forces in the } y\text{-direction, } \sum f_y = 0 \tag{23}$$

$$4.0632 + 1.1772 + C_y + 3.62 + 25.506 + 6.1614 + 9.4021 + F_y = 0$$

$$54.0942 + C_y + F_y = 0$$

$$\text{Sum of forces in the } z\text{-direction, } \sum f_z = 0 \tag{24}$$

$$1263 - 951.6 + C_z + F_z = 0$$

$$\text{A moment in } y\text{-direction about } F, \sum M_y = 0 \tag{25}$$

$$(6.161 \times 28.88) + (25.506 \times 76.43) + (3.629 \times 12.49) + (C_y \times 128.49) + (1.177 \times 160.85) + (4.063 \times 169.33) = 0$$

Table 4 Material comparison for the right solid differential mount

Material	Yield strength (MPa)	FOS	
		Right	Left
Al-3003	124	3.117	2.532
Al-5005	131	3.293	2.674
Al-6061	275	6.913	5.614

$$C_y = -28.569 \text{ N}$$

A moment in z-direction about F , $\sum M_z = 0$ (26)

$$(1263 \times 169.33) + (C_z \times 128.49) = 0$$

$$C_z = -1664.439 \text{ N}$$

Substituting the value of C_y and C_z in Eqs. (23) and (24), we get,

$$F_y = -21.361 \text{ N}$$

$$F_z = 322.572 \text{ N}$$

12 Material Selected for the Differential Mounts

After many iterations of the solid differential mount in different materials, Al-3003 (Table 4) has been chosen as the material for it, since it leads to weight reduction by a large numerical value. These materials were selected based on cost and availability. Table 4 gives comparative study for different materials of solid right and left differential mounts.

13 Shape Optimization

Figure 10 shows the resultant translational force on right and left differential mount, respectively, and also the moment due to braking torque acting on the right differential mount. Keeping bolting points in the base of the legs as fixed, shape optimization was done with a target of 70% weight reduction and achieving maximum stiffness. Figure 11 represents the shape of mounts after weight reduction.

Table 5 depicts the reduction of mass before and after the material removal was done according to the stress distribution.

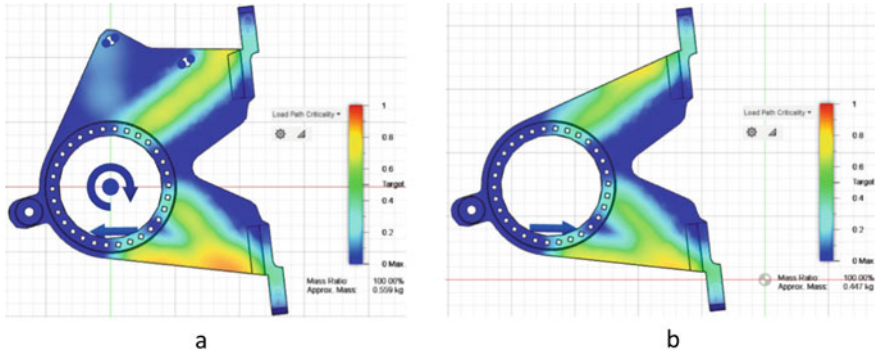


Fig. 10 **a** Resultant stress on the right differential mount; **b** Resultant stress on the left differential mount

Fig. 11 **a** Optimized shape of the right differential mount; **b** Optimized shape of the left differential mount

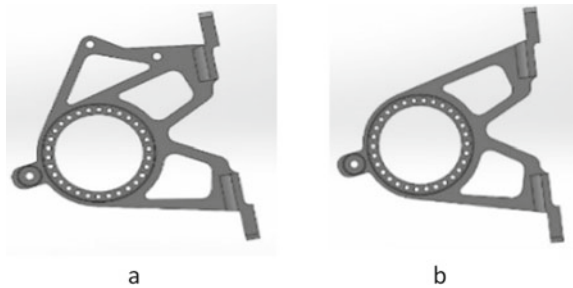


Table 5 Reduction in mass before and after material removal

Differential mount	Initial mass (kg)	Final mass (kg)
Right	0.53475	0.41774
Left	0.43894	0.35947

14 Static Analysis of the Differential Mounts

Static stress analysis on Fusion 360 [17] was performed. Calculated resultant translational forces and moment due to braking torque were given as inputs considering extreme boundary conditions and bolting points as fixed support. Output results were equivalent stress (von Mises), total displacement and FOS (stress) for both differential mounts. Equivalent stress analysis shows the counter of induced stress distribution and points out the maximum and minimum stress points. Maximum stress-induced is 50.92 and 42.67 MPa for left and right differential mounts, respectively. Figure 12 shows the stress distribution patterns.

Total displacement depicts the position of mounts that will undergo extreme to slight displacement. It is observed that maximum displacement is 0.3312 mm and 0.4431 mm for left and right differential mounts, respectively. It is observed that the

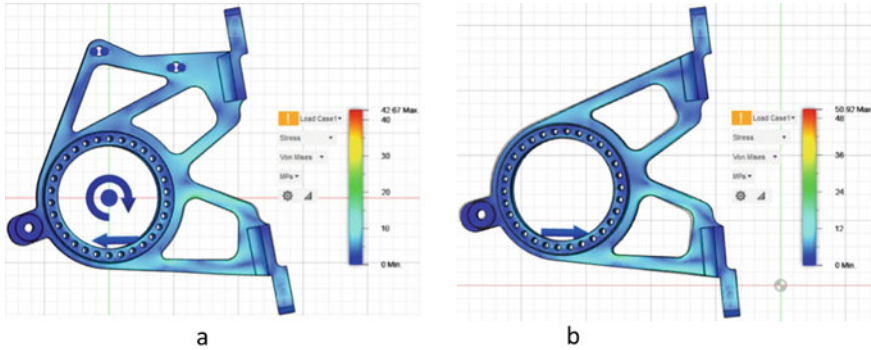


Fig. 12 **a** Stress distribution pattern for the right bearing mount; **b** Stress distribution pattern of the left bearing mount

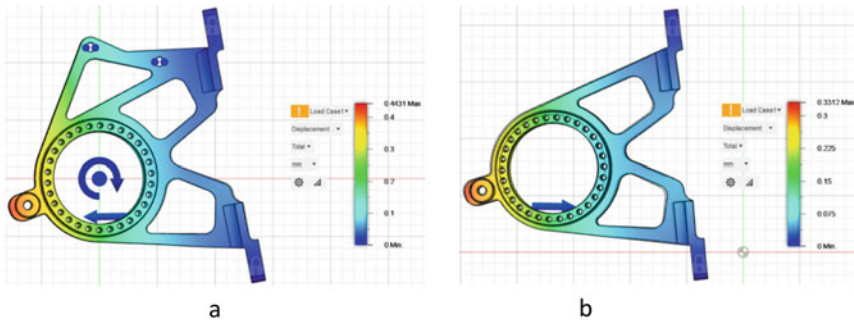


Fig. 13 **a** Displacements in the right differential mount; **b** Displacements in the left differential mount

value of the mount’s extreme displacement is less than half a millimeter, therefore, mounts will not deform under this extreme loading condition. Figure 13 shows the displacements in the mounts.

The factor of safety (FOS) is the ratio of maximum stress-induced to yield strength. FOS of 1 means if the maximum stress is equal to the yield strength and if the stress value increases, the part will fail. So, to keep it on a safer side, this study has a target FOS range of 2–3, which will ensure that if at all the maximum stress induced is more than yield strength during practical application of differential mounts, then it will not fail. FOS of left and right was found to be 2.435 and 2.906, respectively, which is under the target range. Figure 14 depicts the FOS for the differential mounts (Table 6).

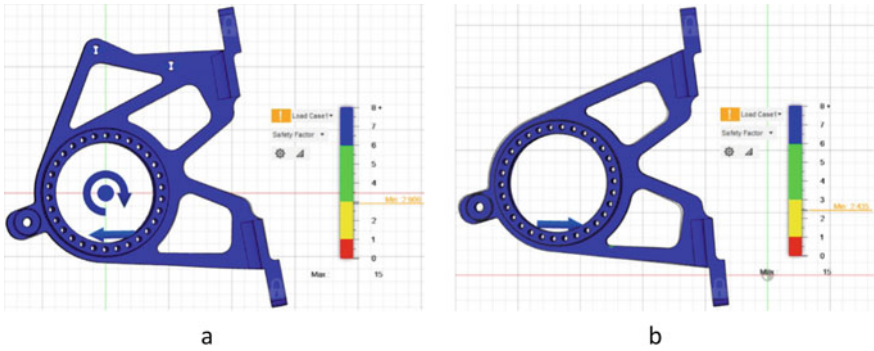


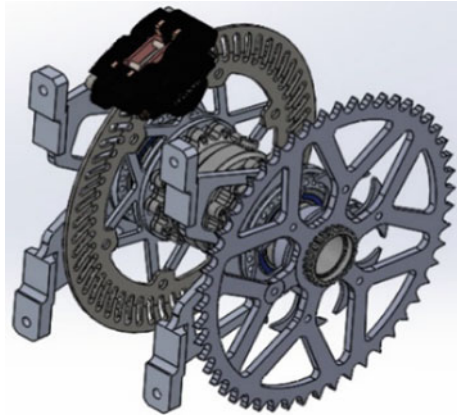
Fig. 14 **a** FOS distribution of the right differential mount; **b** FOS distribution of the left differential mount

Table 6 Stress, displacement, and FOS for both the mounts

Differential mount	Equivalent stress (MPa)	Total displacement (mm)	FOS
Left	50.92	0.3312	2.435
Right	42.67	0.4431	2.906

15 Conclusion

From the research conducted, the design of both the rear inboard brakes and the differential mounts was successfully completed. The material study for the rear brake rotor and differential mounts was also conducted to come up with an optimized working model. The calculations performed were according to the extreme force values expected to improve the reliability of the system. Simulations were done according to the calculated values to check for any scope of improvement in the design. Part consolidation was also done by including the caliper mount in the right differential mount itself leading to the overall weight reduction. The parts designed were in working condition for the mass of the vehicle taken and were in a ready to manufacture condition. Figure 15 depicts the final assembly of all the designed components.

Fig. 15 Final assembly

References

1. Sharma A, Amrute P, Thakur SS, Shrivastav J (2018) Design, analysis and fabrication of braking system with rear inboard brakes baja ATV. *Int Res J Eng Technol* 5(5):4340–4345
2. Rana RH, Jakhiya NH, Savani AK, Bhalodi AK (2017) Optimum design of braking system for a Formula 3 Race cars with numeric computations and thermal analysis. *Int Res J Eng Technol* 4(2):1453–1458
3. James RA (2004) Design of an aluminum differential housing and driveline components for high performance applications. Ph.D. diss., Massachusetts Institute of Technology
4. Scelfo TW (2006) Lightweight Torsen style limited slip differential and rear driveline package for Formula SAE. Ph.D. diss., Massachusetts Institute of Technology
5. Mora LA (2018) Design of a FSAE braking system. Ph.D. diss., Massachusetts Institute of Technology
6. Galbincea ND (2015) Design of the University of Akron's 2015 FSAE electric vehicle braking system
7. Casella A, Deneault A, Donaghey P, Lightbody M, Robinson J, Taylor C (2018) Design and optimization of a formula SAE vehicle. Ph.D. diss., Worcester Polytechnic Institute
8. Zankat CR (2018) Reduction gearbox with inboard braking system for an ATV. *Int J Creative Res Thoughts* 6(2):450–460
9. Chavan K, Kumari C, Pawar P, Bawankar A, Agashe UC (2019) Design, development and manufacturing of braking system for ATV. *Int Res J Eng Technol* 6(4):3605–3609
10. Bulsara A, Lakhani D, Agarwal Y, Agiwal Y (2017) Design and testing of an adjustable braking system for an FSAE vehicle. *Int J Res Eng Technol* 6(10):25–29
11. Formula SAE Rulebook 2021 (2020) Version 1.0. 30 July
12. Wilwood disc brakes technical and parts guide (2013)
13. Student's Guide to Learning SolidWorks® Software, Engineering Design and Technology Series, Dassault Systèmes—SolidWorks Corporation (2020)
14. Arora P, Agrawal MR, Singh PP, Gobinath N, Feroskhan M (2021) Design and analysis of a formula SAE vehicle chain sprocket under static and Fatigue loading conditions. *SAE Int J Mater Manuf* 14(3):275
15. Bhandari VB (2010) Design of machine elements, 4th edn. Tata McGraw-Hill Education
16. Design Data Book of Engineers by PSG College, Kalaikathir Achchagam, Coimbatore (2020)
17. Verma G (2018) Autodesk fusion 360 black book. BPB Publications

A Novel Modeling Approach for Dent Identification and Sizing for Oil and Gas Pipeline



Aawish Kumar, Surya Prakash, Ashish Kumar Srivastava, Rajesh Kumar, and Vimal Kumar Pathak

Abstract This paper presents a novel mathematical modeling approach for the identification of anomalies like dent sizing, ovality sizing, weld sizing through diameter reconstruction for oil and gas pipelines. A novel mathematical model that integrates the best-fit circle (BFC), smallest covering circle (SCC) and largest empty circle (LEC) algorithms are proposed so that the prediction of pipeline features (diameter and dent) becomes very accurate. In the experimental setup, the in-line inspection (ILI) tool was used to obtain the input parameters of algorithms. These ILI tools recorded the data (through arms) systematically and the fundamental structure of the inner side of the pipeline is reconstructed using the data obtained from the ILI tool calipers through a proposed integrated mathematical model. A real-life practical pipeline case study with numerical experimentation for 18-inch pipeline geometry tool data is carried out to highlight the efficacy of proposed algorithms. The algorithm successfully identified all pre-marked 51 dents in a liquid medium, while in gas medium, the total identification was 49 dents.

Keywords Dent identification · Dent sizing · Oil and gas pipeline · ILI tool · Pipeline integrity

1 Introduction

In the last few decades, the use of pipelines has been increased vastly for the transportation of oil and gas throughout nations [1, 2]. Transportation of oil and gas through pipelines is one of the principal means to achieve efficiency. Pipelines are used worldwide for transporting crude oil (approx. 3300×103 km) and final refinery

A. Kumar · S. Prakash
Mechanical Engineering Department, BML Munjal University, Gurgaon, India

A. K. Srivastava (✉) · V. K. Pathak
Mechanical Engineering Department, Manipal University Jaipur, Jaipur, India
e-mail: ashishkumar.srivastava@jaipur.manipal.edu

R. Kumar
Chitkara College of Applied Engineering, Chitkara University, Rajpura, Punjab, India

products (approx. 2600×103 km) [3, 4]. In most cases, the pipelines are laid under the surface of the earth or the seabed. It is worth noting that this makes them difficult to inspect and maintain. Multiple hostile environment aspects lead to their degradation, aging and deterioration. Sometimes, the faults in the pipeline are due to improper laying and commissioning or designing of pipeline structures [5]. Moreover, for optimal performance of pipelines, these assets require extensive maintenance, robust repair and replacement strategies to maintain the pipeline integrity [2, 5].

However, the technology has made the transportation of petroleum products and crude oil is very much safe in the last few decades for long distances, but the database of various accidents still reveals the risk associated with oil and gas pipelines [6]. Some of the failures are very much time-dependent like corrosion or fatigue failure [2, 7], while, others were because of time-independent anomaly that occurs in pipelines such as dent, ovality and wax or debris inner side. Most of the time, the failure in the pipeline is attributed to the unsuccessful estimation or no estimation of variations in the diameter of the pipelines. The regulatory bodies (e.g., PNRB guidelines in India) inspect the geometry of pipelines every five years to ensure asset integrity [8]. The literature shows that there are several non-destructive techniques (NDT) methods that are available to perform the inspection of oil and gas pipelines even underneath the surface or under seabed [2, 5, 9]. The visual examinations or practice of using X-rays is for scrutinizing the pipelines above the ground while underground pipelines require the use of a pipeline inspection gauge (PIG) to perform the inspections [9]. Kishawy and Gabbar [10] have reviewed the pipeline integrity management to present state of art. Xie and Tian [11] investigated the pipeline integrity field while utilizing the in-line inspection (ILI) data. There were minimal studies that had a focus on mathematical modeling for pipeline feature identification. Li et al. [12] presented a study on diameter detectors for curved pipelines. The focus was on analyzing the angle curve impact of the detection arm while it travels through the curved oil pipelines. Caley et al. [13] did performance valuation and calibration of ILI tools of oil and gas pipelines.

In this paper, an efficient, accurate, and suitable algorithm to reconstruct the pipeline diameter to bridge this gap optimally is devised. The mathematical models and algorithms are designed for critical parameters utilizing the integrated approach of the best-fit circle (BFC), smallest covering circle (SCC), and largest empty circle (LEC) so that prediction of pipeline features can be achieved effectively. A real-life practical pipeline case study with numerical experimentation for 18-inch pipeline geometry PIG (the ILI tool) data is provided which showcases the efficacy of proposed algorithms.

2 Mathematical Modeling

2.1 Calibration Method

The calibration process enables the interpretation of digital data obtained from PIG arms into the metric unit. A relation between the known deflection of each arm and its count value was found. A polynomial curve equation is formed between the values. To do so, a polynomial curve is formed in the least square sense to fit the curve on the data set. Let's generalize the straight line to k th degree polynomial as follows-

$$y = a_0 + a_1x + \dots + a_nx_n \tag{1}$$

The residue is given by:

$$R^2 = \sum_{i=1}^n \left[y_i - \left(a_0 + a_1x_1 + \dots + a_{kx_i^k} \right) \right]^2 \tag{2}$$

By, calculating the partial derivatives, obtained equations converts to following matrix:

$$\begin{bmatrix} n & \sum_{i=1}^n x_i & \dots & \sum_{i=1}^n x_i^k \\ \sum_{i=1}^n x_i & \sum_{i=1}^n x_i^2 & \dots & \sum_{i=1}^n x_i^{k+1} \\ \vdots & \vdots & \ddots & \vdots \\ \sum_{i=1}^n x_i^k & \sum_{i=1}^n x_i^{k+1} & \dots & \sum_{i=1}^n x_i^{2k} \end{bmatrix} \begin{bmatrix} a_0 \\ a_1 \\ \vdots \\ a_k \end{bmatrix} = \begin{bmatrix} \sum_{i=1}^n y_i \\ \sum_{i=1}^n x_i y_i \\ \vdots \\ \sum_{i=1}^n x_i^k y_i \end{bmatrix} \tag{3}$$

The above matrix is a type of Vander mode matrix which is in the form of incremental power across its rows and columns [14]. As discussed earlier for given n points (x_i, y_i) and fitted them with polynomial coefficients that are a_0, a_1, \dots , as results in:

$$\begin{bmatrix} y_1 \\ y_2 \\ \vdots \\ y_n \end{bmatrix} = \begin{bmatrix} 1 & x_1 & x_1^2 & \dots & x_1^k \\ 1 & x_2 & x_2^2 & \dots & x_2^k \\ \vdots & \vdots & \vdots & \ddots & \vdots \\ 1 & x_n & x_n^2 & \dots & x_n^k \end{bmatrix} \begin{bmatrix} a_0 \\ a_1 \\ \vdots \\ a_k \end{bmatrix} \tag{4}$$

So, in matrix notation, representation of polynomial fit is given in the form

$$y = Xa. \tag{5}$$

This can be solved by multiplying it with the transpose of X^T .

$$\mathbf{a} = (\mathbf{X}^T \mathbf{X})^{-1} \mathbf{X}^T \mathbf{y}. \quad (6)$$

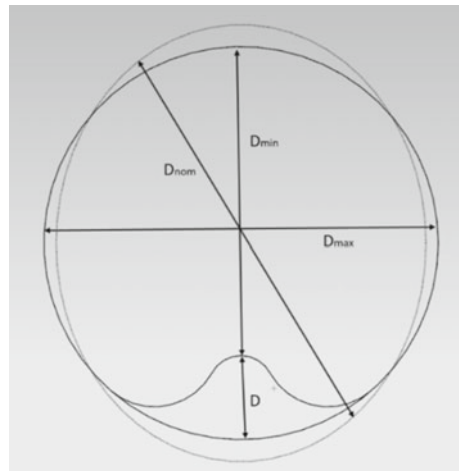
With Eq. 6, polynomial curve fitting of power $n = 1$ is used to determine the linear relation between the fixed and calculated variable of our calibration process. These values are then processed through the above equations. The linear output equation was in the form of $\mathbf{y} = \mathbf{m}\mathbf{x} + \mathbf{c}$. Where slope value was in the range between 4000 counts/in. to 6000 counts/in. and offset value resulted between $-15,000$ counts and $-30,000$ counts. Note that these values vary for all 24 caliper pig arms and none will be the same in any case.

2.2 Sizing of Dent and Ovality

The main objective of any caliper arm is to quantify the internal pipeline diameter along with the identification of pipeline wall anomalies [15]. The Pipeline Defect Assessment Manual (PDAM) guidance includes assessment for many types of pipeline signatures which can be identified for integrity management [16]. This includes corrosion, dents (plain, kinked, on welds, along with welds), gouges, weld defects (seam, girth) and manufacturing defects. The algorithm that is used to identify the size of dents is adopted from [15]. Figure 1 shows the conceptual computation of dent size. Here, D_{dent} : Size of Dent; D_{ov} : Size of Ovality; D_{no} : Nominal Diameter from Best Fit Circle; D_{min} : Minimum Diameter from Largest Empty Circle; D_{max} : maximum Diameter from Smallest Covering Circle, and, $D_{\text{dent}} = D_{\text{nom}} - D_{\text{min}} - (D_{\text{max}} - D_{\text{nom}})/4$.

Here we are subtracting the ovality of internal pipeline diameter (ID) from that instance to get the exact value. Equation 7 shows this arrangement.

Fig. 1 Conceptual computation of dent size



$$D_{ov} = 2 * (D_{max} - D_{nom}) \tag{7}$$

2.3 Best-Fit Circle (D_{nom}) and Achieving BFC

The diameter estimation is achieved by using the algorithm of the best-fit circle. This problem is a very common problem of computer graphics [17–19] and the circle fitting is same as fitting a polynomial curve by using least square method [17–20]. Let, for a given set of point $N = n$ in a given plane $(x_i, y_i), i = 1, 2, 3, \dots, n$; find the circle center point and radius governing equation is as follows:

$$(x - x_0) + (y - y_0) = R^2 \tag{8}$$

Such that the error from the least square method (SM) is minimum and given as:

$$SM = \sum_{i=1}^n \left[\sqrt{(x_i - x_0)^2 + (y_i - y_0)^2} - R \right]^2 \tag{9}$$

The first section uses the sum of the square of differences between circle radius and distance from input point to circle. The second section estimates the coefficient of a quadratic equation of two variables. It reduces to computing the Eigenvector associated with minimum Eigenvalue of the matrix. The first step is to compute the partial derivatives concerning R.

Here, $S = \sqrt{(x_i - x_0)^2 + (y_i - y_0)^2}, \frac{\partial SM}{\partial R} = -2 \sum_{i=1}^n (S - R)$.

Now, setting the value of $\frac{\partial SM}{\partial R} = 0, R = \frac{1}{n} \sum_{i=1}^n (S)$.

Compute partial derivative concerning x_0 and y_0 , by setting obtained derivatives equal to zero yields the following two non-linear relationships in x_0 and y_0 are obtained:

$$x_0 = \overset{\prime}{x} + \overset{\prime}{L} \overset{\prime}{L}_{x_0} = F(x_0, y_0) \tag{12}$$

$$y_0 = \overset{\prime}{y} + \overset{\prime}{L} \overset{\prime}{L}_{y_0} = G(x_0, y_0) \tag{13}$$

where,

$$\overset{\prime}{L} = \frac{1}{n} \sum_{i=1}^n S, \overset{\prime}{L}_{x_0} = \frac{1}{n} \sum_{i=1}^n \frac{x_0 - x_i}{S}, \overset{\prime}{L}_{y_0} = \frac{1}{n} \sum_{i=1}^n \frac{y_0 - y_i}{S}, \overset{\prime}{x} = \frac{1}{n} \sum_{i=1}^n x_i, \overset{\prime}{y} = \frac{1}{n} \sum_{i=1}^n y_i.$$

Now by applying fixed-point iteration, it is easy to solve these equations:

$$x_0 = \overset{\prime}{x}, y_0 = \overset{\prime}{y} \wedge x_{i+1} = F(x_i, y_i), y_{i+1} = G(x_i, y_i)$$

The output of the above equation will give us the radius and center point of the data we need to analyze.

2.4 Largest Empty Circle (D_{min})

If the largest circle of which the center lies in CH (Q) such that no point of Q lies in the interior of the circle is called largest empty circle (LEC) [21]. In solving the sizing problem of pipeline feature, we need D_{min} for identification of the smallest ID that is formed [22]. In this context, “the LEC problem is defined on a set N by finding the largest circle that contains zero points in N and is also centered inside the convex hull of N ”. The LEC has centered at either a vertex on the Voronoi diagram for N . Also, it may be on an intersection between a Voronoi edge and the convex hull of N [23].

Finding the LEC (Convex hull and Delaunay triangulation)

For finding the LEC for a set of point N , construct the convex hull (CH(N)) and Voronoi diagram (V) for a given set of points. For convex hull, first, we need two empty variable U and L for holding the upper and lower vertices of the hull using Jarvis march algorithm to calculate the convex hull [24]. Let, for, $i = 1 \dots N$, take at least two points from L contains. If, there is no counter-clockwise turn, remove the last point from L and for the 2d-arm tool, this will yield L. In such cases, for $i = n, n - 1 \dots 1$, take U contains (at least two points) and the sequence of last two points of U. If $N [i]$ does not make a counter-clockwise turn, here also, remove the last point from U append $N[i]$ to U [24]. Figure 2a, b represents the Convex hull and Delaunay triangulation for data respectively.

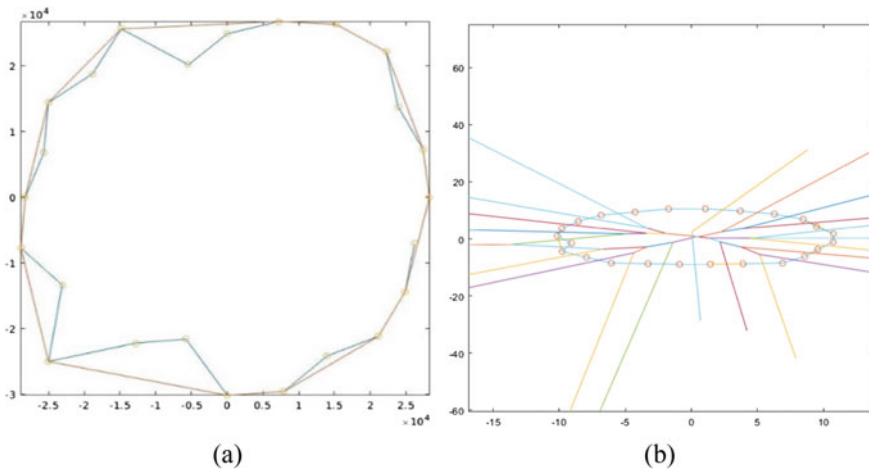
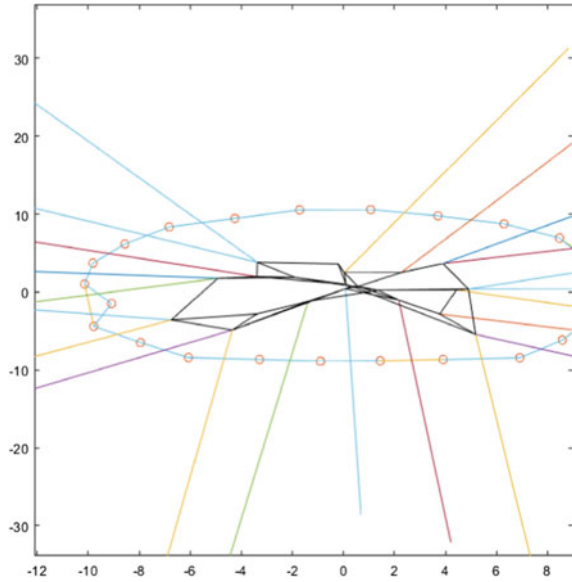


Fig. 2 a Convex hull representation, b Delaunay triangulation for data

Fig. 3 Representation of Voronoi diagram from DT(N)



The Voronoi diagram

Triangles that are near to DT(N) have their vertices connected by an edge in the V(N) dual space [23, 24]. This is the duality between the Voronoi diagram and the Delaunay triangulation which is used further. Okabe et al. [25] provides the coordinates of the Voronoi vertex which correspond to a triangle T 2 DT (P) while it is the center of the circle which circumscribes T. For calculating the circumcircle, the perpendicular bisector creation is used. Finally, the dual vertex in V or (P) is obtained by iterating over all triangles in DT(P). Now, calculating the circumcircle and only those Voronoi edges retained that lies inside the convex hull. Figure 3 shows the representation of Voronoi Diagram from DT(N).

Largest circle identification

After elimination of useless edges, remaining ones are considered as the center of the LEC and to find the radius, we iterate the distance of all edges from all other points to identify the circle that is giving the maximum radius. In our case, this is the simplest and fastest method to identify the center points and radius. Figure 4a, shows the representation of a largest empty circle.

2.5 Smallest Covering Circle

The smallest covering circle (SCC) is the minimum enclosing circle covering the point set with the outline of the closed disk of the smallest area where the disk is defined with its bounding circle [26]. For our pipeline investigation mathematical

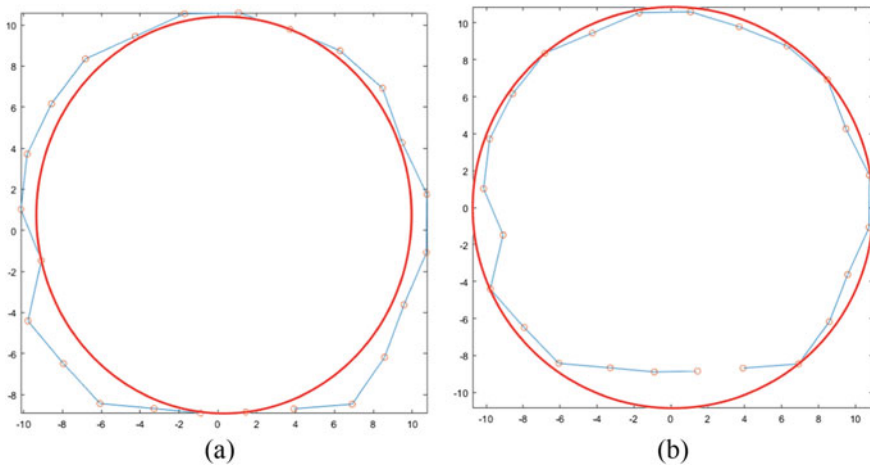


Fig. 4 Representation of, **a** largest empty circle, **b** smallest empty circle

process, we require it to tell us the maximum circle that is forming at any instance. Also, it finds its usage in ovality calculation also. Let there be $N(x_i, y_i)$ no. of points in a 2-D plane, we need to find a circle consisting of all the points inside its circumference and can pass through a maximum of three points from the set of N points [27]. Let $f = (a, b)$ be the assumed circle of the SCC that we need to calculate. It is simple to calculate the distance of all points from assumed circles.

$$d(l, N) = \sqrt{(x - a)^2 + (y - b)^2} \quad (14)$$

For achieving the minimum covering circle, Eq. (14) has to be minimized for all existing points.

Method for finding LEC

Hasan Nasab [27] established that this algorithm's time complexity is much less than those of other older solutions. The general method of achieving this is discussed in 4 steps as: (1) Start with measuring the distances between each pair of points and sort them in chronological order. Choose the point with maximum distance. Refer these points as PP1 and PP2. Take these new points as diameter and generate a circle. Check if all the points are covered inside the new circle, if yes, then it is our solution otherwise move to the following step, (2) Identify the point that is farthest from the center of the previous state. Refer to it as point PP3. Now form a circle from these three-point PP1, PP2 and PP3. Solve Eq. 14 to get values of center point and radius. If this condition also fails then do the next step, (3) Repeat above step to identify the fourth point that is farthest from the center of the previous step. Refer to this point at PP4. Now the circle will be from three-point PP3, PP4 and any from PP1 and PP2, (4) For choosing between PP1 and PP2. Identify the distance between PP1 and PP2 from PP3 and PP4. The point that will be considered that is giving the maximum

difference. Now the final circle will be plotted from that point in determinant series as follows. Figure 4b shows the representation of a smallest empty circle.

3 Time Complexity and Algorithm

Time complexity is the computational complexity that tells about the amount of time required to run an algorithm to produce an acceptable solution. In the case of diameter reconstruction and dent identification from the ILI tool data, the sub-algorithm that is taking the maximum time will also define time complexity. The time taken for BFC algorithm works in $O(n)$ time as it is a single loop algorithm. For its calculation, the number of input points maximized up to 100,000. For the LEC algorithm $O(n \log n)$ time is required as it is the time required for Delaunay triangulation so it dominates [23]. Same process followed for SCC algorithm as given designed by [27], there computational time is $O(n^2)$. Hence, the total computational time for the proposed method is the highest amount of time for LEC. Calibration data (slope and offset) and Run data (counts) are the inputs for the algorithm. Run data is the data of all 24 arms, collected by the tool while moving inside the pipeline. Calibration data consist of slope and offset (in the form of counts) that are obtained after the calibration process.

4 Experimental Verification for Pipeline

The ILI tool used in this study is a PIG that scans the pipeline by traveling through it and collects the data related to diameter, deviations, dents, deposits, internal restrictions etc. The tool is indigenously developed. The number of arms (caliper arm with sensors) in the tool is dependent on the size of the pipeline to provide maximum coverage. This makes the fitting of the electronic challenge, but recent advances in electronics and data storage domain have made the PIGs more accurate, sensitive and compact. The typical PIG used in this study has three main systems, the body, data acquisition system and sensors. The Fig. 5 shows the ILI tool SPYTON18 (Geometry Inspection PIG) prototype device with 24 sensing caliper pig arms for 18 inches pipe diameter which was used for experimentation (the tool make is confidential for trade purposes). Data is recorded through the sensors mounted on caliper arms at a sampling frequency of 500–2000 Hz. The SPYTON18 was equipped with odometers, accelerometer and gyroscope which helps in positioning the location of the signatures (i.e., feature). The sampling frequency of accelerometer and gyroscope was 850 Hz. Hall sensor measures the deflection in arms and produces an output voltage varying from 0 to 5120 milli-volts as the arm deflects. A 16-bit ADC converter interprets this voltage output with a sensitivity of 0.0762 mv/count. First, the calibration of the tool was done to convert the values of counts into deflection manually. Hardware units of SPYTON18 has a minimum bore of 13.5 in. that states that it can measure dent size of range up to 4.5 in.-Height of Arm (Ha).

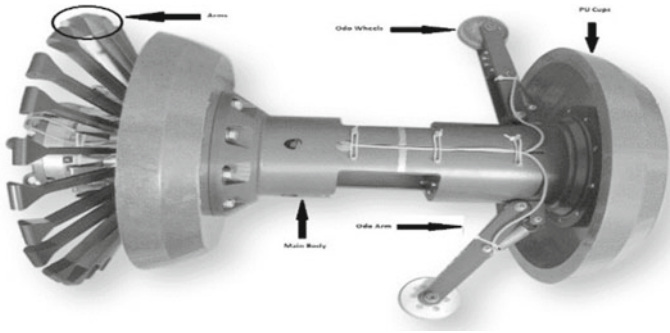
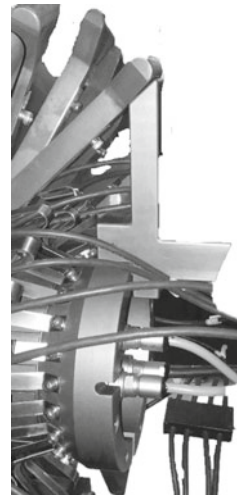


Fig. 5 The ILI tool SPYTON18 (geometry inspection caliper tool)

In the calibration process, known deflection blocks are designed and used. The calibration is a very important step of testing as it helps in conversion of arm data (hall sensor) into known deflection. Total five unique blocks for known deflection value was used. To carry out the process each arm is pressed against each block to record the count values or deflection. Figure 6 shows the metal blocks used for calibration for deflection measurement. Data obtained was then processed with the help of an indigenous developed GUI which uses the algorithm described above in Sect. 2.

A pipeline is set up for experimenting with known dents on it. A total of 51 dents are fashioned on the pipe surface of known shape and location. The ILI tool was forced to pass from this pipeline setup and data from the arms was fetched. The proposed algorithm is deployed to measure the depth of these dents so that the accuracy of the tool can be established. Figure 7a shows the portion of the pipeline

Fig. 6 Metal blocks used for calibration for deflection measurement



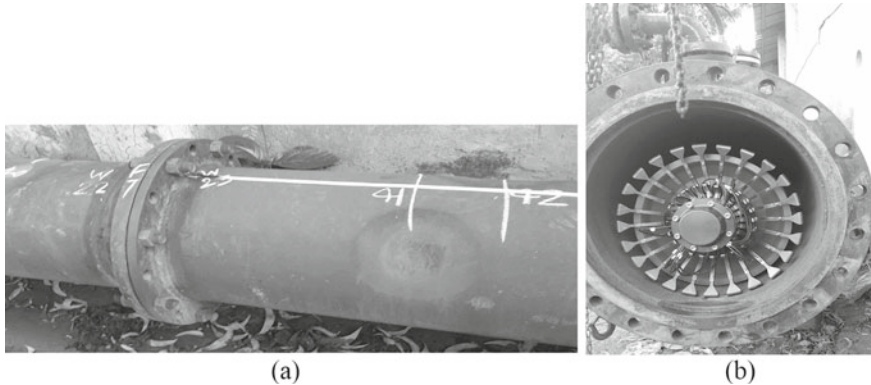


Fig. 7 **a** The portion of the pipeline with known dents fabricated on its surface, **b** The ILI tool in the launcher section of the test loop

with known dents fabricated on its surface. Total 20 runs were conducted with liquid and gas as a media. Figure 7b shows the ILI tool in the launcher section of the test loop. The test parameter is nominal diameter 18", length 50 m, longitudinally welded with a maximum allowable operating pressure of 10 bar.

The algorithm successfully identified all 51 dents in a liquid medium, while in gas medium, total identification was 49 dents. The possible reason for the loss of identification in the gas medium was the operator could not make a smooth transaction of the tool from the launcher to the receiver end. Due to this, a sudden change in pressure difference is created, resulting in instantaneously shooting the tool. This is also evident from the vibrations seen in the plot, which further made the identification of dent difficult by the algorithm. In the experiments, the value of dent feature was within the range of 0.72% of the nominal outer diameter (OD) for the 95% of the population of the dents. These results establish the applicability of the proposed method for accurate sizing of the marked dents in the given pipeline.

5 Conclusion

This study presents a novel mathematical model that integrates the best-fit circle (BFC), smallest covering circle (SCC) and largest empty circle (LEC) algorithms by validating its applicability through a real case study. First, the ILI tool was used to record the data (through arms) systematically and the fundamental structure of the inner side of the pipeline was reconstructed. The tool with 24 sensing caliper pig arms for 18 inches pipe diameter was used and data is recorded by sensors mounted on arms at a sampling frequency of 500–2000 Hz. In the experimental setup, a total of 51 dents is fashioned on the pipe surface of known shape and location. The ILI tool was forced to pass from this pipeline setup and data from the arms was

fetched. The proposed algorithm is deployed to measure the depth of these dents so that the accuracy of the tool can be established. Total 20 runs were conducted with liquid and gas as a media. The test parameter is nominal diameter 18", length 50 m, longitudinally welded with a maximum allowable operating pressure of 10 bar. In the experiments, the algorithm successfully identified all 51 dents in a liquid medium, while in gas medium, total identification was 49 dents. The value of dent feature was within the range of 0.72% of the nominal outer diameter (OD) for the 95% of the population of the dents. These results establish the applicability of the proposed method for accurate sizing of the marked dents in the given pipeline.

Acknowledgements The authors are grateful to Mr. Bhuvnesh Sharma and his team members of TISP Ltd., Baroda, India for their support, insights and providing training to research team members which helped them to accomplish this piece of research work.

References

1. Shi Y, Hao L, Cai M et al (2018) High-precision diameter detector and three-dimensional reconstruction method for oil and gas pipelines. *J Pet Sci Eng* 165:842–849
2. Baker O (1953) Design of pipelines for the simultaneous flow of oil and gas. Society of Petroleum Engineers - Fall Meeting of the Petroleum Branch of AIME, FM 1953
3. Rita T (2014) Worldwide construction report. *Pipeline Gas J* 241:1–6
4. Wang H, Zhu Q (2015) Overview of oil and gas pipelines in the world. *Oil Gas Storage Transp*
5. Shahriar A, Sadiq R, Tesfamariam S (2012) Risk analysis for oil & gas pipelines: a sustainability assessment approach using fuzzy based bow-tie analysis. *J Loss Prev Process Ind* 25:505–523
6. Powell-Price M, Bond J, Mellin B (1998) Accident database: capturing corporate memory. *Inst Chem Eng Symp Ser* 144:133–141
7. Jo Y, Ahn B (2002) Analysis of hazard areas associated with high-pressure natural-gas pipelines. *J Loss Prev Process Ind* 15(3):179–188
8. <https://www.pngrb.gov.in/OurRegulation/approved-guidelines.html>
9. Knickmeyer E (1994) The rolling pig or how does a surveyor creep through a pipeline? *Bull Géodésique* 68:71–76
10. Kishawy H, Gabbar, H (2010) Review of pipeline integrity management practices. *Int J Press Vessels Piping*
11. Xie M, Tian Z (2018) A review on pipeline integrity management utilizing in-line inspection data. *Eng Fail Anal*
12. Li X, Zhang S, Jiao Q et al (2015) Analysis for character of caliper pig passing through curving pipeline. *Oil F Equip* 44:67–71
13. Caleyó F, Alfonso L, Espina-Hernández J et al (2007) Criteria for performance assessment and calibration of in-line inspections of oil and gas pipelines. *Meas Sci Technol*
14. Seiler C, Seiler A (1989) Numerical recipes in C: the art of scientific computing. *Risk Anal* 9(3):415–416
15. Kim D, Cho S, Park S et al (2003) Design and implementation of 30" geometry PIG. *KSME Int J* 17(5):629–636
16. Cosham A, Hopkins P (2002) The pipeline defect assessment manual. In: *Proceedings of IPC* 44, 0–17
17. Wu C, Lee K, Chung Y (2007) A Delaunay triangulation based method for wireless sensor network deployment. *Comput Commun* 30:2744–2752
18. Gander W, Golub G, Strebel R (1994) Least-squares fitting of circles and ellipses. *BIT* 34:558–578

19. Coope I (1993) Circle fitting by linear and nonlinear least squares. *J Optim Theory Appl* 76(2):381–388
20. Moura L, Kitney R (1991) A direct method for least-squares circle fitting. *Comput Phys Commun* 64:57–63
21. Toussaint G (1983) Computing largest empty circles with location constraints. *Int J Comput Inf Sci* 12(5):347–358
22. Lee J, Cho T, Lee J et al (2004) A stochastic search approach for the multidimensional largest empty sphere problem. *Citeseer*, 0–10
23. Schuster M (2008) Largest empty circle problem. In: Proceedings of “Class of 2008 senior conference on computational geometry”, pp 28–37
24. De Berg M, Cheong O, Van Kreveld M et al (2008) *Computational geometry: algorithms and applications*. Springer
25. Okabe A, Boots B, Sugihara K et al (2000) Definitions and basic properties of Voronoi diagrams, Spat Tessellations Concepts Appl Vor diagrams, John Wiley Sons, pp 43–112
26. Mahdi A, Alzubaidi N (2014) Minimum bounding circle of 2D Convex Hull, 3, 2012–2015
27. Hosseini H, Tavana M, Yousefi M (2014) A new heuristic algorithm for the planar minimum covering circle problem. *Prod Manuf Res* 2:142–155

Solution of Lubrication Problems with Deep Neural Network



Saurabh Kumar Yadav and Gananath Thakre

Abstract Reynolds equation is fundamental to model lubrication in bearing and tribological components. In this work, we concentrate on lubrication analysis and solve the governing Reynolds equation with deep neural network. The governing Reynolds equation is converted in deep collocation method. In this work, Deep Neural Networks (DNNs) works as a pressure flow field approximation to obtain flow field. In this work, we have performed the lubrication analysis and analyzed the flow characteristics obtained from Reynold Equation. To get the assurance of the developed programme, we have taken with some bench mark lubrication problems and explore the abilities of this method in Lubrication analysis. In the present work hydrodynamics journal bearing is simulated with Deep Neural Network Model and compared with the results FEM.

Keywords Reynolds equation · Deep learning · Hydrostatic thrust bearing

1 Introduction

In recent years, the use of machine learning techniques has been successfully implemented in various areas of research. Neural Networks have capability to approximate analysis function. The deep neural network function depends on various numerical parameters (the weights and the biases) that have calculated by implementing the learning algorithm [1]. The development of Deep Neural Network is an important tool in learning task and has very fast computation tools. Here, DNN is used as a tool to solve the problem of lubrication in journal bearing. In the past few years, various new numerical methods have been developed by researchers to investigate the bearings. Many researchers used to prefer numerical methods such as FEM and FDM

S. K. Yadav (✉)

Mechanical and Aerospace Engineering Department, Institute of Infrastructure Technology, Research and Management, Ahmedabad, Gujarat, India
e-mail: saurabhme.iitr@gmail.com

G. Thakre

Tribology & Combustion Division, CSIR—Indian Institute of Petroleum, Dehradun, Uttarakhand, India

for the analysis of lubrication problems. In the present work a robust deep learning model has been developed for the analysis of journal bearing. Rahmtabadi et al. [2] has done the simulation of micropolar lubricated journal bearing using GDQ method and demonstrated the accuracy of the results with finite element method. Results of deep learning is compared and validated with results available in open literature and results obtained by conventional FEM. To use this method training data is not required. It works like as mesh less method and concept to Deep learning method. The use of deep learning method in nonlinear Reynolds Equation makes it simple and easy to use.

2 Analysis

The aim of this work is to make a strong fundament in the field of lubrication analysis that enriches deep learning with long standing development in tribology and lubrication field. Reynolds equation with collocation method is used to calculate lubricant flow field. The Reynolds equation for a two-dimensional flow field, where the lubricant is assumed to be incompressible and iso-viscous, is a second-order nonlinear partial differential equation, and it can be expressed in non-dimensional form [1–3]

$$\frac{\partial}{\partial \alpha} \left(\bar{h}^3 \frac{\partial \bar{p}}{\partial \alpha} \right) + \frac{\partial}{\partial \beta} \left(\frac{\bar{h}^3}{12} \frac{\partial \bar{p}}{\partial \beta} \right) = \frac{\Omega}{2} \left[\frac{\partial h}{\partial \alpha} \right] + \frac{\partial \bar{h}}{\partial t} \quad (1)$$

2.1 Fluid Film Thickness Expressions

The nominal fluid film thickness for hydrodynamic two lobe journal bearing, can be expressed in non-dimensional form by following relation [4],

$$h = \frac{1}{\delta} - \left(\bar{X}_J - \bar{X}_L^i \right) \cos \alpha - \left(\bar{Z}_J - \bar{Z}_L^i \right) \sin \alpha \quad (2)$$

where, \bar{X}_J, \bar{Z}_J are the journal centre co-ordinates, \bar{X}_L^i, \bar{Z}_L^i are the bearing lobe centre co-ordinates and $\delta = c_1/c_2$ is the offset factor (non-circular parameter).

Further, the frictional power loss inside the bearing is calculated as

$$\bar{T}_f = \int_{-\lambda}^{+\lambda} \int_0^{2\pi} \left(\bar{h} \frac{\bar{F}_1}{F_0} \frac{\partial \bar{p}}{\partial \alpha} + \frac{\bar{\mu} \Omega}{h F_0} \right) d\alpha d\beta \quad (3)$$

2.2 Implementation of Deep Neural Network (DNN)

In this section, the implementation of point collocation method and deep neural method is discussed. The primary goal of this approach is to obtain the field variable by solving the governing Reynolds equation.

$$\frac{\partial}{\partial \alpha} \left(\bar{h}^3 \frac{\partial \bar{p}_u}{\partial \alpha} \right) + \frac{\partial}{\partial \beta} \left(\frac{\bar{h}^3}{12} \frac{\partial \bar{p}_u}{\partial \beta} \right) = \frac{\Omega}{2} \left[\frac{\partial h}{\partial \alpha} \right] \tag{4}$$

The above partial differential problem is converted into optimization problem by following method.

$$\text{Minimize } \aleph[\bar{p}_u] = \frac{\partial}{\partial \alpha} \left(\bar{h}^3 \frac{\partial \bar{p}_u}{\partial \alpha} \right) + \frac{\partial}{\partial \beta} \left(\frac{\bar{h}^3}{12} \frac{\partial \bar{p}_u}{\partial \beta} \right) - \frac{\Omega}{2} \left[\frac{\partial h}{\partial \alpha} \right] \tag{5}$$

where $\bar{p}_u(\mathbf{x})$ is an output function for a given input \mathbf{x} . The deep neural networks are ANNs obtained by means of following functional[5].

$$\bar{p}_u = A_L(\sigma(A_{L-1}(\sigma(\dots\dots\dots)))) \tag{6}$$

where A_l (with $l = 1, 2, \dots, L$) are affine mapping and σ is activation function, applied element wise.

In collocation method, $\aleph[\bar{p}_u](x_i)$ is evaluated on the complete grid and given set of points located inside the journal bearing domain and construct an optimization function, which tends to $\aleph[\bar{p}_u](x_i) = 0$. To achieve this in the present work mean square error method can be used.

$$\sum_{i=1}^{i=N} \langle \aleph[\bar{p}_u](x_i) \rangle = 0 \tag{7}$$

2.3 Boundary Conditions

Bearing input flow is equal to bearing output flow [6]

- (1) The pressure on external boundary is $\bar{p}_u|_{\beta=\pm 1} = 0.00$.
- (2) At trailing edge of the positive-region $\bar{p}_u = \frac{\partial \bar{p}_u}{\partial \alpha} = 0.00$ is applied to deal with the cavitation problem [7, 8].

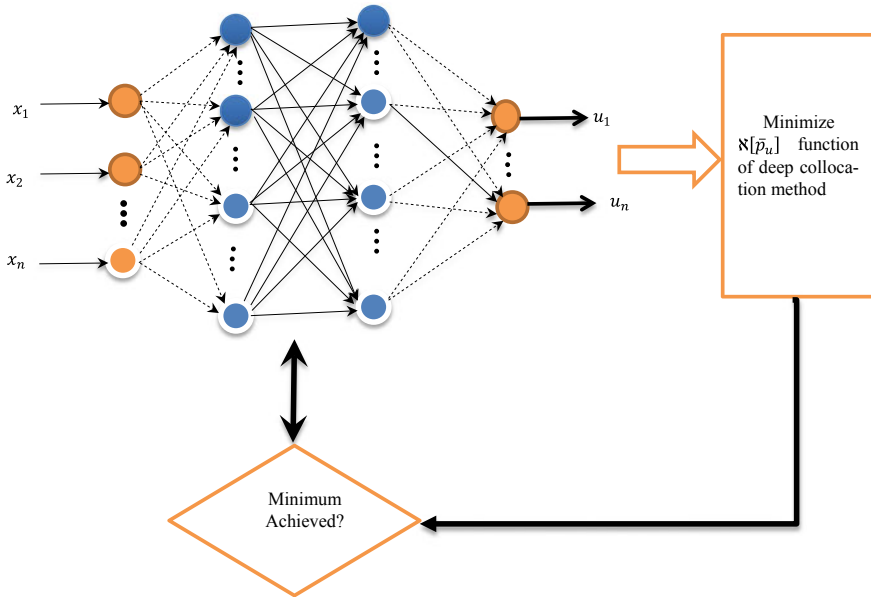


Fig. 1 Solution procedure

3 Solution Procedure

On the basis of above formulation, a solution procedure has been developed and implemented as shown in Fig. 1. The steps involved in obtaining the solution for the field variables using the DEM algorithm are as follows:

1. Initialization, input the neural network parameters and neurons, decide the activation function and optimizer type.
2. Geometry processing and getting collocation points.
3. Generate interior collocation points on grid.
4. Compute minimization function and cost function for boundary condition.
5. Design of Deep neural network for field variable with penalty function.
6. Impose the Reynolds boundary conditions by modifying the neural network design.
7. Perform the neural network training function, calculate weight and biases.
8. Check the minimum convergence criteria and stop the iteration.

4 Results and Discussion

We explored the application of DEM in solving various lubrication problem and Reynolds equation is successfully solved. Here some examples of circular journal

bearing and non-circular journal bearing are compared. A validation study has been performed to check the validity of the developed method.

4.1 Journal Bearing Simulation

As the developed methodology is completely new in the area of lubrication therefore, a validation study has been performed with journal bearing. A comparison study has been presented for increasing value of bearing external load and eccentricity in Table 1. As seen in Table 1 results are in good agreement and maximum percentage difference observed is 4.2%.

As friction coefficient is an important parameter in the bearing design, therefore a comparison study related to friction power loss by using Deep collocation method and Finite element method is performed. The comparison between the values obtained by different methods is presented in Table 2. The results are in good agreement as observed from Table 2.

Table 1 Comparison of parameters with DNN and finite element method

S. N.	Load	Eccentricity		% Difference
		FEM	DNN	
1	1	0.1995	0.1985	0.5012
2	1.2	0.2342	0.229	2.2203
3	1.4	0.2668	0.2602	2.4737
4	1.6	0.2974	0.2870	3.4969
5	1.8	0.3260	0.3123	4.2024
6	2	0.3525	0.3420	2.9787

Table 2 Comparison of parameters friction coefficient

S. N.	Load	μ_{fric}		% Difference
		FEM	DNN	
1	1	8.6458	8.534	0.5012
2	1.2	8.7923	8.5432	2.2203
3	1.4	9.1310	9.0233	2.4737
4	1.6	9.2779	9.2664	3.4969
5	1.8	9.4160	9.2987	4.2024
6	2	9.4026	9.3233	2.9787

Table 3 Comparison of eccentricity for DNN and finite element method

S.N.	Non-dimensional load	Eccentricity		% Difference
		FEM	DNN	
1	1	0.1661	0.1564	5.8398
2	1.2	0.1916	0.1900	0.8350
3	1.4	0.2166	0.2102	2.9547
4	1.6	0.2385	0.2310	3.1446
5	1.8	0.2582	0.2489	3.6018
6	2	0.2770	0.2711	2.1299

Table 4 Comparison of friction coefficient for DNN and Finite element method

S.N.	Non-dimensional load	$\bar{\mu}_{fric}$		% Difference
		FEM	DNN	
1	1	13.3357	13.222	0.8525
2	1.2	13.2381	13.212	0.1971
3	1.4	12.6698	12.6522	0.1389
4	1.6	12.8856	12.6601	1.7500
5	1.8	13.2881	13.1231	1.2417
6	2	13.2780	13.2012	0.5784

4.2 Two Lobe Bearing Simulation

Results of present work is validated for dynamically loaded two lobe non-circular journal bearing. Numerical simulation data is presented in Tables 3 and 4. As shown in Tables 3 and 4, results obtained with Deep collocation method have a good agreement with results obtained with finite element method. The maximum difference obtained in the value of eccentricity is 5.836% and maximum difference obtained in the value of friction power loss is 1.75%.

5 Conclusion

With the help of deep neural network model, lubrication analysis is performed. Lubrication analysis with deep neural network is simple and nonlinear analysis with deep neural network can be easily performed. Reynolds boundary condition has been solved in deep collocation method. This analysis is faster than the conventional analysis. To illustrate the method, applications of DNN are made to simulate a dynamically loaded circular journal bearing and two lobe journals bearing. The computed

results are compared with that of Finite Element Method in the study. The following important conclusions can be drawn from the present study.

1. The deep learning network model will be an important tool in future for the analysis of lubricant analysis.
2. The results obtained with deep neural network are in good agreement in result obtained with Finite Element Method.

Acknowledgements The authors acknowledge the support from the Department of Science and Technology, GOI under the TARE GRANT (No. TAR/2019/000077) and IITRAM, Ahmedabad.

References

1. Yadav SK, Sharma SC (2016) Performance of hydrostatic textured thrust bearing with supply holes operating with non-Newtonian lubricant. *Tribol Trans* 59(3):408–420
2. Kumar V, Sharma SC (2018) Influence of dimple geometry and micro-roughness orientation on performance of textured hybrid thrust pad bearing. *Meccanica* 53(14):3579–3606
3. Yadav SK, Thakre GD, Khatri CB (2021) Improvement in textured hole-entry hybrid journal bearing system by using multi-objective genetic algorithm. *J Braz Soc Mech Sci Eng* 44(1):32
4. Khatri CB, Sharma SC (2017) Influence of couple stress lubricant on the performance of textured two-lobe slot-entry hybrid journal bearing system. *Proc Inst Mech Eng, Part J: J Eng Tribol* 231(3):366–384
5. Samaniego E et al (2020) An energy approach to the solution of partial differential equations in computational mechanics via machine learning: concepts, implementation and applications. *Comput Methods Appl Mech Eng* 362:112790
6. Awasthi R, Jain S, Sharma SC (2006) Finite element analysis of orifice-compensated multiple hole-entry worn hybrid journal bearing. *Finite Elem Anal Des* 42(14–15):1291–1303
7. Nagaraju T, Sharma SC, Jain S (2007) Influence of surface roughness on non-Newtonian thermohydrostatic performance of a hole-entry hybrid journal bearing
8. Anderson CR (1989) Vorticity boundary conditions and boundary vorticity generation for two-dimensional viscous incompressible flows. *J Comput Phys* 80(1):72–97

Structural Integrity Analysis of a Washing Machine Tripod (Front Load) and Redesign Using Taguchi Method



S. P. Gokul Raj, Tenzin Choney, and Lokavarapu Bhaskara Rao

Abstract The main objective of this project is to study the structural analysis of a washing machine tripod, through variable loading conditions and to develop a sound design to neglect all the drawbacks and defects of the present design. Similar to windmills, propellers, cement mixers and utility fans, washing machines have their load acting as a cantilever with a variable rotating load acting on a central axis, due to this rotating load, the load acting changes frequently which directly impacts the integrity of the supporting components, thus in this paper, we study all the potential failures, drawbacks and strains on the system and redesign the tripod of the washing machine for much efficient and safe working process.

Keywords Tripod · Taguchi method · S/N ratio · Minitab

1 Introduction

In this modern age and time, having a washing machine in our households has become a mandatory. With the rapid development in technology, the washing machines have also evolved a lot, and they are generally classified into two types as front load and top load based on the type of loading. Here, we are considering the front-loading washing machines and testing the integrity of a tripod which supports the main rotating shaft of a washing machine and redesign it for a better and efficient work cycle. The part tripod will be analyzed, focusing on the geometry, shape, size and its loading conditions.

S. P. Gokul Raj · T. Choney · L. Bhaskara Rao (✉)
School of Mechanical Engineering, Vellore Institute of Technology, Chennai,
Vandalur-Kelambakkam Road, Chennai, Tamil Nadu 600127, India
e-mail: bhaskarbabu_20@yahoo.com

S. P. Gokul Raj
e-mail: gokulraj.sp2020@vitstudent.ac.in

T. Choney
e-mail: tenzin.choney2020@vitstudent.ac.in

The tripod is mainly used to connect the shaft with the cylinder and to transmit the torque, thus it is one of the most important structural components of a washing machine. The various loading conditions and the change in stress with change in loads are studied to analyze the tripod and make structural changes to it. The main factor for redesign is to study the various stress acting on the component and the resultant strain due to those stresses. The volume and size of the piece are taken into account in order to reduce the amount of material used in the manufacture, which will ultimately lead to cost reduction thus, making the better components cheaper and readily available [1].

1.1 Objective

The main objective of this paper is to use the Taguchi method to study the various loading conditions, stress and strain on a washing machine tripod and analyze the data using the Minitab software to find the optimal conditions for maximum life cycles of the tripod.

2 Current Design

Various parts of the washing machine are presented in Fig. 1.

The current design of the washing machine and tripod [2] is shown in Fig. 1 which consists of a tripod with three arms and a cylindrical drum which is connected with each other through a rear cover using rivets or lock nuts Fig. 2. The schematic diagram given below shows the assembly and the dimensions of the tripod system [3].

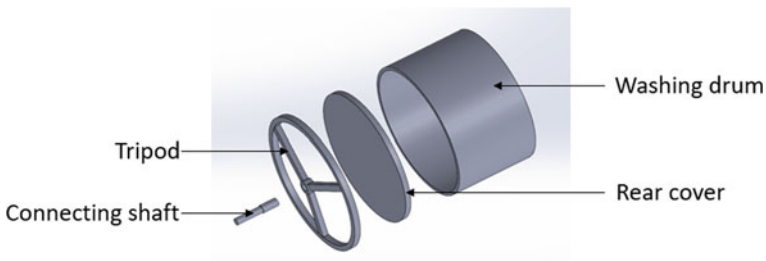


Fig. 1 Current tripod design

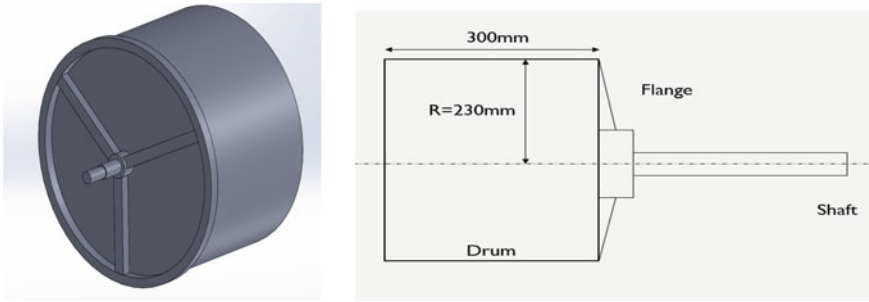


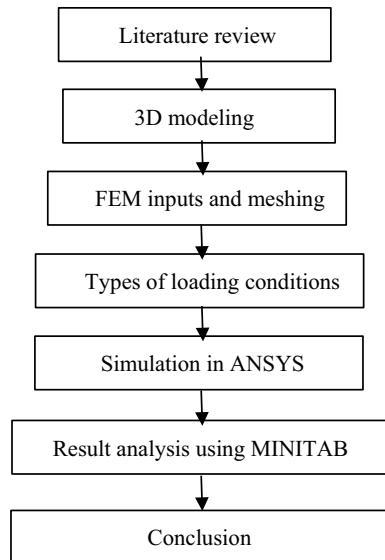
Fig. 2 Assembly dimension of tripod

3 Methodology

The workflow of the present work is given in Flowchart 1.

Literature review over various papers based on the integrity analysis and redesigning using Taguchi methods [4, 5] has been taken, and the important factors and parameters affecting the integrity of a component are studied. The 3D modeling of the tripod is done using solid works [6], and the load analysis is done using ANSYS [7] workbench. The results obtained are then analyzed and studied using Minitab software [8] for optimal configuration [9].

Flowchart 1 Methodology



4 Theoretical Analysis

4.1 Redesigning Factors

Number of supporting arms, shapes, sizes, rotational speed of the drum, and load applied are taken in to account. The connection with the shaft is either with bolts/rivets to keep its relative position with the rest of the parts. The arm selection is mainly based on its characteristics to withstand various loads and stresses during the working of the washing machine [10, 11].

The connections with the cylinder have two main features, the first one is the connection between the arm and the cylinder and the second one is the connection between the shaft and the arm. Thus, based on the above given factors, the current design model will be studied redesigned, tested and analyzed [12].

4.2 Various Testing Condition

We consider 3 different types of loading conditions as shown in Fig. 3a–c, and Fig. 3 represents the distribution of load. Different configuration with number of arm is shown in Fig. 4. Three more types as shown in Fig. 4a–c are considered based upon the structural features (number of arms in the flange).

Based on number of connecting arms.

3D modeling of tripod and meshing

3D modeling of tripod and meshing is shown in Fig. 5. The mesh size and parameters are shown in Fig. 5a–c which were fed into ANSYS workbench and rendered accordingly. Here, we use adaptive sizing for optimal conditions and coarse meshing for more accurate results.

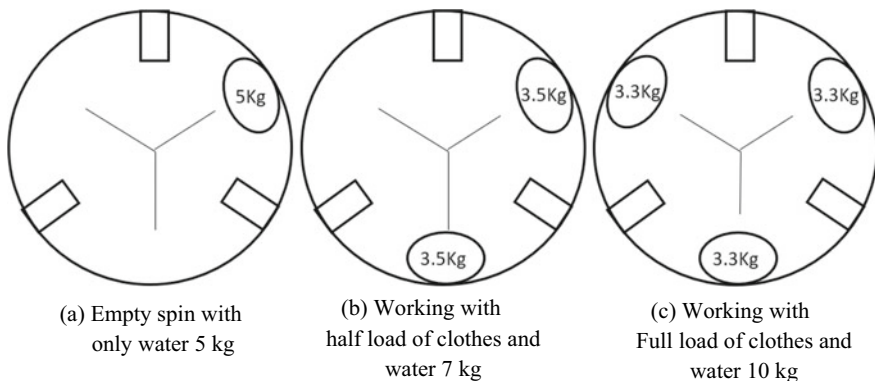


Fig. 3 Different loading conditions of a washing machine

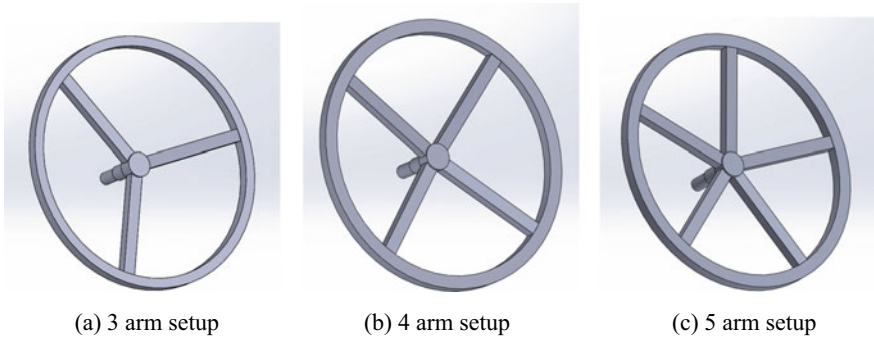


Fig. 4 Different configuration with number of arm

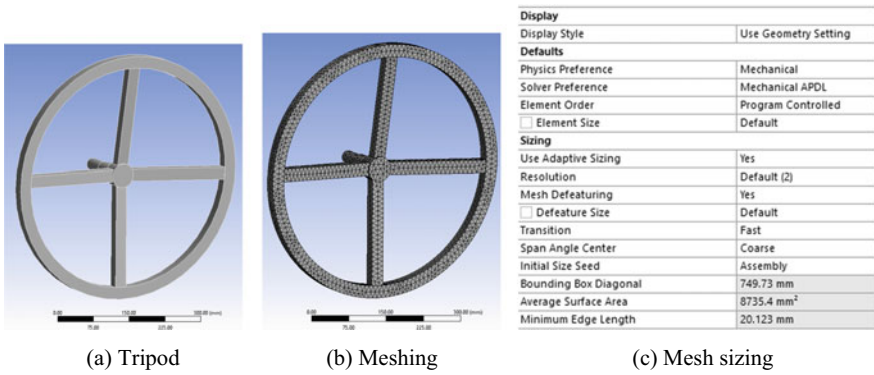


Fig. 5 3D modeling of tripod and meshing

Loading conditions and crack propagation

Figure 6 represents various loading conditions, where the red rotational load implies momentum load acting on the tripod due to the rotation of the drum [13]. The yellow rotational load implies the load due to the rotation of the connecting shaft from the motor, and the connecting shaft is considered only with rotational motion and no linear movements. Also, the load applied on the tripod is considered constant around the edges because during the rotary motion, the load tends to get distributed evenly and it helps in simplifying the loading conditions.

5 Numerical Analysis

The top speed of a regular washing machine varies from 170 to 180 rad/s, and we have taken 5 rad/s difference between each level because the variation in the results is not large enough to be significant. The combinations are presented in Table 1 which

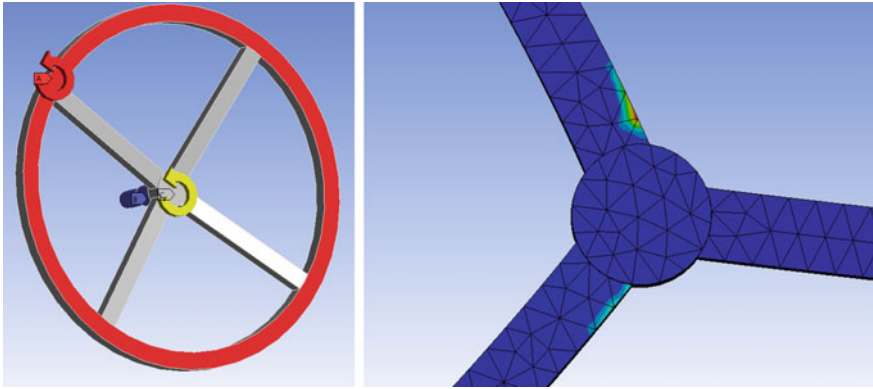


Fig. 6 Loading conditions

Table 1 Various combinations of testing conditions

Factors	Range		
	Low level	Mid-level	High level
Number of connecting arms	3	4	5
Load applied (kg)	5	7	10
Speed (rad/s)	170	175	180

were fed into Minitab and all the various combinations are obtained. The analysis has been carried out for the combinations and the obtained results were tabulated in Table 2.

As given in the combination table presented in Table 2 for the various combination of load, no. of arms and speed then number cycles before failure have been

Table 2 Combination table for the given factors

S. No.	C1	C2	C3	C4
	No. of arms	Load (kg)	Speed	No. of cycles before failure
1	3	5	170	525,260
2	3	7	175	359,000
3	3	10	180	243,000
4	4	5	175	626,000
5	4	7	180	429,000
6	4	10	170	292,500
7	5	5	180	603,260
8	5	7	170	418,300
9	5	10	175	288,000

computed and tabulated using Minitab. The number of cycles before failure for each combination of arms load and speed is calculated by simulating the same in ANSYS workbench [14]. Further using Minitab, the obtained results will be analyzed for the optimal conditions for the maximum number of cycles before failure of the tripod.

6 Result Analysis

For various combination of loads, arms and speed, the mean values have been plotted with which we can identify the highest contributing combination [10] of each factor Table 3.

The response table gives us the general idea of how various factors affect the output which is maximum life cycle [15]. It has been observed from Fig. 7 that the change in load gives the highest variation.

From Table 4, the larger is better format has been considered as we need to find the highest number of cycles for each combination before failure of the tripod.

$$\text{Larger is better} = 10 * \log_{10}(\text{sum}(1/Y^2)/n)$$

S/N ratio

From Fig. 8, it has been observed that the highest value of life cycle of the component can be achieved in each factor, thus we can put together the most optimal configuration for the maximum number of cycles before failure (Table 5).

Regression equation

The variation of speed has little to no effect because the top speed of a regular washing machine varies between 170 and 180 rad/s, and we consider top speed for the worst-case scenario Table 1, thus the change in speed has little effects but has significance in the overall lifetime of the washing machine tripod. The model summary and the coefficients are presented in Tables 6 and 7.

Table 3 Main effect plot of means

Response table for means			
Level	No. of arms	Loading (kg)	Speed
1	375,753	584,840	412,020
2	449,167	402,100	424,333
3	436,520	274,500	425,087
Delta	73,413	310,340	13,067
Rank	2	1	3

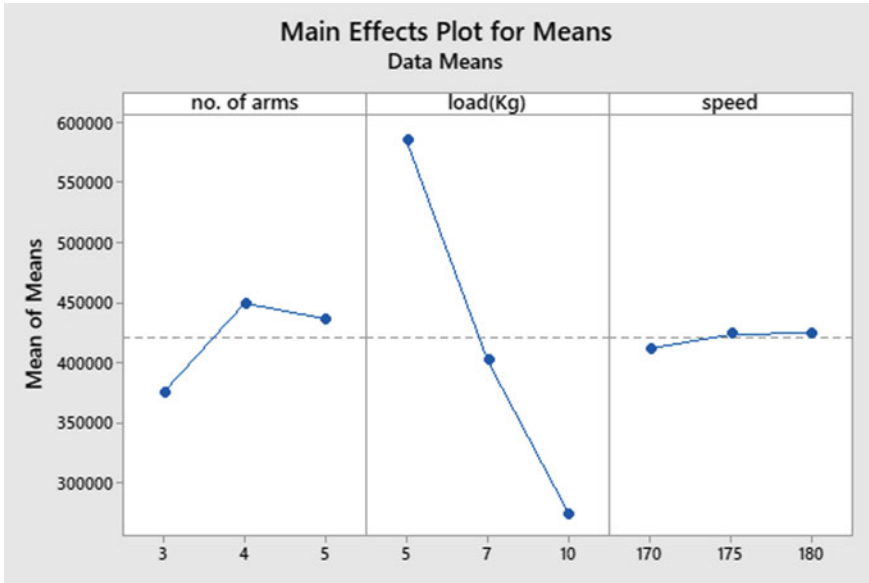


Fig. 7 Main effects plot for means

Table 4 Response for signal-to-noise ratios

Larger is better			
Level	No. of arms	Load (kg)	Speed
1	111.1	115.3	112.1
2	112.6	112.1	112.1
3	112.4	108.7	112.0
Delta	1.6	108.7	112.0
Rank	2	1	3

Regression Analysis: Number of cycles before failure versus load (kg), Speed

Contour and interaction plot analysis

For contour plots, we have three factors as load applied, number of arms in tripod and speed of rotation; thus, we plot contour graphs between them as AB, BC, AB and also plot an interaction graph between all three factors along with the number of cycles before failure as the resulting factor. From these plots, we can identify the change in resulting factor as the two comparing factors change and find the best possible configuration.

Number of cycles before failure versus speed, number of arms

- The fixing the load value of the drum at 7.33 kg and comparing the value of number of cycles versus speed, number of arms as shown in Fig. 9.

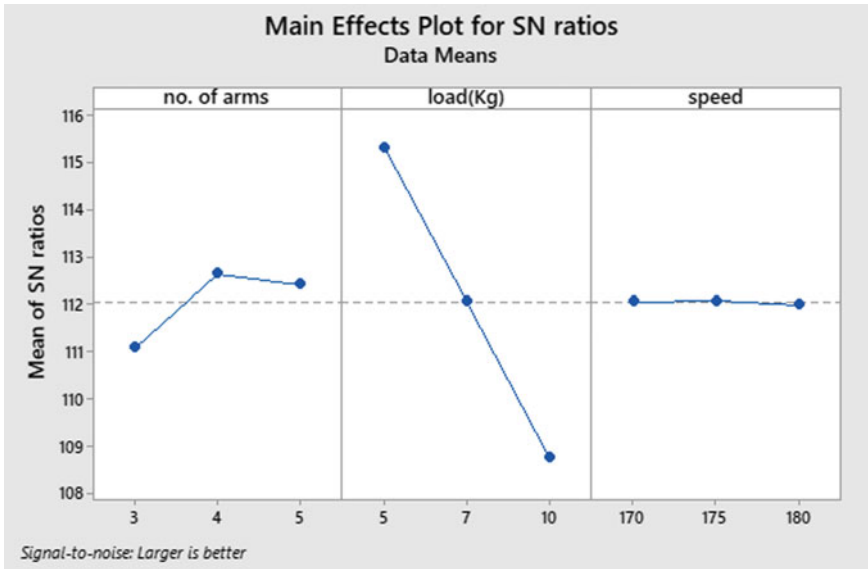


Fig. 8 S/N ratio plot

Table 5 Analysis of variance

Source	DF	Adj SS	Adj MS	F-value	P-value
Regression	3	1.45003E+11	48,334,364,536	22.15	0.003
No. of arms	1	5,538,881,667	5,538,881,667	2.54	0.172
Load (kg)	1	1.39208E+11	1.39208E+11	63.81	0.000
Speed	1	256,106,667	256,106,667	0.12	0.746
Error	5	10,908,867,993	2,181,773,599		
Total	8	1.55912E+11			

Table 6 Model summary

S	R-sq	R-sq (adj)	R-sq (pred)
46,709.5	93.00%	88.81%	83.13%

Table 7 Coefficients

Term	Coef	SE Coef	T-value	P-value	VIF
Constant	514,136	674,236	0.76	0.480	
No. of arms	30,383	19,069	1.59	0.172	1.00
Load (kg)	-60,526	7577	-7.99	0.000	1.00
Speed	1307	3814	0.34	0.746	1.00

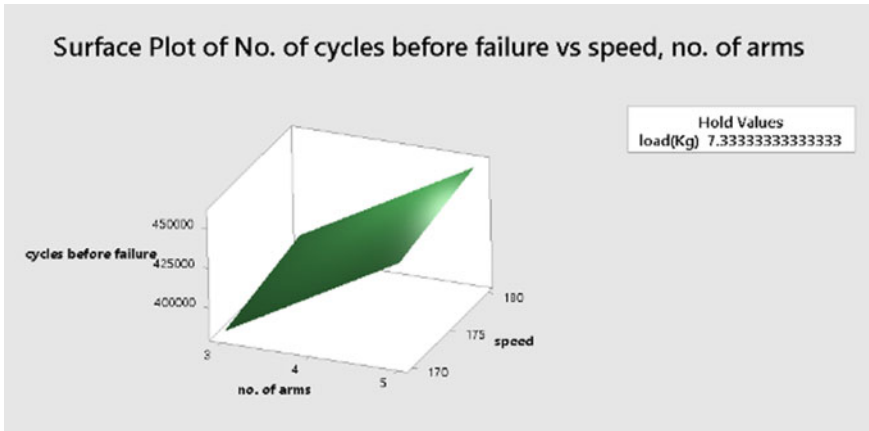


Fig. 9 No. of cycles before failure versus speed, no. of arms

- From Fig. 10, it has been observed that the cycle life increases with decrease in speed and number of arms.

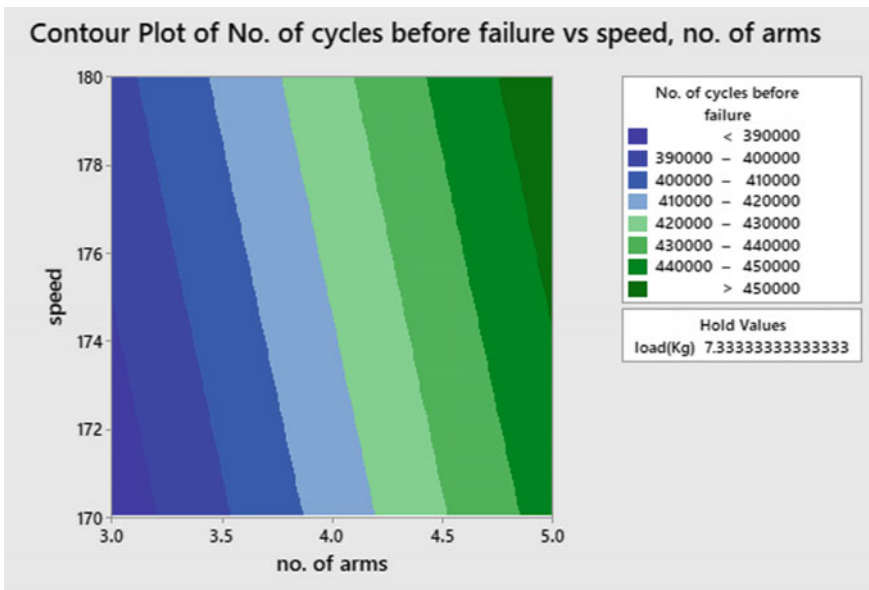


Fig. 10 Contour plot of number of cycles before failure (speed vs. no. of arms)

Number of cycles before failure Versus load, number of arms

- In this plot, we are fixing the speed values of the drum at 175 rad/sec and comparing the value of number of cycles versus load, number of arms as shown in Fig. 11.
- From Fig. 12, it has been observed that the cycle life increases with decrease in load and has a varying effect with the number of arms.
- In this plot Fig. 13, we are fixing the no. of arms as 4 and comparing the value of number of cycles versus speed, load.
- From Fig. 14, it has been observed the cycle life increases with decrease in speed and load.

Number of cycles before failure versus speed, load:

Interaction plot

It has been observed from Fig. 15 that the various combinations of factors and their effect on the result of life cycle.

Normal probability plot

The normal probability plots give us the average range at which the convergence values of each factor and the result lies. Figure 16 gives the graphical plot between the various responses and their S/N ratio, and Fig. 17 gives the plot between the various responses and their means. Figure 18 gives the histogram plot of the frequency and residuals for the number of cycles before failure [16]. Figure 19 represents the residual Vs observation order variation.

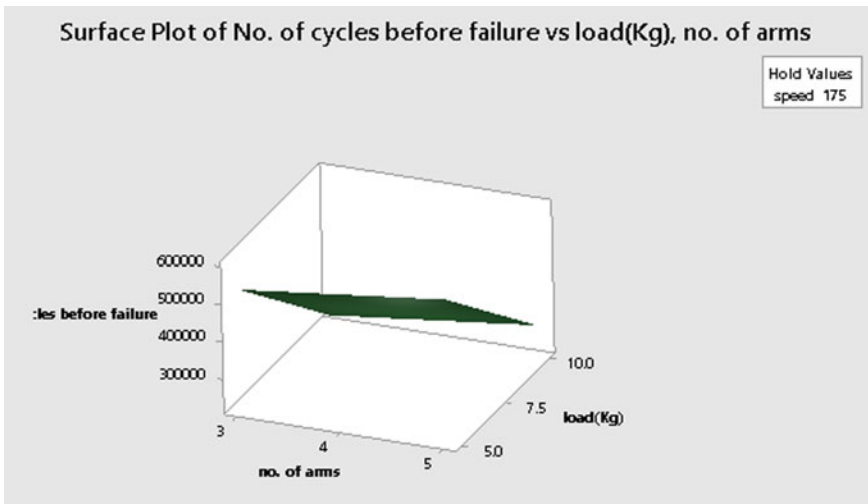


Fig. 11 No. of cycles before failure versus load, no. of arms

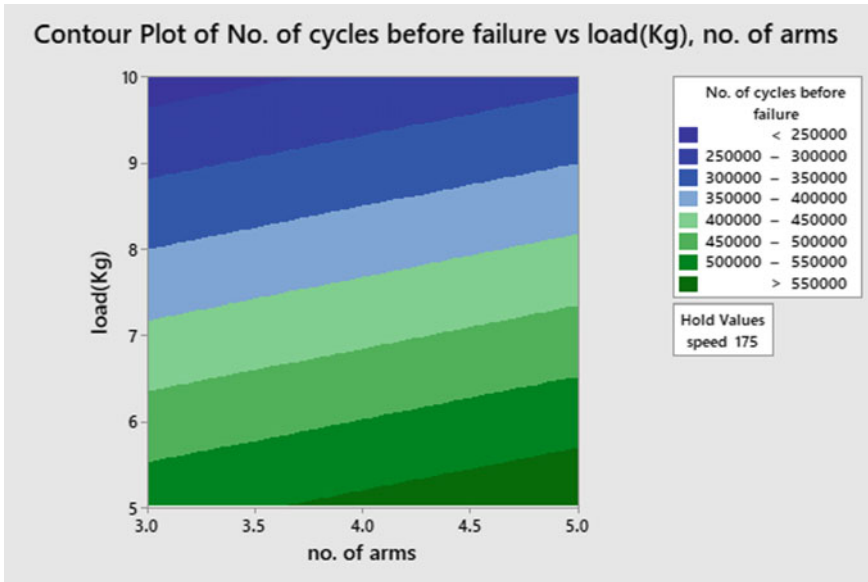


Fig. 12 Contour plot of number of cycles before failure (load vs. no. of arms)

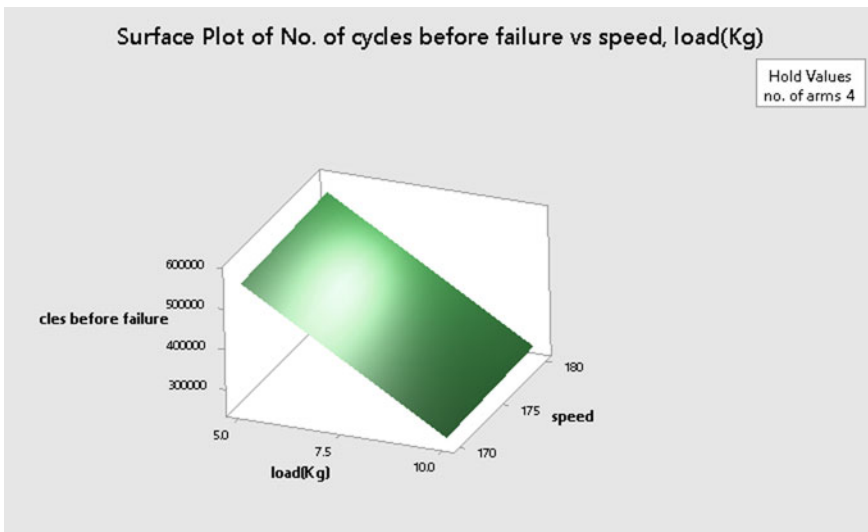


Fig. 13 No. of cycles before failure versus speed, load

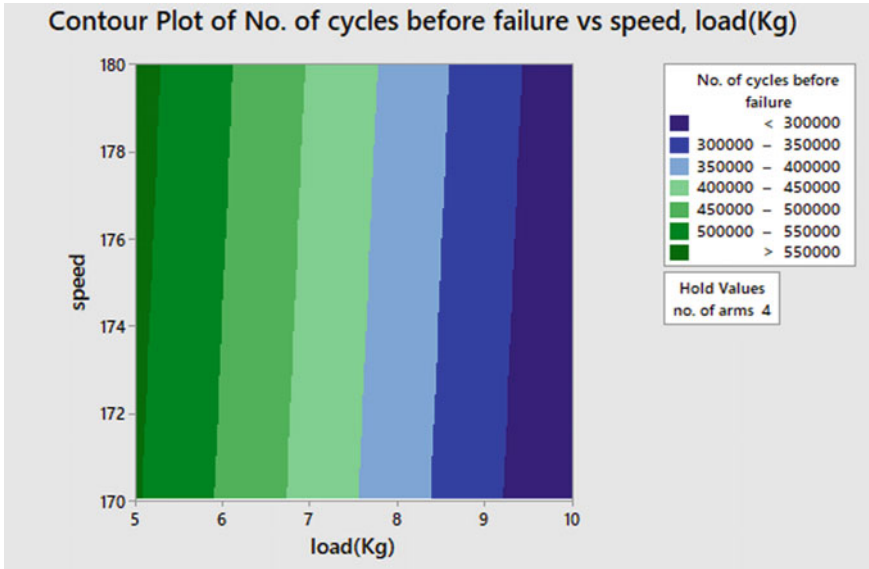


Fig. 14 Contour plot of number of cycles before failure (speed vs load)

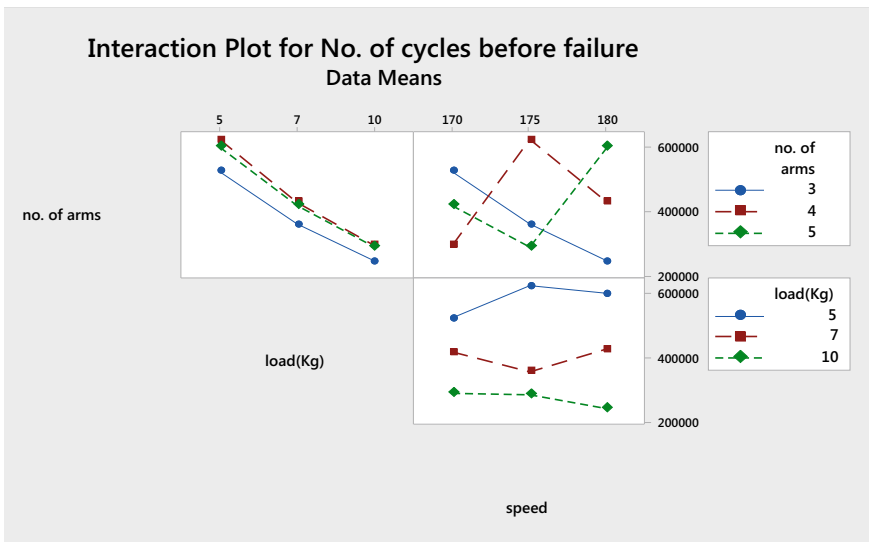


Fig. 15 Interaction plot for life cycle

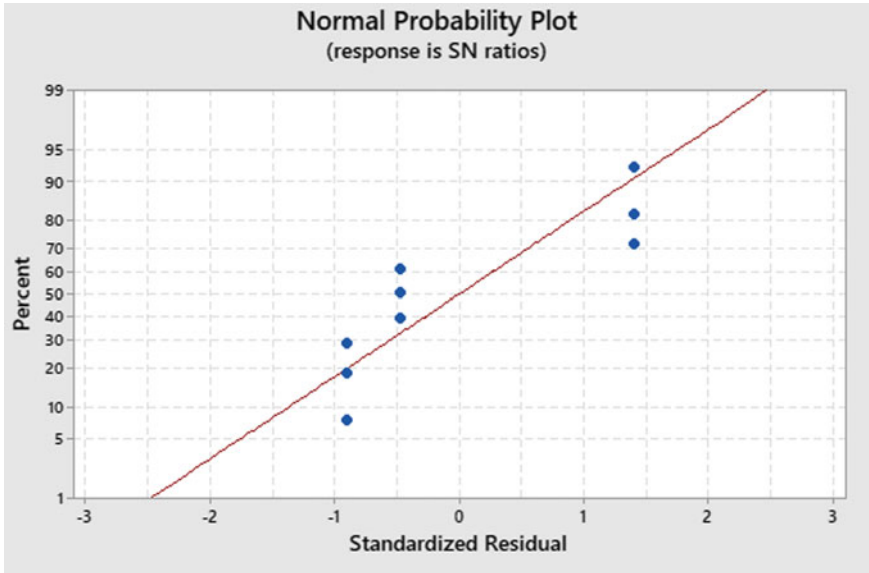


Fig. 16 Standardized residual versus SN ratio percentage

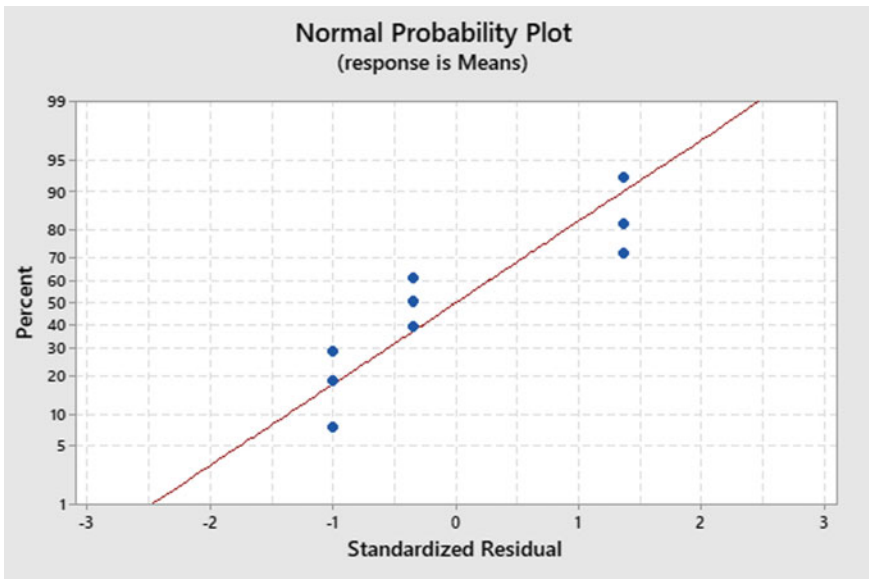


Fig. 17 Standardized residual versus means percentage

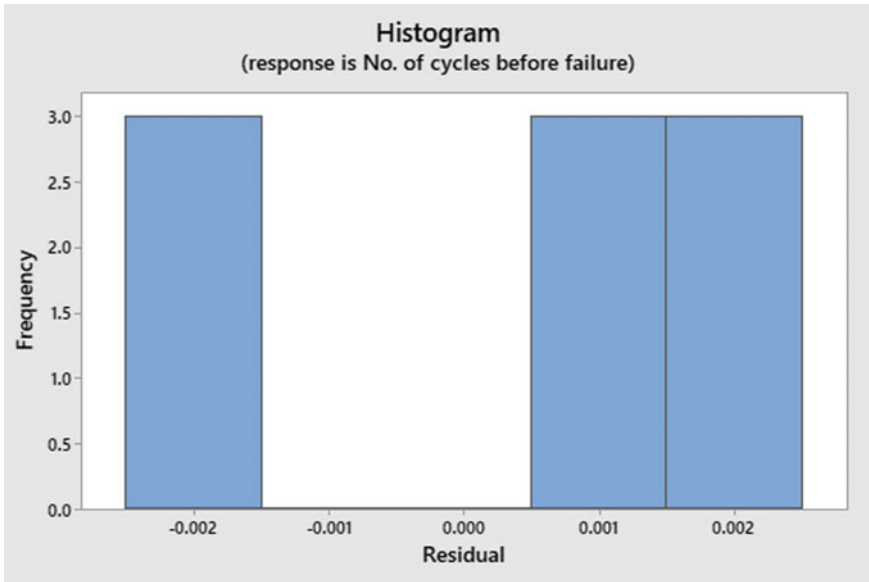


Fig. 18 Histogram

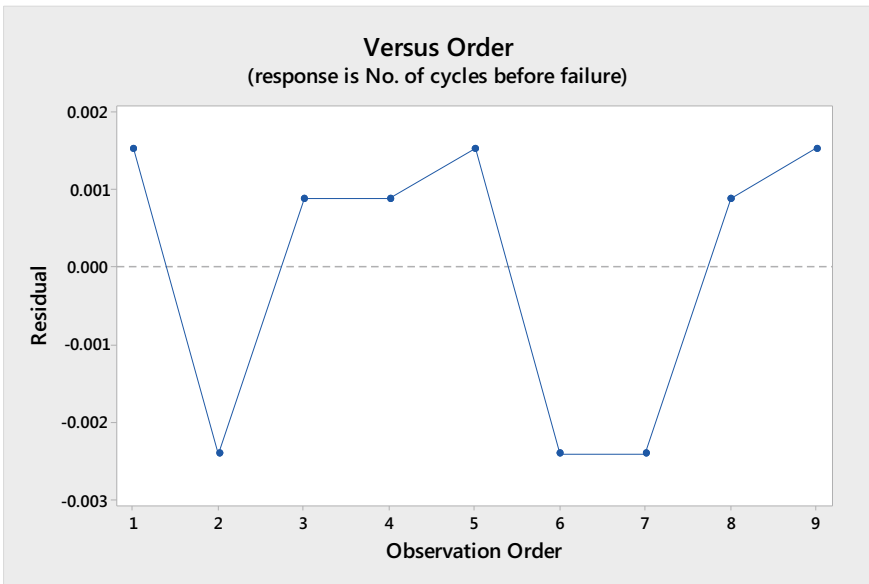


Fig. 19 Residual versus observation order

Table 8 Analysis of variance for transformed response

Source	DF	Seq SS	Contribution (%)	Adj SS	Adj MS	F-value	P-value
No. of arms	2	0.023786	6.12	0.023786	0.011893	880.70	0.001
Load (kg)	2	0.364533	93.86	0.364533	0.182267	13,496.88	0.000
Speed	2	0.000039	0.01	0.000039	0.000019	1.43	0.412
Error	2	0.000027	0.01	0.000027	0.000014		
Total	8	0.388385	100.00				

Versus plot

- From Table 5, it has been observed that the maximum contribution of about 93.86% toward the life cycle of the component is provided by the load applied.
- The second highest contribution is by the number of connecting arms [11] (Table 8).

7 Conclusions

Form the above plots and graphs, we can see that with increase in load and speed, the life cycle of the tripod reduces significantly. Also, that increase in connecting arms of the spider flange has a depreciating return and the optimal arrangement is only 4 arms. With increasing the number of arms, the structural integrity of the component starts collapsing. Considering the load inside the drum varies throughout the washing process with and without water in various cycles the average load should be taken for optimal performance. The maximum speed of a washing machine varies from 170 to 180 rad/s, and we take maximum speed because to provide the worst-case scenarios, thus variation in speed between the limits has little to no effect. Therefore, from the ANOVA table and the regression equation, the optimal arrangement for maximum lifetime of the washing machine is presented in Table 9.

Table 9 Optimal arrangement of factors and their levels

Number of arms in the flange	4
Load	5 kg
Speed	175 rad/s
Total life cycle	429,362

References

1. Unal R, Dean EB (1990) Taguchi approach to design optimization for quality and cost: an overview. In: 1991 Annual conference of the international society of parametric analysts
2. Park J, Jeong S, Yoo H (2021) Dynamic modeling of a front-loading type washing machine and model reliability investigation. *Machines* 9(11):289
3. Cumber P (2021) Visualising mechanics: washing machine dynamics. *Int J Math Educ Sci Technol* 52(4):626–652
4. Tansel İç Y, Yıldırım S (2013) MOORA-based Taguchi optimisation for improving product or process quality. *Int J Prod Res* 51(11):3321–3341
5. Ku KJ, Rao SS, Chen L (1998) Taguchi-aided search method for design optimization of engineering systems. *Eng Optim* 30(1):1–23
6. SolidIreland, Solid Solutions. Solidworks teacher training manual. Solid Solutions Ireland, Arena House, Arena Road, Sandford, Dublin 18 (2006)
7. Thompson MK, Thompson JM (2017) ANSYS mechanical APDL for finite element analysis. Butterworth-Heinemann
8. Minitab Wild DJ (2005) MINITAB release 14:212–212
9. Pokarne RS (2021) Minitab case study Ford industry
10. Gundeboina S (2010) Finite element analysis of a washing machine cylinder
11. Jayasree PK (2020) “Design and engineering” CBS publication basic ideas of designing and engineering for redesigning
12. Jeang A (1996) Optimal tolerance design for product life cycle. *Int J Prod Res* 34(8):2187–2209
13. Unal R, Stanley DO, Russ Joyner C (1993) Propulsion system design optimization using the Taguchi method. *IEEE Trans Eng Manag* 40(3):315–322
14. Sekulic M, Kovac P, Gostimirovic M, Kramar D (2013) Optimization of high-pressure jet assisted turning process by Taguchi method. *Adv Prod Eng Manag* 8(1):5
15. Joshaghani A, Ramezani-pour AA, Ataei O, Golroo A (2015) Optimizing pervious concrete pavement mixture design by using the Taguchi method. *Constr Build Mater* 101:317–325
16. Myers RH, Khuri AI, Vining G (1992) Response surface alternatives to the Taguchi robust parameter design approach. *Am Stat* 46(2):131–139